Table of Contents (İçindekiler)

Volume (Cilt): 10 Number (Sayı): 1
June (Haziran) 2020

PHYSICS

Cladocera and Copepoda (Crustacea) Fauna of Balya District (Balıkesir/Turkey)

Süleyman ÇOLAK[1], Alp ALPER[2,*]

[1]*Balya Atatürk Multi-Program Anatolian High School, Balya, Balıkesir, Turkey*
suleymann88@gmail.com, ORCID: 0000-0001-5903-7551
[2]*Balıkesir University, Faculty of Science and Literature, Department of Biology, Çağış Campus,*
Balıkesir, Turkey
alpalper80@gmail.com, ORCID: 0000-0001-5507-4072

Abstract

In this study, a total of 35 stations including troughs, ponds and streams were sampled between November 2017 and July 2018 in order to determine the Cladocera and Copepoda (Crustacea) fauna of Balya. As a result, a total of 37 species were determined, 21 from Cladocera and 16 from Copepoda. Based on the previous studies, it has been determined that 34 species are recorded for the first time from study area besides 13 species are also determined as new records for Balıkesir fauna.

Keywords: Cladocera; Copepoda; Balya; Balıkesir; Fauna.

Balya İlçesinin (Balıkesir/Türkiye) Cladocera ve Copepoda (Crustacea) Faunası

Öz

Bu çalışmada, Balya'nın Cladocera ve Copepoda (Crustacea) faunasını belirlemek için yalak, gölet ve akarsuların içinde olduğu toplam 35 istasyon Kasım 2017 ile Temmuz 2018 tarihleri arasında örneklendi. Sonuç olarak 21'i Cladocera'dan, 16'sı Copepoda'dan olmak üzere

toplam 37 tür belirlendi. Önceki çalışmalara incelendiğinde 34 türün çalışma alanından ilk kez kaydedildiği, üstelik 13 türün de Balıkesir faunası için yeni kayıt olduğu tespit edildi.

Anahtar Kelimeler: Cladocera; Copepoda; Balya; Balıkesir; Fauna.

1. Introduction

Zooplankton occupies a central position in the pelagic food web, transferring carbon and energy from primary producers to higher trophic levels, and potentially suppressing the abundance of phytoplankton. Cladocerans and copepods are small crustaceans and also the most important members of freshwater zooplankton. They are colonized in any kind of freshwater aquatic body (troughs, ponds, lakes, dams, rivers, etc.) and some other wet habitats (leaf litter, sphagnum mat, caves, tree holes, etc.) [1-3].

The diversity of global freshwater cladocerans and copepods is around 620 and 2814 species respectively [4, 5]. However, the richness of actual species is estimated to be 2-4 times higher [6-8]. Compared to other zoogeographical regions, the Cladocera and Copepoda fauna of the Palearctic is quite rich; 245 cladoceran and 1204 copepod species which is more than twice the number recorded for other regions have been recorded [4, 8, 9]. Biodiversity of the Copepoda and Cladocera fauna of Turkey is over than 240 [9].

Balya district is located in the northwest of Balıkesir. In terms of surface area, it is ranked as 5th with 952 km² among the 20 districts of the province. 70% of the surface of Balya is mountainous, the rest is rugged terrain. The highest point is Akçal Hill (642 m.) located in the east. Animal husbandry is the main source of income due to the rough geography of Balya; therefore, many troughs were built for the livestock. Although suitable land is limited, agricultural activities are also carried out in the district; dams and ponds were built to provide the water needed in irrigation [10].

Although being rich in freshwater resources, Cladocera and Copepoda fauna of Balya have not been researched much so far. The only record in the literature was 3 copepod species which were given from Ilıca pond by Sönmez et al. [11]. So, 35 freshwater resources were sampled in this study in order to reveal Cladocera and Copepoda fauna of Balya.

2. Materials and Methods

The samples were collected from 35 stations (Fig. 1.) for 4 times between November 2017 and July 2018 with a help of 60 µm mesh sized plankton net and/or hand net. The localities of the stations are given in Table 1. Geographical data (altitude and

coordinates) were obtained by using a Magellan eXplorist 610 GPS device. Collected samples were immediately preserved with 70% ethanol. Cladocerans and copepods were extracted from detritus using a Pasteur pipette under an OLYMPUS SZX-16 stereomicroscope. Extracted specimens were stored in 70% ethanol. Specimens were prepared by using the method described by Karaytuğ and Sak [12] and were identified under an OLYMPUS BX-50 microscope equipped with a differential interference contrast attachment. Specimens were identified according to Błędzki and Rybak [2], Rogers and Thorp [3], Einsle [13], Ueda and Reid [14], Wells [15], and relevant other literature.
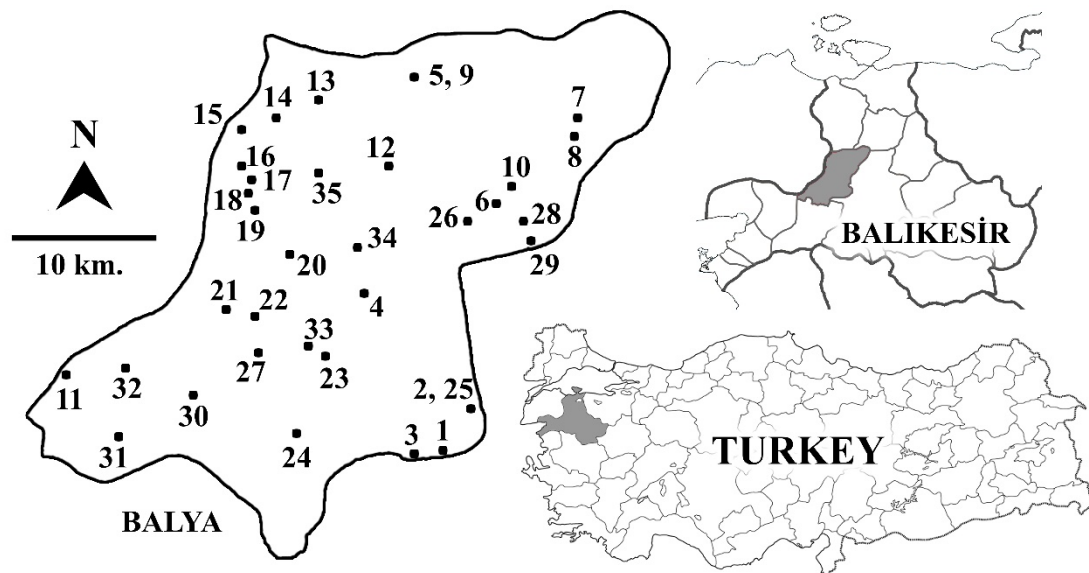
Figure 1: Sampling stations

Table 1: The localities of the stations

Station number	Locality	Type	Coordinate		Altitude (m.)
1	Hacı Hüseyin	Pond	39.67911˚ N	27.66990˚ E	235
2	Ali Demirci I	Pond	39.70834˚ N	27.69579˚ E	269
3	Koca Avşar	Pond	39.67231˚ N	27.64349˚ E	204
4	Kadıköy	Stream	39.77906˚ N	27.60736˚ E	140
5	Koyuneri I	Stream	39.91401˚ N	27.64855˚ E	110
6	Kayalar I	Trough	39.83604˚ N	27.71619˚ E	171
7	Ilıca I	Pond	39.88944˚ N	27.78119˚ E	145
8	Ilıca II	Trough	39.87789˚ N	27.77909˚ E	118
9	Koyuneri II	Trough	39.91472˚ N	27.64840˚ E	121

Station number	Locality	Type	Coordinate		Altitude (m.)
10	Between Ilıca and Kayalar	Stream	39.84483˚ N	27.72702˚ E	146
11	Farsak	Pond	39.73061˚ N	27.36464˚ E	530
12	Ören	Trough	39.85882˚ N	27.62700˚ E	270
13	Değirmendere	Trough	39.90061˚ N	27.57063˚ E	177
14	Mancınık	Trough	39.88962˚ N	27.53625˚ E	189
15	Dereköy I	Trough	39.88034˚ N	27.50861˚ E	206
16	Dereköy II	Trough	39.85821˚ N	27.50773˚ E	267
17	Kara Mustafa I	Trough	39.84784˚ N	27.51548˚ E	352
18	Kara Mustafa II	Trough	39.84295˚ N	27.51332˚ E	344
19	Kara Mustafa III	Trough	39.83192˚ N	27.51980˚ E	432
20	Çalova	Trough	39.80316˚ N	27.54534˚ E	313
21	Doğanlar	Trough	39.76819˚ N	27.49594˚ E	432
22	Doğanlar-Balya Road	Trough	39.76535˚ N	27.51775˚ E	316
23	Balya	Trough	39.74380˚ N	27.57519˚ E	282
24	Göktepe	Trough	39.69258˚ N	27.55242˚ E	391
25	Ali Demirci II	Irrigation canal	39.70834˚ N	27.69579˚ E	269
26	Kayalar II	Pond	39.82528˚ N	27.69250˚ E	200
27	Müstecap I	Trough	39.74285˚ N	27.52187˚ E	251
28	Karlık	Trough	39.82357˚ N	27.73755˚ E	214
29	Söbücealan	Trough	39.81339˚ N	27.74378˚ E	245
30	Çiğdem	Trough	39.71608˚ N	27.46836˚ E	350
31	Çamavşar-Çamucu	Trough	39.69064˚ N	27.40945˚ E	487
32	Çarmık-Yaylacık	Trough	39.73197˚ N	27.41420˚ E	466
33	Müstecap II	Trough	39.74618˚ N	27.56528˚ E	303
34	Semiz-Çukurcak	Trough	39.80881˚ N	27.60152˚ E	366
35	Göloba	Trough	39.85377˚ N	27.57118˚ E	498

3. Results

A total of 37 species were determined, composed of 21 cladocerans and 16 copepods. Identified species and its distribution to the stations and samplings are given in Table 2.

Table 2: Identified species and its distribution to the stations and samplings

	Samplings			
	I	II	III	IV
	November	February	May	July
	Stations			
Cladocera				
Alona quadrangularis (O.F.Müller, 1776)	4	4		
Bosmina longirostris (O.F.Müller, 1776)	1, 2, 7	2, 3, 4, 5, 10	2, 4, 5, 7, 26	2, 3, 7
Ceriodaphnia pulchella Sars, 1862			5	
Ceriodaphnia reticulata (Jurine, 1820)			11	11

	I November	II February	III May	IV July
			Stations	
Chydorus sphaericus (O.F.Müller, 1776)		4	4, 7, 10, 15, 17, 18, 19, 22, 24, 25, 26, 27, 30	33
Coronatella rectangula (Sars, 1862)		4	2, 4	
Daphnia cucullata Sars, 1862	2	2, 3, 10	2, 5, 7, 29	2, 5, 6, 7, 32
Daphnia longispina (O.F.Müller, 1776)	2	2, 3, 10	4, 7	
Daphnia parvula Fordyce, 1901	7	2, 3, 7, 10	2, 7	
Diaphanosoma lacustris Kořinek, 1981			5	2, 5
Disparalona rostrata (Koch, 1841)		4		4, 7
Ilyocryptus agilis Kurz, 1878				4
Ilyocryptus sordidus (Liévin, 1848)	4			
Leydigia leydigi (Schödler, 1863)			10	
Leptodora kindtii (Focke, 1844)				5
Macrothrix hirsuticornis Norman & Brady, 1867			21, 31	
Macrothrix laticornis (Jurine, 1820)			5	
Moina brachiata (Jurine, 1820)			11	2
Moina micrura Kurz, 1875			5, 29	1, 3, 7
Pleuroxus aduncus (Jurine, 1820)			9, 26, 28	
Simocephalus vetulus (O.F.Müller, 1776)			9, 25, 26	
Copepoda				
Achantocyclops robustus (Sars, 1862)			1, 3	
Achantocyclops vernalis (Fischer, 1853)			12, 15	
Bryocamptus pygmaeus (Sars, 1863)			18	
Canthocamptus staphylinus (Jurine, 1820)			10, 20	
Cyclops ankyrae Mann, 1940			11	
Cyclops vicinus Uljanin, 1875	1, 2, 3, 4, 7	1, 2, 3, 4, 5, 7, 10	1, 2, 3, 7	
Diacyclops bisetosus (Rehberg, 1880)			21	
Eucyclops serrulatus (Fischer, 1851)	2, 5, 9	4	3, 9, 10, 14, 22, 24, 25, 26, 27, 29, 30, 31	11, 33, 34, 35
Macrocyclops albidus (Jurine, 1820)			12, 25, 27	
Megacyclops latipes (Lowndes, 1927)			20, 21	
Microcyclops rubellus (Lilljeborg, 1901)			4	
Nitokra hibernica (Brady, 1880)			2	2
Paracyclops chiltoni (Thomson, 1882)		1	14, 24	

	Samplings			
	I	II	III	IV
	November	February	May	July
	Stations			
Paracyclops fimbriatus (Fischer, 1853)			22	6
Thermocyclops oithoinides (Sars, 1863)	7		2, 4, 5, 7,	1, 2, 3, 4, 5, 6, 7, 11, 32
Tropocylops prasinus (Fischer, 1860)	9		10, 22, 24, 26, 27, 28, 29, 30	6, 11, 33, 34

4. Discussion

Analysis of the literature was revealed that the Copepoda fauna of Balya has not been examined sufficiently. The only record in the literature was 3 species (*A. robustus*, *E. serrulatus,* and *T. prasinus*) which were given from Ilıca pond by Sönmez et al. [11]. No record was found in the literature about Cladocera fauna of Balya. So, all taxa identified from the district except 3 copepod species reported previously are new records. In Cladocera, *C. sphaericus* was the most common species followed by *B. longirostris* and *D. cucullata.* In Copepoda, *E. serrulatus* was the most common species followed by *T. prasinus*. It is determined that 13 species are specific to the stations where they are identified (Table 2.).

Turkey is divided into 25 river basins that correspond with its hydrological features by the General Directorate of State Hydraulic Works (GDSH -DSI in Turkish-) [16, 17]. Balıkesir is in the coverage of 3 basins; Marmara, North Aegean and Susurluk. Therefore, many water bodies fed by different streams have spread throughout the province, but only few of them have been studied. A total of 68 species, including 37 cladocerans and 31 copepods were recorded from various water resources (İkizcetepeler Dam Lake, Çaygören Dam Lake, Manyas Dam Lake, Manyas Lake, Gönen Stream) of Balıkesir [11, 18-33]. It is noteworthy that Lake Manyas was studied [18-25] more intensively than other places, 19 species were reported from the lake. A total of 13 species, 6 of the Cladocera (*Ceriodaphnia pulchella*, *Daphnia parvula*, *Diaphanosoma lacustris*, *Ilyocryptus agilis*, *Ilyocryptus sordidus*, and *Macrothrix hirsuticornis*) and 7 of the Copepoda (*Canthocamptus staphylinus*, *Cyclops ankyrae*, *Diacyclops bisetosus*, *Megacyclops latipes*, *Microcyclops rubellus*, *Paracyclops fimbriatus,* and *Thermocyclops*

oithoinides) identified in our study have not been recorded previously from the province; therefore, they are new records for Balıkesir fauna.

Acknowledgement

References

[1] Havens, K.E., *Zooplankton structure and potential food web interactions in the plankton of a subtropical chain-of-lakes*, The Scientific World Journal, 2, 926-942, 2002.

[2] Błędzki, L.A., Rybak, J. I., Freshwater crustacean zooplankton of Europe, Cladocera & Copepoda (Calanoida, Cyclopoida) Key to species identification, with notes on ecology, distribution, methods and introduction to data analysis, Springer International Publishing, Switzerland, 2016.

[3] Rogers, D.C., Thorp, J. H., Keys to Palaearctic fauna, Thorp and Covich's freshwater invertebrates - Volume IV, Elsevier, United Kingdom, 2019.

[4] Boxshall, G.A., Defaye, D., Global diversity of copepods (Crustacea: Copepoda) in freshwater, In: Freshwater animal diversity assessment, Balian, E.V., Lévêque, C., Segers, H., Martens, K. (eds), Springer, pp. 195-207, 2007.

[5] Smirnov, N.N., Physiology of the Cladocera, Academic Press, United Kingdom, 2017.

[6] Humes, A.G., *How many copepods?*, Hydrobiologia, 293, 1-7, 1994.

[7] Adamowicz, S.J., Purvis, A., *How many branchiopod crustacean species are there? Quantifying the components of underestimation*, Global Ecology and Biogeography, 14 (5), 455-468, 2005.

[8] Forró, L., Korovchinsky, N.M., Kotov, A.A., Petrusek, A., Global diversity of cladocerans (Cladocera; Crustacea), In: Freshwater animal diversity assessment, Balian, E. V., Lévêque, C., Segers, H., Martens, K. (eds), Springer, pp. 177-184, 2007.

[9] Ustaoğlu, M.R., *An updated zooplankton biodiversity of Turkish inland waters*, LimnoFish, 1 (3), 151-159, 2015.

[10] Aydın, İ., *Madencilik-şehirleşme ilişkisine farklı bir örnek: Balya*, Marmara Coğrafya Dergisi, 12, 133-147, 2006.

[11] Sönmez, S., Serdar, S., Alper, A., Karaytuğ, S., *A faunistic study on the freshwater Copepoda (Crustacea) of Balıkesir*, Journal of Applied Biological Sciences, 2 (3), 45-49, 2008.

[12] Karaytuğ, S., Sak, S., *A contribution to the marine harpacticoid (Crustacea, Copepoda) fauna of Turkey*, EU Journal of Fisheries & Aquatic Sciences, 23 (3-4), 403-405, 2006.

[13] Einsle, U., Copepoda: Cyclopoida: Genera *Cyclops*, *Megacyclops*, *Acanthocyclops*, SPB Academic Publishing, United Kingdom, 1996.

[14] Ueda, H., Reid, J. W., Copepoda: Cyclopoida: Genera *Mesocyclops* and *Thermocyclops*, SPB Academic Publishing, United Kingdom, 2003.

[15] Wells, J.B.J., *An annotated checklist and keys to the species of Copepoda Harpacticoida (Crustacea)*, Zootaxa, 1568 (1), 1-872, 2007.

[16] Delipınar, Ş., Karpuzcu, M., *Policy, legislative and institutional assessments for integrated river basin management in Turkey*, Environmental Science & Policy, 72, 20-29, 2017.

[17] Uzun, O., Dilek, F., Çetinkaya, G., Erduran, F., Açıksöz, S., *National and regional landscape classification and mapping of Turkey: Konya closed basin, Suğla Lake and its surrounding area*, International Journal of the Physical Sciences, 6 (3), 550-565, 2011.

[18] Noodt, W., *Copepoda, Harpacticoidea aus dem limnischen mesopsammal der Türkei*, İstanbul Üniversitesi Fen Fakültesi Hidrobiyoloji Araştırma Enstitüsü Yayınları, 2 (1), 27-40, 1954.

[19] Kiefer, F., *Freilebende ruderfusskrebse (Crustacea, Copepoda) aus Türkischen binnengewassern, II Cyclopoida und Harpacticoida*, İstanbul Üniversitesi Fen Fakültesi Hidrobiyoloji Araştırma Enstitüsü Yayınları, 2 (4), 108-132, 1955.

[20] Demirhindi, Ü., *The preliminary planktonic investigations in the coastal lagoons and several brackish water lakes of Turkey*, İ. Ü. Fen Fak. Mec., 37 (3-4), 205-232, 1972.

[21] Ustaoğlu, M., Balık, S., Kuş Gölü (Bandırma) zooplanktonu, Ulusal Biyoloji Kongresi, Erzurum, pp. 11-19, 1990.

[22] Gündüz, E., *Türkiye içsularında yaşayan Cladocera (Crustacea) türlerinin listesi*, Turkish Journal of Zoology, 21 (1), 37-45, 1997.

[23] Akbulut, N., Akbulut, A., *The planktonic organisms of lake Manyas*, Hacet. Bull. Nat. Sci. Eng., 29, 9-23, 2000.

[24] Türkmen, E.I. (2018). Manyas Kuş Gölü'nün zooplankton kommunite yapısı, Balıkesir University, Balıkesir/Turkey.

[25] Çelik, K., Manyas (Kuş) Gölü (Balıkesir) plankton ekolojisi, 2 Uluslararası Bandırma ve Çevresi Sempozyumu, Bandırma/Balıkesir, pp. 191-199, 2019.

[26] Alper, A., Çelebi, E., Çam, H., Karaytuğ, S., *Cladocera and Copepoda (Crustacea) fauna of İkizcetepeler Dam Lake (Balıkesir, Turkey)*, Turkish Journal of Fisheries and Aquatic Sciences, 7 (1), 71-73, 2007.

[27] Bozkurt, A., Çelik, K., Sevindik, T.O., *Seasonal variations in the length of zooplankton related to certain physicochemical variables in two freshwater reservoirs*, Crustaceana, 85 (4-5), 447-462, 2012.

[28] Ustaoğlu, M.R., Özdemir Mis, D., Aygen, C., *Observations on zooplankton in some lagoons in Turkey*, J. Black Sea/Mediterranean Environment, 18 (2), 208-222, 2012.

[29] Giritlioğlu, E. (2013). Manyas Barajı zooplankton ekolojisi, Balıkesir University, Balıkesir/Turkey.

[30] Gürleyen, N., Ustaoğlu, M. R., *Zooplankton fauna and seasonal changes of constructed ponds and reservoirs of Gönen Stream (Balıkesir-Turkey)*, Journal of Limnology and Freshwater Fisheries Research, 3 (2), 79-89, 2017.

[31] Çelik, K., Giritlioğlu, E., *Zooplanktonik organizmaların Manyas Barajında (Balıkesir) mevsimsel değişimi ve bazı fiziksel ve kimyasal parametrelerle olan ilişkileri*, Iğdır Üniversitesi Fen Bilimleri Enstitüsü Dergisi, 7 (2), 65-72, 2017.

[32] Bulut, H., Saler, S., *Seasonal variations in zooplankton community of an aquatic ecosystem at Susurluk Basin (Balıkesir-Turkey)*, Fresenius Environmental Bulletin, 27 (4), 2530-2535, 2018.

[33] Çelik, K., Bozkurt, A., Sevindik, T.O., *Seasonal dynamics of the zooplankton community in the temperate eutrophic Çaygören Reservoir (Balıkesir), Turkey related to certain physicochemical parameters of water*, Turkish Journal of Fisheries and Aquatic Sciences, 19 (6), 503-512, 2019.

Toxic Effects of Glyphosate-Based Herbicide on *Melanopsis praemorsa*

Özlem DEMİRCİ[1,*], Feysel ÇAKMAK[2], Ahmet İsmail ÖZKAN[3]

[1]*Dicle University, Science Faculty, Biology Department, Diyarbakır, Turkey*
ozdem22@gmail.com, ORCID: 0000-0001-9511-2010
[2]*Dicle University, Science Faculty, Molecular Biology and Genetics Department, Diyarbakır, Turkey*
feyselcakmak@gmail.com, ORCID: 0000-0002-4827-150X
[3]*Dicle University, Science Faculty, Molecular Biology and Genetics Department, Diyarbakır, Turkey*
aiozkan.13801509@ogr.dicle.edu.tr, ORCID: 0000-0002-4511-2386

Abstract

In the present study, we determined the 24, 48, 72, and 96 h LC_{50} values for a glyphosate-based commercial herbicide (GBH) for the aquatic snail *Melanopsis praemorsa*. We examined subacute toxicity responses from *M. praemorsa* after 30-day exposure to 1/10, 1/5, and 1/2 of the 96 h LC_{50} value using several biochemical markers. Glutathione reductase (GR) and glutathione S-transferase (GST) activities were significantly inhibited when compared to control after 4 days of GBH exposure. On the twentieth day of exposure, GST and GR activities were inhibited in organisms exposed to both $LC_{50}/10$ and $LC_{50}/5$ compared to control. These results showed that chronic GBH exposure inhibited GST, an important detoxifying enzyme. GR, an important oxidative stress marker, was likely inhibited as a result of inhibition of the detoxification mechanism.

Keywords: Melanopsis praemorsa; Biomarkers; Glyphosate-based herbicide.

Glifosat Bazlı Herbisitin *Melanopsis praemorsa* Üzerindeki Toksik Etkileri

Öz

Bu çalışmada, sucul salyangoz *Melanopsis praemorsa* için glifosat bazlı bir ticari herbisit (GBH)'in 24, 48, 72 ve 96 saat LC$_{50}$ değerlerini belirledik. *M. praemorsa*'nın kronik toksisite tepkilerini ve 96 saat LC$_{50}$ değerinin 1/10, 1/5 ve 1/2'sine 30 gün maruz kaldıktan sonra *M. praemorsa*'nın kronik toksisite cevaplarını birkaç biyokimyasal belirteç kullanarak inceledik. Glutatyon redüktaz (GR) ve glutatyon S-transferaz (GST) aktiviteleri, 4 günlük GBH maruziyetinden sonra kontrol ile karşılaştırıldığında istatistiksel olarak anlamlı şekilde inhibe oldu. Yirmi günlük maruz kalma sonucunda, GST ve GR aktiviteleri kontrole karşılaştırıldığında hem LC$_{50}$/10'a hem de LC$_{50}$/5'e maruz kalan organizmalarda inhibe olmuştur. Bu sonuçlar, kronik GBH maruziyetinin önemli bir detoksifiye edici enzim olan GST'yi inhibe ettiğini gösterdi. Önemli bir oksidatif stres belirteci olan GR, detoksifikasyon mekanizmasının inhibisyonu sonucu inhibe edildiği sonucuna varılabilinir.

Anahtar Kelimeler: *Melanopsis praemorsa*; Biyobelirteçler; Glifosat bazlı herbisit.

1. Introduction

Pesticides are xenobiotics that routinely contaminate aquatic areas such as rivers, lakes, and coastal areas [1]. Agricultural area development has markedly increased pesticide use. Pollution of aquatic environments by pesticides usually occurs by surface waters and subsurface drainage after intensive agricultural applications. Pesticides that reach water resources often cause striking toxicity to non-target organisms. Therefore, the evaluation of pesticide effects on aquatic vertebrates and invertebrates is very important [2]. Acute and chronic toxicity tests are frequently used to determine the potential effects of xenobiotics on aquatic populations [3].

Glyphosate has been one of the most widely-used ingredients worldwide since it was introduced to the market in the 1970s. The most important reason for this use is that glyphosate inhibits the 5-enolpyruvyl-shikimate-3-phosphate synthase (EPSPS) enzyme in the shikimate pathway. It functions as a non-selective herbicide to inhibit the synthesis of aromatic acids and many different aromatic compounds in plants, algae, bacteria, and fungi [4, 5]. While this pathway is absent in animals, many studies have shown that glyphosate is toxic to non-target aquatic organisms [6-8]. Due to its high solubility in water and extensive use, exposure of non-target aquatic organisms to this herbicide has caused great concern [9].

Invertebrates are organisms that are widely distributed, represented by many species, and occupy lower levels of the trophic chain. Many bioassays that use aquatic invertebrates have shown that they are more sensitive to xenobiotics than aquatic vertebrates [10]. Many xenobiotics are transferred from invertebrates to vertebrates through accumulation by nutrition. For these

reasons, aquatic invertebrate toxicity testing is a very useful tool for performing the "3Rs principle" (replace, reduce, and refine) in experiments to investigate the safe use of many chemicals [11]. *Melanopsis praemorsa* (Linnaeus, 1758, Buccinum), a gastropod snail, was chosen for this study because it is the most abundant species in the Mediterranean region and exhibits several characteristics: widespread in freshwater, available in all seasons, and able to adapt to laboratory conditions.

Pesticides can accumulate in aquatic organisms and can thus reach humans as the last step in the food chain [2, 12]. Some recent studies have shown that pesticides promote oxidative stress by causing an increase in reactive oxygen species (ROS) [13, 14] Live systems have enzymatic and nonenzymatic antioxidant systems to ameliorate ROS, and their responses are very useful biomarkers for revealing potential toxicity [15]. The antioxidant protection system contains important enzymes such as glutathione reductase (GR) and catalase (CAT). GR catalyses the NADPH-dependent conversion of oxidized glutathione (GSSG) to reduced glutathione (GSH) in the glutathione cycle. GSH is used in hydrogen peroxide (H_2O_2) and organic peroxide detoxification by glutathione peroxidase (GPx) [16]. Without this process, H_2O_2 can be converted to the high reaction hydroxyl radical ($^\cdot$OH) through the Haber-Weiss or Fenton reactions [17, 18]. Glutathione *S*-transferase (GST), an important phase II metabolism enzyme that is part of detoxification mechanisms, can be used as a biomarker to reveal pollutant effects on organisms [19].

Glyphosate-based herbicides (GBHs; e.g., Roundup®) are widely used in aquatic and terrestrial environments. The effects on aquatic organisms such as plants, green algae, fishes, amphibians, and invertebrates have been investigated, and attempts have been made to overcome GBH toxicity in aquatic environments [20-22]. However, studies on snails, an important member of the aquatic ecosystem, are very limited in the literature. The aim of this study was to investigate the biochemical aspects of *M. praemorsa* as bioindicators for realistic evaluation of the effects of GBHs on the aquatic environment.

2. Materials and Methods

2.1. Chemicals

In this study, the effects of a commercial formulation of an herbicide (Roundup®) that contained glyphosate isopropylammonium salt (360 g L^{-1}) as an active ingredient and polyethoxylamine amine as a surfactant were examined. Roundup® was supplied from a local agricultural supply store. The chemicals used for biochemical analyses were obtained from Sigma-Aldrich Chemical Company (USA).

2.2. Acute toxicity assay

The median lethal concentration that caused 50% mortality (LC_{50}) was determined using the semi-static renewal acute toxicity test [23]. Experiments were carried out with 3 replicates and 10 individuals in 5 L glass containers. Dechlorinated tap water was used in all experiments. Organisms were not fed during the acute toxicity test period. Range determination experiments were performed prior to the actual experiment to determine the GBH LC_{50} for the snail. The GBH exposure concentrations were 0.1, 0.3, 0.9, 2.7, 8.1, 24.3, 72.9, 281.7, 656.1, and 1968.3 µg active ingredient (AI) L^{-1}. Inactivity of pesticide-exposed individuals was regarded as evidence of death, at which time dead individuals were removed from the glass containers.

2.3. Test animals and experimental design

Individual *M. praemorsa* (10.1±2 mm in length and 402±4 mg in weight) were obtained from a non-polluted freshwater area on the Dicle University campus (36°54'56.84"N 40°16'28.50"E) at April 2018. Some physicochemical properties of the field were: oxygen amount was 7.40 mL^{-1}, the temperature was 19.4 °C, and pH was 7.04. The concentration of dissolved oxygen in the environment was 7.08, the temperature was 22°C and the pH value was 8.01 during acclimatization and experiments. All experiments were performed at under a 13h:11 h light: dark cycle and the subjects were fed *ad libitum* with *Lactuca sativa* leaves every 24 h to adapt to laboratory conditions. Experiments were carried out in 5 L glass containers under semi-static conditions and with 3 replicates. The experimental setup was prepared in such a way that 30 individuals were at each glass aquaria. Organisms were exposed to the $LC_{50}/10$, $LC_{50}/5$ $LC_{50}/2$ GBH (Roundup®) concentrations for 96 h. No deaths were observed during the experiment. On days 4, 10, 20, and 30, the organisms were sacrificed, washed with distilled water, and stored at -80 °C for enzyme analyses.

2.4. Enzyme analyses

The organisms stored at -80 °C were weighed as a whole and homogenized using four volumes of homogenization phosphate buffer (pH 7.4) under ice condition. Then, samples were centrifuged at 20,000 g for 15 min at 4 °C and the supernatant was assayed for enzyme activities. GST and GR enzyme activities were measured using a microplate reader system [8, 24, 25]. The total protein concentration of each sample was measured according to the Bradford method using bovine serum albumin as a standard [26].

2.5. Statistical analysis

24, 48, 72, and 96 h LC_{50} values were calculated using Probit Analysis [27]. The SPSS statistical software package (version 15.0) was used to statistically evaluate enzyme activities. One-Way ANOVA test was used to determine differences between the control and treatment groups and to demonstrate any dose-dependent changes. The Mann-Whitney *U*-test was used to determine the statistical significance of pairwise comparisons. For all analyses, $p < 0.05$ was considered significant.

3. Results

We first determined the effects of different concentrations of GBH on *M. praemorsa*. The LC_{50} values of GBH were determined for 24, 48, 72 and 96 h exposure as 21.8, 12.6, 10.6 and 9.3 mg L^{-1}, respectively (Table 1). The 96 h LC_{50} concentration was used for subsequent studies to determine changes in GR and GST activities.

GST activity in organisms exposed to both $LC_{50}/5$ and $LC_{50}/2$ concentrations on day 4 of the application was significantly inhibited when compared to control and (Table 2). On day 10 of the application, GST activity in organisms exposed to the $LC_{50}/2$ concentration was significantly inhibited compared to the $LC_{50}/5$ group. After 20 days of exposure, GST enzyme activity in the organisms exposed to all concentrations was different from the control; enzyme activity was decreased at the lowest concentration while it was induced in a concentration dependent manner compared to control, $LC_{50}/5$ and $LC_{50}/10$ groups. GST enzyme activity in individuals exposed to both $LC_{50}/10$ and concentration after 30 days was significantly increased compared to the control.

After 4 days of exposure, the GR activity in $LC_{50}/2$ and $LC_{50}/5$ groups was decreased compared to the control; enzyme activity at the lowest concentration ($LC_{50}/10$) was significantly higher than the other concentrations (Table 2). However, no statistically significant difference was observed between any groups after 10 days. GR activity decreased after 20 d of exposure while the most significant decrease was observed at the lowest concentration. After 30 days, only the individuals exposed to the $LC_{50}/5$ concentration exhibited higher GR activity compared to control (Table 2).

Table 1: The 24 h, 48 h, 72 h and 96 h LC_{50} values of glyphosate-based herbicide (GBH) on *Melanopsis praemorsa*

	Test range (AI)	No tested	LC_{50}			
			24 h	48h	72h	96 h
GBH(mg L^{-1})	1.0-50.0	30	21.7	12.6	10.5	9.3

Table 2: *Melanopsis praemorsa* GST and GR activities during 30 days GBH exposure

Exposure period (Day)	Concentration	GST			GR		
4 d	Control	3.07	±	0.46	3.91	±	0.18
	LC$_{50}$/10	1.83	±	0.05	3.19	±	0.25 [b,c]
	LC$_{50}$/5	1.85	±	0.50*	1.78	±	0.46*,[a]
	LC$_{50}$/2	2.78	±	0.44*	1.77	±	0.05*,[a]
10 d	Control	2.54	±	0.73	2.19	±	0.32
	LC$_{50}$/10	2.37	±	0.44	1.57	±	0.42
	LC$_{50}$/5	2.85	±	0.26 [c]	2.19	±	0.27
	LC$_{50}$/2	1.30	±	0.20 [b]	2.03	±	0.20
20 d	Control	2.70	±	0.12	3.96	±	0.30
	LC$_{50}$/10	1.18	±	0.13*,[b,c]	2.03	±	0.21*,[b,c]
	LC$_{50}$/5	2.01	±	0.21*,[a,c]	3.24	±	0.18*,[a]
	LC$_{50}$/2	3.37	±	0.24*,[a,b]	3.28	±	0.27 [a]
30 d	Control	1.02	±	0.27	1.50	±	0.30
	LC$_{50}$/10	1.77	±	0.17*	2.03	±	0.21
	LC$_{50}$/5	1.72	±	0.32	2.31	±	0.25*
	LC$_{50}$/2	1.34	±	0.22	1.98	±	0.23

Enzyme activities are expressed as nmol/min/mg protein ± standard error (*N*=3).

* $p < 0.05$ compared to control.

[a] $p < 0.05$ compared to LC$_{50}$/10.

[b] $p < 0.05$ compared to LC$_{50}$/5.

[c] $p < 0.05$ compared to LC$_{50}$/2.

4. Discussion

Glyphosate is a broad-spectrum herbicide and currently the most widely used herbicide worldwide. It is used for over 750 different products in agriculture, forestry, and domestic applications. GBHs have begun to be used more intensively and in much wider areas, especially with the increase of glyphosate-resistant genetically-modified products [24]. Glyphosate residues have been found in the air, aquatic environments, and food. Thus, GBHs represent a major threat to the aquatic ecosystem, and the search for effects on non-target aquatic organisms, such as in the present study, will allow a greater understanding of its toxic potential.

The past and present use of many pesticides in agricultural and urban areas has led to their presence in surface and underground water resources [28-31]. Roundup® and other glyphosate-based formulations are used extensively in agricultural areas as well as for weed control in aquatic

areas [32]. Numerous aquatic toxicity studies have been performed with GBHs [33-35]. The toxic effects of the active ingredient (glyphosate) and commercial formulations have been previously compared. These reports revealed that the commercial GBH formulations caused more toxic effects compared to glyphosate alone [36-38]. However, effluents are always contaminated with commercial pesticides. Therefore, investigation of the effect of commercial pesticides on non-target organisms can provide very realistic reports [39]. Many bioassays with aquatic organisms have shown that invertebrates are generally more sensitive to xenobiotics than vertebrates [10]. In particular, gastropods, the most abundant mollusc group, are important bioindicators for many different contaminants such as metals and pesticides [40]. Thus, this study investigated changes in GR and GST enzymes, very important biochemical markers for GBHs, on *M. praemorsa*, a gastropod species with a wide distribution in the Mediterranean.

In our study, we determined the 24, 48, 72 and 96 hours LC_{50} values of GBH for *M. praemorsa* as 21.8, 12.6, 10.6 and 9.3 mg L^{-1}, respectively. In our study, we determined the 24, 48, 72 and 96 hours LC_{50} values of GBH for *M. praemorsa* as 21.8, 12.6, 10.6 and 9.3 mg L^{-1}, respectively. In studies using commercial formulations of Glyphosate, LC_{50} values similar to our results were determined. Bakry et al. [41], Abdel-Ghaffar et al. [42] and Omran et al. [43] determined the 24 h LC_{50} value for *Biomphalaria alexandrina* to be 3.15, 15.062, 41.6 mg L^{-1}, respectively. Different commercial forms of glyphosate were used in these three studies. However, the LC_{50} value is quite different in studies where the active ingredient (AI) of glyphosate is used. For example, Xu et al. [35] 24, 48, 72, 96 h LC_{50} values for freshwater snail (*Pomacea canaliculata*) exposed to glyphosate AI was determined as 178.2, 176.5, 176.2 and 175.1 mg L^{-1}, respectively.

GR activity decreased in the treatment groups (except on exposure days 10 and 30) compared to control. GR is a reliable biomarker that is widely used in aquatic toxicology assessments [44-46]. In some previous studies, GR activity was inhibited in aquatic organisms exposed to pro-oxidants [47-49]. There are two types of glutathione in organisms, GSSG and GSH, and the GSH:GSSG ratio in normal cells is greater than 100:1 [50]. The amount of GSH in tissues usually decreases with short-term oxidant exposure but increases after prolonged exposures. Reduction in GSH levels causes the organs to be more sensitive to xenobiotics. In several studies, moderate oxidative stress increased GSH levels [51]. GR maintains the sulfhydryl groups of both cytosolic proteins in the reduced state by allowing the GSH reserve in cells to remain at the correct level and contributes to the detoxification of many pro-oxidant xenobiotics [3]. Our results revealed that in *M. praemorsa* GR was inhibited compared to control, especially after 4- and 20-day GBH exposure. Contrary to our results, Barky et al. [41] showed a significant

increase in GR activity of freshwater snails (*B. alexandrina*) exposed to GBH. However, in another study done by Bakry et al., [52] similar to our study results, they found that GR activity of a different freshwater snail (*Bulinus truncatus*) exposed to GBH was significantly inhibited. Similar to the GR enzyme in our study, it was found that *M. praemorsa*, exposed to 4 and 20 days GBH, was inhibited compared to the GST enzyme control. GST activity was only induced in organisms exposed to the highest concentration ($LC_{50}/2$) after 20 days compared to control. These results may suggest that GST inhibition is due to an inability to maintain an adequate GSH level or due to GR enzyme inhibition.

In phase II detoxification, GST catalyses the conjugation of xenobiotics with GSH to aid its removal from the organism [53]. Xenobiotics may cause cellular damage. Therefore, cytosolic GST induction is used as a biomarker for environmental pollutants [54, 55]. Many studies demonstrated that GST activity was induced in aquatic organisms exposed to pesticides [5, 48, 56]. Similarly, Khalil [57] reported that GST activity in the freshwater snail *Lanistes carinatus* exposed to chlorpyrifos for 28 days was increased compared to control. However, Lushchak et al. [58] reported that GST and GR enzyme activities in *Carassius auratus* tissues exposed to GBH were generally suppressed. In another study, liver GST activity was inhibited in two different fish species (*Anabas testudineus* (Bloch) and *Heteropneustes fossilis* (Bloch)) after GBH exposure [59]. Similarly, we found that *M. praemorsa* GST activity was generally inhibited after GBH exposure compared to control. The inhibition of detoxification enzymes, when considered independently from reduced GR activity, could make xenobiotics more toxic to an organism and cause metabolic dysfunction [55]. These results provide inexorable evidence that the detoxification mechanism can be inhibited by the GBH.

5. Conclusions

Since glyphosate is a non-selective herbicide, it is used in many different terrestrial and aquatic areas against undesirable vegetation. Thus, glyphosate is one of the most widely used herbicides globally. There are many studies that have investigated its toxic effects, especially for aquatic organisms. The effects of GBHs on the aquatic snail may provide an important contribution to the proper assessment of their aquatic toxicity.

References

[1] Schwarzenbach, R.P., Escher, B.I., Fenner, K., Hofstetter, T.B., Johnson, C.A., Von Gunten, U., Wehrli, B., *The challenge of micropollutants in aquatic systems*, Science, 313, 1072-1077, 2006.

[2] Banaee, M., Sureda, A., Mirvaghefi, A., Ahmadi, K., *Effects of diazinon on biochemical parameters of blood in rainbow trout (Oncorhynchus mykiss)*, Pesticide Biochemistry and Physiology, 99, 1-6, 2011.

[3] de Freitas Tallarico, L., Borrely, S.I., Hamada, N., Grazeffe, V.S., Ohlweiler, F.P., Okazaki, K., Granatelli, A.T., Pereira, I.W., de Bragança Pereira, C.A., Nakano, E., *Developmental toxicity, acute toxicity and mutagenicity testing in freshwater snails Biomphalaria glabrata (Mollusca: Gastropoda) exposed to chromium and water samples*, Ecotoxicology and Environmental Safety, 110, 208-215, 2014.

[4] Duke, S.O., Powles, S.B., *Glyphosate: a once-in-a-century herbicide,* Pest Management Science, 64, 319-325, 2008.

[5] Sayeed, I., Parvez, S., Pandey, S., Bin-Hafeez, B., Haque, R., Raisuddin, S., *Oxidative stress biomarkers of exposure to deltamethrin in freshwater fish, Channa punctatus Bloch*, Ecotoxicology and Environmental Safety, 56, 295-301, 2003.

[6] Folmar, L.C., Sanders, H., Julin, A., *Toxicity of the herbicide glyphosate and several of its formulations to fish and aquatic invertebrates*. Archives of Environmental Contamination and Toxicology, 8, 269-278, 1979.

[7] Lanctôt, C., Navarro-Martín, L., Robertson, C., Park, B., Jackman, P., Pauli, B.D., Trudeau, V.L., *Effects of glyphosate-based herbicides on survival, development, growth and sex ratios of wood frog (Lithobates sylvaticus) tadpoles. II: agriculturally relevant exposures to Roundup WeatherMax® and Vision® under laboratory conditions*, Aquatic Toxicology, 154, 291-303, 2014.

[8] Solomon, K., Thompson, D., *Ecological risk assessment for aquatic organisms from over-water uses of glyphosate*, Journal of Toxicology and Environmental, Health, Part B 6, 289-324, 2003.

[9] Peruzzo, P.J., Porta, A.A., Ronco, A.E., *Levels of glyphosate in surface waters, sediments and soils associated with direct sowing soybean cultivation in north pampasic region of Argentina*, Environmental Pollution, 156, 61-66, 2008.

[10] Achiorno, C.L., de Villalobos, C., Ferrari, L., *Validation test with embryonic and larval stages of Chordodes nobilii (Gordiida, Nematomorpha): Sensitivity to three reference toxicants*, Chemosphere, 81, 133-140, 2010.

[11] Ibrahim, D.M., *Reduce, refine, replace: The failure of the three R's and the future of animal experimentation*, The University of Chicago Legal Forum, 195, 2006.

[12] Özcan Oruç, E., Üner, N., *Marker enzyme assesment in the liver of Cyprinus carpio (L.) exposed to 2,4-D and azinphosmethyl*, Journal of Biochemical and Molecular Toxicology, 16, 182-188, 2002.

[13] Clasen, B., Loro, V. L., Murussi, C. R., Tiecher, T. L., Moraes, B., Zanella, R., *Bioaccumulation and oxidative stress caused by pesticides in Cyprinus carpio reared in a rice-fish system*. Science of the Total Environment, 626, 737-743, 2018.

[14] Parvez, S., Raisuddin, S.J.E.T., *Protein carbonyls: novel biomarkers of exposure to oxidative stress-inducing pesticides in freshwater fish Channa punctata (Bloch)*, Environmental Toxicology and Pharmacology, 20, 112-117, 2005.

[15] Wang, X., Xing, H., Jiang, Y., Wu, H., Sun, G., Xu, Q., Xu, S., *Accumulation, histopathological effects and response of biochemical markers in the spleens and head kidneys of common carp exposed to atrazine and chlorpyrifos*, Food and Chemical Toxicology, 62, 148-158, 2013.

[16] Lukaszewicz-Hussain, A., *Role of oxidative stress in organophosphate insecticide toxicity–Short review*, Pesticide Biochemistry and Physiology, 98, 145-150, 2010.

[17] Kehrer, J.P., *The Haber–Weiss reaction and mechanisms of toxicity,* Toxicology, 149, 43-50, 2000.

[18] Winterbourn, C.C., T*oxicity of iron and hydrogen peroxide: the Fenton reaction*, Toxicology Letters, 82, 969-974, 1995.

[19] Otitoju, O., Onwurah, I.N., *Glutathione S-transferase (GST) activity as a biomarker in ecological risk assessment of pesticide contaminated environment,* African Journal of Biotechnology, 6, 1455-1459, 2007.

[20] Cedergreen, N., Streibig, J.C., *The toxicity of herbicides to non-target aquatic plants and algae: assessment of predictive factors and hazard*, Pest Management Science, 61, 1152-1160, 2005.

[21] Güngördü, A., *Comparative toxicity of methidathion and glyphosate on early life stages of three amphibian species: Pelophylax ridibundus, Pseudepidalea viridis, and Xenopus laevis*, Aquatic Toxicology, 140-141, 220-228, 2013.

[22] Relyea, R.A., *The lethal impact of Roundup on aquatic and terrestrial amphibians*, Ecological Applications, 15, 1118-1124, 2005.

[23] APHA, Standard methods for the examination of water and wastewater. American Public Health Association (APHA): Washington, DC, USA, 2005.

[24] Guyton, K.Z., Loomis, D., Grosse, Y., El Ghissassi, F., Benbrahim-Tallaa, L., Guha, N., Scoccianti, C., Mattock, H., Straif, K., *Carcinogenicity of tetrachlorvinphos, parathion, malathion, diazinon, and glyphosate*, Lancet Oncology, 16, 490, 2015.

[25] Habig, W., Pabst, M., Jakoby, W., *The first enzymatic step in mercapturic acid formation. Glutathione-S-transferase*, The Journal of Biological Chemistry, 249, 7130-7139, 1974.

[26] Bradford, M.M., *A rapid and sensitive method for the quantitation of microgram quantities of protein utilizing the principle of protein-dye binding*, Analytical Biochemistry, 72, 248-254. 1976.

[27] Finney, D.J., Probit analysis. Cambridge University Press, New York. 1952.

[28] Barlas, N., *Determination of organochlorine pesticide residues in aquatic systems and organisms in upper Sakarya Basin, Türkiye*, Bulletin of Environmental Contamination and Toxicology, 62, 278-285, 1999.

[29] Castillo, L.E., Ruepert, C., Solis, E., *Pesticide residues in the aquatic environment of banana plantation areas in the north Atlantic zone of Costa Rica*, Environmental Toxicology and Chemistry, 19, 1942-1950, 2000.

[30] Qian, Y., Matsumoto, H., Liu, X., Li, S., Liang, X., Liu, Y., Zhu, G., Wang, M., *Dissipation, occurrence and risk assessment of a phenylurea herbicide tebuthiuron in sugarcane and aquatic ecosystems in South China*, Environmental Pollution, 227, 389-396, 2017.

[31] Vryzas, Z., Alexoudis, C., Vassiliou, G., Galanis, K., Papadopoulou-Mourkidou, E., *Determination and aquatic risk assessment of pesticide residues in riparian drainage canals in northeastern Greece*, Ecotoxicology and Environmental Safety, 74, 174-181, 2011.

[32] Giesy, J.P., Dobson, S., Solomon, K.R., Ecotoxicological risk assessment for Roundup® herbicide, Reviews of environmental contamination and toxicology, Springer, pp. 35-120, 2000.

[33] Caldas, S.S., Bolzan, C.M., Guilherme, J.R., Silveira, M.A.K., Escarrone, A.L.V., Primel, E.G., *Determination of pharmaceuticals, personal care products, and pesticides in surface and treated waters: method development and survey*, Environmental Science and Pollution Research 20, 5855-5863, 2013.

[34] Nwani, C.D., Lakra, W.S., Nagpure, N.S., Kumar, R., Kushwaha, B., Srivastava, S.K., *Toxicity of the Herbicide Atrazine: Effects on Lipid Peroxidation and Activities of Antioxidant Enzymes in the Freshwater Fish Channa Punctatus (Bloch)*, International Journal of Environmental Research and Public Health, 7, 3298-3312, 2010.

[35] Xu, Y., Li, A.J., Li, K., Qin, J., Li, H., *Effects of glyphosate-based herbicides on survival, development and growth of invasive snail (Pomacea canaliculata)*, Aquatic Toxicology, 193, 136-143, 2017.

[36] Chaufan, G., Coalova, I., Molina, M.d.C.R.d., *Glyphosate commercial formulation causes cytotoxicity, oxidative effects, and apoptosis on human cells: differences with its active ingredient*, International Journal of Toxicology, 33, 29-38, 2014.

[37] Cuhra, M., Traavik, T., Bøhn, T., *Clone-and age-dependent toxicity of a glyphosate commercial formulation and its active ingredient in Daphnia magna*, Ecotoxicology, 22, 251-262, 2013.

[38] Pereira, J.L., Antunes, S.C., Castro, B.B., Marques, C.R., Gonçalves, A.M., Gonçalves, F., Pereira, R., *Toxicity evaluation of three pesticides on non-target aquatic and soil organisms: commercial formulation versus active ingredient*, Ecotoxicology, 18, 455-463, 2009.

[39] Malato, S., Blanco, J., Fernandez-Alba, A., Agüera, A., *Solar photocatalytic mineralization of commercial pesticides: acrinathrin,* Chemosphere, 40, 403-409, 2000.

[40] Oehlmann, J., Schulte-Oehlmann, U., Molluscs as bioindicators, Trace Metals and other Contaminants in the Environment, Elsevier, pp. 577-635, 2003.

[41] Barky, F.A., Abdelsalam, H.A., Mahmoud, M.B., Hamdi, S.A., *Influence of Atrazine and Roundup pesticides on biochemical and molecular aspects of Biomphalaria alexandrina snails*, Pesticide Biochemistry and Physiology, 104, 9-18, 2012.

[42] Abdel-Ghaffar, F., Ahmed, A. K. Bakry, F. Rabei I. and Ibrahim A.J.M., *The impact of three herbicides on biological and histological aspects of Biomphalaria alexandrina, intermediate host of Schistosoma mansoni*, Malacologia, 59, 197-210, 2016.

[43] Omran, N.E., Salama, W.M.J.T., *The endocrine disruptor effect of the herbicides atrazine and glyphosate on Biomphalaria alexandrina snails*, Toxicology and Industrial Health, 32, 656-665, 2016.

[44] Cossu, C., Doyotte, A., Jacquin, M., Babut, M., Exinger, A., Vasseur, P., *Glutathione reductase, selenium-dependent glutathione peroxidase, glutathione levels, and lipid peroxidation in freshwater bivalves, Unio tumidus, as biomarkers of aquatic contamination in field studies*, Ecotoxicology and Environmental Safety, 38, 122-131, 1997.

[45] Di Giulio, R.T., Washburn, P.C., Wenning, R.J., Winston, G.W., Jewell, C.S., *Biochemical responses in aquatic animals: a review of determinants of oxidative stress*, Environmental Toxicology and Chemistry, 8, 1103-1123, 1989.

[46] Regoli, F., Giuliani, M.E., *Oxidative pathways of chemical toxicity and oxidative stress biomarkers in marine organisms*, Marine Environmental Research, 93, 106-117, 2014.

[47] Khatun, S., Ali, M.B., Hahn, E.-J., Paek, K.-Y., *Copper toxicity in Withania somnifera: Growth and antioxidant enzymes responses of in vitro grown plants*, Environmental and Experimental Botany, 64, 279-285, 2008.

[48] Oruc, E.O., Sevgiler, Y., Uner, N., *Tissue-specific oxidative stress responses in fish exposed to 2, 4-D and azinphosmethyl*, Comparative Biochemistry and Physiology Part C: Toxicology & Pharmacology, 137, 43-51, 2004.

[49] Zhang, J., Shen, H., Wang, X., Wu, J., Xue, Y., *Effects of chronic exposure of 2, 4-dichlorophenol on the antioxidant system in liver of freshwater fish Carassius auratus*, Chemosphere, 55, 167-174, 2004.

[50] Di Giulio, R., Meyer, J., Reactive oxygen species and oxidative stress, in: Di Giulio, R., Meyer, J. (eds.), The toxicology of fishes. CRC Press, Boca Raton, pp. 273-324, 2008.

[51] Slaninova, A., Smutna, M., Modra, H., Svobodova, Z., *Reviews Oxidative stress in fish induced by pesticides*, Neuroendocrinology Letters, 30, 2, 2009.

[52] Bakry, F.A., Ismail, S.M., Abd El-Atti, M.S., *Glyphosate herbicide induces genotoxic effect and physiological disturbances in Bulinus truncatus snails*, Pesticide Biochemistry and Physiology, 123, 24-30. 2015.

[53] Mukanganyama, S., Figueroa, C., Hasler, J., Niemeyer, H., *Effects of DIMBOA on detoxification enzymes of the aphid Rhopalosiphum padi (Homoptera: Aphididae)*, Journal of Insect Physiology, 49, 223-229, 2003.

[54] Egaas, E., Sandvik, M., Fjeld, E., Källqvist, T., Goksøyr, A., Svensen, A., *Some effects of the fungicide propiconazole on cytochrome P450 and glutathione S-transferase in brown trout (Salmo trutta)*, Comparative Biochemistry and Physiology Part C: Pharmacology, Toxicology and Endocrinology, 122, 337-344, 1999.

[55] Wang, C., Lu, G., Cui, J., Wang, P., *Sublethal effects of pesticide mixtures on selected biomarkers of Carassius auratus*, Environmental Toxicology and Pharmacology, 28, 414-419, 2009.

[56] Moreira, S., Moreira-Santos, M., Rendón-von Osten, J., Da Silva, E., Ribeiro, R., Guilhermino, L., Soares, A., *Ecotoxicological tools for the tropics: Sublethal assays with fish to evaluate edge-of-field pesticide runoff toxicity*, Ecotoxicology and Environmental Safety, 73, 893-899, 2010.

[57] Khalil, A.M., *Toxicological effects and oxidative stress responses in freshwater snail, Lanistes carinatus, following exposure to chlorpyrifos*, Ecotoxicology and Environmental Safety, 116, 137-142, 2015.

[58] Lushchak, V., Kubrak, O.I., Storey, J.M., Storey, K.B., Lushchak, V.I., *Low toxic herbicide Roundup induces mild oxidative stress in goldfish tissues*, Chemosphere, 76, 932-937, 2009.

[59] Samanta, P., Pal, S., Mukherjee, A.K., Ghosh, A.R., *Biochemical effects of glyphosate based herbicide, Excel Mera 71 on enzyme activities of acetylcholinesterase (AChE), lipid peroxidation (LPO), catalase (CAT), glutathione-S-transferase (GST) and protein content on teleostean fishes*, Ecotoxicology and Environmental Safety, 107, 120-125, 2014.

New Breeding Site of Eleonora's Falcon (*Falco eleonorae*) and Peregrine Falcon (*Falco peregrinus*) in Southern Turkey

Hakan KARAARDIÇ[1],*

[1]Alanya Alaaddin Keykubat University, Faculty of Education, Department of Mathematics and Science Education, Alanya, Antalya, Turkey
hkaraardic@gmail.com, ORCID: 0000-0001-9839-4201

Abstract

In southern Turkey, safety cliffs and islands provide breeding and stopover sites for falcons. But, there is scarce information about their distribution in these regions. In this work, Peregrine falcon (*Falco peregrinus*), Eleonora's falcon (*Falco eleonorae*), Merlin (*Falco columbarius*) and Eurasian Hobby (*Falco subbuteo*) were identified in the studied area. The study was conducted around Adrasan bay on the coast line of southern Turkey from April to October during 2013-2018. The Eleonora's falcon and the Peregrine falcon have successfully bred in this region, regularly. A large breeding colony of the Alpine swift (*Apus melba*) is located close to cliffs in the study area. Both falcon species had many successful attacks on Alpine swifts in the sea. This food abundance may be effective with the safety nesting areas for both Peregrine falcon and Eleonora's falcon.

Keywords: Eleonora's falcon; Migration; Nesting; Peregrine falcon; Southern Turkey.

Türkiye'nin Güneyinde Ada Doğanı (*Falco eleonorae*) ve Gökdoğan (*Falco peregrinus*) Yeni Üreme Alanı

Öz

Türkiye'nin güney kıyı kesiminde yer alan kayalık alanlar ve adalar doğanlara güvenli üreme ve konaklama alanı oluşturmaktadır. Ancak, bölgede bu türlerin yayılışları hakkında yeterli bilgi bulunmamaktadır. Bu çalışmada, Gökdoğan (*Falco peregrinus*), Ada doğanı (*Falco eleonorae*), Boz doğan (*Falco columbarius*) ve Delice doğan (*Falco subbuteo*) belirlenmiştir. Çalışma, 2013-2018 yıllarında Nisan Ekim ayları arasında Türkiye'nin güney kıyılarında Adrasan körfezi çevresinde gerçekleştirilmiştir. Ada doğanı ve Gökdoğan bölgede düzenli olarak başarılı bir şekilde üremiştir. Çalışma alanındaki kayalıklara yakın bir bölgede büyük bir Akkarınlı ebabil (*Apus melba*) üreme kolonisi bulunmaktadır. Her iki Doğan türü de Akkarınlı ebabillere deniz ve ada üstünde saldırılarda bulunmuş, bazılarında başarılı olarak avlandıkları gözlenmiştir. Bu önemli besin bolluğu Gökdoğan ve Ada doğanının bölgeyi güvenli üreme alanı olarak tercih etmesinde etkili olabilir.

Anahtar kelimeler: Ada doğanı; Göç; Yuvalanma; Gökdoğan; Güney Türkiye.

1. Introduction

The coastal line of the western and southern Turkey provides safe resting areas for some migratory birds besides the opportunity for nesting and foraging. Many birds of Prey such as Peregrine falcon (*Falco peregrinus*) and Eleonora's falcon (*Falco eleonorae*) migrate to these areas between breeding and wintering grounds. The Eleonora's falcon breeds in a narrow corridor around the Mediterranean and the eastern Atlantic, from the Canary Islands to the coast of Morocco [1, 2] whereas the Peregrine falcon has a widespread breeding range.

Both falcon species are long-distance migrants that overwinter in Sub-Saharan regions. They mostly use high cliffs for nesting. European breeding populations migrate to their breeding grounds by following different routes viz., Iberian peninsula populations trekk via Tunisia to the south-eastern areas [3], in contrast Aegean Sea populations migrate across the Mediterranean direct to the South [4]. Western and southern Turkey have safe breeding and stopover cliffs and islands for breeding falcons. Information about their distribution in these regions is however scarce. In this study, the new breeding sites of Peregrine falcon and Eleonora's falcon were investigated in south-western Turkey.

2. Materials and Methods

The study was conducted around Adrasan bay along the coast line of southern Turkey (36°18'N, 30°28'E) (Fig. 1). This area covers about 30 km of sea cliffs and small rocky islands. Field observations were carried out between April-October during 2013-2018. Data were

collected once a week in April, May and October, and twice a week during the breeding season i.e. from June to September. Daily observations were recorded while travelling in a boat mostly in the evenings, when the birds were generally more active at this time of the day. After finding nests, active nests were checked regularly and tried to find nesting sites by observing other birds. The data are given in Fig. 2. Certain nests were recognized when the birds observed on the nest, whereas Possible nesting areas within the territory where birds were no observed to indulge in breeding activities.
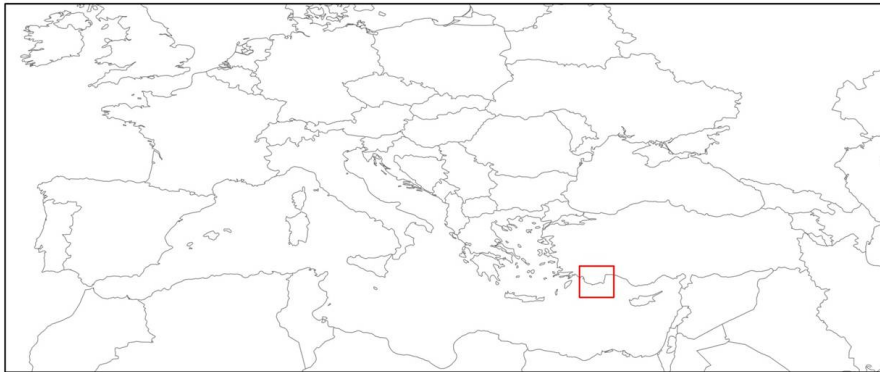
Figure 1: The location of the study area
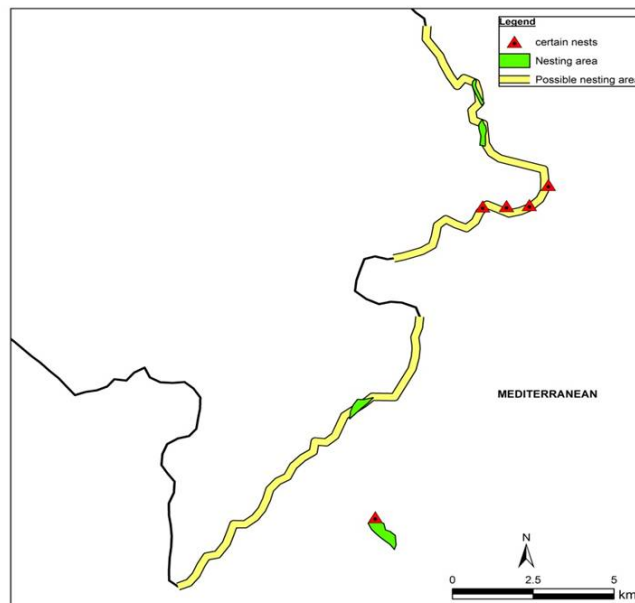
Figure 2: The breeding distribution of falcons. Red triangle shows the nests, which were definitely found and monitored, green colored areas indicate observed pairs but the nest couldn't found, yellow colored areas are also sea cliffs and possible nesting areas

3. Results

During the six-year study, four falcon species were observed to visit the area from April to October viz., Peregrine falcon (*Falco peregrinus*), Eleonora's falcon (*Falco eleonorae*), Merlin

(*Falco columbarius*) and Eurasian Hobby (*Falco subbuteo*). Merlin and Eurasian Hobby are the passing migrants visiting only during in spring and autumn, whereas Peregrine falcon and Eleonora's falcon remain in the area from April to October (Table 1).

Table 1: Observation results of four falcon species according to the months and years

	2013	**2014**	**2015**	**2016**	**2017**	**2018**
April	E,H,M,P	E,H,M,P	E,H,M,P	E,H,M,P	E,H,M,P	E,H,M,P
May	E,H,P	E,H,M,P	E,H,P	E,H,P	E,H,P	E,H,P
June	E,P	E,P	E,P	E,P	E,P	E,P
July	E,P	E,P	E,P	E,P	E,P	E,P
August	E,P	E,P	E,P	E,P	E,P	E,P
September	E,H,M,P	E,M,P	E,H,M,P	E,H,M,P	E,H,M,P	E,M,P
October	E,H,M,P	E,H,M,P	E,H,M	E,H,M,P	E,H,M,P	E,H,M,P

Capital letters in columns indicate observed falcon species. E: Eleonora's falcon,   H: Eurasian hobby, M: Merlin, P: Peregrine falcon.

The Eleonora's falcon and the Peregrine falcon have successfully bred on this region, regularly. The number of brood pairs of both species has been variable in different years, however at least two nests of Eleonora's falcon and one nest of Peregrine falcon had nestlings every year during the study period (Table 2).

Table 2: The number of pairs (nests) of Eleonora's falcon and Peregrine falcon according to the years

		2013	**2014**	**2015**	**2016**	**2017**	**2018**
Eleonora's falcon	Certain	3	3	2	2	3	3
	Observed	5	5	5	5	5	5
Peregrine falcon	Certain	1	1	2	2	1	2
	Observed	2	2	3	3	3	3

Certain, the nest were definitely found; Observed, the nest couldn't find but the pairs were observed around the cliffs.

Eleonora's falcon pairs regularly used the same three nesting sites in 2013 and 2014, but in 2015 pairs did not use the nesting cliff and occupied another site not so far from that used in previous years. Every year five pairs were observed, but only two or three successful nests could be found on the cliffs by using binoculars. Similarly, the Peregrine falcons bred on the cliffs in the same area. The highest pair number was three in all the years during the study period, but mostly just one nest could be found. The number of eggs and hatchlings from each nest could not be determined while observing from the boat. Whereas some young falcons could be observed on their nests, the number of successful fledglings could not be determined (Fig. 3).

Figure 3: Fledglings of Peregrine falcon (*Falco peregrinus*) standing on the slot entry

4. Discussion

Eleonora's falcon mainly breeds on the cliffs of small islands in the Mediterranean in large colonies of up to 630 pairs (Morocco) [3]. According to [5], estimated breeding pairs are 12,299 only on the islands of the Aegean and this is 90% of the World's population of Eleonora's falcon. However, there is only one local study report (unpublished) about the distribution and the breeding site of the species in western (Aegean Sea Region) Turkey.

Several falcon species feed on insects [6], Peregrine falcon feeds on medium-sized birds such as pigeons and doves, waterfowl, songbirds, waders and mammals such as ground squirrels [7-9], according to [1] Eleonora's falcon feeds on primarily insects, but also hunts small migratory birds above the sea. Although there is insufficient information about insects and birds diet of Eleonora's falcon, it is successful in hunting such as wagtails rather than swift species [10]. The study area has a big breeding colony of over 2000 pairs of the Alpine swift (*Apus melba*), on the Pırasalı Island close to the cliffs [11]. Unlike the results of [10], many successful attacks on Alpine swifts were observed during their flights on the sea or above the island near their breeding area. On the other hand, this Alpine swift colony spend pre- and post-breeding time including breeding period longer than northern populations between March and the end of October [12]. Besides the safe nesting areas on the cliffs, food abundance is one of the important features to decide on the

establishment of territories. The number of breeding pairs is not high in comparison to other Eleonora's falcon colonies in the Mediterranean. However, the area is covered with different sized islands and more cliffs. The data about the distribution and breeding pairs of falcons are unsatisfactory. However, this result may help to understand the interactions of falcons and swifts, especially during breeding periods and breeding success of both species groups. Moreover, Peregrine falcon and Eleonora's falcon migrate to the eastern Africa or Madagascar for wintering [2, 13] and Pırasalı Island population of Alpine swift use eastern Africa as wintering grounds [12]. The result of this study is the preliminary of understanding migration and breeding behavior of these species in the eastern Mediterranean.

References

[1] Walter, H., Eleonora's falcon. Adaptations to prey and habitat in a social raptor. Chicago, IL: University of Chicago Press, 1979.

[2] Gschweng, M., Kalko, E.K.V., Querner, U., Fiedler, W. and Berthold, P., *All across Africa: highly individual migration routes of Eleonora's falcon.* Proceedings of the Royal Society B, 275:2887-2896, 2008.

[3] Lopez-Lopez, P., Liminana, R. and Urios, V., *Autumn migration Eleonora's falcon Falco eleonorae tracked by satellite telemetry.* Zoological Studies, 48(4):485-491, 2009.

[4] Kassara, C., Fric, J., Gschweng, M. and Sfenthourakis, S., *Complementing the puzzle of Eleonora's falcon (Falco eleonorae) migration: new evidence from an eastern colony in the Aegean Sea.* Journal of Ornithology, 153:839-848, 2012.

[5] Dimalexis, A., Xirouchakis, S., Portolou, D., Latsoudis, P., Karris, G., Fric, J., Georgiakakis, P., Barboutis, C., Bourdakis, S., Ivovic, M., Kominos, T. and Kakalis, E., *The Status of Eleonora's falcon (Falco eleonorae) in Greece.* Journal of Ornithology, 149:23-30, 2008.

[6] Del Hoyo, J., Elliot, A. and Sargatal, J., Handbook of the birds of the world. Volume 2, New World Vultures to Guineafowl. Lynx Edicion, Barcelona, 1996.

[7] Bradley, M. and Oliphant, L.W., *The diet of peregrine falcons in Rankin Inlet, Northwest territories: An unusually high proportion of mammalian prey,* The Condor, Vol:93, (1): 193-197, 1991.

[8] Rockenbauch, D., Der Wanderfalke in Deutchland und umliegenden Gebieten. Band 2. Koch, Reutlingen, 2002.

[9] Drewitt, E.J.A. and Dixon, N., *Diet and prey selection of urban-dwelling peregrine falcons in southwest England,* British Birds, 101: 58-67, 2008.

[10] Ristow, D., On the insect diet of Eleonora's falcon Falco eleonorae and its importance for coloniality. In *Raptors worldwide* (eds R. D. Chancelor & B.-U. Meyburg), Berlin, Germany, pp. 705-712, 2004.

[11] Karaardıç, H., Köse, F. and Kocakahya, V., *Pırasalı Island: Paradise of Alpine swift (Apus melba) in Adrasan, Kumluca, Turkey.* Tabiat ve İnsan, June:3-10, 2013.

[12] Meier, C., Karaardıç, H., Aymi, R., Peev, S.G., Baechler, E., Weber, R., Witvliet, W. and Liechti, F., *What makes Alpine swift ascend at twilight? Novel geolocators reveal year-round flight behaviour.* Behavioral Ecology and Sociobiology, (2018) 72: 45, 2018.

[13] Mellone, U., Lopez-Lopez, P., Liminana, R. and Urios, V., *Wintering habitats of Eleonora's falcon Falco eleonorae in Madagascar.* Bird Study, 59:1, 29-36, 2012.

Isolation and Identification of *Bacillus* sp. from Root Soil of the *Astragalus gummifer* Lab.: Obtaining and Characterization of α-Amylase

Barış ENEZ[1,*]

[1]*Bingöl University, Vocational School of Technical Science, Veterinary Health Department, Bingöl, Turkey*
benez@bingol.edu.tr, ORCID: 0000-00003-4730-3458

Abstract

α-Amylase (1,4-α D-glucanohydrolase; EC 3.2.1.1) is one of the enzymes that can be used in a number of industrial processes such as bakery, textile, paper, detergents, and is the most important industrial product that plays an important role in the production of bioprotein and the fermentation of starch. The present research aims to the information gap in this area by performing bacterial isolation from the root of *Astragalus gummifer*. Bacterial isolation was performed using serial dilution technique. 16S rRNA analysis was performed for species identification of the microorganism. Isolated microorganism was determined to be gram (+), moving as a result of biochemical tests. Biochemical tests; Catalase, hemolysis, glucose and lactose tests positive (+); indole, H_2S and urease tests showed negative (-) results. Soil samples were analyzed by ICP-MS. As a result of the analysis, it was determined that Al, Cr, Cu, Co, Fe, Pb, Mn and Zn were found in excess amount in the isolated bacteria. The optimal reproductive function of the bacteria was determined at 72 hours, 30 °C and pH 7.0. The maximum production time of α-amylase from Bacillus sp. was 24 hours, 30 °C and pH 7.0. Bacteria identified and found to produce amylase were determined to be used in different biotechnological areas.

Keywords: *Bacillus* sp.; α-Amylase; *Astragalus*; Identification; Optimization.

Astragalus gummifer 'in Kök Topraktan Bacillus sp.'nin İzolasyonu ve Tanımlanması: α-Amilazın Elde Edilmesi ve Karakterizasyonu

Öz

α-Amilaz (1,4-α D-glukanohidrolaz; EC 3.2.1.1) fırıncılık, tekstil, kağıt ve deterjanlar gibi bir dizi endüstriyel işlemde kullanılabilen enzimlerden biridir ve en önemli endüstriyel üründür. Biyoprotein üretiminde ve nişastanın fermantasyonunda önemli rol oynar. Bu araştırmada, literatürde yeterli olmayan *Astragalus gummifer* bitkisinin kökünden bakteri izolasyon yapılarak bu alandaki eksiklik giderildi. Bakteriyel izolasyon seyreltme tekniği kullanılarak yapıldı. Mikroorganizmanın tür tanımlaması için 16 S rRNA analizi yapılmıştır. İzole edilen mikroorganizmanın biyokimyasal testler sonucunda gram (+) ve hareketli olduğu belirlenmiştir. Biyokimyasal testler; Katalaz, hemoliz, glikoz ve laktoz testleri pozitif (+); indol, H_2S ve üreaz testleri negatif (-) sonuçlar göstermiştir. Toprak örnekleri ICP-MS ile analiz edilmiştir. Analizler sonucunda izole edilmiş bakterinin bulunduğu toprakta Al, Cr, Cu, Co, Fe, Pb, Mn ve Zn'nun fazla miktarda olduğu tespit edildi. Bakterilerin optimal üreme koşulları 72 saat, 30 °C ve pH 7.0'da olarak belirlenmiştir. *Bacillus* sp'den maksimum α-amilaz üretim süresi 24 saat, 30 °C ve pH 7.0 idi. Amilaz ürettiği tespit edilen bakterinin farklı biyoteknolojik alanlarda kullanılabileceği görüldü.

Anahtar Kelimeler: *Bacillus* sp.; α-Amilaz; *Astragalus*; Tanımlama; Optimizasyon.

1. Introduction

Alpha amylase (E.C 3.2.1.1) catalyzes the hydrolysis of α-D-(1,4) glycosidic connections in starch components and related carbohydrates [1]. It has a wide range of applications in the fields of starch liquefaction, paper, extraction of textile fabrics, preparation of starch coatings of paints, removal of wallpaper, beer industry, sugar syrup production and sugar induction and pharmaceutical [2-5]. Amylases are produced by plant, animal and microbial sources. When the origins compared; amylases from animal and plant origins are acidic, basic and have low resistance under high temperature conditions. Besides, bacterial and fungal amylases have good stability under these conditions and perform more economical production processes. Therefore; microbial enzymes have been applied in numerous biotechnological areas [6]. This is due to the characteristics of microbial amylases such as bulk production and easy genetic manipulation [7].

Microorganisms play an important role in the production of many industrially important enzymes that play a key role in hydrolyzing complex molecules [8, 9]. Amylase is the first industrially produced enzyme, although some enzymes are produced from microorganisms.

Among extracellular hydrolytic enzymes, amylases have a special status due to their high industrial value and cover about 30% of the enzyme market [10, 11]. Since almost all microorganisms of the genus *Bacillus* synthesize α-amylase, this genus has the potential for bacteria to dominate the enzyme industry [12]. The amylase production of *Bacillus* species varies greatly depending on the composition of moderate and other physical parameters. There is a need to increase amylase production without affecting the overall cost of production [13].

In the present research, bacteria isolation was performed by taking samples from the root soil of *Astragalus gummifer* plant, which is applied in many areas and has an important place especially in medical field. After isolation, bacterial species identification and biochemical tests were performed. Important parameters such as time, temperature and pH were studied to determine the optimal production conditions of the bacteria. Characterization was carried out to obtain maximum α-amylase from the bacterium, which was found to produce α-amylase of industrial importance.

2. Materials and Methods

2.1. Obtaining of biological material

Samples were taken from the root soil of the *Astragalus gummifer* plant found in Karlıova Region of Bingöl at July 2019. Plant sample identified by plant a taxonomist Dr. Ömer KILIÇ. The bacteria that used in the study were obtained from the plant sample.

2.2. Bacterial isolation

In order to obtain microorganism from soil, 1 g sample was taken and 9 ml sterile water was left on it. In this way, 10^{-1} suspension was made. Similarly, 10^{-2}, 10^{-3}, 10^{-4}, 10^{-5}, 10^{-6}, 10^{-7} dilutions were obtained by successive transfers. In order to obtain a single colony, serial dilution samples were smeared on Nutrient Agar (NA) medium and incubated for 1 night at 37ºC.

2.3. Identification of microorganisms and biochemical tests

Biochemical tests were performed to identify selected bacterial sample. As biochemical test; Gram staining, hemolysis, mobility, catalase, amylase, coagulose, and urease tests were performed separately on the bacteria. In addition, 16S rRNA sequence analysis of the isolate was performed by Epi-Gen Biotechnology. The supernatant was used to measure amylase activity. Bacterial growth in the spectrophotometer was measured as 460 nm

2.4. Amylase activity determination

Enzyme activity was performed according to DNS (Dinitrosalicylic acid) method. Bernfeld was used as a method to dissolve in 0.1 M Tris-HCl buffer pH 7.0 for 30 minutes at 37ºC using 0.5% starch as defined. One unit of amylase activity was defined as the amount of enzyme that releases reducing end groups of 1 μmol per minute at 37 ° C [14].

2.5. Protein quantity determination

Protein quantification was performed according to the Lowry method [15].

2.6. Determination of metals in soil

The contents of the soil sample taken for isolation were carried out by ICP-MS.

2.7. Effect of temperature, time and pH on microorganisms and enzyme production

The effects of time, pH and temperature parameters on bacterial growth were evaluated to determine the effect of incubation time 12 - 96. samples were analyzed at 460 nm spectrophotometer.

Temperature parameter, which has a significant effect on development, was examined. For this purpose, bacteria were produced at 25-50 ºC intervals and optimum temperature was determined. In order to determine the effect of pH on microorganism growth, optimum bacterial growth was determined between pH 4.0-10.

Time, pH and temperature effects were investigated to determine the maximum α-amylase production. Enzyme activity was determined from the samples taken for each parameter. After the analysis, spectrophotometry was also measured, and the specific activity was calculated.

2.8. Effect of temperature and pH on α-amylase activity

Maximum enzyme activity temperature and pH parameters were studied. 30-50 ºC to 5 ºC temperature values were studied in increments. Enzyme pH at different pHs between 4.0 and 11.0 were studied. Analysis was performed at 489 nm.

3. Results

3.1. Identification of microorganisms and biochemical tests

Biochemical test results showed that the bacteria were gram (+), bacillus and motile. Catalase, hemolysis, glucose and lactose were found to be positive; Biochemical tests such as

oxidase, H_2S and indole were found to be negative. Detailed results of biochemical tests are given in Table 1.

Table 1: Morphological and biochemical tests of microorganisms

Characters	*Bacillus sp*
Aerobic Growth	+
Gram	+
Catalase	+
Oxidase	-
Glucose	+
Lactose	+
H₂S	-
Indole	-
Motile	+
Urease	-
Hemolysis	+
Amylase	+

Positive:+, Negative:-

16S rRNA analysis was performed to identify single colony-reduced bacteria by dilution technique. As a result of the analysis, it was determined that the bacterium was *Bacillus* sp having 1451 bases. Below is the sequence analysis of the bacteria and the phylogenetic tree drawing

CCTTTTCGGCGGCTGGCTCCATAAAGGTTACCTCACCGACTTCGGGTGTTACA
AACTCTCGTGGTGTGACGGGCGGTGTGTACAAGGCCCGGGAACGTATTCACCGCGG
CATGCTGATCCGCGATTACTAGCGATTCCAGCTTCACGCAGTCGAGTTGCAGACTG
CGATCCGAACTGAGAACAGATTTGTGGGATTGGCTTAACCTCGCGGTTTCGCTGCC
CTTTGTTCTGTCCATTGTAGCACGTGTGTAGCCCAGGTCATAAGGGGCATGATGATT
TGACGTCATCCCCACCTTCCTCCGGTTTGTCACCGGCAGTCACCTTAGAGTGCCCAA
CTGAATGCTGGCAAC…
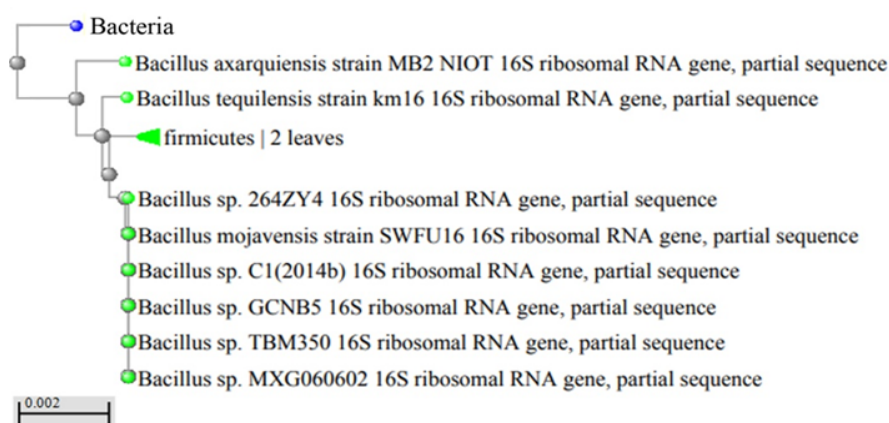
Figure 1: 16S rRNA sequence from Bacillus sp.

3.2. Analysis of sampled soil with ICP-MS

As a result of the analysis, it was determined that the amount of Al, Co, Cr, Cu, Fe, Pb, Mn and Zn in the ppb (mg L^{-1}) level was very low and Ag and Se were less in the soil

Table 2: Soil analysis results

Elements	Values (ppb, mg L^{-1})
Al	14652251
Mn	694114.2
Pb	10053.51
Co	14368.29
Cr	56887.82
Cu	28130.29
Fe	20211887
Zn	37212.81
Se	917.1169

3.3. Effect of temperature, time and pH on microorganism and enzyme production

When the incubation time was examined on microorganism development and enzyme production, it was determined that enzyme production and bacterial growth increased after 12 hours. Bacterial growth was increased depending on the duration of the most reproduction was determined at 72 hours. After this period, bacterial growth was decreased. As shown in Fig. 2, although the bacterial growth was maximum at 72 hours, α-amylase production was found to be highest at 24 hours. A decrease in α-amylase production was observed after 24 hours
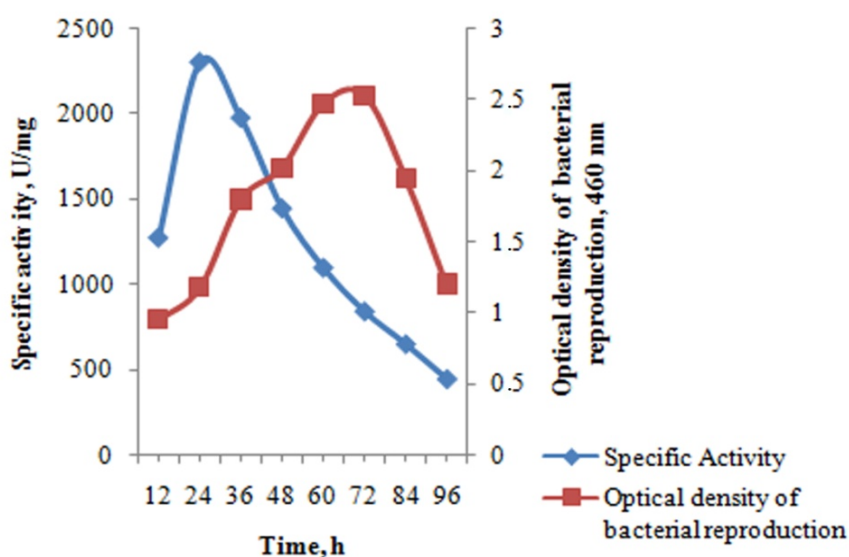
Figure 2: Effect of incubation time on microorganism development and enzyme production

Fermentation temperature and pH are also important parameters that clearly affect enzyme production. To determine the effect of temperature on bacterial growth and enzyme production, was carried out at 25-50 ºC.

Bacterial production increased from 25 ºC and maximum growth was observed at 30 ºC. It was determined that the growth decreased due to increasing temperatures. 50 ºC at the end of the reproduction was determined. When the amylase production is considered, it was observed that the maximum activity was at 30 ºC, as shown in Fig. 3, the specific activity decreases due to the increasing temperature. One unit of amylase activity was defined as the amount of enzyme that releases reducing end groups of 1 µmol per minute at 37 ºC
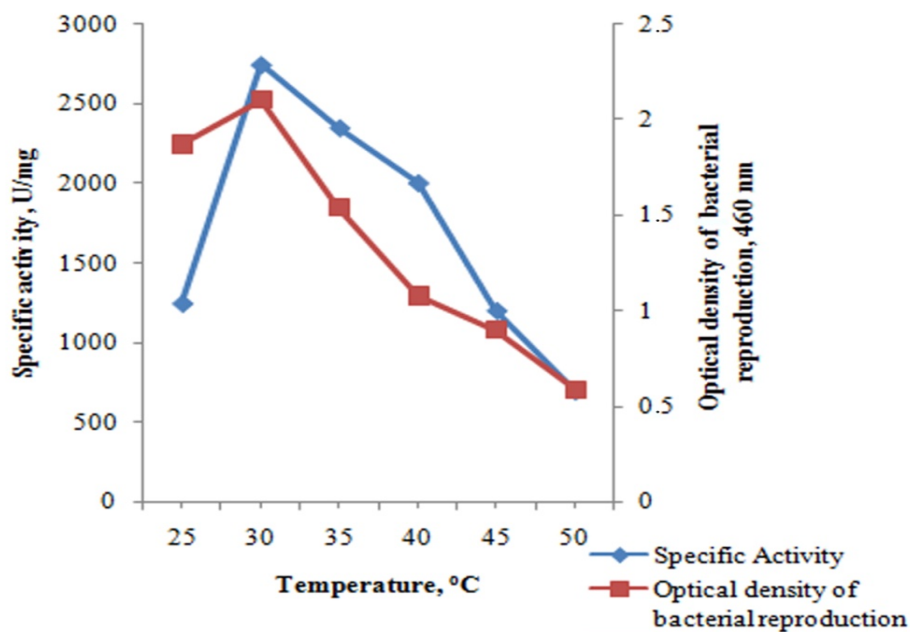
Figure 3: Effect of temperature on bacterial growth and enzyme production

Another important parameter that affects microorganism growth and enzyme production is pH. Bacterial growth was found to be between pH 5.0-10.0. The maximum reproduction pH was determined to be 7.0. At the end of the production, amylase production in pH range of 6.0-8.0 was determined. Maximum production was determined at pH 7.0
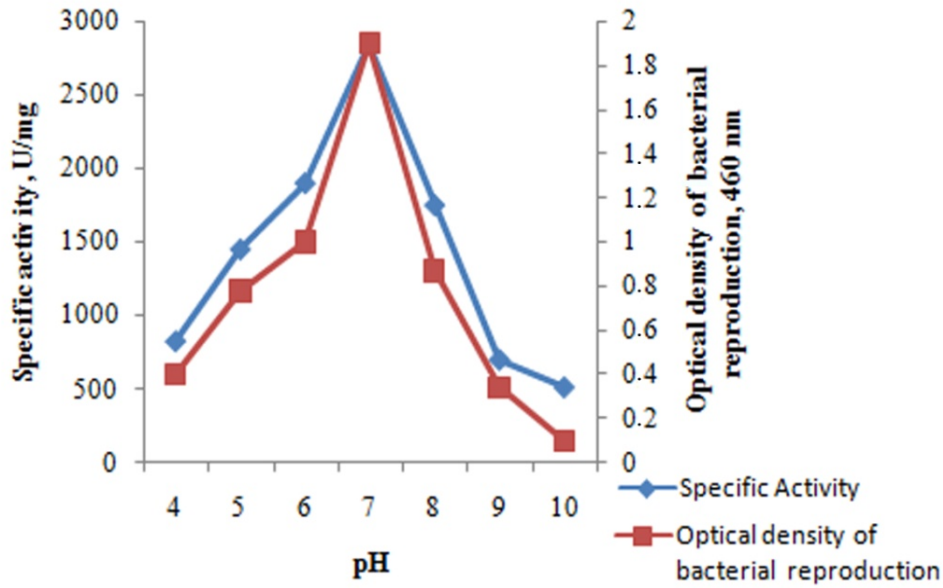
Figure 4: Effect of pH on bacterial growth and enzyme production

3.4. Effect of temperature and pH on enzyme activity

The effect of temperature on enzyme activity was investigated. For this purpose, different temperature media were used during the incubation times in the activity experiment. Thus, at which temperature the enzyme showed more activity was determined. As shown in Fig. 5, the enzyme activity was found to be high between 30-50 °C. Maximum enzyme activity was determined at 45 °C. Enzyme activity decreased due to increasing temperature 50 °C enzyme activity was determined to be 94%.
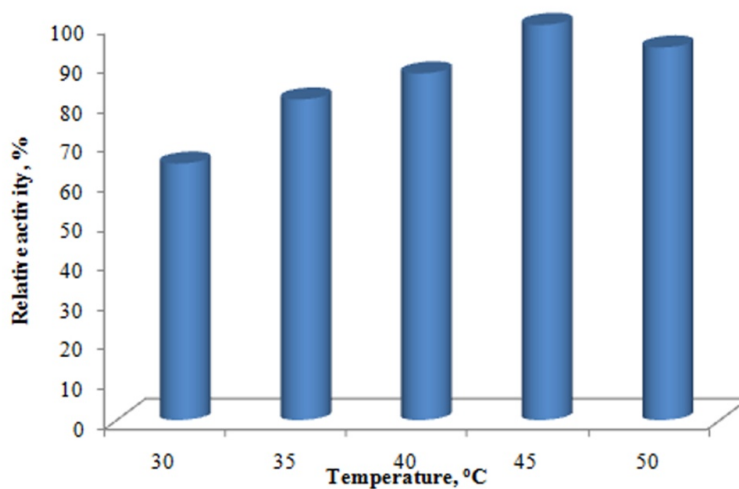
Figure 5: Effect of temperature on amylase activity

The effect of α-amylase on enzyme activity at pH 4.0-11 was investigated. The pH parameter has a significant effect on activity. As a result of the research, the maximum activity of the microorganism at neutral pH (pH 7.0) was determined. Fig. 6 provides detailed data on the effect of pH.
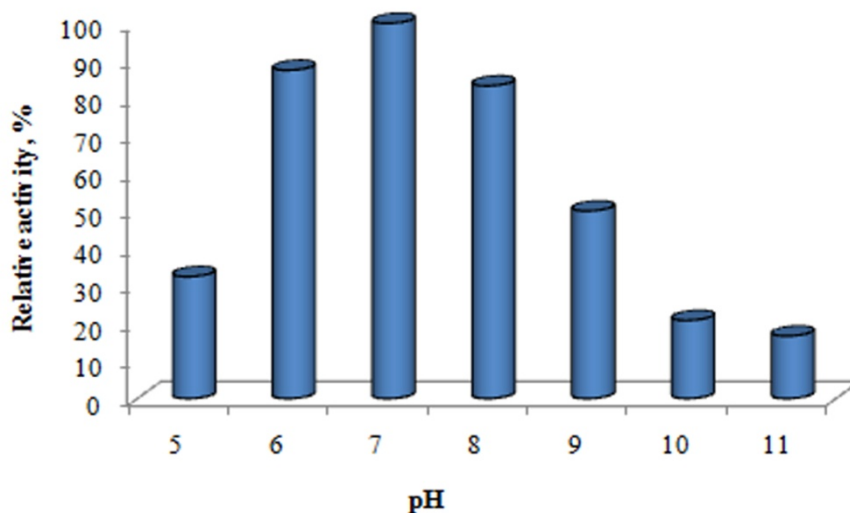
Figure 6: Effect of pH on amylase activity

4. Discussion

When the results of the research were examined, it was found that some researchers had more beneficial results than the results of this study.

For *Bacillus atrophaeus* Enez [16] found that the optimum bacterial production was at 72 hours, 30 ºC and pH 6.0; and the amylase production was at 36 hours, 35 ºC and pH 6.0. Hamilton et al. [17] found that the optimal incubation time from IMD 43 was 41 hours when and the temperature was 40 ºC. According to Asgher et al. [18] for the *Bacillus subtilis* obtained from JS-2004 amylase optimum conditions were found to be at 48 hours at 50 °C and pH 7.0. *Bacillus* sp. they carried out amylase production from EU 04. Behal et al. [19] determined optimal conditions of production at 36 hours and 40 °C, respectively. Saxena et al. [20] determined the optimum amylase production for *Bacillus* sp. that was obtained from PN5 for 60 hours at 60 °C and pH 7.0. Ozdemir et al [21] produced *Bacillus mojavensis* microorganism at 35°C, pH 7.0 and 36 hours for use in biotechnological studies. In their studies on *Bacillus atrophaeus* NRC1, Abd-Elaziz et al. [22] determined the production conditions of the bacteria as pH 6.0, 40 °C and 24 hours.

Although they show activity over a wide temperature range, the activity of amylase from many *Bacillus* species has been observed at 40 °C [3, 23]. Aguloğlu et al. [24] stated that the

maximum amylase activity of *Geobacillus stearotermophilus* bacteria was pH7.0. Wang et al. [25] determined the maximum temperature of the amylase obtained from *Rhizomucor miehei* as 75 °C and pH as 6.0.

5. Conclusions

Bacillus species found in soil flora are of great importance. Detection of these microorganisms and their use in different biotechnology fields is important. Since enzyme technology has developed, studies on industrial enzymes have become more important. Therefore, amylase which has a great industrial importance was simply produced in the present study. In addition, economic processes and optimum conditions were determined and for the production.

References

[1] Gangadharan, D., Sivaramakrishnan S., Nampoothiri, K.M., Sukumaran, R.K., Pandey, A., *Response surface methodology for the optimization of alpha amylase production by Bacillus amyloliquefaciens,* Bioresource Technology, 99, 4597–4602, 2008.

[2] Lévêque, E., Janeček, Š., Haye, B., Belarbi, A., *Thermophilic archaeal amylolytic enzymes*, Enzyme and Microbial Technology, 26, 3–14, 2000.

[3] Ashwini, K., Gaurav, K., Karthik, L., Bhaskara Rao, K.V., *Optimization, production and partial purification of extracellular α-amylase from Bacillus sp.* Marini, Archives of Applied Science Research, 3, 33–42, 2011.

[4] Vijayalakshmi, K., Sushma, S.A., Chander, P., *Isolation and characterization of Bacillus subtilis KC3 for amylolytic activity*, International Journal of Bioscience Biochemistry and Bioinformatics, 2, 33, 2012.

[5] Sanchez, A.C., Ravanal, M.C., Andrews, B.A., Asenjo, J.A., *Heterologous expression and biochemical characterization of a novel cold active α-amylase from the Antarctic bacteria Pseudoalteromonas sp. 2-3*, Protein Expression and Purification, 155, 78–85, 2019.

[6] Elmansy, E.A., Asker, M.S., El-Kady, E.M., Hassanein, S.M., El-Beih, F.M., *Production and optimization of α-amylase from thermo-halophilic bacteria isolated from different local marine environments,* Bulletin of the National Research Centre, 42, 31, 2018.

[7] Souza, P.M., Magalhaes, P.O., *Applications of microbial α-amylase in industry-a review,* Brazilian Journal of Microbiology, 41, 850–61, 2010.

[8] Pandey, A., Nigam, P., Soccol, C.R., Socco, V.T., Singh, D., Mohan, R., *Advances in microbial amylases*, Biotechnology and Applied Biochemistry, 31, 135–52, 2000.

[9] Lipson, D.A., Schadt, C.W., Schmidt, S.K., *Changes in Soil Microbial Community Structure and Function in an Alpine Dry Meadow Following Spring Snow Melt*, Microbial Ecology, 43, 307–314, 2002.

[10] Panneerselvam, T., Elavarasi, S., *Isolation of α-Amylase Producing Bacillus subtilis from Soil*, International Journal of Current Microbiology and Applied, 4: 543–552, 2015.

[11] Schallmey, M., Singh, A., Ward, O.P., *Developments in the use of Bacillus species for industrial production*, Canadian Journal of Microbiology, 50, 1, 2004.

[12] Božić, N., Ruiz, J., Santín, J.L., Vujčić, Z., *Production and properties of the highly efficient raw starch digesting α-amylase from a Bacillus licheniformis ATCC 9945a*, Biochemical Engineering Journal, 53, 203–209, 2011.

[13] Pranay, K., Padmadeo, S.R., Jha, V., Prasad, B., *Screening and identification of amylase producing strains of Bacillus,* Journal of Applied Biology Biotechnology, 1–6, 2019.

[14] Bernfeld, P., Enzymes carbohydrate metabolism, ln Methods ln Enzymology, Academic Press, 17: 149–158, 1955.

[15] Lowry, O.H., Roserbrough, N.J., Farr, A.L., Randall, R., *Protein measure ment with folin phenol reagent,* Journal of Biological Chemistry, 193, 265–275, 1951.

[16] Enez, B., *Işgının Kök Toprağından Bacillus atrophaeus'un İzolasyonu ve Tanımlanması: α-Amilaz'ın Elde Edilmesi ve Karakterizasyonu*, European Journal of Science and Technology, 177, 36–743, 2019.

[17] Hamilton, L.M., Kelly, C.T., Fogarty, W.M., *Production and properties of the raw starch digesting α-amylase of Bacillus sp. IMD 435*, Process Biochemistry, 35, 27–31, 1999.

[18] Asgher, M., Asad, M.J., Rahman, S.U., Legge, R.L., *A thermostable α-amylase from a moderately thermophilic Bacillus subtilis strain for starch processing*, Journal of Food Engineering, 79, 950–955, 2007.

[19] Behal, A., Sharma, M.K., Puri, P., Singh, J., Batra, N., *Characterization of alkaline α-amylase from Bacillus sp. AB 04*, International Journal of Agriculture and Biology, 8, 80–83, 2006.

[20] Saxena, R.K., Dutt, K., Agarwal, L., Nayyar, P., *A highly thermostable and alkaline amylase from a Bacillus sp. PN5*, Bioresource Technology, 98, 260–265, 2007.

[21] Ozdemir, S., Aguloglu Fincan, S., Karakaya, A., Enez, B., *A Novel Raw Starch Hydrolyzing Thermostable α-Amylase Produced by Newly Isolated Bacillus mojavensis SO-10: Purification, Characterization and Usage in Starch Industries*, Brazilian Archives of Biology and Technology, 61:e18160399, 2018.

[22] Abd-Elaziz, A. M., Karam, E.A., Ghanem, M.M., Moharam, M.E., Kansoh, A.L., *Production of a novel α-amylase by Bacillus atrophaeus NRC1 isolated from honey: Purification and characterization,* International Journal of Biological Macromolecules, 148, 292–301, 2020.

[23] Vaseekaran, S., Balakumar, S., Arasaratnam, V., *Isolation and identification of a bacterial strain producing thermostable α-amylase,* Tropical Agricultural Research, 22, 1–11, 2010.

[24] Aguloglu Fincan, S., Enez, B., *Production, purification, and characterization of thermostable α-amylase from thermophilic Geobacillus stearothermophilus,* Starch/Stärke, 66, 182–189. 2014.

[25] Wang, Y., Hu, H., Ma, J., Yan, Q., Liu, H., Jiang, Z., *A novel high maltose-forming α-amylase from Rhizomucor miehei and its application in the food industry*, Food Chemistry, 305, 125447, 2020.

Template Synthesis, Characterization, Antioxidant Effects, DNA Cleavage and Antimicrobial Studies of Zn[II], Ni[II], Mn[II], Cu[II], and Co[II] Complexes Containing Pyridazinone Moiety

Özlem BAKIRCI[1], Hatice Gamze SOGUKOMEROGULLARI[2], Sadin OZDEMIR[3], Mustafa Serkan YALCIN[4], Mehmet SÖNMEZ[1],*

[1]*Department of Chemistry, Faculty of Science and Arts, Gaziantep University, 27310, Gaziantep, Turkey*
vansonmez@hotmail.com or msonmez@gantep.edu.tr, ORCID: 0000-0003-3127-666X
ozlem_bakirci89@hotmail.com, ORCID: 0000-0002-2263-8617
[2]*Medical Services and Techniques Department, Health Services Vocational School, Gaziantep University, 27310 Gaziantep, Turkey*
hgcelikel@gantep.edu.tr, ORCID:0000-0002-0575-8131
[3]*Food Processing Program, Technical Science Vocational School, Mersin University, TR-33343 Yenisehir, Mersin, Turkey*
sadinozdemir@mersin.edu.tr, ORCID: 0000-0001-7384-7358
[4]*Deparment of Chemistry and Chemical Processing Technologies, Technical Science Vocational School, Mersin University, TR-33343 Yenisehir, Mersin, Turkey*
serkanyalcin@mersin.edu.tr, ORCID: 0000-0002-1134-5544

Abstract

In this study, novel five Schiff base metal complexes derived from Zn[II], Ni[II], Mn[II], Cu[II], and Co[II] metal salts and 5-benzoyl-4-hydroxy-2-methyl-6-phenyl-2H-pyridazine-3-one with o-aminophenol have been synthesized using a template method. Metal complexes were characterized by elemental analysis, FT-IR, UV-Vis, Mass and magnetic susceptibility.

Antioxidant effects, DNA cleavage, and antimicrobial studies of synthesized compounds were performed. DPPH scavenging and metal chelating activity was found to increase with concentration. The highest DPPH activity and ferrous ion chelating activity were obtained from compound Zn. DNA cleavage studies indicated that all tested compounds were cleavage active at

the concentration of 100 mg/L. While all the synthesized compounds displayed antibacterial activity against *E. hirae* in order of Mn>Zn=Ni=Co>Cu. The compound Ni only showed antimicrobial activity against all microorganisms tested, especially against *L. pneumophila* subsp. *pneumophila* with inhibition zone value equal to 13 mm.

Keywords: Template synthesis; Schiff base complex; Antioxidant activity; DNA cleavage; Antimicrobial activity.

Piridazinon Yapısı İçeren Zn^{II}, Ni^{II}, Mn^{II}, Cu^{II} ve Co^{II} Komplekslerinin Şablon Sentezleri, Karakterizasyonları, Antioksidan Etkileri, DNA Klevajı ve Antimikrobiyal Etkilerinin Araştırılması

Öz

Bu çalışmada template metodu ile o-aminofenol, 5-benzoil-4-hidroksi-2-metil-6-fenil-2H-piridazin-3-on ve Zn^{II}, Ni^{II}, Mn^{II}, Cu^{II} ve Co^{II} metal tuzlarından türeyen beş yeni Schiff baz kompleksi sentezlenmiştir. Metal kompleksler elemental analiz, FT-IR, UV-Vis, kütle ve manyetik duyarlılık ile karakterize edilmiştir. Sentezlenen bileşiklerin antioksidan etkileri, DNA bölünmesi ve antimikrobiyal çalışmaları yapılmıştır. DPPH süpürme ve metal şelatlama aktivitesinin konsantrasyona bağlı olarak arttığı bulunmuştur. En yüksek DPPH aktivitesi ve demir iyon şelatlama aktivitesi Zn bileşiğinden elde edildi. Sentezlenen tüm bileşikler, Mn>Zn=Ni=Co>Cu sırasına gore *E. hirae*'ye karşı antibakteriyal aktivite sergilerken, sadece Ni bileşiği test edilen tüm organizmalara karşı, özellikle de *L. pneumophila* subsp. *pneumophila*'ya 13 mm'ye eşit inhibisyon zon değerinde antimikrobiyal aktivite göstermiştir.

Anahtar Kelimeler: Template sentez; Schiff baz kompleks; Antioksidan aktivite; DNA bölünmesi; Antimikrobiyal aktivite.

1. Introduction

Oxidative stress is associated with production of reactive oxygen species (ROS) that are responsible for the damage of a range of cellular components [1]. Therefore, antioxidants play a very significant role in the living system in terms of protecting from oxidative stress and other chronic diseases. Nowadays, many scientists have been working on newly synthesized compounds or compounds derived from natural sources due to their antioxidant, anticancer, anticonvulsant, antitubercular, antimicrobial and anti-inflammatory activities [2, 3]. Therefore, the newly synthesized compounds are used in different fields such as molecular biotechnology, genetic engineering, drug designing. Schiff bases containing pyridazine ring are known to possess

a range of biological properties, including antibacterial, antifungal activities etc. [4]. Moreover, pyridazine derivatives and their metal complexes have various pharmacological activities [5-7]. For example, some drugs that contain the pyridazine ring in the structure are used as antihistaminic and sedative drug [6]. Pyridazinone metal complexes are rarely encountered in the literature. The complexes obtained by the template method are very limited. However, when the literature is examined, it has been observed that pyridazinone metal complexes also have antifungal, antibacterial and antitumor activity [4, 7].

In this study, we aimed to examine the antioxidant effects, DNA cleavage, and antimicrobial activities of five newly synthesized Schiff base Zn^{II}, Ni^{II}, Mn^{II}, Cu^{II}, and Co^{II} metal complexes. In order to initiate this investigation the template synthesis and characterization of Schiff base complexes of Zn^{II}, Ni^{II}, Mn^{II}, Cu^{II}, and Co^{II} was initiated and these results are first presented.

2. Materials and Methods

2.1. Chemicals and materials

All the reactants and solvents (95-99 % purity) were purchased from Aldrich or Merck and used without further purification. 5-Benzoyl-4-hydroxy-2-methyl-6-phenyl-2H-pyridazine-3-one was prepared according to the literature procedure [8]. Elemental analyses were measured on a Thermo Scientific Flash EA 2000 CHNS analyzer. Electronic absorption spectra were recorded on a PG Instruments T80+UV/Vis spectrometer. Infrared spectra were measured on a Perkin-Elmer Spectrum 100 FTIR spectrophotometer with an ATR sampling accessory. Mass spectra were obtained on a LC/MS/MS AB/SciEx 3200 Q Trap spectrometer.

2.2. General synthesis method of the complexes (1-5)

A methanolic solution (5 mL) of metal chloride ($ZnCl_2$ (0.068 g), $NiCl_2$ (0.064 g), $MnCl_2 \cdot 2H_2O$ (0.080 g), $CuCl_2 \cdot 2H_2O$ (0.085 g) and $CoCl_2$ (0.064 g), 0.5 mmol) was mixed with a suspension of 5-Benzoyl-4-hydroxy-2-methyl-6-phenyl-2H-pyridazine-3-one (0.153 g, 0.5 mmol) and o-aminophenol (0.055 g, 0.5 mmol) in 15 mL of methanol. The reaction mixture was stirred for 2 hour at 70-80 °C, the precipitate was filtered off, washed with cold MeOH-H_2O (1:1) and Et_2O, the complex was purified from slowly vapor diffusion of Et_2O with a THF-methanol solution of complex and then dried in vacuo (Scheme 1).

[ZnL(H₂O)] complex (1): White solid; Yield 0.043 g (18 %); 185 °C decompose; IR, (ATR)*v*, cm^{-1}: 3285 (O-H); 3059 (C-H)$_{arom.}$; 3028, 2945 (C-H)$_{aliph.}$; 1662 (C=O); 1577 (C=N); 1359 (C-O); 1547 (C=C); 541 (M-O); 514 (M-N). μ_{eff}: Diamagnetic; ^{1}H NMR (400 MHz, d$_6$-

DMSO) δ (ppm);s, singlet; m, multiplet: 7.69-7.25 (m, 14H, Harm), 3.80 (s, 3H, CH$_3$ protons); ^{13}C NMR (400 MHz, d$_6$-DMSO) δ (ppm); δ 196.19 (C-O)$_{pyridazine}$, 163.06 (C=N), 160.31 (C=O)$_{pyridazine}$, 149.19 (C-O)$_{phenyl}$, 138.00 (C=N)$_{pyridazine}$, 137.63 (C-N=), 133.48, 129.63, 128.97, 128.69, 128.47, 116.37 (Aromatic carbons), 40.51 (CH$_3$); UV (DMF, λ$_{max}$ nm, (Abs.)): 328 (0.223), 284 (0.693), 245 (1.724) nm; ESI-MS, m/z: 480.8 [Zn+L+H$_2$O+1]$^+$; Anal. Calc. C$_{24}$H$_{19}$N$_3$O$_4$Zn (478.82): C, 60.20, H, 4.00, N, 8.78 Found: C, 61.07, H, 4.19, N, 8.50%.

[NiL(H$_2$O)] complex (2): Green solid; Yield 0.054 g (23 %); 250 °C decompose; IR, (ATR)*v*, cm^{-1}: 3300 (O-H); 3062 (C-H)$_{arom.}$; 2940 (C-H)$_{aliph.}$; 1664 (C=O); 1578 (C=N); 1362 (C-O); 1548 (C=C); 544 (M-O); 514 (M-N); μ$_{eff}$: 2.55 B.M.; UV (DMF, λ$_{max}$ nm, (Abs.)): 336 (0.237), 285 (0.796), 245 (1.872) nm; ESI-MS, m/z: 473.0 [Ni+L+H$_2$O+1]$^+$; Anal. Calc. C$_{24}$H$_{19}$N$_3$NiO$_4$ (472.12): C, 61.06, H, 4.06, N, 8.90 Found: C, 61.46, H, 4.63, N, 8.69%.

[MnL(H$_2$O)] complex (3): Yellow solid; Yield 0.069 g (30 %); 187 °C decompose; IR, (ATR)*v*, cm^{-1}: 3350 (O-H); 3059 (C-H)$_{arom.}$; 3027, 2826 (C-H)$_{aliph.}$; 1651 (C=O); 1578 (C=N); 1378 (C-O); 1540 (C=C); 532 (M-O); 510 (M-N); μ$_{eff}$: 1.75 B.M.; UV (DMF, λ$_{max}$ nm, (Abs.)): 345 (0.068), 288 (0.339), 245 (1.020) nm; ESI-MS, m/z: 469.7 [Mn+L+H$_2$O+1]$^+$; Anal. Calc. C$_{24}$H$_{19}$MnN$_3$O$_4$ (468.36): C, 61.55, H, 4.09, N, 8.97 Found: C,61.75, H, 4.50, N, 8.46%.

[CuL(H$_2$O)] complex (4): Green solid; Yield 0.039 g (17 %); 335 °C decompose; IR, (ATR)*v*, cm^{-1}: 3150 (O-H); 3059 (C-H)$_{arom.}$; 3027, 2826 (C-H)$_{aliph.}$; 1651 (C=O); 1578 (C=N); 1378 (C-O); 1540 (C=C); 532 (M-O); 510 (M-N); μ$_{eff}$: 2.05 B.M.; UV (DMF, λ$_{max}$ nm, (Abs.)): 310 (0.367), 288 (0.339), 245 (1.020) nm; ESI-MS, m/z: 478.4 [Cu+L+H$_2$O+1]$^+$; Anal. Calc. C$_{24}$H$_{19}$CuN$_3$O$_4$ (476.97): C, 60.43, H, 4.02, N, 8.81 Found: C,60.23, H, 3.89, N, 8.38%.

[CoL(H$_2$O)] complex (5): Brown solid; Yield 0.097 g (42 %); 220 °C decompose; IR, (ATR)*v*, cm^{-1}: 3327 (O-H); 3059 (C-H)$_{arom.}$; 3027, 2935 (C-H)$_{aliph.}$; 1663 (C=O); 1578 (C=N); 1360 (C-O); 1546 (C=C); 541 (M-O); 512 (M-N); μ$_{eff}$: 5.54 B.M; UV (DMF, λ$_{max}$ nm, (Abs.)): 349 (0.222), 285 (0.767), 245 (1.938) nm; ESI-MS, m/z: 472.9 [Co+L+H$_2$O+1]$^+$; Anal. Calc. C$_{24}$H$_{19}$CoN$_3$O$_4$ (472.36): C, 61.02, H, 4.05, N, 8.90 Found: C,61.53, H, 4.57, N, 8.72%.
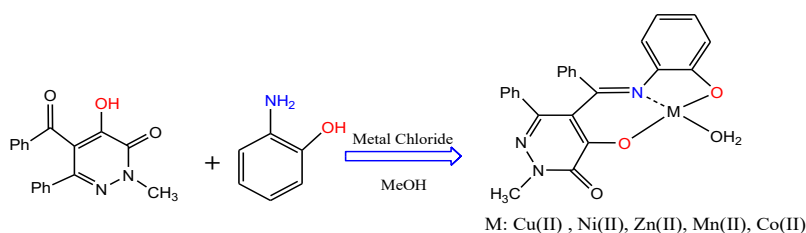
Scheme 1: Template synthesis of Schiff base metal complexes

2.3. DPPH radical scavenging assay

Different solutions (0.5 ml) in dimethylformamide (DMF) of compounds and 2 mL of 2,2-diphenyl-1-picrylhydrazyl radical (DPPH) solution were incubated at 25 ºC in the dark for half an hour [9]. DPPH scavenging activity was measured spectrophotometrically at 517 nm. A control reaction without DMF solution of compounds was performed under the same conditions. DMF solution was used as blank control. Trolox and Ascorbic Acid were used as standards in order to compare with the results. DPPH scavenging activity was determined using following equation:

$$\text{DPPH scavenging activity (\%)} = [1 - (A_{517\,nm,sample}/A_{517\,nm,control})] \times 100 \tag{1}$$

2.4. Ferrous ion chelating activity

Metal chelating effects on ferrous ions displayed by the compounds were applied as reported by Hsu et al. [10]. 1 mL of the synthesized compounds at different concentrations, $FeCl_2 \cdot H_2O$ (0.1 mL 2 mM), ferrozine-1,2,4-triazine (0.2 mL 5 mM), and methanol (3.7 mL) were mixed in test tube and kept waiting for 10 min. The activity was measured spectrophotometrically at 562 nm. A control reaction without extract was performed under the same conditions. Metal chelating effect was calculated as follows:

$$\text{Metal chelating effect (\%)} = [(A_{562nm,control} - A_{562nm,sample}) / A_{562\,nm,control}] \times 100 \tag{2}$$

Ethylene diamine tetra acetic acid (EDTA) was used as the positive control.

2.5. DNA cleavage activity

The DNA cleavage studies were carried out by using agarose gel electrophoresis. A mixture of pBR 322 plasmid DNA (0.1 mg/mL), Tris buffer (50 mMTris–HCl and NaCl buffer, pH 7.2) and the metal complexes (100 mg/L) were incubated at 37 °C for 1.5 hour. After the incubation, the loading buffer was added to the mixture prior to electrophoresis and the reaction mixture was electrophoresed for 1.5 hour at 80 V by using agarose gel. Tris-boric acid-EDTA was used as an electrophoresis buffer. The electrophoresis bands were visualized by UV-A light.

2.6. Antimicrobial activity

Antimicrobial activity of compounds was evaluated by using disk-diffusion method [11] against *Enterococcus hirae* (ATCC 10541), *Bacillus cereus*, *Staphylococcus aureus* (ATCC 6538), *Legionella pneumophila* subsp. *pneumophila* (ATCC 33152), *Pseudomonas aeruginosa* (ATCC 9027), *Escherichia coli* (ATCC 10536), and *Candida albicans*. *B. cereus* and *Candida albicans* were obtained from Siirt Public Hospital.

3. Results and Discussion

Schiff base metal complexes occurred with template effect between coordination sites of o-aminophenol and 5-benzoyl-4-hydroxy-2-methyl-6-phenyl-2H-pyridazine-3-one on a metal center (Scheme 1). New synthesized metal complexes were obtained to the general formula of $ML(H_2O)$ where L is the anion of H_2L. These metal complexes were investigated using various spectroscopic techniques, such as FT-IR, UV-Vis, mass and magnetic susceptibility, elemental analysis, and molar conductivity. The investigation showed that the molar ratio obtained by the complexes was a 1:1 metal-ligand ratio. All of the complexes are air-stable at room temperature in the solid state, soluble in DMF, methanol and insoluble in water. Molar conductivity values measured for 10^{-3} M solution in DMF of these complexes fall in the range 1.41-2.83 μS/cm, indicate the non-electronic nature for the metal complexes [12].

3.1. FT-IR spectra

The infrared spectral bands in the region 3150-3350 cm^{-1} for O-H stretching indicate the presence of coordination water molecule in all the complexes. At the same time, in the spectra of all the complexes show in ν(C-O) at 1359-1378 cm^{-1} on complexation indicate that the phenolic OH group undergoes deprotonation and is coordinated to the metal ions [7]. A broad intensity sharp bands due to ν(C=O) group pyridazine ring appeared at 1651-1664 cm^{-1} in the complexes. The spectra of complexes displaying a band around 1577-1578 cm^{-1} was observed to C=N group stretching. Additionally, the bands in the complexes at 544-532 cm^{-1} and 510-514 cm^{-1} are attributed to the ν(M-O) and ν(M-N) vibrations, respectively [13].

3.2. Electronic spectra and magnetic measurements

In the electronic spectrum of the metal complexes showed bands between 245 and 288 nm, which can be attributed to π– π* transitions of the pyridazine and phenyl aromatic rings. The bands in the 310-349 nm range can be attributed to $n{\rightarrow}\pi$* transitions of imine and carbonyl groups [14]. As expected according to magnetic measurement value of Zn^{II} complex, this complex is diamagnetic, therefore, tetrahedral geometry is suggested for **1**. The observed magnetic moment values (μ_{eff}) of Ni^{II} complex was 2.95 B.M. which this magnetic moment value lie within the range normally found for other tetrahedral Ni^{II} complexes [15]. The magnetic measurement values of Co^{II}, Cu^{II}, and Mn^{II} complexes are 4.02, 2.30 and 5.75 B.M respectively which reveal with tetrahedral geometry [16-18].

45

3.3. Mass spectra

Given that the synthesized complexes, their molecular ion peaks in the mass spectrum have a distinctive; the appearance of this molecular ion peak is strong evidence for the identity of the complexes. Molecular ion peaks of the metal complexes appeared to be in agreement with formula weight after adding on one proton at: m/z: 480.8 $[Zn+L+H_2O+1]^+$,m/z: 473.0 $[Ni+L+H_2O+1]^+$, m/z: 469.7 $[Mn+L+H_2O+1]^+$,m/z: 478.4 $[Cu+L+H_2O+1]^+$, m/z: 472.9 $[Co+L+H_2O+1]^+$.The mass spectrums of the Ni, Co and Zn metal complexes were shown in Fig. 1-3.
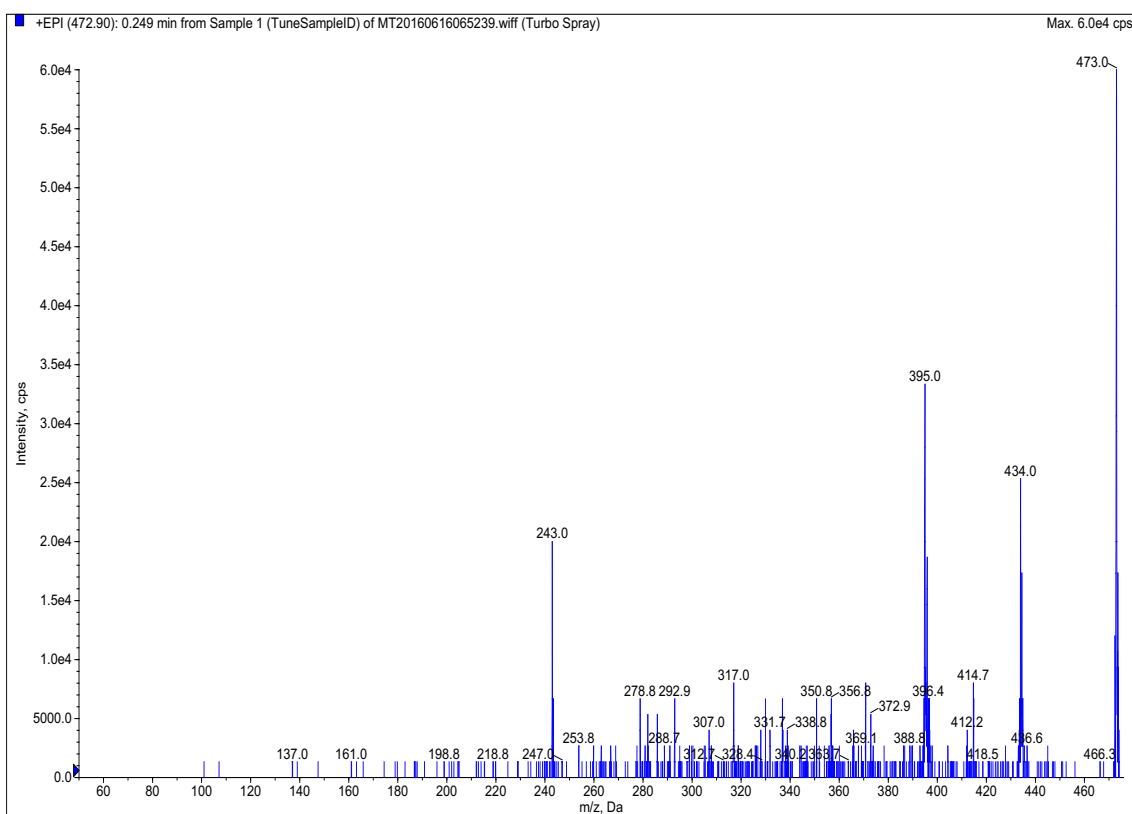
Figure 1: Mass spectrum of Ni(II) complex
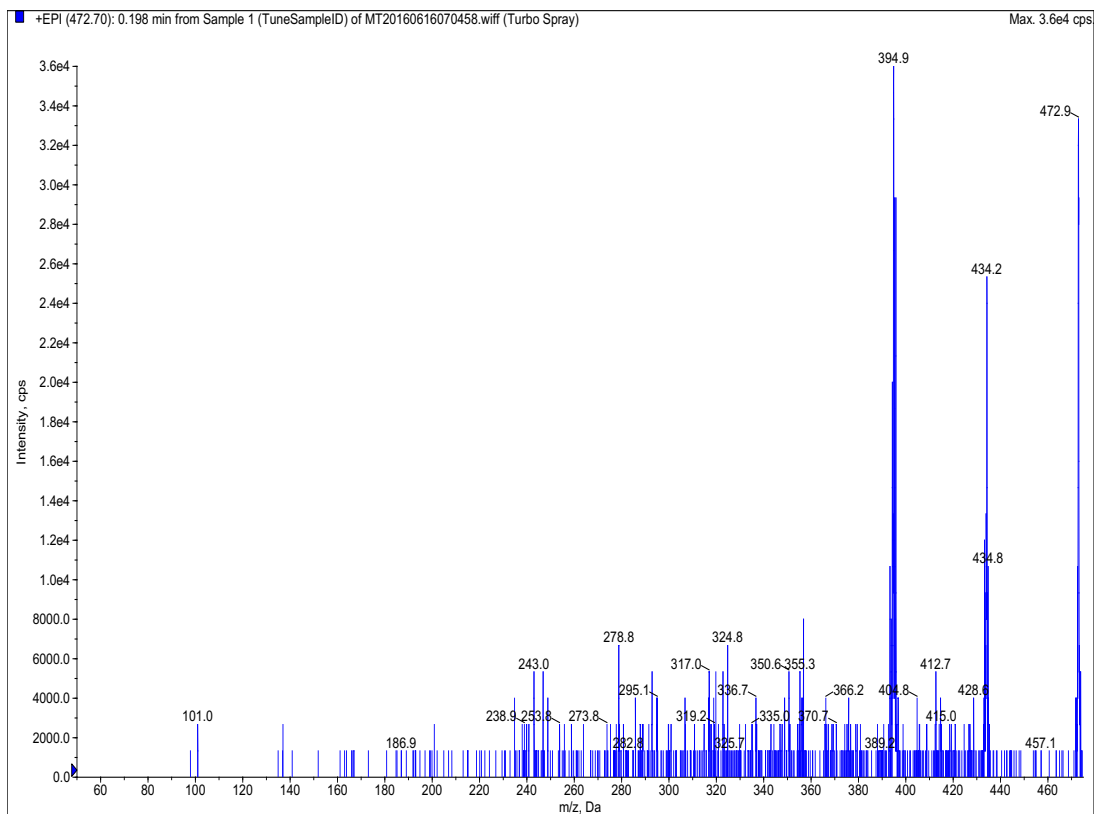
Figure 2: Mass spectrum of Co(II) complex
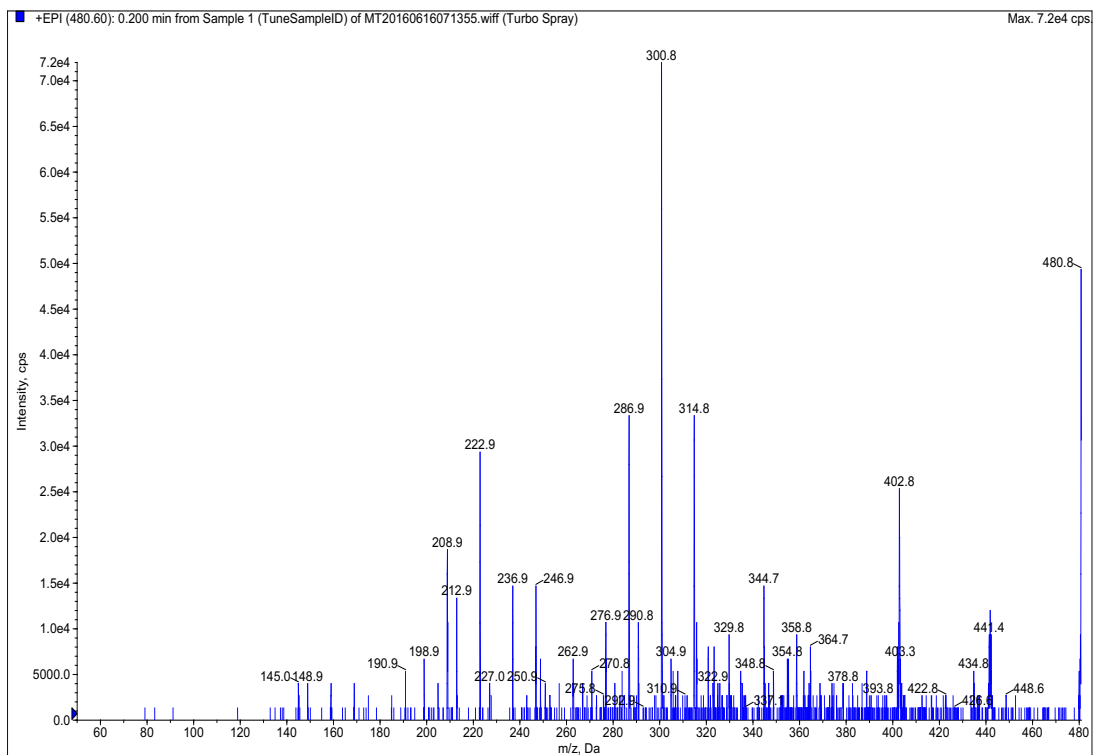
Figure 3: Mass spectrum of Zn(II) complex

3.4. Proton and carbon nuclear magnetic resonance spectra

^{1}H-NMR and ^{13}C-NMR spectrums of the Zn complex (**1**) were recorded in d_6-DMSO as a deuterated solvent. The ^{1}H-NMR spectra of the Zn complex (**1**) exhibits signals due to protons of phenyl and pyridazine rings as multiplex at δ 7.69-7.25 ppm (14 H) and CH$_3$ protons as singlet at 3.80 ppm (3H) (Fig. 4). Water peak was found at 2.51 ppm. Since there are many aromatic rings in the structure of the Zn complex, the aromatic region is complicated in the ^{1}H-NMR spectrum. The[13]C-NMR spectra of the Zn complex (**1**) exhibits signals due to of pyridazine ring (C-O) carbon at 196.19 ppm, azomethine carbon at 163.06 ppm, pyridazine ring carbonyl carbon at 160.31 ppm, phenyl ring (C-O) carbon at 149.19 ppm, pyridazine ring (C=N) carbon at 138.00 ppm, (C-N=) carbon at 137.63 ppm, aromatic carbons at 133.48-116.37 ppm and CH$_3$ carbon at 40.51 ppm (Fig. 5).
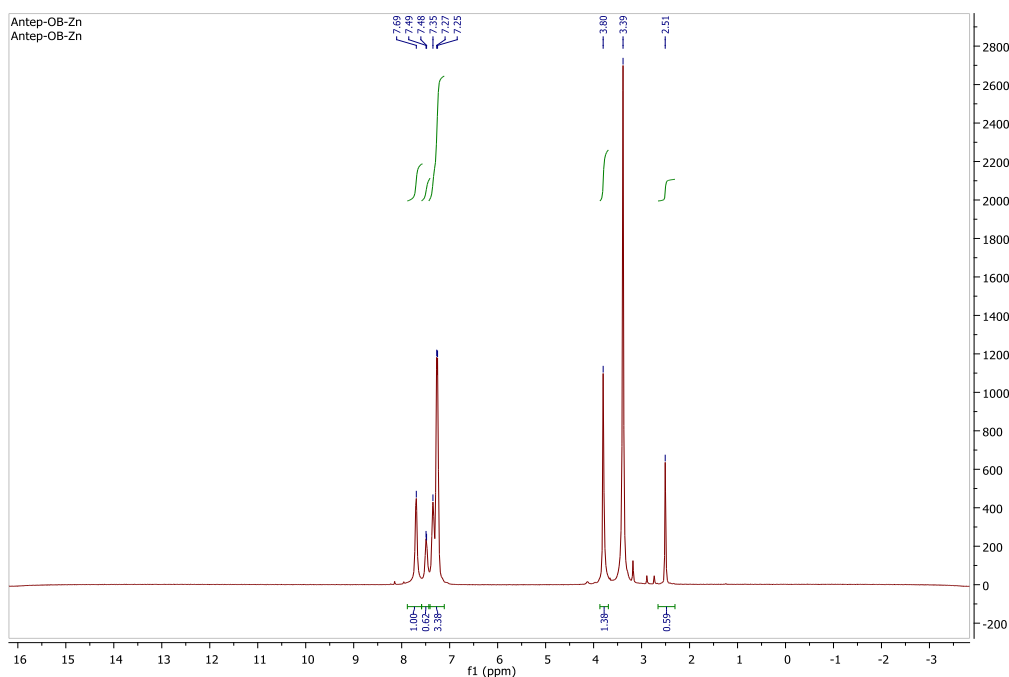
Figure 4: ^{1}H-NMR spectrum of Zn(II) complex
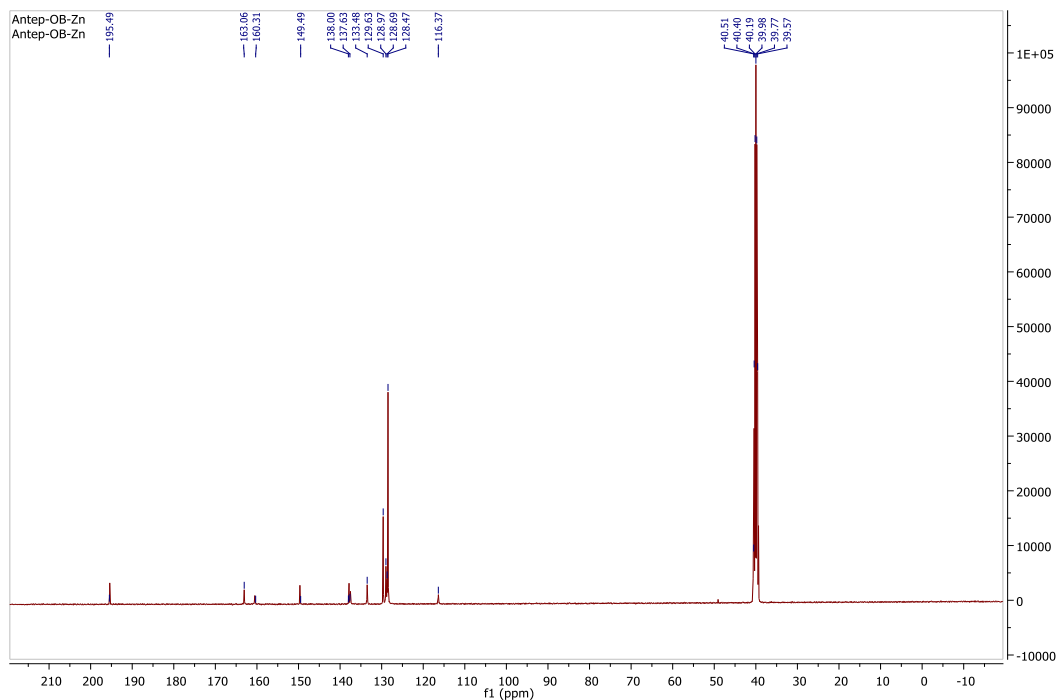
Figure 5: ^{13}C-NMR spectrum of Zn(II) complex

3.5. Antioxidant studies

3.5.1. DPPH scavenging activity

One of the most important factors that cause biological damage is free radicals. DPPH, a free radical compound that is stable at 25 °C and was widely used as a screening method for free radical scavenging activity of organic and inorganic compounds [19]. To determine the DPPH scavenging ability, various concentrations of compounds were tested by comparing with standard Ascorbic acid and Trolox. In Fig. 6, obtained results of the compounds on DPPH radical scavenging activity are presented. While the concentration was increased from 10 mg/L to 200 mg/L, DPPH ability increased from 6.1% to 38.6% mg/L and 17.8% to 84.3% mg/L for Cu and Zn, respectively. It was found that Cu had the lowest DDPH activity, while Zn had the highest. Trolox and Ascorbic acid displayed highest scavenging activity than tested other compounds. Similar results have been reported by Ağırtaş et al. [20]. The IC_{50} values of the novel pyridazine-based Zn^{II}, Ni^{II}, Mn^{II}, Cu^{II} and Co^{II} complexes were found as 46.54, 120.09, 168.99, 269.59, and 152.66 mg/L, respectively. The results indicated that the existence of Zn^{II} may contribute to the antioxidant activity.
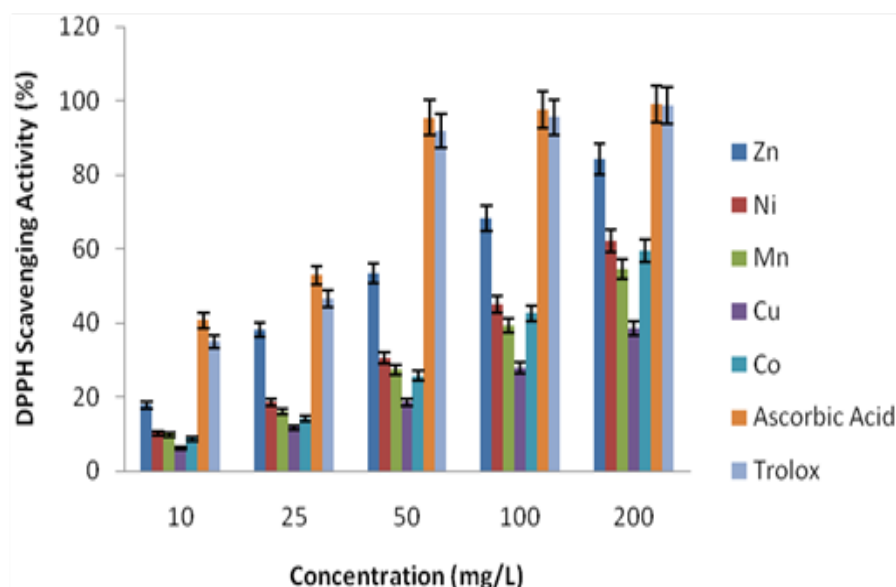
Figure 6: Free radical scavenging activity of the compounds on DPPH radicals

3.6. Metal chelating activity

In order to determine the capability of the tested compounds to bind the oxidation, catalytic ferrous ion was applied in ferrous ion chelating activity test [10]. In this study, chelating activities of DMF solutions of compounds were investigated. As can be seen in Fig. 7, when the concentration of the compounds increased, the metal chelating activities of all tested compounds increased at all tested concentration. The chelating activities of the DMF solutions of compounds at 200 mg/L concentration were 88.9% for Zn^{II}, 80.1% for Ni^{II}, 76.3% for Co^{II}, 53.4% for Mn^{II} and 31.6% for Cu^{II}. The IC_{50} values of pyridazine-based Zn^{II}, Ni^{II}, Mn^{II}, Cu^{II}, and Co^{II} were also determined as 48.82, 52.86, 184.46, 335.42, and 98.52 mg/L, respectively. According to ferrous ion chelating activity of Schiff base metal complexes, Zn^{II} was almost as good chelator as positive control (standard) EDTA.
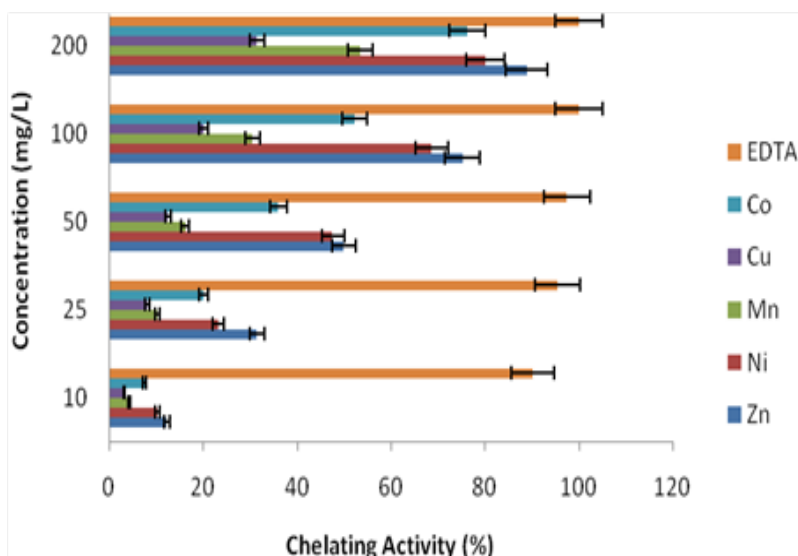
Figure 7: Metal chelating activity of compounds

3.7. Antimicrobial activity

Antimicrobial activity of the five newly synthesized compounds were examined by using disk-diffusion method and results are shown in Fig. 8. According to the results, only *E. hirae* was inhibited by all compounds and the antimicrobial activity was in order of Mn>Zn=Ni=Co>Cu. Compound 2 inhibited all microorganisms and displayed the highest antimicrobial activity against *L. pneumophila* subsp. *pneumophila* with inhibition zone value equal to 13 mm.
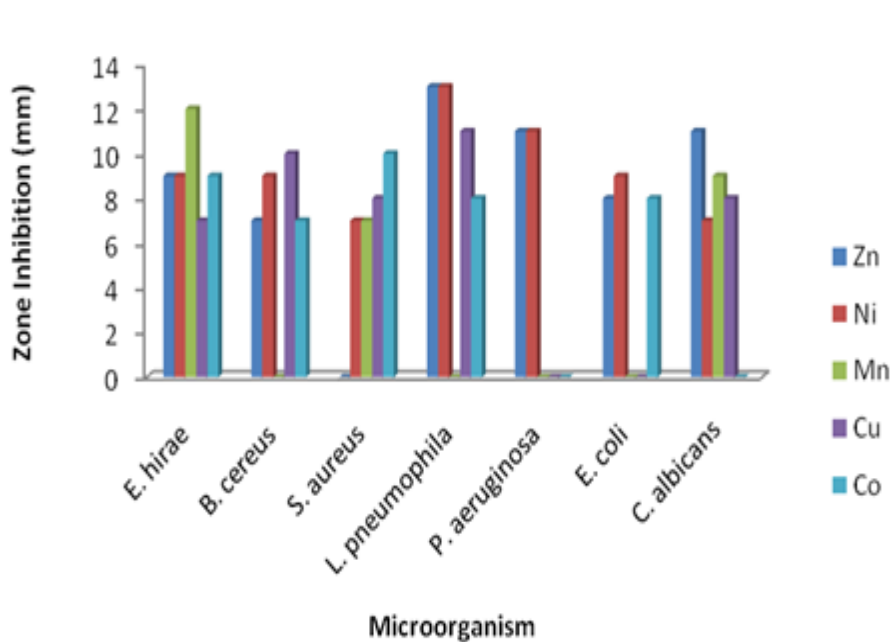
Figure 8: Antimicrobial activity of compounds

3.8. DNA cleavage studies

As seen in Fig. 9, all tested compounds cleaved the supercoiled DNA in varying extents (Lane 2, 3, 4, 5 and 6). The untreated plasmid DNA (Lane 1) and plasmid DNA with 3% DMF (Lane 7) were performed as control groups. Form I (supercoiled DNA) was converted to form II (nicked circular DNA) and form III (linear DNA) at 100 μg/mL concentrations of all complexes. From experimental results we concluded that all of the tested compounds were active in cleavage. Therefore, these metal complexes can be used as alternative anti-cancer medicine after following toxicological test systems.
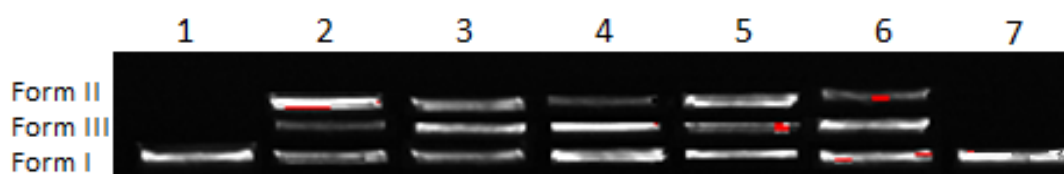
Figure 9: DNA cleavage of the metal complexes. Lane 1, pBR 322 DNA; lane 2, pBR 322 DNA + 100 μg/mL of **Zn**; lane 3, pBR 322 DNA + 100 μg/mL of **Ni**; lane 4, pBR 322 DNA + 100 μg/mL of **Mn**; lane 5, pBR 322 DNA + 100 μg/mL of **Cu**; lane 6, pBR 322 DNA + 100 μg/mL of **Co**; lane 7 pBR 322 DNA + 3%DMF

4. Conclusion

In conclusion, the novel pyridazine-based Zn^{II}, Ni^{II}, Mn^{II}, Cu^{II}, and Co^{II} Schiff base metal complexes have been synthesized using the template method. The metal complexes were characterized by elemental analysis, UV-Vis, FT-IR, Mass, magnetic susceptibility. The newly synthesized compounds displayed antioxidant activity that directly proportional to the concentration of compounds. These compounds displayed moderate DPPH scavenging and metal chelating activity except compound Zn which displayed a potent antioxidant activity compared to the standards. On the basis of DNA cleavage results, all compounds completely broke the structure of form I and form II DNA. Inhibition efficiencies of the compounds were tested against seven microorganisms. According to the inhibition results, compound Ni inhibited all microorganisms and displayed the highest antimicrobial activity against *L. pneumophila* subsp. *pneumophila*. Besides, all compounds inhibited only one microorganism called *E. hirae*. As a result this novel compounds, especially Zn compound can be used as antioxidant agents and anti-cancer drug after mutagenic test assay.

References

[1] Bilgin, R., Yalcin, M.S., Yucebilgic, G., Koltas, I.S., Yazar, S., *Oxidative stress in vivax malaria*, The Korean Journal of Parasitology, 50, 375-377, 2012.

[2] Bajpai, V.K., Baek, K.H., Kang, S.C., *Antioxidant and free radical scavenging activities of taxoquinone, a diterpenoid isolated from Metasequoia glyptostroboides*, South African Journal of Botany, 111, 93–98, 2017.

[3] Gali, R., Banothu, J., Gondru, R., Bavantula, R., Velivela, Y., Crooks, P.A., *One-pot multicomponent synthesis of indole incorporated thiazolylcoumarins and their antibacterial, anticancer and DNA cleavage studies*, Bioorganic & Medicinal Chemistry Letters, 25, 106–112, 2015.

[4] Shebl, M., Adly, O.M.I., Abdelrhman, E.M., El-Shetary, B.A., *Binary and ternary copper(II) complexes of a new Schiff base ligand derived from 4-acetyl-5,6-diphenyl-3(2H)-pyridazinone: Synthesis, spectral, thermal, antimicrobial and antitumor studies*, Journal of Molecular Structure, 1145, 329-338, 2017.

[5] Lin, S., Liu, Z., Hu, Y., *Microwave-enhanced efficient synthesis of diversified 3,6-disubstituted pyridazines*, Journal of Combinatorial Chemistry,9, 742–744, 2007.

[6] Aleeva, G.N., Zhuravleva, M.V., Khafiz'yanova, R.K., *The role of excipients in determining the pharmaceutical and therapeutic properties of medicinal agents*, Pharmaceutical Chemistry Journal, 43, 230-234, 2009.

[7] Sönmez, M., Berber, I., Akbaş, E., *Synthesis, antibacterial and antifungal activity of some new pyridazinone metal complexes*, European Journal of Medicinal Chemistry, 41, 101–105, 2006.

[8] Akbas, E., Berber, I., Sener, A., Hasanov, B., *Synthesis and antibacterial activity of 4-benzoyl-1-methyl-5-phenyl-1H-pyrazole-3-carboxylic acid and derivatives*, Il Farmaco, 60, 23–26, 2005.

[9] Blois, M.S., *Antioxidant determinations by the use of a stable free radical*, Nature, 181, 1199, 1958.

[10] Hsu, C., Chen, W., Weng, Y., Tseng, C., *Chemical composition, physical properties, and antioxidant activities of yam flours as affected by different drying methods*, Food Chemistry, 83, 85–92, 2003.

[11] Kalemba, D., Kunicka, A., *Antibacterial and antifungal properties of essential oils*, Current Medicinal Chemistry, 10, 813–829, 2003.

[12] Roy, S., Mondal, T.K., Layek, A., Saha, R., Sinha, C., *Structure, spectra and electrical conductivity of Copper(I) and Silver(I) phosphino bridging mixed ligand complexes with Coumarinyl Schiff base*, Inorganica Chimica Acta, 469, 523-535, 2018.

[13] Hassan, N., El-Sonbati, A.Z., El-Desouky, M.G., *Synthesis, characterization, molecular docking and DNA binding studies of Cu(II), Ni(II), Zn(II) and Mn(II) complexes*, Journal of Molecular Liquids, 242, 293–307, 2017.

[14] Gao, X.S., Ni, C.C., Ren, X.M., *Syntheses, crystal structures, photoluminescent and magnetic properties of complexes of zinc(II) and copper(II) with Schiff-base ligands derived from 2,6- diacetylpyridine*, Polyhedron, 138, 225-231, 2017.

[15] Fernández-Souto, P., Romero, J., García-Vázquez, J.A., Sousa, A., Perez-Lourido, P., *Electrochemical synthesis of a tetrahedral trinuclear nickel(II) complex with a tridentatedarene phosphinothiol ligand*, Inorganic Chemistry Communications, 26, 28-30, 2012.

[16] Orojloo, M., Zolgharnein, P., Solimannejad, M., Amani, S., *Synthesis and characterization of cobalt (II), nickel (II), copper (II) and zinc (II) complexes derived from two Schiff base ligands: Spectroscopic, thermal, magnetic moment, electrochemical and antimicrobial studies*, Inorganica Chimica Acta, 467, 227-237, 2017.

[17] Khulbe, R.C., Singh, R.P., Bhoon, Y.K., *Copper(II), nickel(II) and cobalt(II) complexes of pyridyl and quinolylhydrazones of isatin and methylisatin: Ligand dependent stereochemistry*, Transition Metal Chemistry, 8, 59-61, 1983.

[18] Adly, O.M.I., Shebl, M., El-Shafiy, H.F., Khalil, S.M.E., Taha, A., Mahdi, M.A.N., *Synthesis, spectroscopic characterization, antimicrobial and antitumor studies of mono-, bi- and tri-nuclear metal complexes of a new Schiff base ligand derived from o-acetoacetylphenol*, Journal of Molecular Structure, 1150, 507-522, 2017.

[19] Kitzberger, C.S.G., Smania, J.A., Pedrosa, R.C., Ferreira, S.R.S., *Antioxidant and antimicrobial activities of shiitake (Lentinula edodes) extracts obtained by organic solvents and supercritical fluids*, Journal of Food Engineering, 80, 631-638, 2007.

[20] Ağırtas, M.S., Cabir, B., Özdemir, S., *Novel metal (II) phthalocyanines with 3,4,5-trimethoxybenzyloxy-substituents: Synthesis, characterization, aggregation behaviour and antioxidant activity*, Dyes and Pigments, 96, 152-157, 2013.

Contribution of Polymorphism in PPARα Untranslated Region to The Development of Axial Spondyloarthritis

Ekrem AKBULUT[1,2,*], Metin ÖZGEN[3,4]

[1]*Munzur University, Faculty of Health Sciences, Department of Physiotherapy and Rehabilitation, Tunceli, Turkey*
[2]*Malatya Turgut Özal University, Faculty of Engineering and Natural Sciences, Department of Bioengineering, Malatya, Turkey*
ekremakbulut@gmail.com, ORCID: https: 0000-0002-7526-9835
[3]*İnönü University, Faculty of Medicine, Department of Rheumatology, Malatya, Turkey*
[4]*Ondokuz Mayıs University, Faculty of Medicine, Department of Rheumatology, Samsun, Turkey*
fmozgen@hotmail.com, ORCID: 0000-0002-6842-2918

Abstract

The study aimed to contribute to the overall understanding of axial spondyloarthritis by investigating the polymorphism in 5' untranslated region of peroxisome proliferator-activated receptor alpha gene in patients. The study included 194 patients and 197 controls recruited. The DNA obtained from the samples was genotyped by multiplex Polymerase Chain Reaction and then Matrix-Assisted Laser Desorption Ionization- Time of Flight Mass Spectrometry. Data were analyzed by logistic regression. Five polymorphic regions analyzed in this study, three of the sites were associated with disease risk. An allele in the rs1800204 polymorphic region ($p < 0.001$), C allele in the rs4253657 polymorphic region ($p = 0.040$) and C allele in the rs13909022 polymorphic region ($p = 0.005$) were associated with disease risk. The association of disease risk could not be detected with G and A alleles in the rs881740 ($p = 0.456$) and rs115640476 ($p = 0.674$) polymorphic regions, respectively. PPARα 5' untranslated region polymorphism, which is

shown to be associated with disease risk, is thought to contribute to the elucidation of the molecular mechanism of the disease. In axial spondyloarthritis, studying the effects of genetic changes in PPARα on other genes with which it interacts will contribute to the full understanding of the molecular mechanism of the disease.

Keywords: Axial spondyloarthritis; Peroxisome proliferator activated receptor alpha; Genetic predisposition; Disease risk.

PPARα Kodlanmayan Bölge Polimorfizminin Aksiyal Spondiloartrit Gelişimine Katkısı

Öz

Bu çalışma peroksizom çoğaltıcılar tarafından aktive edilen reseptör alfa geninin 5' ucu kodlanmayan bölge polimorfizminin aksiyel spondiloartrit hastalığının gelişimine olan katkısını araştırmayı ve hastalığın gelişim mekanizmasının aydınlatılmasına katkı sunmayı amaçlamaktadır. Çalışma 194 hasta ve 197 kontrol ile gerçekleştirildi. Örneklerden elde edilen DNA multipleks PCR sonrası matris aracılı lazer dezorpsiyon iyonizasyon uçuş zamanı kütle spektrometresi yöntemi kullanılarak genotipleme işlemi yapıldı. Elde edilen veriler lojistik regresyon ile analiz edildi. Bu çalışma ile analiz edilen beş polimorfik bölgenin üçü hastalık riski ile ilişkilendirildi. rs1800204 polimorfik bölgesinde A alelinin ($p < 0.001$), rs4253657 için C alelinin ($p = 0.040$) ve rs13909022 için C alelinin ($p = 0.005$) hastalık riski ile ilişkili olduğu tespit edildi. rs881740 polimorfik bölgesi için G aleli ($p = 0.456$) ve rs115640476 için A alelinin ($p = 0.674$) hastalık riski ile ilişkisi tespit edilemedi. Hastalık riski ile ilişkisi gösterilen PPARα 5' kodlanmayan bölge polimorfizminin, hastalığın moleküler mekanizmanın aydınlatılmasına katkı sunacağı düşünülmektedir. Poligenik bir hastalık olan ax-SpA'de, PPARα'daki genetik değişikliklerin etkileştiği diğer genler üzerinde ortaya çıkaracağı etkilerin çalışılması hastalığın moleküler mekanizmasının tam olarak aydınlatılmasını sağlayacaktır.

Anahtar Kelimeler: Aksiyal spondiloartrit; Peroksizom çoğaltıcılar tarafından aktive edilen reseptör alfa; Genetik yatkınlık; Hastalık riski.

1. Introduction

Axial spondyloarthritis (axSpA), a polygenic and chronic inflammatory disease with an unknown pathophysiology, affects the axial skeleton and spine. The most common form of axSpA is ankylosing spondylitis (AS) [1]. More than 7 million people worldwide are estimated to be affected by AS [2]. Peroxisome proliferator-activated receptors (PPARs), known as transcription

factors, are members of the nuclear receptor superfamily involved in the regulation of various essential biological processes. PPAR-alpha (PPARα), a type of PPAR, is a transcription factor that is activated by a fatty acid belonging to a nuclear hormone receptor family [3]. Due to its collective functions in different tissues, PPARα is an important focus of research. Although it is known to play a role in the development of several chronic diseases and in inflammatory processes, their role in the mechanism of disease development has not yet been fully identified. PPARs function as physiological sensors under different stress conditions and are valuable targets for innovative therapies [4]. Single-nucleotide polymorphisms (SNP) that have a high frequency in the human genome are known to provide important data regarding disease susceptibility, risk, etiopathogenesis and prognosis [5-7]. In addition, the gene expression of the sequences expressed as untranslated regions (UTRs) at the 5' and 3' ends of the gene regions on the genome reportedly determine the affinity of the mRNA to the ribosome, post-translational modifications, stability of the protein molecule and the stability of the three-dimensional structure [8].

In this study, we evaluated the contribution of polymorphisms in PPARα 5'untranslated region to the development of axSpA.

2. Materials and Methods

2.1. Study groups

This study included 194 ax-SpA patients (141 male and 53 female; mean age 38.10 ± 11.04; range 18 to 65 years) and 197 controls (99 male and 98 female; mean age 39.61 ± 10.34; range 20 to 69 years) recruited from the department of Rheumatology, İnönü University in Malatya, Turkey. The study protocol was approved by the ethics committee of Malatya Clinical Investigations (2016/44). A complete clinical evaluation was performed for all patients. Healthy individuals were selected for control group. Ethical rules were followed in this study and written consent of volunteers was obtained. Data collection form included information such as gender, age, disease duration, familial disease story and several clinical characteristics (Table 1).

2.2. Genomic DNA isolation

DNA isolation from peripheral blood samples was performed using Invisorb Spin Blood Mini Kit™ (Catalog Number: 1031100300). DNA concentration measurement before multiplex PCR was done using Nanodrop™. To ensure successful multiplex PCR, it was ensured that DNA concentrations were at least 20 ng/µl for each sample.

Table 1: Clinical and demographic data

Demographic Data	Case (n=194)	Control (n=197)	p-Value Odds Ratio (%95CI)
Age (Mean ± SD)	38.10 ± 11.04	39.61 ± 10.34	-
Sex (Male)	%72.7	%50.25	<0.001 2.634(1.728-4.014)
Disease duration (Year ± SD)	8.57 ± 4.72	-	-
Diagnosis delay (Year ± SD)	2.82 ± 1.41	-	-
Diagnosis of lumbar hernia before Ax-SpA (%)	45.36	-	-
Familial Ax-SpA disease story	%28.87	-	<0.001 3.266 (1.888-5.649)
Surgical intervention before symptoms occur	%10.82	%7.11	0.381 1.393 (0.664-2.922)
Suffered severe infectious disease	%11.86	%3.05	0.002 4.434(1.740-11.300)

2.3. Genotyping

Polymorphic regions were amplified by multiplex PCR using designed primer pairs. The reaction was performed as 45 cycles with pre-denaturation at 95°C for 3 min, denaturation at 95°C for 30 sec, binding at 56°C for 30 sec, elongation at 72°C for 1 min and final elongation at 72°C for 5 min. The total volume of reaction was 5 μl with the 2.5 mM of MgCl2, 2 ng of sample DNA, 1 enzyme unit, 0.1 μM of primer and 500 μM of dNTP as the final concentration in PCR. Next, 0.5 ml of Shrimp alkaline phosphatase was added to the samples for dNTP neutralisation after multiplex PCR, and the samples were then incubated at 37°C for 40 min. The samples were further incubated at 85°C for 5 min for enzyme inactivation. Next, 0.041 μl 1X enzyme, 0.940 μl elongation primer and 0.2 μl termination mixture were added to the samples for the identification of the polymorphic base, and PCR was performed as 42 cycles with pre-denaturation at 95°C for 30 sec, denaturation at 95°C for 5 sec, binding at 52°C for 5 sec, elongation at 80°C for 5 sec and final elongation at 75°C for 2 min. After the single-base elongation reaction, 16 μl of ddH2O was added to each sample. The samples were resin-coated before MALDI TOF analysis to optimise background noise. The samples were transferred to 384-element SpectroCHIP® II, and genotype analysis was performed by MALDI TOF. Primer pairs and probe information used in the single-base elongation reaction and multiplex PCR are presented in Table 2.

Table 2: Sequences of Multiplex PCR primers and single base extension probes

SNP Numbers	Primer/Probe Info	Sequence
rs1800204	Forward	ACGTTGGATGAAAGCAAGTGCGCTGGTTTC
	Reverse	ACGTTGGATGTCATACACCAGCTTGAGTCG
	Extension Probe	CCTCACAGGGCTTCTTTC
rs881740	Forward	ACGTTGGATGTTCAGGTACAGTAGGAGGAG
	Reverse	ACGTTGGATGAGCCAAACTGGACCAGCTTC
	Extension Probe	GGGTGAGGAGCAAGCCCAGG
rs4253657	Forward	ACGTTGGATGAACAGTTCTAGCCAGGCACG
	Reverse	ACGTTGGATGTGCCTCCTAGGATCAAGCAG
	Extension Probe	CTTGGAAGGCTGAGG
rs115640476	Forward	ACGTTGGATGTGTCCCTGGGGTTTGGCGCT
	Reverse	ACGTTGGATGACAACCCGAAGACCCAGAGT
	Extension Probe	CGGGTGTTTGGCGCTGCGCGGA
rs139090922	Forward	ACGTTGGATGACACGGAAAGCCCACTCTG
	Reverse	ACGTTGGATGCCCATTTCTTGCAGGAACTC
	Extension Probe	CCGGCGATCTAGAGA

2.4. Statistical analysis

The association of SNP alleles and genotypes with disease predisposition was analysed by logistic regression test (SPSS 24.0, Chicago). Power analysis was performed by using PS Power and Sample Size Program 3.1.2. Hardy-Weinberg equilibrium was evaluated by $\chi 2$ analysis. Demographic data were given as mean ± standard deviation and min/max values. "p" value smaller than 0.05 was regarded as statistically significant.

3. Results

Clinical and demographic data of patients with axSpA and healthy subjects were presented in Table 1. Disease diagnosis was delayed by 2.82 years. In this study, 28% of the patients had a family history of similar disease ($p < 0.001$), 45% of the patients had been diagnosed with lumbar disc herniation before being diagnosed with axSpA. Also 10% of patients had undergone surgery before disease symptoms manifested and 11% of patients had an important infectious disease before disease symptoms were observed ($p = 0.002$). Disease prevalence was 2.6-fold higher in males than in females [$p < 0.001$; OR 95% CI: 2.634 (1.728–4.014)] (Table 1).

In this study, allele and genotype distributions obtained from the analysis of polymorphic regions in PPARα 5'UTR are presented in Table 3. A total of five polymorphic regions were

analyzed. Three of them were associated with disease risk. A allele in the rs1800204 polymorphic region was found to be associated with disease risk (p < 0.001) and a 2-fold increase in disease risk was noted [OR 95% CI: 2.262 (1.462–3.499)]; C allele in the rs4253657 polymorphic region was found to be associated with disease risk (p = 0.040) and a 1.5-fold increase in disease risk was noted [OR 95% CI: 1.561 (1.020–2.391)] and C allele in the rs13909022 polymorphic region was found to be associated with disease risk and a 1.8-fold increase in disease risk was noted [OR 95% CI: 1.851 (1.200–2.855)]. The relationship G and A alleles in the rs881740 and rs115640476 polymorphic regions, were not found to be associated with disease risk (p = 0.456 and p = 0.674, respectively).

Table 3: PPAR-α 5'untranslated region genotyping results

| SNP | Alleles | | Case (n=194) Genotypes | | | | Control (n=197) Genotypes | | | | p-value | OR (95%CI) |
	1	2	11	12	22	MAF	11	12	22	MAF		
rs1800204	A	G	24	109	61	0.405	22	79	96	0.312	< 0.001	2.262 (1.462 – 3.499)
rs4253657	C	T	24	84	86	0.340	14	78	105	0.269	0.040	1.561 (1.020 – 2.391)
rs881740	G	A	57	85	52	0.513	41	97	59	0.454	0.456	1.198 (0.745 – 1.926)
rs115640476	A	G	27	95	72	0.384	36	77	84	0.378	0.674	1.099 (0.709 – 1.702)
rs139090922	C	G	31	94	69	0.402	29	73	95	0.332	0.005	1,851 (1.200 – 2.855)

4. Discussion

axSpA is an inflammatory disease which caused deformation of axial skeleton and consequent movement restriction and labor loss [9-11]. One of the major problems associated with axSpA is the 2 to 5year delay in its diagnosis [12, 13]. Our study is the first in literature to associate polymorphism in PPARα with disease risk and to identify the polymorphism as an alternative genetic target for early diagnosis, elucidation of molecular mechanisms of the disease and disease risk in patients with axSpA. This study showed that prevalence of disease in males was 2.6-fold higher than in females [p < 0.001; OR 95% CI: 2.634 (1.728–4.014)]. This result was consistent with the data obtained in a prevalence study conducted by Esther [14]. The mean delay of 2.82 ± 1.41 years in disease diagnosis observed in our study was showed similarity with the data reported in various studies [13, 15]. 11.86% of the patients (Table 1) had sustained serious

infectious diseases before disease symptoms had manifested [p = 0.002; OR 95% CI: 4.434 (1.740–11.300)]. This finding supports the previously reported statement that microorganism activity may have a role in disease development [16, 17]. 28.87% of the patients had a family history of axSpA [p < 0.001; OR 95% CI: 3.266 (1.888–5.649)] and the results were consistent with the data obtained by Serrano (38.4%) and Wang (36%) regarding the ethnic and community parameters [18, 19].

Although no study has yet elucidated the role of PPARα in axSpA development, several scientific studies have reported that PPARα is associated with the development of different diseases [20-22]. Dhaini et al. state that PPAR polymorphism may be related to the risk of developing cancer [23]. Dong et al. reported that PPAR polymorphism may have a role in the development of diseases such as Type 2 diabetes and metabolic syndrome [24]. Similarly, Andrulionytė et al. reported that the rs1800206 polymorphism increased the risk of developing diabetes [25]. In another study, Qian et al. analyzed the effect of PPARα and other members of the PPAR superfamily on the risk of developing coronary heart disease. In one of the studies, PPARα intron polymorphism (7G/C polymorphism [CC+GC vs GG; p = 0.003; OR 95% CI: 1.42 (1.13–1.78)] and L162V polymorphism [VV+LV vs LL; p = 0.031; OR 95% CI: 0.74 (0.56–0.97)] were found to be associated with the risk of developing coronary heart disease [26]. Fan et al. found that PPARα polymorphism increases the risk of developing atherosclerosis and cardiovascular disease [27].

The human PPARα gene is a 93.2-Kb gene located on chromosome 22 at position 22q12-q13.1 encoding a protein of 468 amino acids [28]. The gene contains a total of 8 exons. The 5' UTR, including the polymorphic regions that are the focus of our study, is encoded by exons 1 and 2 and partially by exon 3 [28, 29]. PPARα has an important role in reducing inflammation. PPARα activity has an effect on neutrophils and macrophages in both acute and chronic inflammatory diseases. Leukotriene B4 (LTB4), a potent chemotactic inflammatory eicosanoid, is an endogenous PPARα ligand. Like other PPARα ligands, it induces the transcription of the genes of β- and PP-oxidation pathways that neutralize and reduce LTB4, to regulate inflammatory response [30]. PPARα regulates the duration of the inflammatory response by limiting cytokine expression and inducing genes that metabolize LTB4 [30].

5. Conclusions

The data obtained from the present study showed that the rs1800204, rs115640476 and rs139090922 polymorphic regions located in 5' UTR of PPARα, which are responsible for suppressing inflammatory response, are increased axSpA risk. Evaluation of results suggests that

changes in 5' UTR can downregulate PPARα expression. This may suppress LTB4-metabolising genes leading to increased LTB4 activity, which ultimately contributes to the prolonged duration of the inflammatory response. The genes that are involved in the inflammatory response and interact with PPARα may offer significant opportunities to completely understand the disease mechanisms and to determine appropriate treatment strategies.

Acknowledgement

Ethical Considerations

Ethical rules were followed in this study and written consent of volunteers was obtained. The study protocol was approved by the ethics committee of Malatya Clinical Investigations (2016/44).

Conflict of Interest

There is no conflict of interest among the authors.

References

[1] Sharma, S.M., Choi, D., Planck, S.R., Harrington, C.A., Austin, C.R., Lewis, J.A., et al., *Insights in to the pathogenesis of axial spondyloarthropathy based on gene expression profiles*, Arthritis Research & Therapy, 11(6), R168, 1-9, 2009.

[2] Dean, L.E., Jones, G.T., MacDonald, A.G., Downham, C., Sturrock, R.D., Macfarlane, G. J., *Global prevalence of ankylosing spondylitis*, Rheumatology, 53, 650-657, 2014.

[3] Dubrac, S., Schmuth, M., *PPAR-alpha in cutaneous inflammation*, Dermato-Endocrinology, 3, 23-26, 2011.

[4] Yessoufou, A., Wahli, W., *Multifaceted roles of peroxisome proliferator-activated receptors (PPARs) at the cellular and whole organism levels*, Swiss Med Wkly, 140, w13071, 2010.

[5] Ruan, W.F., Xie, J.T., Jin, Q., Wang, W.D., Ping, A.S., *The diagnostic and prognostic role of interleukin 12B and Interleukin 6R gene polymorphism in patients with ankylosing spondylitis*, JCR: Journal of Clinical Rheumatology, 24,18-24, 2018.

[6] Wordsworth, B.P., Cohen, C.J., Vecellio, M., *Quantifying the genetic risk for the development of axial spondyloarthropathy: could this become a diagnostic tool?*, Current Opinion in Rheumatology, 30, 319-323, 2018.

[7] Fabris, M., Quartuccio, L., Fabro, C., Sacco, S., Lombardi, S., Ramonda, R., et al., *The-308 TNFα and the-174 IL-6 promoter polymorphisms associate with effective anti-TNFα treatment in seronegative spondyloarthritis*, The Pharmacogenomics Journal, 16, 238, 2016.

[8] Chatterjee, S., Pal, J.K., *Role of 5'-and 3'-untranslated regions of mRNAs in human diseases*, Biology of The Cell, 101, 251-262, 2009.

[9] Sieper, J., Poddubnyy, D., *Axial spondyloarthritis*, The Lancet, 390, 73-84, 2017.

[10] Barlow, J., Wright, C., Williams, B., Keat, A., *Work disability among people with ankylosing spondylitis*, Arthritis Care & Research: Official Journal of The American College of Rheumatology, 45, 424-429, 2001.

[11] Ramonda, R., Marchesoni, A., Carletto, A., Bianchi, G., Cutolo, M., Ferraccioli, G., et al., *Patient-reported impact of spondyloarthritis on work disability and working life: the ATLANTIS survey*, Arthritis Research & Therapy, 18, 78, 2016.

[12] Behar, V.M., Dougados, M., Etcheto, A., Kreis, S., Fabre, S., Hudry, C., et al., *Diagnostic delay in axial spondyloarthritis: A cross-sectional study of 432 patients*, Joint Bone Spine, 84, 467-471, 2017.

[13] Redeker, I., Callhoff, J., Hoffmann, F., Haibel, H., Sieper, J., Zink, A., et al., Determinants of diagnostic delay in axial spondyloarthritis: an analysis based on linked claims and patient-reported survey data, Rheumatology, 58(9), 1634-1638, 2019.

[14] Yi, E., Ahuja, A., Rajput, T., George, A.T., Park, Y., *Clinical economic and humanistic burden associated with delayed diagnosis of Axial Spondyloarthritis: A Systematic Review*, Rheumatology Therapy, 7, 65–87, 2020.

[15] Nie, A., Wang, C., Song, Y., Xie, X., Yang, H., Chen, H., *Prevalence and factors associated with disturbed sleep in outpatients with ankylosing spondylitis*, Clinical Rheumatology, 37, 2161-2168, 2018.

[16] Zhang, L., Zhang, Y.J., Chen, J., Huang, X.L., Fang, G.S., Yang, L.J., et al., *The association of HLA-B27 and Klebsiella pneumoniae in ankylosing spondylitis: A systematic review*, Microbial Pathogenesis, 117, 49-54, 2018.

[17] Braun, J., Sieper, J., *Ankylosing spondylitis*, The Lancet, 369, 1379-90, 2007.

[18] Serrano, P., Navarro-Compán, V., Rodríguez, S., Fernández, M., Zarco, P., de Miguel, E., *SAT0419 Similarities and differences between HLA B27 positive and HLA B27 negative spondyloarthritis: results from the esperanza cohort*, Annals of The Rheumatic Disease, 76(2), 930, 2017.

[19] Wang, R., Gabriel, S.E., Ward, M.M., *Progression of nonradiographic axial spondyloarthritis to ankylosing spondylitis: a population-based cohort study*, Arthritis & Rheumatology, 68, 1415-1421, 2016.

[20] Ruscica, M., Busnelli, M., Runfola, E., Corsini, A., Sirtori, C.R., *Impact of PPAR-alpha polymorphisms-the case of metabolic disorders and atherosclerosis*, Int. J. Mol. Sci., 20(18), 4378, 2019.

[21] Sergeeva, E.G., Berkovich, O.A., Ionova, Z.I., Zaraisky, M.I., Baranova, E.I., *L162v Polymorphism of Par-A gene, A603g polymorphism of tissue factor gene and risk of coronary heart disease in Russian population*, Journal of Bioinformatics and Diabetes, 1(4), 1-11, 2019.

[22] Rashid, A., Jafar, S., Yaqub, R.K., *Role of peroxisome proliferator-activated receptor (PPAR)-α gene in Dyslipidemia*, Rawal Medical Journal, 45(1), 54-57, 2020.

[23] Dhaini, H.R., Daher, Z., *Genetic polymorphisms of PPAR genes and human cancers: evidence for gene–environment interactions*, Journal of Environmental Science and Health, 37(3), 146-179, 2019.

[24] Dong, C., Zhou, H., Shen, C., Yu, L.G., Ding, Y., Zhang, Y.H., et al., *Role of peroxisome proliferator-activated receptors gene polymorphisms in type 2 diabetes and metabolic syndrome*, World Journal of Diabetes, 6(4), 654-661, 2015.

[25] Andrulionytė, L., Kuulasmaa, T., Chiasson, J.L., Laakso, M., Single *Nucleotide Polymorphisms of the Peroxisome Proliferator–Activated Receptor-α Gene (PPARA) Influence the Conversion from Impaired Glucose Tolerance to Type 2 Diabetes: The STOP-NIDDM Trial*, Diabetes, 56, 1181-1186, 2007.

[26] Qian, Y., Li, P., Zhang, J., Shi, Y., Chen, K., Yang, J., et al., *Association between peroxisome proliferator-activated receptor-alpha, delta, and gamma polymorphisms and risk of coronary heart disease: A case–control study and meta-analysis*, Medicine, 95(32), e4299, 1-9, 2016.

[27] Fan, W., Shen, C., Wu, M., Zhou, Z.Y., Guo, Z.R., *Association and interaction of PPARα, δ, and γ gene polymorphisms with low-density lipoprotein-cholesterol in a Chinese Han population*, Genetic Testing and Molecular Biomarkers, 19, 379-386, 2015.

[28] Sher, T., Yi, H.F., McBride, O.W., Gonzalez, F.J., *cDNA cloning chromosomal mapping and functional characterization of the human peroxisome proliferator activated receptor*, Biochemistry, 32, 5598-5604, 1993.

[29] Desvergne, B., Wahli, W., *Peroxisome proliferator-activated receptors: nuclear control of metabolism*, Endocrine Reviews, 20, 649-688, 1999.

[30] Devchand, P.R., Keller, H., Peters, J.M., Vazquez, M., Gonzalez, F.J., Wahli, W., *The PPARα–leukotriene B4 pathway to inflammation control*, Nature, 384(39), 39-43 ,1996.

Avifauna and Important Bird Areas (IBA) of Elazığ Province

Emrah ÇELİK[1,*]

[1]*Igdir University, Vocational School of Technical Sciences, Department of Forestry/Hunting and Wildlife Programme, Igdir, Turkey*
celikemrah822@gmail.com, ORCID: 0000-0003-1274-4122

Abstract

Along with the present study, the bird species and wetland status of Elazig province were investigated. According to the observation between October 2016 and May 2018, 181 species belonging to 18 orders and 44 families were identified. Of the reported species herein, 61 are resident (33.7%), 81 are summer visitors (44.8%), 20 are winter visitors (11.1%), and 19 are passage migrant (10.5%). Among these species, it has been determined that 10 species are threatened with extinction at national and international (IUCN) scale. 1 species as EN (Endangered) (*Neophron percnopterus*), 7 species as NT (Near Threatened) (*Gypaetus barbatus, Aegypius monachus, Circus macrourus, Vanellus vanellus, Limosa limosa, Larus armenicus, Anthus pratensis*), 2 species as VU (Vulnerable) (*Aythya ferina, Streptopelia turtur*) were reported here. Herewith the study, by drawing attention to the wetlands that shape the richness of the bird species in Elazig Province, the bird species that breed and stay in those areas and the threats to the species and habitats and the precautions to be taken were investigated.

Keywords: Biodiversity; Birds; Wetland; Ornithofauna; GIS.

Elazığ İli Avifaunası ve Önemli Kuş Alanları (ÖKA)

Öz

Bu çalışmada Elazığ İlinin kuş türleri ve sulak alan varlığı araştırılmıştır. Araştırmada Ekim 2016 - Mayıs 2018 tarihleri arasında gerçekleştirilen arazi gözlem sonuçları değerlendirilmiş, 18 takım ve 44 familyaya ait 181 tür tespit edilmiştir. Bu türlerden 61'i yerli (% 33.7), 81'i yaz ziyaretçisi (% 44.8), 20'si kış ziyaretçisi (% 11.1) ve 19'u transit göçerdir (% 10.5). Bu türler arasında 10 türün ulusal ve uluslararası (IUCN) ölçeğinde yok olma tehdidi altında olduğu belirlenmiştir. 1 tür EN (Endangered-Tehlikede) (*Neophron percnopterus*), 7 tür NT (Near-Threatened-Yakın gelecekte tehlikede) (*Gypaetus barbatus*, *Aegypius monachus*, *Circus macrourus*, *Vanellus vanellus*, *Limosa limosa*, *Larus armenicus*, *Anthus pra*tensis), 2 tür VU (Vulnarable-Hassas) (*Aythya ferina, Streptopelia turtur*) olarak verilmiştir.

Bu çalışmada, Elazığ İlinin sahip olduğu kuş türlerinin zenginliğini şekillendiren sulak alanlara dikkat çekilerek, bu alanlarda üreyen ve konaklayan kuş türleri ile türlere ve yaşam alanlarına yönelik tehdit unsurları ve alınması gereken tedbirler araştırılmıştır.

Anahtar Kelimeler: Biyoçeşitlilik; Kuşlar; Sulak alan; Ornitofauna; CBS.

1. Introduction

Wetlands are the most productive ecosystems in the world. [1-3]. In addition to the providing biodiversity, wetlands exhibit significant roles in climate control, maintaining the water cycle [4, 5], water treatment and flood prevention [6]. Furthermore, wetlands provide a wide range of biological communities [7, 8], as well as providing significant support to wildlife [9-11]. Birds, which are among the important animals of wildlife, are indicator livings of a healthy ecosystem [12]. Due to the locating on the upper steps of the food chain, the birds possess significant activities and roles for the functioning of the ecosystem [13]. Birds, which spread in almost all of the aquatic and terrestrial ecosystems in the world, are accepted as bio-indicator livings because they respond to any changes deviating from the optimal conditions occurring in the natural ecosystems [12, 14]. Due to the constituting a part of the Palearctic region, Turkey has an important position with respect to the bird migration routes between Europe, Asia and Africa, accommodating the different climatic conditions and different living environments due to its geographical location. Herein it is worthy to note that two important bird migration routes pass through Turkey. Those transitions generally take place through Cyprus and Hatay. Birds enter Anatolia through Cyprus and Hatay. Then, firstly, they cross over the lakes region to Europe and Russia using the straits and the Eastern Black Sea main migration routes, using the wetlands in

the Mediterranean coastline and the transition points of the Taurus Mountains.

All these major reasons significantly increase the biodiversity wealth of Turkey, attracting many national and international researchers. Subsequently, many species lists from different regions of Turkey have been reported [15-34]

The number of bird species was reported as 460 [35], 468 [36] and 502 [37] with random species.

Along with the study, it was targeted to draw attentions towards wetland richness of the bird in Elazig province, breeding and hosting areas, threats to the species, habitats, and finally plausible precautions with recommendations

2. Materials and Methods

2.1. Characteristics of the study area

Elazig is located in the Upper Euphrates part of the Eastern Anatolia region of Turkey. It is adjacent to the provinces of Tunceli in the north, Bingöl in the east, Diyarbakır in the southeast and Malatya in the west (Fig. 1). Elazig province is located between 38° 14'and 39° 11' north latitudes and 38° 22'and 40° 22' east longitudes.
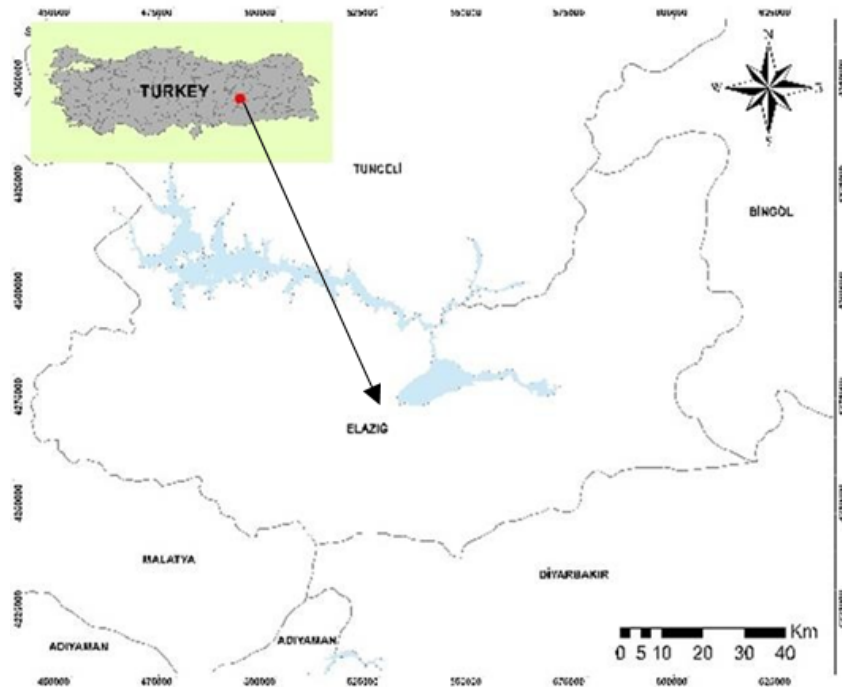
Figure 1: Location map of Elazig province

2.2. Habitat

Regarding the habitat structure of Elazig, there are alpine meadows and small bushes plantations in the higher parts. The dominant vegetation in the high regions is steppe. Forest ecosystems are noticeable in low areas. Some parts have bare vegetation areas and rocky and stony areas (Fig. 2).
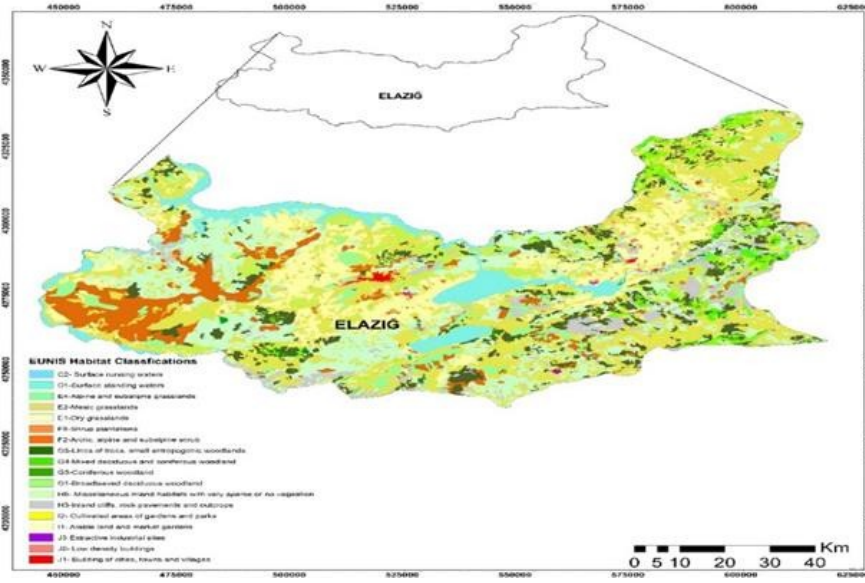
Figure 2: Habitat structure of Elazig province

On the EUNIS habitat types Map formed for Elazig Province, the size and distribution of these habitat types on the areal basis and the number of parts were presented in Table 1 [38].

Table 1: EUNIS habitat types areal sizes and part distributions in Elazig province

EUNIS HABITAT TYPES	Number of Polygons	Area (ha)
C1 Surface stagnant inland waters	9	8065,53
C2 Streams	81	52003,33
E2 Moist meadows	7	18617,14
FB Shrub grove	4	528,144
F5 Lemur, trees and temperate Mediterranean shrubs	3	18,745
G1 Broadleaf deciduous forests	726	128350,1
G3 Conifer forests	253	12592,04
G4 Deciduous and coniferous mixed forests	50	5260,693
H1 Terrestrial underground caves, cave systems	1	0,148
H3 Inner cliffs and rock ledges	3	3010,715
H5 Various indoor habitats with little or no vegetation	683	368241,1
I1 Arable land and gardens	1663	307998,9
J1 City, town and village buildings	329	17112,07
J3 Mine extraction areas	69	1288,275

2.2.1. Criteria used in determining important areas for birds (IBA)

Area and conservation biology are of great importance for living species to form a healthy community and continue their life cycle. The first step is to protect the habitats of living things without damage to the area's natural features. IBAs are determined by scientific criteria accepted all over the world. Sensitivity criterion, one of the two main approaches under the concept of IBA, is used in determining the areas where important populations of bird species, which are in the danger category, are in the world scale. The other criterion is the Uniqueness criterion. This criterion is used to identify areas of importance for narrow-spread species, single biome-dependent species and condensed species [39].

In this study, above-mentioned issues were taken into consideration while determining the areas that can be considered as important for birds.

2.3. Data collection

For the present study, in order to determine the ornithofauna of Elazig province, a 51-day observation study was carried out between October 2016 and May 2018. Detailed information with respect to the observations was presented in Table 2.

Table 2: Information regarding three consecutive year observation in Elazig province

	Jan.	Feb.	March	April	May	June	July	Aug.	Sept.	Oct.	Nov.	Dec.	Total
2016	-	-	-	-	-	-	-	-	3	3	3	-	9
2017	-	-	3	3	4	-	3	3	2	3	3	3	27
2018	3	3	3	3	3	-	-	-	-	-	-	-	15
Total	**3**	**3**	**6**	**6**	**7**	**-**	**3**	**3**	**5**	**6**	**6**	**3**	**51**

Field studies were carried out in accordance with the monthly working schedule. Field observations started early in the morning when the species were active and continued until sunset, when the optical instruments did not get enough images. For birds, the population densities, arrival and departure times, distribution in the study area, status, and locations in the red list were determined.

In order to determine population density and the number of individuals, the line transects and point counts method were used [40].

In determining the species inventory and population density studies, dominant points and habitats where birds are concentrated were taken into consideration, and field scanning was done

with telescope and binoculars.

During observations, camera (Canon-650D), optical zoom lens (Canon 400mm), binoculars, GPS, 1/25000 topographic map, telescope (Konuspot 100mm) and diagnostic books were used as equipment.

3. Results

The results of the study revealed that 181 species belonging to 18 orders and 44 families were identified. Of the reported species herein, 61 are resident (33.7%), 81 are summer visitors (44.8%), 20 are winter visitors (11.1%), and 19 are passage migrant (10.5%) according to the observation between October 2016 and May 2018 (Table 3). Of those identified species, it has been determined that 10 species are threatened with extinction at national and international (IUCN) scale. 1 species as EN (Endangered) (*Neophron percnopterus*), 7 species as NT (Near Threatened) (*Gypaetus barbatus, Aegypius monachus, Circus macrourus, Vanellus vanellus, Limosa limosa, Larus armenicus, Anthus pratensis*), 2 species as VU (Vulnarable) (*Aythya ferina, Streptopelia turtur*) were reported herein.

According to the species identified by order, Podicipediformes 3, Pelecaniformes 9, Suliformes 2, Ciconiiformes 2, Anseriformes 10, Accipiteriformes 18, Falconiformes 3, Galliformes 3, Gruiformes 2, Charadriiformes 23, Columbiformes 5, Cuculiformes 1, Strigiformes 3, Caprimulgiformes 3, Coraciiformes 1, Strigiformes 3, Caprimulgiformes 3, Coraciiformes 1, and Passeriformes are represented by 88 species. The province is mostly represented with Passeriformes and Cuculiformes and Cuculiformes orders are least represented in the province (Fig. 3).
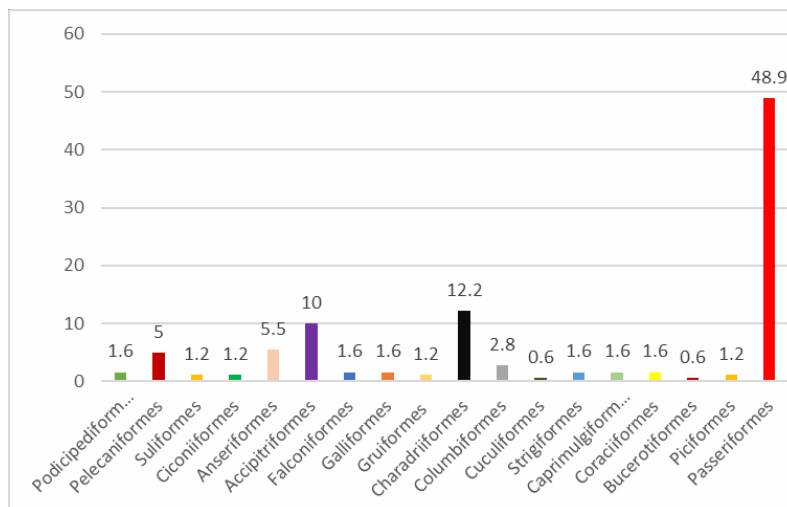
Figure 3: Percentage of the bird species in the area by ordo

Table 3: Bird species and their status determined in Elazig Province

Species list	R.S	O.N.S		IUCN	E.P.S
		Min.	Max.		
Tachybaptus ruficollis	R	2	41	LC	LC
Podiceps cristatus	R	2	29	LC	LC
Podiceps grisegena	SV	1	6	LC	LC
Botaurus stellaris	R	1	2	LC	Depleted
Ixobrychus minutus	SV	1	2	LC	Depleted
Nycticorax nycticorax	R	3	27	LC	Declining
Ardeola ralloides	S	1	5	LC	Depleted
Bubulcus ibis	SV	1	9	LC	LC
Egretta garzetta	R	4	11	LC	LC
Ardea alba	R	2	8	LC	LC
Ardea cinerea	R	3	9	LC	LC
Ardea purpurea	PM	1	2	LC	Declining
Phalacrocorax carbo	R	4	57	LC	LC
Plegadis falcinellus	SV	1	7	LC	LC
Ciconia nigra	PM	1	1	LC	LC
Ciconia ciconia	SV	3	17	LC	LC
Tadorna ferruginea	R	4	518	LC	Depleted
Tadorna tadorna	WV	4	46	LC	LC
Anas crecca	R	2	24	LC	LC
Anas platyrhynchos	R	2	186	LC	LC
Anas acuta	WV	2	87	LC	Declining
Spatula querquedula	WV	4	54	LC	Declining
Spatula clypeata	R	3	19	LC	LC
Netta rufina	SV	1	8	LC	LC
Aythya ferina	WV	4	97	VU	VU
Aythya fuligula	WV	4	27	LC	Declining
Milvus migrans	R	2	19	LC	Depleted
Gypaetus barbatus	R	1	1	NT	VU
Neophron percnopterus	R	1	7	EN	EN
Gyps fulvus	R	1	1	LC	LC
Aegypius monachus	R	1	1	NT	Rare
Circaetus gallicus	SV	1	4	LC	LC
Circus aeruginosus	R	2	5	LC	LC
Circus cyaneus	WV	1	1	LC	LC
Circus macrourus	PM	1	1	NT	NT
Circus pygargus	PM	1	1	LC	LC
Accipiter gentilis	SV	1	1	LC	LC
Accipiter nisus	SV	1	1	LC	LC
Buteo buteo	R	1	5	LC	LC
Buteo rufinus	R	2	7	LC	LC
Clanga pomarina	PM	1	1	LC	LC
Aquila chrysaetos	R	1	1	LC	LC
Hieraaetus pennatus	SV	1	1	LC	LC
Pandion haliaetus	PM	1	1	LC	LC
Falco naumanni	SV	1	3	LC	Depleted
Falco tinnunculus	SV	1	4	LC	Declining
Falco subbuteo	SV	1	2	LC	LC
Alectoris chukar	R	2	7	LC	NT
Perdix perdix	R	1	4	LC	Declining
Coturnix coturnix	SV	1	1	LC	Depleted
Gallinula chloropus	SV	1	1	LC	LC
Fulica atra	R	12	1524	LC	NT
Himantopus himantopus	SV	2	14	LC	LC
Charadrius dubius	SV	2	11	LC	LC

Table 3: (cont.)

Species list	R.S	O.N.S		IUCN	E.P.S
		Min.	**Max.**		
Charadrius hiaticula	PM	1	2	LC	LC
Vanellus vanellus	SV	2	11	NT	VU
Calidris minuta	WV	1	3	LC	LC
Calidris alpina	PM	2	7	LC	Declining
Calidris pugnax	PM	4	15	LC	LC
Gallinago gallinago	WV	1	2	LC	Declining
Scolopax rusticola	WV	1	5	LC	LC
Limosa limosa	WV	2	3	NT	VU
Tringa erythropus	PM	2	4	LC	LC
Tringa totanus	SV	2	17	LC	Declining
Tringa nebularia	WV	3	7	LC	LC
Tringa ochropus	SV	2	4	LC	LC
Tringa glareola	PM	1	3	LC	LC
Actitis hypoleucos	R	2	9	LC	Declining
Chroicocephalus ridibundus	WV	2	11	LC	LC
Larus armenicus	R	7	1427	NT	NT
Larus argentatus	SV	5	17	LC	LC
Gelochelidon nilotica	SV	2	19	LC	Depleted
Sterna hirundo	SV	3	11	LC	LC
Sternula albifrons	SV	4	7	LC	Depleted
Chlidonias leucopterus	SV	3	16	LC	LC
Columba livia	R	2	18	LC	LC
Columba palumbus	SV	2	7	LC	LC
Streptopelia decaocto	R	2	16	LC	LC
Streptopelia turtur	SV	1	5	VU	VU
Spilopelia senegalensis	R	2	14	LC	LC
Cuculus canorus	SV	1	9	LC	LC
Bubo bubo	R	1	1	LC	Depleted
Athene noctua	R	1	4	LC	Depleted
Asio otus	R	1	1	LC	LC
Caprimulgus europaeus	PM	1	1	LC	Depleted
Apus apus	SV	2	57	LC	Declining
Tachymarptis melba	PM	2	152	LC	LC
Alcedo atthis	R	1	4	LC	VU
Merops apiaster	SV	2	19	LC	LC
Coracias garrulus	SV	1	2	LC	Declining
Upupa epops	SV	1	3	LC	LC
Picus viridis	SV	1	1	LC	LC
Dendrocopos syriacus	R	1	1	LC	LC
Melanocorypha calandra	SV	2	11	LC	Declining
Calandrella brachydactyla	SV	2	5	LC	Depleted
Galerida cristata	R	2	19	LC	Declining
Lullula arborea	SV	2	8	LC	Depleted
Alauda arvensis	WV	4	19	LC	Declining
Eremophila alpestris	R	2	7	LC	LC
Riparia riparia	SV	2	34	LC	Depleted
Ptyonoprogne rupestris	R	2	7	LC	LC
Hirundo rustica	SV	5	124	LC	Declining
Delichon urbicum	SV	2	17	LC	Declining
Anthus campestris	SV	1	4	LC	Depleted
Anthus trivialis	SV	1	3	LC	Declining
Anthus spinoletta	SV	1	1	LC	LC
Anthus pratensis	SV	1	2	NT	NT
Motacilla flava	SV	1	7	LC	Declining

Table 3: (cont.)

Species list	R.S	O.N.S Min.	O.N.S Max.	IUCN	E.P.S
Motacilla citreola	SV	1	3	LC	LC
Motacilla cinerea	SV	1	2	LC	LC
Motacilla alba	R	2	8	LC	LC
Cinclus cinclus	SV	1	1	LC	LC
Troglodytes troglodytes	SV	1	1	LC	LC
Muscicapa striata	SV	1	4	LC	Depleted
Ficedula hypoleuca	PM	2	3	LC	LC
Ficedula semitorquata	PM	1	3	LC	Depleted
Cercotrichas galactotes	SV	1	4	LC	Declining
Erithacus rubecula	WV	1	8	LC	LC
Luscinia megarhynchos	SV	1	5	LC	LC
Cyanecula svecica	R	1	4	LC	LC
Irania gutturalis	R	1	4	LC	LC
Phoenicurus ochruros	WV	1	1	LC	LC
Phoenicurus phoenicurus	SV	1	4	LC	LC
Saxicola rubetra	SV	2	4	LC	Declining
Saxicola rubicola	SV	2	7	LC	LC
Oenanthe isabellina	SV	2	7	LC	LC
Oenanthe oenanthe	SV	2	13	LC	Depleted
Oenanthe pleschanka	SV	2	16	LC	LC
Oenanthe hispanica	SV	2	7	LC	LC
Monticola saxatilis	SV	1	2	LC	Declining
Monticola solitarius	SV	1	1	LC	LC
Turdus torquatus	SV	2	7	LC	LC
Turdus merula	R	1	1	LC	LC
Turdus pilaris	WV	1	1	LC	LC
Turdus philomelos	WV	1	1	LC	LC
Turdus viscivorus	R	1	2	LC	LC
Acrocephalus schoenobaenus	SV	1	2	LC	LC
Acrocephalus scirpaceus	SV	1	2	LC	LC
Acrocephalus arundinaceus	SV	1	1	LC	LC
Iduna pallida	SV	1	1	LC	LC
Sylvia nisoria	SV	1	2	LC	LC
Sylvia curruca	SV	1	3	LC	LC
Sylvia communis	PM	1	5	LC	LC
Sylvia atricapilla	SV	1	4	LC	LC
Phylloscopus collybita	R	1	8	LC	LC
Phylloscopus trochilus	SV	1	4	LC	LC
Aegithalos caudatus	PM	1	1	LC	LC
Poecile lugubris	PM	1	2	LC	LC
Cyanistes caeruleus	SV	1	3	LC	LC
Parus major	R	1	6	LC	LC
Sitta neumayer	R	1	3	LC	LC
Oriolus oriolus	SV	1	1	LC	LC
Lanius collurio	SV	1	5	LC	Depleted
Lanius minor	SV	1	4	LC	Declining
Lanius excubitor	WV	1	1	LC	LC
Lanius senator	SV	1	2	LC	Declining
Garrulus glandarius	R	1	5	LC	LC
Pica pica	R	2	34	LC	LC
Pyrrhocorax pyrrhocorax	R	1	1	LC	Declining
Corvus monedula	R	2	47	LC	LC
Corvus frugilegus	R	5	86	LC	LC

Table 3: (cont.)

| Species list | R.S | O.N.S | | IUCN | E.P.S |
		Min.	Max.		
Corvus cornix	R	4	54	LC	LC
Corvus corax	R	1	2	LC	LC
Sturnus vulgaris	SV	4	283	LC	Declining
Pastor roseus	SV	2	32	LC	LC
Passer domesticus	R	4	478	LC	Declining
Passer hispaniolensis	R	2	13	LC	LC
Passer montanus	R	2	11	LC	Depleted
Petronia petronia	R	1	1	LC	LC
Montifringilla nivalis	R	1	1	LC	LC
Fringilla coelebs	R	2	15	LC	LC
Fringilla montifringilla	WV	1	11	LC	LC
Chloris chloris	R	1	3	LC	LC
Carduelis carduelis	R	2	19	LC	LC
Spinus spinus	WV	1	2	LC	LC
Linaria cannabina	R	2	27	LC	Declining
Emberiza citrinella	PM	1	3	LC	Declining
Emberiza cia	SV	1	2	LC	LC
Emberiza hortulana	SV	2	31	LC	Declining
Emberiza melanocephala	SV	2	27	LC	LC
Emberiza calandra	SV	3	41	LC	Depleted

R.S.: Regional Status; **P.M.:** Passage migrant, **W.V.:** Winter visitor, **R.:** Resident, **S.V.:** Summer visitor **O.N.S.:** Observed number of species, **Min. :** Minumum, **Max.:** Maximum, **E.P.S.:** European Population Status

3.1. Important Bird Areas (IBA) proposed

During the study, 4 areas that may be important for birds have been identified. These areas are Karakaya Dam, Hazar Lake, South Keban and Keban Islands. The importance of the areas has been evaluated according to their different habitat structures, species richness and bird mobility. The areas were sorted and determined according to the areas where birds are mostly concentrated in accordance with observations and reproduction activities of the birds in the area.

3.1.1. Karakaya Dam

Karakaya Dam is located between Elazığ and Malatya. The area, where the lake mirror is the widest, is located between Battalgazi-Kale-Baskil districts. The southern part of the lake shore is covered with reed areas. There are fine reed areas around the small streams flowing into the lake. The eastern parts of the dam lake are slightly higher and are surrounded by steppe vegetation and other parts are lower and surrounded by orchards (Fig. 4).
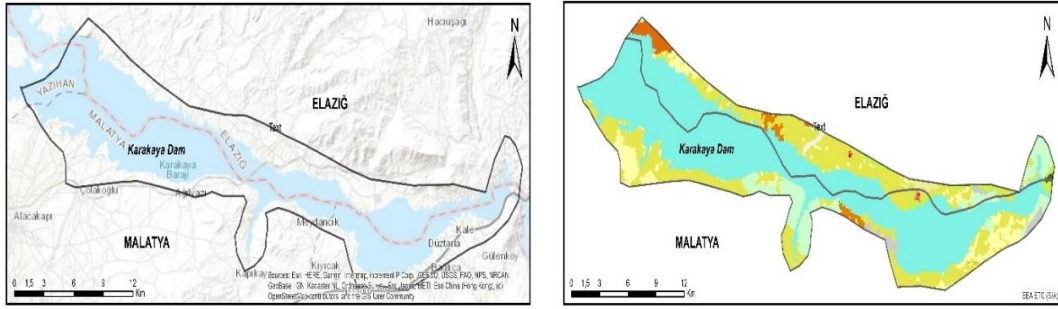
Figure 4: Karakaya Dam Important Bird Area (IBA) topography map and habitat map

With respect to the ornithological importance of Karakaya Dam, it has been determined that various bird species are housed and fed in areas with dense reeds. The bird diversity of the area in the spring period is quite rich. Agricultural lands and orchards around the dam lake positively affect the diversity of birds.

Passerin groups, especially fed with fruit, are very common. In the bays in the dam lake, high numbers of *Podiceps cristatus, Fulica atra* and *Tadorna ferruginea* species were observed as colonies during the winter months. It is also an important habitat for the *Larus armenicus* species, which is endangered on a global scale**.**

3.1.2. Hazar Lake

Hazar Lake is located at the, 25 km southeast of Elazig. There is an island called "Kilise" in the lake and several various sized islets. There are slopes of high sloping steppe character around the lake. On the northern slopes of the lake, there are mixed forests covered with oak and almond trees. There are conifer forests on the southern slopes (Fig. 5).

Two important sources feed the lake water. These sources are "Kürk" and "Zıkkım" creeks. There are reed habitats in places where the streams mix with the lake. These habitats located on the eastern and western coasts of the lake are important breeding and feeding areas for many coasts and waterfowl.

In the area, *Vanellus vanellus, Larus armenicus* and *Fulica atra* species breed. Hazar Lake is an important wintering area for winter visitor species. *Aythya ferina* and *Aythya fuligula* species are seen in herds in the area. Fig. 5 shows the areas where birds breed in the Hazar Lake and its vicinity.
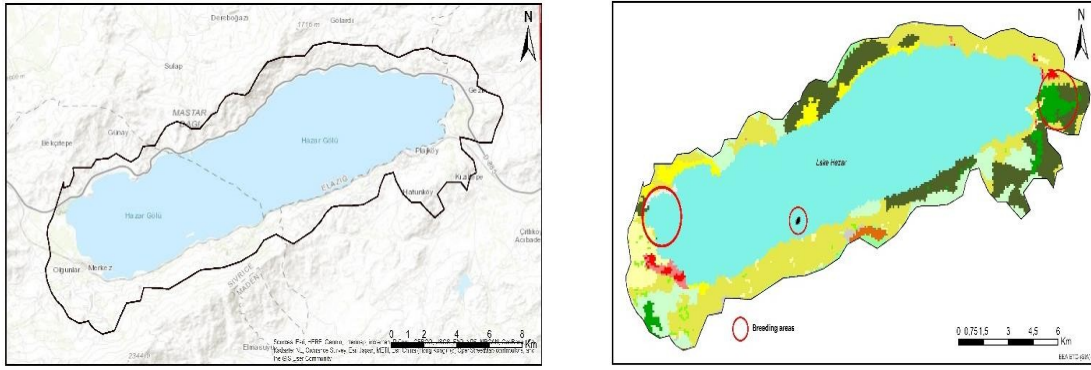
Figure 5: Hazar Lake Important Bird Area (IBA) topography map and habitat map

3.1.3. South Keban Dam

The South Keban Dam, which is the first of the series of dams built on the Euphrates River basin, it forms the southern branch of the Keban Dam system. The southern and western shores of the reservoir are shallower and rich in nutrients compared to other places. In some parts, dune areas were formed as a result of water fluctuations. There are some forest-like habitats on the southern shores of the dam (Fig. 6).
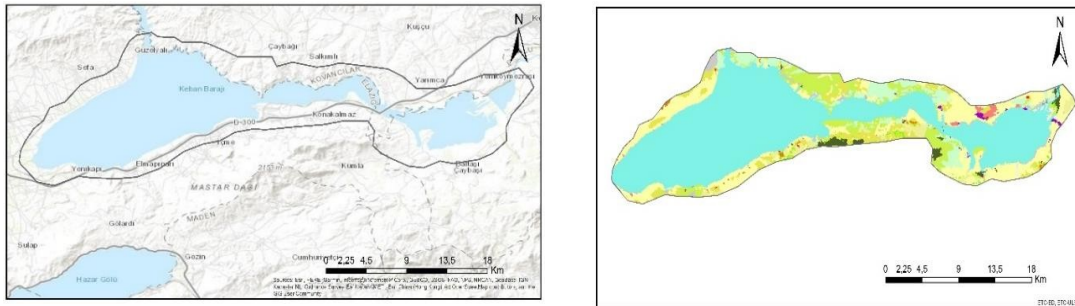
Figure 6: South Keban Dam Important Bird Area (IBA) topography map and habitat map

There is very little data on the bird's presence in the area. Ornithological data related to the area mostly consist of records obtained from mid-winter water bird counts. However, in the periodic observations made within the present study, the presence and importance of the bird was revealed. Due to its different habitat structures (reeds, swamps, wetland meadows, etc.), many different bird species can be found in the region. The lake is used as a feeding and sheltering area by many coasts and waterfowl in the spring period.

During the observations, *Tadorna ferruginea, Anas platyrhynchos, Podiceps cristatus, Fulica atra* and *Tachybaptus ruficollis* species were found in herds along the western and southern shores of the lake. The area is an important habitat for *Larus armenicus,* whose generation is in the NT (Near threatened) category on a global scale. The species is incubated in small islets within the dam lake. *Aythya ferina*, another species in the danger category, is an important winter visitor

for the region.

3.1.4. Keban Islands

Keban Dam is located on the Elazig - Tunceli province border. Large and small islands and peninsulas in the northern part of the dam together with the bays formed by the water are important areas for birds. There are more than 20 large and small islands in the north of the dam. When the habitat structure of the area is examined, it is seen that a large part of the area consists of steppes and very few parts are bushy plantations (Fig. 7).

Keban islands are suitable breeding grounds for *Larus armenicus* and *Nycticorax nycticorax.* In addition, *Aythya ferina* species, which are winter visitors, are frequently seen in the region.
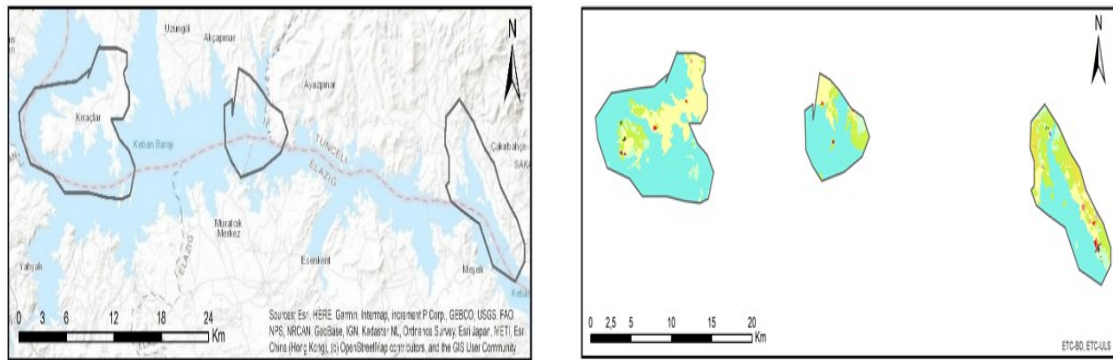
Figure 7: Keban Islands Important Bird Area (IBA) topography map and habitat map

4. Discussion

Wetlands are the most important ecosystems of the earth with their natural functions and economic values [3]. After tropical forests, the ecosystems that produce the highest organic matter from the unit area are wetlands [41]. Wetlands exhibit significant functions in especially forest poor areas [42, 43]. Wetlands make important contributions to biodiversity. It contains many wild livings, especially birds [7, 8]. For that reason, to protect and sustain those natural ecosystems are of the great interest [44].

There are some reports regarding avifauna of Elazig [19, 20, 45-47]. The studies are mostly concentrated in local regions. Ornithological data obtained from previous studies were compared with the present study and the results were discussed.

Distribution area and migration status of 181 bird species in the area are similar with [19, 28, 37].

Almost all the bird species reported in Hazar Lake [19] were observed in the present study. In addition, previously not reported species such as *Accipiter gentilis, Botaurus stellaris, Bubulcus ibis, Calidris minuta, Charadrius hiaticula, Chloris chloris, Cyanecula svecica, Cyanistes caeruleus, Gypaetus barbatus, Iduna pallida, Limosa limosa, Motacilla citreola, Poecile lugubris, Podiceps grisegena, Ptyonoprogne rupestris, Spatula clypeata, Spatula querquedula* were reported herewith the present study.

However, previously reported bird species such as *Columba oenas, Hirundo rupestris, Pyrrhula pyrrhula* [19], *Mareca strepera, Pterocles orientalis, Mareca penelope, Anser albifrons, Larus ichthyaetus, Burhinus oedicnemus, Clamator glandarius*, [45]. *Falco columbarius, Falco vespertinus, Sitta europaea* [46] species were not detected in this study.

According to [19], *Oenanthe pleschanka* species was given as a transit nomad for Elazig. With this study, it was determined that the species is a summer visitor for the region.

Ayvaz (1988) reported information about the reproduction of *Larus argentatus* species in the Hazar Lake and Islands [20]. Herein, it was observed that the species formed a breeding colony on the islands in the Hazar Lake.

The present findings of the study were found to be largely similar to the records [46]. However, *Grus grus* and *Otis tarda* species recorded in the region were not detected during this study.

Kılıç and Eken (2004) drew attention to important wetlands within the borders of Elazig Province, and gave ornithological records about the areas [48]. Ornithological data were compared with the results of the present study and it was observed that they were largely similar. However, *Burchinus oedicnemus, Dendrocopos medius* and *Emberiza cineracea* species, which were previously recorded in the region, were not observed along with the present study.

Kılıç and Eken (2004) reported information about the breeding of the *Nycticorax nycticorax* species in the Keban Islands [48]. These results are consistent with the results of this study. Herein, it was observed that the species formed a breeding colony in Keban Islands.

5. Conclusion and Suggestions

The most important reasons for the richness of Elazig ornithofauna are the wetland potential of the province, the presence of different climatic conditions, the ecosystem diversity and being located near the important bird migration routes. Especially during the migration periods, the birds visit the region intensely. However, there are some threats to birds and their

habitats. It is possible to gather threats against birds in the region under two main headings. These are threats to migratory and domestic birds. Hunting, mining activities, pollution and animal grazing are among these threats. Located in the provincial borders, Hazar Lake is an ornithological rich region for four seasons. However, the environmental pressure on the lake is quite high.

The reed areas in the western part of the lake are breeding and feeding areas suitable for many water and terrestrial bird species that are in the category of danger on a global scale. It was determined that poaching was carried out in breeding areas in April-May, which is the incubation period of birds. It was found that the nests of *Vanellus vanellus* and *Tringa totanus* species, which made their nests on low ground, were damaged and their eggs were broken.

It is obvious that this will affect the reproductive success of the species. Almost all the surroundings of the lake are used for picnic purposes. Domestic wastes left after the picnic or thrown into the lake pollute the lake and its surroundings and subsequently might cause adverse effects on living things.

Another major threat is poaching. Some migratory birds use the region and its immediate vicinity as a transit route. Species such as *Ciconia ciconia, Buteo buteo*, *Apus apus* migrate in herds. Poachers use this situation irresponsibly during migration or in areas where species are accommodated.

There is poaching for domestic species. Duck species are hunted, especially during breeding and migration. Although hunting species are hunted, rifle explosion sound scares other species and causes them to leave the area. It should be ensured that hunting and grazing are not carried out in the incubation period of April-May and the migration period in October-November. Furthermore, the environmental pollution should be prevented by leaving recycling bins in all private or unattended picnic areas around the lake.

Acknowledgement

References

[1] Smardon, R., Estuaries on the Edge, Yucatan Peninsula, Mexico. in Sustaining the World's Wetlands, Springer, New York, NY. 211-266, 2009.

[2] Mitsch, W.J., Gosselink, J.G., Wetlands, John Wiley&Sons: New York, NY, USA. 2015.

[3] Xu, T., Weng, B., Yan, D., Wang, K., Li, X., Bi, W., Liu, Y., *Wetlands of International Importance: Status, threats, and future protection*, International Journal of Environmental Research and Public Health, 16(10), 1818, 2019.

[4] Gibbs, J.P., Wetland loss and biodiversity conservation, Conservation Biology, 14(1), 314-317, 2000.

[5] Hu, S., Niu, Z., Chen, Y., Li, L., Zhang, H*., Global wetlands: Potential distribution, wetland loss, and status*, Science of the Total Environment, 586, 319-327, 2017.

[6] Zedler, J.B., Kercher, S*., Wetland resources: status, trends, ecosystem services, and restorability, Annual Review of Environment and Resources*, 30, 39-74, 2005.

[7] Ghermandi, A., Van Den Bergh, J.C., Brander, L.M., de Groot, H.L., Nunes, P.A., *Values of natural and human-made wetlands: A meta-analysis*, Water Resources Research, 46(12), 2010.

[8] Gray, M.J., Hagy, H.M., Nyman, J.A., Stafford, J.D., *Management of wetlands for wildlife, Wetland techniques*, 803, 121-180, 2013.

[9] King, R.S., Nunnery, K.T., Richardson C.J., *Macro invertebrate assemblage response to highway crossings in forested wetlands: implications for biological assessment*, Wetlands Ecology and Management, 8, 243–256, 2000.

[10] Naugle, D.E., Johnson R.R., Estey M.E., Higgins, K.F., *A landscape approach to conserving wetland bird habitat in the prairie pothole region of eastern South Dakota*, Wetlands, 20, 522–604, 2000.

[11] Odum, H.T., Heavy metals in the environment: using wetlands for their removal: CRC Press LLC, 2016.

[12] Gill, F.B., Ornithology: Freeman Company, USA, 766p. 2007.

[13] Şekercioğlu, Ç.H., Daily, G.C., Ehrlich, P.R., *Ecosystem consequences of bird declines*, Proceedings of the National Academy of Sciences, 101(52), 18042-18047, 2004.

[14] Kiziroğlu, İ., Ekolojik Potpuri: Takav Mat. Yay. A.Ş., 391s. Ankara, 2001.

[15] Danforth, Ch.G., *A Further Contribution to the Ornithology of Asia Minor*, Ibis, 4, 81-894, 1880.

[16] Ergene, S., *Türkiye Kuşları*. İstanbul Üniversitesi Fen Fak. Monografileri (4), 361s. İstanbul, 1945.

[17] Kasparyan, A., *A Preliminary Systematic List of Birds of Turkey*, İstanbul Üniversitesi Fen Fakültesi Mecmuası, 21(1-2), 27-48, 1956.

[18] Kumerloeve, H., Van Gölü-Hakkari Bölgesi (Doğu/Güneydoğu Küçük Asya) Kuşları, 94p. İstanbul, 1969a.

[19] Ayvaz, Y., *Elazığ Hazar Gölü Kuşları*, Atatürk Üniversitesi Fen Fak. Dergisi, 1, 54-64, 1982.

[20] Ayvaz, Y., *The Breeding of the Herring Gull (Larus argentatus),* Journal of Fırat Üniv. 3, 53-60, 1988.

[21] Kiziroğlu, İ., Türkiye Kuşları: OGM Yayınları, Desen Ofset, 314s. Ankara, 1989.

[22] Ayvaz, Y., *Birds of Malatya Pınarbaşı Lake,* Doğa-Tr. Zool., 14, 139-143, 1990.

[23] Bilgin, C., Akçakaya, H.R., Türkiye'nin Biyolojik Zenginlikleri: Çevre Sorunları Vakfı Yayınları, 183-202, 1987.

[24] Turan, N., Türkiye'nin Av ve Yaban Hayvanları / Kuşlar: OGM. Eğt. Dairesi Bşk. Yayın ve Tanıtma Müd. Mat., 274s. Ankara, 1990.

[25] Kasparek, M., Die Vögel der Türkei: eine Übersicht. M. Kasparek, Verlag, 1992.

[26] Ayvaz, Y., *Birds of Elazığ Region*. Doğa-Tr. Zool., 14, 1-10, 1993.

[27] Kasparek, M., Türkiye Kuşları Tür Listesi. 25-88, içinde: Türkiye Omurgalılar Tür Listesi: (Kence, A. & Bilgin, CC eds). Nurol Matbaacılık AŞ, Ankara, 1-183, 1996.

[28] Kirwan, G. M., Martins, R. P., Eken, G., Davidson, P., Checklist of the Birds of Turkey: OSME Sandgrouse Supplement 1, 32p., USA, 1998.

[29] Adızel, Ö. (1998). A research on the ornitofauna of Van Lake Basin, Y.Y.Ü. Graduate School of Natural and Applied Sciences, Department of Biology, Van / Turkey

[30] Çelik, E., Durmuş, A., *Determining the Seasonal Ornithological Potential of the Dönemeç (Engil) Delta and Generate the Digital Maps Using Geographical Information Systems (GIS)*, Iğdır University Journal of the Institute of Science and Technology, 7(3), 73-78, 2017.

[31] Durmuş, A., Çelik, E., *Determination of Ornithological Richness of Erçek Lake, Dönemeç and Bendimahi Deltas (Van/Turkey) in Winter Season and Mapping with Geographic Information System*, International Journal of Scientific & Technology Research, 6(4), 63-66, 2017.

[32] Nergiz, H., Alar, M.M., *Artvin Borçka Karagöl Tabiat Parkı'nın Ornitofaunası*, Bitlis Eren Üniversitesi Fen Bilimleri Dergisi, 8(3), 883-888, 2019.

[33] Çelik, E., *Batman ili ornitofaunası*, Doğu Fen Bilimleri Dergisi, 1(2), 1-10, 2018.

[34] Nergiz, H., *Heybeli Gölü (Bitlis) Kuş Çeşitliliği Üzerine Bir Araştırma*, Iğdır Üniversitesi Fen Bilimleri Enstitüsü Dergisi, 9(2), 692-698, 2019.

[35] Kirwan, G.M., Boyla, K., Castell, P., Demirci, B., Özen, M., Welch, H., Marlow, T., The Birds of Turkey: The Distribution, Taxonomy and Breeding of Turkish Birds: Christopher Helm. London, UK. 2008.

[36] Şekercioğlu, Ç.H., Anderson, S., Akçay, E., Bilgin, R., Can, Ö.E., Semiz, G., Sağlam, İ.K., *Turkey's globally important biodiversity in crisis*, Biological Conservation, 144(12), 2752-2769, 2011.

[37] Kiziroğlu, İ., "Türkiye Kuşları Kırmızı Listesi", Türkiye Tabiatını Koruma Derneği, Ankara. 2008

[38] Anonim, Elazığ İli'nin Karasal ve İç Su Ekosistemleri Biyolojik Çeşitlilik Envanter ve İzleme Projesi, Turunç Peyzaj Tasarım Planlama Uygulama Proje İnşaat Organizasyon ve Danışmanlık Hizm. Ltd. Şti, Nihai Raporu, Eylül. 607s. 2018.

[39] Eken, G., Bozdoğan, M., Karataş, A., Kılıç, D.T., Gem, E., Türkiye'nin Önemli Doğa Alanları-Yeni koruma bölgelerinin seçiminde öncelikli alanlar. Korunan Doğa Alanları Sempozyumu, 8-10 Eylül 2005, Isparta, 133-140. 2005.

[40] Bibby, C. J., Burgess, N. D., Hill, D. A., & Mustoe, S. (2000). Bird census techniques. Elsevier

[41] Can, Ö., Taş, B., *Ramsar Alanı içinde yer alan Cernek Gölü ve sulak alanının (Kızılırmak Deltası, Samsun) Ekolojik ve Sosyo-Ekonomik önemi*, TÜBAV Bilim Dergisi, 5(2), 1-11, 2012.

[42] Adızel, Ö., Durmuş, A., Akyıldız, A., ''The Effects of Pollutants on Birds and Other Organism Living in Lake Van Basin,'' 1st International Eurasian Ornithology Congress, 2004a.

[43] Adızel, Ö., Turan, L., Kiziroğlu, İ., ''The Reasons of Drainage of Van Lake the Effects on Birds and Irritaded Field,'' 1st International Eurasian Ornithology Congress, 2004b.

[44] Green, A.J., Elmberg, J*., Ecosystem services provided by water birds*, Biological Reviews, 89(1), 105-122, 2014.

[45] Anonim, Hazar Gölü Kış Ortası Su Kuşu Sayımı, Doğa Derneği, 2006.

[46] Anonim, Elazığ İli Çevre Durum Raporu, Çevre ve Şehircilik Bakanlığı, Nihai Raporu, 2013a.

[47] Anonim, Elazığ'ın Kuşları Projesi, Mülga Orman ve Su İşleri Bakanlığı, 15. Bölge Müdürlüğü, Elazığ Şube Müdürlüğü, Aralık. 2013b.

[48] Kılıç, D.T., Eken, G., Türkiye'nin Önemli Kuş Alanları 2004 Güncellemesi, Doğa Derneği, Ankara, 2004.

Histopathological and Biochemical Effects of Eugenol on Alcohol-Treated Rat Liver

Hasan YILDIZ[1,*], Eaylettin ÖZTÜRK[2]

[1]Hatay Mustafa Kemal University, Arts and Sciences Faculty, Department of Biology, Hatay, Turkey
yildizh@mku.edu.tr, ORCID: 0000-0001-5486-4005
[2]Hatay Mustafa Kemal University, Graduate School of Natural and Applied Sciences, Department of Biology, Hatay, Turkey
eaylettin@gmail.com, ORCID: 0000-0002-4412-8087

Abstract

The effects of eugenol, which has a high antioxidant capacity, alone and together with ethyl alcohol, an oxidative stress factor, were evaluated histopathologically and biochemically. In this study, 40 Wistar albino female rats weighing 300-390 g were used. Rats were randomly divided into 4 groups of 10 and fed with standard pellet type feed as *ad libitum*. Group 1 (Control group) with 3 ml Serum physiological (Sf)/day via gavage to create the same stress as other groups, Group 2 (Ethyl alcohol group), 40% Ethyl alcohol with 3 ml/day via gavage, Group 3 (Eugenol Group) with 50 mg/kg/day via gavage, Group 4 (Ethical alcohol + Eugenol group) was given for 30 days as 40% Ethyl alcohol 3 ml/day via gavage + 50 mg/kg/day via gavage eugenol 3 ml/day via gavage. At the end of the study, biochemical analyzes and histological preparations were made in blood and liver tissue from rats. When eugenol is consumed together with ethyl alcohol, it was found that ethanol reduces hepatotoxicity on the liver. A statistically significant difference was found in AST, ALT, ALP, LDH and TRIG levels in the eugenol rats compared to the alcohol group rats ($p < 0.05$). However, no significant difference was found between the groups at BILD, BILT, CHOL, AFP and CEA125 levels ($p < 0.05$). The use of eugenol alone increased the value of TAS. It was determined that the use of eugenol alone decreased the TOS values while

increasing the TAS value. According to the biochemical data we obtained, it is possible to say that eugenol reduces the hepatotoxicity formed as a result of ethanol application by changing the oxidant-antioxidant balance in favor of oxidants. The results obtained from histopathological examination of the liver support biochemical data and eugenol have been shown to reduce hepatotoxic effects on the liver when consumed with ethanol.

Keywords: Liver; Eugenol; Ethanol; Hepatotoxicity; Antioxidant; Oxidative stress.

Öjenolün Alkol ile Muamele Edilen Sıçan Karaciğeri Üzerindeki Histopatolojik ve Biyokimyasal Etkileri

Öz

Yüksek antioksidan kapasiteye sahip olan Öjenol maddesinin tek başına ve bir oksidatif stres etkeni olan etil alkol ile beraber tüketilmesi sonucu karaciğer hasarlanması ve oksidatif stres düzeyindeki etkileri histopatolojik ve biyokimyasal olarak değerlendirildi. Bu çalışmada, 300-390 g ağırlığında 40 adet Wistar albino dişi sıçan kullanıldı. Sıçanlar rastgele 10'arlı 4 gruba ayrıldı ve standart pellet tipi yem ile *ad libitum* olarak beslendi. 1. Grup (Kontrol grubu), diğer gruplar ile aynı stresi oluşturmak amacı ile 3 ml Serum fizyolojik (Sf)/gün gavaj ile 2. Grup (Etil alkol grubu), %40'lık Etil alkol 3 ml/gün gavaj ile 3. Grup (Öjenol Grubu), 50 mg/kg/gün gavaj ile, 4. Grup (Etik alkol + Öjenol grubu), %40'lık Etil alkol 3 ml/gün gavaj + 50 mg/kg/gün gavaj ile öjenol 3 ml/gün gavaj yoluyla olacak şekilde 30 gün boyunca verildi. Çalışma sonunda sıçanlardan alınan kan ve karaciğer dokusunda biyokimyasal analizler ve histolojik preparatlar hazırlandı. Öjenol, etil alkol ile beraber tüketildiğinde karaciğer üzerinde etanolün oluşturduğu hepatotoksisiteyi azalttığı tespit edildi. Öjenol grubu sıçanlarda alkol grubu sıçanlara kıyasla AST, ALT, ALP, LDH ve TRİG seviyelerinde istatistiksel olarak anlamlı bir fark bulundu ($p <$ 0.05). Ancak BİLD, BİLT, CHOL, AFP ve CEA125 seviyelerinde gruplar arasında anlamlı bir fark bulunamadı ($p <$ 0.05). Tek başına Öjenol kullanımı TAS değerini arttırırken TOS değerlerini azalttığı belirlendi. Elde ettiğimiz biyokimyasal verilere göre, öjenolün, oksidan-antioksidan dengesini oksidanlar lehine değiştirerek etanol uygulaması sonucunda oluşan hepatotoksisiteyi azalttığını söylemek mümkündür. Karaciğerin histopatolojik incelemesinden elde edilen sonuçlar, biyokimyasal verileri destekler nitelikte olup Öjenolün, etanol ile beraber tüketildiğinde karaciğer üzerinde hepatotoksik etkileri azalttığı görüldü.

Anahtar Kelimeler: Karaciğer; Öjenol; Etanol; Hepatotoksisite; Antioksidan; Oksidatif stres.

1. Introduction

Since ancient times, the relaxing effect of alcohol has been discovered by humans and consumed through the ages. Use of alcohol causes significant, structural, and functional changes especially in the liver depending on the dose taken, duration, individual endurance, diet, and other factors. Oral absorption of alcohol is made through the stomach and small intestine and easily passes into all fluids of the body. Alcohol-induced oxidative stress is much more effective in the liver because alcohol metabolism is primarily carried on in the liver. Alcohol shows its effect depending on destruction product acetaldehyde by various mechanisms and most importantly by increasing lipid peroxidation and free radical levels [1]. Excessive use of alcohol causes 3 different diseases pathologically in the liver: fatty liver, alcoholic hepatitis and cirrhosis. Some enzymes normally found in hepatocytes are mixed into the blood in case of damage to the liver. The levels of enzymes such as aspartate aminotransferase (AST), alanine aminotransferase (ALT) and alkaline phosphatase (ALP) in the blood are important in the context of the indicator of liver damage [2, 3]. The most commonly used liver function tests are serum total bilirubin (BILT), direct bilirubin (BILD), AST, ALT and albumin (ALB) measurements and prothrombin time [4]. Triglyceride (TRIG), cholesterol (CHOL), lactate dehydrogenase (LDH) enzymes are also important parameters that change in ethyl alcohol stress. Synthetic drugs used in the treatment of liver diseases such as corticosteroids, antiviral and immunosuppressive agents can cause negative effects up to serious hepatic damage [5]. Therefore, it is imperative to find more effective and safe agents for the treatment of liver disease. In addition to some natural products (garlic, green tea, grapes, walnuts, etc.), numerous research have been done for the roles of compounds such as L-theanine, vitamin E, N-acetyl cysteine, raksofelast, and betaine in eliminating oxidative stress [6]. The name Eugenol comes from the clove plant (*Eugenia caryophyllata*, Synonym: *Syzygium aromaticum*, Turkish: Karanfil). Clove is one of the most popular and used spices all over the world. It has been a type of spice used in culinary and medical fields for centuries because of its unique smell, taste and aroma as well as containing vitamins, minerals and other nutrients necessary for the body. Eugenol is one of the antioxidative elements that make up a large part of clove extract. It has a colorless, pale yellow, oily appearance and gives the clove its characteristic smell. Eugenol is a member of the allylbenzene class and its molecular weight is 164.20 g/mold. Its closed formula is in the form of $C_{10}H_{12}O_2$ and its open formula is shown in Fig. 1. Eugenol is easily soluble in alcohol or oil but partially dissolved in water [7]. Eugenol is called with more than 44 names and some synonyms; "4-allyl-2-methoxyphenol, 4-allyl-2-methoxy-phenol, 2-methoxy-4- (2-propenyl) -phenol, 2-methoxy-4- (prop-2-en-1-yl) -phenol and 1-Hydroxy-2-Methoxy-4-β-propenylbenzol" [8].
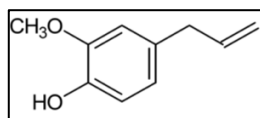
Figure 1: The formula of eugenol [9]

Eugenol can be isolated from the buds, roots and leaves of cloves. It is found mostly in clove oil (80-90%) in nature [10]. In addition, its presence has been shown in studies that have been done using various plants such as Laurel (*Pimenta racemosa*), Tarragon (*Artemisia dracunculus* L.), Cinnamon (*Cinnamomum tamala*), Coconut (*Myristica fragrans*), Basil (*Ocimum basilicum* L. and *Ocimum gratissimum*), Japanese star anise (*Illicium anisatum*) [11-17].

Scientific studies on eugenol and its derivatives have shown that they have anesthetic, analgesic, antimicrobial, antioxidant, antifungal, anti-inflammatory and anticonvulsant, anticancergenic, antimutagenic, and antifumigant properties [18-21]. Because of these properties, it is widely used in medicine, pharmacology, dental care industry, cosmetics, food, agriculture and active packaging materials [22]. It has been reported that the Environment and Working Group (EWG) contains 379 products in different concentrations of eugenol in the cosmetic and personal care database list [23].

In this study, it is aimed to investigate liver damage and changes in oxidative stress level resulting from the consumption of eugenol substance with high antioxidant capacity alone and together with oxidative stress factor (ethanol).

2. Materials and Methods

2.1. Animal material

The rats used in the study obtained from Hatay Mustafa Kemal University Research Experimental Research and Application Center (HMKÜ-DAM). Additionally, the study was approved by the same institution's ethics committee. Date and number of the ethics committee approval is following: 28 December 2017 and 2017/12-2, respectively. In the study, 40 Wistar albino female rats weighing approximately 300-390 g were used. The rats were randomly divided into 4 groups of 10 and fed with standard pellet type feed as *ad libitum*.

2.2. Eugenol

Eugenol with 99% purity was obtained from commercial companies (Sigma-Aldrich Co., USA). The required mixture during the working period was prepared freshly everytime before

use. The eugenol amount calculated for the gavage was mixed homogeneously with the help of the vortex device in sterile water and followed by its application to the animals. This process was repeated before each gavage and the homogenous distribution of eugenol was tried to be provided.

2.3. Ethanol

Pure ethanol used to generate oxidative stress in rats was obtained from commercial companies (Sigma-Aldrich Co., USA) and daily mixed with distilled water (20 ml pure ethanol + 30 ml distilled water) in order to prepare fresh 40% ethanol.

2.4. Experimental application

Rats were randomly divided into 4 groups of 10, and were kept at 25 ± 1 ℃ room temperature for 12 hours light/12 hours dark light period. Rats were adapted to the environment for 4 days and *ad libitum* was fed during the study. Control group (Cont): In order to create the same stress with other groups, 3 ml of saline was administered by gavage. Ethyl alcohol group (Eth): Ethyl alcohol (40%, 3 ml/day) was given by gavage [24]. Eugenol group (Eu): Eugenol was given by gavage at 50 mg/kg bw [25]. Ethyl alcohol and Eugenol group (EthEu): Ethyl alcohol + Eugenol (40% 3ml Ethyl alcohol and 50 mg/kg bw eugenol) were given daily by gavage. Eugenol, prepared freshly every day, was given to the specified study group in warm water and mixed well on the shaker. After physical examination and weighing at the end of the thirtieth day, blood and liver tissues were collected from rats under ketamine/xylazine anesthesia. Vacuum tubes with EDTA were used for complete blood count and analyzes were performed immediately. Vacuum plastic gel tubes were used for biochemical analysis. After centrifugation at 4000 rpm, 15 minutes, + 4ºC after coagulation, the serum was separated and kept at −80ºC until the day of analysis. Liver tissues were placed in 10% formaldehyde for histopathological examination and were subjected to fixation.

2.5. Biochemical analyzes

Determination of AST, ALT, ALP, BILD, BILT, LDH, Gamma glutamyl transferase (GGT), TRIG, Total Chol, Alpha-fetoprotein (AFP) and cancer antigen 125 (CA125) from commercial blood using commercial kits (commercially available) (Advia-1800 and Centaur XP).

2.6. Total antioxidant status (TAS) and total oxidant status (TOS) measurements

Total antioxidant capacity assay developed by Erel Rel brand kit (Rel Assay Kit Diagnostics, Turkey) were measured using. Trolox, a water-soluble analog of vitamin E, was used as a calibrator. The results were expressed as mmol Torolox equiv./lt [26]. Total oxidant capacity

developed by the brand Erel Rel Assay kit (Rel Assay Kit Diagnostics, Turkey) was measured using. Hydrogen peroxide was used as a calibrator. The results were expressed as μmol H_2O_2 equiv./lt [27].

When calculating the Oxydative Stress Index (OSI), which is expressed as the percentage of the ratio of total oxidant capacity to total antioxidant capacity, the mmol value in the TAS result display was converted to μmol in the TOS result display. Results are expressed as "arbitary unit" (AU) and calculated using the formula below [27].

$$OSI = \frac{TOS,\ \mu mol\ H_2 0_2\ equiv./lt}{TAS,\ mmol\ Trolox\ equiv./lt \times 10}$$

2.7. Histopathological examinations

Samples from experimental animals were fixed in 10% formaldehyde solutions. After routine follow-up, 5 μm thick tissue sections were taken from paraffin blocks and stained with Hemotoxylin-Eosin (H&E) and examined under Olympus BX-51 light microscope.

2.8. Statistical analysis

For statistical calculations, ANOVA multiple comparison and Student Newman-Keuls (SNK) tests were used to compare the changes in experimental groups against the Cont groups. Results were determined as mean ± standard deviation (X ± SD) and showed statistical difference of $p < 0.05$. All calculations were made using the Prostate Version 5.04 package program.

3. Results

Greater biological sensitivity to alcohol triggered the use of a female rat in our study. Studies have shown that rats and mice fed a long-term alcoholic diet have more weight loss compared to the Cont group [28, 29]. In our study, weight gain was observed in the Cont group at the end of the 30th day, while weight loss was observed in other groups (Table 1). In the alcohol consuming group, weight loss is thought to be due to possible decreased appetite and decreased food intake as a result of subsequent liver damage.

Table 1: Weights of experimental groups

Groups	1. Day (gr)	30. Day (gr)
Cont	308	324
Eth	322	310
Eu	315	314
EthEu	346	328

Alcohol consumption causes different negative effects on blood cells. Individuals consuming alcohol may suffer from moderate anemia characterized by structurally abnormal RBCs, slightly decreased WBCs, especially neutrophils and moderately decreased platelet count [30]. As a result of the complete blood count, there was a significant difference between the groups in terms of RBC, HGB, HCT MCV, NEU, LYM, MON, EOS parameters, but no significant difference in terms of WBC, PLT, BAS, MCH and MCHC parameters. As shown in Table 2, while RBC, HGB, HCT and PLT values increased in Eth group compared to the Cont group, there was a decrease in WBC, LYM and MCV values. Blood values of the Eug group and the Cont group were close to each other. Our NEU, LYM and MON data are in line with other studies [31, 32].

Biochemical analysis results are presented in Table 3. While there was a statistically significant difference in serum AST, ALT, ALP, LDH and TRIG levels between the Cont group and Eth, Eu and EthEu groups, no significant difference was found in the levels of BILD, BILT, CHOL, AFP and CEA125 ($p < 0.05$). The mean and standard deviation (mean and $\pm$ SD) values of AST values in the Cont group were found to be 131.40 ± 16.27. Eth group has the highest AST value with 165.20 ± 39.82, while Eu group has the lowest AST values with 116.60 ± 11.80.

Table 2: Complete blood count parameters of Control, Ethanol, Eugenol, Ethanol and Eugenol groups

	GROUPS			
	Cont	**Eth**	**Eu**	**EthEu**
WBC (10^3/uL)	6,02 ± 1,08	5,82 ± 0,86	6,80 ± 0,81	5,60 ± 0,67
RBC (10^6/uL)	6,74 ± 0,41	7,74 ± 0,25*	6,95 ± 0,14	6,86 ± 0,27
HGB (g/dL)	12,98 ± 0,67	13,90 ± 0,25*	12,94 ± 0,11	12,96 ± 0,38
HCT (%)	42,88 ± 2,78	45,44 ± 0,98*	42,68 ± 0,84	42,04 ± 1,30
MCV (fL)	62,32 ± 1,20	61,08 ± 2,08	62,14 ± 2,30	59,34 ± 0,81*
PLT (10^3/uL)	656,80 ± 40,49	715,20 ± 85,26	667,40 ± 53,93	651,40 ± 53,39
NEU (10^3/uL)	20,64 ± 2,26	29,10 ± 3,66*	17,56 ± 4,73	37,46 ± 8,76*
LYM (10^3/uL)	70,62 ± 1,95	62,78 ± 5,17	68,40 ± 5,39	52,64 ± 7,43*
MON (10^3/uL)	8,12 ± 0,46	11,76 ± 0,92*	8,98 ± 1,34	10,06 ± 0,60*
EOS (10^3/uL)	0,62 ± 0,22	2,36 ± 1,00*	1,54 ± 0,85*	1,40 ± 1,02*
MCH (pg)	18,80 ± 0,25	18,68 ± 0,76	18,30 ± 0,37	18,38 ± 0,20
MCHC (g/dL)	30,14 ± 0,29	30,52 ± 0,18	30,34 ± 0,35	30,72 ± 0,43

(*) Statistically importance compared with the control group, $p < 0.05$.

Table 3: Some biochemical parameters ın the blood serum of the Control, Ethanol, Eugenol, Ethanol and Eugenol groups

	GROUPS			
	Cont	Eth	Eu	EthEu
AST (U/L)	131,40 ± 16,27	165,20 ± 39,82*	116,60 ± 11,80	121,00 ± 20,23
ALT (U/L)	54,80 ± 3,96	69,75 ± 3,20*	59,00 ± 9,38	56,20 ± 2,58
BILD (mg/dL)	0,034 ± 0,005	0,038 ± 0,008	0,030 ± 0,010	0,034 ± 0,009
BILT (mg/dL)	0,016 ± 0,013	0,032 ± 0,026	0,026 ± 0,017	0,018 ± 0,013
CHOL (mg/dL)	42,60 ± 3,78	43,40 ± 4,61	42,00 ± 3,53	38,00 ± 4,63
LDH (U/L)	1147,75 ± 118,23	1169,20 ± 139,75	979,80 ± 103,34	647,80 ± 156,60*
TRIG (mg/dL)	50,80 ± 5,63	77,20 ± 14,01*	50,40 ± 8,08	54,20 ± 11,56
ALP (U/L)	102,80 ± 12,96	75,40 ± 4,98*	123,20 ± 21,44	77,20 ± 9,73*

(*) Statistically importance compared with the control group, $p < 0.05$.

There was a significant increase in ALT in Eth, Eug and EthEug groups compared to the Cont group ($p < 0.05$). While the highest ALT level belonged to the Eth group to be 69.75 ± 3.20, the lowest ALT level was found in the Cont group to be 54.80 ± 3.96. It was determined that the ALT level decreased in the Eug group compared to the Eth group and increased in comparison with the Cont group. The change between the groups was found to be significant for ALT. Compared to the Cont group, while the BILD level decreased in the Eug group, it did not increase in the Eth group and did not change much in the EthEug group. BILT level increased in all groups except the Cont group. The highest BILT value was found in Eth group with 0.032 ± 0.026. CHOL level did not change significantly between groups however, Eth was the highest group with a value of 43.40 ± 4.61.

There was a significant difference between the groups at the LDH level and Eth group was the highest group with the value of 1169.20 ± 139.75. There was also a significant change in TRIG levels in all groups. When TRIG level was compared, it was the highest Eth group and the lowest group was Eug group. The ALP level was found in the highest Eug group and the lowest in the Eth group. There was a statistically significant difference between the groups for TAS level. Eth group's TAS level was lower than the Cont group. The eugenol group has the highest value with 1.86 ± 0.19, while the EthEug group has the lowest value. Although no significant difference was found between the groups for the TOS level, the TOS level was found to be the highest in the ethanol-treated group with a value of 16.58 ± 4.42 (Table 4).
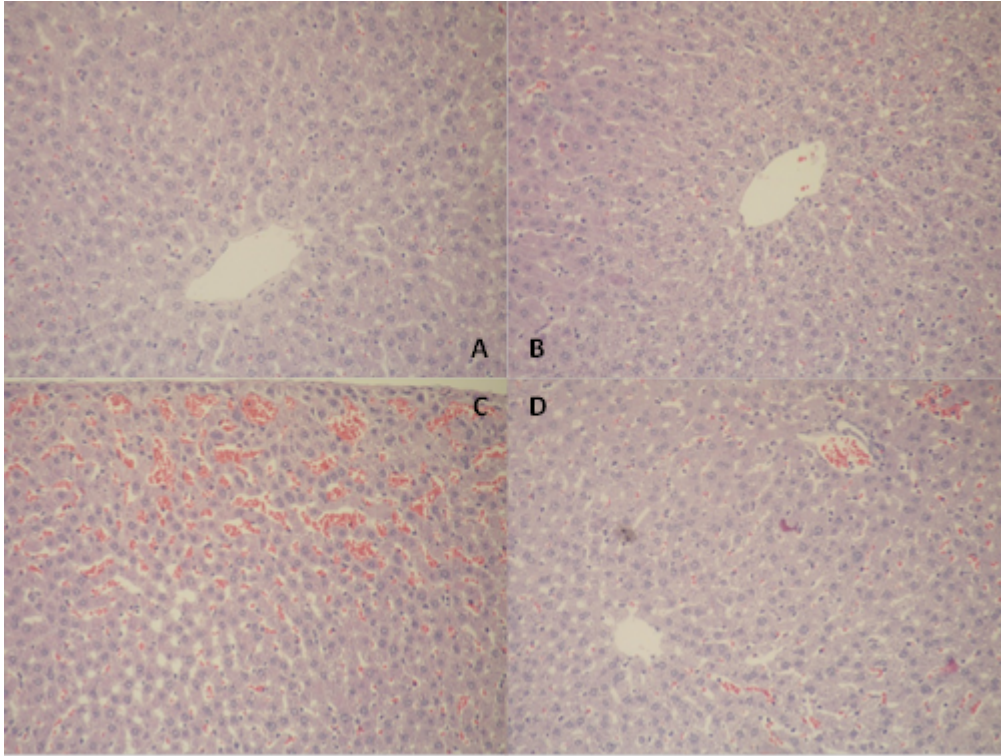
Figure 2: Liver histopathology of Control (A), Eugenol (B), Ethanol (C), Ethanol and Eugenol (D)groups (H&E, X200)
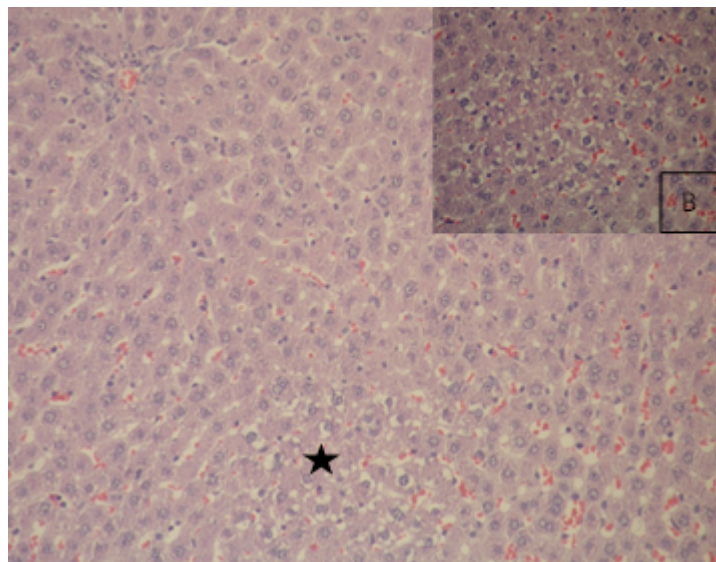
Figure 3: Microvesicular fatty change observed in the liver of Ethanol group rats (asterisk), (H&E, X200), B, Magnified region, indicated by an asterisk (H&E, X400)

Changes in liver histology due to alcohol use, macrovesicular and microvesicular fat accumulation, hepatocyte ballooning, cell infiltration, Mallory-Equivalent body, neutrophilic inflammation, pericular fibrosis, hyaline sclerosis, fibrosis and cholestasis are observed [33]. When the groups are compared histopathologically, there is a significant difference between the Cont group and other groups in terms of degeneration levels (Fig. 2). In the Cont group rats, the liver was observed to have a normal histological structure. Severe diffuse degeneration and microvesicular fatty changes were observed in liver hepatocytes of Eth group rats (Fig. 3). Compared with the Cont group, in the Eth group, intracellular macro and microvesicular fatty accumulation due to alcohol, dense mononuclear cell infiltration, mostly lymphocytes, hydropic degeneration, dual-core structures in some hepatocyte cells, and the presence of erythrocytes in the synophoidal spaces were observed. It was found that degenerations decreased in the group with eugenol added.

Table 4: TAS and TOS parameters in the blood serum of Control, Ethanol, Eugenol, Ethanol and Eugenol groups

	GROUPS			
	Cont	**Eth**	**Eu**	**EthEu**
TAS (mmol/L)	$1,62 \pm 0,25$	$1,49 \pm 0,13$	$1,86 \pm 0,19$	$1,33 \pm 0,09$
TOS (µmol/L)	$12,46 \pm 1,35$	$16,58 \pm 4,42$	$11,86 \pm 1,58$	$13,14 \pm 2,63$
OSI (AU)	$0,77 \pm 0,04$	$1,10 \pm 0,18$	$0,64 \pm 0,05$	$0,98 \pm 0,13$

(*) Statistically importance compared with the control group, $p < 0.05$.

4. Discussion

The extrahepatic metabolism of alcohol is very low. Since 90-95% of alcohol is metabolized in the liver, the organ that is most exposed to harmful effects is the liver. These harmful effects of alcohol are mostly caused by disruption of oxidant and antioxidant balance. Alcohol is metabolized to acetaldehyde by alcoholdehydrogenase in cytosol, cytochrome P450 in microsomes and catalase in peroxisomes [34] . When alcohol is advanced oxidized, it increases the free radical production and disrupts the oxidant-antioxidant system's balance. In order to eliminate or minimize the harmful effects of alcohol, some research have been done on many substances that are synthesized or taken daily and have antioxidant properties. According to literature data, although medicines that help advance modern medicine and renew hepatic cells and protect the liver, many herbal extracts are used to prevent liver diseases [35].

Because of antioxidant feature of eugenol, it is used as a preservative and aroma additive in the food industry and cosmetics industry [36]. In our study, we started from the fact that the

eugenol substance has a high antioxidant activity like olive oil. We aimed to determine what effects it has on the liver when applied directly, without dissolving it in some other solvents. Guenette et al. reported that in rats, the half-life (t1/2) of eugenol in plasma was approximately 14 hours and 18 hours in blood [37].

Depending on alcohol use, moderate anemia characterized by structurally abnormal RBCs, mild deficiency of WBCs, especially neutrophils, and moderately decreased platelet counts have been reported [38, 39].

Yalçın and Yağcı reported that high levels of ethanol intake (15% v/v) in rats decreased the white blood cell and red blood cell counts, hemoglobin concentrations, erythrocyte diameters, erythrocyte sodium and potassium levels compared to the Cont group [40]. Similarly, in our study, WBC, MCV and LYM values in Eth group decreased compared to the Cont group, while RBC, HGB, HCT, PLT, MCH, NEU, MON and other parameters increased.

Gülçin et al. examined the antioxidant activity of clove oil in comparison with synthetic antioxidants. They determined the antioxidant activity of clove oil, BHA, BHT, a-tocopherol and trolox by ferric thiocyanate method in linoleic acid system. As a result, clove oil found 99.7%, under the same conditions, standard antioxidant compounds such as butylated hydroxyanisole (BHA), butylated hydroxytoluene (BHT), a-tocopherol and trolox showed 95.5%, 99.7%, 84.6%, and 95.6% inhibition respectively [41].

Anbu et al examined the effect of ethanol and eugenol administration on lipid levels, lipid peroxidation, enzymatic and non-enzymatic antioxidants. They showed that the levels of SOD, CAT, GST and GPx enzymes increased more than the other groups in the eugenol applied group compared to the other groups. They stated that ethanol intake significantly increased some liver enzymes (AST, ALT, GGT and ALP). In this study, olive oil was used as a solvent agent for eugenol and it was given to other groups in equal amounts except the ethanol group [42]. In another study, extracts of about 30 plants were investigated for their antioxidant properties using DPPH and ABTS radical scavenging capacity test, oxygen radical absorbance capacity (ORAC) test, SOD analysis and ferric reductive antioxidant potential (FRAP) analysis. As a result of the study, researchers showed that clove has strong antioxidant properties and high phenolic content (200 mg GAE/g) [43].

Yogalakshmi et al. pre-treatment with eugenol (10.7 mg/kg bw per day) in rats for 15 days, lipid peroxidation indices, protein oxidation and inflammatory markers and glutathione peroxidase (GPx), superoxide dismutase (SOD), catalase (CAT) and glutathione -S-transferase (GST) has been shown to improve antioxidant status by protecting antioxidants [44]. Binu and his team found that when eugenol (5 mg/kg bw) and arsenic trioxide (As_2O_3) were treated

together, AST and ALT levels were normalized compared to the Cont group and showed hepatoprotective effects with decreased arsenic accumulation [45]. Thuwaini et al., examined the effects of clove extract on liver damage caused by paracetamol and stated that there was a decrease in the amount of albumin in the blood serum and an increase in bilirubin, ALT, AST and ALP levels compared to the Cont group [46]. Muller et al. investigated the liver protective activity of Pecan coconut extract against liver damage caused by ethanol and found increased levels of plasmatic transaminases (ALT, AST) at the end of the study in chronically treated rats with ethanol. As a result, it has been stated that it can be an economical agent to treat liver diseases related to consumption of ethanol from coconut shells [47]. The findings in these studies support our study and similarly, we found a significant increase in AST and ALT levels in Eth group rats ($p<0.05$). ALT distribution among other groups is shown in Fig. 2. AST/ALT ratio decreases in non-alcoholic liver diseases, while AST/ALT ratio increases in alcoholic liver injury [48]. In our study, while AST/ALT ratio in Eth group increased compared to Eug and EthEug group, no increase was found compared to the Cont group.

LDH is an enzyme that is found in many tissues including liver tissue and goes into serum if these tissues are damaged. Abd El Motteleb et al., have shown in their studies that low eugenol dose (10 mg eugenol/kg per day) can protect the liver from ischemia/reperfusion (I/R) damage by reducing lipid peroxidation levels. They found that AST, ALT and LDH levels decreased significantly compared to the I/R group in rats treated with 10mg eugenol [49]. In our study, there was a significant decrease in the LDH level in the Eug and EthEug groups compared to the Eth group. It is possible to state that with this decrease in the LDH level belonging to the Eug and EthEug groups, the tissue damage caused by alcohol decreased.

The fact that the Eth group was found lower than TAS level compared to the Cont group shows the toxic effect of ethanol on antioxidants [50]. The highest TAS level was found in the Eug group. When the TOS level taken into consideration, the Eth group was found to be the highest group, while in the EthEug group was close to the Cont group. This increase in TOS value is due to the strong antioxidant properties of eugenol.

5. Conclusions

In histopathological examination, intracellular macro and microvesicular fat accumulation due to alcohol in the Eth group was observed. Moreover, intense mononuclear cell infiltration, mostly lymphocytes, hydropic degeneration and the presence of erythrocytes in places in the synosoid spaces were also observed. It was found that degenerations decreased in the Eu group.

Our biochemical results, which express the presence of the antioxidant effect of eugenol on liver tissue, supported with histopathologic results.

As a result, an increase in antioxidant parameters was observed while reducing the oxidative stress effects on biochemical parameters and histopathological findings when using only eugenol as an antioxidant agent on the oxidative stress caused by ethanol in the liver of rats. Biochemical and histopathological findings can be stated that eugenol significantly prevents liver damage. Based on the information obtained from our study, we suggest that Eugenol can be used as a drug additive or nutritional supplement to protect health (particularly the liver) against alcohol damage.

Acknowledgement

References

[1] Pandanaboina, S.C., Kondeti, S.R., Rajbanshi, S.L., Kunala, P.N., Pandanaboina, S., Pandanaboina, M.M., Wudayagiri, R., *Alterations in antioxidant enzyme activities and oxidative damage in alcoholic rat tissues: protective role of Thespesia populnea*, Food Chem, 132(1), 150-159, 2012.

[2] Gencer, M., Ceylan, E., Aksoy, N., Uzun, K., *Oksidatif stres benign ve malign akciğer hastalıklarının ayırıcı tanısında belirteç olabilir mi?*, Turkiye Klinikleri Archives of Lung, 6(3), 89-92, 2005.

[3] Guyton, A.C., Hall, J.E., Tıbbi Fizyoloji, Nobel Tıp Kitapevi, 12. Baskı, İstanbul. 937-942, 2013.

[4] Ghany M, H.J., *Approach to the patient with liver disease*, Harrison's Principles of Internal Medicine, Fauci AS (ed). 17th Edition, 1918-1923, 2008.

[5] El-Newary, S.A., Shaffie, N.M., ve Omer, E. A., *The protection of Thymus vulgaris leaves alcoholic extract against hepatotoxicity of alcohol in rat*s, Asian Pacific Journal of Tropical Medicine, 10(4), 361-371, 2017.

[6] Li, S., Tan, H.-Y., Wang, N., Zhang, Z.-J., Lao, L., Wong, C.-W., Feng, Y., *The role of oxidative stress and antioxidants in liver diseases*, Int J Mol Sci, 16(11), 26087-26124, 2015.

[7] NCBI., https://pubchem.ncbi.nlm.nih.gov/compound/3314, Date of access: Mar. 29, 2018.

[8] TOXNET, T.D.N., Eugenol [USP], Date of access: 15.03.2018, from National Library of Medicine, 2018.

[9] Kamatou, G.P., Vermaak, I., Viljoen, A.M., *Eugenol—from the remote maluku islands to the international market place: A review of a remarkable and versatile molecule*, Molecules, 17(6), 6953, 2012.

[10] Tripathi, A.K., Mishra, S., Plant Monoterpenoids (Prospective Pesticides) Ecofriendly Pest Management for Food Security, Chapter 16, 507-524, San Diego: Academic Press, 2016.

[11] Bennett, A., Stamford, I.F., Tavares, I.A., Jacobs, S., Capasso, F., Mascolo, N., Carlo, G. D., *The biological activity of eugenol, a major constituent of nutmeg (Myristica fragrans): Studies on prostaglandins, the intestine and other tissues*, Phytotherapy Research, 2(3), 124-130,1988.

[12] Johnson, C.B., Kirby, J., Naxakis, G., Pearson, S., *Substantial UV-B-mediated induction of essential oils in sweet basil (Ocimum basilicum L.),* Phytochemistry, 51(4), 507-510, 1999.

[13] Dighe, V., Gursale, A., Sane, R., Menon, S., Raje, S., *Quantification of eugenol in Cinnamomum tamala nees and eberm. Leaf powder by high-performance thin-layer chromatography*, JPC - Journal of Planar Chromatography - Modern TLC 18(104), 305-307, 2005.

[14] Ueda-Nakamura, T., Mendonça-Filho, R.R., Morgado-Díaz, J.A., Korehisa Maza, P., Prado Dias Filho, B., Aparício Garcia Cortez, D., Nakamura, C. V., Antileishmanial activity of Eugenol-rich essential oil from Ocimum gratissimum, Parasitology International, 55(2), 99-105, 2006.

[15] Lopes-Lutz, D., Alviano, D.S., Alviano, C.S., Kolodziejczyk, P.P., Screening of chemical composition, antimicrobial and antioxidant activities of Artemisia essential oils, Phytochemistry, 69(8), 1732-1738, 2008.

[16] Howes, M.J., Kite, G.C., Simmonds, M.S., *Distinguishing chinese star anise from Japanese star anise using thermal desorption-gas chromatography-mass spectrometry*, J Agric Food Chem, 57(13), 5783-5789, 2009.

[17] Pragadheesh, V., Yadav, A., Singh, S., Gupta, N., Chanotiya, C., Leaf Essential Oil of Cultivated Pimenta Racemosa (Mill.) J.W. Moore from North India: Distribution of Phenylpropanoids and Chiral Terpenoids, Medicinal & Aromatic Plants, 2(1), 2-4, 2013.

[18] Jaganathan, S.K., Supriyanto, E., *Antiproliferative and molecular mechanism of eugenol-induced apoptosis in cancer cells*, Molecules, 17(6), 6290-6304, 2012.

[19] Guimarães, A.C., Meireles, L.M., Lemos, M.F., Guimarães, M.C.C., Endringer, D.C., Fronza, M., Scherer, R., A*ntibacterial activity of terpenes and terpenoids present in essential oils,* Molecules, 24(13), 2471, 2019.

[20] Li, Z., Veeraraghavan, V.P., Mohan, S.K., Bolla, S.R., Lakshmanan, H., Kumaran, S., Chinnathambi, A., *Apoptotic induction and anti-metastatic activity of eugenol encapsulated chitosan nanopolymer on rat glioma C6 cells via alleviating the MMP signaling pathway*, J Photochem Photobiol B, 203, 2020.

[21] Qian, W., Sun, Z., Wang, T., Yang, M., Liu, M., Zhang, J., Li, Y., *Antimicrobial activity of eugenol against carbapenem-resistant Klebsiella pneumoniae and its effect on biofilms*, Microbial Pathogenesis, 139, 103924, 2020.

[22] Matan, N., Rimkeeree, H., Mawson, A.J., Chompreeda, P., Haruthaithanasan, V., Parker, M., *Antimicrobial activity of cinnamon and clove oils under modified atmosphere conditions*, International Journal of Food Microbiology, 107(2), 180-185, 2006.

[23] EWG, http://www.ewg.org/skindeep/search.php?query=eugenol&h=Search#.Wr3 6zeZrOIV, Date of Access: 10.02.2018, from Environmet Working Group.

[24] Yan, S.L., Wang, Z.H., Yen, H.F., Lee, Y.J., Yin, M.C., *Reversal of ethanol-induced hepatotoxicity by cinnamic and syringic acids in mice*, Food and Chemical Toxicology, 98(B), 119-126, 2016.

[25] Mnafgui, K., Hajji R., Derbali, F., Gammoudi, A., Khabbabi, G., Ellefi, H., Allouche, N., Kadri, A., Gharsallah, N., A*nti-inflammatory, antithrombotic and cardiac remodeling preventive effects of eugenol in isoproterenol-induced myocardial infarction in wistar rat*, Cardiovascular Toxicology, 16(4), 336–344, 2016.

[26] Erel, O., *A novel automated direct measurement method for total antioxidant capacity using a new generation, more stable ABTS radical cation*, Clinical Biochemistry, 37(4), 277-285, 2004.

[27] Erel, O., *A new automated colorimetric method for measuring total oxidant status*, Clin Biochem, 38(12), 1103-1111, 2005.

[28] Larue-Achagiotis, C., Poussard, A.M., Louis-Sylvestre, J., *Alcohol drinking, food and fluid intakes and body weight gain in rats,* Physiol Behav, 47(3), 545-548, 1990.

[29] Bertola, A., Mathews, S., Ki, S.H., Wang, H., Gao, B., *Mouse model of chronic and binge ethanol feeding (the NIAAA model),* Nature protocols, 8(3), 627-637, 2013.

[30] Elanchezhian, T., Y., Mayilsamy, S., Radhakrishnan, S., *Comparison of haematological parameters between alcoholics and non-alcoholics*, Int J Res Med Sci 5(11), 5041-5407, 2017.

[31] Kawashima, Y., Someya, Y., Shirato, K., Sato, S., Ideno, H., Kobayashi, K., Imaizumi, K., *Single administration effects of ethanol on the distribution of white blood cells in rats*, J Toxicol Sci, 36(3), 347-355, 2011.

[32] Sonila, B., Klodeta, M., Andrin, T., Irida, P., *Changes of some blood count variables in correlation with the time of alcohol abuse*, Journal of Addiction Research & Therapy, 6(2), 221, 2015.

[33] Zhang, M.Q., Ren, X., Zhao, Q., Yue, S.-J., Fu, X.-M., Li, X., Wang, C.-Y., *Hepatoprotective effects of total phenylethanoid glycosides from Acanthus ilicifolius L. against carbon tetrachloride-induced hepatotoxicity*, Journal of Ethnopharmacology, (256), 112795, 2020.

[34] Gao, B., Bataller, R., *Alcoholic liver disease: pathogenesis and new therapeutic targets*, Gastroenterology, 141(5), 1572-1585, 2011.

[35] Chattopadhyay, R.R., *Possible mechanism of hepatoprotective activity of Azadirachta indica leaf extract: part II*, J Ethnopharmacol, 89(2-3), 217-219, 2003.

[36] Barboza, J.N., da Silva Maia Bezerra Filho, C., Silva, R.O., Medeiros, J.V.R., de Sousa, D.P., *An overview on the anti-inflammatory potential and antioxidant profile of eugenol*, Oxidative medicine and cellular longevity, 3957262, 2018.

[37] Guenette, S.A., Ross, A., Marier, J.F., Beaudry, F., Vachon, P., *Pharmacokinetics of eugenol and its effects on thermal hypersensitivity in rats*, Eur J Pharmacol, 562(1-2), 60-67, 2007.

[38] Ballard, H.S., *The hematological complications of alcoholism*, Alcohol Health Res World, 21(1), 42-52, 1997.

[39] Xiao, W., *Study on the joint effects of acrylonitrile and alcohol in rats*, Wei Sheng Yan Jiu, 27(5), 295-296 1998.

[40] Yalçın, M., Yağcı, A., *Alterations in some blood parameters after high level ethanol intake,* Uludag Univ. J. Fac. Vet. Med., 24(1-2-3-4), 47-52, 2005.

[41] Gülçin, İ., Elmastaş, M., Aboul-Enein, H.Y., *Antioxidant activity of clove oil – A powerful antioxidant source*, Arabian Journal of Chemistry, 5(4), 489-499, 2012.

[42] Anbu, S., Anuradha, C.V., *Protective effect of eugenol against alcohol-induced biochemical changes in rats,* International Journal of Research in Biotechnology and Biochemistry, 2(2), 13-18, 2012.

[43] Dudonne, S., Vitrac, X., Coutiere, P., Woillez, M., Merillon, J.M., *Comparative study of antioxidant properties and total phenolic content of 30 plant extracts of industrial interest using DPPH, ABTS, FRAP, SOD, and ORAC assays*, J Agric Food Chem, 57(5), 1768-1774, 2009.

[44] Yogalakshmi, B., Viswanathan, P., Anuradha, C.V., *Investigation of antioxidant, anti-inflammatory and DNA-protective properties of eugenol in thioacetamide-induced liver injury in rats,* Toxicology, 268(3), 204-212, 2010.

[45] Binu, P.P., Priya, N.M., Abhilash, S.P., Vineetha, R.C.P., Nair, H.P., *Protective effects of eugenol against hepatotoxicity induced by arsenic trioxide: An antileukemic drug*, Iranian journal of medical sciences, 43(3), 305-312, 2018.

[46] Thuwaini, M., Abdul Mounther, M., Kadhem, H., *Hepatoprotective effects of the aqueous extract of clove (Syzygium aromaticum) against paracetamol-induced hepatotoxicity and oxidative stress in rats*, EJPMR, 3(8), 36-42, 2016.

[47] Muller, L.G., Pase, C.S., Reckziegel, P., Barcelos, R.C., Boufleur, N., Prado, A.C., Burger, M.E., *Hepatoprotective effects of pecan nut shells on ethanol-induced liver damage, exptoxicol pathol,* 65(1-2), 165-171, 2013.

[48] Nyblom, H., Berggren, U., Balldin, J., Olsson, R., *High AST/ALT ratio may indicate advanced alcoholic liver disease rather than heavy drinking*, Alcohol, 39(4), 336-339, 2004.

[49] Abd El Motteleb, D.M., Selim, S.A., Mohamed, A.M., *Differential effects of eugenol against hepatic inflammation and overall damage induced by ischemia/re-perfusion injury*, J Immunotoxicol, 11(3), 238-245, 2014.

[50] Basarslan, S.K., Osun, A., Senol, S., Korkmaz, M., Ozkan, U., Kaplan, I., *Protective effects of intralipid and caffeic acid phenyl esther (CAPE) on neurotoxicity induced by ethanol in rats*, Turk Neurosurg, 27(1), 66-73, 2017.

LCMSMS Analysis of 8-OHdG and Measuring Metallothionein Level for Evaluation of Protective Role of Geraniol in Lead Acetate Administered Rats

Aysel ALKAN UÇKUN[1,*], Ertan YOLOĞLU[2], Miraç UÇKUN[3], Ahmet ÖZKAYA[4]

[1]*Department of Environmental Engineering, Faculty of Engineering, Adıyaman University, Adıyaman, Turkey*
ayseluckun@gmail.com, ORCID: 0000-0002-8957-7476
[2]*Department of Mathematics and Science Education, Faculty of Education, Adıyaman University, Adıyaman, Turkey*
ertanyologlu82@gmail.com, ORCID: 0000-0002-9730-9471
[3]*Department of Food Engineering, Faculty of Engineering, Adıyaman University, Adıyaman, Turkey*
miracuckun@gmail.com, ORCID ID: 0000-0002-9018-8515
[4]*Department of Chemistry, Faculty of Science-Literature, Adıyaman University, Adıyaman, Turkey*
aozkaya@adiyaman.edu.tr, ORCID ID: 0000-0002-0173-3084

Abstract

In this study, DNA damage and metallothionein levels were used as biomarkers to evaluate the protective potential of geraniol, a monoterpen against lead stress, in rats. Hepatic 8-hydroxy-2-deoxyguanosine (8-OHdG) level used as a marker of oxidative DNA damage was measured by LCMSMS. Experimental groups were formed in four ways: control, lead acetate, geraniol and lead acetate + geraniol. Seven animals were used in each group. Geraniol and lead acetate were administered to rats for 30 days. In geraniol administered rats, 8-OHdG and metallothionein levels decreased significantly compared to lead acetate administered rats. The highest DNA damage and metallothionein levels were observed in lead acetate administered rats. According to the results of this study, it can be suggested that geraniol protects cells against lead-caused damage by reducing ROS production. In addition, studies on the measurement of 8-OHdG by LCMSMS in

---

the literature are limited. Therefore, it is thought that the presented study will contribute to the evaluation of the applicability of this method in the literature.

Keywords: 8-hydroxy-2-deoxyguanosine; Metallothionein; Geraniol; Lead; LCMSMS.

Kurşun Asetat Uygulanmış Sıçanlarda Geraniolün Koruyucu Rolünün Değerlendirilmesi için Metallothionein Düzeyinin Ölçülmesi ve 8-OHdG'nin LCMSMS Analizi

Öz

Bu çalışmada, sıçanlarda kurşun stresine karşı bir monoterpen olan geraniolün koruyucu potansiyelini değerlendirmek için DNA hasarı ve metallotiyonein seviyeleri biyobelirteç olarak kullanıldı. Oksidatif DNA hasarının bir belirteci olarak kullanılan hepatik 8-hidroksi-2-deoksiguanozin (8-OHdG) seviyesi LCMSMS ile ölçüldü. Her grupta yedi hayvan kullanıldı. Geraniol ve kurşun asetat 30 gün boyunca uygulandı. Geraniol uygulanan sıçanlarda, 8-OHdG ve metallotiyonein düzeyleri, kurşun asetat uygulananlara kıyasla önemli derecede düşüş göstermiştir. En yüksek DNA hasarı ve metallotiyonein seviyesi, kurşun asetat uygulanan sıçanlarda gözlenmiştir. Bu çalışmanın sonuçlarına göre, geraniolün hücreleri kurşunun yol açtığı hasara karşı ROS üretimini azaltmak suretiyle koruduğu ileri sürülebilir. Ayrıca, literatürde 8-OHdG'nin LCMSMS ile ölçümü konusunda çalışmalar sınırlı sayıdadır. Bu nedenle, sunulan çalışmanın bu yöntemin literatürde uygulanabilirliğinin değerlendirilmesine katkıda bulunacağı düşünülmektedir.

Anahtar Kelimeler: 8-hidroksi-2-deoksiguanozin; Metallotiyonein; Geraniol; Kurşun; LCMSMS.

1. Introduction

Environmental or occupational exposures to numerous chemicals can occur during various periods of human life. Metals such as mercury, cadmium, lead etc. could pose to serious health problems [1, 2]. Lead causes to oxidative stress by increasing free radicals and reducing antioxidant sources [3]. Additionaly lead displaces zinc in many proteins and may cause damage to DNA [4]. Many scientists have suggested that various antioxidant treatments can prevent oxidative stress caused by lead [5]. Herbs and spices have been used as alternative and traditional medicines for many years. Terpenoid compounds found in essential oils of plants such as rose, citronella and coriander have been reported to be beneficial to human health [6]. Geraniol (3,7-dimethylocta-trans-2,6-dien-1-ol) is an acyclic monoterpene alcohol with the chemical formula $C_{10}H_{18}O$. Geraniol was isolated from palmarosa oil and has many biochemical, pharmacological properties and the most important of which is a herbal insect repellent [7]. Geraniol exhibits

antitumor effect against many cancer types and has also been shown by many authors to have antimicrobial activity [8, 9].

Metallothioneins (MTs) are cysteine rich intracellular proteins with low molecular weight that bind to metals such as zinc and copper to provide intracellular metal homeostasis [10, 11]. MTs are responsible for maintaining transition metal ion homeostasis and redox stabilization by protecting the cell against DNA damage and apoptosis [12]. Reduced expression of MT has been observed in liver [13], colon [14] and prostate [15] cancer. The protective role of MT in these cancer types has not been fully explained, but when considering the antioxidant effect and protective properties against DNA damage, this reduction may increase sensitivity to toxin-induced damage [16].

Reactive oxygen species are produced as a result of exposure to environmental factors affecting human health such as xenobiotics, radiation and during normal cellular metabolic functions [17, 18]. Among the cellular biomolecules, DNA is the most affected by reactive oxygen species [19, 20]. An increase in the 8-OHdG level occurs after oxidative DNA damage in the cells [21, 22]. For this, 8-OHdG is an important biomarker used in the monitoring of cancer and other diseases [23]. Purpose of measuring 8-OHdG level in this study was to determine the level of DNA damage caused by reactive oxygen species in rats treated with lead and the protective effect of geraniol against this damage.

Many analytical methods such as including enzyme-linked immunosorbent assay (ELISA), high-performance liquid chromatography with electrochemical detection (HPLC-ECD), gas chromatography-mass spectrometry (GCMS) and liquid chromatography-tandem mass spectrometry (LCMSMS) have been developed to measure 8-OHdG. Recently, due to its specificity, reproducibility, accuracy and structural characterization, there is a great interest in LCMSMS [24]. For these reasons, we preferred to measure the level of 8-OHdG by LCMSMS to estimate lead acetate-induced DNA damage in our study. In the literature, the study of 8-OHdG analysis with LCMSMS is very limited. Therefore, our study will also contribute to the 8-OHdG analysis by LCMSMS.

The objective of this study was to determine whether geraniol had a protective effect against lead damage by changing 8-OHdG and MT levels in rat liver.

2. Materials and Methods

2.1. Animals and experimental procedure

In this study, twenty-eight Wistar albino rats with an average weight of 330 ± 10 g were used. Animals were grown under a standard light / dark cycle with regular temperature and humidity. For the study of animal experiments, approval was obtained from the Ethics Committee of Fırat University, Elazığ, Turkey (Document No: 146/2011-11). Experimental groups were formed in four ways: control, Pb acetate, geraniol and Pb acetate + geraniol. Seven animals were used in each group. Geraniol was administered to animals at 1 day intervals for 30 days by gavage at a dose of 50 mg / kg by dissolving in corn oil. Pb acetate (dissolved in acetic acid) was administered to the animals by adding 500 ppm of Pb acetate to each liter of drinking water daily for 30 days. Only the solvents used to dissolve geraniol and Pb acetate were administered to the animals in the control group. At the end of 30 days, the animals were sacrificed and the liver tissues were removed and stored at -20 for biochemical analysis. The amount of Pb in liver was determined by inductively coupled plasma mass spectrometry (ICP-MS, Perkin Elmer, MA, USA) in Adıyaman University Central Research Laboratory by Ozkaya et al. [25].

2.2. Quantification of 8-hydroxy-2-deoxyguanosine in rat livers by LCMSMS

DNeasy tissue kit (Qiagen) was used for DNA isolation from the control, Pb acetate, geraniol and Pb acetate + geraniol exposed liver of rats. DNA isolation was performed according to the protocol of kit. The level of 8-OHdG in the liver was measured by liquid chromotgraphy tandem mass spectrometry (LCMSMS, Shimadzu Quadropole 8040) in Adıyaman University Central Research Laboratory. Information on LCMSMS analysis conditions is shown in Table 1 and Table 2, respectively. The Inertsil ODS-4 (2.1 mm I.D. × 50 mm L., 3 μm) column was used. Mobil phase A (5 mM ammonium formate in 100% water) and mobil phase B (5 mM ammonium formate in 100% methanol) were used at a flow rate of 0.2 mL min^{-1}. The retention time of 8-OHdG was around 5.16 minutes. The curve was linear ($r^2 = 0.9998$). The calibration curve range prepared from the standards for the calculation of 8-OHdG concentrations was in the range of 1-10 μg/L. The samples were spiked over the samples so that the resulting values corresponded to the calibration curve values, and the total concentration of standart was given to the LCMSMS as 5 μg/L. The standard of 8-OHdG were gotten from Sigma-Aldrich with ≥ 98% purity. This method quantifies the molecular level of DNA damage by measuring the level of 8-OHdG directly. One milliliter purified DNA extract was imported to a vial. Quantitative readings were made in three replicates.

Table 1: LCMSMS conditions

Instrument	Shimadzu Prominence LC-20A/XR Shimadzu LCMS-8040
Mobil phase A	5 mM ammonium formate in 100% water
Mobil phase B	5 mM ammonium formate in 100% methanol
Column	Inertsil ODS-4 (2.1 mm I.D. × 50 mm L., 3 μm)
Column oven temperature	40 °C
Flow rate	0.2 mL/min
Interface current	4.5 kV
Spraying gas flow rate	3 mL/min
Drying gas flow rate	15 mL/min
DL temperature	250 °C
HB temperature	450 °C

Table 2: Gradient mode of LCMSMS

Step	Time	Module	Command	Value
1	2.00	Pumps	Pump B Conc.	5
2	2.01	Pumps	Pump B Conc.	80
3	3.00	Pumps	Pump B Conc.	80
4	3.01	Pumps	Pump B Conc.	5
5	9.00	Controller	Stop	

2.3. Quantification of metallothionein in rat livers by microplate reader

To measure the MT level, the method was used developed by Viarengo et al. [26] which was modified for the microplate reader. The livers were homogenized for one minute at 2000 rpm on ice in 20 mM Tris HCl buffer (pH 8.6) containing 0.5 M sucrose, 0.5 M PMSF and 0.01% b-mercaptoethanol. The homogenates were centrifuged at 15000 g for 30 minutes and the supernatants obtained from this assay were used for analysis. To each 1 ml supernatant was added 1.05 ml of cold (-20 ºC) absolute ethanol and 80 μL of chloroform, and these mixtures were centrifuged for 10 min at 6000 x g at 4 ºC. The mixtures were allowed to incubate for one hour at -20 ° C and then centrifuged for 10 minutes at 6000 x g at 4 °C. Supernatants discharged after centrifugation, the pellets were washed with homogenizing buffer containing 87% ethanol and 1% chloroform and centrifuged at 6000 x g for 10 min at 4 ºC. Finally, the pellets were resuspended in 300 μL 5 mM Tris-HCl buffer (pH 7.0) containing 1 mM EDTA, and 4.2 mL 0.43mM. DTNB buffer containing 0.2 M Na-phosphate (pH 8.0) was added to each sample and then these mixtures were incubated at room temperature for 30 minutes in the dark and centrifuged at 3000 x g for 5 minutes. For the calculation of the MT concentration using GSH as a reference, samples were read at 412 nm absorbance.

2.4. Statistical analysis

In the statistical analysis of the data, computer software package SPSS 22 was used. Data normality was determined using Shapiro-Wilk test ($p < 0.05$). Kruskal Wallis test was used to determine the comparison of biochemical data between groups. Bonferroni Mann Whitney-U test was used to determine whether there was a significant difference within the groups. The statistical significance level was based on $p < 0.05$.

3. Results and Discussion

The levels of Pb determined by ICPMS in rats [25] were shown in Table 3. The concentration of Pb was found significantly higher in Pb acetate (843.7 ± 111 µg/kg) group than the geraniol group (26.0 ± 8.69 µg/kg) ($p < 0.05$). Likewise, the amount of Pb was significantly higher in Pb acetate group than Pb acetate + geraniol group (574.2 ± 58.03 µg/kg) ($p < 0.05$). Pb exposure is known to cause an increase in reactive oxygen species and a decrease in cellular antioxidant capacity. Also it is known that an imbalance in the prooxidant / antioxidant ratio causes damage to membranes, DNA and proteins in tissue and cellular components [27].

Table 3: Pb concentrations in the liver of rats

Group	N	Pb ± S.E. (µg/kg)
Control	7	31.0 ± 9.95
Pb acetate	7	843.7 ± 111[a]
Geraniol	7	26.0 ± 8.69
Pb acetate + Geraniol	7	574.2 ± 58.03[a,b]

[a] : $p < 0.05$ compared with the control group
[b] : $p < 0.05$ compared with the Pb acetate group

The concentrations of 8-OHdG determined by LCMSMS were presented in Table 4. The recovery value was calculated over seven samples and was found in the range of 90% - 105 %. The % relative standard deviation (RSD) value was between 1.23 and 27.64. Measurement of 8-OHdG level in the liver is an integral indicator of many parameters such as free radical production, antioxidant defense system and cellular redox potential [28]. The mean concentration of 8-OHdG in DNA of liver from Pb acetate applied group was in the range of $181 \pm 16.09 – 664 \pm 79.22$ ng L^{-1}. A significant increase was observed in 8-OHdG level in the Pb acetate and Pb acetate+geraniol groups, compared to the control group (406.57 ± 63.07; 124.14 ± 10.04; 93.43 ± 8.7 ng/L respectively), however there was no significant difference between the control and geraniol group. In short, we can say that there was significant DNA damage in the group where Pb is applied alone, compared to the other groups, whereas there was little or no damage in the geraniol-treated groups. Oxidative stress increases ROS production, which can cause oxidative

damage to DNA and proteins [29]. Since 8-OHdG is a product of oxidative DNA damage induced by ROS, its level indirectly reflects the level of ROS in the body [30]. In our study, elevation of the 8-OHdG level in Pb acetate-treated rats may be attributed to oxidative stress resulting in an increase in the amount of free radicals because of metabolic activation between the blood and membrane. Significant declines in the level of 8-OHdG in geraniol administered rats can be interpreted as the reduction of reactive oxygen species by geraniol. At the same time, geraniol may have reduced hepatic DNA damage which caused by Pb acetate. Similarly, Bolin et al. [31] found that 8-OHdG levels increased significantly in rats treated with Pb compared to the control group. Xu et al. [32] exposed rats to different doses of Pb acetate for 4 weeks and as a result they observed an increase in DNA damage along with ROS production. In a study conducted by Liu et al. [33] the liver of rats exposed to 500 mg/L Pb acetate for 75 days by drinking water showed an increase in the 8-OHdG level in parallel with ROS production, and it was suggested that DNA was a target in ROS-induced liver injury, furthermore, the increase of 8-OHdG induced by Pb was effectively suppressed by puerarin. In a study investigating the linkage of Pb-induced DNA damage to oxidative stress, Wang et al. [34] observed that an increase in ROS production in the mitochondria of mice exposed to 0.2% Pb acetate for 42 days was associated with apoptosis induced by caspase 3 activation and 8-OHdG lesion. Tiwari and Kakkar [35] reported that geraniol has antioxidant potential by reducing lipid peroxidation and inhibiting ROS production. It has been reported by Ong et al. [36] that geraniol plays a protective role against liver cancer by inhibiting cell proliferation and DNA damage. Ozkaya et al. [25] observed that 8-OHdG immunoreactivity in rats did not differ significantly between the control and geraniol treated groups, but there was a significant difference between the Pb acetate and Pb acetate + geraniol treated groups. In our study, there was no significant difference between the control and geraniol group in terms of 8-OHdG level.

There are limited studies about the measurement of 8-OHdG level in LCMSMS, which is a marker of DNA damage, so our use of this method will have contributed to the literature. Chen et al. [37] developed a stable isotope dilution by using an automated on-line SPE LCMSMS method to simultaneously measure 8-OHdG and cotinine in human urine. Guo et al. [24] have developed a sensitive, specific and applicable method to detect 8-OHdG in human urine in UPLC-MSMS. They observed higher levels of 8-OHdG in patients with colorectal cancer and tumor metastasis compared to the control group and patients without tumor metastasis respectively. Li et al. [38] determined the levels of 8-OHdG in the livers and kidneys of cetaceans through isotope-dilution LCMSMS and based on the results of the study, it has been suggested that measurement of 8-OHdG by LCMSMS is possible and can be associated with environmental pollutants.

Table 4: Levels of 8-OHdG in the liver of rats

Group	N	Mean ± S.E. (ng/L)	P values (Other groups against control)	P value Pb acetate+Geraniol group against Pb acetate group
Control	7	93.43 ± 8.7		
Pb acetate	7	406.57 ± 63.07[a]	0.002	
Geraniol	7	120.43 ± 23.14	0.405	
Pb acetate+Geraniol	7	124.14 ± 10.04[a,b]	0.047	0.002

[a] : $p < 0.05$ compared with the control group
[b] : $p < 0.05$ compared with the Pb acetate group

Table 5 shows the changes in MT levels between groups. As can be seen in this table, the highest MT level was observed in the Pb acetate group but there was no significant difference between Pb acetate and Pb acetate + geraniol groups (276 ± 6 and 262 ± 2 µmol/gr wet weight tissue; respectively) ($p > 0.05$). The lowest MT level was detected in the geraniol treated group (221 ± 6 µmol/gr wet weight tissue). There was no significant difference between the geraniol treated and control groups in MT levels ($p > 0.05$). Metallothionein is a protein that is slightly induced by lead but more induced by zinc and cadmium. The lead is better bonded to a pre-induced MT by zinc and cadmium so that a lead-thionine complex is formed. In our study, MT levels were higher in Pb acetate group than geraniol treated and control groups. There are many studies showing increases in MT expression due to the protective mechanism of MT against Pb administration. It was observed that MT synthesis was increased in liver, kidney and other tissues of rats exposed to sublethal doses of Pb [39, 40]. MT gene expression was increased by more than 3-fold in cultured human mononuclear blood cells due to Pb exposure [41]. MT expression was significantly increased due to the intra cerebral administration of Pb [42]. Similarly, Ikebuchi et al. [40] observed that when they applied sublethal dose of Pb acetate intraperitoneally to the rats, there was an increase in the synthesis of lead metallothionein and zinc metallothionein. Chidinma et al. [43] observed increased MT expression in mouse livers exposed to different concentrations of Pb. In addition, several studies have shown that geraniol has an antioxidant effect by preventing oxidative stress. Ozkaya and his colleagues [25] suggested that hepatic MDA level, which is an important indicator of lipid peroxidation, was lower in the group where geraniol was administered alone than the group in which Pb acetate was applied alone, and this may be caused by the antioxidant effect of geraniol. Wang et al. [44] stated that at a dose of 250 mg kg^{-1} geraniol can reduce oxidative stress by reducing lipid peroxidation and affecting the activity of GSH and other antioxidant enzymes. Prasad and Muralidhara [45] have also suggested that geraniol can be a promising antioxidant by reducing oxidative stress.

Table 5: The MT levels in the liver of rats

Group	N	MT ± S.E. (μmol/gr wet weight tissue)
Control	7	240 ± 5
Pb acetate	7	276 ± 6[*]
Geraniol	7	221 ± 6
Pb acetate + Geraniol	7	262 ± 2[*]

[*] : $p < 0.05$ compared with the control group

In conclusion, it can be said that Pb causes oxidative and DNA damage in the liver of rats, and geraniol may reduce these damages by inhibiting ROS production. 8-OHdG and MT are also useful biomarkers reflecting lead toxicity in rats. In addition, it can be said that exogenous supplementation of geraniol may play an advantageous role in antioxidant defense of cells to prevent Pb toxicity.

References

[1] Sinicropi, M.S., Amantea, D., Caruso, A., Saturnino, C., *Chemical and biological properties of toxic metals and use of chelating agents for the pharmacological treatment of metal poisoning*, Archives of Toxicology, 84, 501-520, 2010.

[2] Carocci, A., Rovito, N., Sinicropi, M.S., Genchi, G., *Mercury toxicity and neurodegenerative effects*, Reviews of Environmental Contamination and Toxicology, 229, 1-18, 2014.

[3] Silbergeld, E.K., Waalkes, M., Rice, J.M., *Lead as a carcinogen, experimental evidence and mechanisms of action*, American Journal of Industrial Medicine, 38, 316-323, 2000.

[4] Adonaylo, V.N., Oteiza, P.I., *Pb^{2+} promotes lipid peroxidation and alteration in membrane physical properties*, Toxicology, 132, 19-32, 1999.

[5] Garcia, M.T.A., Gonzalez, E.L.M., *Toxic effects of perinatal lead exposure on the brain of rats, involvement of oxidative stress and the beneficial role of antioxidants*, Food Chemistry and Toxicology, 46, 2089-2095, 2008.

[6] Jayachandran, M., Chandrasekaran, B., Namasivayam, N., *Geraniol attenuates fibrosis and exerts anti-inflammatory effects on diet induced atherogenesis by NF-κB signaling pathway*, European Journal of Pharmacology, 762, 102-111, 2015.

[7] Barnard, D.R., Xue, R., *Laboratory evaluation of mosquito repellents against Aedes albopictus, Culex nigripalpus, and Ochlerotatus triseriatus (Diptera, Culicidae)*, Journal of Medical Entomology, 41, 726-730, 2004.

[8] Burke, Y.D., Stark, M.J., Roach, S.L., Sen, S.E., Crowell, P.L., *Inhibition of pancreatic cancer growth by the dietary isoprenoids farnesol and geraniol*. Lipids, 32, 151-156, 1997.

[9] Bard, M., Albrecht, M.R., Gupta, N., Guynn, C.J., Stillwell, W., *Geraniol interferes with membrane functions in strains of Candida and Saccharomyces*, Lipids, 23, 534-538, 1988.

[10] Hamer, D.H., *Metallothionein*, Annual Review of Biochemistry, 55, 913-951, 1986.

[11] Takahashi, S., *Molecular functions of metallothionein and its role in hematological malignancies*, Journal of Hematology and Oncology, 5, 41, 2012.

[12] Cherian, M.G., Jayasurya, A., Bay, B.H., *Metallothioneins in human tumors and potential roles in carcinogenesis*, Mutation Research, 533, 201-209, 2003.

[13] Datta, J., Majumder, S., Kutay, H., Motiwala, T., Frankel, W., Costa, R., Cha, H.C., MacDougald, O.A., Jacob, S.T., Ghoshal, K., *Metallothionein expression is suppressed in primary human hepatocellular carcinomas and is mediated through inactivation of CCAAT/enhancer binding protein alpha by phosphatidylinositol 3-kinase signaling cascade*, Cancer Research, 67, 2736-2746, 2007.

[14] Yan, D.W., Fan, J.W., Yu, Z.H., Li, M.X., Wen, Y.G., Li, D.W., Zhou, C.Z., Wang, X.L., Wang, Q., Tang, H.M., Peng, Z.H., *Downregulation of metallothionein 1F, a putative oncosuppressor, by loss of heterozygosity in colon cancer tissue*, Biochimica et Biophysica Acta, 1822, 918-926, 2012.

[15] Wei, H., Desouki, M.M., Lin, S., Xiao, D., Franklin, R.B., Feng, P., *Differential expression of metallothioneins (MTs) 1, 2, and 3 in response to zinc treatment in human prostate normal and malignant cells and tissues*, Molecular Cancer, 7, 7, 2008.

[16] Zhang, B., Satoh, M., Nishimura, N., Suzuki, J.S., Sone, H., Aoki, Y., Tohyama, C., *Metallothionein deficiency promotes mouse skin carcinogenesis induced by 7,12-dimethylbenz[a]anthracene*, Cancer Research, 58, 4044-4046, 1998.

[17] O'Donovan, P., Perrett, C.M., Zahang, X., Montaner, B., Xu, Y.Z., Harwood, C.A., McGregor, J.M., Walker, S.L., Hanaoka, F., Karran, P., *Azathioprine and UVA light generate mutagenic oxidative DNA damage*, Science, 309, 1871-1874, 2005.

[18] Alan, M.R., Wang, Y., Shah, J., Gordon, S., Fager, M., Butter, PP., Jun, KH., Guardiola-Salmeron, C., Carabe-Fernandez, A., Fan, Y., *Proton beam radiation induces DNA damage and cell apoptosis in glioma stem cells through reactive oxygen species*, Scientific Reports, 5, 13961-13972, 2015.

[19] Krystona, T.B., Georgieva, A.B., Pissisb, P., Georgakilasa, A.G., *Role of oxidative stress and DNA damage in human carcinogenesis*, Mutation Research, 711, 193-201, 2011.

[20] Dizdaroglu, M., *Oxidatively induced DNA damage and its repair in cancer*. Mutation Research, 763, 212-245, 2015.

[21] Cooke, M.S., Evans, M.D., Dizdaroglu, M., Lunec, J., *Oxidative DNA damage, mechanisms, mutation, and disease*, Faseb Journal, 17, 1195-1214, 2003.

[22] Gajewski, E., Rao, G., Nackerdien, Z., Dizdaroglu, M., *Modification of DNA bases in mammalian chromatin by radiationgenerated free radicals*, Biochemistry, 29, 7876-7882, 1990.

[23] Shimoda, R., Nagashima, M., Sakamoto, M., Yamaguchi, N., Hirohashi, S., Yokota, J., Kasai, H., *Increased formation of oxidative DNA damage, 8-hydroxydeoxyguanosine, in human livers with chronic hepatitis*, Cancer Research, 54, 3171-3172, 1994.

[24] Guo, C., Li, X., Wang, R., Yu, J., Ye, M., Mao, L., Zhang, S., Zheng, S., *Association between Oxidative DNA damage and risk of colorectal cancer, Sensitive Determination of Urinary 8-Hydroxy-2-deoxyguanosine by UPLC-MS/MS Analysis*, Scientific Reports, 6, 32581, 2016.

[25] Ozkaya, A., Sahin, Z., Kuzu, M., Saglam, Y.S., Ozkaraca, M., Uckun, M., Yologlu, E., Comakli, V., Demirdag, R., Yologlu, S., *Role of geraniol against lead acetate-mediated hepatic damage and their interaction with liver carboxylesterase activity in rats*, Archives of Physiology and Biochemistry, 124, 80-87, 2017.

[26] Viarengo, A., Ponzano, E., Dondero, F., Fabbri, R., *A simple spectrophotometric method for metallothionein evaluation in marine organisms, an application to Mediterranean and Antarctic molluscs*, Marine Environmental Research, 44, 69-84, 1997.

[27] Hsu, P.C., Guo, Y.L., *Antioxidant nutrients and lead toxicity*, Toxicology, 180, 33-44, 2002.

[28] Kasai, H., *Increased formation of oxidative DNA damage, 8-hydroxydeoxyguanosine, in human livers with chronic hepatitis*, Cancer Research, 54, 3171-3172, 1994.

[29] Dribben, W.H., Creeley, C.E., Farber, N., *Low-level lead exposure triggers neuronal apoptosis in the developing mouse brain*, Neurotoxicology and Teratology, 33, 473-480, 2011.

[30] Courtois, E., Marques, M., Barrientos, A., Casado, S., López-Farré, A., *Lead-induced downregulation of soluble guanylate cyclase in isolated rat aortic segments mediated by reactive oxygen species and cyclooxygenase-2*, Journal of the American Society of Nephrology, 14, 1464-1470, 2003.

[31] Bolin, C.M., Basha, R., Cox, D., Zawia, N.H., Maloney, B., Lahiri, D.K., Cardozo-Pelaez, F., *Exposure to lead and the developmental origin of oxidative DNA damage in the aging brain*, Faseb Journal, 20, 788-790, 2006.

[32] Xu, J., Lian, L.J., Wu, C., Wang, X.F., Fu, W.Y., Xu, L.H., *Lead induces oxidative stress, DNA damage and alteration of p53, Bax and Bcl-2 expressions in mice*, Food Chemistry and Toxicology, 46, 1488-1494, 2008.

[33] Liu, C.M., Ma, J.Q., Sun, Y.Z., *Puerarin protects the rat liver against oxidative stress mediated DNA damage and apoptosis induced by lead*, Experimental Toxicology and Pathology, 64, 575-582, 2012.

[34] Wang, C., Liang, J., Zhang, C., Bi, Y., Shi, X., Shi, Q., *Effect of ascorbic acid and thiamine supplementation at different concentrations on lead toxicity in liver*, Annals of Occupational Hygiene, 51, 563-569, 2007.

[35] Tiwari, M., Kakkar, P., *Plant derived antioxidants-geraniol and camphene protect rat alveolar macrophages against t-BHP induced oxidative stress*, Toxicology in Vitro, 23, 295-301, 2009.

[36] Ong, T.P., Heidor, R., Conti, A.D., Dagli, M.L.Z., Moreno, F.S., *Farnesol and geraniol chemopreventive activities during the initial phases of hepatocarcinogenesis involve similar actions on cell proliferation and DNA damage, but distinct actions on apoptosis, plasma cholesterol and HMGCoA reductase*, Carcinogenesis, 27, 1194-1203, 2006.

[37] Chen, C.Y., Jhou, Y.T., Lee, H.L., Lin, Y.W., *Simultaneous, rapid, and sensitive quantification of 8-hydroxy-2'-deoxyguanosine and cotinine in human urine by on-line solid-phase extraction LC-MS/MS, correlation with tobacco exposure biomarkers NNAL*, Analytical and Bioanalytical Chemistry, 408, 6295-6306, 2016.

[38] Li, C.S., Wu, K.Y., Gou-Ping., Chang-Chien, Chou, C.C., *Analysis of oxidative DNA damage 8-Hydroxy-2'-deoxyguanosine as a biomarker of exposures to persistent pollutants for marine mammals*, Environmental Science and Technology, 39, 2455-2460, 2005.

[39] Dai, S., Yin, Z., Yuan, G., Yu, H., Jia, R., Xu, J., Song, X., Li, L., Shu, Y., Liang, X., He, C., Lv, C., Zhang, W., *Quantification of metallothionein on the liver and kidney of rats by subchronic lead and cadmium in combination*, Environmental Toxicology and Pharmacology, 36, 1207-1216, 2013.

[40] Ikebuchi, H., Teshima, R., Suzuki, K., *Simultaneous induction of Pb-metallothionein-like protein and Zn-thionein in the liver of rats given lead acetate*, Biochemical Journal, 233, 541-546, 1986.

[41] Gillis, B.S., Arbieva, Z., Gavin, I.M., Analysis of lead toxicity in human cells, BMC Genomics, 13, 344, 2012.

[42] Nakao, K., Kibayashi, K., Taki, T., Koyama, H., *Changes in the Brain after Intracerebral Implantation of a Lead Pellet in the Rat*, Journal of Neuroscience, 27, 1925-1934, 2010.

[43] Chidinma, N.C., Adewale, A., Chiaka, A., *Differential expression of metallothionein-1 and cytochrome p450 2a5 (cyp2a5) in mice in response to lead acetate exposure and industrial effluents in Ibadan, Nigeria*, Toxicology and Industrial Health, 32, 1975-1981, 2016.

[44] Wang, J., Su, B., Zhu, H., Chen, C., Zhao, G., *Protective effect of geraniol inhibits inflammatory response, oxidative stress and apoptosis in traumatic injury of the spinal cord through modulation of NF-jB and p38 MAPK*, Experimental and Therapeutic Medicine, 12, 3607-3613, 2016.

[45] Prasad, S.N., Muralidhara, M., *Protective effects of geraniol (a monoterpene) in a diabetic neuropathy rat model, attenuation of behavioral impairments and biochemical perturbations*, Journal of Neuroscience Research, 92, 1205-1216, 2014.

The Effect of Fish Farming on Zooplankton Fauna in Kozan Dam Lake (Adana)

Ahmet BOZKURT[1,*], Cem TUGYAN[1]

[1]*İskenderun Technical University, Faculty of Marine Sciences and Technology, İskenderun, Hatay, Turkey*
ahmet.bozkurt@iste.edu.tr, ORCID: 0000-0001-6673-550X
cemtugyan@hotmail.com, ORCID: 0000-0001-8653-1360

Abstract

The effect of aquaculture on water quality (Dissolved Oxygen, temperature, pH, conductivity, NO_2-N, NO_3-N, NH_4-N, PO_4-P and chlorophyll-*a*) and zooplankton fauna was investigated in Kozan Dam Lake. As a result of the study, it was determined that fish farming did not have a statistically effect on zooplankton fauna and water quality parameters, but it caused some minor changes. In the study, a total of 50 zooplankton species were identified, including 29 from rotifers, 15 from cladocerans and 6 from copepods and *Asplanchna priodonta*, *Polyarthra dolichoptera*, *Bosmina longirostris Ceriodaphnia pulchella* were found in both stations every month during the study. While the reference station had more species in January, February, March, April, May, June, August, October and November than in the cage station, more species were found in the cage station only in September and November than in the reference station. The annual zooplankton abundance was 3.118 ± 3.927 ind/m^3 at the cage station and 2.552 ± 2.452 ind/m^3 at the reference station. Rotifer species and abundance were higher at the cage station whereas cladocer and copepod species and abundance were higher at the reference station. In the study, the species found only in the cage station were *Lecane bulla* and *Disparalona rostrata* while the species found only in the reference station were *Cephalodella gibba*, *Filinia terminalis* and *Macrothrix laticornis*.

Keywords: Zooplankton; Fish farming; Water quality; Kozan Dam Lake.

Kozan Baraj Gölü'nde (Adana) Balık Yetiştiriciliğinin Zooplankton Faunası Üzerine Etkisi

Öz

Kafeste balık yetiştiriciliğinin su kalitesi (Oksijen, sıcaklık, pH, iletkenlik, NO_2-N, NO_3-N, NH_4-N, PO_4-P ve klorofil-*a*) ve zooplankton faunası üzerine etkisi Kozan Baraj Gölü'nde araştırılmıştır. Çalışma sonucunda balık yetiştiriciliğinin, bazı su kalite parametreleri ve zooplankton faunası üzerine istatistiki açıdan bir etkisinin olmadığı, ancak küçük değişikliklere neden olduğu belirlenmiştir. Çalışmada, Rotifera'dan 29, Cladocera'dan 15 ve Copepoda'dan 6 olmak üzere toplam 50 zooplankton türü tespit edildi ve çalışma süresince *Asplanchna priodonta*, *Polyarthra dolichoptera*, *Bosmina longirostris Ceriodaphnia pulchella*'nın her ay bulundukları belirlenmiştir. Referans istasyonunda Ocak, Şubat, Mart, Nisan, Mayıs, Haziran, Ağustos, Ekim ve Kasım (9 ay) aylarında kafes istasyonundakinden daha fazla tür bulunurken, kafes istasyonunda sadece Eylül ve Kasım aylarında (2 ay) referans istasyonundakinden daha fazla tür bulundu. Yıllık zooplankton bolluğu, kafes istasyonunda 3.118 ± 3.927 birey/m³ ve referans istasyonunda 2.552 ± 2.452 birey/m³ idi. Rotifer türleri ve bollukları kafes istasyonunda daha yüksekken kladoser ve kopepod türleri ve bollukları referans istasyonunda daha yüksekti. Çalışmada sadece kafes istasyonunda bulunan türler *Lecane bulla* ve *Disparalona rostrata*, sadece referans istasyonunda bulunan türler *Cephalodella gibba*, *Filinia terminalis ve Macrothrix laticornis* idi.

Anahtar kelimeler: Zooplankton, Balık çiftliği, Su kalitesi, Kozan Baraj Gölü.

1. Introduction

In order to increase fish production, aquaculture was started in dam lakes with a protocol signed between the General Directorate of Agricultural Production (TÜGEM) and the General Directorate of State Hydraulic Works (DSI) in 1994 [1]. As a result, in Turkey, it was established in trout production farm in a cage in many reservoirs.

Good quality in water is essential in fish production [2]. However, due to daily feed intake and routine processes in fish farm, water quality is significantly affected since nitrate, nitrite, ammonium, phosphate, dissolved substances such as inedible feed, food waste and discharge products are directly released into the environment [3-5]. These cause growth disorders in fish, changes in benthos and eutrophication, and they are known to bring many environmental

problems such as chemical contamination, changes in physical parameters, and the spread of diseases caused by parasites and fungi [6, 7].

Since high density fish is usually stocked in cage fish farm, it is inevitable to use drugs and chemicals for fish health. Some of these are antifungals and antibiotics, copper-containing anti-fooling dyes, herbicides and phosphate-containing (Trisodium phosphate) disinfectants.

As an important link in the aquatic food web, zooplankton is one of the essential components of all aquatic ecosystems. In addition, some species of zooplankton are used in various studies as water quality, pollution and eutrophication indicator due to their sensitivity to environmental changes [8-12, 14]

There is a close relationship between the efficiency of the aquatic environment and the diversity and abundance of zooplankton. Zooplanktonic organisms are the main biotic factors of freshwater environments, as they have a significant impact on the growth, survival rate and distribution of fish larvae, as their reproductive periods are short, and their populations grow rapidly and have a renewal feature in a short time.

In this study, the effects of trout production in net cages (600 ton/year) on the water quality and zooplankton fauna were investigated in Kozan Dam Lake. In addition, it is thought that this study will provide data for future water quality, zooplankton and fishing activities.

2. Materials and Methods

The study was carried out between January 2011 and December 2011 in Kozan Dam Lake, which has 6 km^2 lake area, in Adana province Kozan district (Fig. 1). The dam lake was built between 1967 and 1972 for irrigation purposes. The body volume of the dam, which is the rock body fill type, is 1680000 m³, its height from the river bed is 78.50 m, the lake volume at normal water level is 170.34 hm³, and the lake area at normal water level is 6.42 km². It provides irrigation services on an area of 10220 hectares. In addition, electricity production started in the dam lake in 2010/2011 [15].

Zooplankton samples were taken from 4 stations with horizontal and vertical hauls by using 60 μm mesh size plankton nets on monthly basis for systematic analyses. Zooplankton abundance was determined from the samples taken from first two stations (station 1: cage station and station 2: reference station). On the other hand, samples from the first two stations were used to determine the effect of fish production on zooplankton abundance and diversity. Six litres of water samples were collected from every water depths (surface, 1, 2.5, 5, 10, 15, 20, 30 and 40 m) of first and second stations using Nansen Bottles.

One lt and 0.5 lt of water was used for chlorophyll-*a* analysis and chemical analysis respectively. The remaining part (4.5 lt) was filtered from a collector having a mesh size of 60 µm and zooplankton was fixed in 4% formaldehyde in 100 cc glass jars. Dissolved oxygen, water temperature, pH and conductivity were measured directly at the field by means of digital instruments (oxygen and temperature: YSI model 52 oxygen meter; pH: YSI 600 pH meter; conductivity: YSI model 30 salinometer). Merck spectroquant Nova 60 spectrophotometer and it's procedure was used to determine NO_2-N, NO_3-N, NH_4-N, PO_4-P; the method in APHA 1995 was used to determine chlorophyll-*a* spectrophotometrically. Secchi Disk depth was measured using a Secchi Disk with a diameter of 20 cm.
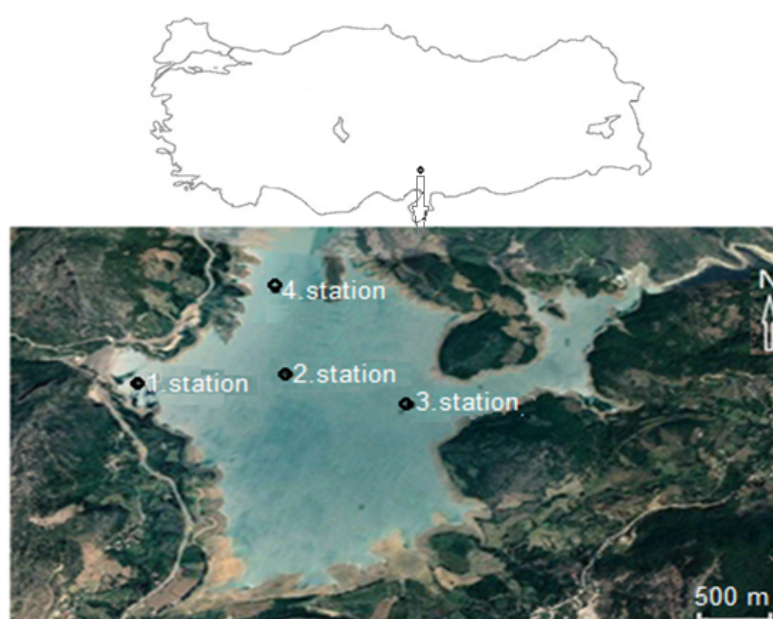
Figure 1: Kozan Dam Lake and sampling stations

The highest depths were 47 m, 44 m, 31 m and 26 m in May, while the lowest depths were 31 m, 26 m, 12 m and 10 m in October at the cage station, reference station, third station and fourth station, respectively.

Species identifications were made using a binocular microscope according to the works of Edmondson [16], Scourfield and Harding [17], Dussart [18], Kiefer and Fryer [19], Koste [20], Negrea [21], Segers [22], De Smet [23, 24], Nogrady and Segers [25], Hołynska et al. [26] and Benzie [27].

Zooplankton count was performed using an invert microscope in a petri dish with 2 mm lines at the bottom. The sample cup was made homogenized by shaking and 2 cc sub-sample was taken from the cup and it was placed in a petri dish and the individuals of each species were

separately counted. This process has been repeated 4-5 times. SPSS package software was used for statistical analyses (t test).

3. Results

Although there are differences between the cage station and the reference station in the water quality parameters (Secchi depth, temperature, chlorophyll-*a*, conductivity, dissolved oxygen, pH, NO_2-N, NO_3-N, NH_4-N and PO_4-P) (Fig. 2), there is no statistical difference.
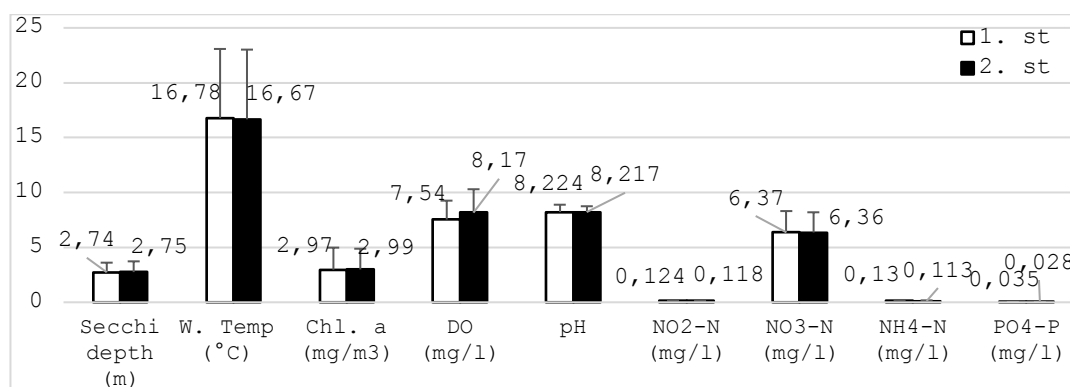
Figure 2: Annual average values of water quality parameters at the cage station and reference stations

The average Secchi Disc depths were very close at both stations, and were determined as 2.74±0.87 at the cage station and 2.75±0.98 at the reference station (Fig. 2).

The temperature was found almost the same at both stations. While the average temperature was 16.78±6.30 °C and 16.67±6.35 °C at the cage station and the reference station respectively. The temperature was higher at the cage station for 8 months (January, February, March, May, July, August, September, October) and at the reference station for 3 months (April, June, November), and it was equal at both stations in December (Fig. 3B).

It was determined that the temperature increased to a depth of 2.5 m from the surface and decreased from this depth to the bottom. The temperature was higher in the cage station at depths of 1, 5, 10, 15, 20 and 30 m (6 depths), while it was higher in the reference station at 0, 2.5 and 40 m depth (3 depths) (Fig. 4a).

The average chlorophyll-a was 2.97±2.013 mg/m3 at the cage station and 2.99±1.89 mg/m3 at the reference station. While chlorophyll-a was high in the cage station for 5 months (January, March, April, August, November), it was higher in the reference station for 7 months (February, May, June, July, September, October and December). Chlorophyll-a, which increased in spring and autumn in both stations, was close to each other in all months (Fig. 3C). Although

116

chlorophyll-a was generally irregular at both stations, it was higher at the first 10 m depth and then decreased to the bottom. While chlorophyll-a was high at 0, 1, 5, 15, 20 m depths at the cage station, it was higher at the reference station at 2.5, 10, 30, 40 m depths (Fig. 4b).
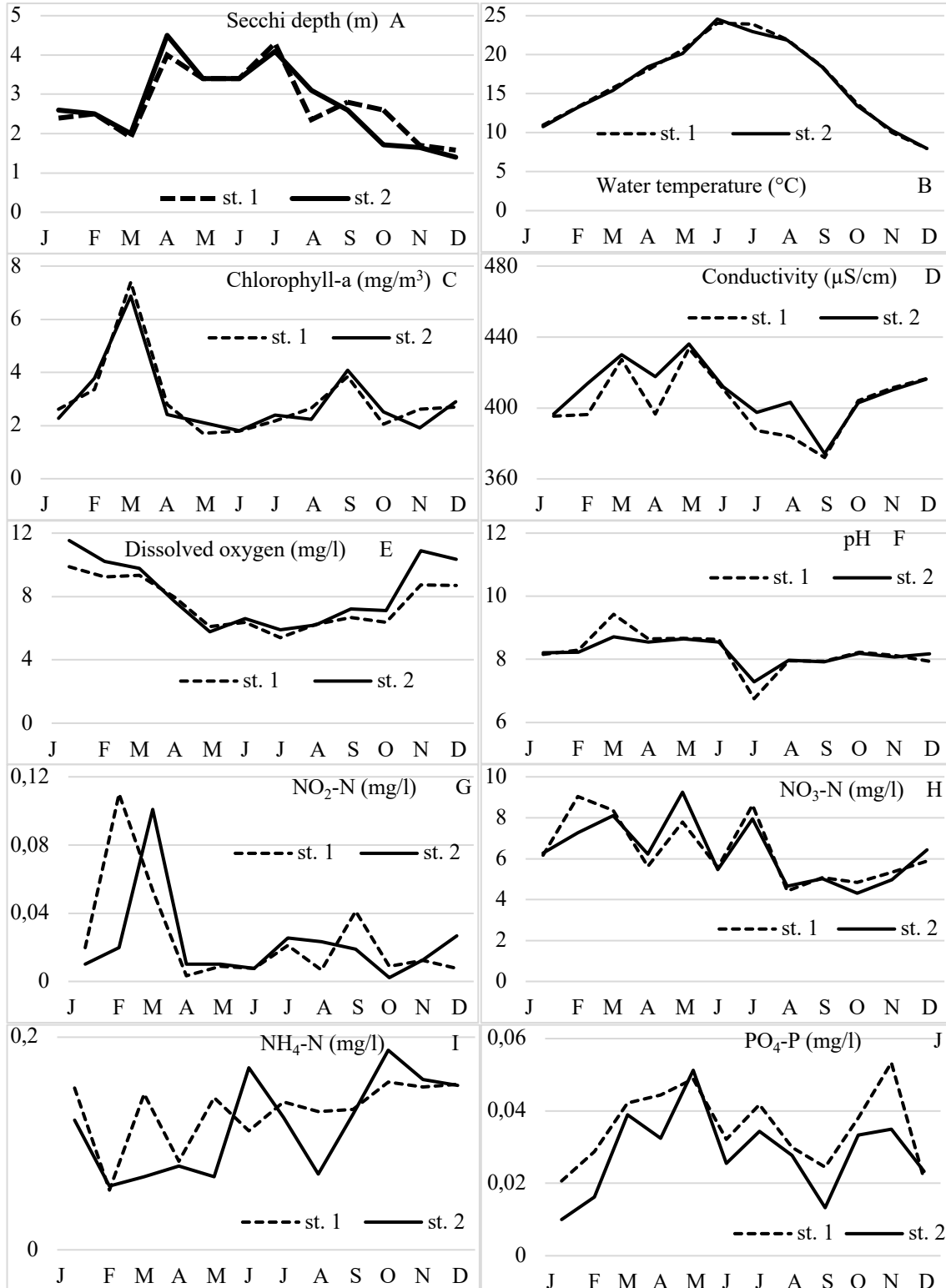
Figure 3: Water quality parameters in the study

The average conductivity was found as 403.14±34.01 µS/cm and 409.12±21.82 µS/cm at the cage station and reference station respectively. Although average conductivity values were close at both stations, it was generally a little higher at the reference station. While the conductivity was higher at the reference station in January, February, March, April, May, June, July, August, September, it was higher at the cage station in October, November and December (Fig. 3D). The conductivity depending on the depth changed irregularly to a depth of 5 m in the reference station and increased up to 40 m from here, while it displayed irregular fluctuations in depth at the cage station. Thus, the conductivity was more in the cage station at depths of 2.5, 5, 15 m, while it was more in the reference station at depths of 0, 1, 10, 20, 30 and 40 m (Fig. 4c).
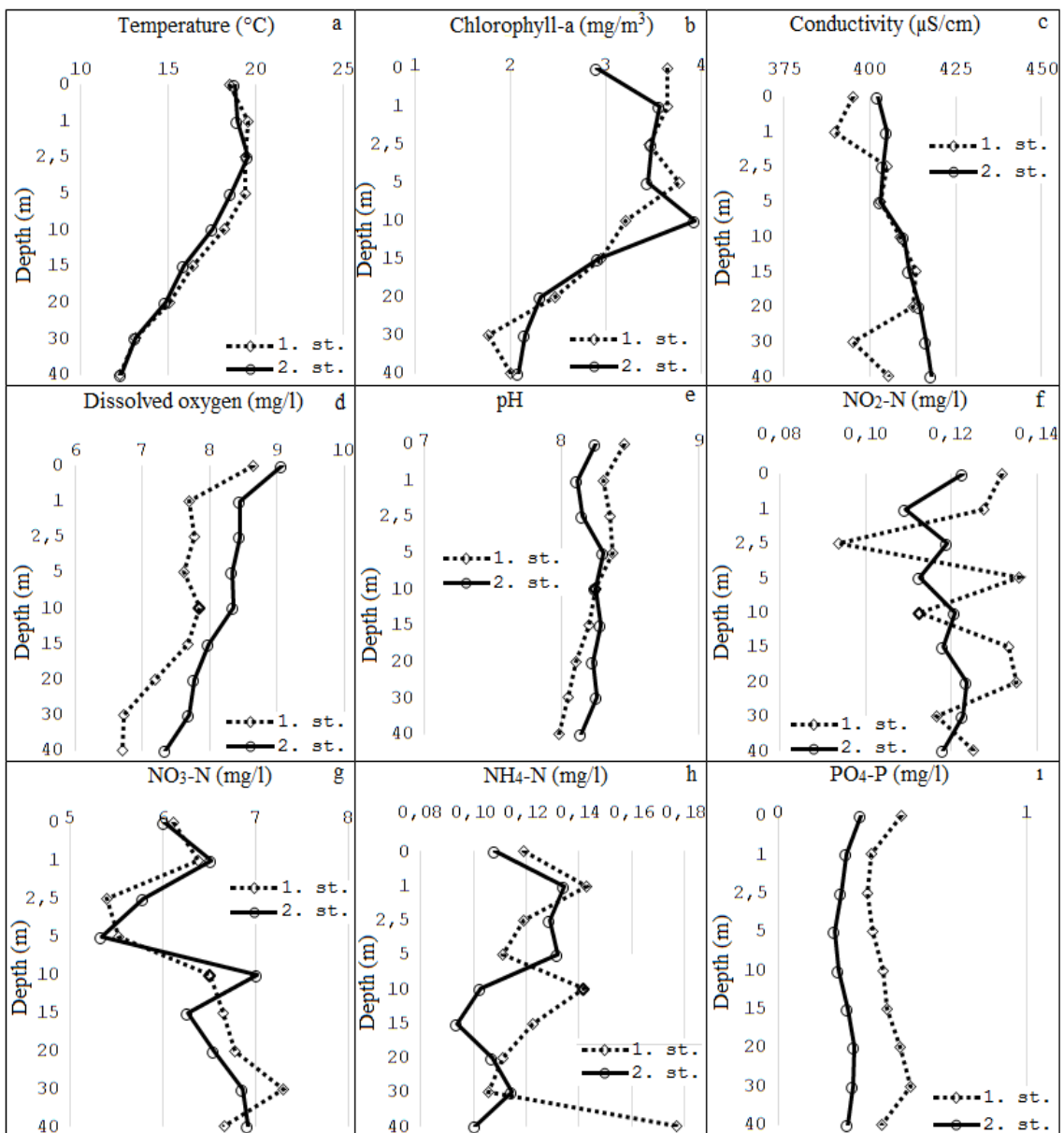
Figure 4: Water quality parameters in different depth in cage and reference stations in Kozan Dam Lake

Average dissolved oxygen values were 7.54±1.72 mg/l at the cage station and 8.17±2.13 mg/l at the reference station. Dissolved oxygen (DO) was high at the reference station in January, February, March, June, July, September, October, November, December, whereas it was high in the cage station in April, May and August (Fig. 3E). At both stations, DO was the most abundant on the surface water and its quantity decreased with increasing depth. DO at all depths was higher at the reference station than cage station (Fig. 4d).

It was determined that the pH was 8.224±0.673 at the cage station and 8.217±0.529 at the reference station, and the monthly average pH values at the stations were almost equal. The pH was higher in the cage station in February, March, April, May, June, September, October, November, while it was higher in the reference station in January, July, August and December (Fig. 3F). In the cage station the pH was high until 10 m depth from the surface but at the reference station it higher from 10 m depth to the bottom. Thus, pH was higher at 0, 1, 2.5, 5 m depths at the cage station, whereas it was higher at 10, 15, 20, 30 and 40 m depths at the reference station (Fig. 4e).

Nitrite nitrogen (NO_2-N) was 0.124±0.05 mg/l and 0.118±0.04 mg/l at the cage station and reference station respectively. NO_2-N was higher in the reference station in March, April, May, June, July, August, November, and December for most of the year, while it was higher in the cage station in January, February, September, October (Fig. 3G). The average NO_2-N values measured in the dam lake showed an irregular increase and decrease in both stations depending on the depth, and an inverse relationship was observed between the stations in terms of nitrogen values. The mean NO_2-N was high at the cage station at 0, 1, 5, 15, 20, 40 m depth, and higher at the reference station at 2.5, 10 and 30 m depths (Fig. 4f).

The mean nitrate nitrogen (NO_3-N) was 6.37±1.94 mg/l at the cage station and 6.36±1.84 mg/l at the reference station. NO_3-N values were higher in the cage station for 7 months (February, March, June, July, September, October, November) and in the reference station for 5 months (January, April, May, August, December); It was detected that the values between the two stations were closer to each other except February, May and July (Fig. 3H). The vertical distribution of NO_3-N at both stations showed irregular fluctuations. NO_3-N was found high in the cage station at depths of 0, 5, 15, 20, 30 m, while it was found more in the reference station at depths of 1, 2.5, 10, 40 m (Fig. 4g).

The average ammonium nitrogen (NH_4-N) was 0.13±0.08 mg/l at the cage station and 0.11±0.06 mg/l at the reference station. NH_4-N values showed monthly irregular increases and decreases at both stations. While NH_4-N was higher at the cage station in January, March, April,

May, July, August, September, December, it was higher at the reference station in February, June, October and November. It was found that the difference between the two stations was high in March, May and June, and closer to each other in other months (Fig. 3I). The vertical distribution of ammonium nitrogen shows irregular fluctuations in both stations. Ammonium nitrogen was found at 0, 1, 10, 15, 20, 40 m depths at the cage station, whereas it was more at the reference station at 2.5, 5, 30 m depths (Fig. 4h).

The average PO_4-P was calculated to be 0.035 ± 0.011 mg/l at the cage station and 0.028 ± 0.012 mg/l at the reference station. PO_4-P was high in the cage station during the months of January, February, March, April, June, July, August, September, October, November, but higher in the reference station in May and December (Fig. 3J). While PO_4-P showed a depth-dependent decrease in both stations, it was higher at all depths in the cage station (Fig. 4i).

In the study, a total of 50 zooplankton species were identified, including 29 from rotifers, 15 from cladocerans and 6 from copepods (Table 1). Seventeen families were identified from Rotifera and Brachionidae was the most species rich family with 7 species, followed by Collothecidae, Hexarthridae, Lecanidae, Lepadellidae, Synchaetidae and Trichocercidae with 2 species each one. The remaining families from Rotifera were found to contain only one species in each one. Seven families found from Cladocera, Chydoridae was the most species rich family with 6 species, followed by Daphniidae with 4 species and other families were represented only one species each one. Two families were detected from Copepoda, Cyclopidae was the richest family with 5 species, but Ameiridae (Harpacticoida) was represented by only one species.

A. priodonta, P. dolichoptera, B. longirostris C. pulchella were found in both stations every month during the study. Collotheca mutabilis, K. quadrata, Pompholyx sulcata, Rotaria rotatoria, D. galeata, D. birgei were found in both stations equal number for several months.

In the study, the species found only in the cage station were L. bulla and D. rostrata while the species found only in the reference station were C. gibba, F. terminalis and M. laticornis. In addition, the species found mostly in the cage station were A. ovalis, C. pelagica, E. dilatata, K. cochlearis and L. lunaris, while the species mostly found in the reference station were N. squamula, S. pectinata, T. capucina, T. similis, D. cucullata, D. longispina, M. micrura, C. vicinus, D. bicuspidatus, M. albidus (Table 2).

The species found only 1 or 2 times during the study are Anuraeopsis fissa, Brachionus quadridentatus, Colurella adriatica, Hexarthra oxyuris, K. tecta, Lepadella acuminata, L. ovalis, Lophocharis salpina, Trichotria tetractis, Leptodora kindtii, Alona quadrangularis, Coronatella

rectangula, Chydorus sphaericus, Leydigia leydigi, Monospilus dispar, Mesocyclops leuckarti, Paracyclops fimbriatus, Nitokra hibernica, and therefore no comment on these species (Table 2).

Table 1: Zooplankton species in the study and their monthly presences

Rotifera	
Anuraeopsis fissa (Gosse, 1851)	*Trichocerca capucina* (Wierzejski and Zacharias, 1893)
Ascomorpha ovalis (Bergendahl, 1892)	*Trichocerca similis* (Wierzejski, 1893)
Asplanchna priodonta (Gosse, 1850)	*Trichotria tetractis* (Ehrenberg, 1830)
Brachionus quadridentatus (Hermann, 1783)	**Cladocera**
Cephalodella gibba (Ehrenberg, 1832)	*Alona quadrangularis* (Müller, 1776)
Collotheca mutabilis (Hudson, 1885)	*Bosmina longirostris* (Müller 1785)
Collotheca pelagica (Rousselet, 1893)	*Ceriodaphnia pulchella* (Sars, 1862)
Colurella adriatica (Ehrenberg, 1831)	*Chydorus sphaericus* (Müller, 1785)
Euchlanis dilatata (Ehrenberg, 1832)	*Coronatella rectangula* (Sars, 1861
Filinia terminalis (Plate, 1886)	*Daphnia longispina* (Müller, 1785)
Hexarthra intermedia (Wiszniewski, 1929)	*Daphnia cucullata* <u>Sars, 1862</u>
Hexarthra oxyuris (Sernov 1903)	*Daphnia galeata* (Sars, 1864)
Keratella cochlearis (Gosse, 1851)	*Diaphanosoma birgei* (Korinek, 1981)
Keratella quadrata (Müller, 1786)	*Disparalona rostrata* (Koch, 1841)
Keratella tecta (Lauterborn, 1900)	*Leptodora kindtii* (Focke, 1844)
Keratella tropica (Apstein, 1907)	*Leydigia leydigi* (Leydig, 1860)
Lecane bulla (Gosse, 1886)	*Macrothrix laticornis* (Jurine, 1820)
Lecane lunaris (Ehrenberg, 1832)	*Moina micrura* (Kurz, 1874)
Lepadella acuminata (Ehrenberg, 1834)	*Monospilus dispar* (Sars, 1861)
Lepadella ovalis (Müller, 1896)	**Copepoda**
Lophocharis salpina (Ehrenberg, 1834)	*Cyclops vicinus* (Uljanin, 1875)
Notholca squamula (Müller, 1786)	*Diacyclops bicuspidatus* (Claus, 1857)
Polyarthra dolichoptera (Idelson, 1925)	*Macrocyclops albidus* (Jurine, 1820)
Pompholyx sulcata (Hudson, 1885)	*Mesocyclops leuckarti* (Claus, 1857)
Rotaria rotatoria (Pallas, 1766)	*Nitokra hibernica* (Brady, 1880)
Synchaeta pectinata (Ehrenberg, 1832)	*Paracyclops fimbriatus* (Fischer, 1853)

The most species were found at the reference station (23 species) in March, followed by 19 species in September (cage station) and December (referance station). The least species was found in both first two stations in July (5 species) (Fig. 5).

While there were more species in the reference station in January, February, March, April, May, June, August, October, November (9 months), more species were found in the cage station only in September and November (2 months). On the other hand, in July, an equal number of species was found at both stations (Fig. 5).

Table 2: Monthly distribution of zooplankton at the cage and reference stations +: available, -: absent)

Species stations	J 1/2	F 1/2	M 1/2	A 1/2	M 1/2	J 1/2	J 1/2	A 1/2	S 1/2	O 1/2	N 1/2	D 1/2	Total 1/2
Rotifera													
A. fissa	-/-	-/-	-/-	-/+	-/-	-/-	-/-	-/-	-/-	-/-	-/-	-/-	0/1
A. ovalis	-/-	-/-	-/-	-/-	+/+	+/+	-/-	+/+	+/+	+/-	+/+	-/-	6/5

A. priodonta	+/+	+/+	+/+	+/+	+/+	+/+	+/+	+/+	+/+	+/+	+/+	+/+	12/12
B. quadridentatus	-/-	-/-	+/-	-/-	-/-	-/-	-/-	-/-	-/-	-/-	-/-	-/-	1/0
C. gibba	-/-	-/-	-/+	-/-	-/-	-/-	-/-	-/-	-/-	-/+	-/-	-/-	0/2
C. mutabilis	-/-	-/-	-/-	+/+	-/+	-/-	-/-	-/-	-/-	-/-	+/+	+/-	3/3
C. pelagica	+/+	+/+	+/+	+/+	-/-	-/-	-/-	-/-	+/+	-/-	+/+	+/-	7/6
C. adriatica	-/-	-/-	-/-	-/+	-/-	-/-	-/-	-/-	-/-	-/-	-/-	-/-	0/1
E. dilatata	-/-	-/-	-/-	-/-	-/-	-/-	-/-	-/-	+/-	-/-	-/-	+/+	2/1
F. terminalis	-/-	-/-	-/+	-/+	-/-	-/-	-/-	-/-	-/-	-/-	-/-	-/+	0/3
H. intermedia	-/-	-/-	+/-	-/-	-/-	-/-	-/-	-/-	-/-	-/+	-/+	-/-	1/2
H. oxyuris	-/-	-/-	-/-	-/-	-/+	-/-	-/-	-/	-/-	-/-	-/-	-/-	0/1
K. cochlearis	-/-	-/-	+/+	+/-	-/-	-/-	-/-	-/-	-/-	-/-	+/+	-/-	3/2
K. quadrata	+/-	-/-	+/+	-/-	+/+	+/+	-/-	-/+	+/+	+/+	-/+	+/-	7/7
K. tecta	-/-	-/-	-/+	-/-	-/-	-/-	-/-	-/-	-/-	-/-	-/-	-/-	0/1
K. tropica	-/-	-/-	-/-	+/-	-/+	-/-	-/-	-/-	-/-	-/-	-/-	-/-	1/1
L. bulla	-/-	-/-	-/-	-/-	-/-	+/-	-/-	-/-	+/-	-/-	-/-	-/-	2/0
L. lunaris	-/-	-/-	+/-	-/-	-/+	-/-	+/-	+/-	+/-	+/-	+/-	-/-	6/1
L. acuminata	-/-	-/-	-/+	-/-	-/-	-/-	-/-	-/-	-/-	-/-	-/-	-/-	0/1
L. ovalis	-/-	-/-	-/+	-/-	-/-	+/-	-/-	-/-	-/-	-/-	-/-	-/-	1/1
L. salpina	-/-	-/-	-/-	-/-	-/-	-/-	-/-	-/-	-/-	-/-	-/+	-/-	0/1
N. squamula	-/+	-/-	-/+	-/-	-/-	-/-	-/-	-/-	-/-	-/-	+/-	-/-	1/2
P. dolichoptera	+/+	+/+	+/+	+/+	+/+	+/+	+/+	+/+	+/+	+/+	+/+	+/+	12/12
P. sulcata	+/-	-/-	-/+	-/+	-/-	+/+	-/-	-/-	+/+	+/-	-/-	-/-	4/4
R. rotatoria	+/+	-/-	+/+	-/-	-/-	-/-	-/-	-/-	+/+	-/-	-/-	+/+	4/4
S. pectinata	+/+	+/+	+/+	+/+	-/-	-/+	-/-	-/-	-/-	-/-	+/+	+/+	6/7
T. capucina	-/-	-/+	-/-	-/-	-/-	+/+	-/+	-/-	-/-	-/-	-/-	-/-	1/3
T. similis	-/+	+/+	+/+	+/+	+/+	-/+	-/+	-/+	-/+	-/-	+/-	+/+	6/10
T. tetractis	-/-	-/+	-/-	-/-	-/-	-/-	-/-	-/-	-/-	-/-	-/-	-/-	0/1
Cladocera													
B. longirostris	+/+	+/+	+/+	+/+	+/+	+/+	+/+	+/+	+/+	+/+	+/+	+/+	12/12
C. pulchella	+/+	+/+	+/+	+/+	+/+	+/+	+/+	+/	+/+	+/+	+/+	+/+	12/12
D. cucullata	-/-	-/-	-/+	-/+	-/-	+/+	+/-	+/+	+/+	-/-	-/-	-/-	4/5
D. galeata	-/-	-/-	+/+	-/-	-/-	+/+	-/-	-/-	-/-	-/-	-/-	-/-	2/2
D. longispina	-/+	+/+	+/+	+/-	+/+	-/+	-/+	-/-	-/+	-/-	+/-	-/+	5/8
D. birgei	-/+	-/-	+/-	-/-	-/-	+/+	+/+	+/+	+/+	+/+	+/+	-/-	7/7
L. kindtii	-/-	-/-	-/-	-/-	-/-	+/-	-/-	-/-	-/-	-/-	-/-	-/-	1/0
M. micrura	-/-	-/-	-/+	-/-	-/-	+/+	-/-	-/-	+/+	-/+	-/-	-/+	2/5
A. quadrangularis	-/-	-/-	-/-	-/-	-/-	-/-	-/-	-/-	-/-	+/+	-/-	-/-	1/1
C. rectangula	-/-	-/-	-/-	-/-	-/-	-/-	-/-	-/-	-/-	+/-	-/-	-/+	1/1
C. sphaericus	-/-	-/-	-/-	-/-	+/-	-/-	-/-	-/-	-/-	-/-	-/-	-/-	1/0
D. rostrata	+/-	-/-	-/-	-/-	-/-	-/-	-/-	-/-	-/-	-/-	-/-	+/-	2/0
L. leydigi	-/-	-/-	-/-	-/-	-/-	-/-	-/-	-/+	-/-	-/-	-/-	-/-	0/1
M. laticornis	-/-	-/-	-/-	-/-	-/-	-/-	-/-	-/-	-/-	-/+	-/-	-/+	0/2
M. dispar	-/-	-/-	-/-	-/-	-/-	-/-	-/-	-/-	-/-	-/+	-/-	-/-	0/1
Copepoda													
C. vicinus	+/+	+/+	+/+	+/-	-/+	+/+	+/+	+/+	+/+	-/+	+/+	+/+	10/11
D. bicuspidatus	-/+	-/+	+/-	-/+	-/+	+/+	-/+	-/-	+/-	-/-	+/-	+/+	5/7
M. albidus	-/-	-/+	-/+	-/+	-/-	-/-	-/-	-/-	+/+	-/-	-/-	-/+	1/5
M. leuckarti	-/-	-/-	-/-	-/-	+/-	-/-	-/-	-/-	-/-	-/-	-/-	-/-	1/0
P. fimbriatus	-/-	-/-	-/-	-/-	-/-	-/-	-/-	-/-	-/-	+/+	-/-	-/-	1/1
N. hibernica	-/-	-/-	-/-	-/-	-/-	-/-	-/-	-/-	-/-	-/-	-/-	-/+	0/1
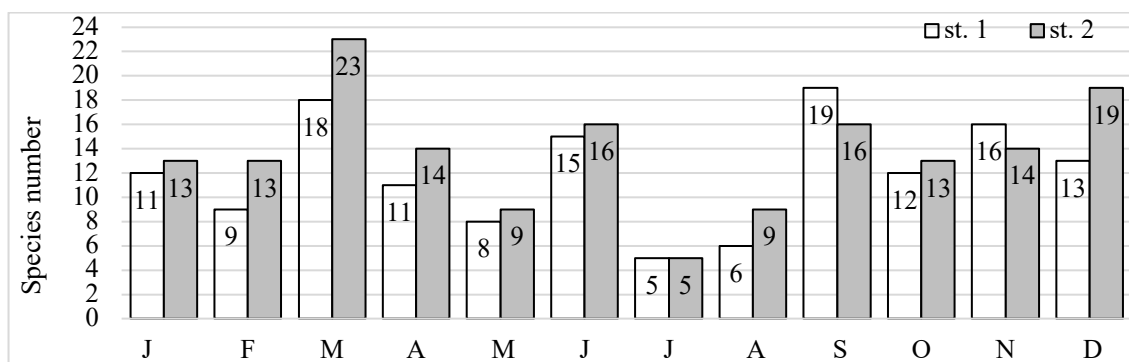
Figure 5: Species number of cage and reference stations according to months.
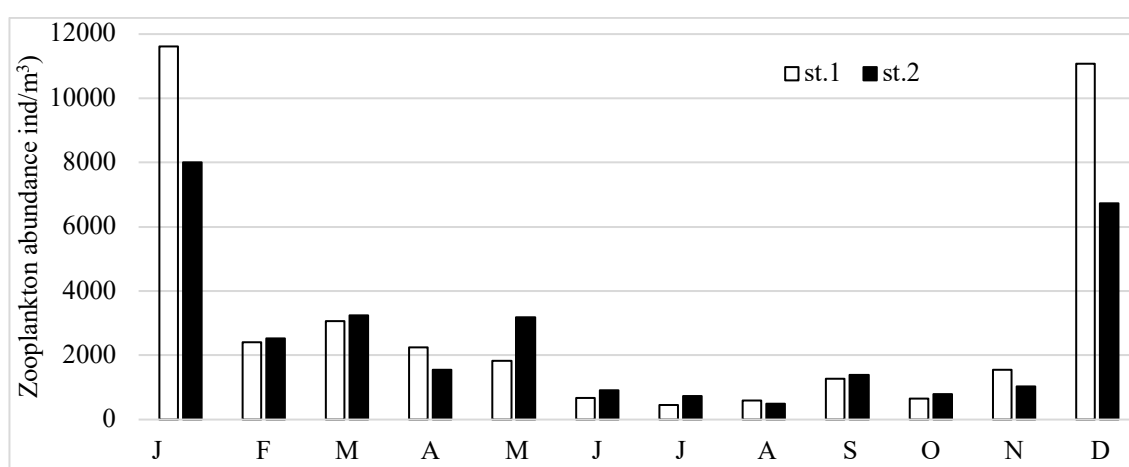
Figure 6: Abundance of zooplankton in cage and reference stations according to the months (ind/m³)

The annual zooplankton density was 3.118±3.927 ind/m³ at the cage station and 2.552±2.452 ind/m³ at the reference station. It was found that zooplankton was the most abundant at the reference station (11.607 ind/m³) in January and December (11.069 ind/m³), and at least at the reference station in July (460 ind/m³). While the amount of zooplankton was high at the reference station in February, March, May, June, July, September and October (7 times), it was high at the cage station (5 times) in January, April, August, November and December (Fig. 6).

The abundance of zooplankton varied at the cage and reference stations during the sampling periods, but was not statistically significant. While Rotifera was more abundant at the cage station, Cladocera and Copepoda were more abundant at the reference station. Thus, A*scomorpha ovalis, Asplanchna priodonta, Colletheca pelagica*, *Lecane lunaris*, *Polyarthra dolichoptera*, *Synchaeta pectinata*, *Trichocerca capucina* (Rotifera); *Daphnia longispina* (Cladocera) were abundant at the cage station, while other species (*Keratella quadrata*, *Pompholyx sulcata*, *Trichocerca similis* from Rotifera; *Bosmina longirostris*, *Cephalodella pulchella*, *Daphnia cucullata*, *D. galeata*,

Diaphanosoma birgei, *Moina micrura*, *Coronatella rectangula* from Cladocera; *Cyclops vicinus*, *Diacyclops bicuspidatus* and *Paracyclops fimbriatus* from Copepoda) were more abundant at the reference station (Table 3).

Table 3: Abundance of zooplankton species at cages and reference stations (ind/m^3)

Stations	1. st.	2. st.
Rotifera		
Ascomorpha ovalis	1980±3890.16	905±1117.71
Asplanchna priodonta	689±412.15	592±357.23
Colletheca pelagica	1336±1159.44	796±666.45
Keratella quadrata	552±452.53	740±1333.16
Lecane lunaris	378±23.54	350±60
Polyarthra dolichoptera	2955±2550.28	2460±1828.26
Pompholyx sulcata	515±107.61	859±860.67
Synchaeta pectinata	23567±2783	16498±20163.54
Trichocerca capucina	1705±978	1079±1170.46
Trichocerca similis	246±7.23	447±174.37
Cladocera		
Bosmina longirostris	365±121.15	591±225.73
Cephalodella pulchella	422±203.06	508±235.96
Daphnia cucullata	333±117.92	464±253.47
D. galeata	311±110	431±145
D. longispina	604±313.52	475±301.91
Diaphanosoma birgei	509±214.82	516±200.56
Moina micrura	310±76	342±91.27
Coronatella rectangula	252±49	260±97
Chydorus sphaericus	236±102	184±66
Copepoda		
Cyclops vicinus	410±212.14	551±291.23
Diacyclops bicuspidatus	277±56.61	320±126.82
Paracyclops fimbriatus	241±68	271±89
Copepodit	687±711.24	538±313.39

The abundance of zooplankton species at the cage and reference stations is as in Table 4. The density of rotifers was more abundant at the cage station (3941±1154 ind/m^3), while cladocer (1569±2443 ind/m^3) and copepod (600±445 ind/m^3) were more abundant at the reference station (Table 4).

4. Discussion

Kozan Dam Lake irrigates approximately 10220 ha of agricultural land and generates electricity. The streams feeding the dam are Kırksu and Düzağaç Creek. For this purpose, there is a water flow and mixture in the reservoir, which has continuous water inlet and outlet. This situation causes vertical and horizontal mixing of the reservoir water. Therefore, it was found that

there was no significant difference between zooplankton and water quality parameters at different depths of both stations.

The effects of cage fish farming have been analysed by various researchers and it was reported that nitrogen, phosphor and organic material load in sediment were significantly affected by these changes. Researches have shown that negative effects vary according to fish farm capacity, currents, change ratio and total volume of water and the technology used in fish farming [28-30].

Table 4. Abundance of zooplankton species at two stations in Kozan Dam Lake (ind/m^3)

Months	J		F		M		A		M		J	
Species	1	2	1	2	1	2	1	2	1	2	1	2
Rotifera												
A. ovalis	-	-	-	-	-	-	-	-	9910	2828	254	250
A. priodonta	857	460	610	564	943	817	333	250	-	-	-	-
C. pelagica	-	-	594	257	3416	429	619	1239		254	-	-
K. quadrata	-	-	-	-	1558	4 285	503	250	309	309	372	250
L. lunaris	-	-	-	-	-	-	-	-	-	-	-	-
P.dolichoptera	3 728	2406	3220	3650	396	6074	8623	2714	-	-	-	483
P. sulcata	-	-	-	-	-	-	-	-	-	-	625	250
S. pectinata	61496	48380	2206	3974	13476	14998	2148	1962		-		1415
T. capucina	-	-	-	-	-	-	-	-		-	1705	1906
T. similis	-	-	-	-	-	-	-	-	1938	1644	-	483
Average	22027	17082	1658	2111	3958	5321	2445	1283	4052	1259	739	720
Cladocera												
B.longirostris	9382	8553	9336	8529	244	250	1427	914	586	750	315	561
C. pulchella	303	481	1906	1600	2555	3153	1316	2913	602	4140	738	935
D. cucullata	-	-	-	-	-	-	-	-	-	-	500	742
D. galeata	-	-	-	-	-	-	-	-	-	-	311	431
D. longispina	-	-	824	857	447	1318	1538	2235	904	11965		750
D. birgei	-	-	-	-	-	-	-	-	-	-	505	624
M. micrura	-	-	-	-	-	-	-	-	-	-	-	-
C. rectangula	-	-	-	-	-	-	-	-	-	-	-	-
C. sphaericus	-	-	-	-	-	-	-	-	252	-	-	-
Average	4843	4517	4022	3662	1082	1574	1427	2021	586	5618	474	674
Copepoda												
C. vicinus	503	963	244	260	-	250	250	-	-	750	250	620
D.bicuspidatus	378	258	-	510	1000	-	-	-	-	-	252	250
P. fimbriatus	-	-	-	-	-	-	-	-	-	-	-	-
Average	441	611	244	385	1000	250	250	-	-	750	251	435
copepodit	617	830	299	343	1787	534	299	744	1132	379	1486	1416
Rotifera												
A. ovalis	-	-	741	241	478	955	255	-	242	252	-	-
A. priodonta	-	-	-	-	1436	955	830	1181	246	255	254	253
C. pelagica	-	-	-	-	1762	1954			1356	1164	268	274
K. quadrata	-	-	-	245	370	249	259	260	490	550	-	258
L. lunaris	380	-	375	-	-	-	-	-	-	-	-	-
P.dolichoptera	-	-	-	-	2810	3686	1427	842	1097	554	2342	1729
P. sulcata	-	-	-	-	410	1467	509	-	-	-	-	-
S. pectinata	-	-	-	-	-	-	-	-	5490	2939	56584	41820
T. capucina		252	-	-	-	-	-	-	-	-	-	-
T. similis	-	-	-	601	238	-	-	-	250	-	251	258
Average	380	252	558	362	1072	1544	656	761	1310	952	11940	7432

Table 4: continued

Months	J		A		S		O		N		D	
Species	**1**	**2**	**1**	**2**	**1**	**2**	**1**	**2**	**1**	**2**	**1**	**2**
Cladocera												
B.longirostris	334	506	412	564	1388	1496	300	1348	1681	2031	5451	3468
C. pulchella				243	1235	1437	383	356	251	488	252	545
D. cucullata	254		332	404	246	246	-	-	-	-	-	-
D. galeata	-	-	-	-	-	-	-	-	-	-	-	-
D. longispina		256	-	-	-	251	-	-	241		-	263
D. birgei	500	591	869	608	345	740	586	258	248	274	-	-
M. micrura	-	-	-	-	-	406		277	-	-	-	-
C. rectangula	-	-	-	-	-		252	260	-	-	-	-
C. sphaericus	-	-	-	-	-	-		-	-	-	-	-
Average	**363**	**451**	**538**	**455**	**804**	**763**	**380**	**500**	**605**	**931**	**2852**	**1425**
Copepoda												
C. vicinus	625	1465	822	406	491	970	-	254	251	488	253	1628
D.bicuspidatus	-	-	-	-	246	-	-	-	251	-	258	262
P. fimbriatus	-	-	-	-	-	-	241	271	-	-	-	-
Average	**625**	**1465**	**822**	**406**	**369**	**970**	**241**	**263**	**251**	**488**	**256**	**945**
copepodit	625	-	247	800	430	922	-	-	371	597	262	547
Average rotifer	Cage st. 3941±1154 ind/m^3					Reference st. 3132 ± 8721 ind/m^3						
Average cladocer	Cage st. 1239±2103 ind/m^3					Reference st.1569±2443 ind/m^3						
Average copepod	Cage st. 514±406 ind/m^3					Reference st. 643±347 ind/m^3						

The effects of cage fish farming have been analysed by various researchers and it was reported that nitrogen, phosphor and organic material load in sediment were significantly affected by these changes. Researches have shown that negative effects vary according to fish farm capacity, currents, change ratio and total volume of water and the technology used in fish farming [28-30].

It has been reported that the most common effect of fish farming in lakes leads to a decrease in dissolved oxygen, pH values and Secchi Disk depth and causes an increase in suspended solids, nutrients, electrical conductivity and chlorophyll-*a* [31-33, 28]. However, Cornel and Whoriskey [34] reported that pH did not change in the cage station and reference station, and that fish farming did not affect the pH value. In another study at rainbow trout farm, pH and dissolved oxygen did not change significantly between stations, while nutrients (N, P) (excluding nitrite nitrogen) were higher in cage stations similar to those above [35]. Similarly, some other researchers declared that there was no difference between the cage station and reference station in terms of nitrite nitrogen and nitrate nitrogen [29]. Interestingly, Cornel and Whoriskey [34] reported that N and P levels may be the same at the cage station and the reference station in the fish farm that produce below their capacity.

The difference between the two stations in terms of water quality parameters is very small and close to each other and our findings are consistent with the literature findings in the other studies given above.

Determined water quality parameters; temperature (16.78±6.3°C), pH (8.224±0.623), nitrite nitrogen (0,124±0,05 mg/l), nitrate nitrogen (6.37±1.94 mg/l), NH$_4$-N (0.13±0.08 mg/l) and phosphate (0.035±0.01 mg/l) values were higher in cage station but dissolved oxygen (8.17±2.13 mg/l), conductivity (401.91 ±99.07 µS/cm), chlorophyll-*a* (8.86±2.81 mg/m^3) and sechi depth (2.75±0,98 m) were higher in reference station.

In the study, dissolved oxygen was close to each other at both stations, but it was higher in cold months, especially in the January, November and December reference stations. On the other hand, the vertical distribution of dissolved oxygen was higher at the reference station at all depths. This shows that fish farming in cage is also in agreement with previous studies, which caused a decrease in dissolved oxygen and Secchi Depth and an increase in nitrogen and phosphate compounds, especially in the places where cages are located.

Some of previous researchers reported that primary productivity increase in cage station due to the nutrients coming from feed and metabolism wastes and this increased the abundance of zooplanktonic organisms [35-37, 6]. Matsumura-Tundisi and Tundisi [38, 39] reported that zooplankton diversity and abundance changed in cage stations due to increased nutrients, phytoplankton, conductivity, bacteria, food item and other factors.

In a study carried out in a tilapia farm, Santos et al., [40] reported only small changes in zooplankton levels. Guo and Li [6] reported that Rotifera was found in small quantity in cage station, however it was more abundant in the station that was outside of the cage. Cladocera was more abundant in the cage station and less abundant in the other station and finally Copepoda abundance was the same in both stations.

During the study, more species were found in the reference station for 9 months, while more species were found in the cage station for 2 months. In parallel to Guo and Li [6] this result shows that the fish farming in lakes has a negative impact on zooplankton species diversity because fewer species have been identified at the cage station in the vast majority of the year.

Contrary to the number of species, the abundance of zooplankton was higher in the cage station (3.118±3.927 ind/m^3) than reference station (2.552±2.452 ind/m^3).

It has been reported that most zooplankton species (except *Lepadella ovalis*, *Trichocerca capucina*, *Leptodora kindtii*, *Diacyclops bicuspidatus*, *Mesocyclops leuckarti*, *Paracyclops fimbriatus*) found in the study can be found in water bodies of various productivity levels and sizes in different geographic regions and are tolerant to changes in water quality [41-46]. All species in the study were widespread in Turkey and worldwide because they were found in almost

all regions of Turkey [47-59] and they were reported from lots of study inland waters of Turkey [60, 58].

In terms of monthly availability, in parallel with the above declarations, Ascomorpha ovalis, Asplanchna priodonta, Collotheca pelagica, C. mutabilis, Euchlanis dilatata, Hexarthra intermedia, Keratella cochlearis, K. quadrata, Notholca squamula, Polyarthra dolichoptera, Pompholyx sulcata, Rotaria rotatoria, Synchaeta pectinata, Trichocerca capucina, Bosmina longirostris, Ceriodaphnia pulchella, Daphnia cucullata, Daphnia galeata, Diaphanosoma birgei, Cyclops vicinus and Diacyclops bicuspidatus were found equal number or very close each other in both stations.

Abundance of the species (Asplanchna priodonta, Keratella quadrata, Polyarthra dolichoptera, Pompholyx sulcata, Trichocerca capucina, Ceriodaphnia pulchella, Daphnia cucullata, D. galeata, D. longispina, Diaphanosoma birgei, Coronatella rectangula, Cyclops vicinus, Diacyclops bicuspidatus, Paracyclops fimbriatus) were found close to each other in both stations as above. As they are resistant to environmental variables, it is seen that these species are not affected by low level changes in water quality parameters related to aquaculture activities.

In terms of abundance, the eutrophication indicator *Ascomorpha ovalis*, *Colletheca pelagica*, *Lecane lunaris*, *Synchaeta pectinata* and *Chydorus sphaericus* are expected to predominate in the cage station. It is interesting that *Bosmina longirostris*, which is an indicator of eutrophication, is dominant at the reference station. The reason why it is scarce in the cage station is thought to be over-consumed by the local fish around the cage. There is not enough data to explain that *Trichocerca similis* and *Moina micrura* are more dominant at the reference station.

In terms of monthly availability, *Cephalodella gibba*, *Filinia terminalis* and *Macrothrix laticornis* which are widespread and tolerant to environmental changes [61-63, 42, 43], have never been found at the cage station during the study. On the other hand, *Lecane bulla* and *Disparalona rostrata*, which have ecological characteristics similar to the above species, have never been found at the reference station. This can be explained by the fact that these species are in the dam lake only in a very small part of the year (2-3 months).

Cosmopolitan widespread species, *T. similis*, *Daphnia longispina*, *Moina micrura*, *Macrocyclops albidus* were more dominant at the reference station but widespread cosmopolitan *Lecane lunaris* was found dominant in cage station. Since the zooplankton found in the reference station are generally large in size, we think that they are consumed by fish that feed on waste feed around the cage, and therefore they are less in the cage station.

5. Conclusions

Our study is about comparing the effect of fish farming in lakes on water quality and zooplankton in two stations. It was determined that fish farming caused little changes (degradation) in water quality, rotifers were found in the area where they were fish production area, more in terms of species diversity and abundance, and cladocerans and copepods were found more in the area outside the place of fish production area.

References

[1] Anonymous, *Sekizinci beş yıllık kalkınma planı su ürünleri ve su ürünleri sanayii özel ihtisas komisyonu raporu* Ankara. DPT: 2275-ÖİK. 588, 2001.

[2] Boyd, C.A., McNevin, A., *Aquaculture*. Aquaculture, Resource Use, and the Environment, 1-337, 2015.

[3] Aşır, U., *Kesikköprü Baraj Gölü'nde ağ kafeslerde gökkuşağı alabalığının (Oncorhynchus mykiss Walbaum,1972) pelet ve ekstrude yemle besiciliğinden kaynaklanan azot-fosfor yükünün tahmini*. Doktora Tezi, Ankara Üniversitesi, Fen Bilimleri Enstitüsü, 2007.

[4] Das, P.C., Ayyappan, S., Jena, J., *Comparative changes in water quality and role of pond soil after application of different levels of organic and inorganic inputs*. Aquaculture Research, 36(8), 785-798, 2005.

[5] Tavares, L., Sipaúba, H., Millan, R.N., Santeiro Magalhães, R., *Characterization of a plankton community in a fish farm*. Acta Limnologica Brasiliensia, 22(1), 60-69, 2010.

[6] Guo, L., Li, Z., *Effects of nitrogen and phosphorus from fish cage-culture on the communities of a shallow lake in middle Yangtze River basin of China*. Aquaculture 226, 201-212, 2003.

[7] Guo, L., Li, Z., Xie, P., Ni, L., *Assessment effects of cage culture on nitrogen and phosphorus dynamics in relation to fallowing in a shallow lake in China*. Aquaculture International, 17, 229-241, 2009.

[8] Buhungu, S., Donou, M., Ntakimazi, G., Bonou, C.A., Montchowui, E., *Identification of characteristic zooplankton species in the Kinyankonge River basin, Burundi*. International Journal of Aquatic Biologia, 7(2), 71-84, 2019.

[9] Dede, A.N., *Study on Rotifers zooplankton and pollution indicators species in Bhima River near Sangam Village, Dist. Solapur*. (M.S). Asian Journal of Multidisciplinary Studies, 4(3), 13-15, 2016.

[10] Gutkowska, A., Paturej, E., Kowalska, E., *Rotifer trophic state indices as ecosystem indicators in brackish coastal waters*. Oceanologia, 55(4), 887–899, 2013.

[11] Kutama, R.M., Abubakar, M.M., Balarabe, M.L., *The plankton as indicators of water quality in Kusalla Reservoir*: A shallow manmade lake. IOSR Journal of Pharmacy and Biological Sciences, 9(3), 12-15, 2014.

[12] Loria, K., *Freshwater zooplankton communities as indicators of habitat quality: testing responses to multiple disturbances*. Undergraduate Honors Theses, University of Colorado, Boulder, 35, 2017.

[13] Neto, A.J.G., Silva, L.C., da Saggio, A.A., Rocha, O., *Zooplankton communities as eutrophication bioindicators in tropical reservoirs*. Biota Neotropica 14(4), 1-12, 2014.

[14] Parmar, T.K., Rawtani, D., Agrawal, Y.K., *Bioindicators: the natural indicator of environmental pollution.* Frontiers In Life Science, 9(2), 110-118, 2016.

[15] Anonymous, *Adana tarımsal sulama altyapısının analizi, sulamanın sorunları ve çözüm önerileri.* T.C. Gıda Tarım ve Hayvancılık Bakanlığı Adana Zirai Üretim İşletmesi Tarımsal Yayım ve Hizmetiçi Eğitim Merkezi Müdürlüğü. Adana, 2013.

[16] Edmondson, W.T., *Methods and Equipment, in Fresh-Water Biology*, Second Education, John Wiley and Sons, New-York. Inc 1194-1202, 1959.

[17] Scourfield, D.J., Harding, J.P., *Fresh-Water Biology* As. Sci. Publ. New York, 1966.

[18] Dussart, B., *Les Copepodes des Eaux Continentales dÕ Europe Occidentale, Tome I, Calanoides et Harpacticoides.*, Editions N. Boubee; et cie, Paris, 499, 1967.

[19] Kiefer, F., Fryer, G., *Das Zooplankton der Binnengewässer*, 2, 1-380. (E. Schweizerbart'sche Verlagsbuchhandlung, Stuttgart), 1978.

[20] Koste, W., *Die Radertiere Mitteleuropas Ein Bestimmungswerk, Begründet Von Max Voigt.* Überordnung Monogononta. 2 Auflage Neubearbeitet Von II. Tefelband Berlin Stutgart, 234, 1978.

[21] Negrea, S.T., *Fauna Republicii Socialiste Romania Vol*. 4, 12. Crustacea Cladocera. Academia Republicii Socialiste Romania, Bucaresti, 339, 1983.

[22] Segers, H., *Rotifera. Volume 2: The Lecanidae (Monogonota).* Guides to the identification of the microinvertebrates of the continental waters of the world 6. SPB Academic Publishing, The Hague, 1995.

[23] De Smet, W.H., *The Prolidae (Monogononta).* Vol. 4. SPB Academic Publishing, Amsterdam, 1996.

[24] De Smet, W.H., *The Dicranophoridae (Monogononta)*. Vol. 5. SPB Academic, 1997.

[25] Nogrady, T., Segers, H., *Rotifera vol. 6*: *Asplanchnidae, Gastropodidae, Lindiidae, Microcodidae, Synchaetidae, Trochosphaeridae and Filinia*. Guide to the identification of the microinvertebrates of to the continental waters of the world. (Guides to the identification of the microinvertebrates of the continenta waters of the world 12 (ed. H.J. Dumont), Backhuys Publishers, 264, 2002.

[26] Hołynska, M., Reid, J.W., Ueda, H., *Copepoda: Cyclopoida genera Mesocyclops and Thermocyclops*. In: Ueda H, Reid JW, editors. Guides to the identification of the microinvertebrates of the continental waters of the world. Leiden: Backhuys Publishers. 213, 2003.

[27] Benzie, J.A.H., *The Genus Daphnia (including Daphniopsis) (Anomopoda: Daphniidae).* Backhuys Publishers, Leiden: 377, 2005.

[28] Phillips, M.J., Beveridge, M.C.M., Ross, L.G., *The environmental impact of salmonid cage culture on inland fisheries*: present status and future trends. Journal of Fish Biology, 27(Suppl. A), 123-137, 1985.

[29] Stirling, H.P., Dey, T., *Impact of intensive cage fish farming on the phytoplankton and periphyton of a scottish freshwater loch.* Hydrobiologia, 190, 193-214, 1990.

[30] Pitta, P., Karakassis, I., Tsapakis, M., Zivanovic, S., *Natural vs. mariculture induce variability in nutrients and plankton in the eastern Mediterranean.* Hydrobiologia, 391, 181-194, 1999.

[31] Rast, W., Holland, M., *Eutrophication of lakes and reservoirs: a framework for making management decisions*. Ambio, 17, 2-12, 1988.

[32] Weglenska, T., Bownik-Dylinska, L., Ejsmont Karabin, J., Spodniewska, I., *Plankton structure and dynamics, phosphorus and nitrogen regeneration by zooplankton in Lake Glebokie polluted by aquaculture*. Ekologia Polska, 35(1), 173-208, 1987.

[33] Beveridge, M., *Cage and pen fish farming carrying capacity models and environmental impact.* FAO Fisheries Technical Paper, 255, 131, 1984.

[34] Cornel, G.E., Whoriskey, F.G., *The effects of rainbow trout (Oncorhynchus mykiss) cage culture on the water quality, zooplankton, benthos and sediments of Lac du Passage, Quebec*. Aquaculture, 109, 101-117, 1993.

[35] Demir, N., Kırkağaç, M.U., Pulatsu, S., Bekcan, S., *Influence of trout cage culture on water quality, plankton and benthos in an anatolian dam lake.* The Israeli Journal of Aquaculture -Bamidgeh, 53 (3-4), 115-127, 2001.

[36] Atay, D., Demir N., *The Effects of Chicken Manure on the Phytoplankton Primary Production in Carp Ponds*. Acta Hydrobiologica, 40(4), 215-225, 1998.

[37] Kırkağaç, M., Köksal, G., *Sazan havuzlarında Piliç Gübresinin Zooplankton Verimliliğine Etkisi*, X. Ulusal Su Ürünleri Sempozyumu, Cilt II, 548-562, Adana, 1999.

[38] Matsumura-Tundisi, T., Tundisi, J.G., *Calanoida (Copepoda) species composition changes in the reservoirs of São Paulo State (Brazil in the last twenty years*. Hydrobiologia 504, 215-222, 2003.

[39] Matsumura-Tundisi, T., Tundisi, J.G., *Plankton richness in a eutrophic reservoir (Barra Bonita Reservoir, SP, Brazil)*. Hydrobiologia, 542, 367-378, 2005.

[40] Santos, R.M., Rocha, G.S., Rocha, O., Santos Wisniewski, M.J., *Influence of net cage fish cultures on the diversity of the zooplankton community in the Furnas Hydroelectric Reservoir*, Areado, MG, Brazil. Aquaculture Research, 40, 753-776, 2009.

[41] Hutchinson, G.E., *A treatise on limnology*. Vol. 2: Introduction to lake biology and the limnoplankton. New York: Wiley 1115, 1967.

[42] Ruttner-Kolisko, A., *Plankton rotifers, biology and taxonomy*. Biological Station Lunz of the Austrian Academy of Science, Stutgart, 146, 1974.

[43] Braioni, M.G., Gelmini, D., *Guide per il reconoscimento delle specie animali delle acque interne Italiane: Rotiferi monogononti. Italy*: Consiglio Nazionalie delle Ricerche, 181, 1983.

[44] Ryding, S.O., Rast, W., *The control of eutrophication of lakes and reservoirs*. Man and The Biosphere Series Volume I. The Parthenon Publishing Group, Lancaster, 1989.

[45] Ramdani, M., Flower, R.J., Elkhiati, N., *Zooplankton (Cladocera, Ostracoda), chironomidae and benthic fauna remains in sediment cores from nine North African wetland lakes*: The CASSARINA Project. Aquatic Ecology, 35 (3-4), 389-403, 2001.

[46] Eldredge, L.G., Evenhuis, N.L., *Hawaii's biodiversity*: a detailed assessment of the numbers of species in the Hawaiian Islands. Bishop Museum Occasional Papers, 76, 1-28, 2003.

[47] Güher, H., *A fanustic study on the freshwater Cladocera (Crustacea) species in Turkish Thrace (Edirne, Tekirdağ, Kırklareli)*. Turkish Journal of Zoology, 24, 237-244, 2000.

[48] Alper, A., Çelebi, E., Çam, H., Karaytuğ, S., *Cladocera and Copepoda (Crustacea) fauna of İkizcetepeler Dam Lake (Balıkesir, Turkey)*. Turkish Journal of Fisheries and aquatic sciences, 7(1), 71-73. 2007.

[49] Dirican, S., Musul, H., *Çamlıgöze Baraj Gölü (Sivas-Türkiye) zooplanktonu faunası üzerine bir çalışma,* Süleymen Demirel Üniversitesi Fen Bilimleri Dergisi, 12(1), 1721, 2008.

[50] Saler, S., İpek, N., *Cladocer and Copepoda (Crustacea) fauna of Seli Stream (Elazığ Turkey)*. Journal of FisheriesSciences.com, 3(4), 318-322, 2009.

[51] Yıldız, Ş., Özgökçe, M.S., Karaca, F., Polat, E., *Zooplankton composition of Van Lake Coastline in Turkey*. African Journal of Biotechnology, 9 (48), 8248-8252, 2010.

[52] Günsel, S., Emir Akbulut, N., *The investigation of the zooplanktonic organisms of Delice River and its arms in Kızılırmak River Basin (Turkey)*. Hacettepe Journal of Biology and Chemistry, Special Issue, 309-316, 2012.

[53] Apaydın Yağcı, M., *Seasonal zooplankton community variation in Karataş Lake*. Iranian Journal of Fisheries Sciences. 12(2), 265-276, 2013.

[54] Güher, H., *A checklist for zooplankton (Rotifera, Copepoda, Cladocera) of European Turkey inland waters*. Ege Journal of Fisheries and Aquatic Sciences, 31(4), 221-225, 2014.

[55] Saler, S., İpek Alış, N., *Zooplankton of Hancağız Dam Lake (Gaziantep-Turkey)*. Journal of Survey in Fisheries Sciences. 1(1), 45-54, 2014.

[56] Apaydın Yağcı, M., Yilmaz, S., Yazıcıoğlu, O., Polat, N., *The zooplankton composition of Lake Ladik (Samsun, Turkey)*. Turkish Journal of Zoology 39(4), 652-659, 2015.

[57] Güher, H., Çolak, Ş., *Süloğlu Baraj Gölü'nün (Edirne) zooplankton (Rotifera, Cladocera, Copepoda) faunası ve mevsimsel değişimi*. Trakya University Journal of Natural Sciences, 16(1), 17-24, 2015.

[58] Ustaoğlu, M.R., *An updated zooplankton biodiversity of Turkish inland waters*. LimnoFish, 1(3), 151-159, 2015.

[59] Gürel, Ö., Saler, S*., Zooplankton of Orduzu Lake (Malatya*). Fırat University Turkish Journal of Science & Technology, 27(1), 21-28, 2015.

[60] Ustaoğlu, M.R., Balık, S., Özdemir Mis, D., The rotifer fauna of Lake Sazlıgöl (Menemen-İzmir). Turkish Journal of Zoology, 28, 267-272, 2004.

[61] Einsle, U., *Ökologische Studien an einer pelagisch lebenden Population von Diacyclops bicuspidatus (Crust. Cop.)*. Gewäss Abwäss 39-40, 102-117, 1965 (in German).

[62] Monchenko, V.I., *Cyclopidae*. Fauna of Ukraine 27(3). Kyiv, Ukraine: Naukova Dumka Publisher. 1974.

[63] Dussart, B.N., Defaye, D., *Repertoire mondial des Copepodes Cyclopoides*. Paris, France, CNRC, 1985 (in French).

A Comparative Study of Different Solvents on the Toxic and Antioxidant Properties of *Digitalis ferruginea* L. subsp. f*erruginea*

Arzu KASKA[1,*]

[1]*Department of Science and Mathematics, Faculty of Education, Pamukkale University, Denizli, Turkey*
akaska@pau.edu.tr, ORCID: 0000-0002-0166-1818

Abstract

Digitalis plants have different biological actions, including antioxidant and antimicrobial activities. In addition, some members of this genus are used in traditional Turkish medicine as diuretics and tonics**.** The purpose of the present study is to compare the antioxidant, toxic activity and phenolic profile of two extracts of *D. ferruginea* L. subsp. *ferruginea*. The radical scavenging capacities in the hydromethanolic extract were higher than the hydroethanolic extract. The same extract was effective in total antioxidant (β-carotene, 83.75% and phosphomolybdenum 111.5 µg/mg) and metal chelating activities. The hydromethanolic extract (75.91 mgGAEs/g) exhibited higher phenolic content than hydroethanolic extract (70 mgGAEs/g). There were no statistical differences between the flavonoid and tannin contents of the extracts. The HPLC results determined major phenolics: 2,5 dihydroxybenzoic, vanillic and caffeic acid. In addition, this plant is also rich in polyphenolic content as well as toxic activity. The present data could provide significant information regarding its potential use in the pharmaceutical industry.

Keywords: *Digitalis ferruginea* L. subsp. *ferruginea;* HPLC; Toxicity; Antioxidant capacity.

Digitalis ferruginea L. subsp. *ferruginea* 'nin Toksik ve Antioksidan Özellikleri Üzerine Farklı Çözücülerin Karşılaştırmalı Bir Çalışması

Öz

Digitalis bitkilerinin antioksidan ve antimikrobiyal aktiviteler dahil olmak üzere farklı biyolojik etkileri vardır. Ayrıca, bu cinsin bazı üyeleri geleneksel Türk tıbbında diüretik ve tonik olarak kullanılmaktadır. Bu çalışmanın amacı, *D. ferruginea* L. subsp. *ferruginea*'nın iki ekstresinin antioksidan, toksik aktivite ve fenolik profilini karşılaştırmaktır. Hidrometanolik ekstrakt'daki radikal süpürme kapasiteleri hidroetanolik ekstrakt'dakinden daha yüksektir. Aynı ekstrakt, toplam antioksidan (β-karoten, %83.75 ve fosfomolibdenum 111.5 µg/mg) ve metal şelatlama aktivitelerinde de etkili olmuştur. Hidrometanolik ekstrakt (75.91 mgGAEs /g), hidroetanolik ekstraktdan (70 mgGAEs/ g) daha yüksek fenolik içerik sergilemiştir. Ekstraktların flavonoid ve tanen içeriği arasında istatistiksel fark bulunmamıştır. HPLC ile önemli fenolikler saptanmıştır: 2,5 dihidroksibenzoik, vanilik ve kafeik asit. Ek olarak, bu bitki aynı zamanda polifenolik içerik ve toksik aktivite bakımından da zengindir. Mevcut veriler, bu bitkinin ilaç endüstrisindeki potansiyel kullanımı hakkında önemli bilgiler sağlayabilir.

Anahtar Kelimeler: *Digitalis ferruginea* L. subsp. *ferruginea;* HPLC; Toksisite; Antioksidant kapasite.

1. Introduction

Generated in the body or by external factors, free radicals are highly reactive chemical species that can cause damage to cells, organelles, DNA, and other biomolecules. This action can result in diseases, including cancer, as well as cardiovascular and neurodegenerative conditions [1-3]. Remedies for ailments such as these are often prohibitively expensive and their cost could result in an unsurmountable financial burden for some patients. The discovery and development of effective therapies, and their being readily available and reasonably priced on the market, is therefore crucial for the general population. Moreover, natural antioxidants are a prerequisite for the prevention and/or cure of diseases caused by free radicals. Plants are a resource that contain a diversity of therapeutic molecules, and the development of these properties can result in novel remedies. Consequently, the study of such plants is highly beneficial in the development of novel therapeutic agents [1, 2, 4]. Many researchers are therefore searching for natural antioxidants that are potent but safe, in particular those sourced from medicinal plants. There are various plants among the Plantaginaceae family that have been shown to have different pharmacological actions, including antioxidant, antimicrobial, antidiabetic, anti-inflammatory and toxicological activities [5-8]. Moreover, some members of *Digitalis* genus (Plantaginaceae family) are used in traditional

Turkish medicine as diuretics and tonics [5]. In this study, the antioxidant properties, toxic effects and total bioactive compounds of the hydroethanolic and hydromethanolic extracts of *D. ferruginea* L. subsp. *ferruginea* were evaluated and the phenolic compound of the hydromethanolic extract was determined.

2. Materials and Methods

2.1. Plant material and preparation of the extracts

The plant material was collected from Denizli, Turkey, in August 2018 and it was identified and stored with voucher specimens (*D. ferruginea L.* subsp. *ferruginea*; Herbarium No: 2018-5-2) at the private herbarium of Dr. M. Çiçek. To obtain the hydroethanolic and hydromethanolic extracts, 30 g of dried plant material (aerial parts) was added to 300 mL of a solution containing ethanol: water (70:30, w:w) and methanol: water (70:30, w:w) respectively and shaking at 50° C for 6 h in a temperature controlled shaker. The combined extracts was evaporated using a rotary evaporator under vacum at $40\text{-}50^{\circ}$ C. The samples were lyophilized and kept at -20° C. The details of preparation of the extracts followed those given by Kaska et al. [9].

2.2. Total bioactive compounds and quantification of phenolic compounds by HPLC

With reference to Kaska et al. [10], the total phenolic, flavonoid and tannin content (by the standard Folin-Ciocalteu method), flavonoids (by $AlCl_3$ method) and tannin (by the vanillin–HCl method) were determined. The results were expressed as mg of Gallic acid (mg GAE/g sample), Quercetin (mg QEs/g sample) and Catechin (mg CEs/g sample) equivalents for phenolic, flavonoid and tannin content respectively.

The phenolic profile of the hydromethanolic extract of *D. ferruginea* L. subsp. *ferruginea* was determined using previously described method Caponio et al. [11] using reversed-phase high performance liquid chromatography. The details of this method were given in Kaska and Mammadov [12].

2.3. Antioxidant activity

The radical scavenging (DPPH (2,2-Diphenyl-1-picrylhydrazyl radical) and ABTS (2,2'-azino-bis (3-ethylbenzothiazoline-6-sulfonic acid))), total antioxidant (phosphomolybdenum and β-carotene/linoleic acid) and metal chelating activities were evaluated by the method described by Kaska et al. [10] and EDTA (Ethylenediaminetetraacetic acid), BHT (Butylated hydroxytoluene) and TROLOX (6-hydroxy-2,5,7,8-tetramethylchromane-2-carboxylic acid) were used as standards for these methods. The ferric ion reducing antioxidant power procedure followed are those given by

135

Kaska and Mammadov [12] and results were expressed as mg of ascorbic acid equivalents (AA) per milliliter of extract.

2.4. Brine shrimp lethality assay

The brine shrimp lethality bioassay was used to investigate the toxicity of *D. ferruginea* L. subsp. *ferruginea* [13]. The details of determining the toxicity were given in Kaska and Mammadov [12]. The EPA Probit Analysis Program was used for data analysis.

2.5. Statistical analysis

The experimental results were analyzed using the MINITAB Statistical Package Program and the results expressed as mean ± SE (Standard Error). To see how the groups differed from each other, the variations between the different extracts were tested with Analysis of Variance (ANOVA) and Tukey ($p < 0.05$), and the different groups were shown with different letters in the same column. If there were only two groups then a t-test was used.

3. Results and Discussion

3.1. Total phenolic, flavonoid, tannin content and phenolic composition

The content of the bioactive compound in the different *D. ferruginea* L. subsp. *ferruginea* extracts are existed in Table 1.

Table 1: Total bioactive compound of *D. ferruginea* L. subsp. *ferruginea* extracts

Sample	Total phenolic content (mg GAEs/g)	Total flavonoid content (mg QEs/g)	Total tannin content (mg CEs/g)
Hydroethanolic	70 ± 1.2 b	37.94 ± 2 a	35.43 ± 1.7 a
Hydromethanolic	75.91 ± 1.9 a	34.19 ± 0.26 a	34.55 ± 2.4 a

The statistical differences were given as different letters ($p < 0.05$).

The procedure was based on the Folin-Ciocalteu reagent. This is frequently used for ascertaining and quantifying total phenols, as it assesses the capacity of phenols to react with oxidizing agents [14]. In the present study total phenolic content was determined using the Folin–Ciocalteu method [15]. There were statistical differences ($t = 2.71$, $df = 11$, $p < 0.05$) in the total phenolic contents of the hydroethanolic and hydromethanolic extracts of *D. ferruginea* L. subsp. *ferruginea.*

In this study, an AlCl₃ colorimetric method was employed to explore the factors influencing the determination of total flavonoids in *D. ferruginea* L. subsp. *ferruginea*. The AlCl₃ colorimetric assay is a simple, feasible, reproducible and stable method [16]. There were no statistical differences in the total flavonoid (t = 1.86, df = 7, p > 0.05) and the tannin contents (t = 0.30, df = 12, p > 0.05) of the hydroethanolic and hydromethanolic extracts.

This study determined that total phenolic, flavonoid and tannin content of the extracts varied in accordance with the solvent. Similar to these results, the studies of Kaska et al. [10] found that the total phenolic, flavonoid and tannin content differed according to the solvents used on *Nepeta cadmea*.

The results for phenolic compositions of the hydromethanolic extract of *D. ferruginea* L. subsp. *ferruginea* by HPLC analysis are presented in Table 2.

Table 2: Phenolic components in the hydromethanolic extract of *D. ferruginea* L. subsp. *ferruginea*

No	Phenolic component	Approximate Rt (min)	µg/g*
1	Gallic acid	6.8	3.55
2	2,5 dihydroxybenzoic acid	17.2	20690.02
3	Chlorogenic acid	18.2	1222.44
4	3,4 dihidroxybenzoic acid	10.7	26.23
5	4-hidroxybenzoic acid	15.7	54.39
6	Cinnamic acid	71.1	208.10
7	Quercetin	70.4	138.49
8	*p*-coumaric acid	26.1	195.37
9	Ferulic acid	30.1	296.63
10	Caffeic acid	22.7	2761.59
11	Vanilic acid	19.2	5728.93
12	Epicatechin	21.3	1074.11
13	Rutin	45.6	34.14

* based on dry weights

Some of the phenolics determined in this study, such as caffeic, chlorogenic, ferulic and *p*-coumaric acid were obtained from Plantaginaceae plants used in previous studies [7, 8, 17].

Phenolic compounds comprise a broad range of chemical substances, with varied chemical structures and disparate biological activities, involving as many as 8000 diverse compounds [18, 19]. Phenolic compounds can function as hydrogen donors or to chelate metal ions (viz. iron and

copper) by impeding the oxidation of low-density lipoproteins (LDL). These features of phenolic compounds are related to a reduction in the risk of contracting neurodegenerative diseases, for example cardiovascular diseases [20] and gastrointestinal cancers [21]. In plant foods phenolic compounds are pervasive and hence significant amounts are ingested on a daily basis. Furthermore, the antioxidant activities of phenolic compounds are nowadays becoming increasingly well-known, and researchs on the use of natural substances or food ingredients including phenolic antioxidants are continuing to be of great interest to the food industry [22]. For this reason, the plants' phenolic compounds analyses are very important in the understanding of these plant's medicinal value.

3.2. Antioxidant capacity

The antioxidant capacity by phosphomolybdenum assay can be assessed by the reduction of molybdenum to a green molybdenum complex by the antioxidant compounds present in the plant extracts [23].

The antioxidant capacity with a phosphomolybdenum assay of extracts are given in Table 3. These findings indicate that hydroethanolic and hydromethanolic extracts from *D. ferruginea* L. subsp. *ferruginea* possess antioxidant capacities. The antioxidant activities were found to be statistically different between the hydroethanolic and hydromethanolic extracts ($t = 11.81$, $df = 9$, $p < 0.001$). As previously reported by Kaska and Mammadov [12] and Nickavar and Esbati [24], these findings also showed that the high antioxidant capacities of the hydromethanolic extract is due to the presence of the high phenolic content.

Table 3: Antioxidant properties of *D. ferruginea* L. subsp. *ferruginea*

Sample	DPPH (IC$_{50}$, µg/mL)	ABTS (IC$_{50}$, µg/mL)	Phosphomolybdenum (µg/mg)	Power reducing (mg/mL)
hydroethanolic	292.47 ± 9.10 a	308.43 ± 16.5 a	60.94 ± 1.7 b	0.38 ± 0.02 b
hydromethanolic	197.54 ± 23.9 b	222.80± 18.4 b	111.5 ± 3.9 a	0.31 ± 0.03 b
TROLOX	20.43 ± 1.12 c	26.44 ± 1.08 c	nt	nt
BHT	31.76 ± 1.72 c	27.10 ± 0.36 c	nt	1.15 ± 0.02 a
EDTA	nt	nt	nt	nt

TROLOX, BHT and EDTA: standard antioxidants.
The statistical differences were given as different letters ($p < 0.05$). nt: not tested

In this study, according to the results of the inhibition of linoleic acid oxidation for hydroethanolic and hydromethanolic extracts, similar to that of the phosphomolybdenum method,

the hydromethanolic extract from *D. ferruginea* L. subsp. *ferruginea* (85.57±0.62%) showed stronger antioxidant capacities than those in the hydroethanolic extract (72.30±2.20%) (Fig. 1).

In addition, the hydromethanolic exract's activity was found to be significantly different from that of the BHT (93.71±0.23%) and TROLOX (94.81±1.15%) antioxidant activities ($F_{3,28} = 65.42$ p < 0.001). These findings demonstrate that hydroethanolic and hydromethanolic extracts were found to effectively inhibit linoleic acid oxidation, showing that they have strong antioxidant properties.
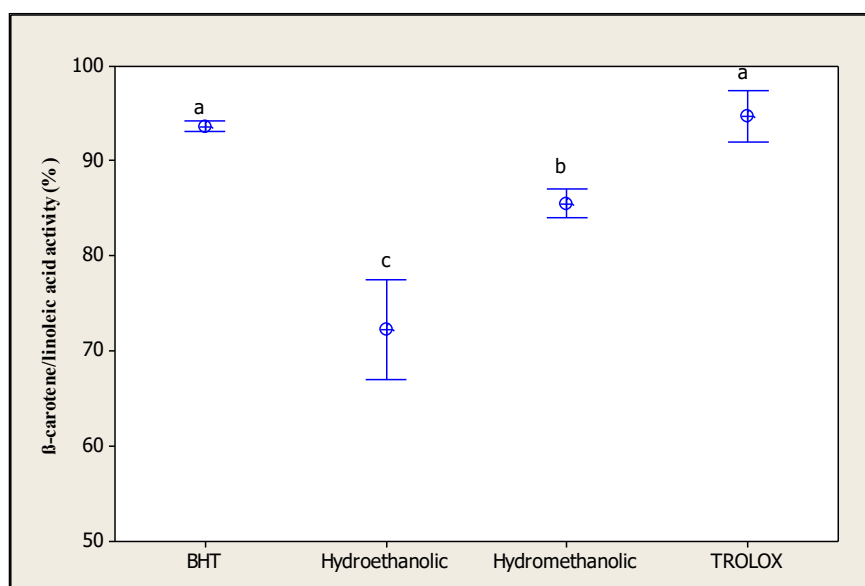
Figure 1: The β-carotene/linoleic acid activity (%) of *D. ferruginea* L. subsp. *ferruginea*

When the hydromethanolic and hydroethanolic extract of *D. ferruginea* L. subsp. *ferruginea* were compared with the methanol extract from *D. ferruginea* L. subsp. *ferruginea* (78.59%) [7], the β-carotene/linoleic acid activity of the hydroethanolic extract was lower, while the hydromethanolic extract's antioxidant activity was higher than those of the methanol extract of this species. It is known that the antioxidant efficacy of the resulting extracts is strongly affected by the type of solvent used and is a polarity of this solvent [25]. This is because the type of solvents and polarity may modify the single electron transfer and the hydrogen atom transfer, both of which are crucial to the measurement of antioxidant capacity [26]. So it is very important to investigate the plants' antioxidant activities using a of variety solvents.

DPPH and ABTS radical-scavenging assays offer a redox-functioned proton ion for unstable free radicals and perform a vital role in the human body for the stabilization of detrimental free radicals [27].

Moreover, ABTS and DPPH assays are commonly used for evaluating the volume of antioxidants in natural products; both are spectrophotometric techniques, which are based on the quenching of stable colored radicals (ABTS or DPPH). They reveal the radical scavenging ability of antioxidants, even when found in complex biological amalgams, such as plant or food extracts [28]. It is known that in the ABTS and DPPH assay, when antioxidant activity transpires, the capacity to eradicate hydroxyl radicals or superoxide radicals through physiologic action or oxidation is calculated with a high index indicating a powerful antioxidant capacity [27].

DPPH is one of the most stable free radicals and is frequently used in the evaluation of radical scavengers in natural foods. The DPPH assay method is very straightforward and fast for the manual analysis of antioxidant contents [29].

In the current study, the DPPH radical scavenging activity of different extracts of *D. ferruginea* L. subsp. *ferruginea* is expressed in terms of IC_{50} (µg/mL) values (Table 3). A reduction in the IC_{50} value signifies a higher level of antioxidant activity. The DPPH free radical scavenging activity of the hydroethanolic and hydromethanolic extracts were significantly different from each other and IC_{50} values of these extracts were found to be different from the BHT and TROLOX IC_{50} values ($F_{3,28}$ 106.24 p < 0.001).

Hydrogen donating ability is related to the effect of antioxidants on DPPH [30]. The results obtained in this study suggested that extracts from the *D. ferruginea* L. subsp. *ferruginea* contained a large amount of radical scavenging compounds with hydrogen donating abilities.

The ABTS radical-scavenging measurement method, frequently used when calculating antioxidant activity, exploits the fact that ABTS free radicals become stable by taking a hydrogen ion from the antioxidant, thereby relinquishing their blue colors [27].

In the ABTS radical scavenging assay, the IC_{50} values for hydroethanolic and hydromethanolic extracts are shown in Table 3.

The hydroethanolic and hydromethanolic extracts investigated in present study demonstrated a scavenging capacity. These samples were significantly different from each other and the IC_{50} values of the all extracts were found to be statistically different from the BHT and TROLOX IC_{50} values ($F_{3,28} = 132.55$ p < 0.001).

Free radicals cause a loss of fluidity in the membranes lipids, a denaturating of the proteins and cell lysis. In addition, they produce mutagenesis and carcinogenesis, by modifying the bases in nucleic acids Antioxidants protect the body from free radicals, [31, 32]. Natural antioxidants in the plants are of a greater benefit when compared with synthetic ones. This is because, due to

their natural origin, the use of natural antioxidants from plants does not induce side effects [33, 34]. As a result, the investigation of biological activity in plants as a potential source of natural antioxidants are very important. The hydroethanolic and hydromethanolic extracts of *D. ferruginea* L. subsp. *ferruginea* tested in this study showed a radical scavenging capacity.

Metal ion chelating capacity is noteworthy, as it decreases the concentration of transition metal, which catalyzes lipids through oxidation [35]. Consistent with the results, the plant extracts are not as beneficial as the standard EDTA; nevertheless, the reduction of the concentration – dependent color formation in the presence of the extracts – reveals iron chelating activity. Figure 2 shows the comparison of hydroethanolic (29.79 ± 0.7 %) and hydromethanolic (39.06 ± 1.27%) extracts from *D. ferruginea* L. subsp. *ferruginea* with EDTA (88.27 ± 1.18%) for metal ion chelating activity. The Metal ion chelating activities were found to be statistically different between the hydroethanolic, hydromethanolic extracts and EDTA ($F_{2,21}$ = 835.07 p < 0.001).
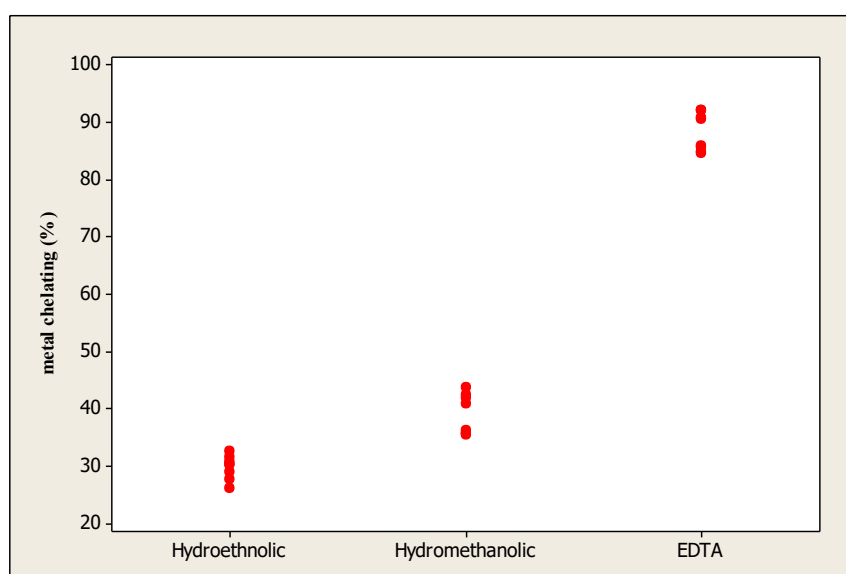
Figure 2: The Metal chelating activity of *D. ferruginea* L. subsp. *ferruginea*

The ferric ion reducing method is based on the reduction of ferric (Fe^{3+}) to ferrous (Fe^{2+}), in the presence of antioxidants. Substances exhibiting a reduction potential respond to potassium ferricyanide, forming potassium ferrocyanide that also reacts with $FeCl_3$ to create a deep Prussian blue complex that has maximum absorbance at 700 nm. The quantity of the complex created is directly relative to the reducing power of the test sample [36].

In this study, hydroethanolic and hydromethanolic extracts from *D. ferruginea* L. subsp. *ferruginea* were investigated for reducing capacity and there were no statistically differences among the reducing activities of hydroethanolic and hydromethanolic extracts ($F_{2,21}$ = 468.98,

p < 0.001). The reducing power is a very important feature for the estimation of the antioxidant activity [37]. This antioxidant activity is attributed to the presence of natural antioxidants such as phenolic compounds in *D. ferruginea* L. subsp. *ferruginea.*

3.3. Brine shrimp lethality assay

The Brine Shrimp Lethality Assay is a valuable method for an assessment of the toxic potential of various plant extracts. This assay is also easily mastered, is of little cost, and utilizes only a small amount of the test material. In addition, applied with *Artemia salina* nauplii. The Brine Shrimp Lethality test turned out to be significantly correlated with several other animal models. The preliminary toxicity data obtained by conducting the this assay gives LC_{50} values for further toxicity studies [38-40].

The lethality of the extracts of *D. ferruginea* L. subsp. *ferruginea* to brine shrimp was determined on *A. salina* after 24 hours of exposure to the test solutions, by following the procedure of Meyer et al. [13]. The hydroethanolic and hydromethanolic extracts showed potential toxic activity, having an LC_{50} value of 281.497 and 107.437 μg/ml respectively. The result obtained from the brine shrimp lethality bioassay of *D. ferruginea* L. subsp. *ferruginea* can be used as a guide for the isolation of toxic components from the hydroethanolic and hydromethanolic extracts of this plant.

4. Conclusions

Testing the antioxidant properties of natural products has attracted growing interest in recent years. This is largely due to antioxidants being able to neutralize harmful free radicals. According to the findings, hydroethanolic and hydromethanolic extracts of *D. ferruginea* L. subsp. *ferruginea* were found to be a valuable antioxidant in various *in vitro* methods. In addition, this plant exhibited toxic effects and has various polyphenolic compounds that possess beneficial properties. The findings shown here will supply new data for further investigations of this species. The results of this study could provide additional information for the potential use of this plant for the pharmaceutical industry. However, further research would be required before such uses could be proposed with confidence.

Acknowledgement

References

[1] Ahmed, D., Khan, M.M., Saeed, R., *Comperative analysis of phenolics, flavonoids and antioxidant and antibacterial potential of methanolic, hexanic and aqueous extracts from Adiantum caudatum leave*, Antioxidants. 4, 394-409, 2015.

[2] Valko, M., Leibfritz, D., Moncol, J., Cronn, M.T.D., Mazur, M., Telser, J., *Free redicals and antioxidants in normal physiological functions and human disease*, International Journal of Biochemistry Cell Biology, 39, 44-84, 2007.

[3] Percival, M., *Antioxidants*, Clinical Nutrition İnsights. 10: 1–4, 1998.

[4] Frey, F.M, Meyers, R., *Antibacterial activity of traditional medicinal plants used by Haudenosaunee peoples of New York State,* BMC Complementary and Alternative Medicine 2010, 10:64.

[5] Benli, M., Yigit Kayhan, N., Geven, F., Güney, K., Bingöl, M.U., *Antimicrobial activity of endemic Digitalis lamarckii Ivan from Turkey,* Indian Journal of Experimental Biology, 47, 218–221, 2009.

[6] Tusevski, O., Kostovska, A, Iloska, A, Trajkovska, L, Simic, S.G., *Phenolic production and antioxidant properties of some Macedonian medicinal plants,* Central European Journal of Biology, 9, 888-900, 2014.

[7] Katanić, J., Ceylan, R., Matić, S., Boroja, T., Zengin, G., Aktumsek, A., Mihailović, V., Stanić S*., Novel perspectives on two Digitalis species: Phenolic profile, bioactivity, enzyme inhibition, and toxicological evaluation*, South African Journal of Botany, 109:50–57, 2017.

[8] Adom, M.B., Taber, M., Mutalabisi, M.F, Amri, M.S., Kudos, M.B.A., Sulaiman, M.W.A.W., Sengupta P., Susanti D., *Chemical constituents and medical benefits of Plantago major,* Biomedicine &Pharmacotherapy, 96:348-360, 2017.

[9] Kaska, A., Çiçek, M., Mammadov, R., *Biological activities, phenolic constituents and mineral element analysis of two endemic medicinal plants from Turkey: Nepeta italica subsp. cadmea and Teucrium sandrasicum,* South African Journal of Botany, 124, 63–70, 2019.

[10] Kaska, A., Deniz, N., Cicek, M., Mammadov, R., *Evaluation of antioxidant properties, phenolic compounds, anthelmintic, and cytotoxic activities of various extracts isolated from Nepeta cadmea: an endemic plant for Turkey*, Journal of *Food* Science, 83, 1552–1559, 2018.

[11] Caponio, F., Alloggio, V., Gomes, T., *Phenolic compounds of virgin olive oil: influence of paste preparation techniques.* Food Chemistry, 64, 203–209, 1999.

[12] Kaska, A., Mammadov, R., *Antioxidant properties, proximate analysis, phenolic compounds, anthelmintic and cytotoxic screening of Teucrium sandrasicum, an endemic plant for Turkey*, Italian Journal of Food Science, 31,332-346, 2019.

[13] Meyer, B.N., Ferrigni, N.R., Putnam, J.E., Jacobsen, L.B., Nichols, D.E., McLaughlin, J.L., *Brine shrimp: a convenient general bioassay for active plant constituents.* Planta Medica. 45, 31–34, 1982.

[14] Peterson, G.L., *Review of the folin phenol protein quantitation method of lowry, rosebrough, farr, randall*, Analytical Biochemisrty, 100(2), 201-220, 1979.

[15] Slinkard, K., Singleton, V.L., *Total Phenol Analysis: Automation and Comparison with Manual Methods*, American Journal of Enology and Viticulture. 28, 49-55, 1977.

[16] Liu, H., Song, Y., Zhang, X., *Determination of total flavonoids in Leek by AlCl$_3$ colorimetric assay*, Chemical Engineering Transactions, 59, 775-780, 2017.

[17] Xu, J., Tong, C., Fu, Q., Guo, K., Shi, S., Xiao, Y., *Comprehensive polyphenol profile of Plantago depressa using high-speed countercurrent chromatography off-line with high-performance liquid chromatography-diode array detector-quadrupole time-of-flight tandem mass spectrometry*, eFOOD, 1-12, 2019.

[18] Martinez-Valverde, I., Periago, M.J., Ros, G*., Significado nutricional de los compuestos fenolicos de la dieta*, Archivos Latinoamericanos de Nutricion, 50 (1), 5-18, 2000.

[19] Santos-Sanchez, N.F., Salas-Coronado, R., Vaillanueva-Canongo, C., Hernandez-Carlos, B. Chapter: *Antioxidant compounds and their antioxidant mechanism*, Antioxidants, 1-28, 2019.

[20] Paran, E., Novack, V., Engelhard, Y.N., Hazan-Halevy, I., *The effects of natural antioxidants from tomato extract in treated but uncontrolled hypertensive patients*, Cardiovascular Drugs and Therapy, 23 (2),145-151, 2009.

[21] Yoshida, M., Sakai, T., Hosokawa, N., Marui, N., Matsumoto, K., Fujioka, A. et al., *The effect of quercitin on cell cycle progression and growth of human gastric cancer cells*, FEBS Letters, 260 (1), 10-13, 1990.

[22] Ho, C.T., *Phenolic compounds in foods*. Phenolic Compounds in Food and Their Effects on Health II. Chapter I, pp.2-7, 1992.

[23] Prieto, P., Pineda, M., Aguilar, M., *Spectrophotometric quantitation of antioxidant capacity through the formation of a phosphomolybdenum complex: specific application to the determination of vitamin E,* Analytical Biochemistry, 269, 337–341, 1999.

[24] Nickavar, B., Esbati, N., *Evaluation of the Antioxidant Capacity and Phenolic Content of Three* Thymus *Species,* Journal of Acupuncture and Meridian Studies, 5(3), 119-125, 2012.

[25] Sultana, B., Anwar, F., Ashraf, M., *Effect of extraction solvent/technique on the antioxidant activity of selected medicinal plant extracts*, Molecules, 14, 2167-2180, 2009.

[26] Pérez-Jiménez, J., Saura-Calixto, F., *Effect of solvent and certain food constituents on different antioxidant capacity assays,* Food Research International, 39, 791– 800, 2006.

[27] Lee, K.J., Oh, Y.C., Cho, W.K., Ma, J.Y., *Antioxidant and Anti-inflammatory activity determination of one hundred kinds of pure chemical compounds using offline and online screening HPLC assay*, Evidence-Based Complemetary and Alternative Medicine. 1-13, 2015.

[28] Sujarwo, W., Keim, A.P., *Spondias pinnata (L.f.) Kurz. (Anacardiaceae): Profiles and zpplications to diabetes*, Chapter 27-Bioactive Food as Dietary Intervantions for Diabetes. 395-405, 2019.

[29] Burda, S., Oleszek, W., *Antioxidant and antiradical activities of flavonoids*, Journal of Agricultural and Food Chemistry, 49 (6), 2774-9, 2001.

[30] Zin, Z.M, Abdul, A., *Antioxidative activity of extracts from Mengkudu (Morinda citrifolia L.) root, fruit and leaf,* Food Chemistry, 78, 227-231, 2002.

[31] Nimse, S.B, Pal, D., *Free radicals natural antioxidants and their reaction mechanism*, RSC Advances, 5, 2015.

[32] Dean, R.T, Fu, S., Stocker, R,, Davies, M., *Biochemisrty and pathology of radical-mediated protein oxidation*, Biochemisrty Journal, 324, 1-18, 1997.

[33] Rohman, A., Riyanto, S., Yuniarti, N., Saputra, W.R, Utami, R., *Antioxidant activity total phenolic and total flavonoid of extracts and fractions of red fruit (Pandanus conoideus Lam.)* International Food Research Journal, 17, 97-106, 2010.

[34] Zheng, W., Wang, Y.S., *Antioxidant activity and phenolic compounds in selected herbs,* Journal of Agricultural and Food Chemistry, 49, 5165-5170, 2001.

[35] Mohan, S.C., Balamurugan, V., Salini, S.T., Rekha, R., *Metal ion chelating activity and hydrogen peroxide scavenging activity of medicinal plant Kalanchoe pinnata*, Journal of Chemical and Pharmaceutical Research, 4, 197-202, 2012.

[36] Kumar, C.S., Loh, W.S., Ooi, C.W., Quah, C.K., Fun, H.K., *Structural correlation of some heterocyclic chalcone analogues and evaluation of their antioxidant potential*, Molecules, 18 (10), 11996-12011, 2013.

[37] Ksouri, R., Megdiche, W., Falleh, H., Trabelsi, N., Boulaaba, M., Smaoui, A., Abdelly, C., *Influence of biological, environmental and technical factors on phenolic content and antioxidant activities of Tunisian halophytes*, Compes Rendus Biologie, 31, 865-873, 2008.

[38] Hamidi, M.R., Jovanova, B., Panovska, T.K., *Toxicological evaluation of the plant products using Brine Shrimp (Artema salina L.) model*, Macedonian pharmaceutical bulletin, 60(1), 9-18, 2014.

[39] Gadir, S.A., *Assessment of bioactivity of some Sudanese medicinal plants using Brine Shrimp (Artemia salina) lethality assay.* Journal of Chemical and Pharmaceutical Research, 4, 5145-5148, 2012.

[40] Naidu, J.R., Ismail, R., Sasidharan, S., *Acute oral toxicity and Brine shrimp lethality of methanol extracts of Mentha spicata L. (Lamiaceae)*, Tropical Journal of Pharmaceutical Research, 13, 101-107, 2014.

Gall Forming Wasp Species of Oak Forests in Bolu

Serap MUTUN[1], Serdar DİNÇ[1,]*

[1]*Bolu Abant İzzet Baysal University, Faculty of Science and Art, Department of Biology, Bolu, Turkey*
smutun@ibu.edu.tr, ORCID: 0000-0002-0838-3857
dinc_s@ibu.edu.tr, ORCID: 0000-0002-8920-2738

Abstract

Oak cynipid galls were collected between 2006-2019 to reveal species diversity of oak gall wasps (Hymenoptera, Cynipidae, Cynipini) in Bolu. Collected galls were brought to laboratory and kept at room temperature in jars covered by tulle until adult cynipid wasps emerged. As a result, 44 species from 8 genera showed that *Andricus* is the most specious genus with 26 species. Our results indicate that Bolu bears high gall wasp species diversity. In this study, new distribution ranges are provided for most of the cynipid species previously reported for Turkey.

Bolu Meşe Ormanlarında Gal Oluşturan Arı Türleri

Öz

Meşe gal arısı (Hymenoptera, Cynipidae, Cynipini) çeşitliliğini belirleyebilmek için 2006-2019 yılları arasında Bolu'da arazi çalışmaları yapılmıştır. Toplanan mazılar laboratuvara getirilerek kavanozlara konulmuş ve tülle kapatılarak oda sıcaklığında ergin gal arısı elde edilene dek tutulmuşlardır. Çalışma sonucunda belirlenen 8 cinse ait toplam 44 cynipid türü belirlenmiş, 26 tür ile A*ndricus* cinsinin en fazla tür sayısına sahip grup olduğu belirlenmiştir. Sonuçlar

Bolu'da gal arısı çeşitliliğinin yüksek olduğunu ortaya koymuştur. Bu çalışma ile Türkiye'nin meşe gal arısı türleri için yeni lokasyonlar belirlenmiştir.

Anahtar Kelimeler: Cynipidae; Hymenoptera; Meşe mazı arısı; Çeşitlilik; Bolu.

1. Introduction

Different arthropod groups from insects to acaroid species and other organisms from bacteria, fungi to viruses induce galls on a variety of plant taxa [1]. Among insects, the majority of gall-inducing species are gall wasps (Hymenoptera, Cynipidae, Cynipini) that are represented by more than 1400 species classified under 40 genera with worldwide distribution [2]. In the northern hemisphere, the Nearctic region with nearly 700 cynipid species is richer than the Palearctic region, which hosts roughly around 300 species [3, 4]. Gall forming cynipids prefer different parts of predominantly oak species from the family Fagaceae as their hosts [5]. They form their galls in roots, leaves, shoots, branches, stems, flowers, and other parts of oak trees [6].

At the junction of three phytogeographic regions, 24 taxa including species, subspecies and varieties are known to exist in nearly 5.938.527 hectares area in the Turkish forests [7, 8]. Until recent years, there have not been many studies in oak gall wasps despite the richness in the host plant species in Turkey. However, there is currently an increase in these obligate guests of oaks [9-18]. A recent checklist study reported 148 species under 25 genera of cynipids representing 9 tribes [19]. The tribe Cynipini hosts 110 species under 12 genera and galls variety of oak taxa from Quercus, Cerris and Ilex sections. Majority of the species are from the genus *Andricus* with 77 species followed by *Cynips*, *Neuroterus* and other genera. A recent study added two new records for the Turkish cynipid fauna [20]. Despite the acceleration in oak gall wasp research the Turkish oak cynipid gall wasp fauna still remains little-known, and it is estimated that the number of gall wasp species is much higher than the current reports.

With this study, we aim to contribute to the knowledge of the Turkish oak cynipid fauna with special emphasis given to Bolu since it is rich in oaks. Bolu is located in the northwestern part of Turkey which is an important city being in the passageway between Anatolia and the Thrace considering its floral elements. Among a variety of oak species and their natural hybrids *Quercus petraea* (Mattuschka) Liebl., *Q. robur* L. ve *Q. pubescens* Willd. are the dominant oak species in the forestry areas of Bolu. This paper gives species diversity as well as new distribution localities of some Turkish oak gall wasp species since so far, no study was carried out to determine oak gall wasp fauna of the studied area.

2. Materials and Methods

The materials examined in this study were collected between May and November from 2006 to 2019 from Bolu Province located in the western part of the Black Sea area of Turkey. Oak cynipid galls were collected from *Quercus petraea*, *Q. pubescens*, *Q. robur* and *Q. infectoria*. Coordinates of the sampling sites were recorded using a Garmin model Geographic Positioning System (GPS). After collecting galls, they were put in a plastic bag and brought into the laboratory. All gall samples were kept in jars covered by tulle under laboratory conditions until cynipid wasps emerged from the galls. Both gall and adult gall wasp morphologies were used for the identification of specimens by the authors following the key provided in Melika 2006 [6]. The materials are kept in Abant Izzet Baysal University, Department of Biology, Molecular Zoology Laboratory, Bolu.

3. Results and Discussion

In this study, a total of 44 species under 8 genera (listed below) from the tribe Cynipini were recorded from Bolu.

Andricus aries (Giraud, 1859)

Material examined: Gerede Dağkara Village, N 40° 47′ E 32° 22′, 09-07-2008, 1 gall, Gölköy, N 40° 71′ E 31° 51′, 26-09-2011, 1 gall, Seben Ekiciler Village, N 40° 25′ E 31° 31′, 09-07-2008, 2 galls, Güneyce Village, N 40° 21′ E 31° 28′, 09-07-2008, 3 galls, Kazanuçuran, N 40° 28′ E 31° 32′, 09-07-2008, 1 gall. Host: *Quercus pubescens*, *Q. petraea*.

Andricus bulgaricus Vassileva-Samnalieva, 1977

Materyal examined: Gölköy, N 40° 71′ E 31° 51′, 14-10-2011, 1 gall, Mengen Gökçesu near Çaydeğirmeni Road, N 41° 16′ E 32° 04′, 18-07-2006, 22 galls, Host: *Quercus petraea*.

Andricus caputmedusae (Hartig, 1843)

Material examined: Gölköy, N 40° 71′ E 31° 51′, 17-09-2011, 3 galls, Göynük Çamlıca Village, N 40° 13 E 30° 56′, 19-08-2010, 5 galls, Kumcuk Village, N 40° 22′ E 30° 43′, 19-08-2010, 6 galls, Kürnuç Village, N 40° 13′ E 30° 41′, 19-08-2007, 4 galls, Kıbrıscık Belen Village, N 40° 22′ E 31° 70′, 15-07-2009, 7 galls, Kılkara Village, N 40° 24′ E 31° 46′, 15-07-2009, 3 galls. Host: *Quercus petraea*, *Q. infectoria*.

Andricus coriarius (Hartig, 1843)

Material examined: Gölköy, N 40° 71´ E 31° 51´, 12-09-2011, 4 galls, Göynük Karacalar Village, N 40° 22´ E 30° 37´, 19-08-2010, 2 galls, Ahmetbeyler Village, N 40° 12´ E 30° 50´, 19-08-2010, 3 galls, Mengen Çubuk Village, N 40° 59´ E 32° 04´, 14-10-2011, 2 galls, Karakaya village, N 40° 54´ E 31° 57´, 05-08-2009, 2 galls. Host: *Quercus petraea*.

Andricus coronatus (Giraud, 1859)

Material examined: Dörtdivan Çetikören Village, N 40° 41´ E 31° 59´, 27-07-2006, 7 galls, Yağbaşlar Village, N 40° 40´ E 31° 58´, 27-07-2009, 5 galls, Kındıra Village, N 40° 48´ E 31° 58´, 27-07-2006, 6 galls, Gölköy, N 40° 71´ E 31° 51´, 14-10-2011, 17 galls, Göynük Arıkçayırı Village, N 40° 28´ E 30° 54´, 19-08-2009, 9 galls, Mengen Babahızır Village, N 40° 54´ E 32° 03´, 14-07-2007, 8 galls, Çubuk Village, N 40° 59´ E 32° 04´, 14-07-2007, 4 galls. Host: *Quercus petraea*.

Andricus corruptrix (Schechtendal, 1870)

Material examined: Gölköy, N 40° 71´ E 31° 51´, 01-10-2010, 7 galls, Hamidiye area, N 40° 67´ E 31° 58´, 29-10-2010, 9 galls, Kütükçüler, N 40° 45´ E 31° 37´, 21-08-2011, 5 galls, Tokmaklar, N 40° 48´ E 31° 46´, 21-08-2011, 8 galls. Host: *Quercus petraea*, *Q. pubescens*.

Andricus curvator Hartig, 1840

Material examined: Gerede Aktaşkurtlar, N 40° 50´ E 32° 31´, 22-07-2009, 1 gall, Macarlar Village, N 40° 49´ E 32° 31´, 22-07-2009, 5 galls, Ertuğrulköy Village, N 40° 49´ E 32° 21´, 11-06-2011, 3 galls, Salur-Karapazar, 40° 47´ E 32° 22´, 11-06-2011, 5 galls, Gölköy, N 40° 71´ E 31° 51´, 11-06-2011, 2 galls, Kıbrıscık near Alan Village, N 40° 22´ E 31° 45´, 13 galls, Geriş N 40° 22´ E 31° 47´, 11-06-2011, 3 galls, Yeniçağa Saray-Yamanlar, N 40° 47´ E 32° 22´, 11-06-2011, 1 gall. Host: *Quercus petraea*, *Q. pubescens*.

Andricus foecundatrix (Hartig, 1840)

Material examined: Dörtdivan Çetikören, N 40° 39´ E 31° 59´, 27-07-2006, 2 galls, Kındıra Village, N 40° 48´ E 31° 50´, 27-07-2007, 1 gall, Yağbaşlar Vilage, N 40° 39´ E 31° 59´, 27-07-2009, 2 galls, Gölköy, N 40° 71´ E 31° 51´, 12-09-2011, 6 galls, Kıbrıscık Kılkara Village, N 40° 24´ E 31° 46´, 15-07-2009, 3 galls, near Belen Village, N 40° 25´ E 31° 45´, 17-07-2009, 3 galls. Host: *Quercus petraea*, *Q. robur*.

Andricus gallaeurnaeformis (Fonscolombe, 1832)

Material examined: Near Gölköy, N 40° 71´ E 31° 51´, 10-10-2019, 11 galls, Mudurnu Ekinören Village, N 40° 33´ E 31° 01´, 12-08-2006, 5 galls, Göllüören Village, N 40° 28´ E 31° 35´, 12-08-2006, 3 galls, Samsaçavuş Village, N 40° 29´ E 31° 02´, 12-08-2006, 4 galls. Host: *Quercus petraea*.

Andricus gallaetinctoriae (Olivier, 1791)

Material examined: Gölköy, N 40° 71´ E 31° 51´, 01-09-2011, 8 galls, Gerede Aktaşkurtlar, N 40° 50´ E 32° 31´, 22-08-2010, 4 galls, Macarlar Village, N 40° 49´ E 32° 31´, 22-08-2010, 6 galls, Mengen Karakaya Village, N 40° 54´ E 31° 57´, 05-08-2009, 4 galls, Mudurnu, N 40° 34´ E 31° 04´, 10-08-2010, 5 galls, Samsaçavuş Village, N 40° 29´ E 31° 02´, 12-08-2009, 7 galls. Host: *Quercus petraea*.

Andricus glutinosus Giraud, 1859

Material examined: Dörtdivan Çetikören, N 40° 39´ E 31° 59´, 17-09-2007, 4 galls, Kındıra Village, N 40° 48´ E 31° 50´, 17-09-20019, 6 galls, Yağbaşlar Vilage, N 40° 39´ E 31° 59´, 17-09-2009, 5 galls, Gölköy, N 40° 71´ E 31° 51´, 01-10-2011, 9 galls, Mengen, N 40° 59´ E 32° 03´, 14-10-2011, near Dorukhan, N 41° 00´ E 32° 03´, 05-08-2009, 1 gall, Başyellice Village, N 41° 07´ E 32° 58´, 05-08-2009, 5 galls. Host: *Quercus petraea*.

Andricus grossulariae Giraud, 1859

Material examined: Mengen Babahızır, N 40° 54´ E 32° 03´, 14-05-2011, 1 gall, Gökçesu, N 41° 26´ E 32° 24´, 18-07-2006, 1 gall. Host: *Quercus petraea*, *Q. robur*.

Andricus infectorius (Hartig, 1843)

Material examined: Dörtdivan Çetikören, N 40° 39´ E 31° 59´, 17-09-2007, 6 galls, Kındıra Village, N 40° 48´ E 31° 50´, 17-09-2007, 8 galls, Yağbaşlar Village, N 40° 39´ E 31° 59´, 17-09-2009, 9 galls, Seben Kozyaka Village, N 40° 25´ E 31° 31´, 09-07-2008, 5 galls, Çeltikdere Village, N 40° 25´ E 31° 31´, 09-07-2008, 5 galls, Gerede Dağkara Village, N 40° 19´ E 31° 39´, 09-07-2008, 2 galls, Gölköy, N 40° 71´ E 31° 51´, 19-09-2011, 5 galls, Mengen Avşar Village, N 40° 44´ E 31° 52´, 27-07-2009, 1 gall. Host: *Quercus petraea*.

Andricus inflator Hartig, 1840

Material examined: Abant, N 40° 71′ E 31° 51′, 04-09-2011, 6 galls, Gerede Macarlar Village, N 40° 49′ E 32° 31′, 22-09-2010, 7 galls, Salur-Karapazar, N 40° 47′ E 32° 22′, 11-09-2011, 3 galls, Gölköy, N 40° 71′ E 31° 51′, 02-09-2011, 7 galls , Göynük Karacalar Village, N 40° 22′ E 30° 37′, 10-09-2008, 6 galls, Kıbrıscık Belen Village, N 40° 22′ E 31° 70′, 15-09-2009, 6 galls, Mengen Babahızır, N 40° 54′ E 32° 03′, 14-05-2011, 6 galls, Mengen Gökçesu, N 41° 26′ E 32° 24′, 18-07-2006, 3 galls,, Seben Alpagut Village, N 40° 45′ E 31° 34′, 21-09-2011, 1 gall. Host: *Quercus infectoria*.

Andricus kollari (Hartig, 1843)

Material examined: Dörtdivan Çetikören, N 40° 39′ E 31° 59′, 17-09-2007, 7 galls, Gerede Aktaşkurtlar, N 40° 50′ E 32° 31′, 22-07-2009, 4 galls, Gölköy, N 40° 71′ E 31° 51′, 11-10-2011, 10 galls, Göynük Arıkçayırı, N 40° 28′ E 30° 54′, 19-08-2008, 9 galls, Akçaalan, N 40° 28′ E 30° 55′, 05-08-2010, 4 galls Mengen, N 40° 59′ E 32° 03′, 14-10-2011, 5 galls, Mudurnu Ekinören Village, N 40° 33′ E 31° 01′, 12-08-2009, 7 galls, Gelinözü, N 40° 27′ E 31° 05′, 12-08-2009, 3 galls, Göllüören Village, N 40° 28′ E 31° 35′, 12-08-2009, 2 galls, Taşkesti, N 40° 34′ E 31° 04′, 12-08-2009, 5 galls, Taşlık Village, N 40° 11′ E 31° 11′, 12-08-2009, 9 galls, Seben Kozyaka, N 40° 25′ E 31° 31′, 09-07-2008, 8 galls. Host: *Quercus petraea*.

Andricus lignicolus (Hartig, 1843)

Material examined: Gerede Aktaşkurtlar, N 40° 50′ E 32° 31′, 22-08-2009, 2 galls, Macarlar Village, N 40° 49′ E 32° 31′, 22-08-2009, 3 galls, Gölköy, N 40° 71′ E 31° 51′, 01-11-2011, 1 gall, Göynük Arıkçayırı, N 40° 28′ E 30° 54′, 19-08-2008, 6 galls, Akçaalan, N 40° 28′ E 30° 55′, 05-08-2010, 2 galls, Mengen Dereköy-Bürnük, N 40° 57′ E 32° 08′, 05-08-2010, 12 galls, Karacalar Village, N 40° 57′ E 32° 14′, 05-08-2010, 3 galls, Mudurnu Ekinören Village, N 40° 33′ E 31° 01′, 12-08-2009, 4 galls. Host: *Quercus petraea*, *Q. infectoria*, *Q, robur*.

Andricus lucidus (Hartig, 1843)

Material examined: Dörtdivan Çetikören, N 40° 39′ E 31° 59′, 17-09-2007, 8 galls, Kındıra Village, N 40° 48′ E 31° 50′, 17-09-2007, 9 galls, Yağbaşlar Vilage, N 40° 39′ E 31° 59′, 17-09-2009, 6 galls, Gölköy, N 40° 71′ E 31° 51′, 10-11-2011, 1 gall, Göynük, Arıkçayırı, N 40° 28′ E 30° 54′, 10-09-2008, 2 galls, Karacalar Village, N 40° 22′ E 30° 37′, 10-09-2008, 3 galls, Kumcuk Village N 40° 22′ E 30° 43′, 10-08-2008, 4 galls, Mengen Avşar Village, N 40° 44′ E 31° 52′, 27-07-2009, 6 galls, Karakaya village, N 40° 54′ E 31° 57′, 25-08-2009, 2 galls. Host: *Quercus petraea*.

Andricus malpighii (Adler, 1881)

Material examined: Gölköy, N 40° 71´ E 31° 51´, 11-10-2011, 15 galls, Abant, N 40° 71´ E 31° 51´, 04-06-2011, 12 galls, Aladağ, N 40° 40´ E 31° 38´, 09-07-2008, 17 galls. Host: *Quercus petraea*.

Andricus mitratus (Mayr, 1870)

Material examined: Aladağ, N 40° 40´ E 31° 38´, 09-09-2008, 9 galls, Dörtdivan Çetikören, N 40° 39´ E 31° 59´, 17-09-2007, 8 galls, Yağbaşlar Vilage, N 40° 39´ E 31° 59´, 27-07-2009, 3 galls, Kındıra Village N 40° 48´ E 31° 50´, 27-09-2007, 7 galls, Gölköy, N 40° 71´ E 31° 51´, 26-08-2011, 8 galls, Kıbrıscık Kılkara Village, N 40° 24´ E 31° 46´, 18-09-2009, 5 galls, Mengen Çubuk Village, N 40° 59´ E 32° 04´, 14-08-2007, 9 galls, Karakaya village, N 40° 54´ E 31° 57´, 05-08-2009, 8 galls, Seben Çeltikdere, N 40° 22´ E 31° 45´, 15-08-2009, 13 galls, Güneyce Village, N 40° 21´ E 31° 28´, 09-08-2008, 6 galls. Host: *Quercus petraea*, *Q. infectoria*, *Q. pubescens*.

Andricus quercusramuli (Linnaeus, 1761)

Material examined: Abant, N 40° 71´ E 31° 51´, 04-06-2011, 8 galls, Aladağ, N 40° 40´ E 31° 38´, 09-07-2008, 7 galls, Dörtdivan Çetikören, N 40° 39´ E 31° 59´, 17-06-2007, 12 galls, Kındıra Village, N 40° 48´ E 31° 50´, 17-06-2007, 6 galls, Gerede Aktaşkurtlar, N 40° 50´ E 32° 31´, 22-06-2009, 5 galls, Gölköy, N 40° 71´ E 31° 51´, 14-7-2011, 21 galls, Göynük Arıkçayırı, N 40° 28´ E 30° 54´, 10-06-2008, 7 galls, Kürnuç Village, N 40° 13´ E 30° 41´, 17-09-2011, 9 galls, Kıbrıscık Belen Village, N 40° 22´ E 31° 70´, 18-06-2009, 11 galls, Mengen Çubuk Village, N 40° 59´ E 32° 04´, 14-6-2011, 4 galls, Mudurnu Ekinören Village, N 40° 33´ E 31° 01´, 12-06-2009, 5 galls. Host: *Quercus petraea*, *Q. infectoria*.

Andricus quercustozae (Bosc, 1792)

Material examined: Aladağ, N 40° 40´ E 31° 38´, 09-07-2008, 12 galls, Dörtdivan, Çetikören, N 40° 39´ E 31° 59´, 17-09-2007, 7 galls, Yağbaşlar Vilage, N 40° 39´ E 31° 59´, 27-07-2009, 9 galls, Kındıra Village, N 40° 48´ E 31° 50´, 27-07-2007, 6 galls, Gölköy, N 40° 71´ E 31° 51´, 26-08-2011, 8 galls, Kıbrıscık Belen Village, N 40° 22´ E 31° 70´, 18-09-2009, 4 galls, Kılkara Village, N 40° 24´ E 31° 46´, 18-09-2009, 7 galls, Mengen Çubuk Village, N 40° 59´ E 32° 04´, 14-07-2007, 2 galls, Karakaya village, N 40° 54´ E 31° 57´, 05-08-2009, 4 galls, Seben Çeltikdere, N 40° 22´ E 31° 45´, 15-07-2009, 3 galls, Güneyce Village, N 40° 21´ E 31° 28´, 09-07-2008, 9 galls, Kozyaka, N 40° 25´ E 31° 31´, 09-07-2008, 8 galls. Host: *Quercus petraea*, *Q. infectoria*.

Andricus solitarius (Fonscolombe, 1832)

Material examined: Mengen Gökçesu, N 41° 21′ E 32° 10′, 18-07-2006, 5 galls. Host: *Quercus petraea*.

Andricus stefanii (Kieffer, 1897)

Material examined: Mengen Çubuk Village, N 40° 59′ E 32° 04′, 14-10-2011, 2 galls, Gölköy, N 40° 71′ E 31° 51′, 09-10-2011, 5 galls, Seben Kozyaka N 40° 25′ E 31° 31′, 09-07-2008, 1 gall, Yeniçağ Saray-Yamanlar, N 40° 47′ E 32° 22′, 11-06-2011, 2 galls. Host: *Quercus petraea*.

Andricus sternlichti Bellido, Pujade-Villar, Melika, 2003

Material examined: Gölköy, N 40° 71′ E 31° 51′, 09-10-2011, 10 galls, Hamidiye area, N 40° 67′ E 31° 58′, 29-10-2010, 13 galls, Kıbrıscık Belen Village, N 40° 22′ E 31° 70′, 18-09-2009, 7 galls, Kılkara Village, N 40° 24′ E 31° 46′, 18-09-2009, 2 galls, Mudurnu Nallıhan Road, N 40° 28′ E 31° 11′, 12-06-2009, 8 galls. Host: *Quercus petraea, Q. pubescens*.

Andricus theophrastea (Trotter, 1866)

Material examined: Gölköy, N 40° 71′ E 31° 51′, 09-10-2011, 5 galls, Hamidiye area, N 40° 67′ E 31° 58′, 29-10-2010, 9 galls, Kütükçüler, N 40° 45′ E 31° 37′, 21-08-2011, 1 gall, Tokmaklar, N 40° 48′ E 31° 46′, 21-08-2011, 3 galls, Göynük Akçaalan, N 40° 28′ E 30° 55′, 05-08-2010, 2 galls, Arıkçayırı, N 40° 28′ E 30° 54′, 19-08-2008, 4 galls, Bulanık Village, N 40° 24′ E 30° 46′, 19-08-2010, 1 gall, Karacalar Village, N 40° 22′ E 30° 37′, 10-09-2008, 2 galls, Kumcuk Village, N 40° 22′ E 30° 43′, 19-08-2010, 3 galls. Host: *Quercus petraea*.

Andricus tomentosus (Trotter, 1901)

Material examined: Hamidiye area, N 40° 67′ E 31° 58′, 21-09-2009, 15 galls. Host: *Quercus petraea*.

Biorhiza pallida (Olivier, 1791)

Material examined: Gerede Aktaşkurtlar, N 40° 50′ E 32° 31′, 22-06-2010, 5 galls, Macarlar Village, N 40° 49′ E 32° 31′, 22-06-2010, 8 galls, Salur-Karapazar, 40° 47′ E 32° 22′, 11-06-2011, 7 galls, Gölköy, N 40° 71′ E 31° 51′, 02-06-2011, 14 galls, Göynük Akçaalan, N 40° 28′ E 30° 55′, 05-06-2010, 9 galls, Arıkçayırı, N 40° 28′ E 30° 54′, 19-06-2008, 8 galls, Karacalar Village, N 40° 22′ E 30° 37′, 10-06-2008, 6 galls, Kıbrıscık Belen Village, N 40° 22′

E 31° 70´, 15-06-2009, 9 galls, Mengen Babahızır, N 40° 54´ E 32° 03´, 14-06-2011, 7 galls, Gökçesu, N 41° 16´ E 32° 04´, 06-06-2011, 3 galls, Mudurnu, N 40° 28´ E 31° 11´, 12-06-2009, 2 galls, Seben Alpagut Village, N 40° 45´ E 31° 34´, 21-06-2011, 2 galls. Host: *Quercus petraea*, *Q. infectoria*.

Cerroneuroterus lanuginosus (Giraud, 1859)

Material examined: Aladağ, N 40° 40´ E 31° 38´, 09-07-2008, 13 galls, Abant, N 40° 71´ E 31° 51´, 04-09-2011, 21 galls, Mengen Çubuk Village, N 40° 59´ E 32° 04´, 14-07-2007, 8 galls. Host: *Quercus petraea*.

Cerroneuroterus minutulus (Giraud, 1859)

Material examined: Abant, N 40° 71´ E 31° 51´, 04-09-2011, 15 galls, Gölköy, N 40° 71´ E 31° 51´, 26-08-2011, 7 galls, Kıbrıscık Belen Village, N 40° 22´ E 31° 70´, 18-09-2009, 3 galls, Kılkara Village, N 40° 24´ E 31° 46´, 18-09-2009, 4 galls, Mengen Çubuk Village, N 40° 59´ E 32° 04´, 14-07-2007, 6 galls, Karakaya village, N 40° 54´ E 31° 57´, 05-08-2009, 5 galls, Seben Çeltikdere, N 40° 22´ E 31° 45´, 15-07-2009, 2 galls, Güneyce Village, N 40° 21´ E 31° 28´, 09-07-2008, 2 galls, Kozyaka, N 40° 25´ E 31° 31´, 09-07-2008, 7 galls. Host: *Quercus petraea*, *Q. infectoria*.

Chilaspis nitida (Giraud, 1859)

Material examined: Abant, N 40° 71´ E 31° 51´, 04-09-2011, 10 galls, Gölköy, N 40° 71´ E 31° 51´, 26-08-2011, 8 galls. Host: *Quercus petraea*.

Cynips agama Hartig, 1840

Material examined: Aladağ, N 40° 40´ E 31° 38´, 09-07-2008, 5 galls, Dörtdivan Çetikören, N 40° 39´ E 31° 59´, 17-09-2007, 8 galls, Kındıra Village, N 40° 48´ E 31° 50´, 27-07-2007, 3 galls, Gölköy, N 40° 71´ E 31° 51´, 26-08-2011, 6 galls, Kıbrıscık Kılkara Village, N 40° 24´ E 31° 46´, 18-09-2009, 4 galls, Mengen, Çubuk Village, N 40° 59´ E 32° 04´, 14-07-2007, 7 galls, Seben Çeltikdere, N 40° 22´ E 31° 45´, 15-07-2009, 5 galls, Güneyce Village, N 40° 21´ E 31° 28´, 09-07-2008, 2 galls, Kozyaka N 40° 25´ E 31° 31´, 09-07-2008, 4 galls. Host: *Quercus petraea*, *Q. infectoria*.

Cynips disticha Hartig, 1840

Material examined: Abant, N 40° 71´ E 31° 51´, 04-09-2011, 13 galls, Gerede Aktaşkurtlar, N 40° 50´ E 32° 31´, 22-09-2009, 8 galls, Ertuğrulköy Village, N 40° 49´ E 32° 21´, 11-09-2011,

7 galls, Gölköy, N 40° 71′ E 31° 51′, 26-05-2011, 16 galls, Mengen, N 40° 59′ E 32° 03′, 14-10-2011, Mudurnu Güllüören Village, N 40° 28′ E 31° 35′, 14-10-2011 3 galls, Taşkesti, N 40° 34′ E 31° 04′, 12-08-2009, 11 galls, near Taşlık Village, N 40° 11′ E 31° 11′, 14-10-2011, 5 galls. Host: *Quercus petraea*, *Q. pubescens*.

Cynips divisa Hartig, 1840

Material examined: Dörtdivan Yağbaşlar Village, N 40° 40′ E 31° 58′, 27-07-2009, 14 galls, Gerede Aktaşkurtlar, N 40° 50′ E 32° 31′, 22-07-2009, 21 galls, Macarlar Village, N 40° 49′ E 32° 31′, 22-07-2009, 3 galls, Gölköy, N 40° 71′ E 31° 51′, 14-10-2011, 1 gall, Kıbrıscık Kılkara Village, N 40° 24′ E 31° 46′, 15-07-2009, 3 galls, near Belen Village, N 40° 25′ E 31° 45′, 17-07-2009, 3 galls, Hamidiye Village, N 40° 73′ E 31° 54′, 14-10-2011, 7 galls. Host: *Quercus petraea*.

Cynips longiventris Hartig, 1840

Material examined: Abant, N 40° 71′ E 31° 51′, 04-09-2011, 1 gall, Gerede, N 40° 40′ E 32° 19′, 05-09-2007, 2 galls, Dörtdivan Çetikören, N 40° 39′ E 31° 59′, 17-09-2007, 7 galls, Kındıra Village, N 40° 48′ E 31° 50′, 17-09-2007, 9 galls, Gerede Aktaşkurtlar, N 40° 50′ E 32° 31′, 22-09-2009, 7 galls, Macarlar Village, N 40° 49′ E 32° 31′, 22-09-2009, 6 galls, Gölköy, N 40° 71′ E 31° 51′, 02-06-2011, 20 galls, Kıbrıscık Kılkara Village, N 40° 24′ E 31° 46′, 18-09-2009, 8 galls, near Mudurnu-Göynük Road, N 40° 42′ E 31° 25′, 04-09-2007, 2 galls, Seben Çeltikdere, N 40° 22′ E 31° 45′, 15-08-2008, 3 galls. Host: *Quercus petraea*, *Q. infectoria*.

Cynips quercus (Fourcroy, 1785)

Material examined: Abant, N 40° 71′ E 31° 51′, 04-09-2011, 17 galls, Göynük Akçaalan Village, N 40° 28′ E 30° 55′, 19-08-2007, 11 galls, Arıkçayırı Village, N 40° 28′ E 30° 54′, 19-08-2007, 10 galls, Göynük Kürnuç Village, N 40° 13′ E 30° 41′, 19-08-2007, 7 galls, Kumcuk Village, N 40° 22′ E 30° 43′, 19-08-2007, 5 galls, Gölköy, N 40° 71′ E 31° 51′, 15-10-2011, 15 galls. Host: *Quercus petraea*.

Cynips quercusfolii (Linnaeus, 1758)

Material examined: Abant, N 40° 71′ E 31° 51′, 04-09-2011, 8 galls, Aladağ, N 40° 40′ E 31° 38′, 09-07-2008, 7 galls, Dörtdivan Çetikören, N 40° 39′ E 31° 59′, 17-09-2007, 12 galls, Kındıra Village, N 40° 48′ E 31° 50′, 17-09-2007, 6 galls, Gerede Aktaşkurtlar, N 40° 50′ E 32° 31′, 22-07-2009, 5 galls, Gölköy, N 40° 71′ E 31° 51′, 14-10-2011, 21 galls, Göynük Arıkçayırı, N 40° 28′ E 30° 54′, 10-09-2008, 7 galls, Bulanık Village, N 40° 24′ E 30° 46′, 15-09-2010, 2

galls, Kumcuk Village, N 40° 22´ E 30° 43´, 17-09-2011, 4 galls, Kürnüç Village, N 40° 13´ E 30° 41´, 17-09-2011, 9 galls, Kıbrıscık Belen Village, N 40° 22´ E 31° 70´, 18-09-2009, 11 galls, Kılkara Village, N 40° 24´ E 31° 46´, 18-09-2009, 7 galls, Mengen Çubuk Village, N 40° 59´ E 32° 04´, 14-10-2011, 4 galls, Karakaya village, N 40° 54´ E 31° 57´, 25-08-2009, 1 gall, Mudurnu Ekinören Village, N 40° 33´ E 31° 01´, 12-08-2009, 5 galls, Taşkesti, N 40° 34´ E 31° 04´, 12-08-2009, 7 galls, Seben Çeltikdere, N 40° 22´ E 31° 45´, 15-07-2009, 6 galls. Host: *Quercus petraea*, *Q. infectoria*.

Neuroterus albipes (Schenck, 1863)

Material examined: Abant, N 40° 71´ E 31° 51´, 04-09-2011, 21 galls. Host: *Quercus petraea*.

Neuroterus anthracinus (Curtis, 1838)

Material examined: Aladağ, N 40° 40´ E 31° 38´, 09-07-2008, 8 galls, Abant, N 40° 71´ E 31° 51´, 04-09-2011, 12 galls, Dörtdivan Çetikören, N 40° 39´ E 31° 59´, 17-09-2007, 4 galls, Yağbaşlar Vilage, N 40° 39´ E 31° 59´, 27-07-2009, 6 galls, Kındıra Village, N 40° 48´ E 31° 50´, 27-07-2007, 3 galls, Gölköy, N 40° 71´ E 31° 51´, 14-10-2011, 1 gall, Mengen Çubuk Village, N 40° 59´ E 32° 04´, 14-07-2007, 4 galls, Karakaya village, N 40° 54´ E 31° 57´, 05-08-2009, 6 galls. Host: *Quercus petraea*.

Neuroterus numismalis (Fourcroy, 1785)

Material examined: Abant, N 40° 71´ E 31° 51´, 04-09-2011, 15 galls, Dörtdivan Çetikören, N 40° 39´ E 31° 59´, 17-09-2007, 2 galls, Kındıra Village, N 40° 48´ E 31° 50´, 17-09-2007, 7 galls, Göynük, Arıkçayırı, N 40° 28´ E 30° 54´, 10-09-2008, 11 galls, Bulanık Village, N 40° 24´ E 30° 46´, 15-09-2010, 8 galls, Mengen, N 40° 59´ E 32° 03´, 14-10-2011, 12 galls, Gökçesu, N 41° 16´ E 32° 04´, 06-06-2011, 6 galls, Seben near Alpagut Village, N 40° 45´ E 31° 34´, 21-08-2011, 3 galls. Host: *Quercus petraea*, *Q. pubescens*.

Neuroterus politus Hartig, 1840

Material examined: Abant, N 40° 71´ E 31° 51´, 04-05-2011, 6 galls, Gerede Macarlar Village, N 40° 49´ E 32° 31´, 22-04-2010, 7 galls, Salur-Karapazar, 40° 47´ E 32° 22´, 11-05-2011, 3 galls, Gölköy, N 40° 71´ E 31° 51´, 02-05-2011, 7 galls, Göynük Arıkçayırı, N 40° 28´ E 30° 54´, 19-04-2008, 3 galls, Karacalar Village, N 40° 22´ E 30° 37´, 10-05-2008, 6 galls, Kıbrıscık Belen Village, N 40° 22´ E 31° 70´, 15-04-2009, 6 galls, Mengen Babahızır, N 40° 54´

E 32° 03′, 14-05-2011, 6 galls, Mudurnu Nallıhan Road, N 40° 28′ E 31° 11′, 12-05-2009, 3 galls, Seben Alpagut Village, N 40° 45′ E 31° 34′, 21-04-2011, 1 gall. Host: *Quercus petraea*.

Neuroterus quercusbaccarum (Linnaeus, 1758)

Material examined: Abant, N 40° 71′ E 31° 51′, 04-09-2011, 9 galls, Dörtdivan Çetikören, N 40° 39′ E 31° 59′, 17-09-2007, 13 galls, Kındıra Village, N 40° 48′ E 31° 50′, 17-09-2007, 16 galls, Gölköy, N 40° 71′ E 31° 51′, 03-06-2011, 2 galls, Kıbrıscık Belen Village, N 40° 22′ E 31° 70′, 18-09-2009, 5 galls, Kılkara Village, N 40° 24′ E 31° 46′, 18-09-2009, 8 galls, Mengen Avşar Village, N 40° 86′ E 31° 84′, 06-06-2011, 10 galls, Gökçesu, N 41° 16′ E 32° 04′, 06-06-2011, 4 galls, Mudurnu Ekinören Village, N 40° 33′ E 31° 01′, 12-08-2009, 15 galls, Taşkesti, N 40° 34′ E 31° 04′, 12-08-2009, 17 galls, Seben Çeltikdere, N 40° 22′ E 31° 45′, 15-07-2009, 16 galls. Host: *Quercus petraea*, *Q. pubescens*.

Neuroterus tricolor (Hartig, 1841)

Material examined: Abant, N 40° 71′ E 31° 51′, 04-09-2011, 22 galls, Dörtdivan Çetikören, N 40° 39′ E 31° 59′, 17-09-2007, 11 galls, Kındıra Village, N 40° 48′ E 31° 50′, 17-09-2007, 8 gall, Yağbaşlar Vilage, N 40° 39′ E 31° 59′, 17-09-2009, 7 galls, Gölköy, N 40° 71′ E 31° 51′, 10-11-2011, 2 galls, Göynük, Arıkçayırı, N 40° 28′ E 30° 54′, 10-09-2008, 3 galls, Karacalar Village, N 40° 22′ E 30° 37′, 10-09-2008, 3 galls, Mengen Avşar Village, N 40° 44′ E 31° 52′, 27-07-2009, 10 galls. Host: *Quercus petraea*, *Q. infectoria*.

Pseudoneuroterus saliens (Kollar, 1857)

Material examined: Abant, N 40° 71′ E 31° 51′, 04-09-2011, 3 galls, Gölköy, N 40° 71′ E 31° 51′, 10-11-2011, 2 galls, Dörtdivan Kındıra Village, N 40° 48′ E 31° 50′, 17-09-2007, 1 gall, Göynük Karacalar Village, N 40° 22′ E 30° 37′, 10-09-2008, 2 galls, Seben Çeltikdere, N 40° 22′ E 31° 45′, 15-07-2009, 2 galls. Host: *Quercus cerris*, *Q. petraea*, *Q. infectoria*.

Trigonaspis synaspis Hartig, 1841

Material examined: Abant, N 40° 71′ E 31° 51′, 04-09-2011, 9 galls, Gerede, N 40° 40′ E 32° 19′, 05-09-2007, 4 galls, Dörtdivan Çetikören, N 40° 39′ E 31° 59′, 17-09-2007, 5 galls, Kındıra Village, N 40° 48′ E 31° 50′, 17-09-2007, 3 galls, Gerede Aktaşkurtlar, N 40° 50′ E 32° 31′, 22-09-2009, 6 galls, Macarlar Village, N 40° 49′ E 32° 31′, 22-09-2009, 6 galls, Gölköy, N 40° 71′ E 31° 51′, 14-105-2011, 7 galls, Kıbrıscık Kılkara Village, N 40° 24′ E 31° 46′, 18-09-2009, 3 galls, Seben Çeltikdere, N 40° 22′ E 31° 45′, 15-08-2008, 2 galls. Host: *Quercus petraea*, *Q. pubescens*.

With this study, we found 44 cynipid species belonging to 8 different genera from the tribe Cynipini in Bolu. We determined that *Andricus* genus is the most specious group in Bolu which is represented by 26 species. The other genera members in the studied area include *Biorhiza* with one species, *Cerroneuroterus* with 2 species, *Chilaspis* with one species, *Cynips* and *Neuroterus* with 6 species each, *Pesudoneuroterus* and *Trigonaspis* genera are with one species.

5. Conclusions

This is the first detailed work on oak cynipids found in Bolu where all the given cynipid species in this study are recorded for the first time from the studied area. Latest studies on this parasitic insect group of oaks are becoming more popular and requires more attention. Reviewing the literature, it seems the cynipid fauna of Turkey has not yet been completed and requires further detailed investigation.

References

[1] Ronquist, F., Liljeblad, J., *Evolution of the gall wasp-host plant association*, Evolution, 55, 2503-2522, 2001.

[2] Stone, G.N., Cook, J.M., *The structure of cynipid oak galls: patterns in the evolution of an extended phenotype*, Proceedings of the Royal Society of London B, 265, 979-988, 1998.

[3] Stone, G.N., Schönrogge, R.A., Atkinson, K., Bellido, D., Pujade-Villar, J., *The population biology of oak gallwasps (Hymenoptera: Cynipidae)*, Annual Review of Entomology 47, 633-668, 2002.

[4] Abe, Y., Melika, G., Stone, G.N., *The diversity and phylogeography of cynipid gallwasps (Hymenoptera: Cynipidae) of the Oriental and Eastern Palearctic Regions, and their associated communities*, Oriental Insects, 41, 169-212, 2007.

[5] Oğurlu, İ., Avcı, M., "*Kasnak meşesi Quercus vulcanica (Boiss. and Held.) Kotschy' da zarar yapan böcekler*," in Kasnak Meşesi ve Türkiye Florası Sempozyumu, pp. 657-671, 1998.

[6] Melika, G., Gallwasps of Ukraine: Cynipidae. Schmalhausen Institute of Zoology, National Academy of Sciences of Ukraine, 646 pp (2 vols), 2006.

[7[Yılmaz, H., *Quercus* L. (Ed. Ü. Akkemik), Türkiye'nin Doğal-Egzotik Ağaç ve Çalıları. Ankara: Orman Genel Müdürlüğü Yayınları, 338-356, 2018.

[8] OGM (Orman Genel Müdürlüğü / General Directorate of Forestry). (2019, November 11). Ormancılık İstatistikleri. https://www.ogm.gov.tr/ ekutuphane/Sayfalar/Istatistikler.aspx.

[9] Melika, G., Stone, G.N., *A new species of cynipid gall wasp from Turkey (Hymenoptera: Cynipidae)*, Folia Entemolica Hungarica, 62, 127–131, 2001.

[10] Kıyak, S., Kılıç, T., Katılmış, Y., *A contribution to the knowledge of the Cynipini fauna of Turkey (Hymenoptera: Cynipidae)*, Munis Entomology & Zoology, 3(1), 523-536, 2008.

[11] Katılmış, Y., Kıyak, S., *Checklist of Cynipidae of Turkey, with a New Genus Record*, Journal of Natural History, 42(31-32), 2161-2167, 2008.

[12] Katılmış, Y., Kıyak, S., *New records of oak gallwasps of the genus Andricus (Burgsdorf, 1783) from Turkey (Hymenoptera: Cynipidae)*, Zoology in the Middle East, 48, 108-109, 2009.

[13] Katılmış Y., Kıyak, S., *Oak gallwasps (Hymenoptera: Cynipidae) fauna of inner-western Anatolian*, Munis Entomology & Zoology, 6(2), 735-757, 2011.

[14] Mutun, S., Dinç, S., *Contribution of the Turkish Cynipidae fauna with one new record*, Journal of Applied Biological Sciences, 5(3), 83-85, 2011.

[15] Mete, Ö., Demirsoy, A*., Kemaliye'nin (Erzincan, Türkiye) gal arısı faunası üzerine bir ön çalışma ve Türkiye için yeni bir kayıt*, Hacettepe Journal of Biology & Chemistry, 351-363, 2012.

[16] Dinç, S., Mutun, S., Melika, G., *A new species of Andricus Hartig Oak Gall Wasp from Turkey (Hymenoptera: Cynipidae, Cynipini)*, North-Western Journal of Zoology, 10(1), 122-127, 2014.

[17] Mutun, S., Dinç, S., Bozsó, M., Melika, G., *Four New Species of Andricus Hartig Oak Gallwasp From Turkey (Hymenoptera: Cynipidae, Cynipini)*, Zootaxa, 3760(2), 241-259, 2014.

[18] Katılmış, Y., Azmaz, M., *Investigation on the inquilines (Hymenoptera: Cynipidae, Synergini) of oak galls from Inner-Western Anatolia, Turkey*, Turkish Journal of Zoology, 39(1), 168-173, 2015.

[19] Azmaz, M., Katılmış, Y., *Updated species list of Cynipidae (Hymenoptera) from Turkey*, Zootaxa. 4303(3), 361-378, 2017.

[20] Bayrak, S., Avcı, M., *Gall forming Cynipini (Hymenoptera: Cynipidae) species in Isparta oak forests*, Munis Entomology & Zoology, 14(2), 552-564, 2019.

Preparation and Characterization of Polyvinyl Alcohol/Activated Carbon (PVA/AC) Composite and Its Use in the Adsorption of 4-Nitrophenol (4-NP)

Hatice KARAER YAĞMUR[1],*

[1]*Dicle University, Faculty of Science, Department of Chemistry, Diyarbakır, Turkey*
profhatice23@hotmail.com, ORCID: 0000-0002-3728-1825

Abstract

In this study, polyvinyl alcohol-activated carbon (PVA/AC) composite was synthesized and characterized by SEM, FTIR, DLS and TGA-DSC measurement. The zero point charge for the PVA/AC was determined as approximately 3 pH. The efficiency of PVA/AC as a cheap adsorbent for removal of 4-nitrophenol (4-NP) from aqueous solution was researched at 298, 318 and 328 K. For this purpose, Freundlich and Langmuir isotherm models were used. According to the results, adsorption of 4-NP onto composite best fitted to Freundlich model. The pseudo-first-order, pseudo-second-order and intraparticle diffusion models were utilized to study the adsorption kinetics. The experimental consequences fitted with the pseudo-first-order model. According to Arrhenius equation, Ea was calculated as 14.13 kJmol^{-1}. Thermodynamic parameters were also calculated, which revealed that the adsorption process is endothermic, not spontaneous.

Keywords: Adsorption; Activated carbon; Polyvinyl alcohol; 4-nitrophenol (4-NP); Zero point charge.

Polivinil Alkol/Aktif Karbon (PVA/AC) Kompozitinin Hazırlanması ve Karakterizasyonu ve 4-Nitrofenol (4-NP) Adsorpsiyonunda Kullanımı

Öz

Bu çalışmada polivinil alkol/aktif karbon (PVA/AC) kompoziti sentezlendi ve SEM, FTIR, DLS ve TGA-DSC ölçümleriyle karakterize edildi. PVA/AC için sıfır noktası yükü yaklaşık 3 pH olarak belirlenmiştir. Sulu çözeltiden 4-nitrofenolün (4-NP) uzaklaştırılması için ucuz bir adsorban olarak PVA / AC'nin etkinliği 298, 318 ve 328 K'de araştırıldı. Bu amaçla Freundlich ve Langmuir izoterm modelleri kullanıldı. Sonuçlara göre, 4-NP'nin kompozit üzerine adsorpsiyonunda Freundlich model en uygundu. Adsorpsiyon kinetiklerini incelemek için psödo birinci derece, psödo ikinci derece ve partikül içi difüzyon modelleri kullanıldı.Deneysel sonuçlar psödo birinci derece modeline uydu. Arrhenius denklemine göre Ea, 14.13 kJmol^{-1} olarak hesaplandı. Termodinamik parametreler hesaplandı, adsorpsiyon sürecinin endotermik olduğu kendiliğinden olmadığı belirlendi.

Anahtar Kelimeler: Adsorpsiyon; Aktif karbon; Polivinil alkol; 4-nitrofenol (4-NP); Sıfır nokta yükü.

1. Introduction

Activated charcoals (ACs) are known homogeneous materials having high surface area and microporous structure. Moreover, they are widely used in industrial applications as adsorbent and catalyst. The features of AC adsorption depend primarily upon size of particle, porosity, ash contents, carbonization degree and activation process [1]. Moreover, they are efficiently used both in purification of drinking water and different industrial applications and in hemoperfusion and based on hemofiltration therapies [2]. Polyvinyl alcohol (PVA) is a water-soluble synthetic polymer and is known as a cheap polymer and not poisonous [3]. Between artificial polymers, PVA has received amazing interest owing to its convenient physicochemical and viscoelastic features and is widely utilized for several biomedical functions for wound dressing and tissue engineering since it is a biodegradable as well as biocompatible artificial polymer [4]. Phenolic compounds have been widely utilized in the production of chemicals such as explosives, dyes, pesticides, solvents and can stay in aqueous media for a long time. Phenols have been encountered in both wastewater and in whole natural aquatic systems, and have toxic features even at low concentrations. 4-nitrophenol (4-NP) is one of the phenol derivatives which is toxic. 4-NP has a hydroxyl group at the opposite side of a nitro group on the benzene ring and is generally found in wastewater especially with pesticides, herbicides and petrochemicals [5]. Elimination of the phenolic compounds from water is an interesting field due to their high stability and solubility, and the development of environmentally friendly techniques for elimination of phenolic compounds from polluted water is still an important significant topic. Currently, several methods,

such as separation of membrane, adsorption and exchange of ion have been utilized for the elimination of phenolic compounds from industrial effluents. Adsorption method is one of the efficient and preferred processes due to its simplicity and high effectiveness [6]. There are many studies in the literature on activated carbon. However, the studies on polyvinyl alcohol/activated carbon and 4-nitrophenol (4-NP) are limited.

In this study, a new polymer-based composite was prepared from PVA and AC. The composite was characterized by FTIR, DLS, SEM-EDX, TGA-DSC and Zeta sizer. Furthermore, the point of zero charge of PVA/AC composite was determined. Then, PVA/AC composite was used as an adsorbent for the removal of 4-nitrophenol (4-NP) from aqueous solution. Finally, the adsorption of 4-NP by the PVA/AC composite from aqueous solution was studied both thermodynamically and kinetically.

2. Materials and Methods

2.1. Materials

PVA (Poly(vinyl alcohol)) was supplied from Sigma–Aldrich (average molecular weight (M_W): 30,000-70,000 $gmol^{-1}$ and 90% hydrolyzed). AC (Activated charcoal, black powder, 100-400 mesh) and 4-Nitrophenol (4-NP) were bought from Sigma and Sigma–Aldrich (M_W: 139.11 $gmol^{-1}$) respectively.

2.2. Preparation of PVA/AC composite

The composite was synthesized according to a reported procedure [2, 7]. A solution of PVA was synthesized from PVA (5 g) and distilled water (100 mL) at 90 °C with vigorous stirring. Then, an aqueous solution of PVA and10 mL sulfuric acid was mechanically stirred in a 500 mL beaker, and temperature of the mixture was diminished to 60 °C. Subsequently, AC (2.5 g) was added and stirred. The mixture was cooled to room temperature and kept in an ice bath for 30 min. 5 mL of 25% glutaraldehyde solution was added to the cooled solution and the mixture was stirred by a magnetic stirrer for about 3h. PVA/AC composite was acquired after washing with distilled water. It was dried in an oven at about 80 °C. Scheme 2 shows the PVA/AC preparation (Scheme 2).
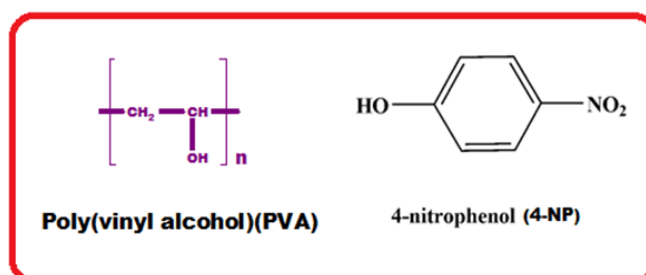
Scheme 1: The chemical structure of materials
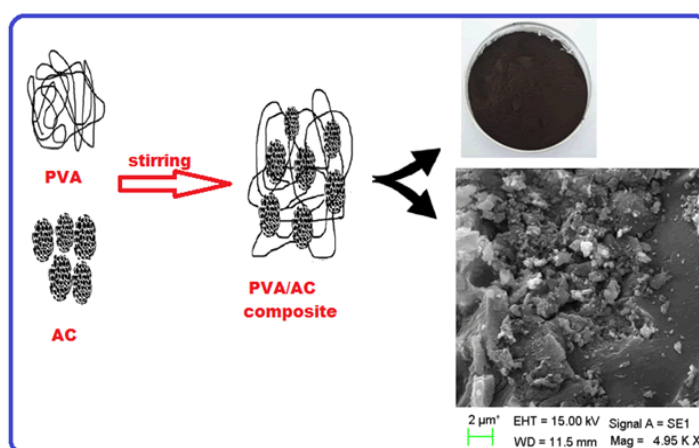
Scheme 2: Schematic representation of PVA/AC composite preparation

2.3. Characterization

The chemical structure of the composite was elucidated by using FTIR spectroscopy (A Perkin Elmer spectrometer-ATR sampling accessory between the wavelengths of 4000–450 cm^{-1}). TGA–DTA analysis was carried out between 20 and 1000 °C (Perkin Elmer, in N$_2$, rate 10°C min^{-1}). DSC analysis of the composite was performed between 25 and 450 °C (Perkin Elmer Pyris sapphire, in N$_2$, rate 10 °C min^{-1}). Surface structure of the composite was identified by using of SEM (scanning electron microscope, JEOL, JSM-7100 model). The conductivity measurements were performed by Keithley Electrometer (Keithley 2400, Ohio, USA). The pellet was pressed on hydraulic press at 1687 kg/cm^2. Iodine doping was performed by exposing the pellet to iodine steam at 25 ^{o}C in a desiccator. Particle dimension of the PVA/AC was detected by using the DLS (dynamic light scattering) method. Zeta potential measurement of the PVA/AC was performed using a ZetaSizer Nano-ZS (Malvern Nano ZS90).

2.4. Determination of the point of zero charge (pHzpc)

The point of zero charge was determined by a reported procedure [8, 9]. The procedure can be described as follows: to a series of 50 mL conical flasks, 30 mL of 0.1M NaCl solution was added. pH values of the initial NaCl solutions (initial pH) were adjusted in the range of 2 to 12 of using 0.1 M HCl / NaOH solutions. After a constant value of initial pH had been reached, 0.015 g of PVA/AC composite was added into each conical flask and caped them immediately. These samples were shaken for 48 h, after which pH was measured for each sample (pH$_f$). The pH variation (ΔpH = pH$_f$ − pH$_i$) was plotted against the pH$_i$, and the point of intersection of the resulting curve at which ΔpH = 0 was the pHzpc value.

2.5. Adsorption kinetics and isotherms

The sorption studies were performed on the composite by use of 4-NP (Scheme 1) and can be classified as three parts: (a) effect of temperature (b) defining of a kinetic model and isotherm model (c) thermodynamic studies. Kinetic studies were performed agitating 100 ml of solution of a constant 4-NP concentration with 0.1 g of the composite at the shaking rate 120 rpm, 298, 313 and 328 K, natural pH. Adsorption equilibrium studies were performed by 0.05 g of composite with 100 mL of 4-NP solution of in the range of 50 to 500 mgL^{-1} concentrations at 298, 313 and 328 K (S.R:120 rpm for 4h). The equilibrium phenol concentration was measured via a UV-visible spectroscopy (λ_{max}:348 nm for 4-NP, Cary 100 Bio UV-visible spectrophotometer). The capacity of adsorption (qe, mg g^{-1}) may be computed by the following equations:

$$qe = (Co-Ce) \, V/m \tag{1}$$

V (L), Co (mgL^{-1}), m (g) and Ce (mg L^{-1}) are the volume of the solution, initial concentration, the adsorbent mass and equilibrium concentration of phenol in the solution, respectively.

3. Results and Discussion

3.1. FTIR

FTIR spectra of PVA and PVA/AC were shown in Fig. 1. The PVA has –CH$_2$, –CH and –OH groups with C-C backbone and is known as a polar polymer. The formation of intermolecular and free bonded hydroxyl groups of AC and PVA were observed at 3317 cm^{-1}. The aliphatic stretching peak of C-H was observed at 2971 cm^{-1} and 2901 cm^{-1}. The peaks at 1702 cm^{-1} and 1667 cm^{-1} are due to C=O and C-O stretching, respectively. The peaks at around 1596 cm^{-1} and 1409 cm^{-1} are corresponding to C=C vibrations and the C-H aliphatic bending, respectively. The

peak at 1080 cm^{-1} (PVA) was defined C-O stretching peak in alcohols. The broadening of C-O peak (1080 cm^{-1}) occurred with the existence of a new peak at 1049 cm^{-1} in the composite is attributed to the interfacial covalent reaction between AC and PVA. The peak at 829 cm^{-1} (PVA) for C-H bending in the PVA/AC sample shifted to 809 cm^{-1} with AC addition [4].
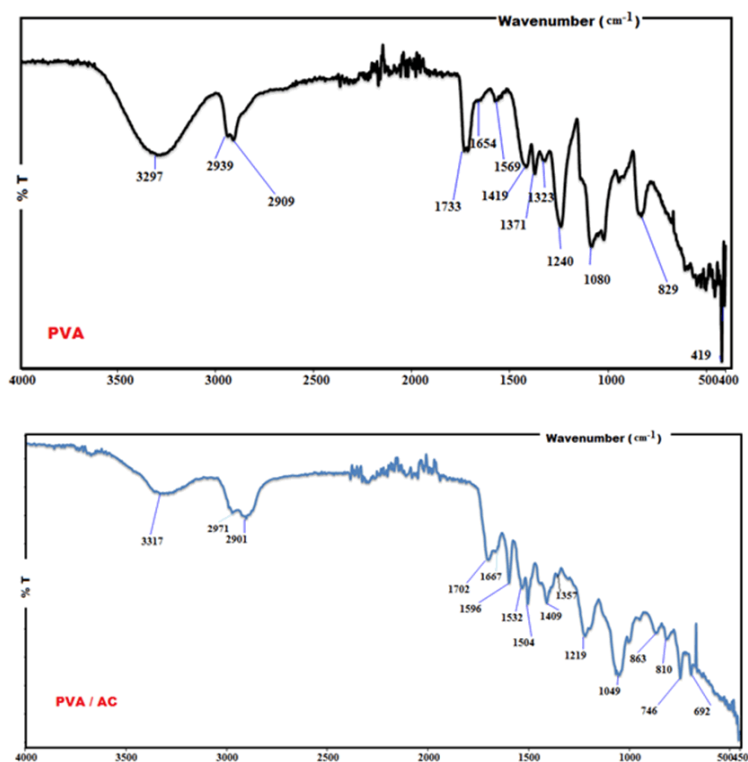
Figure 1: FTIR spectra of the PVA and PVA/AC

3.2. SEM-EDX analysis

The surface morphology of PVA/AC composite was determined by using SEM (Fig. 2). EDX has been defined as the elements on the composite surface. Fig. 2, shows the SEM images of the composite. One can easily see in the Fig. 2 that the surface of the composite is amorphous and not regular, which shows a relatively high surface area. EDX analysis shows that the composite is composed commonly of carbon (Fig. 2(B)). The peaks related to oxygen are low and there were no other different atoms (N, P, S.) present in the composite.
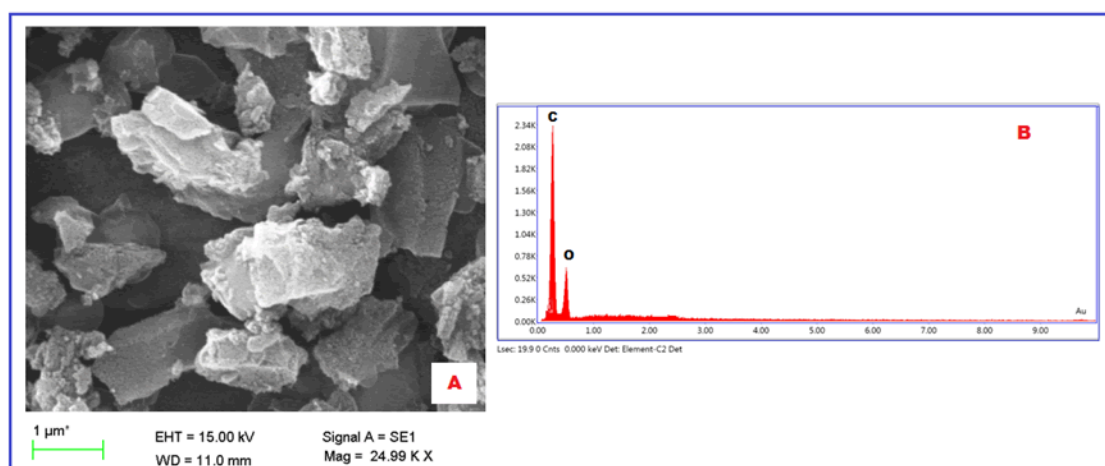
Figure 2: SEM image of composite (A) and EDX spectra of composite (B)

3.3. Dynamic light scattering (DLS)

633 nm diode laser was used in the instrument. The PVA/AC composite was diluted by using of pure water before measurement. The D-values (D10, D50 and D90) were usually used for describing particle size distributions. D10, D50 and D90 are the intercepts for 10%, 50% and 90% of the cumulative mass [10]. Size distribution of the PVA/AC particles was found as < 14.3 μm < 299 μm < 1170 μm for D10, D50 and D90% cumulative mass, respectively. For example, if the D50 is 299 μm, for PVA/AC particles, this means that 50% of the PVA/AC particles has a size of 299 μm or smaller. An additional parameter to show the width of the size distribution is the span. The span of a volume-based size distribution is determined as Span = (D90–D10)/D50 and gives an indication of how far the 10 percent and 90 percent points are apart, normalized with the midpoint [10]. The value of span PVA/AC was calculated as 3.86.

3.4. Thermal studies

TGA, DTA, DTG and DSC are defined as Thermogravimetric analysis, Differential Thermal Analysis, Differential Thermogravimetry and Differential Scanning Calorimetry respectively. TGA, DTG, DTA and DSC curves of the composite were given in Fig. 3. Based on TGA analysis, Tonset (the initial degradation temperatures) of the PVA/AC composite was defined as 170 °C. The values of temperature of T_{20} (20%, weight losses) and T_{50} (50%, weight losses) were defined as 233 and 446 °C, respectively. Tmax was defined from the DTG curves as 194 and 433°C. The endothermic and exothermic peaks were not observed in DTA curve of the composite. The glass transition temperature (Tg) and the change in the specific heat (Δ_{Cp}) during the glass transition of the composite were computed from its DSC curve as 147 °C and 0.106 J/g °C.
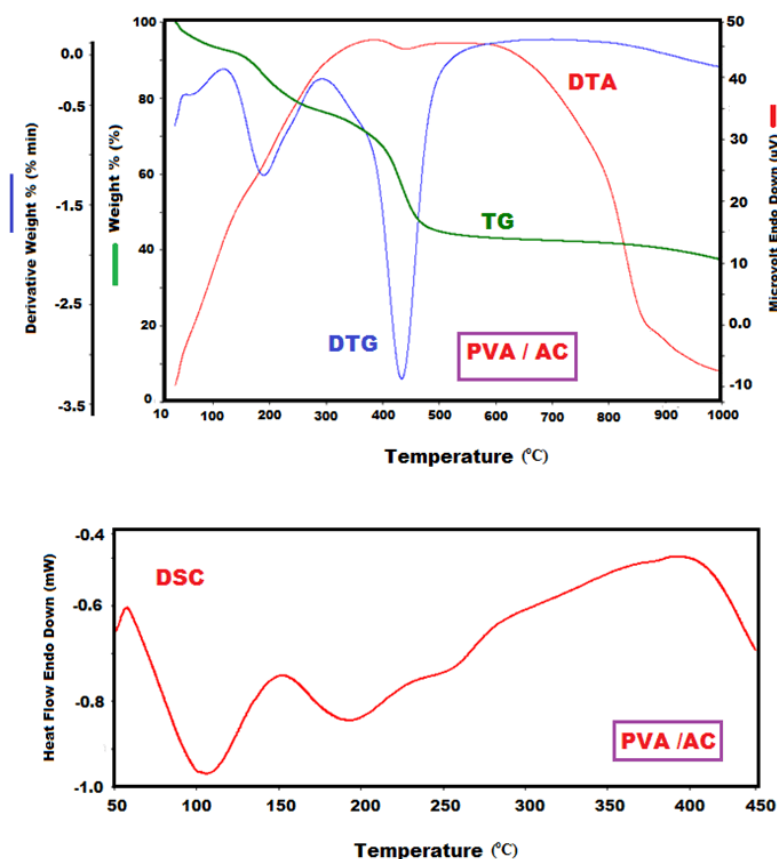
Figure 3: TGA and DSC analysis curves of the PVA/AC

3.5. Conductivity of the composite

The composite pellet was doped with iodine vapors at 25 ^{o}C in desiccators for 24 h. It was observed that the conductivity of the PVA/AC increased slightly but then tended to level-off. The conductivities of doped and undoped pressed PVA/AC pellets were determined as 2.44×10^{-5} S cm^{-1} and 2.09×10^{-4} S cm^{-1}, respectively.

3.6. Point of zero charge

The sorbent surface to charge positively or negatively depends on concentration of protons in the solution. The pHpzc results of the experiments were determined with the PVA/AC composite, where the pH ranged from 2 to 12. Fig. 4 shows that the pHpzc of the PVA/AC was approximately 3. In other words, at this pH, the PVA/AC surface has zero charge [9]. Therefore, when solution pH increases above pHpzc, the surface of PVA/AC is negatively charged, when it decreases below the pHpzc value the surface of PVA/AC is positively charged because of protonation [11, 12].

167

4-NP is a weak acid (pKa value of 7.15). If initial pH of the solution is in acidic range, particularly less than 3, the most of 4-NP molecules remain in molecular form and at the same time the PVA/AC surface possesses positive charge due to pHpzc (i.e. 3). If initial pH of the solution is in alkaline range, the dissociation of 4-NP into 4-NP anions takes place and at the same time the PVA/AC surface possesses negative charge (because pH > pHpzc). In this state electrostatic repulsion dominates between the adsorbate and adsorbent surface, resulting in a considerable decrease in percentage removal of 4-NP in alkaline range. At pH of 3.0 the net charge on the PVA/AC surface was zero, hence, there was no electrostatic repulsion and hence the removal of 4-NP is more than that in alkaline range [13]. Fig. 5 shows the zeta potential curves of PVA/AC in three replicates. Zeta potential value of PVA/AC was -17.8 mV. Therefore, the PVA/AC composite has a negative surface charge and may be moved towards a positively polarized electrode under an electric field [14]. Nanoparticles with zeta potential greater than +30mV or less than –30mV are considered strongly cationic and strongly anionic respectively [15]. Paralikar [16] reported that negative zeta potential value of the particles might be owing to adsorption of OH^- ions on adsorbent. OH^- ion helps in preventing the aggregation.
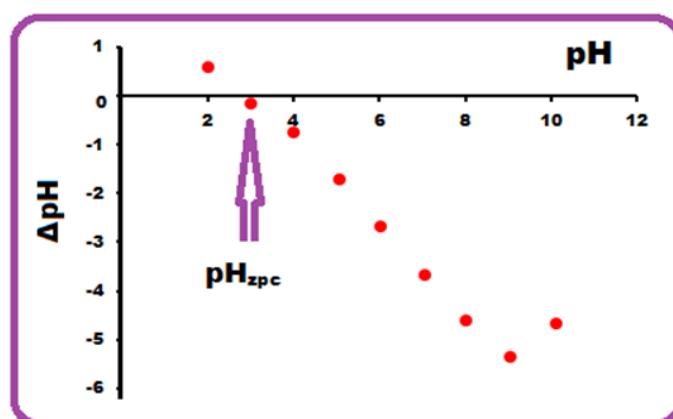
Figure 4: Zero point charge of PVA/AC at 298 K
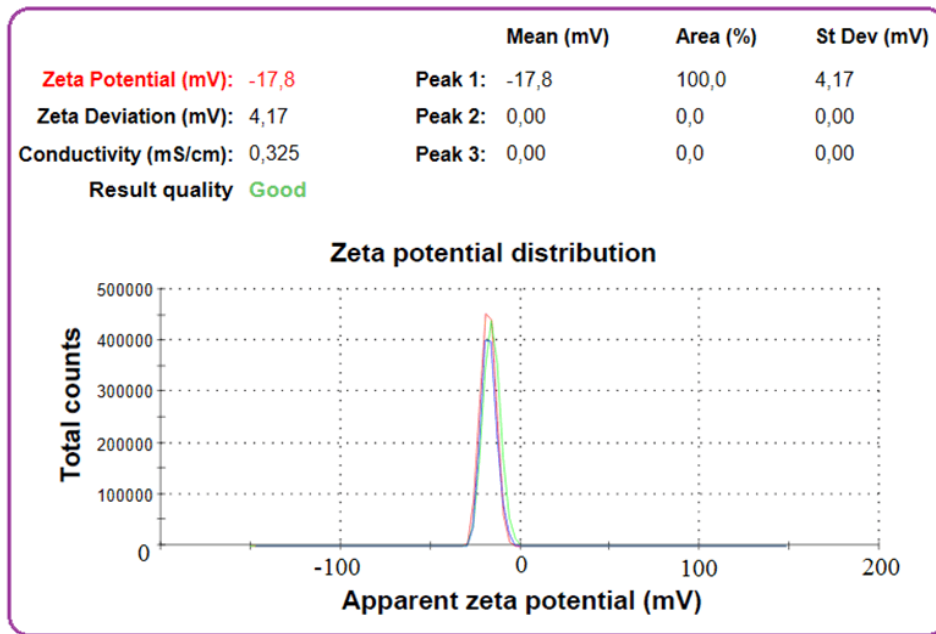
Figure 5: Zeta potential curves obtained for water suspensions of PVA/AC

3.7. Kinetic study

3.7.1. Effect of temperature

The effect of contact time on the sorption of 4-NP by the PVA/AC was researched for 200 min by using initial 4-NP concentration of 100 mg/L. Fig. 6 shows the quantity of adsorbed 4-NP (qe, mg g^{-1}) at 298, 313 and 328 K. The values of qe (mg g^{-1}) increased from 298 to 313 K, indicating that the adsorption of 4-NP on the PVA/AC composite is endothermic. Three different kinetic models (Lagergren(PFO), Ho-Mckay(PSO) and Weber-Morris) were used to understand the adsorption process:

Pseudo-first order (PFO)

$$\log (q_e - q_t) = \log q_e - k_1 \, t \, / \, 2.303 \tag{2}$$

Pseudo-second order (PSO)

$$t \, / \, q_t = 1 \, / \, k_2 \, q_e^2 + t \, / \, q_e \tag{3}$$

Intra particle diffusion(Weber-Morris)

$$q_t = k_{id} \, t^{1/2} + C \tag{4}$$

169
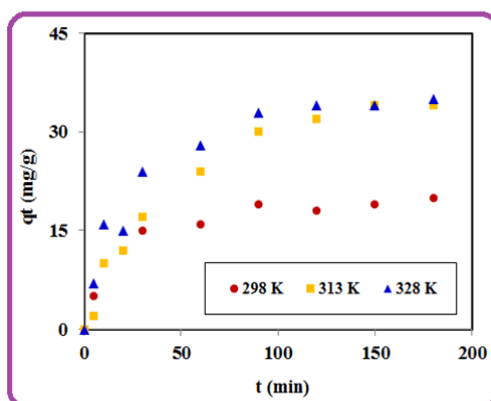
Figure 6: Adsorption kinetic of 4-NP on the composite at 298, 313, 328 K

qe (mg g^{-1}) and qt (mg g^{-1}) are the quantity of adsorbed at equilibrium and at any contact time of adsorption t (min), respectively; PFO, PSO and intraparticle diffusion rate constants were defined as k_1 (min^{-1}), k_2 (g mg^{-1} min^{-1}), and k_{id} (mg g^{-1} min$^{-1/2}$) respectively. Based on Eqn.(2), the plot of log (qe–qt) versus t, and based on Eqn.(3) the plot of t/qt versus t and based on Eqn. (4) the plot of qt versus t^{½} should each give a straight line for the respective model to be applicable [17]. The rate constants, qe and correlation coefficient values (R^2) were shown in Table 1. Table 1 and Fig. 7 show the kinetic models of sorption for 4-NP. Based on the results (Table 1), PFO model has higher values of correlation coefficients (R^2) compared to PSO model. Moreover, the computed qe values agreed with the experimental qe data in the case of the PFO model [18]. Feyzi et al. used raw and modified activated carbon from walnut and pistachio shell in order to remove Dimethyl sulfide from model fuel. Results showed that adsorption kinetic could be determined by pseudo-first order kinetic model [19]. Nam et al. synthesized active carbon from peanut shell with KOH activation for the adsorption of H$_2$S. According to their results, adsorption kinetic was determined as the pseudo-first order model owing to its higher R^2 and smaller difference between qe,exp and qe,calc as compared to the pseudo-second order model [20]. Moreover, the best-fitted model can be determined using the normalized standard deviation (Δq_e (%)) and average relative error (ARE) [21, 22]. The equations of the functions are given as follows:

$$\Delta q_e(\%) = 100 \times \sqrt{\frac{1}{n-1}\sum_{i=1}^{n}\left[\frac{q_{t,meas}-q_{t,cal}}{q_{t,meas}}\right]^2} \tag{5}$$

$$ARE = \frac{100}{n}\sum_{i=1}^{n}\left[\frac{q_{t,meas}-q_{t,cal}}{q_{t,meas}}\right] \tag{6}$$

q$_{t.meas}$(mg/g), q$_{t.cal}$(mg/g) and n are the experimental and calculated equilibrium adsorption capacity and value the number of data points respectively. The values of Δqe and ARE were

shown in Table 1. Low ARE and Δq_e (%) values indicate the accurate fitting of the model [21, 23]. According to our experimental results (Table 1), it may be seen that the pseudo-first order (PFO) model seems to be suitable for modelling the adsorption of 4-NP on PVA/AC.

Table 1: Kinetic data

	Pseudo First Order (PFO)						Pseudo Second Order (PSO)					Intra-Particle Diffusion Model	
T (K)	$q_{e,exp}$ (mg g⁻¹)	$q_{e,calc}$ (mg g⁻¹)	$k_1 \times 10^3$ (min⁻¹)	R^2	Δq_e (%)	ARE	$q_{e,calc}$ (mg g⁻¹)	$k_2 \times 10^3$ (g mg⁻¹ min⁻¹)	R^2	Δq_e (%)	ARE	k_{id} (mgg⁻¹ min⁻¹ᐟ²)	R^2
298	21	19.17	17.50	0.8647	3.1	0.97	20.58	4.36	0.9928	0.005	0.22	1.36	0.8639
313	35	34.40	23.26	0.9932	0.61	0.19	43.86	0.48	0.8680	9.0	2.81	2.94	0.8003
328	35	32.64	29.48	0.9857	2.4	0.75	38.02	1.57	0.9685	3.0	0.97	2.63	0.9131
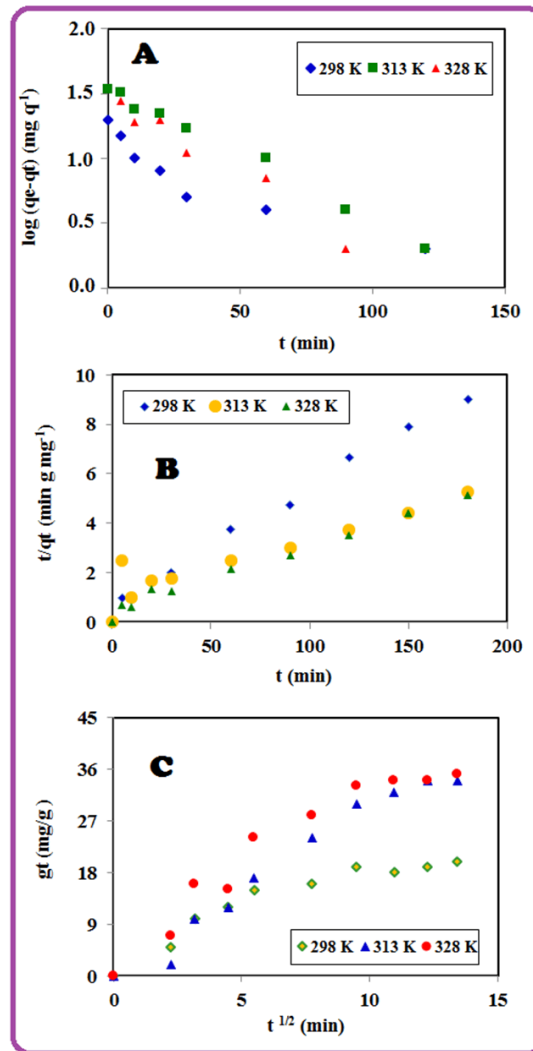
Figure 7: Fitting of Lagergren (PFO) (A), Ho-Mckay (PSO) (B) and intra-particle diffusion (Weber-Morris) (C) kinetic models

3.7.2. Activation parameters

The adsorption type was defined by using the PFO rate constants(k_1) at 298, 313, 328 K and the Arrhenius eqn. (7),

$$\log k_1 = \log A - E_a/2.303RT \tag{7}$$

where E_a, k_1, A, R and T are the activation energy (Jmol^{-1}), the PFO rate constant(min^{-1}), the Arrhenius factor (gmol^{-1}min^{-1}), the gas constant (8.314 J K^{-1} mol^{-1}) and the temperature (K) respectively.

The slope of the plot of ln k_1 versus 1/T was used to evaluate E_a (Figure not given). Physical adsorption has low activation energies (between 5–40 kJ mol^{-1}), while chemical chemisorption has higher ones (40–800 kJ mol^{-1}) [24, 25]. Based on the results, the adsorption of 4-NP on the composite is physisorption because of E_a=14.13 kJmol^{-1}.

3.8. Adsorption isotherm parameters

The adsorption isotherms studies for evaluating adsorption process are essential to attain some information about the nature of interaction of 4-NP with adsorbent and to evaluate the applicability and efficiency of any adsorbent [26]. Fig. 8 shows adsorption isotherms at different temperature. The surface property can be determined as a multilayer or monolayer by using of adsorption isotherms. The Langmuir (8) and Freundlich (9) isotherm models are usually used to detect the adsorption isotherm.

$$C_e/q_e = 1/b Q_{max} + C_e/Q_{max} \tag{8}$$

q_e (mgg^{-1}), C_e (mgL^{-1}), Q_{max} (mgg^{-1}) and b (Lmg^{-1}) are the quantity of phenol adsorbed at equilibrium, the remaining concentration of phenol in solution at equilibrium, maximum adsorption capacity and Langmuir constant respectively which are relative to adsorption energy [27, 28]. The Langmuir model is monolayer adsorption isotherm. According to Langmuir isotherm, surface of adsorbent is homogeneous, energetically uniform [28]. Linear representation of Langmuir isotherm may be described by Eqn. (8). The $Q_{max}$and b values were computed from the slopes and intercept of the linear plot of C_e/q_e versus C_e in Fig. 9 (A).

$$\log q_e = \log k + (1/n) \log C_e \tag{9}$$

k(mg/g) and n are the adsorbent capacity, the heterogeneous factor respectively and connected to intensity of Freundlich isotherm. According to Freundlich isotherm, adsorbent surface is heterogenous [29] and adsorption capacity is relative to the concentration of adsorbed

phenol at equilibrium. Freundlich isotherm is convenient adsorption at high concentrations and not convenient for low concentration range [30]. The values of k and n may be acquired from the slope and intercept of linear plot of log qe versus log Ce [31]. In Fig. 9 (B) for based on Eqn. (9). The adsorption isotherm parameters, correlation coefficients (R^2) and values error RMSE (root mean squared error) were given in Table 2. The values of RMSE (Eqn.10) can be calculated by the following equations [21]:

$$RMSE = \sqrt{\frac{1}{n-1}\sum_{n=1}^{n}(q_{e,meas} - q_{e,cal})^2} \tag{10}$$

qe.meas (mg g^{-1}), qe.cal (mg g^{-1}) and n are the experimental, calculated equilibrium adsorption capacity and the value the number of data points respectively. According to Table 2, the Freundlich model provided a higher correlation coefficient (R^2 = 0.7973, 0.8883 and 0.8513) as compared to Langmuir isotherm model (R^2 = 0.3780, 0.5450 and 0.7290). It can be seen that the values of RMSE obtained from Freundlich were lower than those from the Langmuir. Low RMSE values indicate the accurate fitting of the model [21, 23]. According to the Freundlich isotherm, the significance of n value is as follows: adsorption process is chemical (n < 1), linear (n = 1), or physical (n > 1) [18]. From Table 2, the values of n are 1.2, 1.47 and 1.58 at 298, 313 and 328 K respectively. So, the adsorption of 4-NP on PVA/AC was a physical process due to n > 1.

Based on these results, the Freundlich isotherm model was the best-fitted adsorption isotherm model for the adsorption of 4-NP on PVA/AC. So, the adsorption of 4-NP on the PVA/AC occurred on nonhomogeneous adsorptive sites [31].

Table 2: Equilibrium parameters

T (K)	Langmuir isotherm				Freundlich isotherm			
	Q_{max} (mg g^{-1})	b (L mg^{-1})	R^2	RMSE	k (mg g^{-1})	n	R^2	RMSE
298	217.39	0.00214	0.3780	22	1.25	1.20	0.7973	18
313	238.10	0.00297	0.5450	16	2.32	1.47	0.8883	14
328	138.89	0.00536	0.7290	17	2.45	1.58	0.8513	13
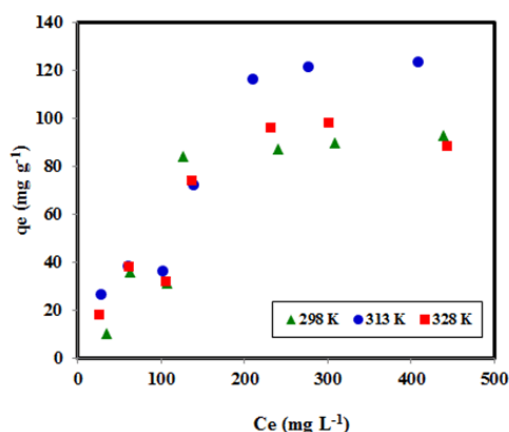
Figure 8: Adsorption isotherm of 4-NP on PVA/AC at different temperature
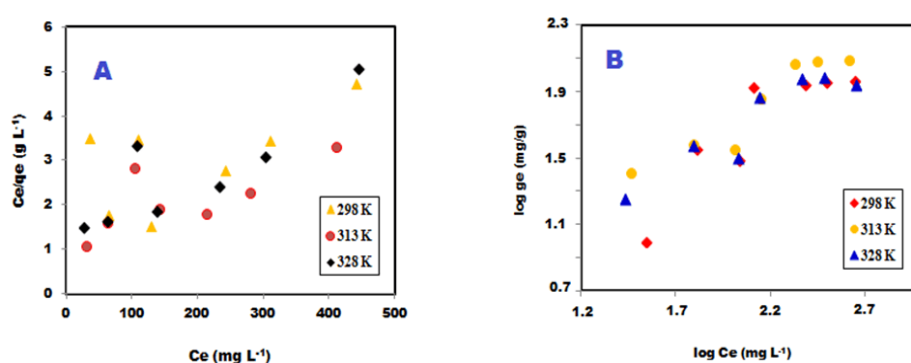
Figure 9: Langmuir (A) and Freundlich isotherm (B) plots for 4-NP removal by PVA/AC

3.9. Adsorption thermodynamics

The standard Gibbs energy change (ΔG^o), standard enthalpy change (ΔH^o) and standard entropy change (ΔS^o) which are thermodynamic parameters. They are essential to predict the feasibility and mechanism of adsorption process. ΔG^o was computed by using Eqn. (11). Kc (L/g) was calculated by using the Langmuir constants Q_{max} and b (Kc =Q_{max}x b) (Fig. 10) and known as equilibrium constant [26]. R and T had been explained before.

$$Kc = Q_{max} \text{ x } b \tag{11}$$

The thermodynamic parameters ΔH^o and ΔS^o were computed by using the slope and intercept of the plot of ln Kc versus 1/T, Fig. 10. The ΔG^0 was computed as 1.91, 0.91 and 0.82 kJ mol^{-1} at 298, 313 and 328 K respectively. Physical adsorption was reconfirmed because of ΔG^o being >-20 kJ mol^{-1} regardless of the temperature, because these ΔG^o values are positive. Therefore, this reaction is nonspontaneous. As the adsorption temperatures increased, accordingly the absolute values increased, which means the process becomes more non spontaneous at higher

temperatures [32]. According to Fig. 10, ΔS^0 and ΔH^o were calculated as 37.32 J mol^{-1} K^{-1} and 12.88 kJ mol^{-1} respectively. Owing to the positive ΔH^o values, adsorption process is endothermic for 4-NP. Consequently, increasing the temperature from 298 to 328 K causes an increase in phenol adsorption on the PVA/AC. In addition, if the magnitude of ΔH if lies between 80–200 kJ/mol process of the adsorption may be considered as chemical whereas physical adsorption usually is seen in a range of 2.1–20.9 kJ/mol or $\leq$40 kJ/mol [33]. In this way, adsorption of 4-NP on PVA/AC composite is physical in the nature (ΔH^o were calculated as 12.88 kJ mol^{-1}). Positive ΔS^o values show the increasing randomness in phenol solution-sorbent interface during the sorption process [27].
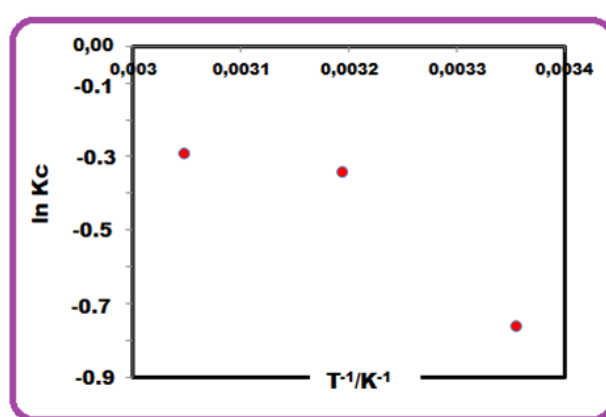
Figure 10: Van't Hoff plot of ln Kc versus 1/T

4. Conclusion

In this study, PVA/AC composite was synthesized and characterized. The adsorption of 4-NP from aqueous solution was investigated by utilizing as an adsorbent PVA/AC. This adsorbent can be used for the elimination of 4-NP from aqueous solution. There were two kinds of the adsorption process parameters. They were kinetics and thermodynamic parameters and both of them were calculated. According to results, adsorption process was determined as endothermic. The adsorption isotherms were determined by Langmuir and Freundlich models. The adsorption data was better fitted by the Freundlich isotherm model due to RMSE and R^2 values. Adsorption kinetic model was determined as a pseudo-first-order kinetic model. All the results on the sorption of 4-NP on PVA/AC indicate the applicability of the adsorption study.

Acknowledgement

References

[1] Aljeboree, A., Alshirifi, A., Alkaim, A., *Kinetics and equilibrium study for the adsorption of textile dyes on coconut shell activated carbon*, Arabian Journal of Chemistry, 10, 3381-3393, 2017.

[2] Wang, H., *Preparation and properties of porous poly (vinyl alcohol)/powdered activated carbon composite*, Material Science and Advanced Technologies in Manufacturing, 852, 117-120, 2014.

[3] Jia, Z., Li, Z., Li, S., Li, Y., Zhu, R., *Adsorption performance and mechanism of methylene blue on chemically activated carbon spheres derived from hydrothermally-prepared poly (vinyl alcohol) microspheres*, Journal of Molecular Liquids, 220, 56–62, 2016.

[4] Kaur, T., Thirugnanam, A., *Effect of Porous Activated Charcoal Reinforcement on Mechanical and In-Vitro Biological Properties of Polyvinyl Alcohol Composite Scaffolds*, Journal of Materials Science & Technology, 33(7), 734–743, 2017.

[5] Kumar, A., Kumar, S., Kumar, S.,Gupta, D., *Adsorption of phenol and 4-nitrophenol on granular activated carbon in basal salt medium: equilibrium and kinetics,* J. Hazard. Mater., 147, 155–166, 2007.

[6] Liu, S., Wang, J., Huang, W., Tan, X., Dong, H., Goodman, B., Du, H., Lei, F., Diao, K., *Adsorption of phenolic compounds from water by a novel ethylenediamine rosin-based resin: Interaction models and adsorption mechanisms*, Chemosphere, 214, 821-829, 2019.

[7] Ivanov, A., Kozynchenko, O., Mikhalovska, L., Tennison, S., Jungvid, H., Gunko, V., Mikhalovsky, S., *Activated carbons and carbon-containing poly(vinyl alcohol) cryogels: characterization, protein adsorption and possibility of myoglobin clearance*, Phys. Chem. Chem. Phys., 14, 16267–16278, 2012.

[8] Swamy, M., Nagabhushana, B., Krishna, R., Kottam, N., Raveendra, R., Prashanth, P., *Fast adsorptive removal of methylene blue dye from aqueous solution onto a wild carrot flower activated carbon: isotherms and kinetics studies*, Desalination and Water Treatment, 71, 399–405, 2017.

[9] Silva, M., Santos, M., Júnior, M., Fonseca, M., Filho, E., *Natural Palygorskite as an Industrial Dye Remover in Single and Binary Systems*, Materials Research,19, 1232-1240, 2016.

[10] Trivedi, M., Sethi, K., Panda, P., and Jana, S., *A comprehensive physicochemical, thermal, and spectroscopic characterization of zinc (II) chloride using X-ray diffraction, particle size distribution, differential scanning calorimetry, thermogravimetric analysis/differential thermogravimetric analysis, ultraviolet-visible, and Fourier transform-infrared spectroscopy*, International Journal of Pharmaceutical Investigation, 7, 33-40, 2017.

[11] Cuevas, L., Villacura, E., Toloza, C., *Magellan Peat (Sphagnum Magallanicum) As Natural Adsorbent OfRecalcitran Synthetic Dyes*, J. Soil Sc. Plant Nutr., 8,31-43, 2008.

[12] Haddad, M., Mamouni, R., Saffaj, N., Lazar, S., *Removal of a cationic dye – Basic Red 12– from aqueous solution by adsorption onto animal bone meal*, Journal of the Association of Arab Universities for Basic and Applied Sciences, 12, 48–54, 2012.

[13] Dhorabe, P., Lataye, D., Ingole, R., *Removal of 4-nitrophenol from aqueous solution by adsorption onto activated carbon prepared from Acacia glauca sawdust*, Water Science & Technology, 73, 2016, doi: 10.2166/wst.2015.575.

[14] Chartarrayawadee, W., Moulton, S., Too, C., Wallace, G., *Fabrication of Graphene Electrodes by Electrophoretic Deposition and Their Synergistic Effects with PEDOT and Platinum*, Chiang Mai J. Sci., 40, 750-762, 2013.

[15] El-Naggar, N., Hussein, M., El-Sawah, A., *Phycobiliprotein-mediated synthesis of biogenic silver nanoparticles, characterization, in vitro and in vivo assessment of anticancer activities*, Scientific Reports, 8, 2018, doi:10.1038/s41598-018-27276-61.

[16] Paralikar, P., *Biogenic Synthesis of Silver Nanoparticles Using Leaves Extract of EpiphyllumOxypetalum and its Antibacterial Activity*, Austin Journal of Biotechnology & Bioengineering, 1, 2014.

[17] Bulut, Y., Karaer, H., *Adsorption of Methylene Blue from Aqueous Solution by Crosslinked Chitosan/Bentonite Composite*, Journal of Dispersion Science and Technology, 36,61-67, 2015.

[18] Salehi, E., Farahani, A., *Macroporous chitosan/polyvinyl alcohol composite adsorbents based on activated carbon substrate*, J Porous Mater., 24,1197–1207, 2017.

[19] Feyzi, F., Jalilvand, H., Dehghani, M., *Adsorption of dimethyl sulfide from model fuel on raw and modified activated carbon from walnut and pistachio shell origins:kinetic and thermodynamic study*, doi.org/10.1016/j.colsurfa.2020.124620.

[20] Nam, H., Nam, H., Wang, S., *Preparation of activated carbon from peanut shell with KOH activation and its application for H_2S adsorption in confined space*, Journal of Environmental Chemical Engineering, 8, 103683, 2020.

[21] Fajri, L., Nawi, M., Sabar, S., Nawawi, N., *Preparation of immobilized activated carbon-polyvinyl alcohol composite for the adsorptive removal of 2,4-dichlorophenoxyacetic acid*, Journal of Water Process Engineering, 25, 269–277, 2018.

[22] Almeida, V., Vargas, A., Nogami, E., *NaOH-activated carbon of high surface area produced from coconut shell: Kinetics and equilibrium studies from the methylene blue adsorption*, Chemical Engineering Journal 174, 117– 125, 2011.

[23] Tseng, T., Wu, F., Juang, R., *Characteristics and applications of the Lagergren's first-order equation for adsorption kinetics*, Journal of the Taiwan Institute of Chemical Engineers 41, 661–669, 2010.

[24] Wang, L., Zhang, J., Wang, A., *Fast removal of methylene blue from aqueous solution by adsorption onto chitosan-g-poly(acrylic acid)=attapulgite composite*. Desalination, 266: 33–39, 2011.

[25] Gürses, A., Hassani, A., Kırans, M., Açıslı, O., Karaca, S., *Removal of methylene blue from aqueous solution using by untreated lignite as potential low-cost adsorbent: kinetic, thermodynamic and equilibrium approach*, J. Water Process Eng., 2,10-21, 2014.

[26] Daga, K., Gehlot, P., *Use of Polyvınylalcohol Coated Carbon Black for Removal of Lınear AlkylbenzeneSulphonate (Las) From Wastewater*, Nature Environment and Pollution Technology © Technoscience Publications, 6,725-730, 2007.

[27] Karaer, H., Kaya, I., *Synthesis, characterization of magnetic chitosan/active charcoal composite and using at the adsorption of methylene blue and reactive blue4*, Microporous and Mesoporous Materials, 232,26-38, 2016.

[28] Iqbal, M., Ashiq, M., *Adsorption of dyes from aqueous solutions on activated charcoa*, Journal of Hazardous Materials B, 139,57–66, 2007.

[29] Karaer, H., Uzun, İ., *Adsorption of basic dyestuffs from aqueous solution by modified chitosan*, Desalination and Water Treatment, 51, 2294-2305, 2013.

[30] Negma, N., AbdElWahed, M., Hassan, A., Kana, M., *Feasibility of metal adsorption using brown algae and fungi: Effect of biosorbents structure on adsorption isotherm and kinetics*, Journal of Molecular Liquids, 264, 292–305, 2018.

[31] Kyzas, G., Deliyanni, E., Lazaridis, N., *Magnetic modification of microporous carbon for dye adsorption,* Journal of Colloid and Interface Science, 430,166–173, 2014.

[32] Kim, Y., Kim, J., *Isotherm, kinetic and thermodynamic studies on the adsorption of paclitaxel onto Sylopute*, J. Chem. Thermodynamics, 130,104–113, 2019.

[33] Mahida, V., Patel, M., *Removal of some most hazardous cationic dyes using novel poly(NIPAAm/AA/N-allylisatin) nanohydrogel*, Arabian J. Chem., 9, 430-442, 2016.

Preparation and Characterization of Some Schiff Base Compounds

Nurcan BERBER[1,*], Mustafa ARSLAN[2]

[1]*Çanakkale University, Ezine Vocational High School, Çanakkale, Turkey*
nberber@comu.edu.tr, ORCID: 0000-0002-1595-585X
[2]*Sakarya University, Department of Chemistry, Faculty of Art and Sciences, Sakarya, Turkey*
marslan@sakarya.edu.tr, ORCID: 0000-0003-0796-4374

Abstract

Schiff bases (imines) have been frequently used in various fields such as medicine, pharmaceutical purposes due to their various biological properties. In this study, nine new imine compounds (3a-h) were synthesized from 1-naphthyl amine with aromatic aldehydes in MeOH and their chemical structures were defined by 1H/13C NMR, IR and elemental analysis studies. We observed a singlet one hydrogen of the imines (–CH=N–) at 8.56–8.86 ppm in the 1H NMR spectra and also carbon of the Schiff bases (–CH=N–) at 158.2-163.4 ppm in the 13C NMR spectra. Also the IR spectra displayed the (–C=N–) characteristic absorption band at around 1600 cm $^{-1}$. The obtained characteristic peaks at the expected locations proved the structural accuracy of the synthesized new derivative Schiff bases.

Keywords: Schiff bases; Imines; 2-naphthylamine; Aromatic Aldehyde.

Bazı Schiff Baz Bileşiklerinin Hazırlanması ve Karakterizasyonu

Öz

Schiff bazları (iminler), çeşitli biyolojik özellikleri nedeniyle tıp, farmasötik amaçlar gibi çeşitli alanlarda sıkça kullanılmaktadır. Bu çalışmada, 1-naftil aminden MeOH içerisinde aromatik aldehitler ile dokuz yeni imin bileşiğinin (3a-h) sentezi yapılarak ve kimyasal yapıları;

1H/13C NMR, IR ve elemantel analiz yöntemleri aydınlatılmıştır. 1H/13C NMR analiz sonuçları incelendiğinde iminlerin (–CH=N–) protonu 8.56-8.86 ppm ve karbonunun ise 158.2-163.4 ppm de geldiği gözlemlenmiştir. Ayrıca IR spektrumundada (–C=N–) piki 1600 cm $^{-1}$ civarında görülmüştür. Elde edilen bu karakteristik piklerin beklenen yerlerde gelmesi sentezlenen yeni türev Shifft bazların yapısal doğruluğunu kanıtlamıştır.

Anahtar Kelimeler: Schiff bazları; İminler; 2-naftilamin; Aromatik aldehit.

1. Introduction

Generally, Schiff bases (imines) occur from primary amines and carbonyl compounds (aldehydes or ketones, in Scheme 1) and were first synthesized in 1869 by the German chemist Hugo Schiff [1, 2]. The bond formed by reaction with aldehyde is called azomethine or aldimine, while the bond formed by reaction with ketone is called imine or ketimine.
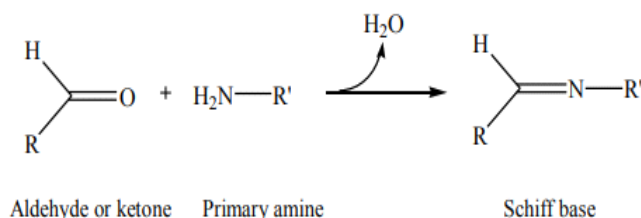
Scheme 1: General route for synthesis of a imines

Imines can also be represented by the general formula $RCH = NR'$, wherein R and R' are alkyl or alkyl substituents [3-5]. Many imines have been worked due to their very varying structural properties and used as chelating ligands in coordination Chemistry [6-12]. This interest in Schiff bases can be explained due to their availability in many areas, such as biological systems, medicine, and also in new technologies [9, 13-15]. In addition these, imines are important intermediates and multipurpose starting materials for the synthesis of many reaction such as Mannich bases [16, 17], indoles [18, 19], betalactam [20, 21], pyrimidine derivatives [22]. Compounds obtained from these reactions accompanied by Schiff bases have been used in the treatment of various diseases due to their biological activity [23]. Many reagents have been used for the synthesis of imines such as Lewis acids [24-27], metal complex [28, 29], metal-free conditions [30, 31], promoted by microwave irradiation [32] and ultrasound radiation [33].

In this study, nine new imine compounds (3a-h) were synthesized from 1- naphthyl amine with aromatic aldehydes in MeOH and their chemical structures were defined by 1H/13C NMR, IR, and elemental analysis studies. The evaluation of the analysis results had proved the accuracy of the synthesized structures.

2. Materials and Methods

All starting materials and reagents were commercially available and used without further purification except where indicated. Analytical thin-layer chromatography (TLC) was carried out on precoated plates (silica gel 60 F254), and spots were visualised with ultraviolet (UV) light. Melting points were determined on a Yanagimoto micro-melting point apparatus and were uncorrected. IR spectra were measured on a SHIMADZU Prestige-21 (200 VCE) spectrometer. 1H/13C NMR spectra were measured on spectrometer at VARIAN Infinity Plus 300 and at 75 MHz, respectively. 1H/13C chemical shifts are referenced to the internal deuterated solvent. Chemical shift values (δ) are given in ppm. The elemental analysis was carried out with a Leco CHNS-932 (St. Joseph, Michigan) instrument. All chemicals were purchased from Merck (Darmstadt, Germany), Alfa Aesar (Ward Hill, MA), and Sigma-Aldrich (Taufkirchen, Germany).

2.1. General procedure for synthesis of compounds

R:4-H-, 4-CH$_3$-, 4-NO$_2$-, 4-Cl-, 4-OCH$_3$-,
2,3-OCH$_3$-, 4-OH-, 3,4-OH-
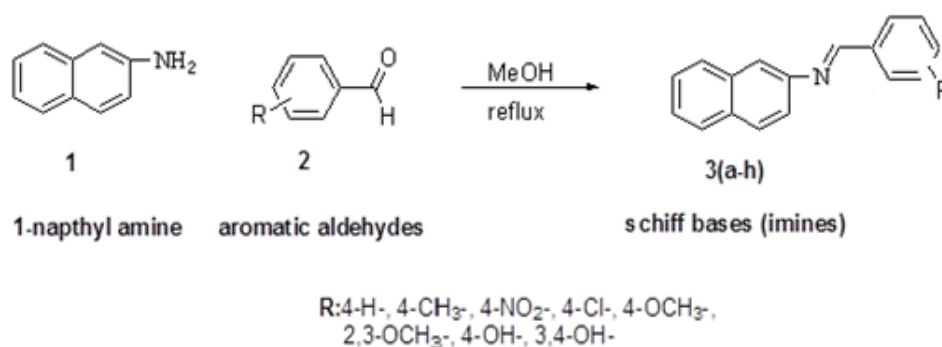
Scheme 2: Synthesis of new schiff base compounds (3a-h)

2.1.1. General procedure for the synthesis of substituted benzylidenyl amino naphthalenes(3a-h):

Mixture of 1-naphthylamine (1) (1.0 mmol) and aromatic aldehydes derivatives (2) (1.0 mmol) were stirred and refluxed for 3 hours in MeOH (15 ml). After completion of the reaction, the mixture was left cooling to room temperature and poured on cold water (50 ml). The product (3) was filtered and dried (in Scheme 2).

N-(benzylidene)napthy-amine(3a); yellow solid; m.p. 121-123 ºC; (91%) yield. IR (KBr,cm^{-1}): 3018 (aromatic C-H), 2926 (azomethine C-H), 1600 (Ar-CH=N-Ar), 1560 (-C=C-). 1H NMR (300 MHz, DMSO, δ, ppm): 7.26-8.27 (12H, m, Ar-H), 8.80 (1H,s,Ar-CH=N-). 13C NMR (75 MHz, DMSO, δ, ppm): 158.2 (Ar-CH=N-Ar), 142.3 (-Ar-N=), 133.5 (-Ar-H), 130.1-

119.3 (other aromatic karbon). Anal. Calcd. for $C_{17}H_{13}N$ %: C 88.28, H 5.66, N 6.06; found: C 88.30, H 5.20, N 6.09.

N-(4-methylbenzylidene)napthy-amine(3b); light yellow solid; m.p. 69-71 °C; (89%) yield. IR(KBr,cm^{-1}): 3023 (aromatic C-H), 2935 (azomethine C-H), 1605 (Ar-CH=N-Ar), 1562 (-C=C-), 1354 (-CH$_3$). 1H NMR (300 MHz, DMSO, δ, ppm): 2.35 (s,3H,-CH$_3$), 7.24-8.20 (11H,m,Ar-H), 8.78 (1H,s,Ar-CH=N-Ar). 13C NMR (75 MHz, DMSO, δ, ppm): 158.2 (Ar-CH=N-Ar), 142.3 (-Ar-N=), 140.5 (-Ar-CH$_3$), 130.1-119.3 (other aromatic karbon). Anal. Calcd. for $C_{18}H_{15}N$ %: C 88.13, H 6.16, N 5.71; found: C 88.20, H 6.20, N 5.80.

N-(4-Nitrobenzylidene)naphthalene-1-amine (3c); dark yellow solid; m.p. 160-162 °C; (85%) yield. IR(KBr, cm^{-1}): 3018 (aromatic C-H), 2955 (azomethine C-H), 1603 (Ar-CH=N-Ar), 1568 (-C=C-), 1332 (-N=O). 1H NMR (300 MHz, DMSO, δ, ppm): 7.36-8.57 (11H, m, Ar-H), 8.86 (1H,s,-Ar-CH=N-Ar). 13C NMR (75 MHz, DMSO, δ, ppm): 158.2 (-CH=N-), 142.3 (-Ar-N=), 143.5 (-Ar-NO$_2$), 130.1-119.3 (other aromatic karbon). Anal. Calcd. for $C_{17}H_{12}N_2O_2$ %: C 73.90, H 4.38, N 10.14, O 11.58 ; found: C 73.92, H 4.25, N 10.07, O 11.50.

N-(4-Chlorobenzylidene)naphthalene-1-amine (3d); yellow solid; m.p. 103-105 °C; (78%) yield. IR (KBr, cm^{-1}): 3020 (aromatic C-H), 2947 (azomethine C-H), 1620 (Ar-CH=N-Ar), 1558 (-C=C-), 1108-1035 (-C-Cl). 1H NMR (300 MHz, DMSO, δ, ppm): 7.23-8.21 (11H,m,Ar-H), 8.64 (1H,s,Ar-CH=N-Ar). 13C NMR (75 MHz, DMSO, δ, ppm): 158.2 (-C=N-), 142.3 (-Ar-N=), 135.3 (-Ar-Cl), 130.1-119.3 (other aromatic karbon). Anal. Calcd. for $C_{17}H_{12}NCl$ %: C 77.84, H 4.55, Cl 13.34, N 5.30; found: C 76.99, H 4.49, Cl 13.30, N 5.26.

N-(4-methoxybenzylidene)napthy-amine(3e); yellow solid; m.p. 75-77 °C; (79%) yield. IR (KBr, cm^{-1}): 3024 (aromatic C-H), 2943 (azomethine C-H), 1654 (Ar-CH=N-Ar), 1547 (-C=C-), 1128 (CH$_3$-O-). 1H NMR (300 MHz, DMSO, δ, ppm): 3.68 (s,3H,–OCH$_3$), 7.12-7.90 (11H,m,Ar-H), 8.60 (1H,s,Ar-CH=N-Ar). 13C NMR (75 MHz, DMSO, δ, ppm): 162.4 (4-OMe-Ar-), 160.0 (-CH=N-), 142.3 (-Ar-N=), 130.1-119.3 (other aromatic karbon), 56.7 (-O-CH$_3$). Anal. Calcd. for $C_{18}H_{15}NO$ %: C 82.73, H 5.50, N 5.36, O 6.12; found: C 82.80, H 5.49, N 5.20, O 6.09.

N-(2,3-dimethoxybenzylidene)napthy-amine(3f); yellow solid; m.p. 85-87 °C; (74%) yield. IR (KBr, cm^{-1}): 3018 (aromatic C-H), 2945 (azomethine C-H), 1660 (Ar-CH=N-Ar), 1547 (-C=C-), 1137 (CH$_3$-O-). 1H NMR (300 MHz, DMSO, δ, ppm): 3.63 (s,6H,–OCH$_3$), 7.12-7.90 (10H,m,Ar-H), 8.58 (1H,s,Ar-CH=N-Ar). 13C NMR (75 MHz, DMSO, δ, ppm): 160.2 (-CH=N-), 142.3 (-Ar-N=), 141.3 (2-CH$_3$O-Ar-), 139.3 (3-CH$_3$O-Ar-), 130.1-119.3 (other aromatic

karbon), 58.2 (-O-CH$_3$). Anal. Calcd. for C$_{19}$H$_{17}$NO$_2$ %: C 78.73, H 5.80, N 4.81, O 10.98; found: C 78.80, H 5.79, N 4.80, O 10.95.

N-(4-hydroxybenzylidene)napthy-amine(3g); yellow solid; m.p. 91-93 °C; (85%) yield. IR (KBr, cm^{-1}): 3320 (O-H), 3024 (aromatic C-H), 2958 (azomethine C-H), 1615 (Ar-CH=N-Ar), 1558 (-C=C-). 1H NMR (300 MHz, DMSO, δ, ppm): 4.68 (s,1H,–OH), 6.90-7.80 (11H,m,Ar-H), 8.56 (1H,s,Ar-CH=N-Ar). 13C NMR (75 MHz, DMSO, δ, ppm): 161.3 (4-OH-Ar), 160.2 (-CH=N-), 142.3 (-Ar-N=), 130.1-119.3 (other aromatic karbon), 58.2 (-O-CH$_3$). Anal. Calcd. for C$_{17}$H$_{13}$NO %: C 82.73, H 5.50, N 5.36, O 6.12; found: C 82.80, H 5.49, N 5.20, O 6.09.

N-(3,4-dihydroxybenzylidene)napthy-amine(3h); yellow solid; m.p. 98-100 °C; (78%) yield. IR (KBr, cm^{-1}): 3400-3320 (-O-H), 3028 (aromatic C-H), 2960 (azomethine C-H), 1610 (Ar-CH=N-Ar), 1560 (-C=C-). 1H NMR(300 MHz, DMSO, δ, ppm): 4.73 (s,2H,–OH), 6.90-7.80 (10H,m,Ar-H), 8.56 (1H,s,Ar-CH=N-Ar). 13C NMR (75 MHz, DMSO, δ, ppm): 160.2 (Ar-CH=N-Ar), 142.3 (-Ar-N=), 139.3 (4-OH-Ar-), 136.9 (3-OH-Ar-), 130.1-119.3 (other aromatic karbon). Anal. Calcd. for C$_{17}$H$_{13}$NO$_2$ %: C 77.55, H 4.98, N 5.32, O 12.15; found: C 77.63, H 5.00, N 5.20, O 12.09.

3. Results

In our research,the Schiff base benzylidene aminonaphthalenes (3a-h) were prepared by refluxing an appropriate amount of 1-naphthylamine with the different aromatic aldehydes in methanol under mildexperimental conditions. [34]. For purification, the products obtained were poured on cold water and filtered. The efficiency of the products obtained was between 74-91%conversion. In addition, the reaction mechanism of the Schiff bases obtained was considered to be as outlined in Scheme 3.
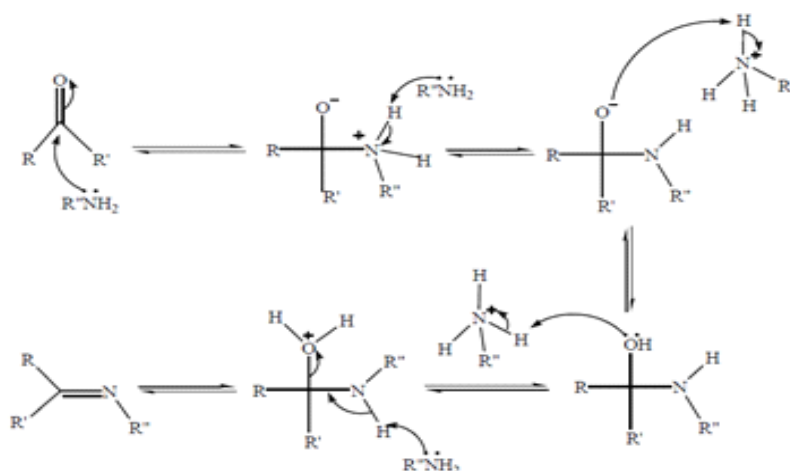
Scheme 3: Reaction mechanism of schiff base synthesis

The structures of the synthesized all compounds were characterized with the help of their 1H/^{13}C NMR, IR and Mass spectroscopic studies. The spectral data results showed that all the compounds (3a-h) were successfully synthesized. Some physical properties and analytical data of the imines compounds were summarized in Table 1.

Table 1: New Schiff base compounds (3a-h)

Compound	Product	Melting Point (°C)	Yield (%)
3a		121-123	91
3b		69-71	89
3c		160-162	85
3d		103-105	78
3e		75-77	79
3f		85-87	74
3g		91-93	85
3h		98-100	78
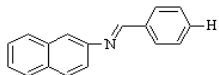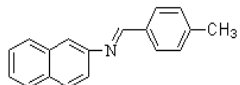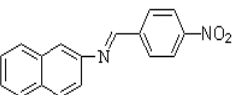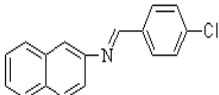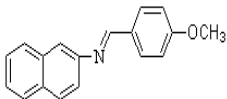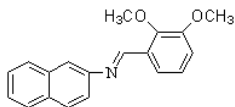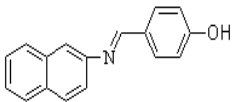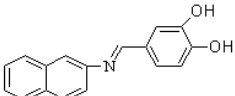
4. Discussion

According to the literature research, all spectral data of the synthesized Schiff Bases (3a-h) were found to be consistent with the expected results. In the IR spectra displayed characteristic absorption bands at around 3438, 3020, 2960, 1620, 1480, 1330 cm^{-1} regions, confirming the presence of (-O-H), aromatic (C-H), azomethine (C-H), (C=N), (C=C) respectively [35, 18]. A strong absorption band at 1558-1660 cm^{-1} was due to (C=N) vibration [36]. The absorption bands at 3012- 3139 cm^{-1} and 1568-1547 cm^{-1} belonged to the stretching frequency of the aromatic ring. The strong absorption band in the region 1137-1128 cm^{-1} arose from vibrations of the (CH$_3$O-)

group present in 3e, 3f. Compounds 3g and 3h gave rise to a strong band at 3400-3320 cm^{-1} due to stretching vibrations of the (-O–H) bond [31]. Also, compound 3d had strong (-C-Cl) peak nearly at 850 cm^{-1}. Compound 3c has (-NO$_2$)group. This stretching was observed at 1548 cm^{-1} as very strong peak. The infrared spectral data of the Schiff base matched the expected range and total IR results were given in Table 2.

Table 2: IR spectral data (cm^{-1})

Compound	Aromatic C-H	Azomethine C-H	C=N	Aromatic C=C
3a	3018	2926	1600	1560
3b	3023	2935	1605	1562
3c	3018	2955	1603	1568
3d	3020	2947	1620	1558
3e	3024	2943	1654	1547
3f	3018	2945	1660	1547
3g	3024	2958	1615	1558
3h	3028	2960	1610	1560

Further, we observed a singlet of integration intensity equivalent to one hydrogen at 8.56–8.86 ppm in the 1H NMR spectra of the Schiff bases, indicating the presence of the azomethine proton (–CH=N–) [37, 38]. The peaks of naphthalene aromatic and phenyl group protons appeared as multiple signal at 7.26-8.57 ppm. Also compounds 3e and 3f (–O-CH$_3$) protons were found 3.63 ppm as singlet signal. The peak at 2.35 ppm was due to three methyl protons (s,-CH$_3$) in 3b. Finally, signal of (-OH) groups protons in compounds 3g and 3h were observed nearly at 4.00 ppm. The 1H NMR spectroscopy provided an additional support for the formation of Schiff base derivatives and total 1H NMR results were given in Table 3.

Table 3: 1H NMR chemical shifts (ppm)

Compound	Aromatic C-H	Azomethine C-H
3a	8.80	7.26-8.27
3b	8.78	7.24-8.20
3c	8.86	7.36-8.57
3d	8.64	7.23-8.21
3e	8.60	7.12-7.90
3f	8.58	7.12-7.90
3g	8.56	6.90-7.80
3h	8.56	6.90-7.80

For compound 3(a-h), characteristic 13C-NMR signal of the azomethine group (-C=NH) was observed at 158.2-163.4 ppm. This characteristic peak has been found for the others at 162.4(4-OMe-Ar-), 143.5(-Ar-NO$_2$), 142.3(-Ar-N=), 135.3(-Ar-Cl), 139.3(4-OH-Ar), 136.9(3-OH-Ar), and 58.2(-O-CH$_3$), respectively. Furthermore, signal of aromatic carbons (compound 3) were observed at 130.1-119.3 ppm. The purity of all imine compounds was confirmed by mass analysis.

5. Conclusions

The structure of the newly synthesized compounds was elucidated on the basis of elemental analysis and spectral data. When all analysis results of the synthesized compounds were examined, the presence of characteristic peaks proving the formation of imine was observed and the synthesis of the compounds was successful. Also, this synthesis has quite environmentally friendly synthesis method because methanol was used as solvent and no need to any catalysts.

References

[1] Schiff, H., *Untersuchungen über salicinderivate*, Justus Liebigs Annalen der Chemie, 150 (2), 193-200, 1869.

[2] Patel, P.R., Thaker, B.T., Zele, S., *Preparation and characterisation of some lanthanide complexes involving a heterocyclic β–diketone*, NISCAIR-CSIR, India, 38A(6), 563-567, 1999.

[3] Berg, M.A., *The bromine addition products of the schiff bases*, Bulletin de la Societe Chimique de France, 37, 637-641, 1925.

[4] Hania, M.M., *Synthesis of some imines and investigation of their biological activity,* Journal of Chemistry, 6(3), 629-632, 2009.

[5] Cohen, A.B., *The interaction of α-1-antitrypsin with chymotrypsin, trypsin and elastase,* Biochimica et Biophysica Acta (BBA)-Enzymology, 391(1), 193-200, 1975.

[6] Badwaik, V.B., Deshmukh, R.D., Aswar A.S., *Transition metal complexes of a schiff base: synthesis, characterization, and antibacterial studies,* Journal of Coordination Chemistry, 62(12), 2037-2047, 2009.

[7] Hussain, Z., Yousif, E., Ahmed, A., Altaie, A., *Synthesis and characterization of schiff's bases of sulfamethoxazole*, Organic and Medicinal Chemistry Letters, 4(1), 1, 2014.

[8] Yamada, S., *Advancement in stereochemical aspects of schiff base metal complexes,* Coordination Chemistry Reviews, 190, 537-555, 1999.

[9] Sharaby, C.M., Amine, M.F., Hamed, A.A., *Synthesis, structure characterization and biological activity of selected metal complexes of sulfonamide schiff base as a primary ligand and some mixed ligand complexes with glycine as a secondary ligand*, Journal of Molecular Structure, 1134, 208-216, 2017.

[10] Abbaspour, A., Esmaeilbeig, A.R., Jarrahpour, A.A., Khajeh, B., Kia, R., *Aluminium (III)-selective electrode based on a newly synthesized tetradentate schiff base*, Talanta, 58(2), 397-403, 2002.

[11] Pfeiffer, P., Breith, E., Lubbe, E., Tsumaki, T., *Tricyclische orthokondenzierte nebenvolenzringe*, Annalen der Chemie, 503, 84-127, 1933.

[12] Redshaw, C., *Use of metal catalysts bearing schiff base macrocycles for the ring opening polymerization (ROP) of cyclic esters*, Catalysts, 7(5), 165-176, 2017.

[13] Tiwari, V., Meshram, J., Ali, P., *Microwave assisted synthesis of of quinolinyl thiazolidinones using zeolite as an efficient and recyclable activation surface: SAR and biological activity*, Der Pharma Chemica, 2(3), 187-195, 2010.

[14] Mistry, K.M., Desai, K.R., *Synthesis of novel heterocyclic 4-thiazolidinone derivatives and their antibacterial activity*, Journal of Chemistry, 1(4), 189-193, 2004.

[15] Hania, M.M., *Synthesis of some imines and investigation of their biological activity*, Journal of Chemistry, 6(3), 629-632, 2009.

[16] Movrin, M., Maysinger, D., *Biologically active n-mannich bases of isatin-3-(phenyl)-imines (author's transl),* Die Pharmazie, 34(9), 535-536, 1979.

[17] Abdulghani, J.A., Nada, M.A., *Synthesis characterization and biological activity study of new schiff and mannich bases and some metal complexes derived from isatin and dithiooxamide*, Bioinorganic Chemistry and Applications, 2011, 15, 2011.

[18] Ebrahimi, H., Hadi, J.S., Al-Ansari, H.S., *A new series of schiff bases derived from sulfa drugs and indole-3-carboxaldehyde: synthesis, characterization, spectral and DFT computational studies*, Journal of Molecular Structure, 1039, 37-45, 2013.

[19] Nafia, R.A., Fadhil, L.F., *Synthesis and characterization of new indole schiff bases and study effect of the compounds on lymphatic cell in metaphase in human blood*, Journal of Pharmaceutical Sciences and Research, 11(4), 1319-1326, 2019.

[20] Berber, N., Arslan, M., Bilen, Ç, Sackes, Z., Gençer, N., Arslan, O., *Synthesis and evaluation of new phthalazine substituted β-lactam derivatives as carbonic anhydrase inhibitor*s, Russian Journal of Bioorganic Chemistry, 41(4), 414-420, 2015.

[21] Turan, B., Şendil, K., Şengül, E., Gültekin, M.S., Taslimi, P., Gulcin, I., Supuran, C.T., *The synthesis of some β-lactams and investigation of their metal-chelating activity, carbonic anhydrase and acetylcholinesterase inhibition profiles*, Journal of Enzyme Inhibition and Medicinal Chemistry, 31(sup1), 79-88, 2016.

[22] Ostrowski, S., Wolniewicz, A.M., *An approach to fused pyrimidine derivativesvia schiff bases of aromaticortho-nitrocarbaldehydes. An investigation of substituent effects on the reaction course*, Chemistry of Heterocyclic Compounds, 36(6), 705-713, 2000.

[23] Woodward, R.B., Heusler, K., Gosteli, J., Naegeli, P., Oppolzer, W., Ramage, R., Ranganathan, S., Vorbrüggen, H., *The total synthesis of cephalosporin C[1]*, Journal of the American Chemical Society, 88(4), 852-853, 1966.

[24] Marcantoni, E., Palmieri, A., Petrini, M., *Recent synthetic applications of α-amido sulfones as precursors of n-acylimino derivatives*, Organic Chemistry Frontiers, 6(13), 2142-2182, 2019.

[25] Elmacı, G., Duyar, H., Aydıner, B., Yahaya, I., Seferoglu, N., Sahin, E., Çelik, S.P., Açık, L., Seferoglu, Z., *Novel benzildihydrazone based schiff bases: syntheses, characterization, thermal properties, theoretical DFT calculations and biological activity studies,* Journal of Molecular Structure, 1184, 271-280, 2019.

[26] Elmacı, G., Duyar, H., Aydıner, B., Seferoglu, N., Naziri, M.A., Sahin, E., Seferoglu, Z., *The syntheses, molecular structure analyses and DFT studies on new benzil monohydrazone based schiff bases*, Journal of Molecular Structure, 1162, 37-44, 2018.

[27] Elmacı, G., Aktan, E., Seferoglu, N., Hökelek, T., Seferoglu, Z., *Synthesis, molecular structure and computational study of (Z)-2-((E)-4-nitrobenzylidene) hydrazone)-1, 2-diphenylethan-1-one,* Journal of Molecular Structure, 1099, 83-91, 2015.

[28] Beck, J.F., *Ortho metallated acetophenone imines as ligands for transition and main group metals: synthesis and organometallic reactivity and the hydroamination of allenes using a palladium allyl triflate 3-iminophosphine precatalyst*, Diss. University of Toledo, 2011.

[29] Shelke, V.A., Jadhav, S.M., Patharkar, V.R., Shankarwar, S.G., Munde, A.S., Chondhekar, T.K., *Synthesis, spectroscopic characterization and thermal studies of some rare earth metal complexes of unsymmetrical tetradentate schiff base ligand*, Arabian Journal of Chemistry. 5(4), 501-507, 2012.

[30] Xu, J., Zhuang, R., Bao, L., Tang, G., Zhao, Y., *KOH-mediated transition metal-free synthesis of imines from alcohols and amines*, Green Chemistry, 14(9), 2384-2387, 2012.

[31] Kozlov, N.G., Basalaeva, L.I., Skakovskaya, E.Y., *Synthesis of benzo [a] phenanthridine derivatives by condensation of n-arylmethylene-2-naphthylamines with 5-phenyl-and-5-(p-Methoxyphenyl)-1, 3-cyclohexanediones*, Russian Journal of General Chemistry, 72(8), 1238-1242, 2002.

[32] Blackburn, L., Taylor, R.J., *In situ oxidation imine formation reduction routes from alcohols to amines*, Organic Letters, 3(11), 1637-1639, 2001.

[33] Vázquez, M.Á., Landa, M., Reyes, L., Miranda, R., Tamariz, J., Delgado, F., *Infrared irradiation: effective promoter in the formation of n-benzylideneanilines in the absence of solvent*, Synthetic Communications, 34(15), 2705-2718, 2004.

[34] Goszczyńska, A., Kwiecień, H., Fijałkowski, K., *Synthesis and antibacterial activity of schiff bases and amines derived from alkyl 2-(2-formyl-4-nitrophenoxy) alkanoates*, Medicinal Chemistry Research, 24(9), 3561-3577, 2015.

[35] Sharma, S., Singh, T., Mittal, R., Saxena, K.K., Srivastava, V.K., Kumar, A., *A study of anti-inflammatory activity of some novel α-amino naphthalene and β-amino naphthalene derivatives,* Archiv der Pharmazie: An International Journal Pharmaceutical and Medicinal Chemistry, 339(3), 145-152, 2006.

[36] Arora, K., Parmar, A., *Simulation of IR spectra of some organic compounds-a review*, IOSR Journal of Applied Chemistry (IOSR-JAC), 6(1), 10-24, 2013.

[37] Kozlov, N.G., Yakubovich, L.S., Murashko, V.L., *Condensation of ethyl cydopentanone-2-carboxylate with N-arylmethylene-2-naphthylamines*, Russian Journal of Electrochemistry, 36(6), 777-780, 2000.

[38] Güngör, Ö.Ö., *Intramolecular proton transfer equilibrium in salicylidene-and naphthalene-based tetraimine schiff base*, Gazi University Journal of Science, 30(1), 191-214, 2017.

Adıyaman University Journal of Science

https://dergipark.org.tr/en/pub/adyujsci

Synthesis of Some New Carbazole-Metal Complexes and Their Thermal, Electronic, Spectral and Catalytic Alkene Oxidation Properties

Selma BAL[1],*

[1]*Kahramanmaras Sutcu Imam University, Faculty of Sciences and Literature, Department of Chemistry, 46050, Kahramanmaras, Turkey*
selmabal@ksu.edu.tr, ORCID: 0000-0001-9547-8717

Abstract

Two new ligands [(*E*)-4-chloro-2-((9-ethyl-9H-carbazol-3-yl)methyleneamino)phenol, (*E*)-2-bromo-4-chloro-6-((9-ethyl-9H-carbazol-3-yl)methyleneamino)phenol] and their Cobalt (II), Manganese (II) and Nickel (II) complexes have been synthesized and characterized through various spectroscopic techniques (NMR, UV, IR, Mass etc.). Synthesized compounds have been examined for their catalytic activities in the oxidation reactions of styrene and cyclohexene. Manganese (II) complexes of both ligands showed the highest catalytic activity in alkene oxidations. Synthesized complex compounds proved that they could be used as catalysts in organic reactions requiring high temperatures. Electronic features of all the new compounds have also been reported for the first time with this paper.

Keywords: Catalysis; Complex; Schiffbase.

Bazı Yeni Karbazol-Metal Komplekslerinin Sentezi ve Termal, Elektronik, Spektral ve Katalitik Alken Oksidasyon Özellikleri

Öz

İki yeni ligant [(*E*)-4-kloro-2-((9-etil-9H-karbazol-3-yl)metilenamino)fenol, (*E*)-2-bromo-4-chloro-6-((9-etil-9H-karbazol-3-yl)metilenamino)fenol] ile bunların kobalt (II), mangan (II) ve nikel(II) kompleksleri sentezlenmiş ve yapıları değişik spektroskopik yöntemlerle (NMR, UV, IR, Mass etc.) karakterize edilmişlerdir. Sentezlenen bileşiklerin katalitik aktiviteleri stiren ve siklohekzenin oksidasyon reaksiyonları üzerinde incelenmiştir. Her iki ligantın Mangan (II) kompleksleri alken oksidasyonlarında en yüksek aktiviteyi göstermiştir. Sentezlenen kompleks bileşiklerin katalizör olarak yüksek sıcaklık isteyen katalitik reaksiyonlarda kullanılabilirliği termal analizlerle kanıtlanmıştır. Bu yeni bileşiklerin elektronik özellikleri de ilk kez bu çalışma ile rapor edilmektedir.

Anahtar Kelimeler: Kataliz; Kompleks; Şifbazı.

1. Introduction

Schiff base ligands and their metal complexes have been studied and are still being studied extensively for years due to their synthetic flexibilities. They have captured many attention in the fields relating antimicrobial activity, catalytic activity especially in the reactions including alkene epoxidations [1-6], epoxide ring openings [7-9]. Among alkene epoxidation reactions, styrene and cyclohexene oxidation reactions captured quite high attention due to their versatile usage as starting materials in many synthetic organic reactions. In the literature, we have previously synthesized some carbazole derived Schiff bases and examined their catalytic activity towards the oxidation reactions of both cyclohexene and styrene [10]. Schiff base complexes were and are still being examined for their catalytic activities towards many different organic reactions [11-15]. Also, various Schiff base ligands are being examined for their biological effects like antimicrobial, anticancer and antitumour activities [16-21]. In many research carried out worldwide use carbazole moiety in the syntheses of new organic compounds and these organic compounds have been studied for their various features like thermal, electrochemical, electroluminescent features [22], as catalysts for the hydrogenation of alkenes [23], as ligands toward catalytic nitrogen fixation [24] and as photosensitizers (PS) [25]. Recently, a carbazole based Schiff base derivative was synthesized and used for detection of HSO_4^- ion in aqueous medium [26]. In addition above all, many different metal coordination compounds of different Schiff bases have been and are still being used in various kinds of oxidation reactions of both saturated and unsaturated hydrocarbons [27-29].

This work, first of all, deals with the synthesis and purification of 9-ethyl-3-carbazole carboxaldehyde from N-ethyl carbazole. Then it moves on to the synthesis and characterization of the two new Schiff bases and their Copper(II), Cobalt(II) and Nickel(II) complexes. All these

newly synthesized compounds have been examined for their catalytic, thermal and electronic features.

2. Experimental

9-Ethylcarbazole, Phosphorus(V) oxychloride, 2-amino-4-methylphenol, 2-aminophenol, acetate salts of Manganese(II) Cobalt(II) and Nickel(II) were purchased from Sigma Aldrich. Nuclear Magnetic Resonance spectra were recorded on a Bruker AV 400 MHz spectrometer in the solvent CDCl$_3$. Infrared spectra were obtained using KBr discs on a Shimadzu 8300 FTIR spectrophotometer in the region of 400-4000 cm^{-1}. Ultra-violet spectra were run in ethanol on a Schimadzu UV-160 A spectrophotometer. Mass spectra of the ligand were recorded on a LC/MS APCI AGILENT 1100 MSD spectrophotometer. The oxidation products were analyzed with a gaschromatograph (Shimadzu, GC-14B) equipped with a SAB-5 capillary column and a flame ionization detector. Elemental analyses were performed on a LECO CHNS 932 elemental analyzer and the metal analyses were carried out on an Ati Unicam 929 Model AA Spectrometer in solutions prepared by decomposing the compounds in aquaregia and subsequently digesting them in conc. HCl. Chemical composition analysis by EDAX was performed with an EDAX; Rönteckx flash detector analyzer associated to a scanning electron microscope (SEM, Leo-Evo 40xVP). The energy spectrum of characteristic X-rays is measured with Bruker energy dispersive X-ray spectroscope (EDX) by a high resolution Si (Li) detector. Incident electron beam energies from 3 to 30 keV had been used. In all cases, the beam was at normal incidence to the sample surface and the measurement time was 100 s. All the EDAX spectra were corrected by using the ZAF correction, which takes into account the influence of the matrix material on the obtained spectra. Further, the presence of metals in the complexes was detected by an energy dispersive X-ray fluorescence (EDXRF) spectrometer and its percentage is estimated using CATXRF Program.

Thermal analyses of synthesized ligand and its metal complexes were carried out on a Perkin-Elmer Thermogravimetric Analyzer TG/DTA 6300 instrument under nitrogen atmosphere between the temperature range 30 °C and 800 °C at a heating rate of 10 °C/min. Magnetic measurements were carried out by the Gouy method using Hg[Co(SCN)$_4$] as calibrant.

2.1. Synthesis of the ligands

Formylation of 9-ethyl carbazole was done by using Vilsmeier formylating agents DMF and POCl$_3$ (1:1), 24h reflux at 85 °C [10, 30, 31]. The mono aldehyde was separated by flash

chromatography with ethyl acetate/hexane (1:10) as eluent. 1 mmol N-ethylcarbazole-3-carbaldehyde was then reacted with 1 mmol 2-amino-4-chlorophenol to give (E)-4-chloro-2-((9-ethyl-9H-carbazol-3-yl)methyleneamino)phenol (L^1) and with 1 mmol 2-amino-6-bromo-4-chlorophenol to give (E)-2-bromo-4-chloro-6-((9-ethyl-9H-carbazol-3-yl)methyleneamino)phenol (L^2). Reactions were carried out in 30 mL ethanol under reflux for 9 hours. The resulting precipitates were recrystallized from methanol. Fig. 1 represents the whole reaction scheme for the synthesized componds.

R=H: **L^1** (*E*)-4-chloro-2-((9-ethyl-9*H*-carbazol-3-yl)methyleneamino)phenol
R=Br: **L^2** (*E*)-2-bromo-4-chloro-6-((9-ethyl-9*H*-carbazol-3-yl)methyleneamino)phenol
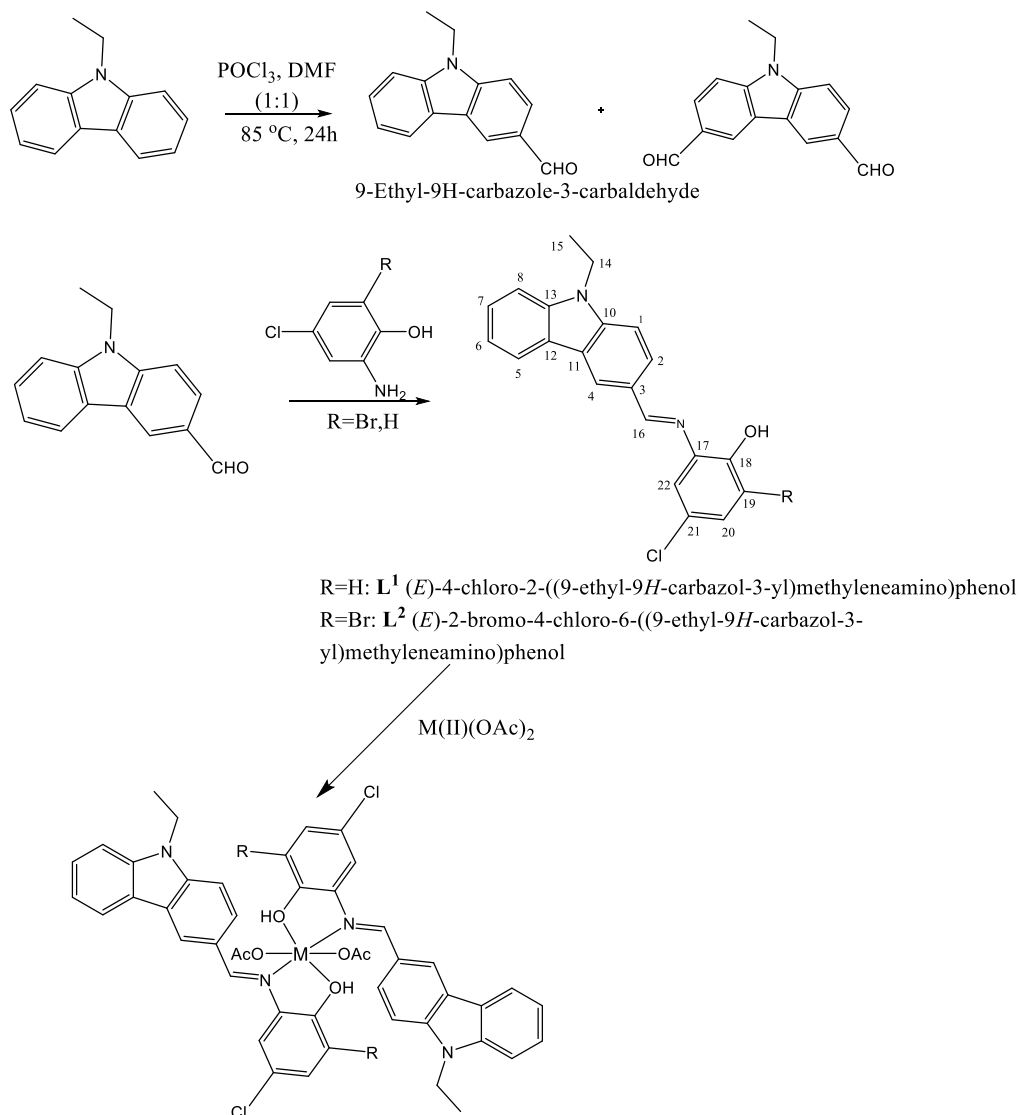
Figure 1: Synthesis scheme and the proposed structures for the synthesized compounds

2.1.1. L^1 (*E*)-4-chloro-2-((9-ethyl-9H-carbazol-3-yl)methyleneamino)phenol

$C_{21}H_{17}ClN_2O$. Yield: 90%, m.p.: 78-88 °C. Elemental Analysis, found % (calculated %): C 72.3(72.31) H 5.04(4.91) N 8.0(8.03), UV-Vis (ethanol) (λ_{max}, nm): 241, 292, 330. FT-IR (KBr,

cm−1): 3040(C-H)$_{Ar}$; 2973(C-H); 1590(C=C)$_{Ar}$; 3380, 3312(OH); 1619(CH=N). ^{1}H NMR(CDCl$_3$): δ 8.2(H-1, d, J= 8.6 Hz); 8.06(H-2, dd, J= 8.6 & 1.4 Hz); 8.6 (H-4, d, J= 1.2 Hz);7.5 (H-5, H-7, H-8 overlapped); 7.3 (H-6, H-22 overlapped); 4.4 (2H-14, q, J= 7.2 Hz); 1.5 (3H-15, t, J= 7.2 Hz);8.7 (H-16, s); 6.94 (H-19, d, J= 8.6 Hz); 7.1 (H-20, dd, J= 8.6 Hz, 2.4 Hz); 10.0 (OH, s). ^{13}C NMR(CDCl$_3$): δ 127.5 (C-1); 126.5 (C-2); 128.5 (C-3); 123.3 (C-4); 120.8 (C-5); 120.0 (C-6); 108.9 (C-7); 109.0 (C-8); 142.4 (C-10); 123 (C-11); 122.7 (C-12); 140.6 (C-13); 37.9 (C-14); 13.9 (C-15);159.3 (C-16); 137.0 (C-17); 150.7 (C-18); 115.7 (C-19);116.2 (C-20); 126.6 (C-22). Mass spectrum (LC/MS APCI): m/z 349.0 [M+H]$^+$.

2.1.2. (L^2) (*E*)-2-bromo-4-chloro-6-((9-ethyl-9H-carbazol-3 yl)methyleneamino) phenol

C$_{21}$H$_{16}$BrClN$_2$O.Yield: 84%, m.p.: 85-90°C. Elemental Analysis, found % (calculated %): C 59.3(58.97) H 4.02(3.77) N 6.3(6.55), UV-Vis (ethanol) (λ$_{max}$, nm): 235, 276, 293, 333. FT-IR (KBr, cm−1): 3041(C-H)$_{Ar}$; 2850, 2918(C-H); 1587(C=C)$_{Ar}$; 3350, 3550(OH); 1622(CH=N). ^{1}H NMR(CDCl$_3$): δ 8.3(H-1, d, J= 8 Hz); 8.03 (H-2, dd, J= 8.6 & 1.5 Hz); 8.5 (H-4, d, J= 1.2 Hz); 7.45 (H-5, d, J= 8 Hz overlapped with H-8); 7.33 (H-6, ddd, J= 8 & 7.1 & 1.2 Hz); 7.53 (H-7, ddd, J= 8 & 7 & 1.2 Hz); 7.45 (H-8,d, J= 8 Hz overlapped with H-5); 4.4 (2H-14, q, J= 7.2 Hz); 1.5 (3H-15, t, J= 7.2 Hz); 8.7 (H-16, s); 7.4 (H-20, d, J= 2.3 Hz); 7.2 (H-22, d, J= 2.3 Hz); 10.1 (OH, s); ^{13}C NMR(CDCl$_3$): δ 126.7 (C-1); 126.6 (C-2); 128.5 (C-3); 123.4 (C-4); 120.8 (C-5); 120.0 (C-6); 108.9 (C-7); 109.1 (C-8); 142.6 (C-10); 123.1 (C-11); 122.8 (C-12); 140.6 (C-13); 37.9 (C-14); 13.9 (C-15);160.5 (C-16); 137.6 (C-17); 148.2 (C-18); 129.9 (C-19);115.4 (C-20); 126.6 (C-22). Massspectrum (LC/MS APCI): m/z 427.0 [M]$^+$.

2.2. Synthesis of the complex compounds

Synthesized ligands were reacted with the acetate salts of Nickel, Cobalt and Manganese with the ratio 2:1. The ligands were first dissolved in ethanol in a round bottom flask. The appropriate metal salt which was also dissolved in ethanol were added into this solution slowly. The mixtures were refluxed for 24 hours. The resulted precipitates were recrystallized from methanol.

Co(L^{1}H)$_2$(OAc)$_2$

C$_{46}$H$_{40}$Cl$_2$CoN$_4$O$_6$.Yield: 64%, m.p.: 94-117°C. Elemental Analysis, found % (calculated %): C 63.51(63.17) H 5.01(4.61) N 6.21(6.41), Co 6.81(6.74). UV-Vis (ethanol) (λ$_{max}$, nm): 239, 276, 295, 334, 442. FT-IR (KBr, cm−1): 3049(C-H)$_{Ar}$; 2975(C-H); 1591(C=C)$_{Ar}$; 3550, 3322(OH); 1621(CH=N). 539 (M-N); 613 (M-O)$_{asym}$; 584(M-O)$_{sym}$. Massspectrum (LC/MS APCI): found m/z (Caculated m/z) 875.3 (874.6) [M]$^+$. μ$_{eff}$ B.M.: 4.61.

Mn(L¹H)₂(OAc)₂

$C_{46}H_{40}Cl_2MnN_4O_6$.Yield: 56%, m.p.: 90-110 °C. Elemental Analysis, found % (calculated %): C 63.84(63.46) H 4.77(4.63) N 6.33(6.43), Mn 6.26(6.31). UV-Vis (ethanol) (λ_{max}, nm): 236, 275, 294, 332, 443. FT-IR (KBr, cm−1): 3047(C-H)$_{Ar}$; 2974(C-H); 1592(C=C)$_{Ar}$; 3338(OH); 1620(CH=N). 538 (M-N); 613 (M-O)$_{asym}$; 589(M-O)$_{sym}$. Massspectrum (LC/MS APCI): found m/z (Caculated m/z) 870.0 (870.7) [M]⁺. μ_{eff} B.M.: 6.01.

Ni(L¹H)₂(OAc)₂

$C_{46}H_{40}Cl_2NiN_4O_6$.Yield: 55%, m.p.: 100-120 °C. Elemental Analysis, found % (calculated %): C 63.64(63.18) H 4.31(4.61) N 6.11(6.41), Ni 6.36(6.71) UV-Vis (ethanol) (λ_{max}, nm): 238, 278, 294, 336, 446. FT-IR (KBr, cm−1): 3044(C-H)$_{Ar}$; 2974(C-H); 1586(C=C)$_{Ar}$; 3480(OH); 1615(CH=N). 537 (M-N); 610 (M-O)$_{asym}$; 572(M-O)$_{sym}$. Massspectrum (LC/MS APCI): found m/z (Caculated m/z) 876.0 (875.4) [M+H]⁺. μ_{eff} B.M.: 3.07

Co(L²H)₂(OAc)₂

$C_{46}H_{38}Br_2Cl_2CoN_4O_6$. Yield: 71%, m.p.: 100-123 °C. Elemental Analysis, found % (calculated %): C 53.47(53.51) H 4.12(3.71) N 5.52(5.43), Co 5.59(5.71) UV-Vis (ethanol) (λ_{max}, nm): 231, 277, 291, 325, 447FT-IR (KBr, cm−1): 3040(C-H)$_{Ar}$; 2850, 2918(C-H); 1587(C=C)$_{Ar}$; 3350, 3243(OH); 1622(CH=N). 538 (M-N); 613 (M-O)$_{asym}$; 587(M-O)$_{sym}$. Massspectrum (LC/MS APCI): found m/z (Caculated m/z) 1034.0 (1034.5) [M+2H]⁺. μ_{eff} B.M.: 4.60.

Mn(L²H)₂(OAc)₂

$C_{46}H_{38}Br_2Cl_2MnN_4O_6$. Yield: 68%, m.p.:89-117 °C. Elemental Analysis, found % (calculated %): C 53.68(53.72) H 3.93(3.72) N 5.67(5.45), Mn 5.544(5.34) UV-Vis (ethanol) (λ_{max}, nm): 236, 275, 294, 332, 443. FT-IR (KBr, cm−1): 3047(C-H)$_{Ar}$; 2974(C-H); 1592(C=C)$_{Ar}$; 3338(OH); 1620(CH=N). 538 (M-N); 613 (M-O)$_{asym}$; 589(M-O)$_{sym}$. Massspectrum (LC/MS APCI): found m/z (Caculated m/z) 1029.0 (1029.5) [M+H]⁺. μ_{eff} B.M.: 5.88.

Ni(L²H)₂(OAc)₂

$C_{46}H_{38}Br_2Cl_2NiN_4O_6$. Yield: 77%, m.p.: 127-135 °C. Elemental Analysis, found % (calculated %): C 53.39(53.52) H 4.65(3.71) N 5.48(5.43), Ni 5.75(5.69) UV-Vis (ethanol) (λ_{max}, nm): 232, 276, 292, 328, 446. FT-IR (KBr, cm−1): 3040(C-H)$_{Ar}$; 2883(C-H); 1589(C=C)$_{Ar}$; 3544, 3322(OH); 1620(CH=N). 510 (M-N); 614 (M-O)$_{asym}$; 570(M-O)$_{sym}$. Massspectrum (LC/MS APCI): found m/z (Caculated m/z) 1032.0 (1032.2) [M]⁺. μ_{eff} B.M.: 3.27

3. Results and Discussion

3.1. Spectral analysis

Both synthesized ligands L^1 and L^2 gave similar signals in their proton (Fig. 2 and Fig. 3) and carbon NMR spectra (Fig. S1 and Fig. S2). Ethyl group on the Nitrogen in the carbazole unit were seen at 4.4ppm (2H-14) as quarted (J = 7.2 Hz) and at 1.5 ppm (3H-15) as triplet (J = 7.2 Hz). The imine protons for both ligands were seen at 8.7 ppm.

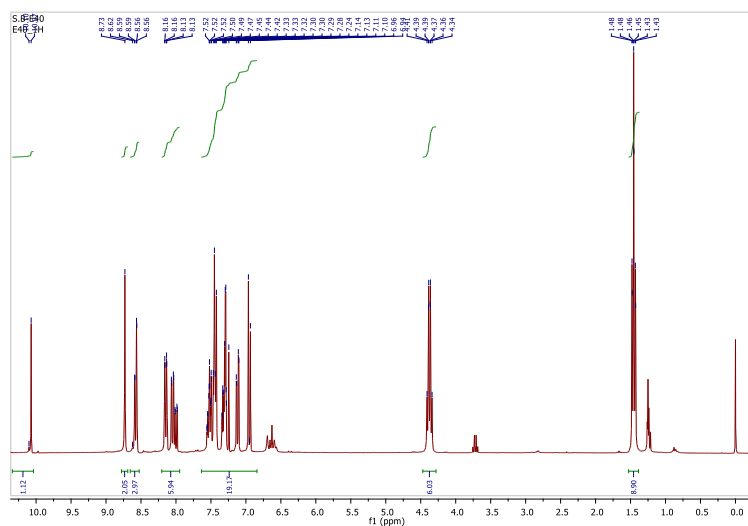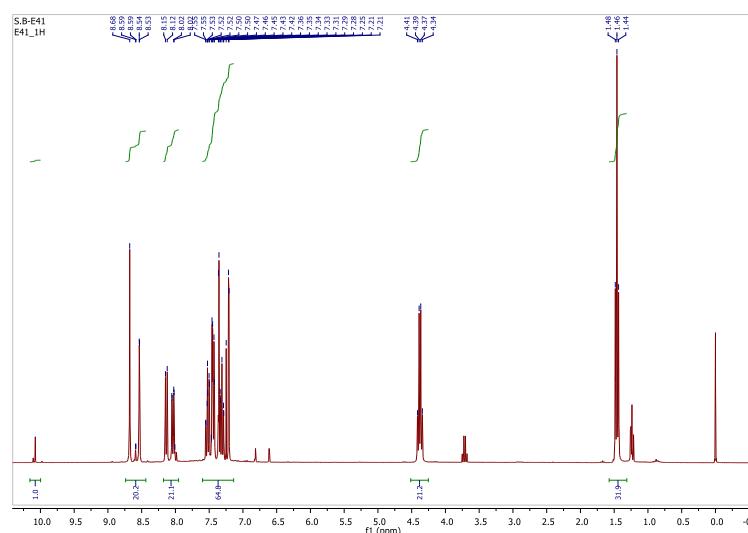**Figure 2:** ^{1}H NMR Spectrum of L^1

Figure 3: ^{1}H NMR Spectrum of L^2

Among the carbazole aromatic ring protons in ligand L^1, next to the imine proton signal, the doublet at 8.6 ppm (d, J = 1.2 Hz) belongs to H-4 and the two signals appearing next to H-4 belongs to H-1 [δ 8.2 (d, J = 8.6 Hz)] and H-2 [δ 8.03 (dd, J = 8.6 & 1.4 Hz)]. We can see the rest of the aromatic protons between 6.9 ppm and 7.6 ppm for both ligands. We could clearly see the phenolic aromatic protons H-19 and H-20, belonging L^1, at 6.94 ppm (d, J = 8.6 Hz) and at 7.1 ppm (dd, J = 8.6 & 2.4 Hz). H-22 on this ring were observed as overlapped with H-6 at 7.3. ^{1}H NMR spectrum of L^2 showed two sharp doublets, one at 7.4 ppm (J = 2.3 Hz), the other at 7.2

ppm (J = 2.3 Hz) belonging to H-20 and H-22 on the phenolic ring respectively. Both ligands showed the hydroxyl proton at 10.0 ppm as a weak singlet. ^{13}C NMR spectra of the ligands revealed the imine carbon signals at 159.3 ppm for L^{1}and at 160.5 ppm for L^2. The ethyl group on the carbazole unit were seen at δ 37.9 and at δ 13.9 for both ligands. The rest of the aromatic carbons were seen between 100 ppm and 154 ppm.

In the IR spectra of the ligands L^1 and L^2, we were able to see weak signals at 1619 and 1622 cm^{-1} respectively, corresponding the imine streching frequency. This vibration was slightly shifted in their complexes. Aromatic C-H vibrations were seen at around 3050 cm^{-1} and the aliphatic vibrations were between 2918 and 2975 cm^{-1}. The NMR spectra of the ligands gave hydroxyl signals at around 10.1 ppm and the IR spectra of the ligands showed hydroxyl stretchings between 3312 and 3380 cm^{-1}. Since all the synthesized complexes have uncoordinated two molecule of waters, their IR spectra revealed hydroxyl stretchings between 3243 cm^{-1} and 3550 cm^{-1}. For the substitution patterns of the benzene rings present in L^1 and their complexes, we could clearly see the sharp signals between 800 cm^{-1} and 808 cm^{-1} corresponding to two adjacent hydrogens on the phenolic rings. Similarly, for L^2 and its complexes, the weak signals at around 805 cm^{-1} corresponded to two isolated hydrogens in their phenolic rings. M-N streching frequencies for all the complexes were observed between 510 cm^{-1} and 539 cm^{-1}. The IR spectra of all the complexes revealed M-O streching frequencies both as symmetric and asymmetric in the ranges 570-589 cm^{-1} and 610-614 cm^{-1} respectively [32].

IR spectra of all the complexes gave three intense bands belonging to asymmetric and symmetric carboxylate strechings, which proves the chelation of the carboxyls with metals. It is known that there are three possible carboxylate coordination modes: unidentate, bidentate and bridging. Also, the splitting value of carboxylate streching bands ($\Delta = V_{as} - V_s$) are frequently used to attempt to distinguish between the three carboxylate coordination modes [33]. Deacon and Phillips [34] sought to correlate the difference, Δ, between the asymmetric and symmetric strechings of carboxylates in a number of acetate and trifluoroacetate complexes. They concluded that unidentate acetate coordination is generally associated with Δ values higher than 200 cm^{-1}, bridging coordination shows lower Δ values than 150 cm^{-1} and the compounds with very low Δ values ($\ll$ 150 cm^{-1}) are generally indicative of bidentate acetate chelation. In all of our synthesized complexes, these Δ values were calculated (Table 1) and they were found to be much higher than 200 cm^{-1}, which proves unidentate chelating of acetates.

Table 1: Asymmetric and symmetric IR values of carboxylate coordinations and the difference between them.

Complexes	$V_{asymmetric}$	$V_{symmetric}$	Δ (V_{asym} - V_{sym})
$[Co(L^1H)_2(OAc)_2]2H_2O$	1679, 1573	1231	448, 342
$[Mn(L^1H)_2(OAc)_2]2H_2O$	1679,1542	1233	446, 309
$[Ni(L^1H)_2(OAc)_2]2H_2O$	1678, 1567	1231	447, 336
$[Co(L^2H)_2(OAc)_2]2H_2O$	1679, 1571	1231	448, 340
$[Mn(L^2H)_2(OAc)_2]2H_2O$	1675, 1538	1230	445, 308
$[Ni(L^2H)_2(OAc)_2]2H_2O$	1660, 1532	1234	426, 298

UV-visible spectra of the ligands and the complexes showed absorption bands between 231 nm and 446 nm. The spectra of the complexes showed some bands in the high-energy region at 323-336 nm which can be assigned to charge transfer L-M bands [35, 36]. The complex compounds showed d-d transitions between 442 nm and 447 nm. The EDAX spectra of all the complexes showed characteristic K_{α} and L_{α} values for all the coordinated metals. In addition to the energy dispersive X-ray analysis (EDAX), scanning electron microscopy (SEM) images of all complexes provided valuable information concerning surface morphology (Fig. S3 and Fig. S4). While the EDAX images confirms the existence of the metals and the purity of the complexes, SEM photographs display uniform and homogeneous matrixes of the synthesized complexes.

Additionally, spectrochemical analyses by EDXRF (energy dispersive X-ray fluorescence) were performed on all the complexes to detect the presence of metals in them. As it is known, this technique is based on the fact that the chemical elements emit characteristic radiation when subjected to appropriate excitation [37, 38]. The inner Shell vacancies in the atoms of elements, created by excitation, are filled by transition of electrons from outer orbitals leading to emission of characteristic X-rays [39]. The energy spectra of characteristic X-rays are measured by a high resolution Si(Li) detector. The concentration values were calculated using the net area under the K_{α} peaks of Cobalt, Manganese and Nickel. The results are given in Table 2 and they are in good agreement with the calculated values.

Table 2: Metal percentages estimated by EDXRF

Compouds	Chemical Formula	Calculated Values (%)	Experimental Values (EDXRF) (%)
$Co(L^1H)_2(OAc)_2$	$C_{46}H_{40}Cl_2CoN_4O_6$	6.74	7 ± 0.6
$Mn(L^1H)_2(OAc)_2$	$C_{46}H_{40}Cl_2MnN_4O_6$	6.31	6 ± 0.6

Ni(L^{1}H)$_2$(OAc)$_2$	C$_{46}$H$_{40}$Cl$_2$NiN$_4$O$_6$	6.71	7 ± 0.6
Co(L^{2}H)$_2$(OAc)$_2$	C$_{46}$H$_{38}$Br$_2$Cl$_2$CoN$_4$O$_6$	5.71	6 ± 0.6
Mn(L^{2}H)$_2$(OAc)$_2$	C$_{46}$H$_{38}$Br$_2$Cl$_2$MnN$_4$O$_6$	5.34	6 ± 0.6
Ni(L^{2}H)$_2$(OAc)$_2$	C$_{46}$H$_{38}$Br$_2$Cl$_2$NiN$_4$O$_6$	5.69	6 ± 0.6

Mass spectra of the complex compounds showed parental ion peaks. In addition, some other distinctable fragments were also observable. For example, the carbazole unit with the phenolic ring (C$_{21}$H$_{17}$ClN$_2$O) were seen at around 348 m/z and the phenolic ring with the imine group (C$_7$H$_4$ClNO) were observable at 154 m/z for the complexes of L^1. Same fragments (C$_{21}$H$_{16}$BrClN$_2$O, C$_7$H$_3$BrClNO) for L^2 complexes were seen at around 427 m/z and at 233 m/z. Magnetic susceptibility studies revealed the geometries of all the complexes to be octahedral. For the Manganese complexes the magnetic moments were calculated as 6.01 and 5.88 B.M. [41]. The Cobalt complexes gave these values as 4.60 B.M. and 4.61 B.M. [40]. The Nickel complexes, also revealed their characteristic magnetic moment values as 3.07 B.M. and 3.27 B.M., suggesting octahedral geometry [41].

3.2. Thermal analysis

As we all know, Thermal Analysis is a method used to examine the thermal behaviour (e.g. thermal stability and composition) of the various compounds isolated by researchers world-wide. In this work, the Thermogravimetric investigation of the isolated ligands and their complexes was carried out on Perkin-Elmer TGA 6300 instrument with nitrogen atmosphere starting at 30^{0}C with a heating rate of 10 ^{0}C/min. Themal analysis studied for these new compounds revealed useful information about the decompositions of both ligands and the complexes (Fig. S5 and Fig S6). For example, examination of TG graphics of L^1 and its complexes showed well defined degradation steps that are in agreement with the proposed structures. Their decomposition starts between the temperatures 90 ^{o}C and 120 ^{o}C. Nickel (II) complex of L^1 was the most temperature resistant with a degradation temperature starting at 100 ^{o}C and its TG graphic revealed two steps of degradation, one with the loss of carbazole unit with 43.9 % (Calc. 44 %) and the other was the loss of phenolic ring with the imine group [34 % (Calc. 34.5 %)]. The residual part of this complex gave the total masses of NiO and the two coordinated acetates. Cobalt (II) and Manganese (II) complexes of L^1 showed similar degradations in their TG graphics, which can be divided in two steps. The first steps corresponded to two phenolic rings with the imine group and the second step belonged to the mass loss of two carbazoles and the two coordinated acetates. Metallic Manganese was the residual mass found for Mn(L^{1}H)$_2$(OAc)$_2$ and oxygenated Cobalt

was recorded as the residual part for the Cobalt complex of this ligand. The ligand L^1 itself also revealed two degradation steps consisting of the carbazole unit and the phenolic part with the imine group. Thermal analysis of the other ligand L^2 revealed a mass loss assigned as the residual part consisting of bromide and the ethyl group. Between 100 °C and 420 °C, the mass loss of the phenolic group without the bromide occurred with 35.7 % (Calc. 35.8 %). Above 420 °C, the mass loss of 39.3 % (Calc. 38.9 %) was attributed to the carbazole without the ethyl group. Among complexes of L^2, Nickel complex was the most temperature resistant with degradation temperature starting at 135 °C. Manganese and Nickel complexes showed quite similar degradation patterns in their TG graphics. For example, both revealed a mass loss belonging to the phenolic groups ($2 \times C_7H_4BrClNO$). The second step shows mass losses of the carbazoles and the coordinated acetates mainly. Cobalt (II) complex of L^2, however, revealed the residual part with a mass loss of 33.8 % (Calc. 33.3 %), which corresponds to the total masses of two bromines, two acetates and Cobalt oxide. The experimental values obtained for the ligands and the complexes were all in agreement with the calculated values. All the results for the thermal analysis are listed in Table 3.

Table 3: Thermal results of synthesized compounds

| Compound	M.W.	T/°C	MassLoss % Found(Calc.)	Assignment	Residual % Found(Calc.)
L^1	348	80-450	42.7(42.6)	C_7H_5ClNO	
		450-700	56.5(56.2)	$C_{14}H_{13}N$	
$Ni(L^1H)_2(OAc)_2$	875	100-450	34(34.5)	$2(C_7H_5ClNO)$	22.1(21.5) (NiO), 2(AcO)
		550-800	43.9(44)	$2(C_{14}H_{12}N)$	
$Co(L^1H)_2(OAc)_2$	875	94-525	35(34.8)	$2(C_7H_5ClNO)$	8.8(8.5) (CoO)
		525-800	56.2(56.7)	$2(C_{14}H_{12}N)$, 2(AcO)	
$Mn(L^1H)_2(OAc)_2$	870	90-520	35.4(35.5)	$2(C_7H_5ClNO)$	6(6.3) (Mn),
		520-670	58.6(58.2)	$2(C_{14}H_{12}N)$, 2(AcO)	
L^2	427	85-420	35.7(35.8)	C_7H_4ClNO	25(25.3) (CH_3CH_2), Br
		420-800	39.3(38.9)	$C_{12}H_8N$	
$Ni(L^2H)_2(OAc)_2$	1032	130-475	44.4(44.8)	$2(C_7H_4BrClNO)$	
		475-800	55.6(55.2)	$2(C_{14}H_{12}N)$, 2(AcO), NiO	
$Co(L^2H)_2(OAc)_2$	1032	100-465	28.9(29.3)	$2(C_7H_4ClNO)$	33.8(33.3) (CoO), 2(AcO), 2Br
		465-800	37.3(37.4)	$2(C_{14}H_{12}N)$	
$Mn(L^2H)_2(OAc)_2$	1028	85-600	45.5(45.2)	$2(C_7H_4BrClNO)$	6.5(6.5) (MnO)
		600-800	48.0(48.3)	$2(C_{14}H_{12}N)$, 2(AcO)	

All thermal analyses were done under nitrogenatmosphere between the temperature range 30 °C and 800 °C at a heating rate of 10 °C/min.

3.3. Cyclic voltammetry

Cyclic voltammogram studies of the title compounds were run in CH_3CN (1×10^{-3} M–0.1 M NBu_4BF_4 as supporting electrolyte at 293 K. Unless otherwise stated, all potentials quoted refer to measurements run at a scan rates ('v') of 50, 100, 250, 500, 750 and 1000 mV s^{-1} and against an internal ferrocene–ferrocenium standard. The electrochemical curves of the synthesized ligands at 50, 100, 250, 500, 750 and 1000 mV s^{-1} scan rates are shown in the Fig. 4 and Fig. 5. As shown in Fig. 4 , our ligand L^1 shows many reversible processes in all of its scan rates and a few irreversible ones. Especially at 1000 mV/s, it showed only the reversible processes. In this scan rate, both forward and reverse scans showed a total of twelve potentials, each halve shared by anodic and catodic peaks. Examination of the complexes of L^1 revealed that the Nickel (II) and Cobalt (II) complexes showed mostly the reversible processes in all of their scan rates. Manganese (II) complex of L^1, however, showed pseudo-reversible redox processes too. In these pseudo-reversible processes , the anodic peak potentials were recorded between -0.69 V and -0.76 V and the cathodic potentials were seen between -1.17 V and -1.19 V at scan rates 250, 500, 750 and 1000 mVs^{-1}. Our second ligand L^2 also revealed many reversible processes, however, it showed irreversible redoxes too. For the scan rates 250, 500, 750 and 1000 mVs^{-1} at -0.569 V, -0.621 V, -0.613 V, -0.589 V for the forward scan and at -0.388 V, -0.376 V, -0.364 V, -0.364 V peak potentials for the reverse scan revealed their anodic to cathodic ratio values were around 1.6 (I_{pa}/I_{pc}), proving their irreversable nature. Among the complexes of L^2, Cobalt (II) complex revealed mainly reversible processes, only for the scan rates 50 mVs^{-1} ve 100 mVs^{-1}, it showed pseudo-reversible redoxes at -0.913 V and -0.929 V for anodic potentials and at -1.186 V and -1.322 V for cathodic potentials. Nickel (II) and Manganese (II) complexes of the same ligand revealed both reversible and pseudo-reversible processes. For all the synthesized metal complexes, one can say that the redox process occur with a simple one-electron processes [M(II)/M(I)]. For the ligands, we can draw the redox scheme in Fig. 6. The results of these experiments can be gathered in a table which can be seen in the supporting file.
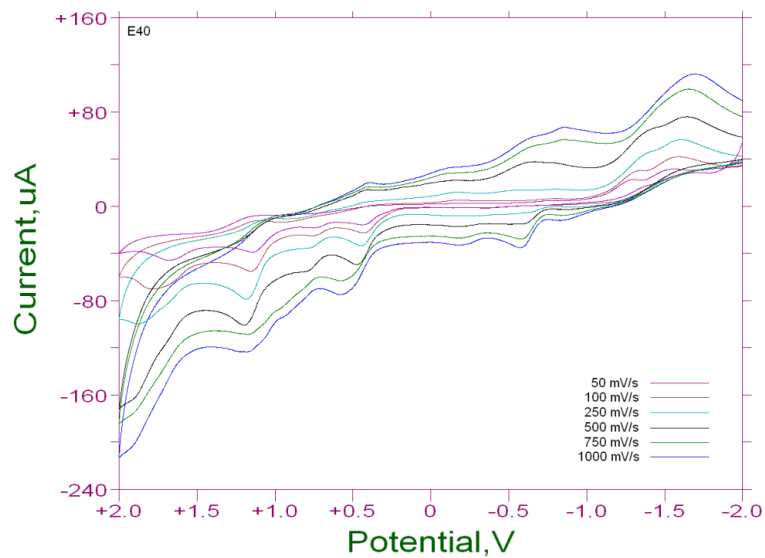
Figure 4: Cyclic Voltammogram for Ligand L^1
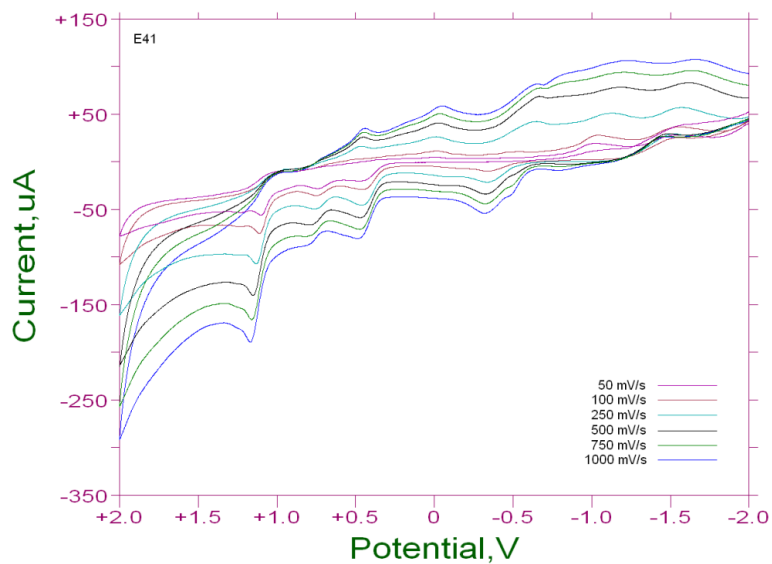
Figure 5: Cyclic Voltammogram for Ligand L^2
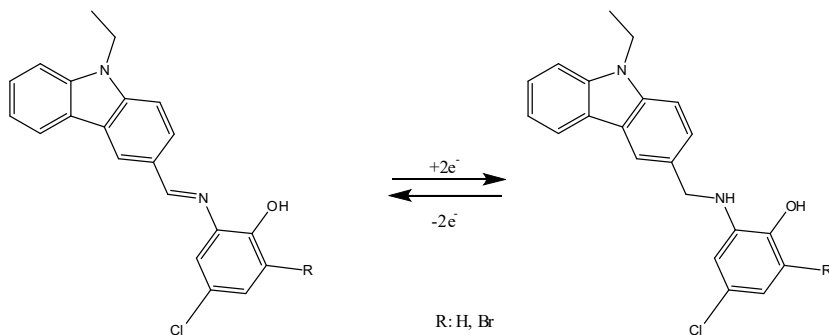
Figure 6: Redox scheme for L^1 and L^2

3.4. Catalytic activity

Catalytic activities of the synthesized coordination compounds revealed high performances towards the oxidation reactions of styrene and cyclohexene (Tables 4 and 5). Among the complexes of our ligands, Manganese (II) complexes were the most effective catalysts in the alkene oxidations. In literature, although differet oxidants used, Manganese complexes of similar schiff bases revealed high styrene oxide yields as catalysts in the oxidation reactions of styrene [42]. Styrene oxide selectivities for our Manganese complexes of L^1 and L^2 were recorded as 58.7% and 55.2% and the same complexes gave cyclohexene oxide selectivities as 40% and 42.7% respectively. Cobalt (II) complex of the ligands showed slightly more activity than the Nickel (II) complex in the oxidation reactions of styrene. On the other hand, their catalytic activities were quite similar in cyclohexene oxidations. Compared to our previous study [43] and some other studies [44, 45], although different oxidants and conditions used, high selectivities were obtained in our studies in the oxidation reactions of both styrene and cyclohexene.

Table 4: Styreneoxidation results

	Catalyst	Styrene Conversion (%)	Selectivity (%) StyreneOxide	Benzaldehyde	BenzoicAcid	Others
1	$Mn(L^1H)_2(OAc)_2$	80.9	58.7	35.0	4.2	2.1
2	$Ni(L^1H)_2(OAc)_2$	67.2	38.7	41.4	9.6	10.3
3	$Co(L^1H)_2(OAc)_2$	71.3	42.9	37.6	11.1	8.4
4	$Mn(L^2H)_2(OAc)_2$	78.7	55.2	33.6	5.7	5.5
5	$Ni(L^2H)_2(OAc)_2$	66.5	34.5	47.2	10.3	8.0
6	$Co(L^2H)_2(OAc)_2$	70.0	40.0	35.4	13.3	11.3

Others: Phenylacetaldehyde, 1-phenylethane-1,2-diol
Reaction temperature: 70 ºC (343.15 K), Solvent: Acetonitrile

Table 5: Cyclohexeneoxidation results

	Catalyst	Cyclohexene Conversion (%)	Selectivity (%) Cyclohexeneoxide	2-Cyclohexene-1-ol	Others
1	$Mn(L^1H)_2(OAc)_2$	70.1	40.0	22.2	37.8
2	$Ni(L^1H)_2(OAc)_2$	65.7	30.4	19.5	50.1
3	$Co(L^1H)_2(OAc)_2$	62.3	33.4	21.0	45.6
4	$Mn(L^2H)_2(OAc)_2$	73.6	42.7	26.4	30.9
5	$Ni(L^2H)_2(OAc)_2$	61.4	31.1	18.4	50.5
6	$Co(L^2H)_2(OAc)_2$	60.5	28.8	20.6	50.6

Others: 2-Cyclohexene-1-one, 2-cyclohexene-1-hydroperoxide
Reaction temperature: 70 ºC (343.15 K), Solvent: Acetonitrile

4. Conclusion

With this work, heading from N-ethylcarbazole, two novel schiff bases and their Cobalt (II), Nickel (II) and Manganese (II) complexes have been synthesized. All the spectral analysis supported the proposed structures of these newly synthesized compounds. All the synthesized

compounds have also been examined for their catalytic, thermal and electronic features. Good results have been obtained for the catalytic activities of the complex compounds in alkene oxidation reactions, especially Manganese (II) complex was the most effective in these reactions as catalyst.

Acknowledgement

References

[1] Rayati, S., Salehi, F., *Green oxidation of olefins and methyl phenyl sulfide with hydrogen peroxide catalyzed by an oxovanadium(IV) Schiff base complex encapsulated in the nanopores of zeolite-Y.*, Journal of Iranian Chemical Society, 12, 309-315, 2015.

[2] Hassana, H.M.A., Saada, E.M., Soltana, M.S., Betiha, M.A., Butle, I.S., Mostafa, S.I., *A palladium(II) 4-hydroxysalicylidene Schiff-base complex anchored on functionalized MCM-41: An efficient heterogeneous catalyst for the epoxidation of olefins*, Applied Catalysis A-General, 488, 148-159, 2014.

[3] Mavrogiorgoua, A., Papastergioua, M., Deligiannakis, Y., Louloudi, M., *Activated carbon functionalized with Mn(II) Schiff base complexes as efficient alkene oxidation catalysts: Solid support matters*, Journal Of Molecular Catalysis A-Chemical, 393, 8-17, 2014.

[4] Maiti, M., Sadhukhan, D., Thakurta, S., Zangrando, E., Pilet, G., Signorella, S., Bellú, S., Mitra, S., *Catalytic efficacy of copper(II) and cobalt(III) Schiff base complexes in aklene epoxidation*, Bulletin of Chemical Society of Japan, 87, 724-732, 2014.

[5] Shit, S., Saha, D., Saha, D., Row, T.N.G., Rizzoli, C., *Azide/thiocyanate incorporated cobalt(III)-Schiff base complexes: Characterizations and catalytic activity in aerobic epoxidation of olefins*, Inorganica Chimica Acta, 415, 103-110, 2014.

[6] Heshmatpour, F., Rayati, S., Hajiabbas, M.A., Abdolalian, P., Neumüller, B., *Copper(II) Schiff base complexes derived from 2,20 -dimethyl-propandiamine: Synthesis, characterization and catalytic performance in the oxidation of styrene and cyclooctene*, Polyhedron, 31, 443-450, 2012.

[7] Liu, D.F., Zhu, L.Q., Wu, J., Wu, L.Y., Lu, X.Q., *Ring-opening copolymerization of epoxides and anhydrides using Manganese(III) asymmetrical Schiff base complex catalysts*, RSC Advances, 5(5), 3854-3859, 2015.

[8] Wu, L.Y., Fan, D.D., Lü, X.Q., Lu, R., *Ring-opening Copolymerization of Cyclohexene Oxide and Maleic Anhydride Catalyzed by Mononuclear [Zn(L)(H2O)] or Binuclear [Zn2(L)(OAc)2(H2O)] Complex Based on the Salen-type Schiff-base Ligand*, Chinese Journal of Polymmer Science, 32(6), 768-777, 2014.

[9] Maleev, V.I., Chusov, D.A., Yashkina, L.V., Ikonnikov, N.S., II'in, M.M., *Asymmetric ring opening of epoxides with cyanides catalysed by chiral binuclear titanium complexes*, Tetrahedron-Asymmetry, 25, 838-843, 2014.

[10] Bal, S., Bal, S.S., Cobalt(II) and Manganese(II) Complexes of NovelSchiff Bases, *Synthesis, Characterization, and Thermal, Antimicrobial, Electronic, and Catalytic Features*, Advances in Chemistry, 2014, 1-12, 2014.

[11] Kadw, E., Bala, M.D., Friedrich, H.B., *Characterisation and application of montmorillonite-supported Fe Schiff base complexes as catalysts for the oxidation of n-octane*, Applied Clay Science, 95, 340-347, 2014.

[12] Noshiranzadeh, N., Emami, M., Bikas, R., S´lepokura, K., Lis, T., *Synthesis, characterization and catalytic reactivity of Mn(III) complexes with a scorpion-like bis(phenolate) ligand: Selective oxidation of primary alcohols to aldehydes*, Polyhedron, 72, 56-65, 2014.

[13] Wang, P., Dong, Z., Lei, Y., Du, Y., Li, H., Yang, H., Nie, Y., Ma, J., *Highly selective oxidation of alcohols catalyzed by Cu(II)-Schiff base-SBA-15 with hydrogen peroxide in water*, Journal of Porous Materials, 20, 277-284, 2013.

[14] Das, A., Kureshy, R.I., Maity, N.Ch., *Subramanian PS, Khan NH, R.Abdi SH, Suresh E, Bajaj HC. Synthesis and characterization of new chiral Cu(II)-N₄ complexes and their application in the asymmetric aza-Henry reaction*, Dalton Transactions, 43, 12357-12364, 2014.

[15] Amirnasr, M., Bagheri, M., Farrokhpour, H., Schenk, K.J., Mereiter, K., Ford, P.C., *New Zn(II) complexes with N2S2 Schiff base ligands. Experimental and theoretical studies of the role of Zn(II) in disulfide thiolate-exchange*, Polyhedron, 71, 1-7, 2014.

[16] Chandra, S., Vandana, K.S., *Synthesis, spectroscopic, anticancer, antibacterial and antifungal studies of Ni(II) and Cu(II) complexes with hydrazine carboxamide, 2-[3-methyl-2-thienyl methylene]*, Spectrochimica Acta Part A-Molecular and Biomolecular Spectroscopy., 135, 356-363, 2015.

[17] Nagesh, G.Y., Raj, K.M., Mruthyunjayaswamy, B.H.M., *Synthesis, characterization, thermal study and biological evaluation of Cu(II), Co(II), Ni(II) and Zn(II) complexes of Schiff base ligand containing thiazole moiety*, Journal of Molecular Structure, 1079, 423-432, 2015.

[18] Zhao, X.J., Xue, L.W., Zhang, C.X., *Schiff Base Copper(II) and Zinc(II) Complexes: Synthesis, Structures, and Antimicrobial Activities*, Synthesis and Reactivity in Inorganic Metal-Organic And Nano-Metal Chemistry, 45, 516-520, 2015.

[19] Proetto, M., Liu, W., Hagenbach, A., Abram, U., Gust, R., *Synthesis, characterization and in vitro antitumour activity of a series of novel platinum(II) complexes bearing Schiff base ligands*, European Journal of Medicinal Chemistry, 53, 168-175, 2012.

[20] Scozzafava, A., Menabuoni, L., Mincione, F., Mincione, G., Supuran, C.T., *Carbonic anhydrase inhibitors: synthesis of sulphonamides incorporating dtpa tails and of their zinc complexes with powerful topical antiglaucoma properties*, Bioorganic and Medicinal Chemistry Letters, 11(4), 575-582, 2001.

[21] Scozzafava, A., Supuran, C.T., *Carbonic Anhydrase and Matrix Metalloproteinase Inhibitors: Sulfonylated Amino Acid Hydroxamates with MMP Inhibitory Properties Act as Efficient Inhibitors of CA Isozymes I, II, and IV, and N-Hydroxysulfonamides Inhibit Both These Zinc Enzymes*, Journal of Medicinal Chemistry, 43, 3677-3687, 2000.

[22] Jiang, T., Wang, F., Tang, C., Zhang, X., Cao, X., Tao, Y., Huang, W., *Carbazole/phenylpyridine hybrid compound as dual role of efficient hostand ligand of iridium complex: Well matching of host-dopant for solution-processed green phosphorescent OLEDs*, Dyes Pigments, 150:130-138, 2018.

[23] Ott, J.C, Blasius, C.K, Wadepohl, H., Gade, L.H., *Synthesis, Characterization, and Reactivity of a High-Spin Iron(II) Hydrido Complex Supported by a PNP Pincer Ligand and Its Application as a Homogenous Catalyst for the Hydrogenation of Alkenes*, Inorganic Chemistry, 57, 3183-3191, 2018.

[24] Higuchi, J., Kuriyama, S., Eizawa, A., Arashiba, K., Nakajima, K., Nishibayashi, Y., *Preparation and reactivity of iron complexes bearing anionic carbazole-based PNP-type pincer ligands toward catalytic nitrogen fixation*, Dalton Transactions,;47, 1117-1121, 2018.

[25] Yu, Z.-J., Chen, H., Lennox, A.J.J., Yan, L.-J., Liu, X.-F., Xu, D.-D., Chen, F., Xu, L.-X., Li, Y., Wu, Q.-A., Luo, S.-P., *Heteroleptic copper(I) photosensitizers with carbazole-substitutedphenanthroline ligands: Synthesis, photophysical properties and applicationto photocatalytic H$_2$ generation*, Dyes and Pigments, 162, 771-775, 2019.

[26] Yingjun, L., Nan, Z., Jihong, L., Kun, J., Siyuan, W., *Detection of HSO$_4^-$ Ion with a Colorimetric and Fluorescent Probe Based on Hydrolysis Reaction of Carbazole-Derived Schiff Base in Aqueous Medium*, Chinese Journal of Organic Chemistry, 38, 3026-3031, 2018.

[27] Zarnegaryan, A., Pahlevanneshan, Z., Moghadam, M., Tangestaninejad, S., Mirkhani, V., Mohammdpoor-Baltork, I., *Copper(II) Schiff base complex immobilized on graphene nanosheets: a heterogeneous catalyst for epoxidation of olefins*, Jounal of Iranian Chemical Society, 16, 747-756, 2019.

[28] Hazra, S., Rocha, B.G.M., Guedes da Silva, M.F.C., Karmakar, A., Pombeiro, A.J.L., *Syntheses, Structures, and Catalytic Hydrocarbon Oxidation Properties of N-Heterocycle-Sulfonated Schiff Base Copper(II) Complexes*, Inorganics, 7, 17, 2019.

[29] Zakeri, H., Rayati, S., Zarei, G., *Synthesis and characterization of a Mn-Schiff base complex anchored on modified MCM-41 as a novel and recyclable catalyst for oxidation of olefins*, Applied Organomettalic Chemistry, 32, 4593, 2018.

[30] Yoon, K.R., Ko, S-O, Lee, S.M., Lee, H., *Synthesis and characterization of carbazole derived nonlinear optical dyes*, Dyes and Pigments, 75, 567-573, 2007.

[31] Grigoras, M., Antonoaia, N.-C., *Synthesis and characterization of some carbazole-based imine polymers*, European Polymer Journal, 41, 1079-1089, 2005.

[32] Hester, R.E., Plane, R.A., *Metal-Oxygen bonds in complexes: Raman spectra of trisacetylacetonato and trisoxalato complexes of Aluminum, Gallium and Indium*, Inorganic Chemistry, 3, 513-517, 1964.

[33] Finnie, K.S., Bartlett, J.R., Woolfrey, J.L., *Vibrational Spectroscopic Study of the Coordination of (2,2'-Bipyridyl-4,4'-dicarboxylic acid)ruthenium(II) Complexes to the Surface of Nanocrystalline Titania*, Langmuir, 14, 2744-2749, 1998.

[34] Deacon, G.B., Phillips, R.J., *Relationships Between the Carbon-Oxygen Stretching Frequencies of Carboxylato Complexes and The Type of Carboxylate Coordination*, Coordination Chemistry Reviews, 33, 227-250, 1980.

[35] Ispir, E., *The synthesis, characterization, electrochemical character, catalytic and antimicrobial activity of novel, azo-containing schiff bases and their metal complexes, Dyes and Pigments*, 82, 13-19, 2009.

[36] Kurtoglu, M., Ispir, E., Kurtoglu, N., Toroglu, S., Serin, S., *New soluble coordination chain polymers of nickel(II) and copper(II) ions and their biological activity*, Transition Metal Chemistry, 30, 765-770, 2005.

[37] Sawhney, K.J.S., Tiwari, M.K., Singh, A.K., Nandedkar'in, R.V., Joshi, S.K. et al. (Eds.). Proceedings of Sixth National Seminar on X-ray Spectroscopy and Allied Areas, pp. 130, 1998.

[38] Tiwari, M.K., Singh, A.K., Sawhney, K.J., *Analysis of stainless steel samples by energy dispersive X-ray fluorescence (EDXRF) spectrometry*, Bulletin of Materials Science, 24, 633-638, 2001.

[39] Roy, G.B., *Synthesis and study of physico-chemical properties of a new chiral Schiff baseligand and its metal complex*, Inorganica Chimica Acta, 362, 1709-1714, 2009.

[40] El-Seıdy, A.M.A., *In situ room temperature synthesis and characterization of salicylaldehyde phenylhydrazone metal complexes, their cytotoxic activity on MCF-7 cell line, and their ınvestigation as antibacterial and antifungal agents*, Synthesis and Reactivity in Inorganic Metal-Organic And Nano-Metal Chemistry, 45, 437-446, 2015.

[41] Shennar, K.A., Butcher, R.J., Greenaway, F.T., *Co(II), Cu(II), Mn(II) and Ni(II) complexes of maleic hydrazide,* Inorganica Chimica Acta, 425, 247-254, 2015.

[42] Yang, Q., Lei, Y., Wang, P., *Synthesis, X-Ray Structural Characterization, and Catalytic Property of a Manganese (II) Complex With 2-Bromo-6-[(3-cyclohexylammoniopropylimino)methyl]phenolate and Thiocyanate Ligands*, Synthesis and Reactivity in Inorganic Metal-Organic And Nano-Metal Chemistry, 44, 1208-1211, 2014.

[43] Bal, S., Orhan, B., Connolly, J.D., Digrak, M., Koytepe, S., *Synthesis and characterization of some Schiff bases, their metal complexes and thermal, antimicrobial and catalytic features*, Journal of Thermal Analysis And Calorimetry, 121, 909-917, 2015.

[44] Mukherjee, S., Samanta, S., Roy, B.C., Bhaumik, A., *Efficient allylic oxidation of cyclohexene catalyzed by immobilized Schiff base complex using peroxides as oxidants*, Applıed Catalysis A-General, 301, 79-88, 2006.

[45] Islam, S.M., Mondal, P., Mukherjee, S., Roy, A.S., Bhaumik, A., *A reusable polymer anchored copper(II) complex catalyst for the efficient oxidation of olefins and aromatic alcohol*, Polymers For Advanced Technologies, 22, 933-941, 2011.

Microwave-Assisted Rapid Synthesis of C@Fe₃O₄ Composite for Removal of

Microplastics from Drinking Water

Gökhan ELMACI[1],*

[1]*Department of Chemistry, School of Technical Sciences, Adıyaman University, TR-02040 Adıyaman, Turkey*
gelmaci@adiyaman.edu.tr, ORCID: 0000-0002-7235-0021

Abstract

Filtration is a basic requirement for the production of clean drinking water. However, filtering of large-scale drinking water is a time-consuming and costly process. Addressed herein is a new approach to the removal of microplastics, defined as dangerous organic pollutants, from water. As magnetic adsorbent, highly porous and well dispersed C@Fe₃O₄ composites were produced by a facile and rapid one-pot microwave synthesis method in minutes. The prepared C@Fe₃O₄ composites were used as an adsorbent in water contaminated with microplastics. The obtained results revealed that the microplastics adhered to the composite surface and were successfully removed from the water with an external magnet. In this point, this study provides a new approach to the rapid, effective, and low-cost removal of microplastic pollutants from drinking water.

Keywords: Filtration; Magnetic composites; Microwave-assisted synthesis; Micropollutant.

İçme Suyundan Mikroplastiklerin Uzaklaştırılması İçin C@Fe₃O₄ Kompozitinin Mikrodalga Destekli Hızlı Sentezi

Öz

Filtrasyon, temiz içme suyu için temel bir gerekliliktir. Bununla beraber, büyük miktarda içme suyunun filtrelenmesi zaman alıcı ve maliyetli bir işlemdir. Tehlikeli bir organik kirletici olarak tanımlanan mikroplastiklerin sudan uzaklaştırılmasına yeni bir yaklaşım sunulmaktadır. Manyetik adsorban olarak, son derece gözenekli ve iyi dağılmış $C@Fe_3O_4$ kompoziti dakikalar içinde kolay ve hızlı mikrodalga destekli sentez yöntemiyle üretildi. Hazırlanan $C@Fe_3O_4$ kompoziti, mikroplastiklerle kirletilmiş suda bir adsorban olarak kullanıldı. Elde edilen sonuçlar, mikroplastiklerin kompozit yüzeye yapıştığını ve harici bir mıknatısla sudan başarıyla çıkarıldığını ortaya koydu. Bu noktada, bu çalışma mikroplastik kirleticilerin içme suyundan hızlı, etkili ve düşük maliyetli olarak uzaklaştırılmasına yeni bir yaklaşım sunmaktadır.

Anahtar Kelimeler: Filtrasyon; Manyetik kompozitler; Mikrodalga destekli sentez; Mikrokirletici.

1. Introduction

In recent years, magnetic materials have attracted a great attention because they can be produced effectively and efficiently from abundant raw materials [1, 2]. These materials can be used in different roles such as absorbents, catalysts, capacitors, energy storage systems, and sensors in various applications [3-9]. Especially, magnetic composites are used in the field of catalytic decomposition and removal of organic pollutants in environmental applications [10-12]. In addition, magnetic property significantly reduces recovery costs after the use of the material [10, 13]. This advantage allows the repeated use of these materials in many applications such as catalytic process and filtering systems [5, 14-16]. As a result of these advantages, magnetic materials will become more important in the future in terms of their potential applications. Therefore, the production of their composites in a cheap, fast, and an efficient way plays a vital role.

Microwave-assisted synthesis technology has been emerging as an alternative method for higher efficiency, selectivity, and large-scale production of nanoparticles compared to the conventional synthesis methods [17-23]. This technology is a fast synthesis technique that consumes relatively low energy [24, 25]. In particular, it provides efficient heating, which leads to a uniform size distribution of nanoparticles [23, 26, 27]. Thanks to controlled heating, it prevents the formation of many side reactions, and thus provides efficiency and repeatability in the production of nanoparticles [28-30]. Therefore, microwave technology is an indispensable part of green chemistry [19, 31].

The low-cost and fast production of magnetic composites have gained increasing interest as filtering materials to obtain clean drinking water [32, 33]. Carbon-based magnetic materials

are used to remove heavy metal ions, organic dyes, and microbial contaminants from water [34, 35]. In addition, microplastics are defined as organic pollutants that are becoming increasingly dangerous to human health [36-38]. New composites are being developed as an alternative to traditional filter materials such as natural minerals, zeolites, and porous carbon absorbents used to clean drinking water [39-41]. Due to its porous structure and high surface area, carbon-based magnetic composites can be an alternative to conventional filter materials to remove microplastic pollutants from drinking water [42, 43].

The present paper introduces a rapid synthetic strategy, which allows the production of highly porous and well dispersed C@Fe₃O₄ composites in minutes. Furthermore, the produced C@Fe₃O₄ composites were evaluated to remove microplastic pollutants from drinking water.

2. Experimental

2.1. Chemicals and materials

The reagent grade chemicals, Polystyrene beads (3μm), Glucose, FeCl₃, FeCl₂. 4H₂O and Ammonium hydroxide (30-32%) were purchased from Sigma-Aldrich. All reactions were carried out using deionized water (resistivity < 18 MΩ·cm).

2.2. Instrumentation

The TGA analysis was carried out with a HITACHI SII 7300 with a heating rate of 2 °C min^{-1} under an air atmosphere. The XRD (X-ray diffraction) patterns were performed on a Pan Analytical Empyrean instrument with Cu Kα radiation (λ = 1.54056 Å) from 3 to 70° (2θ) at a scanning rate of 2° min^{-1}. The micro-morphology and structure of sample were examined using Scanning electron microscopy, and Transmission electron microscopy (SEM, ZEISS Sigma 300; TEM, Hitachi HT 7700). The magnetic properties were performed on a VSM device (Quantum Designed Physical Property Measurement System) in the magnetic field range of ±20 kOe. The Brunauer−Emmett−Teller (BET) specific surface area of C@Fe₃O₄ was calculated by nitrogen sorption isotherms that were measured on a Micromeritics 3Flex instrument, to obtain the surface area. Microwave-irradiated reactions were conducted on a microwave reactor (Discover SP, CEM, Matthews, NC, USA).

2.3. Preparation of C@Fe₃O₄ composite

1.02 g of FeCl₃, 2.45 g of FeCl₂. 4H₂O was dissolved in a 80 mL of de-ionized water, and then 5 mL of 0.1M NH₄OH solution added over it dropwise. The solution was refluxed under microwave irradiation according to the desired program (200 W, 100 °C, hold for 10 min). 2 g of

glucose was dissolved in 5 mL of de-ionized water, then glucose solution added over as-prepared Fe_3O_4 suspension. The suspension was refluxed under microwave irradiation at 130 °C for 10 min. Finally, the $C@Fe_3O_4$ composite was filtered, washed with deionized water several times, and then dried at 70°C for 12 h.

2.4. Micropollutant removal batch studies

Drinking water samples were obtained from the local market in Turkey and used without further purification or any treatments in the micropollutant removal studies. In a sample batch study, an appropriate amount of polystyrene beads were dispersed in the drinking water for 30 min in an ultrasonic bath. Then, the resulting suspensions were treated with the produced $C@Fe_3O_4$ composites in order evaluate their micropollutant removal efficiencies from the drinking water samples.

3. Results and Discussion

Powder XRD was used to confirm the crystal structure of $C@Fe_3O_4$ composite. Fig. 1a shows the XRD diffraction pattern of $C@Fe_3O_4$. The X-ray diffraction pattern of the $C@Fe_3O_4$ exhibits a broad peak centered at 22.21°, which is attributed to amorphous carbon support. The peaks of Fe_3O_4 at 30.28°, 35.63°, 36.754°, 43.36°, 53.93°, 57.942°, and 63.58° are consistent with the (220), (311), (222), (400), (422), (511), and (440) of the standard card of Fe_3O_4 (JCPDS 65–3107) (Fig. 1a). XRD data confirms the presence of both magnetic Fe_3O_4 and amorphous carbon in the composite structure.

Separation of the produced composite from the suspended solution with an external magnet is an important feature to reduce recovery costs and saving time. Thus, synthesis of magnetite, which exhibit relatively high magnetization among other magnetic metal oxides, was chosen. The magnetic properties of $C@Fe_3O_4$ composite were investigated using VSM device (Quantum Designed Physical Property Measurement System). Fig. 1b display a representative magnetization curve of $C@Fe_3O_4$ measured at room temperature, which exhibit typical superparamagnetic behavior and the saturation magnetization of the $C@Fe_3O_4$ is 48.3 emu/g.

The solution containing Fe^{2+} and Fe^{3+} salts forms the highly soluble ferrihydrite ($Fe(OH)_3$) in basic medium [44]. It is then possible that $Fe(OH)_3$ can react with Fe^{2+} species and precipitate as magnetite (Fe_3O_4). The following reaction takes place (predictably) during microwave-assisted synthesis; $2Fe(OH)_3 + Fe^{2+} \rightarrow Fe_3O_4 + 2H_2O + 2H^+$.
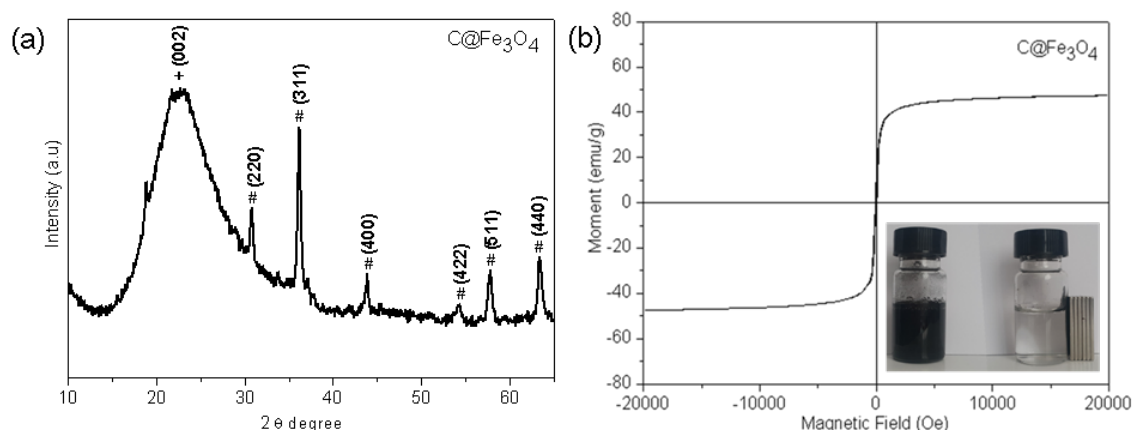
Figure 1: (a) XRD pattern of C@Fe$_3$O$_4$, (b) room temperature magnetization curve of C@Fe$_3$O$_4$

Thanks to the microwave-assisted controlled heating, this suspension was completely transformed into the nearly monodisperse Fe$_3$O$_4$ nanoparticles with a uniform size within a short period of 10 min (Scheme 1).
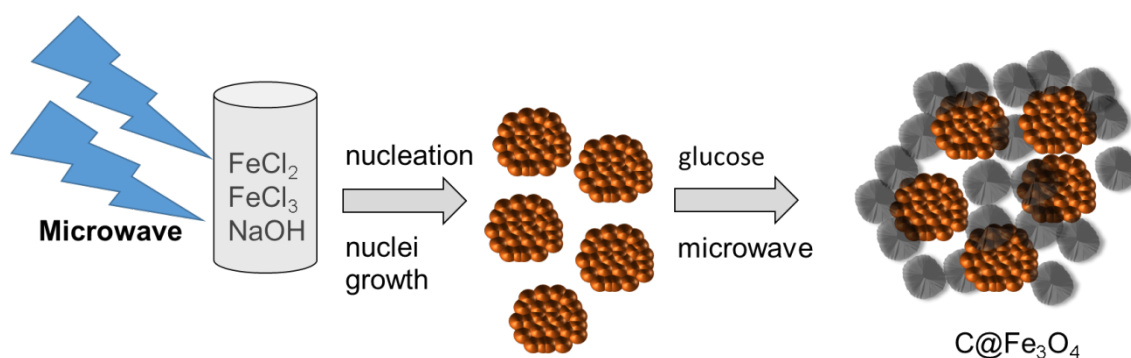

Scheme 1: Schematic of the synthesis procedure of C@Fe$_3$O$_4$

SEM and TEM analysis techniques were used to investigate the shape and size of the particles forming the components of the composite. SEM image of Fe$_3$O$_4$ particles in the composite revealed that the average diameter was ~90 nm, producing an interconnected porous network with carbon support seen in Fig. 2a. In addition, TEM image shows that carbon support has a spherical shape with an average size of ≈40 nm decorated with spherical Fe$_3$O$_4$ (Fig. 2b).
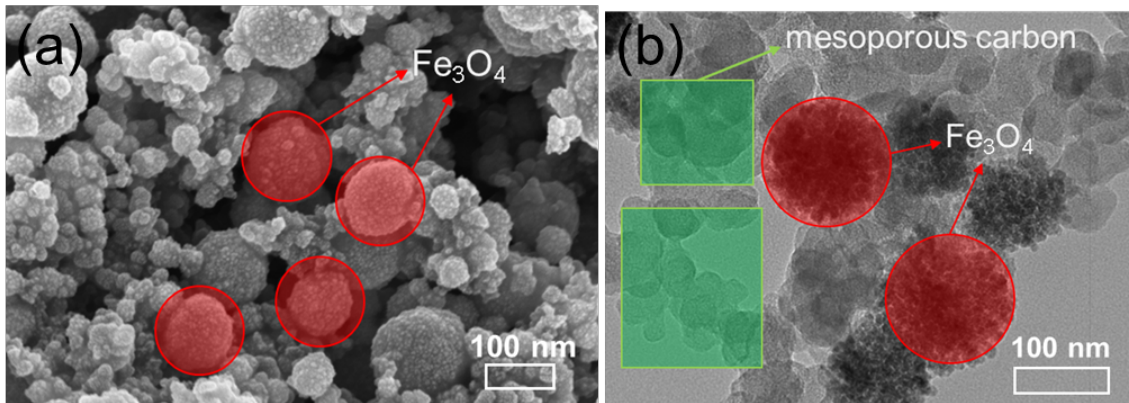
Figure 2: (a) SEM image of C@Fe$_3$O$_4$, (b)TEM image of C@Fe$_3$O$_4$

Thermal stability of the C@Fe$_3$O$_4$ was characterized by TGA (Fig. 3a). The first weight-loss in the temperature range of ca. 30−120 °C might result from the loss of adsorbed water. The second weight-loss broader range of ca. 250−450 °C was presumably due to the decomposition of the C@Fe$_3$O$_4$, in which the carbon support oxidized to CO$_2$. This is followed by a more drastic weight loss starting at ca. 450 °C, revealing a nearly complete decomposition of the Fe$_3$O$_4$ to Fe$_2$O$_3$.On the other hand, the porosity information on C@Fe$_3$O$_4$ composite was characterized by a N$_2$ adsorption-desorption study, and the BET surface area of C@Fe$_3$O$_4$ was measured to be 250.1 m^2/g.
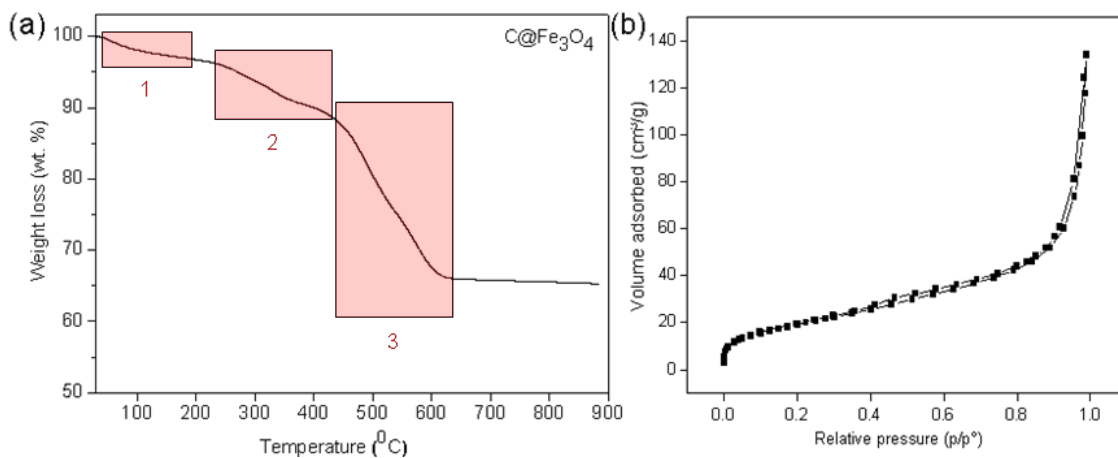

Figure 3: (a) TGA curve of C@Fe$_3$O$_4$, (b)Nitrogen adsorption-desorption isotherm of C@Fe$_3$O$_4$

Microplastics are defined among common aquatic pollutants with a size range of 0.1 μm - 5 mm [45, 46]. The main source of these pollutants is the result of mechanical and chemical decomposition of large quantities of plastics produced. Microplastics transported to the seas and lakes by wastewater threaten all aquatic life [47]. In addition, these pollutants are also a great threat to mammals through the food chain. Moreover, its toxicity to living organism in the

growing period is even higher [45-47]. Therefore, these organic pollutants should be removed from water sources with effective and low-cost methods. For this purpose, $C@Fe_3O_4$ composite was produced as a model sorbent by microwave-assisted synthesis method to remove microplastics from water. Polystyrene beads were used to represent microplastics as organic pollutants.

20 mg of polystyrene beads were dispersed in 20 ml of water for 30 minutes in the sonicator. Then 5 mg of composite was added to this suspension and the heterogeneous mixture was sonicated for 30 minutes. The suspension containing composite and polystyrene beads were separated by an external magnet from the drinking water in 2 minutes (Fig. 4b). Then, this structure was examined in detail with SEM and EDX measurements. SEM image shows that the $C@Fe_3O_4$ composite adheres to the surface of polystyrene beads (Fig. 4a). In this way, polymer beads suspended in water were easily separated with the help of an external magnet (Fig. 4b). Furthermore, the energy dispersive X-ray (EDX) elemental mapping clearly confirms that the $C@Fe_3O_4$ composite completely cover on the polystyrene beads (Fig. 4a).
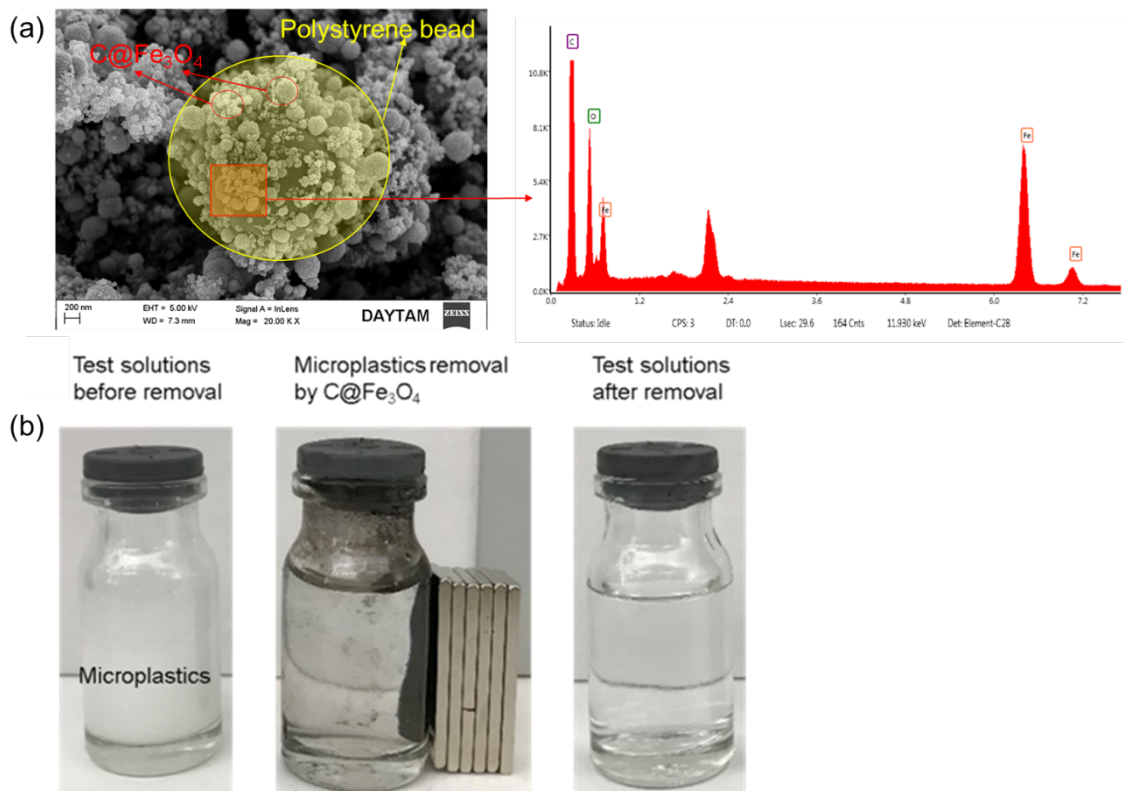
Figure 4: (a) SEM and EDX images of micro-sized polystyrene beads covered $C@Fe_3O_4$ composite, (b) Microplastics removal by magnetic $C@Fe_3O_4$. SEM image of micro-sized polystyrene beads covered $C@Fe_3O_4$ composite

4. Conclusions

In summary, we prepared highly porous and well dispersed C@Fe$_3$O$_4$ composite by a facile and rapid one-pot microwave synthesis method in minutes. The introduced microwave process led to the production of homogeneous particle size distribution Fe$_3$O$_4$ (~ 90nm) and high surface area carbon support (250.1 m^2/g), using low-cost starting materials. Furthermore, C@Fe$_3$O$_4$ composite was used as an adsorbent in water contaminated with microplastics. The microplastics adhered to the composite surface and were successfully removed from the water with an external magnet. Overall, this study provides a new approach to the rapid, effective, and low-cost removal of microplastic pollutants from drinking water samples.

Acknowledgement

References

[1] Ahmadian-Fard-Fini, S., Salavati-Niasari, M., Ghanbari, D., *Hydrothermal green synthesis of magnetic Fe$_3$O$_4$-carbon dots by lemon and grape fruit extracts and as a photoluminescence sensor for detecting of E. coli bacteria*, Spectrochimica Acta Part a-Molecular and Biomolecular Spectroscopy, 203, 481-493, 2018.

[2] Maensiri, S., Sangmanee, M., Wiengmoon, A. Magnesium Ferrite (MgFe$_2$O$_4$) Nanostructures Fabricated by Electrospinning., Nanoscale Res. Lett., 4, 221-228, 2009.

[3] Hajalilou, A., Kianvash, A., Lavvafi, H., Shameli, K., *Nanostructured soft magnetic materials synthesized via mechanical alloying: a review.*, Journal of Materials Science: Materials in Electronics, 29, 1690-1717, 2018.

[4] Zhukov, A. Novel Functional Magnetic Materials, Springer, 2016.

[5] Elmaci, G., Ozer, D., Zumreoglu-Karan, B., *Liquid phase aerobic oxidation of benzyl alcohol by using manganese ferrite supported-manganese oxide nanocomposite catalyst*, Catalysis Communications, 89, 56-59, 2017.

[6] Elmaci, G., Frey, C.E., Kurz, P., Zümreoğlu-Karan, B., *Water oxidation catalysis by birnessite@ iron oxide core–shell nanocomposites*, Inorganic Chemistry, 54, 2734-2741, 2015.

[7] Elmacı, G., Frey, C.E., Kurz, P., Zümreoğlu-Karan, B., *Water oxidation catalysis by using nano-manganese ferrite supported 1D-(tunnelled), 2D-(layered) and 3D-(spinel) manganese oxides*, Journal of Materials Chemistry A, 4, 8812-8821, 2016.

[8] Kayili, H.M., Ertürk, A.S., Elmacı, G., Salih, B., *Poly (amidoamine) dendrimer coated magnetic nanoparticles for the fast purification and selective enrichment of glycopeptides and glycans*, Journal of Separation Science, 42, 3209-3216, 2019.

[9] Elmacı, G., Özgenç, G., Kurz, P., Zumreoglu-Karan, B., *Enhanced water oxidation performances of birnessite and magnetic birnessite nanocomposites by transition metal ion doping*, Sustainable Energy & Fuels, 4, 3157-3166, 2020.

[10] Gómez-Pastora, J., Dominguez, S., Bringas, E., Rivero, M.J., Ortiz, I., Dionysiou, D.D., *Review and perspectives on the use of magnetic nanophotocatalysts (MNPCs) in water treatment*, Chemical Engineering Journal, 310, 407-427, 2017.

[11] Xiao, D., Lu, T., Zeng, R., Bi, Y., *Preparation and highlighted applications of magnetic microparticles and nanoparticles: a review on recent advances*, Microchimica Acta, 183, 2655-2675, 2016.

[12] Karan, B., *Degradation of Crystal Violet Dye from Waters by Layered MnO_2 and Nanocomposite-$MnO_2@$ $MnFe_2O_4$ Catalysts*, Hacettepe Journal of Biology and Chemistry, 45, 573-580, 2018.

[13] Negin, C., Ali, S., Xie, Q., *Application of nanotechnology for enhancing oil recovery– A review*, Petroleum, 2, 324-333, 2016.

[14] Chen, H., Wang, X., Bi, W., Wu, Y., Dong, W., *Photodegradation of carbamazepine with $BiOCl/Fe_3O_4$ catalyst under simulated solar light irradiation*, Journal of colloid and interface science, 502, 89-99, 2017.

[15] Tudorache, M., Opris, C., Cojocaru, B., Apostol, N.G., Tirsoaga, A., Coman, S.M., et al., *Highly efficient, easily recoverable, and recyclable re–SiO_2–Fe_3O_4 catalyst for the fragmentation of lignin*, ACS Sustainable Chemistry & Engineering, 6, 9606-9618, 2018.

[16] Fan, R., Min, H., Hong, X., Yi, Q., Liu, W., Zhang, Q., et al., *Plant tannin immobilized $Fe_3O_4@$ SiO_2 microspheres: A novel and green magnetic bio-sorbent with superior adsorption capacities for gold and palladium*,Journal of Hazardous Materials, 364, 780-790, 2019.

[17] Kumar, A., Kuang, Y., Liang, Z., Sun, X., *Microwave Chemistry, Recent Advancements and Eco-Friendly Microwave-Assisted Synthesis of Nanoarchitectures and Their Applications: A Review*, Materials Today Nano, 100076, 2020.

[18] Singh, R., Kumar, R., Singh, D., Savu, R., Moshkalev, S., *Progress in microwave-assisted synthesis of quantum dots (graphene/carbon/semiconducting) for bioapplications: a review*, Materials Today Chemistry, 12, 282-314, 2019.

[19] Zuliani, A., Balu, A.M., Luque, R., *Efficient and environmentally friendly microwave-assisted synthesis of catalytically active magnetic metallic Ni nanoparticles*, ACS Sustainable Chemistry & Engineering, 5, 11584-11587, 2017.

[20] Ertürk, A.S., Elmacı, G., *PAMAM dendrimer functionalized manganese ferrite magnetic nanoparticles: microwave-assisted synthesis and characterization. Journal of Inorganic and Organometallic Polymers and Materials*, 28, 2100-2107, 2018.

[21] Ertürk, A.S., *Controlled Production of Monodisperse Plant Mediated AgNP Catalysts Using Microwave Chemistry: A Desirability Function Based Multiple Response Optimization Approach*, ChemistrySelect, 4, 9300-9308, 2019.

[22] Koca, M., Ertürk, A.S., Umaz, A., *Microwave-assisted intermolecular aldol condensation: Efficient one-step synthesis of 3-acetyl isocoumarin and optimization of different reaction conditions*, Arabian Journal of Chemistry, 11, 538-545, 2018.

[23] Elmaci, G., *Microwave Assisted Green Synthesis of Ag/AgO Nanocatalyst as An Efficient OER Catalyst in Neutral Media*, Hittite Journal of Science & Engineering, 7, 61-65, 2020.

[24] de Medeiros, T.V., Manioudakis, J., Noun, F., Macairan, J.-R., Victoria, F., Naccache, R., *Microwave-assisted synthesis of carbon dots and their applications*, Journal of Materials Chemistry C, 7, 7175-7195, 2019.

[25] Gaudino, E.C., Cravotto, G., Manzoli, M., Tabasso, S.,*From waste biomass to chemicals and energy via microwave-assisted processes*, Green Chemistry, 21, 1202-1235, 2019.

[26] Schneider, T., Löwa, A., Karagiozov, S., Sprenger, L., Gutiérrez, L., Esposito, T., et al., *Facile microwave synthesis of uniform magnetic nanoparticles with minimal sample processing*, Journal of Magnetism and Magnetic Materials, 421, 283-291, 2017.

[27] Elmacı, G., *Magnetic Hollow Biocomposites Prepared from Lycopodium clavatum Pollens as Efficient Recyclable Catalyst*, ChemistrySelect, 5, 2225-2231, 2020.

[28] Ragupathi, C., Vijaya, J.J., Kennedy, L.J., *Preparation, characterization and catalytic properties of nickel aluminate nanoparticles: A comparison between conventional and microwave method*, Journal of Saudi Chemical Society, 21, 231-239, 2017.

[29] Xu, S., Zhong, G., Chen, C., Zhou, M., Kline, D.J., Jacob, R.J., et al., *Uniform, scalable, high-temperature microwave shock for nanoparticle synthesis through defect engineering*, Matter, 1, 759-769, 2019.

[30] Cai, Y., Piao, X., Gao, W., Zhang, Z., Nie, E., Sun, Z.,*Large-scale and facile synthesis of silver nanoparticles via a microwave method for a conductive pen*, RSC Advances, 7, 34041-34048, 2017.

[31] Wang, M., Wang, Z., Wei, L., Li, J., Zhao, X., *Catalytic performance and synthesis of a Pt/graphene-TiO$_2$ catalyst using an environmentally friendly microwave-assisted solvothermal method*, Chinese Journal of Catalysis, 38, 1680-1687, 2017.

[32] Li, B., Zhou, F., Huang, K., Wang, Y., Mei, S., Zhou, Y., et al., *Environmentally friendly chitosan/PEI-grafted magnetic gelatin for the highly effective removal of heavy metals from drinking water*, Scientific Reports, 7, 1-9, 2017.

[33] Puente-Urbina, A., Montero-Campos, V.,*Porous materials modified with Fe$_3$O$_4$ nanoparticles for arsenic removal in drinking water*, Water, Air, & Soil Pollution, 228, 374, 2017.

[34] Latibari, S.T., Sadrameli, S.M., *Carbon based material included-shaped stabilized phase change materials for sunlight-driven energy conversion and storage: An extensive review*, Solar Energy, 170, 1130-1161, 2018.

[35] Ribeiro, R.S., Silva, A.M., Figueiredo, J.L., Faria, J.L., Gomes, H.T., *Catalytic wet peroxide oxidation: a route towards the application of hybrid magnetic carbon nanocomposites for the degradation of organic pollutants. A review*,Applied Catalysis B: Environmental, 187, 428-460, 2016.

[36] Fossi, M.C., Baini, M., Panti, C., Galli, M., Jiménez, B., Muñoz-Arnanz, J., et al., *Are whale sharks exposed to persistent organic pollutants and plastic pollution in the Gulf of California (Mexico) First ecotoxicological investigation using skin biopsies*, Comparative Biochemistry and Physiology Part C: Toxicology & Pharmacology, 199, 48-58, 2017.

[37] Liu, G., Zhu, Z., Yang, Y., Sun, Y., Yu, F., Ma, J., *Sorption behavior and mechanism of hydrophilic organic chemicals to virgin and aged microplastics in freshwater and seawater*, Environmental Pollution, 246, 26-33, 2019.

[38] Jiang, J.-Q., *Occurrence of microplastics and its pollution in the environment: A review*, Sustainable Production and Consumption, 13, 16-23, 2018.

[39] Chandrakala, B., Vasudha, D., Yaseen, M., Aravinda, H., *Purification of water using low cost adsorbents-fly ash and activated carbon*, International Journal of Advanced Research in Science and Technology, 3, 1237-1242, 2018.

[40] Pandey, S. A., *Comprehensive review on recent developments in bentonite-based materials used as adsorbents for wastewater treatment*, Journal of Molecular Liquids, 241, 1091-1113, 2017.

[41] Yadav, K.K., Gupta, N., Kumar, V., Khan, S.A., Kumar, A., *A review of emerging adsorbents and current demand for defluoridation of water: bright future in water sustainability*, Environment International, 111, 80-108, 2018.

[42] Namvari, M., Namazi, H., *Preparation of efficient magnetic biosorbents by clicking carbohydrates onto graphene oxide*, Journal of Materials Science, 50, 5348-5361, 2015

[43] Soares, S.F., Fernandes, T., Trindade, T., Daniel-da-Silva, A.L., *Surface engineered magnetic biosorbents for water treatment. In: Green Adsorbents for Pollutant Removal*, Springer, , 301-342, 2018.

[44] Hansel, C.M., Benner, S.G., Fendorf, S., *Competing Fe (II)-induced mineralization pathways of ferrihydrite*, Environmental Science & Technology, 39, 7147-7153, 2005.

[45] Cole, M., Lindeque, P., Halsband, C., Galloway, T.S., *Microplastics as contaminants in the marine environment: a review*, Marine Pollution Bulletin, 62, 2588-2597, 2011.

[46] do Sul, J.A.I., Costa, M.F., *The present and future of microplastic pollution in the marine environment*, Environmental Pollution, 185, 352-364, 2014.

[47] Sharma, S., Chatterjee, S., *Microplastic pollution, a threat to marine ecosystem and human health: a short review*, Environmental Science and Pollution Research, 24, 21530-21547, 2017.

On Δ-Uniform and Δ-Pointwise Convergence on Time Scale

Mustafa Seyyit SEYYİDOĞLU[1,*], Ayşe KARADAŞ[2]

[1]*Uşak University, Department of Mathematics, Uşak, Turkey*
seyyit.seyyidoglu@usak.edu.tr, ORCID: 0000-0001-9129-1373
[2]*Uşak University, Institute of Science and Technology, Uşak, Turkey*
aysekaradas9496@gmail.com, ORCID: 0000-0000-0000-0000

Abstract

In this article, we define the concept of Δ-Cauchy, Δ-uniform convergence and Δ-pointwise convergence of a family of functions $\{f_j\}_{j\in\mathbb{J}}$, where $\mathbb{J}$ is a time scale. We study the relationships between these notions. Moreover, we introduced sufficient conditions for interchangeability Δ-limitation with Riemann Δ-integration or Δ-differentiation. Also, we obtain the analogue of the well-known Dini's Theorem.

Keywords: Δ-Convergence; Δ-Cauchy; Statistical convergence.

Zaman Skalası Üzerinde Δ-Düzgün ve Δ-Noktasal Yakınsaklık

Öz

Bu makalede $\mathbb{J}$ bir zaman skalası olmak üzere, $\{f_j\}_{j\in\mathbb{J}}$ fonksiyon ailesi için Δ-Cauchy, Δ-düzgün yakınsaklık ve Δ-noktasal yakınsaklık kavramları verilerek bu kavramlar arasındaki ilişkiler incelenmiştir. Δ-limit ile Riemann Δ-integrali ve Δ-türevin yer değişme problemi araştırılarak Dini Teoreminin farklı bir versiyonu elde edilmiştir.

Anahtar Kelimeler: Δ-Yakınsaklık; Δ-Cauchy; İstatistiksel yakınsaklık.

1. Introduction and Preliminaries

The time scale calculus was introduced in 1989 by German mathematician Stefan Hilger [1]. It is a unification of the theory of differential equations with that of difference equations. This theory was developed to a certain extent in [2] by Hilger.

The notion of statistical convergence for complex number sequences was introduced by Fast in [3]. Schoenberg gave some properties of this concept [4]. Fridy progressed with the statistically Cauchy and showed the equivalence of these concepts in [5].

In recent years, there are many studies based on the density function, which is defined on some subsets of time scale. For instance, first author and Tan [6] gave the notions of Δ-Cauchy and Δ-convergence of a function defined on time scale by using Δ-density. The notion of m- and (λ, m)- uniform density of a set and the concept of m- and (λ, m)- uniform convergence on a time scale were presented by Altin et al. [7]. Also, Altin et al. gave λ-statistical convergence on time scale and examined some of its features [8]. Some fundamental properties of Lacunary statistical convergence and statistical convergence on time scale investigated by Turan and Duman in [9].

Let $\mathcal{S}$ be the collection of all subsets of time scale $\mathbb{J}$ in the form of $[a, b)$, where $[a, a) = \emptyset$. Then $\mathcal{S}$ is a semiring on $\mathbb{J}$. The set function m defined by $m([a, b)) = b - a$ is a measure on $\mathcal{S}$. The outer measure $m^*: \mathcal{S} \to [0, \infty]$ generated by m is defined by

$$m^*(A) := \inf \left\{ \sum_{n=1}^{\infty} (b_n - a_n) : A \subset \bigcup_{n=1}^{\infty} [a_n, b_n) \right\}.$$

The family of all m^*-measurable (it is also called Δ-measurable) sets $\mathcal{M} = \mathcal{M}(m^*)$ is a σ-algebra and it is well known that from the measure theory the restriction of m^* to $\mathcal{M}$, which we denote by μ_Δ, is a measure. This measure is called Lebesgue Δ-measure on $\mathbb{J}$.

Definition 1. [5] Let $A \subset \mathbb{N}$, and

$$A_n = \sum_{m \leq n, m \in A} 1.$$

The asymptotic density of A is defined by $\delta(A) = lim_n n^{-1} A_n$, which is also called natural density. The real number sequence $x = (x_n)$ is statistically convergent to l if for each $\epsilon > 0$, $\delta(\{n \in \mathbb{N}: |x_n - l| \geq \epsilon\}) = 0$; in this case we write st-lim $x = l$.

From now on we assume that sup $\mathbb{J} = \infty$ and $\mathbb{J}$ has a minimum for the time scale $\mathbb{J}$.

Definition 2. (Δ -Density) [6] Let B be a subset of $\mathbb{J}$ such that $B \in \mathcal{M}$ and $a = \min \mathbb{J}$. Δ-density of B in $\mathbb{J}$ is defined by

$$\delta_\Delta(B) := \lim_{j \to \infty} \frac{\mu_\Delta(B \cap [a,j])}{\sigma(j) - a}$$

provided that this limit exists.

A property of points of $\mathbb{J}$ is said to hold Δ-almost everywhere (or Δ-almost all $j \in \mathbb{J}$) if the set of points in $\mathbb{J}$ at which it fails to hold has zero Δ-density. The expression Δ-almost everywhere abbreviated to Δ-a.e.

Definition 3. (Δ -Convergence) [6] If for every $\epsilon > 0$, the inequality $|g(j) - l| < \epsilon$ holds Δ-a.e. on $\mathbb{J}$, then $g: \mathbb{J} \to \mathbb{R}$ is called Δ-convergent to $l \in \mathbb{R}$ (or has Δ-limit). In this case we write $\Delta\text{-}lim_{j \to \infty} f(j) = l$.

Definition 4. (Δ-Cauchy) [6] The function $g: \mathbb{J} \to \mathbb{R}$ is Δ-Cauchy provided that for each $\epsilon > 0$, there exist $K = K(\epsilon) \subset \mathbb{J}$ and $j_0 \in \mathbb{J}$ such that $\delta_\Delta(K) = 1$ and $|g(j) - g(j_0)| < \epsilon$ holds for all $j \in K$.

Note that the Δ-density, Δ-Cauchy and Δ-Convergence coincide with the natural density, statistical Cauchy and statistical convergence respectively whenever $\mathbb{J}$ is the natural numbers.

2. Δ-Pointwise and Δ-Uniform Convergence

In this section, we will deal with the family of functions $\{f_j\}_{j \in \mathbb{J}}$ whose elements defined on any subset of real numbers.

Definition 5. (Δ-Pointwise Convergence) Let $B \subset \mathbb{R}$ and for each $j \in \mathbb{J}$, f_j and f be real valued functions on B. The family $\{f_j\}_{j \in \mathbb{J}}$ converges Δ-pointwise to f on B, if for each given $\epsilon > 0$ and $t \in B$, the inequality $|f_j(t) - f(t)| < \epsilon$ holds Δ-a.e. on $\mathbb{J}$. This notion is abbreviated as $\{f_j\}_{j \in \mathbb{J}} \to f$ on B.

Definition 6. (Δ-Uniform Convergence) Let $B \subset \mathbb{R}$ and for each $j \in \mathbb{J}$, f_j and f be real valued functions on B. The family $\{f_j\}_{j \in \mathbb{J}}$ converges Δ-uniformly to f on B, if for each given $\epsilon > 0$, the inequality $|f_j(t) - f(t)| < \epsilon$ holds Δ-a.e. on $\mathbb{J}$ and for all $t \in B$. In this case we write $\{f_j\}_{j \in \mathbb{J}} \rightrightarrows f$ on B.

Definition 7. (Δ-Uniform Cauchy) Let $B \subset \mathbb{R}$ and $\{f_j\}$ be a family of real valued functions defined on B. The family $\{f_j\}_{j \in \mathbb{J}}$, Δ-uniform Cauchy on B, if for all $\epsilon > 0$ there exists a subset $K = K(\epsilon)$ of $\mathbb{J}$ and $j_0 \in \mathbb{J}$ such that $\delta_\Delta(K) = 1$ and $|f_j(t) - f_{j_0}(t)| < \epsilon$ for all $j \in K$ and for all $t \in B$.

Example 8. Let $\mathbb{J} = [0, \infty)$ and $B \subset \mathbb{R}$. We denote the irrational and rational numbers in $[0, \infty)$ by $\mathbb{I}_{[0,\infty)}$ and $\mathbb{Q}_{[0,\infty)}$, respectively. We consider the functions $f_j : B \to \mathbb{R}$ ($j \in \mathbb{J}$) defined as;

$$f_j(t) = \begin{cases} \sin jt, & j \in \mathbb{Q}_{[0,\infty)} \\ 0, & j \in \mathbb{I}_{[0,\infty)} \end{cases}.$$

Since the set $\mathbb{Q}_{[0,\infty)}$ has zero density in $\mathbb{J}$, the density of $\mathbb{I}_{[0,\infty)}$ is one. Hence, $\{f_j\}_{j \in \mathbb{J}} \rightrightarrows f = 0$ on B.

It is easily seen that Δ-uniform convergence implies Δ-pointwise convergence, but the converse is not always true as we can see from the following counter-examle.

Example 9. Let $\mathbb{J} = [1, \infty)$ and $j \in \mathbb{J}$. Consider the functions $f_j : [0, \infty) \to \mathbb{R}$ defined as;

$$f_j(t) = \begin{cases} \frac{t}{j}, & j \in \mathbb{Q}_{[1,\infty)} \\ 0, & j \in \mathbb{I}_{[0,\infty)} \end{cases}.$$

Although $\{f_j\}_{j \in \mathbb{J}}$ is Δ-pointwise convergent to $f = 0$, it is not Δ-uniform convergent.

The proof of the following theorem is clear.

Theorem 10. Let $(f_n)_{n \in \mathbb{N}}$ be a sequence of real valued functions defined on $B \subset \mathbb{R}$. If $(f_n)_{n \in \mathbb{N}}$ converges uniformly (pointwise) to f, then $\{f_n\}_{n \in \mathbb{N}}$ converges Δ-uniformly (Δ-pointwise) to f.

Theorem 11. Let $\{f_j\}_{j \in \mathbb{J}}$ be a family of real valued functions defined on $B \subset \mathbb{R}$. If $\{f_j\}_{j \in \mathbb{J}} \to f$ on B, then $\{f_j\}_{j \in \mathbb{J}} \rightrightarrows f$ on B if and only if

$$\Delta - \limsup_{j \to \infty} \sup_{t \in B} |f_j(t) - f(t)| = 0.$$

Theorem 12. Let $\{f_j\}_{j \in \mathbb{J}}$ be a family of real valued functions defined on $B \subset \mathbb{R}$. $\{f_j\}_{j \in \mathbb{J}} \rightrightarrows f$ on B if and only if it is Δ-uniform Cauchy on B.

Proof. Necessity is obvious. Let $\{f_j\}_{j \in \mathbb{J}}$ be Δ-uniform Cauchy on B. For a given $\epsilon > 0$ there exists $j_0 \in \mathbb{J}$ and $K \subset \mathbb{J}$ such that $\delta_\Delta(K) = 1$, the inequality

$$|f_j(t) - f_{j_0}(t)| < \frac{\epsilon}{2}, \tag{1}$$

holds for all $j \in K$ and $t \in B$. Let $g_t: \mathbb{J} \to \mathbb{R}$ defined by $g_t(j) = f_j(t)$ for each $t \in B$. For each fixed t

$$|g_t(j) - g_t(j_0)| = |f_j(t) - f_{j_0}(t)| < \epsilon,$$

holds Δ-a.e. on $\mathbb{J}$. Therefore, the functions g_t, $(t \in B)$ are Δ-Cauchy. These functions have Δ-limit. Let $f(t) = \Delta\text{-}\lim_{j\to\infty} g_t(j)$. As $j \to \infty$, the Δ-limit of (1) yields

$$|f(t) - f_{j_0}(t)| \le \frac{\epsilon}{2}. \tag{2}$$

In view of inequalities (1) and (2), one can get

$$|f_j(t) - f(t)| \le |f_j(t) - f_{j_0}(t)| + |f_{j_0}(t) - f(t)| < \epsilon,$$

for all $j \in K$ and for all $t \in B$.

Theorem 13. Let $\mathbb{T}$ and $\mathbb{J}$ be two time scales and $[\alpha, \beta] \subset B \subset \mathbb{T}$. If $f_j \in C_{rd}(B, \mathbb{R}) := \{f | f: B \to \mathbb{R} \text{ is } rd - continuous\}$ for all $j \in \mathbb{J}$, and $\{f_j\}_{j \in \mathbb{J}} \rightrightarrows f$, then $f \in C_{rd}(B, \mathbb{R})$ and

$$\Delta - \lim_{j\to\infty} \int_\alpha^\beta f_j(t)\Delta t = \int_\alpha^\beta f(t)\Delta t.$$

Proof. Let any positive ϵ be given. In accordance with Δ-uniform convergence, the time scale $\mathbb{J}$ has a subset K such that $\delta_\Delta(K) = 1$ and the inequality

$$|f_j(t) - f(t)| < \frac{\epsilon}{3},$$

holds for all $j \in K$ and for all $t \in B$.

Let $j_0 \in K$ and $t_0 \in B$ are arbitrary. We consider two cases. In the first case we assume that t_0 is left-dense. From rd-continuity of f_{j_0}, we can find $\delta > 0$ such that

$$|f_{j_0}(\xi) - f_{j_0}(\eta)| < \frac{\epsilon}{3},$$

for any $\xi, \eta \in (t_0 - \delta, t_0)$. If $t_n \to t_0^-$ as $n \to \infty$, then there exists natural number n_0 such that $n, m > n_0$ imply $t_m, t_n \in (t_0 - \delta, t_0)$ and

$$|f_{j_0}(t_n) - f_{j_0}(t_m)| < \frac{\epsilon}{3}. \tag{3}$$

Hence, for $m, n > n_0$, we have

$$|f(t_n) - f(t_m)| = |f(t_n) - f_{j_0}(t_n) + f_{j_0}(t_n) - f_{j_0}(t_m) + f_{j_0}(t_m) - f(t_m)|$$

$$\leq |f(t_n) - f_{j_0}(t_n)| + |f_{j_0}(t_n) - f_{j_0}(t_m)|$$

$$+|f_{j_0}(t_m) - f(t_m)|$$

$$< \epsilon. \tag{4}$$

Therefore, the function f has finite left-sided limit at t_0.

In the second case we assume that t_0 is right-dense. Then all functions f_j are continuous at t_0. If $t_n \to t_0$ as $n \to \infty$, then there exists natural number n_0 such that $n, m > n_0$ imply $t_m, t_n \in (t_0 - \delta, t_0 + \delta)$ and (3-4) holds. This is implies continuity of f at t_0. Therefore, f is Riemann Δ-integrable on every subinterval $[\alpha, \beta] \subset B$. So, we obtain the inequality

$$\left| \int_\alpha^\beta f_j(t)\Delta t - \int_\alpha^\beta f(t)\Delta t \right| \leq \int_\alpha^\beta |f_j(t) - f(t)|\Delta t < \frac{\epsilon}{3}(\beta - \alpha),$$

for every $j \in K$ that completes our proof.

Theorem 14. Le*t* $\mathbb{T}$ and $\mathbb{J}$ be two time scales and $[\alpha, \beta] \subset \mathbb{T}$. Suppose that the functions

$$f_j : [\alpha, \beta] \to \mathbb{R} \qquad (j \in \mathbb{J})$$

satisfies the following conditions on $[\alpha, \beta]$:

1. f_j has Hilger derivative and its Hilger derivative f_j^Δ is rd-continuous,

2. $\{f_j\}_{j \in \mathbb{J}} \to f$,

3. $\{f_j^\Delta\}_{j \in \mathbb{J}} \rightrightarrows g$.

Then f has Hilger derivative on $[\alpha, \beta]$ and $f^\Delta(t) = g(t)$ for all $t \in [\alpha, \beta]$.

Proof. g is rd-continuous on $[\alpha, \beta]$ by Theorem 13 and so g is Riemann Δ-integrable on this interval. By the help of Theorem 13, we have

$$\int_\alpha^t g(s)\Delta s = \Delta - \lim_{j \to \infty} \int_\alpha^t f_j^\Delta f(s)\Delta s = \Delta - \lim_{j \to \infty} (f_j(t) - f_j(\alpha)) = f(t) - f(\alpha),$$

for all $t \in [\alpha, \beta]$. Since the left hand-side of the last equality has Hilger derivative, the right hand-side also has, and it follows that $f^{\Delta}(t) = g(t)$ for all $t \in [\alpha, \beta]$.

Theorem 15. (Dini's Theorem**)** *Let* X *be a compact metric space. Let* $f: X \to \mathbb{R}$ *be a continuous function and the functions* $f_j: X \to \mathbb{R}$, $(j \in \mathbb{J})$ *are continuous for* Δ-*almost all* $\mathbb{J}$. *If the following two conditions are satisfied:*

1. $\{f_j\}_{j \in \mathbb{J}} \to f$ on X,

2. $f_j(x) \le f_i(x)$ for all $x \in X$ and Δ-almost all $i, j \in \mathbb{J}$ such that $i < j$,

then $\{f_j\}_{j \in \mathbb{J}} \rightrightarrows f$ on X.

Proof. There exists a subset $K_1 \subset \mathbb{J}$ with Δ-density 1. Moreover, for each $j \in K_1$ the functions f_j are continuous, and

$$f_j(x) \le f_i(x) \quad \text{for all} \quad x \in X,$$

holds for all $i, j \in K_1$ such that $i < j$. For each $j \in K_1$, define $g_j = f_j - f$. Then $\{g_j\}_{j \in K_1}$ is a family of continuous functions on the compact metric space X that converges Δ-pointwise to 0. Furthermore,

$$0 \le g_j(x) \le g_i(x),$$

for all $x \in X$ and $i, j \in K_1$ such that $i < j$.

Let $\epsilon > 0$ and define

$$G_j = \{x \in X : g_j(x) < \epsilon\}, \quad (j \in K_1).$$

Since g_j is continuous, then G_j is an open set and $G_i \subset G_j$ for each $i, j \in K_1$ such that $i < j$.

Let $x_0 \in X$ be arbitrary. Since Δ-$\lim_{j \to \infty} g_j(x_0) = 0$, then there exists a subset $K_2 \subset \mathbb{J}$ such that $\delta_{\Delta}(K_2) = 1$ and the inequality $|g_j(x_0)| < \epsilon$ holds for all $j \in K_2$. If we set $K = K_1 \cap K_2$ then $\delta_{\Delta}(K) = 1$ and $g_j(x_0) = |g_j(x_0)| < \epsilon$ for all $j \in K$. Thus $x_0 \in G_j$ for all $j \in K$, and thus, we have

$$X = \bigcup_{j \in K} G_j.$$

Since K is compact and $G_i \subset G_j$ when $i < j$, then there is a $j_0 \in K$ with $G_{j_0} = X$. Then we have $G_j = X$ for all $j \in K$ such that $j > j_0$. This implies that $f_j(x) - f(x) = g_j(x) < \epsilon$ for all $x \in X$ and $j \in K$ such that $j > j_0$. Consequently, $\{f_j\}_{j \in \mathbb{J}} \rightrightarrows f$ on X.

References

[1] Hilger, S., *Ein maßkettenkalkül mit anwendung auf zentrumsmannigfaltigkeiten,* PhD Thesis, 1989.

[2] Hilger, S., *Analysis on measure chains—a unified approach to continuous and discrete calculus*, Results in Mathematics 18, 1-2, 18-56, 1990.

[3] Fast, H., *Sur la convergence statistique*, Colloquium Mathematicae, 2(3-4), 1951.

[4] Schoenberg, I.J,.*The integrability of certain functions and related summability methods*, The American Mathematical Monthly, 66(5), 361-775, 1959.

[5] Fridy, J.A., *On statistical convergence*, Analysis,5(4), 301-314, 1985.

[6] Seyyidoğlu, M.S., Tan, N.Ö,. *A note on statistical convergence on time scale, Journal of Inequalities and Applications*, 2012(1), 219, 2012.

[7] Altın, Y., Koyunbakan, H., Yılmaz, E., *Uniform statistical convergence on time scales, Journal of Applied Mathematics*, vol. 2014, 6 pages, 2014.

[8] Yılmaz, E., Altın, A., Koyunbakan, H., *λ-Statistical convergence on time scales*, Dynamics of Continuous, Discrete and Impulsive Systems Series A: Mathematical Analysis, 23, 69-78, 2016.

[9] Ceylan, T., Duman, O*., Fundamental Properties of Statistical Convergence and Lacunary Statistical Convergence on Time Scales*, Filomat, 31(14), 2017.

Inverse Spectral Problems for Second Order Difference Equations with

Generalized Function Potentials by aid of Parseval Formula

Bayram BALA[1,*]

[1]*Harran University, Department of Mathematics, Şanlıurfa, Turkey.*
bbala@harran.edu.tr, ORCID: 0000-0001-6515-6039

Abstract

In the present study we are investigated inverse spectral problems for spectral analysis and two spectra of matrix J by using equality which is equivalance Parseval formula. The matrix J is $N \times N$ tridiagonal almost-symmetric matrix. The mean of almost-symmetric is the entries above and below the main diagonal are the same except the entries a_M and c_M.

Keywords: Parseval formula; Spectral analysis; Two spectra.

Parseval Formülü yardımıyla Genelleşmiş Fonksiyon Katsayılı İkinci Mertebeden Fark Denklemleri için Ters Spektral Problemler

Öz

Bu çalışmada, Parseval formülü ile eşdeğer olan eşitlik kullanılarak J matrisinin spektral analizine göre ve iki spektrumuna göre ters spektral problemleri incelenmiştir. J, $N \times N$ tipinde hemen hemen simetrik üçköşegensel matristir. Hemen hemen simetriklik, a_M ve c_M elemanları dışında matrisin köşegeninin altında ve üstündeki elemanları eşit olmasıdır.

Anahtar Kelimeler: Parseval formülü; Spektral analiz; İki spektrum.

1. Introduction

Consider the second order difference equation

$$a_{n-1}y_{n-1} + b_n y_n + a_n y_{n+1} = \lambda \rho_n y_n, \quad a_{-1} = c_{N-1} = 1, \quad n \in \{0,1,...,N-1\}, \tag{1}$$

with the boundary conditions

$$y_{-1} = y_N = 0, \tag{2}$$

where $y = \{y_n\}_{n=0}^{N-1}$ is column vector which is solution of the second order difference equation, ρ_n is constant

$$\rho_n = \begin{cases} 1, & 0 \leq n \leq M \\ \alpha, & M < n \leq N-1 \end{cases}, \quad \alpha \in \mathbb{R}^+ - \{1\}, \tag{3}$$

and $a_n,\ b_n \in \mathbb{R},\quad a_n > 0$ are coefficients of Eqn. (1),

$$\begin{aligned} c_n &= a_n/\alpha, \quad n \in \{M, M+1, ..., N-2\}, \\ d_n &= b_n/\alpha, \quad n \in \{M+1, M+2, ..., N-1\}. \end{aligned} \tag{4}$$

Now, we can write the Eqn. (1) by definition of ρ_n

$$\begin{cases} a_{n-1}y_{n-1} + b_n y_n + a_n y_{n+1} = \lambda y_n, & n \in \{0,1,...,M\}, \\ c_{n-1}y_{n-1} + d_n y_n + c_n y_{n+1} = \lambda y_n, & n \in \{M+1, M+2, ..., N-1\}. \end{cases}$$

J is $N \times N$ tridiagonal almost-symmetric matrix and the entries of J are the coefficients of Eqn. (1).

$$
J = \begin{bmatrix}
b_0 & a_0 & 0 & \cdots & 0 & 0 & 0 & 0 & \cdots & 0 & 0 & 0 \\
a_0 & b_1 & a_1 & \cdots & 0 & 0 & 0 & 0 & \cdots & 0 & 0 & 0 \\
0 & a_1 & b_2 & \cdots & 0 & 0 & 0 & 0 & \cdots & 0 & 0 & 0 \\
\vdots & \vdots & \vdots & \ddots & \vdots & \vdots & \vdots & \vdots & \ddots & \vdots & \vdots & \vdots \\
0 & 0 & 0 & \cdots & b_{M-1} & a_{M-1} & 0 & 0 & \cdots & 0 & 0 & 0 \\
0 & 0 & 0 & \cdots & a_{M-1} & b_M & a_M & 0 & \cdots & 0 & 0 & 0 \\
0 & 0 & 0 & \cdots & 0 & c_M & d_{M+1} & c_{M+1} & \cdots & 0 & 0 & 0 \\
0 & 0 & 0 & \cdots & 0 & 0 & c_{M+1} & d_{M+2} & \cdots & 0 & 0 & 0 \\
\vdots & \vdots & \vdots & \ddots & \vdots & \vdots & \vdots & \vdots & \ddots & \vdots & \vdots & \vdots \\
0 & 0 & 0 & \cdots & 0 & 0 & 0 & 0 & \cdots & d_{N-3} & c_{N-3} & 0 \\
0 & 0 & 0 & \cdots & 0 & 0 & 0 & 0 & \cdots & c_{N-3} & d_{N-2} & c_{N-2} \\
0 & 0 & 0 & \cdots & 0 & 0 & 0 & 0 & \cdots & 0 & c_{N-2} & d_{N-1}
\end{bmatrix}.
$$

So, the eigenvalue problem $Jy = \lambda y$ is equivalent problem (1)-(3) which is discrete form Sturm-Liouville problem with discontinuous coefficients

$$
\frac{d}{dx}\left[p(x)\frac{d}{dx}y(x) \right] + q(x)y(x) = \lambda\rho(x)y(x), \quad x \in [a,b],
$$
$$
y(a) = y(b) = 0,
$$

(5)

where $\rho(x)$ is a piecewise function

$$
\rho(x) = \begin{cases} 1, & a \le x \le c \\ \alpha^2, & c < x \le b \end{cases}, \quad \alpha^2 \ne 1.
$$

H. Hochstadt made significant contributions to the development of the inverse problem for second order difference equations. He studied inverse problem for Jacobi matrices in [1-4]. Later, G. Guseinov has pioneered for inverse problem of infinite symmetric tridiagonal matrices. He considered different kinds of inverse spectral problems for second order difference equation; such as the inverse spectral problems of spectral analysis for infinite Jacobi matrices in [5], the inverse spectral problems for the infinite non-self adjoint Jacobi matrices from generalized spectral function in [6, 7], and the inverse spectral problems for same matrices from spectral data and two spectra in [8-12]. The inverse spectral problem for discrete form of Sturm-Liouville problem with continuous coefficients has been studied in [13] and the inverse spectral problem with spectral parameter in the initial conditions has been studied by M. Manafov in [14]. The eigenvalues and eigenfunctions and the inverse problem for Sturm-Liouville operator with discontinuous coefficients which is the same problem given by (5) are investigated by E. Akhmedova and H.

Huseynov in [15, 16], respectively. Bala et al. are studied inverse spectral problem for almost symmetric tridiagonal matrices from generalized spectral function in [17] and they examined inverse spectral problems for same matrices from spectral data and two spectra in [18]. Finite dimensional inverse problems are investigated by H. Huseynov in [19].

Also, Parseval equality of discrete Sturm-Liouville equation with periodic generalized function potentials is studied by Manafov et al. in [20]. At the same time a new approach for higher-order difference equations and eigenvalue problems is examined by Bas and Ozarslan in [21].

The goal of this article is to study inverse spectral problems of the problem (1)-(3) for spectral analysis and two spectra by using Parseval formula.

2. Direct Problem for Spectral Analysis

The matrix J has N number eigenvalues $\lambda_1, \lambda_2, ..., \lambda_N$ and N number eigenvectors $v_1, v_2, ..., v_N$, which form an orthonormalized basis. Assume that the eigenvalues are real. We bring to mind the algorithm of structure for the matrix J eigenvalues and eigenvectors.

Let $P_n(\lambda)$ be a solution of Eqn. (1)

$$a_{n-1}P_{n-1}(\lambda) + b_n P_n(\lambda) + a_n P_{n+1}(\lambda) = \lambda \rho_n P_n(\lambda), \quad n \in \{0, 1, ..., N-1\}, \tag{6}$$

with initial conditions

$$P_{-1}(\lambda) = 0, \quad P_0(\lambda) = 1, \tag{7}$$

and the degree of polynomial $P_n(\lambda)$ is n.

Lemma 1. The following equality holds:

$$\det(J - \lambda I) = (-1)^N a_0 a_1 ... a_M c_{M+1} ... c_{N-1} P_N(\lambda).$$

Proof. See [17].

According to Lemma 1, the roots of the equation $P_n(\lambda)$ are equal the eigenvalues of J, and eigenvectors corresponding eigenvalues λ_k, $k = \overline{1, N}$ will be

$$\Re(\lambda_k) = \left(P_0(\lambda_k), P_1(\lambda_k), ..., P_{N-1}(\lambda_k)\right)^T.$$

Assuming that $v_k = \dfrac{\Re(\lambda_k)}{\sqrt{\beta_k}}$, where $\beta_k = \sum\limits_{j=0}^{N-1} P_j^2(\lambda_k)$. Thus, we have the complete

orthonormalized system of eigenvectors of the matrix J. The numbers β_k are called normalized numbers of the problem (1)-(3).

Lemma 2. Eigenvalues of matrix J are different.

Proof. Because of eigenvalues λ_k, $k = 1, 2, ..., N$ are the roots of polynomial $P_N(\lambda)$, we

must show that $P_N'(\lambda_k) \neq 0$. Firstly, take the derivative equation Eqn. (6) by λ, we have

$$a_{n-1}P_{n-1}'(\lambda) + b_n P_n'(\lambda) + a_n P_{n+1}'(\lambda) = \lambda \rho_n P_n'(\lambda) + \rho_n P_n(\lambda). \tag{8}$$

Now, if the Eqn. (8) is multiplied by $P_n(\lambda)$ and the Eqn. (6) is multiplied by $P_n'(\lambda)$, the

second result is substracted from the first, for $n \in \{0, 1, ..., N-1\}$ we obtain

$$a_{n-1}\left(P_{n-1}'(\lambda) P_n(\lambda) - P_n'(\lambda) P_{n-1}(\lambda)\right) - a_n\left(P_n'(\lambda) P_{n+1}(\lambda) - P_{n+1}'(\lambda) P_n(\lambda)\right) = \rho_n P_n^2(\lambda). \tag{9}$$

For $\lambda = \lambda_k$ and summing n from 0 to $N-1$, pay attention to Eqn. (7) and $P_N(\lambda_k) = 0$

we have

$$a_{N-1} P_N'(\lambda_k) P_{N-1}(\lambda_k) = \sum\limits_{j=0}^{M} P_j^2(\lambda) + \sum\limits_{j=M+1}^{N-1} \alpha P_j^2(\lambda). \tag{10}$$

As a result, $P_N'(\lambda_k) \neq 0$.

According to Lemma 2, we can assume that $\lambda_1 < \lambda_2 < ... < \lambda_N$. The following Lemma is about Parseval equality.

Lemma 3. The expansion formula which is equivalent Parceval equality, can be written as below:

$$\sum\limits_{j=1}^{N} \frac{\eta}{\beta_j} P_m(\lambda_j) P_n(\lambda_j) = \delta_{mn}, \quad m, n = \overline{0, N-1}, \tag{11}$$

where η is defined by

$$\eta = \begin{cases} 1, & m \text{ or } n \le M \\ \alpha, & m \text{ or } n > M \end{cases}, \tag{12}$$

and δ_{mn} is the Kronecker delta.

For $n = m = 0$ in the Eqn. (11) and from conditions (7) we obtain following equality

$$\sum_{j=1}^{N} \frac{1}{\beta_j} = 1. \tag{13}$$

Thus, we get eigenvalues $\{\lambda_k\}_{k=1}^{N}$ and eigenvectors v_j, $j = 1, 2, ..., N$ corresponding $\{\lambda_k\}_{k=1}^{N}$. So, we can say that the direct spectral problem of spectral analysis is solved.

Now let's try to answer the following question:

If we know eigenvalues $\{\lambda_k\}_{k=1}^{N}$ and eigenvectors $\{v_k\}_{k=1}^{N}$ of matrix J, is it possible to reconstruct the matrix J by using the following formula

$$Ju = \sum_{k=1}^{N} \lambda_k (u, v_k) v_k, \quad u \in l_2 (0, N-1),$$

where $(u, v) = \sum_{j=0}^{N-1} u_j \bar{v}_j$ scalar product.

It is clear that eigenvalues of J is not sufficient for reconstruct matrix J. On account of this we must have some more information about eigenvectors.

Definition 4. The collection of quantitites $\{\lambda_k, \beta_k\}$ are called spectral data for the matrix J.

Additional we will need the presentation of entries of the matrix J by the polynomial $P_n(\lambda)$. For $\lambda = \lambda_j$ the Eqn. (6) is multiplied by $\dfrac{\eta}{\beta_j} P_m(\lambda_j)$, then summing by j from 1 to N and using Lemma 3, we have

$$a_n = \sum_{j=1}^{N} \frac{\eta^2 \lambda_j}{\beta_j} P_n(\lambda_j) P_{n+1}(\lambda_j), \quad n = \overline{0, N-2} - M,$$

$$b_n = \sum_{j=1}^{N} \frac{\eta^2 \lambda_j}{\beta_j} P_n^2(\lambda_j), \quad n = \overline{0, N-1},$$

where η is defined by (12). It is clear that $\rho_n = \eta = \alpha$ for m or $n > M$. Then, we can write these equalities as below:

$$a_n = \sum_{j=1}^{N} \frac{\lambda_j}{\beta_j} P_n(\lambda_j) P_{n+1}(\lambda_j), \quad n = \overline{0, M-1}, \tag{14}$$

$$a_M = \sum_{j=1}^{N} \frac{\alpha \lambda_j}{\beta_j} P_M(\lambda_j) P_{M+1}(\lambda_j), \quad c_M = \sum_{j=1}^{N} \frac{\lambda_j}{\beta_j} P_M(\lambda_j) P_{M+1}(\lambda_j), \tag{15}$$

$$c_n = \sum_{j=1}^{N} \frac{\alpha \lambda_j}{\beta_j} P_n(\lambda_j) P_{n+1}(\lambda_j), \quad n = \overline{M+1, N-2}, \tag{16}$$

$$b_n = \sum_{j=1}^{N} \frac{\lambda_j}{\beta_j} P_n^2(\lambda_j), \quad n = \overline{0, M}, \tag{17}$$

$$d_n = \sum_{j=1}^{N} \frac{\alpha \lambda_j}{\beta_j} P_n^2(\lambda_j), \quad n = \overline{M+1, N-1}. \tag{18}$$

3. Inverse Problem of Spectral Analysis

The inverse problem of spectral analysis is reconstruct matrix J by using the collection quantities $\{\lambda_k, \beta_k\}$.

Theorem 5. Let an arbitrary collection $\{\lambda_k, \beta_k\}$ of matrix is J. In order for this collection to be spectral data for some matrix which have form J, it is necessary and sufficient that the following conditions are satisfied:

(i) $\lambda_k \neq \lambda_j$,   (ii) $\sum_{j=1}^{N} \frac{1}{\beta_j} = 1$,   (iii) $a_n > 0, \quad n = \overline{0, N-2}$.

Lemma 6. Let λ_k, $k = \overline{1, N}$ are distinct real numbers and for the positive numbers β_k, $k = \overline{1, N}$ be given that $\sum_{j=1}^{N} \dfrac{1}{\beta_j} = 1$. Then there exists unique polynomials $P_k(\lambda)$, $k = \overline{0, N-1}$ with $\deg P_j(\lambda) = j$ and positive leading coefficients satisfying the conditions (11).

Now, we will give another method for a kind of approach to the solution of the inverse spectral problem which is called the Gelphand-Levitan-Marchenko method.

Let $R_n(\lambda)$ be a solution of the Eqn. (1) satisfying the conditions

$$R_{-1}(\lambda) = 0, \quad R_0(\lambda) = 1,$$

in the case $a_n \equiv 1$, $b_n \equiv 0$.

Recall that $P_n(\lambda)$ is a polynomial of degree n, so it can be expressed as

$$P_n(\lambda) = \gamma_n \left(R_n(\lambda) + \sum_{k=0}^{n-1} \chi_{n,k} R_k(\lambda) \right), \quad n \in \{0, 1, ..., M, ..., N\}, \tag{19}$$

where γ_n and $\chi_{n,k}$ are constants. There is a connection between coefficients a_n, b_n, c_n, d_n and $\gamma_n, \chi_{n,k}$.

Then we can write the equalities

$$a_n = \frac{\gamma_n}{\gamma_{n+1}} \quad (0 \leq n \leq M), \quad \gamma_0 = 1,$$

$$c_n = \frac{\gamma_n}{\gamma_{n+1}} \quad (M < n \leq N-2), \quad c_M = \frac{\gamma_M}{\alpha \gamma_{M+1}}, \tag{20}$$

$$b_n = \chi_{n,n-1} - \chi_{n+1,n} \quad (0 \leq n \leq M), \quad \chi_{0,-1} = 0,$$

$$d_n = \chi_{n,n-1} - \chi_{n+1,n} \quad (M < n \leq N-1). \tag{21}$$

Now, we can write from Eqn. (19)

$$\sum_{j=1}^{N} \frac{\eta}{\beta_j} P_n\left(\lambda_j\right) R_m\left(\lambda_j\right) = \gamma_n\left[G_{nm} + \sum_{k=0}^{n-1} \chi_{n,k} G_{km}\right],$$ (22)

where η is defined by (12) and

$$G_{nm} = \sum_{j=1}^{N} \frac{\eta}{\beta_j} R_n\left(\lambda_j\right) R_m\left(\lambda_j\right).$$ (23)

Since the expansion

$$R_j\left(\lambda\right) = \sum_{k=0}^{j} w_k^{(j)} P_k\left(\lambda\right)$$

holds, then from Eqn. (11) we have

$$\sum_{j=1}^{N} \frac{1}{\beta_j} P_n\left(\lambda_j\right) R_m\left(\lambda_j\right) = \frac{1}{\eta\gamma_n} \delta_{nm}, \quad n \geq 0, \quad s = \overline{0, n}.$$

Considering the Eqn. (22) we get

$$G_{nm} + \sum_{k=0}^{n-1} \chi_{n,k} G_{km} = 0, \quad m = \overline{0, n-1}, \quad n \geq 1,$$ (24)

$$G_{nn} + \sum_{k=0}^{n-1} \chi_{n,k} G_{kn} = \frac{1}{\eta\gamma_n^2}, \quad n = \overline{0, N-1}.$$ (25)

Eqn. (24) is important for the solution of inverse spectral problem. Firstly, G_{nm} are determined by using Eqn. (23) and then quantities $\chi_{n,k}$, $k = \overline{0, n-1}$ are found from system of Eqn. (24). Thus we can find unknowns γ_n with aid of $\chi_{n,k}$ from Eqn. (25).

Lemma 7. For any fixed n the system of Eqn. (24) is identically solvable.

Proof. It is clear that

$$v_n = \left(\frac{R_n\left(\lambda_1\right)}{\sqrt{\beta_1}}, \frac{R_n\left(\lambda_2\right)}{\sqrt{\beta_2}}, ..., \frac{R_n\left(\lambda_N\right)}{\sqrt{\beta_N}}\right), \quad n = \overline{0, N-1},$$

are linear independent and from the Eqn. (23), we have

$$G_{ns} = (v_n, v_s).$$

The basic determinant of the system (24)

$$\det\{G_{ij}\}_{i,j=0}^{n-1} = \det\{(v_i, v_j)\}_{i,j=0}^{n-1}. \tag{26}$$

Lemma 8. Let G_{nm}, $m = \overline{0, n-1}$ be a solution of the system (24). Then

$$G_{nm} + \sum_{k=0}^{n-1} \chi_{n,k} G_{km} > 0, \quad n = \overline{0, \mathrm{N}-1}.$$

Proof. See [19].

Therefore we can determine the entries of the matrix J from the formulas Eqn. (20) and Eqn. (21).

4. Inverse Problem for Two Spectra

Consider the boundary value problem

$$a_{n-1} y_{n-1} + b_n y_n + a_n y_{n+1} = \lambda \rho_n y_n, \quad n = \overline{1, N-1}, \tag{27}$$

with the boundary conditions

$$y_0 = y_N = 0, \tag{28}$$

where ρ_n is defined in (3). Now, the matrix of coefficients of Eqn. (27) is denoted by J_1 which has the same form with matrix J. If we delete the first row and the first column of the matrix J then we have $N-1 \times N-1$ tridiagonal matrix J_1 which has $N-1$ number eigenvalues μ_k, $k = \overline{1, N-1}$. Assume that eigenvalues of matrix J_1 are distinct and real. Thus we can write

$$\mu_1 < \mu_2 < ... < \mu_{N-1}.$$

The solution of Eqn. (27) is denoted by $\{Q_n(\lambda)\}$ provided that $Q_0(\lambda) = 0$, $Q_1(\lambda) = 1$. It is clear that the eigenvalues μ_j, $j = \overline{1, N-1}$ are zeros of the polynomial $Q_N(\lambda)$. While we determine entries of J, we will use eigenvalues of matrices J and J_1.

Now we will give an important lemma for the inverse spectral problem according to the two spectra.

Lemma 9. The eigenvalues of matrices J and J_1 alternate, i.e.

$$\lambda_1 < \mu_1 < \lambda_2 < \mu_2 < ... < \lambda_{N-1} < \mu_{N-1} < \lambda_N.$$

Proof. See [19].

Additionally, we can find the normalized numbers β_k by aid of two spectrums $\lambda_1, \lambda_2, ..., \lambda_N$ and $\mu_1, \mu_2, ..., \mu_{N-1}$ of the matrices J and J_1 respectively. Assume that

$$f_n(\lambda) = Q_n(\lambda) + m(\lambda) P_n(\lambda), \tag{29}$$

and require that $f_N(\lambda) = 0$. $m(\lambda)$ is a meromorphic function,

$$m(\lambda) = -\frac{Q_N(\lambda)}{P_N(\lambda)}, \tag{30}$$

its poles and zeros coincide with the eigenvalues of the problem (1)-(2) and (27)-(28), respectively. We see that the function $f_n(\lambda)$ satifies the equation

$$a_{n-1}f_{n-1}(\lambda) + b_n f_n(\lambda) + a_n f_{n+1}(\lambda) = \lambda \rho_n f_n(\lambda). \tag{31}$$

Now, if the equality Eqn. (31) is multiplied by $P_n(\lambda_k)$ and the Eqn. (6) (for $\lambda = \lambda_k$) is multiplied by $f_n(\lambda)$ then the second result is substracted from the first and sum by n, we obtain:

$$(\lambda - \lambda_k) \sum_{n=1}^{N-1} \rho_n f_n(\lambda) P_n(\lambda_k) = \sum_{n=1}^{N-1} \left\{ \begin{matrix} a_{n-1}\left(f_{n-1}(\lambda)P_n(\lambda_k) - P_{n-1}(\lambda_k)f_n(\lambda)\right) \\ -a_n\left(f_n(\lambda)P_{n+1}(\lambda_k) - P_n(\lambda_k)f_{n+1}(\lambda)\right) \end{matrix} \right\}$$

or

$$(\lambda - \lambda_k) \sum_{n=1}^{N-1} \rho_n f_n(\lambda) P_n(\lambda_k) = -a_0,$$

and then for $\lambda \to \lambda_k$, we have

$$\beta_k = \frac{a_0 P_N'(\lambda_k)}{Q_N(\lambda_k)}.$$

On the other hand from Lemma 1, we get

$$\det(J - \lambda I) = (-1)^N a_0 a_1 ... a_M c_{M+1} ... c_{N-1} P_N(\lambda),$$

$$\det(J_1 - \lambda I) = (-1)^{N-1} a_1 ... a_M c_{M+1} ... c_{N-1} Q_N(\lambda)$$

and from these equalities we can find

$$P_N(\lambda) = \frac{(\lambda - \lambda_1)...(\lambda - \lambda_N)}{a_0 a_1 ... a_M c_{M+1} ... c_{N-1}}, \qquad Q_N(\lambda) = \frac{(\lambda - \mu_1)...(\lambda - \mu_{N-1})}{a_1 ... a_M c_{M+1} ... c_{N-1}}.$$

As a result

$$\beta_k = \frac{\prod_{\substack{j=1 \\ j \neq k}}^{N}(\lambda_k - \lambda_j)}{\prod_{j=1}^{N-1}(\lambda_k - \mu_j)}. \tag{32}$$

Theorem 10. Let the collections $\{\lambda_k\}_{k=1}^{N}$, $\{\mu_k\}_{k=1}^{N-1}$ to be real numbers. These collections are spectrums of the $N \times N$ and $N-1 \times N-1$ tridiagonal almost-symmetric matrices J and J_1, respectively, it is necessary and sufficient that they are alternate as below:

$$\lambda_1 < \mu_1 < \lambda_2 < \mu_2 < ... < \lambda_{N-1} < \mu_{N-1} < \lambda_N.$$

5. Conclusion

While solving the inverse spectral problem from two spectra, firstly we determine the normalized numbers β_k of the matrix J by using the eigenvalues $\{\lambda_k\}_{k=1}^{N}$, $\{\mu_k\}_{k=1}^{N-1}$ of the matrices J and J_1, respectively. Thus, we reduce the problem from two spectra to spectral analysis, and then we determine the values G_{nm}, $\chi_{n,k}$ and γ_n from the formulas (23)-(25) by aid of the eigenvalues λ_k and the normalized numbers β_k of the matrix J.

Consequently, the entries a_n, b_n, c_n and d_n are found from the Eqn. (20) and Eqn. (21).

Thus, the matrix J is reconstructed by using Parseval formula.

References

[1] Hochstadt, H., *On some inverse problems in matrix theory*, Archiv der Mathematik, 18(2), 201-207, 1967.

[2] Hochstadt, H., *On the construction of a Jacobi matrix from spectral data*, Linear Algebra and Its Applications, 8(5), 435-446, 1974.

[3] Hochstadt, H., *On the construction of a Jacobi matrix from mixed given data*, Linear Algebra and its Applications, 28, 113-115, 1979.

[4] Fu, L., Hochstadt, H., *Inverse theorems for Jacobi matrices*, Journal of Mathematical Analysis and Applications, 47(1), 162-168, 1974.

[5] Gasymov, M.G., Guseinov, G.Sh., *On inverse problems of spectral analysis for infinite Jacobi matrices in the limit-circle case*, In Soviet Mathematics Doklady, 40, 627-630, 1990.

[6] Guseinov, G.Sh., *Determination of an infinite non-selfadjoint Jacobi matrix from its generalized spectral function*, Matematicheskie Zametki, 23, 237-248, 1978; English transl.: Mathematical Notes, 23, 130-136, 1978.

[7] Guseinov, G.Sh., *The inverse problem from the generalized spectral matrix for a second order non-selfadjoint difference equation on the axis*, Izvetsiya Akademii Nauk Azerb. SSR Ser. Fiz.-Tekhn. Mat. Nauk, 5, 16-22, 1978 (in Russian)

[8] Guseinov, G.Sh., *An inverse spectral problem for complex Jacobi matrices*, Communications in Nonlinear Science and Numerical Simulation, 15(4), 840-851, 2010.

[9] Guseinov, G.Sh., *Construction of a complex Jacobi matrix from two-spectra*, Hacettepe Journal of Mathematics and Statistics, 40(2), 2011.

[10] Guseinov, G. Sh., *On construction of a complex finite Jacobi matrix from two-spectra*, Electronic Journal of Linear Algebra, 26, 101-120, 2013.

[11] Guseinov, G.Sh., *On a discrete inverse problem for two spectra*, Discrete Dynamics in Nature and Society, 14 pages, 2012.

[12] Guseinov, G.Sh., *On an inverse problem for two spectra of finite Jacobi matrices*, Applied Mathematics and Computation, 218(14), 7573-7589, 2012.

[13] Guseinov, G.Sh., *Inverse spectral problems for tridiagonal N by N complex hamiltonians*, Symmetry Integrability and Geometry: Methods and Applications, 28 pages, 2009.

[14] Manafov, M.D., Bala, B., *Inverse spectral problems for tridiagonal N by N complex hamiltonians with spectral parameter in the initial conditions*, Adıyaman Üniversitesi Fen Bilimleri Dergisi, 3(1), 20-27, 2013.

[15] Akhmedova, E.N., Huseynov, H.M., *On eigenvalues and eigenfunctions of one class of Sturm-Liouville operators with discontinuous coefficients*, Transactions of National Academy of Sciences of Azerbaijan Series of Physical-Technical and Mathematical Sciences, 23-4, 7-18, 2003.

[16] Akhmedova, E.N., Huseynov, H.M., *On inverse problem for Sturm-Liouville operators with discontinuous coefficients*, Transactions of Saratov University, (Izv. Sarat. Univ.), 10(1), 3-9, 2010.

[17] Bala, B., Kablan, A., Manafov, M.Dzh., *Direct and inverse spectral problems for discrete Sturm-Liouville problem with generalized function potential*, Advances in Difference Equations, 2016(1), 172, 2016.

[18] Huseynov, H.M., *Finite dimensional inverse problems*, Transactions of National Academy of Sciences of Azerbaijan Series of Physical-Technical and Mathematical Sciences, 21(1), 80-87, 2001.

[19] Bala, B., Manafov, M.Dzh., Kablan, A., *Inverse spectral problems for spectral data and two spectra of N by N tridiagonal almost-symmetric matrices*, Applications and Applied Mathematics, 14(2), 12 pages, 2019.

[20] Manafov, M.Dzh., Kablan, A., Bala, B., *Parseval equality of discrete Sturm-Liouville equation with periodic generalized function potentials*, AIP Conference Proceedings. Vol. 1991. No. 1. AIP Publishing, 2018.

[21] Baş, E., Özarslan, R., *A new approach for higher-order difference equations and eigenvalue problems via physical potentials*, The European Physical Journal Plus, 134(6), 253, 2019.

Non-null Surfaces with Constant Slope Ruling with Respect to Osculating Plane

Ayşe YAVUZ[1,*], Fatma ATEŞ[2], Yusuf YAYLI[3]

[1]*Necmettin Erbakan University, Faculty of A.K.E., Department of Mathematics and Sciences Education, Konya, Turkey*
ayasar@erbakan.edu.tr, ORCID: 0000-0002-0469-3786
[2]*Necmettin Erbakan University, Faculty of Science, Department of Mathematics-Computer Sciences, Konya, Turkey*
fgokcelik@erbakan.edu.tr, ORCID: 0000-0002-3529-1077
[3]*Ankara University, Faculty of Science, Department of Mathematics, Ankara, Turkey*
yayli@science.ankara.edu.tr, ORCID: 0000-0003-4398-3855

Abstract

The main purpose of this study is to investigate surface with a constant slope ruling with respect to osculating plane by using Frenet Frame according to casual characters in Minkowski space. In accordance with this purpose, surface with constant slope ruling with respect to osculating plane in Minkowski Space is defined and many features of this surface are investigated. In addition, examples of the given characterizations are obtained and the geometrical structures of these examples are be examined and visualized.

Keywords: Ruled surface; Surface with constant slope; Minkowski space.

Oskülatör Düzleme Göre Dayanak Eğrisi Sabit Eğimli Null Olmayan Yüzeyler

Öz

Bu çalışmanın amacı, Minkowski uzayında Frenet çatısını kullanarak oskülatör düzleme göre dayanak eğrisi sabit eğimli yüzeyleri incelemektir. Bu amaç doğrultusunda, Minkowski uzayında Frenet çatısını kullanarak oskülatör düzleme göre dayanak eğrisi sabit eğimli yüzeylerin

---

tanımları elde edilmiştir ve bu yüzeylerin birçok özelliği ayrı ayrı ele alınmıştır. Elde edilen yüzeylerin örnekleri incelenerek görselleri elde edilmiştir.

Anahtar Kelimeler: Regle yüzeyler; Sabit eğimli yüzeyler; Minkowski uzayı.

1. Introduction

Curves and surfaces are geometric structures that are frequently encountered in daily life. The most known curve helix which is an important curve has a lot of applications. In the 3-dimensional Euclidean space, if the angle between a fixed direction and each tangent is constant, such a curve is called a helix curve. The path that a bean follows as it grows around the stick follows, the sequence of molecules in the structure of the DNA, the carbon nanotubes, the progression of the screw, the path that the flying creatures are heading towards the point source or the prey and the way the ants walk on a tree from point A to point B are all examples of helix curves.

Ruled surface in 3-dimensional Minkowski space is a special surface which is formed by moving a line given in 3-dimensional Minkowski space along a given curve. The line is the generating line of the ruled surface and the given curve is the base curve of the surface. The ruled surface is one of the most important topic of differential geometry.

Minkowski space is more interesting than the Euclidean space because curves and surfaces have different casual characters such as timelike, spacelike or null (lightlike). In the literature, studies involving the subject of curves and surfaces in Minkowski space are very common [1-4]. Therefore, ruled surfaces in Minkowski space can be classified according to the Lorentzian character of their ruling and surface normal.

Firstly, K. Malecek and others defined a surface with a constant slope with respect to the given plane in Euclidean Space in [5]. In this study, we give definition of surfaces with a constant slope ruling with respect to osculating plane by using Frenet frame Minkowski spaces. Many features of these surfaces are examined and characterized. In addition, examples of the given characterizations are given and the geometrical structures of these examples are visualized using the Mathematica program. It is shown that rotational surface and one sheet rotational hyperboloid have constant slopes. The conditions are given for being a torsal surface in Minkowski space.

2. Preliminaries

A vector v tangent to a semi-Riemanian manifold M is spacelike if $g(v, v) > 0$ or $v = 0$, null if $g(v, v) = 0$ and $v \neq 0$, timelike if $g(v, v) < 0$. The norm of a tangent vector v is given

by $|v| = \sqrt{|g(v,v)|}$. A curve in a manifold M is a smooth mapping $\alpha: I \to M$, where I is an open interval in the real line R. A curve α in a semi-Riemannian manifold M is spacelike if all of its velocity vectors $\alpha'(s)$ are spacelike, null if all of its velocity vector $\alpha'(s)$ are null, timelike if all of its velocity vectors $\alpha'(s)$ are timelike.

In this study we give the Frenet frames and formulas in the Minkowski space $E_1{}^3$ with metric $g = -dx_1{}^2 + dx_2{}^2 + dx_3{}^2$.

A curve $\alpha(s)$ in $E_1{}^3$ has different causal characters. We consider that $\alpha(s)$ is spacelike or timelike separately and construct their Frenet frame $\{t, n, b\}$.

If α is spacelike, we take the arclength parameter s or α such that $g(\alpha'(s), \alpha'(s)) = 1$. $t(s)$ is the velocity or unit tangent vector field of $\alpha(s)$. If $\alpha''(s) \neq 0$, then $\alpha''(s)$ is perpendicular to $t(s)$, so we take $n(s) = \lambda\alpha''(s)$, $\lambda \in R$ and $\lambda > 0$. Depending on the causal character of $\alpha''(s)$ we have the different cases.

If $g(\alpha''(s), \alpha''(s)) > 0$, the principal normal vector field $n(s)$ is then the normalized vector field $\alpha''(s)$. The binormal vector field $b(s)$ is the unique timelike unit vector field perpendicular to the spacelike plane $\{t(s), n(s)\}$ at every point $\alpha(s)$ of α, such that $\{t, n, b\}$ has the same orientation as $E_1{}^3$. The Frenet formulas are, in matrix notation,

$$\begin{bmatrix} t'(s) \\ n'(s) \\ b'(s) \end{bmatrix} = \begin{bmatrix} 0 & \kappa(s) & 0 \\ -\kappa(s) & 0 & \tau(s) \\ 0 & \tau(s) & 0 \end{bmatrix} \begin{bmatrix} t(s) \\ n(s) \\ b(s) \end{bmatrix}$$

If $g(\alpha''(s), \alpha''(s)) < 0$, the principal normal vector field $n(s)$ is then the normalized timelike vector field $\alpha''(s)$. The binormal vector field $b(s)$ is the unique spacelike unit vector field perpendicular to the timelike plane $\{t(s), n(s)\}$ at every point $\alpha(s)$ of a, such that $\{t, n, b\}$ has the same orientation as $E_1{}^3$. The Frenet formulas are, in matrix notation,

$$\begin{bmatrix} t'(s) \\ n'(s) \\ b'(s) \end{bmatrix} = \begin{bmatrix} 0 & \kappa(s) & 0 \\ \kappa(s) & 0 & \tau(s) \\ 0 & \tau(s) & 0 \end{bmatrix} \begin{bmatrix} t(s) \\ n(s) \\ b(s) \end{bmatrix}$$

If $g(\alpha''(s), \alpha''(s) = 0$, to rule out straight lines and points of inflexion on a, we shall suppose that $\alpha''(s) \neq 0$. The principal normal vector field $n(s)$ is then the vector field $\alpha''(s)$. The binormal vector field $b(s)$ is the unique null vector field perpendicular to $t(s)$ at every point $\alpha(s)$ of α, such that $g(n, b) = 1$. The Frenet formulas are, in matrix notation,

$$\begin{bmatrix} t'(s) \\ n'(s) \\ b'(s) \end{bmatrix} = \begin{bmatrix} 0 & \kappa(s) & 0 \\ 0 & \tau(s) & 0 \\ -\kappa(s) & 0 & -\tau(s) \end{bmatrix} \begin{bmatrix} t(s) \\ n(s) \\ b(s) \end{bmatrix},$$

where the curvature κ can only take two values; 0 , when a is a straight line, or 1 in all other cases. If $\alpha(s)$ is a straight line, then $\alpha''(s) = 0 = t'(s)$ which means that $\kappa = 0$. If $\alpha(s)$ is not a straight line, then there exists an interval I on which $\alpha''(s) \neq 0$ [6].

Let x and y be future pointing (or past pointing) timelike vectors in $R_1{}^3$. Then there is a unique real number $\theta > 0$ such that $< x, y >= -\|x\|\|y\|\cos h\theta$.

Let x and y be spacelike vectors in $R_1{}^3$ that span a timelike vector subspace. Then there is a unique real number $\theta > 0$ such that $< x, y >= \|x\|\|y\|\cos h\theta$.

Let x and y be spacelike vectors in $R_1{}^3$ that span a spacelike vector subspace. Then there is a unique real number $\theta > 0$ such that $< x, y >= \|x\|\|y\|\cos\theta$.

Let x be a spacelike vector and y be a timelike vector in $R_1{}^3$. Then there is a unique real number $\theta > 0$ such that $< x, y >= \|x\|y\sinh\theta$. [7].

Surface of rotation or surface of revolution are formed from circles centered on one of the axes with variable radii and the ruled surfaces are formed from lines along some fixed curve, but in variable direction. A surface is called surface of rotation, if it is obtained by rotation of a regular curve $t \rightarrow (r(t), h(t))$ around the 2-axis, in other words if it admits parameterization form as following

$$f(t, \phi) = (r(t)\cos\phi, r(t)\sin\phi, h(t)).$$

Let $\alpha = \alpha(s)$ be a curve in Minkowski space and $X = X(s)$ be vector field along α, we have the parametrization for the ruled surface M in $R_1{}^3$

$$\varphi(s, v) = \alpha(s) + v.X(s),$$

where the curve $\alpha = \alpha(s)$ is called based curve and $X = X(s)$ is called a director curve of the ruled surface [8].

If the angle between $X(s)$ and (spacelike or timelike) osculating (rectifying, normal) plane is constant, then the surface $\varphi(s, v)$ is called a constant slope surface with respect to (spacelike or timelike) osculating (rectifying, normal) planes to the curve α [9].

3. Non-null Surfaces with Constant Slope Ruling with respect to Osculating Plane

Non-null surface with a constant slope ruling with respect to given plane is a term used of surfaces whose generating lines have the same $\boldsymbol{\sigma}$ deviation from the plane. $\boldsymbol{\sigma}$ is called the slope with respect to the plane. The ruled surface is defined by

$$\varphi(s, v) = \alpha(s) + v.X(s),$$

where $\alpha(s)$ is a base curve and $X(s)$ is a direction vector. Surface with a constant slope ruling with respect to given plane in Minkowski space is a surface whose generating lines have the same σ slope with respect to the given plane by direction vectors. The casual character of the direction vectors are changed according to character of the curve α given following cases.

Case 3.1. If $\alpha(s)$ is a spacelike base curve with the principal spacelike normal vector field $n(s)$, then the generating line of the surface is given as follows

$$X(s) = \sigma e_1 + \cos w(s)t(s) + \sin w(s)n(s),$$

and the surface with a constant slope ruling is parameterized by

$$\phi(s, v) = \alpha(s) + v(\sigma e_1 + \cos w(s)t(s) + \sin w(s)n(s)).$$

Case 3.2. If the curve $\alpha(s)$ is spacelike and its normal vector field $n(s)$ is timelike, then the generating line of the surface is given by

$$\bar{X}(s) = \cosh w(s)t(s) + \sinh w(s)n(s) + \sigma(-e_3),$$

and the surface with a constant slope ruling is parameterized by

$$\bar{\phi}(s, v) = \alpha(s) + v(\cosh w(s)t(s) + \sinh w(s)n(s) + \sigma(-e_3)).$$

Case 3.3. If the $\alpha(s)$ is timelike base curve with $n(s)$ spacelike, then the generating line of the surface is given as follows

$$\tilde{X}(s) = \sinh w(s)t(s) + \cosh w(s)n(s) + \sigma e_3,$$

and the surface with a constant slope ruling is parameterized by

$$\tilde{\phi}(s, v) = \alpha(s) + v(\sinh w(s)t(s) + \cosh w(s)n(s) + \sigma e_3).$$

3.1. Rotational non-null surface with a constant slope ruling with respect to osculating plane

In a surface with a constant slope ruling, if we take the base curve α is pseudo circle and the director vector is given by constant angle, then we obtain the rotational surface. The circle is given by the vector functions in Minkowski space. We have different cases as following:

Case 3.1.1. The $\alpha(s)$ is a spacelike circle and its normal vector field n is a spacelike vector. Then the curve $\alpha(s)$ is given by

$$\alpha(s) = \left(0, rcos\left(\tfrac{s}{r}\right), rsin\left(\tfrac{s}{r}\right)\right),$$

and its Frenet frame are obtained as follows

$$t(s) = \left(0, -sin\left(\tfrac{s}{r}\right), cos\left(\tfrac{s}{r}\right)\right),$$

$$n(s) = \left(0, -cos\left(\tfrac{s}{r}\right), -sin\left(\tfrac{s}{r}\right)\right),$$

$$b(s) = -e_1 = (-1,0,0).$$

The surface with a constant slope ruling $\varphi(s, v)$ with respect to osculating plane is obtained by

$$\varphi(s, v) = \alpha(s) + v.X(s),$$

where $X(s) = \sigma e^1 + cos\, w(s)t(s) + sin\, w(s)n(s)$, with $w(s)$ is a constant.

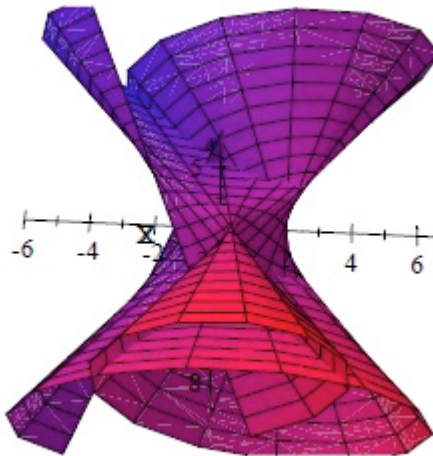The surface has the parametric representation as follows

$$x = \sigma v,$$

$$y = rcos\left(\tfrac{s}{r}\right) - vsin\left(w(s) + \left(\tfrac{s}{r}\right)\right),$$

$$z = rsin\left(\tfrac{s}{r}\right) + vcos\left(w(s) + \left(\tfrac{s}{r}\right)\right),$$

$s \in [0,2\pi r], v \in R$. The Cartesian representation of the surface $\varphi(s, v)$ is obtained as follows

$$\sigma^2(y^2 + z^2) - (x - \sigma rsin\, w(s))^2 = \sigma^2 r^2 cos^2 w(s).$$

Figure 1: Example of the surface for $\sigma = \sqrt{3}, r = 2, \ u = [0, 10]$

Case 3.1.2. If the circle $\alpha(s)$ is a spacelike and its normal vector field $n(s)$ is a timelike vector then the curve $\alpha(s)$ is given by

$$\alpha(s) = \left(rcosh\left(\frac{s}{r}\right), rsinh\left(\frac{s}{r}\right), 0\right),$$

and its Frenet - Serret frame vectors are obtained as follows

$$t(s) = \left(sinh\left(\frac{s}{r}\right), cosh\left(\frac{s}{r}\right), 0\right),$$

$$n(s) = \left(cosh\left(\frac{s}{r}\right), sinh\left(\frac{s}{r}\right), 0\right),$$

$$b(s) = -e_3 = (0,0,-1).$$

The rotational surface with a constant slope ruling given as follows

$$\bar{\varphi}(s, v) = \alpha(s) + v\bar{X}(s),$$

with the directional vector

$$\bar{X}(s) = cosh\, w(s)t(s) + sinh\, w(s)n(s) - \sigma e_3,$$

and $w(s) = const., g(X, X) = 1 + \sigma^2 > 0$, then the vector $\bar{X}$ is a spacelike vector. The parametric representation of the spacelike surface $\bar{\varphi}(s, v)$ as follows;

$$\bar{\varphi}(s, v) = \left(rcosh\left(\frac{s}{r}\right) + vsinh\left(w + \left(\frac{s}{r}\right)\right), rsinh\left(\frac{s}{r}\right) + vcosh\left(w + \left(\frac{s}{r}\right)\right), -v\sigma\right).$$

In the Cartesian coordinate system the equation of the surface is written by

246

$$\sigma^2(x^2 + y^2) + (z + \sigma r sinh\, w(s))^2 = \sigma^2 r^2 cosh^2 w(s).$$

Case 3.1.3. The rotational surface with a constant slope ruling generated by timelike circle $\alpha(s) = \left(rsinh\left(\frac{s}{r}\right), rcosh\left(\frac{s}{r}\right), 0\right)$ in the timelike plane

$$\tilde{\varphi}(s, v) = \alpha(s) + v\tilde{X}(s),$$

where

$$\tilde{X}(s) = sinh\, w(s)t(s) + cosh\, w(s)n(s) + \sigma e_3,$$

$(w(s) = const.)$. After the similar calculations we have the surface as follows

$$(z + \sigma r cosh\, w(s))^2 - \sigma^2(y^2 - x^2) = \sigma^2 r^2 sinh^2 w(s).$$

Remark 3.1.1. In all cases, each rotational surfaces with the constant slope $\sigma, \sigma \in (0, \infty)$ is a rotational one sheet hyperboloid.

3.2. Torsal non-null surface with constant slope ruling with respect to osculating plane

A generatrix of a ruled surface is torsal, if for its each point there is one and the same tangent plane on the surface. A surface is developable if and only if it is a torsal ruled surface. In this section, we will investigate the conditions necessary for the surface to be a torsal surface.

Case 3.2.1. Frenet-Serret vectors of the spacelike circle $\alpha(s)$ can be expressed as follows

$$t(s) = (0, cos\beta(s), sin\beta(s)),$$

$$n(s) = (0, -sin\beta(s), cos\beta(s)),$$

Derivatives of the vector functions Frenet-Serret trihedron are given by

$$t'(s) = \beta'(s).n(s),$$

$$n'(s) = -\beta'(s).t(s),$$

The partial derivatives $\left(\frac{d\varphi(s,v)}{ds}\right)$ of the vector functions can be expressed as follows

$$\left(\frac{d\varphi(s, v)}{ds}\right) = \left(1 - vw'(s)sin\, w(s) - v\beta'(s)sin\, w(s)\right)t(s)$$

$$+vcos\, w(s).\left(\beta'(s) + w'(s)\right)n(s).$$

In the last equation vector function defines the direction vectors of the tangents to the parametric curves for the constant v.

So $v = 0$, $(\frac{d\varphi(s,v)}{ds}) = t(s)$ and for $v = 1$,

$$(\frac{d\varphi(s,v)}{ds}) = (1 - w'(s)\sin w(s) - \beta'(s)\sin w(s))t(s) + (\cos w(s)\beta'(s)$$

$$+\cos w(s)w'(s))n(s).$$

These vectors must be linearly dependent, so we obtained

$$\cos w(s) = 0,$$

$$w(s) = \left(\frac{k\pi}{2}\right), k\varepsilon Z,$$

or

$$\beta'(s) + w'(s) = 0,$$

$$w(s) = -\beta(s) + c, c = const..$$

Remark 3.2.1. The surface $\varphi(s,v)$ is developable if and only if $det(t, X, X') = 0$. So, we calculate this equation as follows;

$$det(t, X, X')) = \begin{vmatrix} 1 & 0 & 0 \\ 0 & \cos w(s) & \sin w(s) \\ 0 & 1 - w'\sin w - \beta'\sin w & \cos w(\beta' + w') \end{vmatrix},$$

$$\cos w(s)(\beta'(s) + w'(s)) = 0.$$

Case 3.2.2. If the circle $\alpha(s)$ is spacelike curve and its normal vector $n(s)$ is timelike, then the curve's Frenet-Serret vectors are

$$t(s) = (cosh\beta(s), sinh\beta(s), 0),$$

$$n(s) = (sinh\beta(s), cosh\beta(s), 0).$$

Derivatives of the these vectors are

$$t'(s) = \beta'(s).n(s),$$

$$n'(s) = \beta'(s).t(s).$$

The partial derivative $(\frac{d\bar{\varphi}(s,v)}{ds})$ of the vector functions are,

$$\left(\frac{d\bar{\varphi}(s,v)}{ds}\right) = [1 + v.w'(s).\sinh w(s) + v\beta'(s)\sinh w(s)]t(s)$$

$$+ v\cosh w(s).\left(\beta'(s)w'(s)\right)n(s),$$

for $v = 0$, $\left(\frac{d\bar{\varphi}(s,v)}{ds}\right) = t(s)$, and for $v = 1$,

$$(\frac{d\bar{\varphi}(s,v)}{ds}) = [1 + w'(s)\sinh w(s) + \beta'(s)\sinh w(s)]t(s) + \cosh w(s).(\beta'(s)$$

$$+ w'(s)).n(s)$$

If it is considered that the vector obtained for $v = 1$ and the vector obtained for $v = 0$ are linearly dependent the following equation is obtained as follows

$$\cosh w(s).(w'(s) + \beta'(s)) = 0.$$

Thus

$i)\cosh w(s) = 0$,

or

$ii)w'(s) + \beta'(s) = 0,$

and $w(s) = -\beta(s) + c.$

Case 3.2.3. The rotational surface generated by timelike circle $\alpha(s)$ curve's Frenet-Serret from vectors in timelike plane are

$$t(s) = (\sinh\beta(s), \cosh\beta(s), 0),$$

$$n(s) = (\cos\beta(s), \sinh\beta(s), 0).$$

The partial derivative $(\frac{d\tilde{\varphi}(s,v)}{ds})$ of the vector functions are

$$(\frac{d\tilde{\varphi}(s,v)}{ds}) = [1 + v.w'(s).\cosh w(s) + v\beta'(s)\cosh w(s)]t(s) + v\sinh w(s).(\beta'(s)$$

$$+ w'(s))n(s),$$

for $v = 0$,

$$\left(\frac{d\widetilde{\varphi}(s,v)}{ds}\right) = t(s),$$

and for $v = 1$,

$$\left(\frac{d\widetilde{\varphi}(s,v)}{ds}\right) = (1 + w'(s)\cosh w(s) + \beta'(s)\cosh w(s))t(s) + \sinh w(s).(\beta'(s)$$
$$+ w'(s)).n(s).$$

Thus,

$$i)\ sinh\ w(s) = 0 \Rightarrow w(s) = 0,$$

or

$$ii)\ w'(s) + \beta'(s) = 0,\ w(s) = -\beta(s) + c.$$

4. Generalized Non-null Surface with Constant Slope Ruling with respect to Osculating Plane

Generating lines of the surface are given by points on the curve $X(s)$ and they have the constant slope with respect to the osculating planes to the curve at every point on the curve $X(s)$. The surface will be called generalized surface with constant slope ruling with respect to the osculating planes. The definitions of this type surface according to casual characters in Minkowski space are described in the following cases.

Case 4.1. The generalized surface with constant slope ruling with respect to osculating plane of the spacelike curve (whose normal vector is spacelike) is given as follows

$$M(s, v) = \alpha(s) + v(u(s)).,$$

such that

$$u(s) = sin\ w(s)t(s) + cos\ w(s)n(s) + \sigma b(s).$$

Case 4.2. The generalized surface with constant slope ruling with respect to osculating plane with spacelike curve and timelike normal vector is defined as follows

$$M^-(s, v) = \alpha(s) + v(\bar{u}(s)),$$

with following generating line

$$\bar{u}(s) = cosh\ w(s)t(s) + sinh\ w(s)n(s) + \sigma b(s).$$

Case 4.3. The generalized surface with constant slope ruling with respect to the osculating plane with timelike curve and spacelike normal vector is defined by
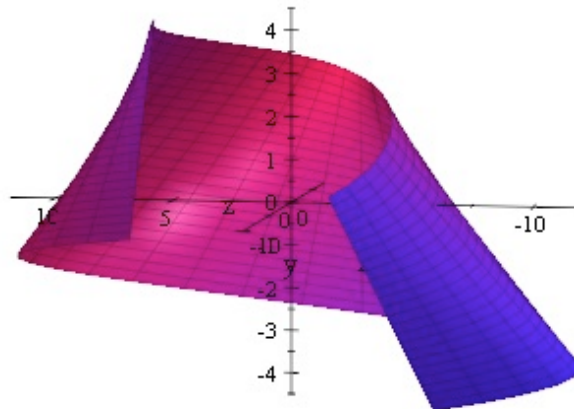
$$\tilde{M}(s,v) = \alpha(s) + v(\tilde{u}(s)),$$

where

$$\tilde{u}(s) = sinh\, w(s)t(s) + cosh\, w(s)n(s) + \sigma b(s).$$

Example 4.1. Let the curve parameterized by vector function

$$\alpha(s) = \left(8cos\left(\frac{s}{2}\right), 8sin\left(\frac{s}{2}\right), \sqrt{6\left(\frac{s}{2}\right)} \right).$$

The generalized surface with constant slope ruling with respect to the osculating plane for $s \in [0,30]$, $w(s) = (\frac{2s}{10\sqrt{2}})$ and $\sigma = \left(\frac{1}{5}\right)$ is shown in following Fig. 2.

Figure 2: Example of the surface for $s \in [0,30]$, $w(s) = (\frac{2s}{10\sqrt{2}})$ and $\sigma = \left(\frac{1}{5}\right)$

4.1. Developable of generalized non-null surface with constant slope ruling with respect to the osculating plane

In this subsection, we investigate the developable condition for the generalized surface with constant slope ruling with respect to the osculating plane with Frenet Frame in Minkowski Space and give some relations and special cases about developable condition.

251

Theorem 4.1.1. The generalized surface $M(s, v)$ with constant slope ruling of the spacelike curve (whose normal vector is spacelike) is developable surface if and only if

$$\tau(cos^2 w(s) - \sigma^2) = \sigma sin \, w(s)(\kappa - w'(s)),$$

where the functions κ and τ are the first and second curvatures of the spacelike base curve, respectively.

Proof. If the surface $M(s, v)$ is developable surface, then it satisfies the following equality

$$det(t, u(s), u(s)') = 0.$$

It is calculated $det(t, u(s), u(s)')$ for the surface $M(s, v)$

$$u(s)' = (cos \, w(s)(w'(s) - \kappa))t(s) + (sin \, w(s)(\kappa - w'(s)) + \sigma \tau)n(s) + (\tau cos \, w(s)b(s)),$$

$$det(t, u(s), u(s)') = \tau(cos^2 w(s) - \sigma^2) - \sigma sin \, w(s)(\kappa - w'(s)) = 0.$$

So developable condition for generalized surface with constant slope ruling with respect to the osculating plane $M(s, v)$ is given by

Remark 4.1.1. If $cos \, w(s) = x^1 = const.$ and $sin \, w(s) = x_2 = const.$

$$\left(\frac{\tau}{\kappa}\right) = \left(\frac{\sigma x_2}{x_1{}^2 - \sigma^2}\right),$$

then the surface $M(s, v)$ is developable if and only if the base curve $\alpha(s)$ is a helix.

Theorem 4.1.2. The surface $\bar{M}(s, v)$ is developable surface if and only if

$$\tau(sin \, h^2 w(s) - \sigma^2) = \sigma cosh \, w(s)(\kappa + w'(s)).$$

Proof. If the surface $\bar{M}(s, v)$ is developable, then it satisfies the following equality

$$\bar{u}(s)' = \left(sinh \, w(s)(w'(s) - \kappa)\right)t(s) + \left(cosh \, w(s)(\kappa - w'(s)) + \sigma \tau\right)n(s)$$
$$+ \left(\tau sinh \, w(s)\right)b(s),$$

$$det(t, \bar{u}(s), \bar{u}(s)') = \tau(sinh^2 w(s) - \sigma^2) - \sigma cosh \, w(s)(\kappa - w'(s)) = 0.$$

So developable condition for the surface $\bar{M}(s, v)$ is obtained as follows

$$\tau(sinh^2 w(s) - \sigma^2) = \sigma cosh \, w(s)(\kappa - w'(s)).$$

Remark 4.1.2. The surface $\bar{M}(s, v)$ is developable surface if and only if the base curve is a helix with

$$\left(\frac{\tau}{\kappa}\right) = \left(\frac{\sigma x_1}{x_2{}^2 - \sigma^2}\right),$$

where $\cos w(s) = x^1 = const.$ and $\sin w(s) = x_2 = const.$

Theorem 4.1.3. The surface $\widetilde{M}(s, v)$ is developable surface if and only if

$$\tau(\cos h^2 w(s) + \sigma^2) = \sigma \sinh w(s) \left(\kappa + w'(s)\right).$$

Proof. By taking derivative of $\tilde{u}(s)$ is obtained as follows

$$\tilde{u}(s)' = (\sinh w(s)(w'(s) - \kappa))t(s) + (\cosh w(s)(\kappa - w'(s)) + \sigma\tau)n(s)$$
$$+ (\tau \sinh w(s))b(s).$$

Then

$$\tau(\cosh^2 w(s) + \sigma^2) - \sigma \sinh w(s)(\kappa + w'(s)) = 0.$$

Thus, the condition that ensures the surface can be developable is as following

$$\tau(\cos h^2 w(s) + \sigma^2) = \sigma \sinh w(s)(\kappa + w'(s)).$$

Remark 4.1.3. We can say that the surface $\widetilde{M}(s, v)$ is developable if and only if the base curve is a helix with

$$\left(\frac{\tau}{\kappa}\right) = \left(\frac{\sigma \sinh b}{\cosh^2 b + \sigma^2}\right),$$

where $\cos w(s) = x_1 = const$ and $\sin w(s) = x_2 = const.$

4.2. Striction line of generalized non-null surface with constant slope ruling with respect to osculating plane

The striction point on a surface is the foot of the common normal between two consecutive generators (or ruling). The set of striction points defines the striction curve given by [10]

$$\beta = \alpha(s) - \left(\frac{<t,X>}{<X',X'>}\right).X(s).$$

Theorem 4.2.1. The striction line on $M(s,v)$ is given by

$$\beta = \alpha(s) - \left(\frac{\cos w(s)\big(\kappa - w'(s)\big)}{\big(\kappa - w'(s)\big)^2 + \tau^2\big(\sigma^2 - \cos^2 w(s)\big) + 2\sin^2 w(s)\big(\kappa - w'(s)\big)\sigma\tau}\right)u(s).$$

Proof. By taking derivative of $u(s)$ is calculated as

$$u(s)' = (\cos w(s)(w'(s) - \kappa))t(s) + (\sin w(s)(\kappa - w'(s)) + \sigma\tau)n(s) + (\tau\cos w(s)b(s))$$

and

$$<t, u(s)> = \cos w(s)(\kappa - w'(s)),$$

$$<u(s)', u(s)'> = (\kappa - w'(s))^2 + \tau^2(\sigma^2 - \cos^2 w(s)) + 2\sin^2 w(s)(\kappa - w'(s))\sigma\tau.$$

Theorem 4.2.2. The striction line on surface $\bar{M}(s,v)$ is given as follows

$$\beta = \alpha(s) - \left(\frac{-\sinh w(s)\big(\kappa + w'(s)\big)}{\big(\kappa + w'(s)\big)\big(\big(\kappa + w'(s)\big) - 2\cosh w(s)\sigma\tau\big) + \tau^2\big(\sigma^2 + \sinh^2 w(s)\big)}\right)u(s).$$

Proof. By taking derivative of $\bar{u}(s)$ is obtained as follows

$$\bar{u}(s)' = (\sinh w(s)(w'(s) - \kappa))t(s) + (\cosh w(s)(\kappa - w'(s)) + \sigma\tau)n(s)$$
$$+ (\tau\sinh w(s))b(s)$$

and

$$<t, \bar{u}(s)> = -\sinh w(s)(\kappa + w'(s)),$$

$$<\bar{u}(s)', \bar{u}(s)'> = (\kappa + w'(s))((\kappa + w'(s)) - 2\cosh w(s)\sigma\tau) + \tau^2(\sigma^2 + \sinh^2 w(s)).$$

If the obtained values are written in place of the striction line equation, then the proof is completed.

Theorem 4.2.3. The striction line on surface $\tilde{M}(s,v)$ is defined by

$$\beta = \alpha(s) - \left(\frac{\cosh w(s)\big(\kappa + w'(s)\big)}{\big(\cosh^2 w(s)(\kappa - w'(s))^2 + [\sinh w(s)(\kappa - w'(s)) - \sigma\tau]\big)^2} + \cosh^2 w(s)\tau^2\right)\tilde{u}(s).$$

Proof. Proof of the theorem can be obtained by making calculations similar to the proof of the previous two theorems.

References

[1] Erdoğdu M., Yavuz A., *Some Characterizations for Involute-Evolute Curve Couples with Constant Curvatures in Minkowski Space*, Afyon Kocatepe University Journal of Science and Engineering,. 19, 031303, 605-614, 2019.

[2] Erdoğdu, M., *Parallel frame of non-lightlike curves in Minkowski space-time*, International Journal of Geometric Methods in Modern Physics, 12, 16 pages, 2015.

[3] López, R., *Differential geometry of curves and surfaces in Lorentz-Minkowski space.* International Electronic Journal of Geometry, 7, 44-107, 2014.

[4] Kaya, F.E., Yavuz, A., *Harmonic curvatures of the strip in Minkowski space.* Asian-European Journal of Mathematics, Vol. 11, No. 04, 1850061, 2018.

[5] Malecek, K., Szarka, J., Szarkova, D., Surfaces *with Constant Slope with Their Generalisation*, The Journal of Polish Society for Geometry and Engineering Graphics, 19, 67-77, 2009.

[6] Walrave, J., *Curves and Surfaces in Minkowski Space*, Ph. D. thesis, K. U. Leuven, Fac. of Science Leuven, 1995.

[7] Önder, M., Uğurlu, H.H., *Frenet Frames and Invariants of Timelike Ruled Surfaces*, Ain Shams Engineering Journal, 4(3), 507-513, 2013.

[8] Wolfgang, K., *Differential Geometry: Curves Surfaces Manifolds,* ISBN-13: 978-0821839881, American Mathematical Society, 2002.

[9] Yaylı, Y., Zıplar, E., *Ferret-Serret motion and ruled surfaces with constant slope*, International Journal of the Physical Science, 6(29), 6727-6734, 2011.

[10] Do Carmo, M.P., *Differential Geometry of Curves and Surfaces*, Prentice Hall, ISBN New Jersy, 1976.

The New Travelling Wave Solutions of Time Fractional Fitzhugh-Nagumo Equation with Sine-Gordon Expansion Method

Orkun TAŞBOZAN[1], Ali KURT[2,*]

[1]*Hatay Mustafa Kemal University, Faculty of Science and Literature, Department of Mathematics, Hatay, Turkey*
otasbozan@mku.edu.tr, ORCID: 0000-0001-5003-6341
[2]*Pamukkale University, Faculty of Science and Literature, Department of Mathematics, Denizli, Turkey*
akurt@pau.edu.tr, ORCID: 0000-0002-0617-6037

Abstract

Authors aimed to employ the sine-Gordon expansion method to acquire the new exact solutions of fractional Fitzhugh-Nagumo equation which is a stripped type of the Hodgkin-Huxley model that expresses in extensive way activation and deactivation dynamics of neuron spiking. By using the wave transformations, by the practicality of chain rule and applicability of the conformable fractional derivative, the fractional nonlinear partial differential equation (FNPDE) changes to a nonlinear ordinary differential equation. So the exact solution of the considered equation can be obtained correctly with the aid of efficient and reliable analytical techniques.

Keywords: Sine-Gordon expansion method; Fitzhugh-Nagumo Equation; Conformable derivative.

Zaman Kesirli Fitzhugh-Nagumo Denkleminin Sine-Gordon Açılım Yöntemi İle Yeni Yürüyen Dalga Çözümleri

Öz

---

* Corresponding Author   DOI: 10.37094/adyujsci.515011

Yazarlar, nöron artışının, geniş bir aktivasyon ve deaktivasyon dinamiğini ifade eden Hodgkin-Huxley modelinin sade bir tipi olan kesirli Fitzhugh-Nagumo denkleminin yeni tam çözümlerini elde etmek için sine-Gordon açılım yöntemini kullanmayı amaçladılar. Dalga dönüşümleri, zincir kuralının pratikliği ve conformable kesirli türevin uygulanabilirliği kullanılarak, lineer olmayan kesirli mertebeden kısmi diferansiyel denklem, lineer olmayan adi diferansiyel denkleme dönüşür. Böylece, ele alınan denklemin tam çözümü etkin ve güvenli analitik tekniklerin yardımı ile doğru bir biçimde elde edilebilir.

Anahtar Kelimeler: Sine-Gordon açılım yöntemi; Fitzhugh-Nagumo denklemi; Conformable türev.

1. Introduction

Fractional calculus that is gone by the name of as arbitrary order differentiation and integration is as old as known calculus. At the beginning fractional derivation was seen as a great paradox in L'Hospital's letter to Liouville who asked firstly about arbitrary order derivation. So the survey of the fractional calculus has been started. In the last decades many scientists dealt with this subject to explain complexity and nonlinearity of the natural events with more accuracy. But they need some tools for modeling these natural phenomenons. So they expressed some definitions as a tool for modeling physical, engineering and social problems mathematically. Especially Grunwald-Letnikov, Riemann-Liouville and Caputo type fractional order derivation and integration definitions are the most popular ones as modeling tools [1-3]. But recently scientists recognized some deficiencies of these definitions. For instance Riemann-Liouville fractional order derivative of a constant is not zero. Both Riemann-Liouville and Caputo derivative definitions do not satisfy the chain rule. Also these definitions do not satisfy the rule for derivative of quotient of two functions and derivative of product of two functions. To annihilate these deficiencies recently Khalil et al. [4] expressed a new definition called "conformable fractional derivative and integral".

Definition 1. Let $f : [0, \infty) \rightarrow \mathbb{R}$ be a function. The αth order *"conformable fractional derivative"* (CFD) of f is expressed by,

$$T_\alpha(f)(t) = \lim_{\varepsilon \to 0} \frac{f(t + \varepsilon t^{1-\alpha}) - f(t)}{\varepsilon},$$

for all $t > 0, \alpha \in (0,1)$ [4].

Definition 2. Let f be α-differentiable over some $(0,a), a > 0$ and $\lim\limits_{t \to 0^+} f^{(\alpha)}(t)$ subsists then $f^{(\alpha)}(0) = \lim\limits_{t \to 0^+} f^{(\alpha)}(t)$. The *"conformable fractional integral"* of a function f starting from $a \geq 0$ is defined as:

$$I_\alpha^a(f)(t) = \int_a^t \frac{f(x)}{x^{1-\alpha}} dx,$$

where considered integral is by means of Riemann improper integral, also, $\alpha \in (0,1]$ [4].

Basic properties of CFD are declared in [4, 5]. The conformable fractional calculus aroused scientist's great interest and huge amount of implementation of this derivative is visible in the literature [6-9]. Korkmaz [10] constructed the solutions of the conformable fractional RLW-Burgers, potential KdV, and CRWP equations by using the modified Kudryashov method. Rosales et al. [11] used the conformable Laplace transform to get the solution of the classical Drude model. Srivastava et al. [12] employed the conformable DTM to evaluate an numerical solution of the SIR epidemic model of childhood disease. Sabiu et al. [13] evaluated analytical solution for the conformable fractional (3+1) dimensional mKdV equation.

In this article authors established the traveling wave solutions of time fractional Fitzhugh-Nagumo Equation

$$D_t^\alpha u - D_x^2 u = u(u-s)(1-u), \tag{1}$$

which arises in nonlinear reaction-diffusion, the transmission of nerve impulses models [14, 15], circuit theory and the area of population genetics [16] as mathematical models. In Eqn. (1) $\alpha \in (0,1)$ and $D_t^\alpha u$ means CFD of function $u(x,t)$.

2. A Brief Description of Implemented Method

The sine-Gordon expansion method is represented briefly in this section. Regarded method relying on the sine-Gordon equation [17] and complex wave transformation [18].

Regard the sine-Gordon equation [19];

$$u_{xx} - u_{tt} = v^2 \sin(u), \tag{2}$$

considering $u = u(x,t)$ and v is constant. Supposing the transformation $u = u(x,t) = U(\varrho)$, $\varrho = \mu(x - ct)$ in the Eqn. (2) led to,

$$U'' = \frac{v^2}{\eta^2(1-c^2)}\sin(U).$$

(3)

By regulating the Eqn. (3), it turns into

$$\left[\left(\frac{U}{2}\right)'\right]^2 = \frac{v^2}{\eta^2(1-c^2)}\sin^2\left(\frac{U}{2}\right) + W,$$

(4)

where W is a constant. Choosing $W = 0$, $\varphi(\varrho) = \dfrac{U}{2}$, $o^2 = \dfrac{v^2}{\eta^2(1-c^2)}$ and replacing in Eqn. (4), we get,

$$\varphi' = o\sin(\varphi),$$

(5)

also establishing $o = 1$ in Eqn. (5), yields

$$\varphi' = \sin(\varphi).$$

(6)

The solution of (6) can be evaluated by the method of separation of variables, we have,

$$\sin(\varphi) = \sin(\varphi(\varrho)) = \frac{2\vartheta e^\varrho}{\vartheta^2 e^{2\varrho} + 1}\Big|_{\vartheta=1} = \operatorname{sech}(\varrho),$$

(7)

$$\cos(\varphi) = \sin(\varphi(\varrho)) = \frac{\vartheta^2 e^{2\varrho} - 1}{\vartheta^2 e^{2\varrho} + 1}\Big|_{\vartheta=1} = \tanh(\varrho)$$

(8)

regarding ϑ is constant. For obtaining following conformable PDE's solution;

$$G(u, D_t^\alpha u, D_x u, D_{xx} u, D_t^\alpha D_t^\alpha u, \ldots),$$

(9)

we use the wave transform $\varrho = kx + w\dfrac{t^\alpha}{\alpha}$. So the time fractional nonlinear PDE turns into an integer order ODE

$$G(U, U'(\varrho), U''(\varrho), U'''(\varrho), \ldots),$$

(10)

Suppose that the solution of Eqn. (10)

$$U(\varrho) = \sum_{i=1}^{n} \tanh^{i-1}(\varrho) \left[B_i \sec h(\varrho) + A_i \tanh(\varrho) \right] + A_0, \tag{11}$$

then due to Eqn. (7) and Eqn. (8), Eqn. (11) can be reorganized as

$$U(\varphi) = \sum_{i=1}^{n} \cos^{i-1}(\varphi) \left[B_i \sin(\varphi) + A_i \cos(\varphi) \right] + A_0. \tag{12}$$

In the Eqn. (10) using the balancing principle n can be examined. Equating the coefficients of $\cos^i(\varphi)$ and $\sin^i(\varphi)$ to zero yields a system. Solving obtained system by using software Mathematica the values of A_i, B_i, k and w can be derived. At the end substituting all the obtained the results for A_i, B_i, η and c in Eqn. (11), the solutions can be derived.

3. Wave Solutions of Time Fractional Fitzhugh-Nagumo Equation

We employ above expressed method to acquire the traveling wave solutions of fractional Fitzhugh-Nagumo equation (1). Regarding the wave transform and chain rule [5] to the Eqn. (1) led to

$$wU' - k^2 U'' = U(U - s)(1 - U), \tag{13}$$

where the prime defines derivative of function U with respect to ϱ. Applying the balancing procedure between the terms U'' and U^3 gives $n = 1$. Suppose that the solution of Eqn. (12) is as follows

$$U = B\sin(\varrho) + A\cos(\varrho) + C. \tag{14}$$

Subrogating Eqn. (14) into Eqn. (13) and equating all the coefficients of $\cos^i(\varrho)$ and $\sin^i(\varrho)$ to be zero, we get the following solution sets

Set 1:

$$A = \frac{s-1}{2}, B = \frac{1}{2}\sqrt{-s^2 + 2s - 1}, C = \frac{s+1}{2}, k = \frac{s-1}{\sqrt{2}}, w = \frac{1}{2}(s-1)(s+1), \tag{15}$$

Set 2:

$$A = -\frac{1}{2}, B = 0, C = \frac{1}{2}, k = -\frac{1}{2\sqrt{2}}, w = -\frac{1}{4}(1-2s), \tag{16}$$

Set 3:

$$A = -\frac{s}{2}, B = 0, C = \frac{s}{2}, k = -\frac{s}{2\sqrt{2}}, w = -\frac{1}{4}(s-2)s, \tag{17}$$

Set 4:

$$A = \frac{1-s}{2}, B = 0, C = \frac{s+1}{2}, k = -\frac{s-1}{2\sqrt{2}}, w = -\frac{1}{4}(s^2-1). \tag{18}$$

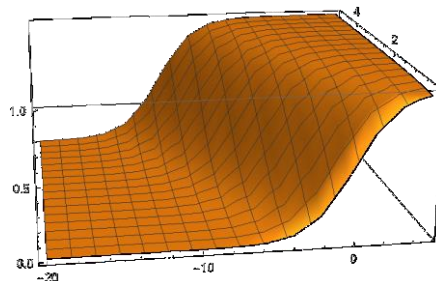Based on these solution sets, we acquire the following solutions respectively,

$$u_1(x,t) = \frac{1}{2}(s-1)\tanh\left(\frac{(s^2-1)t^\alpha}{2\alpha} + \frac{(s-1)x}{\sqrt{2}}\right)$$

$$+ \frac{1}{2}\sqrt{-s^2+2s-1}\operatorname{sech}\left(\frac{(s^2-1)t^\alpha}{2\alpha} + \frac{(s-1)x}{\sqrt{2}}\right) + \frac{s+1}{2},$$

$$u_2(x,t) = \frac{1}{2}\tanh\left(\frac{x}{2\sqrt{2}} - \frac{(2s-1)t^\alpha}{4\alpha}\right) + \frac{1}{2},$$

$$u_3(x,t) = \frac{1}{2}s\tanh\left(\frac{(s-2)st^\alpha}{4\alpha} + \frac{sx}{2\sqrt{2}}\right) + \frac{s}{2},$$

$$u_4(x,t) = \frac{s+1}{2} - \frac{1}{2}(1-s)\tanh\left(\frac{(s-1)x}{2\sqrt{2}} - \frac{(1-s^2)t^\alpha}{4\alpha}\right).$$

The 3D graphics of the obtained solutions are given as follows

Figure 1: The 3D graphical illustration of $u_2(x,t)$ for $s=-1$, $\alpha=0.9$
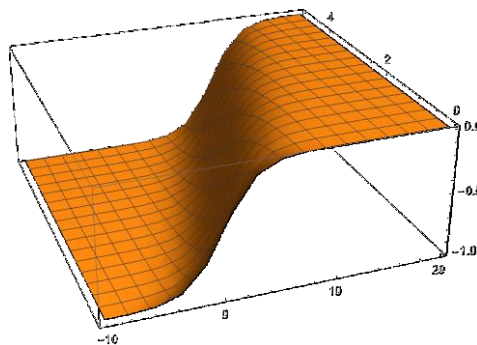
Figure 2: The 3D graphical representation of $u_3(x,t)$ for $s = -1$, $\alpha = 0.9$
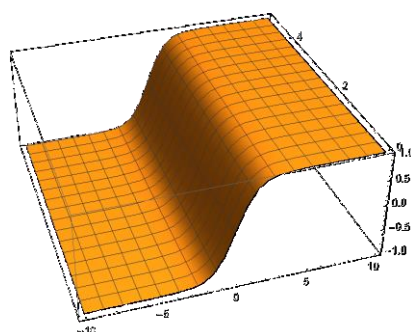
Figure 3: The 3D graphics of $u_4(x,t)$ for $s = -1$, $\alpha = 0.9$

4. Conclusions

In this study authors obtained the new traveling wave solutions of time fractional Fitzhugh-Nagumo equation with the aid of sine-Gordon expansion method. Obtained results show that the method is applicable, accurate and efficient for acquiring the analytical solutions of FPDEs in conformable sense. Also 3D graphical representations are given for the obtained results. Although authors used the advantages of CFD. In other fractional derivative definitions, the considered equations can't be turned into ODE with integer order by using wave transform. Also all the solutions are verified by putting them into the considered equation.

References

[1] Miller, K.S., Ross, B., *An Introduction to the Fractional Calculus and Fractional Differential Equations*, John Wiley &Sons, New York, 1993.

[2] Kilbas, A., Srivastava, H.M., Trujillo, J.J., Theory and Applications of Fractional Differential Equations, Elsevier, San Diego, 2006.

[3] Podlubny, I., Fractional Differential Equations, Academic Press,San Diego, 1999.

[4] Khalil, R., Al Horani, M., Yousef, A., Sababheh, M., *A new definition of fractional derivative*, Journal of Computational and Applied Mathematics, 264, 65-70, 2014.

[5] Abdeljawad, T., *On conformable fractional calculus*, Journal of Computational and Applied Mathematics, 279, 57-66, 2015.

[6] Çenesiz, Y., Kurt, A., Taşbozan, O., *On the New Solutions of the Conformable Time Fractional Generalized Hirota-Satsuma Coupled KdV System,* Annals of West University of Timisoara-Mathematics and Computer Science, 55(1), 37-50, 2017.

[7] Taşbozan, O., Şenol, M., Kurt, A., Özkan, O., *New solutions of fractional Drinfeld-Sokolov-Wilson system in shallow water waves*, Ocean Engineering, 161, 62-68, 2018.

[8] Taşbozan, O., Çenesiz, Y., Kurt, A., Baleanu, D., *New analytical solutions for conformable fractional PDEs arising in mathematical physics by exp-function method*, Open Physics, 15(1), 647-651, 2017.

[9] Kurt, A., Taşbozan, O., Baleanu, D., *New solutions for conformable fractional Nizhnik-Novikov-Veselov system via G'/G expansion method and homotopy analysis methods*, Optical and Quantum Electronics, 49(10), 333, 2017.

[10] Korkmaz, A., *Explicit exact solutions to some one-dimensional conformable time fractional equations*, Waves in Random and Complex Media, 29(1), 124-137, 2019.

[11] Rosales, J.J., Godnez, F.A., Banda, V., Valencia, G.H., *Analysis of the Drude model in view of the conformable derivative*, Optik, 178, 1010-1015, 2019.

[12] Srivastava, H.M., Gunerhan, H., *Analytical and approximate solutions of fractional-order susceptible-infected-recovered epidemic model of childhood disease*, Mathematical Methods in the Applied Sciences, 42(3), 935-941, 2019.

[13] Sabiu, J., Jibril, A., Gadu, A.M., *New exact solution for the (3 +1)conformable space time fractional modified Kortewegde-Vries equations via Sine-Cosine Method*, Journal of Taibah University for Science, 13(1), 91-95, 2019.

[14] Fitzhugh, R., *Impulse and physiological states in models of nerve membrane*, Biophys. J., 1, 445-466, 1961.

[15] Nagumo, J.S., Arimoto, S., Yoshizawa, S., *An active pulse transmission line simulating nerve axon*, Proc. IRE, 50, 2061-2070, 1962.

[16] Aronson, D.G., Weinberger, H.F., *Multidimensional nonlinear diffusion arising in population genetics*, Adv. Math., 30, 33-76, 1978.

[17] Yan, C., *A simple transformation for nonlinear waves*, Physics Letters A, 224(1), 77, 1996.

[18] Çenesiz, Y., Kurt, A., *New fractional complex transform for conformable fractional partial differential equations*, Journal of Applied Mathematics, Statistics and Informatics, 12, 2, 2016.

[19] Rubinstein, J., *Sine-Gordon Equation*, Journal of Mathematical Physics, 11(1), 258-266, 1970.

Comparison of Jordan (σ, τ) - Derivations and Jordan Triple (σ, τ) - Derivations in Semiprime Rings

Emine KOÇ SÖGÜTCÜ[1,*], Öznur GÖLBAŞI[2]

[1]*Cumhuriyet University, Faculty of Science, Department of Mathematics, 58140, Sivas, Turkey*
eminekoc@cumhuriyet.edu.tr, ORCID: 0000-0002-8328-4293
[2]*Cumhuriyet University, Faculty of Science, Department of Mathematics, 58140, Sivas, Turkey*
ogolbasi@cumhuriyet.edu.tr, ORCID: 0000-0002-9338-6170

Abstract

Let R be a 3!-torsion free semiprime ring, τ, σ two endomorphisms of R, $d: R \to R$ be an additive mapping and L be a noncentral square-closed Lie ideal of R. An additive mapping $d: R \to R$ is said to be a Jordan (σ, τ) −derivation if $d(x^2) = d(x)\sigma(x) + \tau(x)d(x)$ holds for all $x, y \in R$. Also, d is called a Jordan triple (σ, τ) −derivation if $d(xyx) = d(x)\sigma(yx) + \tau(x)d(y)\sigma(x) + \tau(xy)d(x)$, for all $x, y \in R$. In this paper, we proved the following result: d is a Jordan (σ, τ) −derivation on L if and only if d is a Jordan triple (σ, τ) −derivation on L.

Keywords: Semiprime ring; Jordan derivation; Jordan triple derivation; (σ, τ) -derivation; Jordan (σ, τ) derivation; Jordan triple (σ, τ)-derivation.

Yarıasal halkalarda Jordan (σ,τ)- Türevler ve Jordan Üçlü (σ,τ)-Türevlerin Karşılaştırılması

Öz

R bir 3!-torsion free yarıasal halka, τ ve σ iki endomorfizm, $d: R \to R$ toplamsal dönüşüm ve L merkez tarafından kapsanmayan R halkasının bir kare kapalı Lie ideali olsun. $d: R \to R$

toplamsal dönüşümü her $x, y \in R$ için $d(x^2) = d(x)\sigma(x) + \tau(x)d(x)$ koşulunu sağlıyorsa d dönüşümüne Jordan (σ, τ) −türev denir. Ayrıca, $d: R \to R$ toplamsal dönüşümü her $x, y \in R$ için $d(xyx) = d(x)\sigma(yx) + \tau(x)d(y)\sigma(x) + \tau(xy)d(x)$ koşulunu sağlıyorsa d dönüşümüne Jordan üçlü (σ, τ) −türev denir. Bu çalışmada, d bir L üzerinde Jordan (σ, τ) −türev olması için gerek ve yeter koşul d dönüşümünün L üzerinde Jordan üçlü (σ, τ) −türev olmasıdır sonucu ispatlanmıştır.

Anahtar kelimeler: Yarıasal halka; Jordan türev; Jordan üçlü türev; (σ, τ) −türev; Jordan (σ, τ) −türev; Jordan üçlü (σ, τ) −türev.

1. Introduction

R is an associative ring with center Z. A ring R is prime ring if $xRy = (0)$ implies $x = 0$ or $y = 0$, and semiprime ring if $xRx = (0)$ implies $x = 0$. An additive subgroup L of R is said to be a Lie ideal of R if $[L, R] \subseteq L$. A Lie ideal L is said to be square-closed if $a^2 \in L$ for all $a \in L$. An additive mapping $d: R \to R$ is called a derivation (resp. Jordan derivation) if $d(u_1 u_2) = d(u_1)u_2 + u_1 d(u_2)$ (resp. $d(u_1{}^2) = d(u_1)u_1 + u_1 d(u_1)$) holds for all $u_1, u_2 \in R$. Let σ and τ be endomorphisms of R. An additive mapping $d: R \to R$ is said to be a (σ, τ) −derivation (resp. Jordan (σ, τ) −derivation) if $d(uv) = d(u)\sigma(v) + \tau(u)d(v)$ (resp. $d(u^2) = d(u)\sigma(u) + \tau(u)d(v)$) holds for all $u, v \in R$. A Jordan triple derivation $d: R \to R$ is an additive mapping satisfying $d(u_1 u_2 u_1) = d(u_1)u_2 u_1 + u_1 d(u_2)u_1 + u_1 u_2 d(u_1)$, for all $u_1, u_2 \in R$. Also, d is called a Jordan triple (σ, τ) −derivation if $d(u_1 u_2 u_1) = d(u_1)\sigma(u_2 u_1) + \tau(u_1)d(u_2)\sigma(u_1) + \tau(u_1 u_2)d(u_1)$, for all $u_1, u_2 \in R$.

We can invetigate that every derivation is a Jordan derivation, but the opposite is not usually true. This result by Herstein [1] was shown in a prime ring of 2- torsion free. The same result was proved by Cusack in [2] to the semiprime rings. The same result was generalized to the Lie ideal of the semiprime ring in [4].

In [4], Jing and Lu, has proven to be a derivation of any of the Jordan triple derivation on prime rings. Vukman [5], examined the results for the semiprime rings. Hence, Rehman and Koç Söğütcü has transferred it Lie ideal of the semiprime ring in [6].

In [7] Herstein proved that each Jordan derivation of the prime ring is a Jordan triple derivation, while Bresar is a derivation of each Jordan triple derivation of a semiprime ring in [8]. In [9], the relation between Jordan triple derivation and Jordan derivation is given.

In this paper, we present the results corresponding to Jordan triple (σ, τ) −derivation and Jordan (σ, τ) −derivation.

2. Results

Lemma 1. [10, Corollary 2.1] Let R be a 2-torsion free semiprime ring, L be a Lie ideal of R such that $L \nsubseteq Z(R)$ and a,b∈L.

i) If $aLa = (0)$, then $a = 0$.

ii) If $aL = (0)$ (or $La = (0)$), then $a = 0$.

iii) If L is square-closed and $aLb = (0)$, then $ab = 0$ and $ba = 0$.

Lemma 2. [6, Theorem 2.1] Let R be a 2-torsion free semiprime ring, $\alpha, \beta \epsilon Aut(R)$ and $L \nsubseteq Z(R)$ be a nonzero square-closed Lie ideal of R. If an additive mapping $d: R \to R$ satisfying

$$d(u_1 u_2 u_1) = d(u_1)\alpha(u_2 u_1) + \beta(u_1)d(u_2)\alpha(u_1) + \beta(u_1 u_2)d(u_1), \text{ for all } u_1, u_2 \in L.$$

and $d(u_1), \beta(u_2) \in L$, then d is a (α, β) −derivation on L.

Lemma 3. Let R be a 2-torsion free semiprime ring, $L \nsubseteq Z(R)$ is a square-closed Lie ideal of R, τ, σ two endomorphisms of R, $\sigma(L) = L$ and $a, b \in L$. If $a\sigma(ub) + \tau(bu)a = 0$, for all $u \in L$ then $a\sigma(ub) = 0$.

Proof. By the hypothesis, we have

$$a\sigma(ub) + \tau(bu)a = 0. \tag{1}$$

Then replacing u by $4ubv, v \in U$ in Eqn. (1) and by 2-torsion freeness, we get $a\sigma(ubvb) + \tau(bubv)a = 0$.

Application ofEqn. (1) yields that

$$-\tau(bu)a\sigma(vb) + \tau(bu)\tau(bv)a = 0.$$

Again using Eqn. (1), we get $a\sigma(ub)\sigma(vb) = 0$.

Using $\sigma(L) = L$, we obtain that $a\sigma(ub)L\sigma(b) = 0$, and so $a\sigma(ub)La\sigma(ub) = 0$. By Lemma 1, we get $a\sigma(ub) = 0$, for all $u \in L$.

Theorem 4. Let R be a 3!-torsion free semiprime ring, τ, σ two endomorphisms of R, $d: R \to R$ an additive mapping, $L \nsubseteq Z(R)$ be a nonzero square-closed Lie ideal of R and

$d(L), \tau(L) \subseteq L, \sigma(L) = L$. Then d is a Jordan (σ, τ) −derivation on L if and only if d is a Jordan triple (σ, τ) −derivation on L.

Proof. We obtain that

$$d(u_1{}^2) = d(u_1)\sigma(u_1) + \tau(u_1)d(u_1), \text{ for all } u_1 \in L. \tag{2}$$

Replacing u_1 by $u_1 + u_2$ in Eqn. (2), using d is an additive mapping and $u_1 \circ u_2 = u_1 u_2 + u_2 u_1$, we see that

$$d(u_1{}^2) + d(u_1 \circ u_2) + d(u_2{}^2) = d(u_1)\sigma(u_1) + \tau(u_1)d(u_1) + d(u_1)\sigma(u_2) +$$
$$d(u_2)\sigma(u_1) + +\tau(u_1)d(u_2) + \tau(u_2)d(u_1) + d(u_2)\sigma(u_2) + \tau(u_2)d(u_2).$$

By the Eqn. (2), we have

$$d(u_1 \circ u_2) = d(u_1)\sigma(u_2) + d(u_2)\sigma(u_1) + \tau(u_1)d(u_2) + \tau(u_2)d(u_1), \tag{3}$$

for all $u_1, u_2 \in L$. Since $u_1{}^2 \circ u_2 + 2u_1 u_2 u_1 = u_1 \circ (u_1 \circ u_2)$, we find

$$d(u_1{}^2 \circ u_2 + 2u_1 u_2 u_1) = d(u_1 \circ (u_1 \circ u_2)), \text{ for all } u_1, u_2 \in L.$$

By the Eqn. (3), we see that

$$d(u_1{}^2 \circ u_2 + 2u_1 u_2 u_1) = d(u_1)\sigma(u_1)\sigma(u_2) + \tau(u_1)d(u_1)\sigma(u_2) + d(u_2)\sigma(u_1{}^2)$$

$$+\tau(u_1{}^2)d(u_2) + \tau(u_2)d(u_1)\sigma(u_1) + \tau(u_2)\tau(u_1)d(u_1)$$

$$+d(2u_1 u_2 u_1).$$

On the other hand,

$$d\big(u_1 \circ (u_1 \circ u_2)\big) = d(u_1)\sigma(u_1 u_2) + d(u_1)\sigma(u_2 u_1) + d(u_1)\sigma(u_2)\sigma(u_1)$$

$$+d(u_2)\sigma(u_1)\sigma(u_1) + \tau(u_1)d(u_2)\sigma(u_1) + \tau(u_2)d(u_1)\sigma(u_1)$$
$$+ \tau(u_1)d(u_1)\sigma(u_2) + \tau(u_1)d(u_2)\sigma(u_1) + \tau(u_1)\tau(u_1)d(u_2)$$
$$+ \tau(u_1)\tau(u_2)d(u_1) + \tau(u_1 u_2)d(u_1) + \tau(u_2 u_1)d(u_1).$$

After comparing the above two equations, we get

$$2d(u_1 u_2 u_1) = 2d(u_1)\sigma(u_2 u_1) + 2\tau(u_1)d(u_2)\sigma(u_1) + 2\tau(u_1 u_2)d(u_1),$$

for all $u_1, u_2 \in L$.

That is,

$$d(u_1 u_2 u_1) = d(u_1)\sigma(u_2 u_1) + \tau(u_1)d(u_2)\sigma(u_1) + \tau(u_1 u_2)d(u_1).$$

Reverse, we see that

$$d(u_1 u_2 u_1) = d(u_1)\sigma(u_2 u_1) + \tau(u_1)d(u_2)\sigma(u_1) + \tau(u_1 u_2)d(u_1), \tag{4}$$

for all $u_1, u_2 \in L$.

Replacing u_2 by $4u_1 u_2 u_1$ in Eqn. (4), using Eqn. (4) and 2-torsion freeness of R, this implies that

$$d(u_1{}^2 u_2 u_1{}^2) = d(u_1)\sigma(u_1 u_2 u_1{}^2) + \tau(u_1)d(u_1 u_2 u_1)\sigma(u_1) + \tau(u_1{}^2 u_2 u_1)d(u_1)$$

$$= d(u_1)\sigma(u_1 u_2 u_1{}^2) + \tau(u_1)d(u_1)\sigma(u_2 u_1)\sigma(u_1) + \tau(u_1)\tau(u_1)d(u_2)\sigma(u_1)\sigma(u_1)$$

$$+\tau(u_1)\tau(u_1 u_2)d(u_1)\sigma(u_1) + \tau(u_1{}^2 u_2 u_1)d(u_1).$$

On the other hand, replacing u_1 by $u_1{}^2$ in Eqn. (4), we have

$$d(u_1{}^2 u_2 u_1{}^2) = d(u_1{}^2)\sigma(u_2 u_1{}^2) + \tau(u_1{}^2)d(u_2)\sigma(u_1{}^2) + \tau(u_1{}^2 u_2)d(u_1{}^2).$$

Comparing the expressions and let us write $A(u_1) = d(u_1{}^2) - d(u_1)\sigma(u_1) - \tau(u_1)d(u_1)$ for brevity, we get

$$A(u_1)\sigma(u_2 u_1{}^2) + \tau(u_1{}^2 u_2)A(u_1) = 0.$$

By Lemma 3, we get $A(u_1)\sigma(u_2)\sigma(u_1{}^2) = 0$, for all $u_1, u_2 \in L$ and using $\sigma(L) = L$, we have

$$A(u_1)u_2\sigma(u_1{}^2) = 0, \text{ for all } u_1, u_2 \in \text{L}. \tag{5}$$

Multiplying $\sigma(u_1{}^2)$ on the left and $A(u_1)$ on the right hand side of Eqn. (5), we see that

$$\sigma(u_1{}^2)A(u_1)u_2\sigma(u_1{}^2)A(u_1) = 0, \text{ for all } u_1, u_2 \in L.$$

Lemma 1 leads to

$$\sigma(u_1{}^2)A(u_1) = 0, \text{ for all } u_1 \in L. \tag{6}$$

Replacing u_2 by $4\sigma(u_1{}^2)u_2 A(u_1)$ in Eqn. (5) and by 2-torsion freeness, we have

$$A(u_1)\sigma(u_1{}^2)u_2 A(u_1)\sigma(u_1{}^2) = 0, \text{ for all } u_1, u_2 \in L.$$

Using Lemma 1, we have

$A(u_1)\sigma(u_1{}^2) = 0$ for all $u_1 \in L$. (7)

Replacing u_1 by u_1+u_2 in Eqn. (7), we obtain that

$$
\begin{aligned}
0 \;=\;& A(u_1 + u_2)\sigma((u_1 + u_2)^2) \\
=\;& (d(u_1{}^2) - d(u_1)\sigma(u_1) - \tau(u_1)d(u_1) + d(u_2{}^2) - d(u_2)\sigma(u_2) - \tau(u_2)d(u_2) \\
& +d(u_1 \circ u_2) - d(u_1)\sigma(u_2) - d(u_2)\sigma(u_1) \\
& -\tau(u_1)d(u_2) - \tau(u_2)d(u_1))\sigma((u_1 + u_2)^2).
\end{aligned}
$$

Let us write $B(u_1, u_2) = d(u_1 \circ u_2) - d(u_1)\sigma(u_2) - d(u_2)\sigma(u_1) - \tau(u_1)d(u_2) - \tau(v)d(u_1)$, for brevity. For all $u_1, u_2 \in L$,

$$(A(u_1) + A(u_2) + B(u_1, u_2))\sigma((u_1 + u_2)^2) = 0.$$

Using Eqn. (7) and $(u_1 + u_2)^2 = u_1{}^2 + u_1 \circ u_2 + u_2{}^2$, we have

$$
\begin{aligned}
0 =\;& A(u_2)\sigma(u_1{}^2) + A(u_1)\sigma(u_2{}^2) + A(u_1)\sigma(u_1 \circ u_2) + A(u_2)\sigma(u_1 \circ u_2) \\
& +B(u_1, u_2)\sigma(u_1{}^2) + B(u_1, u_2)\sigma(u_2{}^2) + B(u_1, u_2)\sigma(u_1 \circ u_2).
\end{aligned}
$$
(8)

Replacing u_1 with $-u_1$ in Eqn. (8) and using $A(-u_1) = A(u_1)$ and $B(-u_1, u_2) = -B(u_1, u_2)$, we get

$$
\begin{aligned}
0 =\;& A(u_2)\sigma(u_1^2) + A(u_1)\sigma(u_2^2) - A(u_1)\sigma(u_1 \circ u_2) - A(u_2)\sigma(u_1 \circ u_2) \\
& -B(u_1, u_2)\sigma(u_1{}^2) - B(u_1, u_2)\sigma(u_2{}^2) + B(u_1, u_2)\sigma(u_1 \circ u_2).
\end{aligned}
$$
(9)

Combining Eqn. (8) with Eqn. (9), we have

$$2A(u_1)\sigma(u_1 \circ u_2) + 2A(u_2)\sigma(u_1 \circ u_2) + 2B(u_1, u_2)\sigma(u_1{}^2) + 2B(u_1, u_2)\sigma(u_2{}^2) = 0.$$

By 2-torsion freeness, we have

$$A(u_1)\sigma(u_1 \circ u_2) + A(u_2)\sigma(u_1 \circ u_2) + B(u_1, u_2)\sigma(u_1{}^2) + B(u_1, u_2)\sigma(u_2{}^2) = 0. \quad (10)$$

Replacing u_1 by $2u_1$ in Eqn. (8), we find

$$
\begin{aligned}
0 =\;& 4A(u_2)\sigma(u_1^2) + 4A(u_1)\sigma(u_2^2) + 8A(u_1)\sigma(u_1 \circ u_2) + 2A(u_2)\sigma(u_1 \circ u_2) \\
& +8B(u_1, u_2)\sigma(u_1{}^2) + 2B(u_1, u_2)\sigma(u_2{}^2) + 4B(u_1, u_2)\sigma(u_1 \circ u_2).
\end{aligned}
$$

Using Eqn. (8) and Eqn. (9) in the last equation, we get

$6\,A(u_1)\sigma(u_1 \circ u_2) + 6B(u_1, u_2)\sigma(u_1{}^2) = 0$, for all $u_1, u_2 \in L$.

By 3!-torsion freeness, we have

$$A(u_1)\sigma(u_1 \circ u_2) + B(u_1, u_2)\sigma(u_1{}^2) = 0, \tag{11}$$

for all $u_1, u_2 \in L$.

Right multiplication of Eqn.(11) by A(u_1), we have

$A(u_1)\sigma(u_1 \circ u_2)A(u_1) + B(u_1, u_2)\sigma(u_1{}^2)A(u_1) = 0$.

Using Eqn.(6), we find that

$A(u_1)\sigma(u_1 u_2)A(u_1) + A(u_1)\sigma(u_2 u_1)A(u_1) = 0$, for all $u_1, u_2 \in L$.

Since $\sigma(L) = L$, we have

$$A(u_1)\sigma(u_1)u_2 A(u_1) + A(u_1)u_2\sigma(u_1)A(u_1) = 0, \tag{12}$$

for all $u_1, u_2 \in L$.

Replacing u_2 by $2u_2\sigma(u_1)$ in the above relation and by 2-torsion freeness, we get

$A(u_1)\sigma(u_1)u_2\sigma(u_1)A(u_1) + A(u_1)u_2\sigma(u_1{}^2)A(u_1) = 0$, for all $u_1, u_2 \in L$.

Again using Eqn. (6), we get

$A(u_1)\sigma(u_1)u_2\sigma(u_1)A(u_1) = 0$, for all $u_1, u_2 \in L$.

and so

$\sigma(u_1)A(u_1)\sigma(u_1)u_2\sigma(u_1)A(u_1)\sigma(u_1) = 0$, for all $u_1, u_2 \in L$.

By Lemma 1, we have

$\sigma(u_1)A(u_1)\sigma(u_1) = 0$, for all $u_1 \in L$.

Right multiplication of Eqn. (12) by $\sigma(u_1)$ and using the last equation, we see that

$A(u_1)\sigma(u_1)u_2 A(u_1)\sigma(u_1) = 0$, for all $u_1, u_2 \in L$.

Again using Lemma 1, we have

$$A(u_1)\sigma(u_1) = 0, \text{ for all } u_1 \in L. \tag{13}$$

Replacing u_1 by u_1+u_2, we have

$$0 = A(u_1 + u_2)\sigma(u_1 + u_2) = (A(u_1) + A(u_2) + B(u_1, u_2))\sigma(u_1 + u_2).$$

Using Eqn. (13), we get

$$A(u_1)\sigma(u_2) + A(u_2)\sigma(u_1) + B(u_1, u_2)\sigma(u_1) + B(u_1, u_2)\sigma(u_2) = 0.$$

Replacing u_1 by $-u_1$ in the above relation, we have

$$A(u_1)\sigma(u_2) + B(u_1, u_2)\sigma(u_1) = 0, \tag{14}$$

for all $u_1, u_2 \in L$.

Right multiplication of Eqn. (14) by $\sigma(u_1)A(u_1)$, we find

$$A(u_1)\sigma(u_2)\sigma(u_1)A(u_1) + B(u_1, u_2)\sigma(u_1{}^2)A(u_1) = 0.$$

Using Eqn. (6), we see

$$A(u_1)\sigma(u_2)\sigma(u_1)A(u_1) = 0$$

and so $\sigma(u_1)A(u_1)u_2\sigma(u_1)A(u_1) = 0.$

By Lemma 1, we have

$$\sigma(u_1)A(u_1) = 0, \text{ for all } u_1 \in L.$$

Right multiplication of Eqn. (14) by $A(u_1)$ and using the last equation

$$A(u_1)\sigma(u_2)A(u_1) = 0, \text{ for all } u_1, u_2 \in L.$$

By Lemma 1 and $\sigma(L) = L$, we get $A(u_1) = 0$, for all $u_1 \in L$. We conclude that d is a Jordan (σ, τ)-derivation.

Corollary 5. Let R be a 3!-torsion free semiprime ring, τ, σ two endomorphisms of R, $d: R \to R$ an additive mapping, $L \nsubseteq Z(R)$ be a nonzero square-closed Lie ideal of R, $\sigma, \tau \epsilon Aut(R)$ and $d(L), \tau(L) \subseteq L, \sigma(L) = L$. If d is a Jordan $(\sigma, \tau)-$derivation on L, then d is $(\sigma, \tau)-$derivation on L.

Proof. By Theorem 4 and Lemma 2, we get the required results.

3. Conclusions

Our study is about the comparison of Jordan triple (σ, τ) -derivation and Jordan (σ, τ)-derivation. Using this theorem, each Jordan (σ, τ)-derivation has been shown to be a (σ, τ)-derivation.

Acknowledgement

References

[1] Herstein, I.N., Jordan derivations of prime rings, Proceedings of the American Mathematical Society, 8, 1104-1110, 1957.

[2] Cusack, J.M., *Jordan derivations on rings,* Proceedings of the American Mathematical Society, 53, 321-324, 1975.

[3] Gupta, V., *Jordan derivations on Lie ideals of prime and semiprime rings,* East-West Journal of Mathematics, 9 (1), 47-51, 2007.

[4] Jing, W., Lu, S., *Generalized Jordan derivations on prime rings and standard opetaror algebras,* Taiwanese Journal of Mathematics, 7, 605-613, 2003.

[5] Vukman, J., *A note on generalized derivations of semiprime rings,* Taiwanese Journal of Mathematics, 11, 367-370., 2007.

[6] Rehman, N., Koç Sögütcü, E., *Lie idelas and Jordan Triple (α,β)-derivations in rings,* Communications Faculty of Sciences University of Ankara Series A1-Mathematics and Statistics, 69(1), 528-539, 2020. (doi: 10.31801/cfsuasmas.549472)

[7] Herstein, I.N., *Topics in ring theory*, The University of Chicago Press, Chicago, London, 1969.

[8] Bresar, M., *Jordan mappings of semiprime rings,* Journal of Algebra, 127, 218-228, 1989.

[9] Fošner, M., Ilišević, D., *On Jordan triple derivations and related mappings,* Mediterranean Journal of Mathematics, 5, 415-427, 2008.

[10] Hongan, M., Rehman, N., Al-Omary, R. M., *Lie ideals and Jordan triple derivations in rings*, Rendiconti del Seminario Matematico della Università di Padova, 125,147-156, 2011. (doi: 10.4171/RSMUP/125-9).

Kuratowski Theorems in Soft Topology

Müge ÇERÇİ[1], Gültekin SOYLU[2, *]

[1]*Haliç University, Department of Mathematics, İstanbul, Turkey*
mugecerci@halic.edu.tr, ORCID: 0000-0001-9018-463X
[2]*Akdeniz University, Department of Mathematics, Antalya, Turkey*
gsoylu@akdeniz.edu.tr, ORCID: 0000-0003-2640-5690

Abstract

This paper deals with the soft topological counterparts of concepts introduced by Kuratowski. First the closure operator is investigated in the soft topological setting and afterwards the Kuratowski Closure-Complement Theorem is stated and proved.

Keywords: Soft topology; Kuratowski closure operator; Kuratowski Closure-Complement Theorem.

Soft Topolojideki Kuratowski Teoremleri

Öz

Bu çalışmada Kuratowski tarafından ortaya konan bazı topolojik kavramların Soft topolojideki karşılıkları ele alınmıştır. Öncelikle kapanış operatörü soft topolojide tanımlanmış ve incelemesi yapılmış daha sonra Kuratowski Kapanış-Tümleyen Teoremi ifade edilmiş ve kanıtlanmıştır.

Anahtar Kelimeler: Soft topoloji; Kuratowski kapanış operatörü; Kuratowski Kapanış-Tümleyen Teoremi.

---

1. Introduction

Various theories have been proposed with the purpose of dealing with different types of uncertainties. Besides to probability theory the most known ones are the theory of fuzzy sets [1], the theory of vague sets [2], the theory of rough sets [3]. Nevertheless not suprisingly all these theories have their own drawbacks. In 1999, Molodtsov [4] introduced the notion of soft set theory claiming to overcome the drawbacks of the theories mentioned above. Molodtsov proposed applications of this new tool in several directions, such as smoothness of functions, game theory, operations research, Riemann integration, Perron integration, probability, theory of measurement. After the introduction of soft sets, several researchers started to extend the theory in different paths. In 2003, Maji et al [5] defined and studied several fundamental notions of soft set theory. The outcome of soft set theory in algebraic structures was introduced by Aktaş and Çağman [6]. They not only defined the notion of soft groups but also obtained most of their basic properties. In 2011, Shabir and Naz [7] brought to light the idea of soft topological spaces. They interestingly observed that a soft topological space is actually a parameterized family of topological spaces.

This paper participates to all those discussions in the direction of soft topological spaces. First the concept of Kuratowski closure operator is introduced in the soft topological setting. The correspondence of a closure operator with a soft topology is given. In addition the well-known Kuratowski Closure-Complement Theorem is stated and proved for soft topological spaces.

2. Preliminaries

In this section, the fundamental definitions and results of soft set theory and its topology are presented. They may be found in earlier studies [4 , 5, 7-10].

Definition 1. Let U denote the universe of discourse and E be a set of parameters. Let $\wp(U)$ denote the power set of U and A be a non-empty subset of E. A pair (F, A) is called a soft set over U, where F is a mapping given by $F: A \longrightarrow \wp(U)$.

Basically, a soft set over U is a parametrized family of subsets of the universe U. In the sequel U will allways be the universe of discourse and E the set of parameters unless stated otherwise.

For the sake of simplicity we hereafter will suppose any given soft set (F, A) over U with parameters set E is extended as following:

$$F': E \to \wp(U), F'(e) = \begin{cases} F(e) & ,if\, e \in A \\ \varnothing & ,if\, e \in E - A \end{cases}.$$ By this extension we will denote any given

soft set (F, A) by (F, E) just by replacing F' with F.

Definition 2. Let U be an initial universe set and E be an universe set of parameters. Let (F, E) and (G, E) be soft sets over a common universe set U. Then (F, E) is a soft subset of (G, E), denoted by $(F, E) \stackrel{\sim}{\subset} (G, E)$, if for all $e \in E$, $F(e) \subset G(e)$.

(F, E) is called a soft super set of (G, E), if (G, E) is a soft subset of (F, E). We denote it by $(F, E) \stackrel{\sim}{\supset} (G, E)$.

Definition 3. Two soft set (F, E) and (G, E) over a common universe U are said to be soft equal if, (F, E) is a soft subset of (G, E) and (G, E) is a soft subset of (F, E).

Definition 4. A soft set (F, E) over U is said to be the empty soft set denoted by Φ_E if for all $e \in E$, $F(e) = \emptyset$.

Definition 5. A soft set (F, E) over U is said to be an absolute soft set denoted by U_E if for all $e \in E$, $F(e) = U$.

Clearly $U_E^c = \Phi_E$ and $\Phi_E^c = U_E$.

Definition 6. The union (H, E) of two soft sets (F, E) and (G, E) over the common universe U, denoted $(F, E) \stackrel{\sim}{\cup} (G, E)$, is defined as $H(e) = F(e) \cup G(e)$, for all $e \in E$.

Definition 7. The intersection (H, E) of two soft sets (F, E) and (G, E) over the common universe U, denoted $(F, E) \stackrel{\sim}{\cap} (G, E)$, is defined as $H(e) = F(e) \cap G(e)$, for all $e \in E$.

Definition 8. The complement of a soft set (F, E) is denoted by $(F, E)^c$ and is defined by $(F, E)^c := (F^c, E)$, where $F^c: E \longrightarrow \wp(U)$ is a mapping given by $F^c(e) = U - F(e)$, for all $e \in E$.

Proposition 9. Let (F, E) and (G, E) be the soft sets over U. Then

i) $\left((F, E) \stackrel{\sim}{\cup} (G, E) \right)^c = (F, E)^c \stackrel{\sim}{\cap} (G, E)^c$,

ii) $\left((F, E) \stackrel{\sim}{\cap} (G, E) \right)^c = (F, E)^c \stackrel{\sim}{\cup} (G, E)^c$.

Definition 10. Let U be an initial universe and E be the non-empty set of parameters. The difference (H, E) of two soft sets (F, E) and (G, E) over U, denoted by $(F, E)\widetilde{\backslash}(G, E)$, is defined as $H(e) = F(e)\backslash G(e)$, for all $e \in E$.

Definition 11. Let (F, E) be a soft set over U and $u \in U$. We say that $u \widetilde{\in} (F, E)$ read as u belongs to the soft set (F, E) whenever $u \in F(e)$, for all $u \in E$.

Note that for any $u \in U$, $u \widetilde{\notin} (F, E)$ if $u \notin F(e)$, for some $e \in E$.

Definition 12. Let Y be a non-empty subset of U, then Y_E denotes the soft set (Y, E) over U for which $Y(e) = Y$, for all $e \in E$.

Definition 13. Let $u \in U$, then (u, E) denotes the soft set over U for which $u(e) = \{u\}$, for all $e \in E$.

Definition 14. Let τ be a collection of soft sets over U, then τ is said to be a soft topology on U if

T1) Φ_E,U_E belong to τ,

T2) The union of any number of soft sets in τ belongs to τ,

T3) The intersection of any two soft sets in τ belongs to τ.

The triplet (U, τ, E) is called a soft topological space over U.

Definition 15. Let (U, τ, E) be a soft topological space over U, then the members of τ are said to be soft open sets in U.

Definition 16. Let (U, τ, E) be a soft topological space over U. A soft set (F, E) over U is said to be a soft closed set in U, if its complement $(F, E)^c$ belongs to τ.

Proposition 17. Let (U, τ, E) be a soft topological space over U and E be the non-empty set of parameters. Then

i) Φ_E,U_E are closed soft sets over U,

ii) The intersection of any number of soft closed sets is a soft closed set over U,

iii) The union of any two soft closed sets is a soft closed set over U.

Definition 18. Let (U, τ, E) be a soft space over U and (F, E) be a soft set over U. Then the soft closure of (F, E), denoted by $\overline{(F, E)}$ is the intersection of all soft closed super sets of (F, E).

Clearly $\overline{(F, E)}$ is the smallest soft closed set over U which contains (F, E).

Theorem 19. Let (U, τ, E) be soft topological space over U and (F, E), (G, E) are soft sets over U. Then the following hold:

i) $\Phi_E = \overline{\Phi_E}$ and $U_E = \overline{U_E}$,

ii) $(F, E) \tilde{\subseteq} \overline{(F, E)}$,

iii) (F, E) is a soft closed set if and only if $(F, E) = \overline{(F, E)}$,

iv) $\overline{\overline{(F, E)}} = \overline{(F, E)}$,

v) $(F, E) \tilde{\subseteq} (G, E)$ implies $\overline{(F, E)} \tilde{\subseteq} \overline{(G, E)}$,

vi) $\overline{(F, E) \tilde{\cup} (G, E)} = \overline{(F, E)} \tilde{\cup} \overline{(G, E)}$,

vii) $\overline{(F, E) \tilde{\cap} (G, E)} \tilde{\subseteq} \overline{(F, E)} \tilde{\cap} \overline{(G, E)}$.

Definition 20. Let (U, τ, E) be a soft topological space over U then soft interior of soft set (F, E) over U is denoted by $(F, E)°$ and is defined as the union of all soft open sets contained in (F, E).

Thus $(F, E)°$ is the largest soft open set contained in (F, E).

Theorem 21. Let (U, τ, E) be a soft topological space over U and (F, E), (G, E) are soft sets over U. Then the followings hold:

i) $\Phi_E° = \Phi_E$ and $U_E° = U_E$,

ii) $(F, E)° \tilde{\subseteq} (F, E)$,

iii) $((F, E)°)° = (F, E)°$,

iv) (F, E) is a soft open set if and only if $(F, E)° = (F, E)$,

v) $(F, E) \tilde{\subseteq} (G, E)$ implies $(F, E)° \tilde{\subseteq} (G, E)°$,

vi) $((F,E) \mathbin{\widetilde{\cap}} (G,E))^{\circ} = (F,E)^{\circ} \mathbin{\widetilde{\cap}} (G,E)^{\circ}$,

vii) $(F,E)^{\circ} \mathbin{\widetilde{\cup}} (G,E)^{\circ} \mathbin{\widetilde{\subseteq}} ((F,E) \mathbin{\widetilde{\cup}} (G,E))^{\circ}$.

Theorem 22. Let (F,E) be a soft set of soft topological space over U. Then

i) $((F,E)^c)^{\circ} = \left(\overline{(F,E)}\right)^c$,

ii) $\overline{((F,E)^c)} = ((F,E)^{\circ})^c$,

iii) $(F,E)^{\circ} = \left(\overline{((F,E)^c)}\right)^c$.

Definition 23. Let (U,τ,E) be a soft topological space over U then the soft boundary of soft set (F,E) over U is denoted by $\underline{(F,E)}$ and defined as $\underline{(F,E)} = \overline{(F,E)} \mathbin{\widetilde{\cap}} \overline{((F,E)^c)}$.

Remark 24. From the above definition it follows directly that the soft sets (F,E) and $(F,E)^c$ have same soft boundary.

Theorem 25. Let (F,E) be a soft set of soft topological space over U. Then the followings hold:

(1) $(\underline{(F,E)})^c = (F,E)^{\circ} \mathbin{\widetilde{\cup}} ((F,E)^c)^{\circ} = (F,E)^{\circ} \mathbin{\widetilde{\cup}} (F,E)_{\circ}$

(2) $\overline{(F,E)} = (F,E)^{\circ} \mathbin{\widetilde{\cup}} \underline{(F,E)}$

(3) $\underline{(F,E)} = \overline{(F,E)} \mathbin{\widetilde{\cap}} \overline{((F,E)^c)} = \overline{(F,E)} \mathbin{\widetilde{\backslash}} (F,E)^{\circ}$

(4) $(F,E)^{\circ} = (F,E) \mathbin{\widetilde{\backslash}} \underline{(F,E)}$.

3. Soft Kuratowski Closure Operator

Theorem 26. Let (U,τ,E) be a soft topological space. The operator $\varphi: \wp(U_E) \to \wp(U_E)$, defined by $\tilde{\varphi}((F,E)) = \overline{(F,E)}$ satisfies following properties:

K1) $(F,E) \mathbin{\widetilde{\subseteq}} \tilde{\varphi}((F,E))$,

K2) $\tilde{\varphi}(\tilde{\varphi}((F,E))) = \tilde{\varphi}((F,E))$,

K3) $\tilde{\varphi}((F,E) \mathbin{\widetilde{\cup}} (G,E)) = \tilde{\varphi}((F,E)) \mathbin{\widetilde{\cup}} \tilde{\varphi}((G,E))$,

K4) $\tilde{\varphi}(\Phi_E) = \Phi_E$.

Conversely for any operator $\tilde{\varphi}\colon \wp(U_E) \to \wp(U_E)$ satisfying these four conditions there exists a unique soft topology $\tau_{\tilde{\varphi}}$ on U such that for all $(F,E) \widetilde{\subset} U_E$ the soft closure of (F,E) is just $\tilde{\varphi}((F,E))$.

Proof. (K1)-(K4) are obvious from Theorem 19.

For the second part of the theorem let us define $\tau_{\tilde{\varphi}}$ as following:

$$\tau_{\tilde{\varphi}} = \{(F,E) \widetilde{\subset} U_E \colon \tilde{\varphi}((F,E)^c) = (F,E)^c\}$$

We will show that the family $\tau_{\tilde{\varphi}}$ is a soft topology on U_E.

T1) $\tilde{\varphi}(U_E^c) = \tilde{\varphi}(\Phi_E)$ and by (K4) $\tilde{\varphi}(\Phi_E) = \Phi_E$ therefore $U_E \in \tau_{\tilde{\varphi}}$. $\tilde{\varphi}(\Phi_E^c) = \tilde{\varphi}(U_E)$ and since by (K1) $U_E \subset \tilde{\varphi}(U_E)$ we obeserve that $\tilde{\varphi}(U_E) = U_E$ and $\Phi_E \in \tau_{\tilde{\varphi}}$.

T2) Let $(F,E), (G,E) \in \tau_{\tilde{\varphi}}$ then we have $\tilde{\varphi}((F,E)^c) = (F,E)^c$ and $\tilde{\varphi}((G,E)^c) = (G,E)^c$. Now by the Morgan's $\tilde{\varphi}(((F,E) \widetilde{\cap} (G,E))^c) = \tilde{\varphi}((F,E)^c \widetilde{\cup} (G,E)^c)$ and by (K3) $\tilde{\varphi}((F,E)^c \widetilde{\cup} (G,E)^c) = \tilde{\varphi}((F,E)^c) \widetilde{\cup} \tilde{\varphi}((G,E)^c) = (F,E)^c \widetilde{\cup} (G,E)^c = ((F,E) \widetilde{\cap} (G,E))^c$ which means that $(F,E) \widetilde{\cap} (G,E) \in \tau_{\tilde{\varphi}}$.

T3) Let $(F_i,E) \in \tau_{\tilde{\varphi}}$ for $\forall i \in I$. For $\forall i \in I$ we have $(F_i,E) \widetilde{\subset} \widetilde{\underset{i\in I}{\cup}} (F_i,E)$ therefore,

$U_E \widetilde{\setminus} \widetilde{\underset{i\in I}{\cup}} (F_i,E) \widetilde{\subset} U_E \widetilde{\setminus} (F_i,E)$ and with help of (K3) it can be seen that for $\forall i \in I$, $\tilde{\varphi}\left(U_E \widetilde{\setminus} \widetilde{\underset{i\in I}{\cup}} (F_i,E)\right) \widetilde{\subset} \tilde{\varphi}(U_E \widetilde{\setminus} (F_i,E))$. Since each (F_i,E) is a member of $\tau_{\tilde{\varphi}}$ we have $\tilde{\varphi}(U_E \widetilde{\setminus} (F_i,E)) = U_E \widetilde{\setminus} (F_i,E)$ thus, $\tilde{\varphi}\left(U_E \widetilde{\setminus} \widetilde{\underset{i\in I}{\cup}} (F_i,E)\right) \widetilde{\subset} \widetilde{\cap} (U_E \widetilde{\setminus} (F_i,E))$ and finally by De Morgan's

$$\tilde{\varphi}\left(U_E \widetilde{\setminus} \widetilde{\underset{i\in I}{\cup}} (F_i,E)\right) \widetilde{\subset} \left(U_E \widetilde{\setminus} \widetilde{\underset{i\in I}{\cup}} (F_i,E)\right). \tag{1}$$

On the other hand by (K1),

$$U_E \widetilde{\setminus} \widetilde{\underset{i\in I}{\cup}} (F_i,E) \widetilde{\subset} \tilde{\varphi}\left(U_E \widetilde{\setminus} \widetilde{\underset{i\in I}{\cup}} (F_i,E)\right). \tag{2}$$

Combining Eqn. (1) and Eqn. (2) we get the equality $\tilde{\varphi}\left(U_E \widetilde{\setminus} \widetilde{\underset{i\in I}{\cup}} (F_i,E)\right) = U_E \widetilde{\setminus} \widetilde{\underset{i\in I}{\cup}} (F_i,E)$ hence

$$\widetilde{\underset{i\in I}{\cup}} (F_i,E) \in \tau_{\tilde{\varphi}}.$$

Once we have seen that $\tau_{\tilde{\varphi}}$ is a soft topolgy the property (K2) will help us showing that $\tilde{\varphi}((F,E)) = \overline{(F,E)}$:

Since by (K2) $\tilde{\varphi}(\tilde{\varphi}((F,E))) = \tilde{\varphi}((F,E))$ we have by definition of $\tau_{\tilde{\varphi}}$, $\tilde{\varphi}((F,E))^c \in \tau_{\tilde{\varphi}}$ and therefore $\tilde{\varphi}((F,E))$ is a soft closed set which means,

$$\overline{(F,E)} \widetilde{\subseteq} \tilde{\varphi}((F,E)). \tag{3}$$

For the reverse inclusion we first observe that since $\overline{(F,E)}$ is a closed set, by definition of $\tau_{\tilde{\varphi}}$, $\tilde{\varphi}((\overline{(F,E)})) = \overline{(F,E)}$. Additionally we have $(F,E) \widetilde{\subseteq} \overline{(F,E)}$ and by (K1) $\tilde{\varphi}((F,E)) \widetilde{\subseteq} \tilde{\varphi}(\overline{(F,E)}) = \overline{(F,E)}$ which is the required inclusion,

$$\tilde{\varphi}((F,E)) \widetilde{\subseteq} \overline{(F,E)}. \tag{4}$$

Thus by Eqn. (3) and Eqn. (4) $\tilde{\varphi}((F,E)) = \overline{(F,E)}$. The operator $\tilde{\varphi}$ in this theorem is called to be a Kuratowski soft closure operator.

Example 27. Let $U = \mathbb{R}$, $E = \{e_1, e_2, \ldots, e_n\}$ and $\tilde{\varphi}: \wp(\mathbb{R}_E) \to \wp(\mathbb{R}_E)$ be defined as following:

$$\tilde{\varphi}((F,E)) = \begin{cases} \Phi_E, & \text{if } (F,E) = \Phi_E; \\ (F,E) \, \widetilde{\cup} \, (\sqrt{2}, E), & \text{if } (F,E) \neq \Phi_E; \end{cases}$$

$\tilde{\varphi}$ is a soft Kuratowski closure operator.

It can be easily verified that $\tilde{\varphi}$ satisfies (K1)-(K4). The topology generated by $\tilde{\varphi}$ is

$$\tau_{\tilde{\varphi}} = \left\{ (F,E) : (\sqrt{2}, E) \widetilde{\subseteq} (F,E)^c \right\} \widetilde{\cup} \, U_E.$$

For sure the duallity between closednes and opennes of soft sets in soft topological spaces reflects a dual concept to Soft Closure Operators: In the sequel we introduce the Soft Interior Operator.

Theorem 28. In a soft topological space (X, τ, E) the operator $\widetilde{\Psi}: \wp(U_E) \to \wp(U_E)$, $\widetilde{\Psi}((F,E)) = (F,E)°$ satisfies following properties:

I1) $\widetilde{\Psi}((F,E)) \widetilde{\subseteq} (F,E)$,

I2) $\widetilde{\Psi}(\widetilde{\Psi}((F,E))) = \widetilde{\Psi}((F,E))$,

I3) $\widetilde{\Psi}((F,E) \, \widetilde{\cap} \, (G,E)) = \widetilde{\Psi}((F,E)) \, \widetilde{\cap} \, \widetilde{\Psi}((G,E))$,

I4) $\widetilde{\Psi}(U_E) = U_E$.

Conversely, suppose that the operator $\widetilde{\Psi}: \wp(U_E) \to \wp(U_E)$ satisfies the 4 conditions given above then there exists a soft topology $\tau_{\widetilde{\Psi}}$ on U such that for each $(F,E) \widetilde{\subseteq} U_E$ the soft interior of (F,E) is just $\widetilde{\Psi}((F,E))$.

Proof. The first part of the theorem is obvious from Theorem 21. For the converse part it can be first varified that $\tilde{\varphi}((F,E)) = U_E \widetilde{\setminus} \widetilde{\Psi}((F,E)^c)$ is a soft Kuratowski closure. Afterwards it can be seen that for the topology $\tau_{\widetilde{\Psi}} = \left\{(F,E) \widetilde{\subseteq} U_E : \widetilde{\Psi}((F,E)) = (F,E)\right\}$ we have the equality $(F,E)^{\circ} = \widetilde{\Psi}((F,E))$.

Example 29. Let $U = \mathbb{R}$, $E = \{e_1, e_2, \ldots, e_n\}$ and $\widetilde{\Psi}: \wp(\mathbb{R}_E) \to \wp(\mathbb{R}_E)$ be defined as following:

$$\widetilde{\Psi}((F,E)) = \begin{cases} \mathbb{R}_E, & \text{if } (F,E) = \mathbb{R}; \\ (F,E) \widetilde{\setminus} (\sqrt{2}, E), & \text{if } (F,E) \neq \mathbb{R}. \end{cases}$$

$\widetilde{\Psi}$ is a soft interior operator and the corresponding soft topology is the family

$$\tau_{\widetilde{\Psi}} = \left\{(F,E) \in \wp(\mathbb{R}_E): (F,E)) \widetilde{\cap} (\sqrt{2}, E) = \Phi_E\right\}.$$

4. Soft Kuratowski Closure-Complement Theorem

The Kuratowski Closure-Complement Theorem which was first proved by the Polish mathematician Kazimierz Kuratowski in 1922 can be given by using soft sets as follows:

Theorem 30. Let (U, τ, E) be a soft topological space and (F,E) be a soft set over U. The number of different soft sets obtained by soft complementing and soft closing the set (F,E) can not exceed 14. Moreover, this number can be attained for a soft set in the soft standard topology.

Several proofs of the classical version of this theorem are demonstrated by different mathematicians. The way we have choosen is analoguous to the proof of Strabel [11] but before going to the proof of the theorem, we will review some algebraic notions that are in connection with the operators used in the proof. Given a soft topological space (U, τ, E) define the soft complement operator a and the soft closure operator b on soft subsets $(F,E) \widetilde{\subseteq} U_E$ by $a(F,E) = U_E \widetilde{\setminus} (F,E)$ and $b(F,E) = \overline{(F,E)}$, respectively. Obviously $aa(F,E) = (F,E)$. Starting with any soft topological space (U, τ, E), possible distinct operators on (U, τ, E) that can be obtained by composing the elements of the set $\{a, b\}$ yield to a monoid with the identity element aa. This monoid is called the Kuratowski monoid on (U, τ, E).

For any soft topological space (U, τ, E), a natural partial order on the Kuratowski monoid exists.(U, τ, E) If $\circ_1$ and $\circ_2$ are elements of the Kuratowski monoid on (U, τ, E), we define the partial order $\leq$ as $\circ_1 \leq \circ_2$ if for every $(F, E) \tilde{\subseteq} U_E$, $\circ_1 (F, E) \leq \circ_2 (F, E)$.

After this short introduction we are ready for the proof of the theorem.

Proof. Let (U, τ, E) be a soft topological space. We mentioned above that $aa = id$. At the same time $bb = b$. Therefore it can be easily observed that a member of the Kuratowski monoid on (U, τ, E) has to be equivalent to one of the operators: *id*, a, b, ab, ba, *aba*, *bab*, *abab*, *baba*, *ababa*, *babab*, *abab ... ab*, *baba ... ba*, *abab ... aba* or *baba ... bab*.

We will now obtain that $bab = babababab$. Firstly,

$$aba\big((F, E)\big) = ab\big(U_E \tilde{\backslash} (F, E)\big)$$

$$= a\left(\big(U_E \tilde{\backslash} (F, E)\big)^{\circ} \tilde{\cup} \underline{(F, E)}\right)$$

$$= (F, E)^{\circ}$$

Now $ababab \leq bab$ since $ababab(F, E)$ is the interior of $bab(F, E)$. By the fact that $bb = b$, it follows that $bababab \leq bbab = bab$. Also, $abab \leq b$ since $abab(F, E)$ is the interior of $b(F, E)$. Hence, $babab \leq bb = b$. Then $ababab \geq ab$, and therefore $bababab \geq bab$. We conclude that $bab = bababab$. From this it can be deduced that any word on $\{a, b\}$ that is longer than 7 places has to be equivalent to a word of length at most 7. Thus, for any soft topological space (U, τ, E), each operator in the Kuratowski monoid on (U, τ, E) is equivalent to at least one of the following:

$id, a, b, ab, ba, aba, bab, abab, baba, ababa, babab, ababab, bababa, abababa$

Therefore, for a soft topological space (U, τ, E), the Kuratowski monoid on (U, τ, E) can have order at most 14 and hence for any $(F, E) \tilde{\subseteq} U_E$, there are at most 14 distinct soft sets that can be obtained via soft closures and soft complements of (F, E).

To complete the proof of the theorem we need to show that this bound of 14 can be attained for a soft set. The following set will serve to this objective. $(F, E) \tilde{\subseteq} \mathbb{R}_E$ given by

$$(F, E) = \left\{\big(e_1, (0,1)\big), \big(e_2, (1,2)\big), \big(e_3, \{3\}\big), \big(e_4, [4,5] \cap \mathbb{Q}\big)\right\}$$

attains the bound of 14; that is, we can produce 14 distinct soft sets from (F, E) by taking soft complements and soft closures. These soft sets are:

$$id(F,E) = \{(e_1,(0,1)),(e_2,(1,2)),(e_3,\{3\}),(e_4,[4,5] \cap \mathbb{Q})\}, \tag{i}$$

$$a(F,E) = \begin{Bmatrix} (e_1,(-\infty,0] \cup [1,+\infty)), (e_2,(-\infty,1] \cup [2,+\infty)), \\ (e_3,(-\infty,3] \cup (3,+\infty)), (e_4,(-\infty,4) \cup (5,+\infty) \cup ([4,5] \cap I)) \end{Bmatrix}, \tag{ii}$$

$$b(F,E) = \{(e_1,[0,1]),(e_2,[1,2]),(e_3,\{3\}),(e_4,[4,5])\}, \tag{iii}$$

$$ab(F,E) = \begin{Bmatrix} (e_1,(-\infty,0) \cup (1,+\infty)), (e_2,(-\infty,1) \cup (2,+\infty)), \\ (e_3,(-\infty,3) \cup (3,+\infty)), (e_4,(-\infty,4) \cup (5,+\infty)) \end{Bmatrix}, \tag{iv}$$

$$ba(F,E) = \begin{Bmatrix} (e_1,(-\infty,0] \cup [1,+\infty)), (e_2,(-\infty,1] \cup [2,+\infty)), \\ (e_3,\mathbb{R}),(e_4,\mathbb{R}) \end{Bmatrix}, \tag{v}$$

$$aba(F,E) = \{(e_1,(0,1)),(e_2,(1,2))\}, \tag{vi}$$

$$bab(F,E) = \begin{Bmatrix} (e_1,(-\infty,0] \cup [1,+\infty)), (e_2,(-\infty,1] \cup [2,+\infty)), \\ (e_3,\mathbb{R}),(e_4,(-\infty,4] \cup [5,+\infty)) \end{Bmatrix}, \tag{vii}$$

$$abab(F,E) = \{(e_1,(0,1)),(e_2,(1,2)),(e_4,(4,5))\}, \tag{viii}$$

$$baba(F,E) = \{(e_1,[0,1]),(e_2,[1,2])\}, \tag{ix}$$

$$ababa(F,E) = \begin{Bmatrix} (e_1,(-\infty,0) \cup (1,+\infty)), (e_2,(-\infty,1) \cup (2,+\infty)), \\ (e_3,\mathbb{R}),(e_4,\mathbb{R}) \end{Bmatrix}, \tag{x}$$

$$babab(F,E) = \{(e_1,[0,1]),(e_2,[1,2]),(e_4,[4,5])\}, \tag{xi}$$

$$ababab(F,E) = \begin{Bmatrix} (e_1,(-\infty,0) \cup (1,+\infty)), (e_2,(-\infty,1) \cup (2,+\infty)), \\ (e_3,\mathbb{R}),(e_4,(-\infty,4) \cup (5,+\infty)) \end{Bmatrix}, \tag{xii}$$

$$bababa(F,E) = \begin{Bmatrix} (e_1,(-\infty,0] \cup [1,+\infty)), (e_2,(-\infty,1] \cup [2,+\infty)), \\ (e_3,\mathbb{R}),(e_4,\mathbb{R}) \end{Bmatrix}, \tag{xiii}$$

$$abababa(F,E) = \{(e_1,(0,1)),(e_2,(1,2))\}. \tag{xiv}$$

References

[1] Zadeh, L.A., *Fuzzy sets*, Information and Control, 8(3), 338–353, 1965.

[2] Gau, W.-L., Buehrer, D.J., *Vague sets*, IEEE Transactions on Systems, Man, and Cybernetics, 23(2), 610–614, 1993.

[3] Pawlak, Z., *Rough sets*, International Journal of Computer & Information Sciences, 11(5), 341–356, 1982.

[4] Molodtsov, D., *Soft set theory-first results*, Computers & Mathematics with Applications, 37(4-5), 19–31, 1999.

[5] Maji, P.K., Biswas, R., Roy, A.R., *Soft set theory*, Computers & Mathematics with Applications, 45(4-5), 555–562, 2003.

[6] Aktaş, H., Çağman, N., *Soft sets and soft groups*, Information Sciences, 177(13), 2726–2735, 2007.

[7] Shabir, M., Naz, M., *On soft topological spaces*, Computers & Mathematics with Applications, 61(7), 1786–1799, 2011.

[8] Çağman, N., Karataş, S., Enginoğlu, S., *Soft topology*, Computers & Mathematics with Applications, 62(1), 351–358, 2011.

[9] Feng, F., Jun, Y:B., Zhao, X., *Soft semirings*, Computers & Mathematics with Applications, 56(10), 2621–2628, 2008.

[10] Hussain, S., Ahmad, B., *Some properties of soft topological spaces*, Computers & Mathematics with Applications, 62(11), 4058–4067, 2011.

[11] Strabel, G., *The Kuratowski Closure-Complement Theorem*, Accessed on 15.02.2019. www.mathtransit.com/2009 strabel.pdf, 2009.

On (p, q)-Rogers-Szegő Matrices

Adem ŞAHİN[1],*

[1]Tokat Gaziosmanpaşa University, Faculty of Education Tokat, Türkiye
adem.sahin@gop.edu.tr, ORCID: 0000-0001-5739-4117

Abstract

In the present article, we have discussed the (p, q)-numbers, the Rogers-Szegő polynomial and the (p, q)-Rogers-Szegő polynomial and have defined the (p, q)-matrices and the (p, q)-Rogers-Szegő matrices. We have presented some algebraic properties of these matrices and have proved them. In particular, we have obtained the factorization of these matrices, their inverse matrices, as well as the matrix representations of the (p, q)-numbers, the Rogers-Szegő polynomials and the (p, q)-Rogers-Szegő polynomials.

Keywords: (p, q)-analogue; (p, q)-Rogers-Szegő polynomials; (p, q)-Rogers-Szegő matrix.

(p, q)-Rogers-Szegő Matrisleri Üzerine

Öz

Bu çalışmada, (p, q)-sayılarını, Rogers-Szegő polinomunu ve (p, q)-Rogers-Szegő polinomunu ele aldık ve (p, q)-matrislerini ve (p, q)-Rogers-Szegő matrislerini tanımladık. Bu matrislere ait bazı özellikleri verdik ve bunların ispatlarını yaptık. Özellikle, bu matrislerin

çarpanlara ayrılışını, bunların ters matrislerini ve (p,q)-sayılarının, Rogers-Szegő polinomlarının ve (p,q)-Rogers-Szegő polinomlarının matris temsillerini elde ettik.

Anahtar Kelimeler: (p,q)-analoji; (p,q)-Rogers-Szegő polinomu; (p,q)-Rogers-Szegő matrisi.

1. Introduction

The q-binomial is defined as;

$$\begin{bmatrix} m \\ s \end{bmatrix}_q = \frac{(q;q)_m}{(q;q)_s (q;q)_{m-s}}, \text{ and } (a;q)_m = \prod_{j=0}^{m-1}(1-aq^j). \tag{1}$$

Another way to present the q-binomial is;

$$\begin{bmatrix} m \\ s \end{bmatrix}_q = \frac{[m]_q!}{[s]_q![m-s]_q!}$$

where $[m]_q = \dfrac{1-q^m}{1-q}$ and $[m]_q! = [1]_q[2]_q...[m]_q$.

The q-oscillator algebra is an important part of the quantum groups [1- 3]. Accordingly, the (p,q)-oscillator algebra was presented in [4] and studied in [5-6]. The (p,q)-number $[m]_{p,q}$ was introduced as a result of the studies on the (p,q)-oscillator. The (p,q)-number is defined as;

$$[m]_{p,q} = \frac{p^m - q^m}{p-q}.$$

And it is obvious that;

$$\lim_{p\to 1}[m]_{p,q} = [m]_q.$$

The (p,q)-binomial coefficient is defined as;

$$\begin{bmatrix} m \\ s \end{bmatrix}_{p,q} = \frac{(p,q;p,q)_m}{(p,q;p,q)_s(p,q;p,q)_{m-s}} = \frac{[m]_{p,q}!}{[s]_{p,q}![m-s]_{p,q}!}, \text{ and } (a,b;p,q)_m = \prod_{s=0}^{m-1}(ap^s - bq^s)$$

where $[0]_{p,q}! = 1$ and $[m]_{p,q}! = [1]_{p,q}[2]_{p,q}...[m]_{p,q}$.

After the presentation of the (p,q)-number, the (p,q)-calculus studied in [1, 4, 7-9].

Recently, many researchers have studied the q analogue of number sequences and polynomials, see [10-13]. The Rogers-Szegő polynomials were shown up in the studies of Rogers [14, 15] and were discussed by Szegő [16]. The single variable Rogers-Szegő polynomial is defined as;

$$H_m(x) = \sum_{k=0}^{m} \begin{bmatrix} m \\ s \end{bmatrix}_q x^s .$$

The Rogers-Szegő polynomials satisfy the recursion in [17, p. 49] given as;

$$H_{m+1}(x) = (1+x)H_m(x) + x(q^m - 1)H_{m-1}(x) .$$

Jagannathan and Sridhar [18] defined the (p,q)-Rogers-Szegő polynomial using the (p,q)-number and showed that it is related to the (p,q)-oscillator. The (p,q)-Rogers-Szegő polynomial is defined as;

$$H_m(x,p,q) = \sum_{s=0}^{m} \begin{bmatrix} m \\ s \end{bmatrix}_{p,q} x^s .$$

This polynomial is a natural generalization of the Rogers-Szegő polynomial as;

$$\lim_{p \to 1} H_m(x,p,q) = H_m(x) .$$

Additionally, some matrices associated with the number sequences and the polynomials were studied. For example, in [19] the authors studied the k-Fibonacci matrix and the symmetric k-Fibonacci matrix, in [20] the authors studied the Pell matrix. Lee et al. [21] gave the factorization of the Fibonacci matrix. In [10] the authors studied the $(q;x;s)$-Fibonacci and Lucas matrices. Fonseca and Petronilho [22] gave explicit inverses of some tridiagonal matrices. Some of the important works on the number sequences are determinant and permanent representations [23-28].

2. (p,q)-Matrices and Rogers-Szegő Polynomial

Definition 1. The $n \times n$ lower triangular (p,q)-matrices $\mathbf{N}_n^{p,q} = [a_{rs}]$ are defined by

$$a_{rs} = \begin{cases} [r-s+1]_{p,q}, & r-s \geq 0 \\ 0, & otherwise. \end{cases}$$

Theorem 2. Let $\mathbf{N}_n^{p,q}$ are (p,q)-matrices, then

$$(\mathbf{N}_n^{p,q})^{-1} = [b_{rs}] = \begin{cases} 1, & r = s \\ -(p+q), & r-s=1 \\ pq, & r-s=2 \\ 0, & \text{otherwise.} \end{cases}$$

Proof. It suffices to prove that $\mathbf{N}_n^{p,q}(\mathbf{N}_n^{p,q})^{-1} = I_n$. It is obvious, for $r < s$,

$$\sum_{k=0}^{n} a_{rk}b_{ks} = 0 \text{ and for } r = s, \ \sum_{k=0}^{n} a_{rk}b_{ks} = a_{rr}b_{rr} = 1. \text{ For } r > s > 0 \text{ we have}$$

$$\sum_{k=0}^{n} a_{rk}b_{ks} = \sum_{k=s}^{s+2} a_{rk}b_{kr} = [r-s+1]_{p,q} + [r-s]_{p,q}(-p-q) + [r-s-1]_{p,q}\,pq$$
$$= [r-s+1]_{p,q} - ([r-s]_{p,q}(p+q) + [r-s-1]_{p,q}(-pq)) = 0$$

which implies that $\mathbf{N}_n^{p,q}(\mathbf{N}_n^{p,q})^{-1} = I_n$.

Definition 3. The $n \times n$ tridiagonal matrices $\mathbf{H}_n^q = [h_{rs}]$ are defined by

$$h_{rs} = \begin{cases} -1, & s-r=1 \\ x+1, & r=s \\ x(q^{r-1}-1), & r-s=1 \\ 0, & \text{otherwise.} \end{cases} \tag{3}$$

Theorem 4. Let $\widehat{\mathbf{H}}_n^q$ be a lower triangular matrix defined as

$$\widehat{\mathbf{H}}_n^q = \begin{bmatrix} 1 & 0 & & 0 \\ & & & 0 \\ & -\mathbf{H}_n^q & & \\ & & & 1 \end{bmatrix}. \tag{4}$$

Then, $(\widehat{\mathbf{H}}_n^q)^{-1} = [\bar{h}_{ij}] = \begin{cases} H_{i-j}(x), & i \geq j \\ 0, & \text{otherwise.} \end{cases}$

Proof. It is obvious by using matrix product.

3. (p, q) Rogers-Szego Matrices

Definition 5. The $n \times n$ lower triangular (p,q)-Rogers-Szegő matrices $\mathbf{R}_n^{p,q} = [r_{ij}]$ are defined by

$$r_{ij} = \begin{cases} H_{i-j}(x,p,q), & i-j \geq 0 \\ 0, & \text{otherwise.} \end{cases}$$

The sequence $h_n(x,p,q)$ is defined by $h_0(x,p,q) = 1$, $h_1(x,p,q) = x+1$ and

$$h_n(x,p,q) = (x+1)h_{n-1}(x,p,q) + \sum_{s=1}^{n-1} (-1)^{n-s} H_{n-s+1}(x,p,q) h_{s-1}(x,p,q).$$

Definition 6. The $n \times n$ lower Hessenberg matrices $\mathbf{S}_n^{p,q} = [a_{rs}]$ are defined by

$$a_{rs} = \begin{cases} H_{r-s+1}(x,p,q), & r-s \geq -1 \\ 0, & \text{otherwise.} \end{cases}$$

Lemma 7. [28] Let H_n be an $n \times n$ lower Hessenberg matrix for all $n \geq 1$ and define det(H_0) = 1. Then, $\det(H_1) = a_{11}$ and for $n \geq 2$

$$\det(H_n) = a_{s+1,s+1} \det(H_{s-1}) + \sum_{k=1}^{s-1} [(-1)^{s-k} a_{s,k} \prod_{j=k}^{s} a_{j,j+1} \det(H_{k-1})].$$

Lemma 8. For $n \geq 1$, $\det(\mathbf{S}_n^{p,q}) = h_n(x,p,q)$.

Proof. $\det(\mathbf{S}_1^{p,q}) = h_1(x,p,q) = x+1$. Suppose that the result is true for all $m \leq n$. We prove it for $m = n+1$. Actually, by using Lemma 7 we have

$$\det(\mathbf{S}_{n+1}^{p,q}) = s_{n+1,n+1} \det(\mathbf{S}_n^{p,q}) + \sum_{i=1}^{n} [(-1)^{n+1-i} s_{n+1,i} \prod_{j=i}^{n} s_{j,j+1} \det(\mathbf{S}_{i-1}^{p,q})]$$

$$= (x+1) \det(\mathbf{S}_n^{p,q}) + \sum_{i=1}^{n} [(-1)^{n+1-i} H_{n+2-i+1}(x,p,q) \det(\mathbf{S}_{i-1}^{p,q})]$$

$$= (x+1) \det(\mathbf{S}_n^{p,q}) + \sum_{i=1}^{n} [(-1)^{n+1-i} H_{n+2-i}(x,p,q) h_{i-1}(x,p,q)]$$

$$= h_{n+1}(x,p,q).$$

Lemma 9. Let $n \geq 1$ then,

$$H_n(x,p,q) = \sum_{k=1}^{n} (-1)^{k+1} h_k(x,p,q) H_{n-k}(x,p,q).$$

Proof. From the previous definition of $h_n(x,p,q)$ we know $h_0(x,p,q) = 1$ and

$$h_n(x,p,q) = (x+1)h_{n-1}(x,p,q) + \sum_{k=1}^{n-1} (-1)^{n-k} H_{n-k+1}(x,p,q) h_{k-1}(x,p,q).$$

Using this equation, we have;

$$h_n(x,p,q) - (x+1)h_{n-1}(x,p,q) + H_2(x,p,q)h_{n-2}(x,p,q) - ... + H_{n-1}(x,p,q)h_1(x,p,q)$$
$$-H_n(x,p,q)h_0(x,p,q) = 0$$
$$\Rightarrow H_n(x,p,q) = h_n(x,p,q) - (x+1)h_{n-1}(x,p,q) + H_2(x,p,q)h_{n-2}(x,p,q) - ...$$
$$+H_{n-1}(x,p,q)h_1(x,p,q).$$

Theorem 10. Let $\mathbf{R}_n^{p,q}$ be the (p,q)-Rogers-Szegő matrices, then

$$(\mathbf{R}_n^{p,q})^{-1} = [t_{ij}] = \begin{cases} (-1)^{i-j} h_{i-j}(x,p,q), & i-j \geq 0 \\ 0, & \text{otherwise.} \end{cases}$$

Proof. The proof runs like in Theorem 2 using Lemma 9.

Corollary 11. Let $\mathbf{R}_n^{p,q}$ be the (p,q)-Rogers-Szegő matrices and $\widehat{\mathbf{H}}_n^q$ be the lower triangular matrices in Eqn. (4). Then, $\mathbf{R}_n^{1,q} = (\widehat{\mathbf{H}}_n^q)^{-1}$.

Theorem 12. Let $\mathbf{D}_n^{p,q} = [d_{rs}]_{n \times n}$ be an $n \times n$ lower Hessenberg matrix defined as

$$d_{rs} = \begin{cases} -1, & r+1 = s \\ (-1)^{r-s} h_{r-s+1}(x,p,q), & r-s \geq 0 \\ 0, & \text{otherwise.} \end{cases}$$

Then,

$$\det \mathbf{D}_n^{p,q} = H_n(x,p,q).$$

Proof. The proof runs like in Lemma 8 using Lemma 7.

The following two corollaries are easy consequences of known results in the literature.

Corollary 13. Let $N_n = [n_{ij}]$ be an $n \times n$ tridiagonal matrix defined as

$$n_{ij} = \begin{cases} -1, & j-i=1 \\ p+q, & i=j \\ -pq, & i-j=1 \\ 0, & \text{otherwise.} \end{cases}$$

Then, $\det N_n = [n+1]_{p,q}$, where $i = \sqrt{-1}$.

Proof. $\det N_1 = [2]_{p,q} = p+q$. Suppose that the result is true for all the $m \leq n-1$. We prove it for $m = n$.

$$N_n([1]_{p,q}, \ldots, [n]_{p,q})^T = (0, \ldots, 0, [n+1]_{p,q})^T.$$

In fact, using Cramer's rule we have

$$[n]_{p,q} = \frac{\det(N_{n-1})[n+1]_{p,q}}{\det(N_n)} \Rightarrow [n+1]_{p,q} = \frac{\det(N_n)[n]_{p,q}}{\det(N_{n-1})}.$$

We obtain $\det N_n = [n+1]_{p,q}$.

Therefore, $\det N_n = [n+1]_{p,q}$ holds for all positive integers n.

Corollary 14. Let $\mathbf{H}_n^q$ be the matrix in Eqn. (3). Then, $\det \mathbf{H}_n^q = H_n(x)$.

Proof. The proof runs like in Corollary 13.

If we multiply the rth row by $(-1)i^r$ and the sth column by $(-i)^{s+2}$ of the matrices N_n, $\mathbf{H}_n^p$ and $\mathbf{D}_n^{p,q}$, then the determinant is not altered [23]. In addition, there is a connection between the determinant and permanent of the Hessenberg matrix [26, 29]. Then, it is clear that the following corollaries holds.

Corollary 15. Let $\mathbf{E}_n^{p,q} = [e_{ij}]$ be an $n \times n$ Hessenberg matrix defined as

$$e_{st} = \begin{cases} i, & t-s=1 \\ i^{3(s-t)} h_{s-t+1}(x,p,q), & s-t \geq 0 \\ 0, & \text{otherwise.} \end{cases}$$

Then, $\det \mathbf{E}_n^{p,q} = H_n(x,p,q)$, where $i = \sqrt{-1}$.

Corollary 16. Let $H_n(x,p,q)$ be (p,q)-Rogers-Szegő polynomial, $\overline{\mathbf{D}}_n^{p,q} = [\overline{d}_{ij}]$ and $\overline{\mathbf{E}}_n^{p,q} = [\overline{e}_{ij}]$ be an $n \times n$ Hessenberg matrices defined as

$$\overline{d}_{ij} = \begin{cases} 1, & j-i=1 \\ (-1)^{i-j} h_{i-j+1}(x,p,q), & i-j \geq 0 \\ 0, & \text{otherwise,} \end{cases} \qquad \overline{e}_{st} = \begin{cases} -i, & t-s=1 \\ (i)^{3(s-t)} h_{s-t+1}(x,p,q), & s-t \geq 0 \\ 0, & \text{otherwise.} \end{cases}$$

Then, $per\overline{\mathbf{D}}_n^{p,q} = per\overline{\mathbf{E}}_n^{p,q} = H_n(x,p,q)$, where $i = \sqrt{-1}$.

Corollary 17. Let $H_n(x)$ be Rogers-Szegő polynomial, then

$$\det \mathbf{D}_n^{1,q} = \det \mathbf{E}_n^{1,q} = per\overline{\mathbf{D}}_n^{1,q} = per\overline{\mathbf{E}}_n^{1,q} = H_n(x).$$

Proof. Proof is obvious from equation $\lim_{p \to 1} H_n(x,p,q) = H_n(x)$.

Corollary 18. Let $[n]_{p,q}$ be a (p,q)-number and $M_n = [m_{st}]$ be an $n \times n$ tridiagonal matrix defined as

$$m_{st} = \begin{cases} -i, & t-s=1 \\ p+q, & s=t \\ ipq, & s-t=1 \\ 0, & \textit{otherwise.} \end{cases}$$

Then, $\det M_n = [n+1]_{p,q}$, where $i = \sqrt{-1}$.

Corollary 19. Let $\mathbf{K}_n^q = [k_{st}]$ be an $n \times n$ tridiagonal matrix defined as

$$k_{st} = \begin{cases} -i, & t-s=1 \\ 1+x, & t=s \\ ix(q^{s-1}-1), & s-t=1 \\ 0, & \textit{otherwise.} \end{cases}$$

Then, $\det \mathbf{K}_n^q = H_n(x)$.

4. Factorization of (p, q)-Rogers-Szegő Matrix

The lower triangular matrix $K_n = [k_{ij}]_{n \times n}$, is defined by

$$k_{ij} = H_{i-1}(x, p, q) - pH_{i-2}(x, p, q) - qH_{i-2}(x, p, q) + pqH_{i-3}(x, p, q).$$

Theorem 20. Let $\mathbf{R}_n^{p,q}$ be (p,q)-Rogers-Szegő matrices and $\mathbf{N}_n^{p,q}$ be (p,q)-matrices. Then,

$$\mathbf{R}_n^{p,q} = K_n \mathbf{N}_n^{p,q}.$$

Proof. It suffices to prove that $\mathbf{R}_n^{p,q}(\mathbf{N}_n^{p,q})^{-1} = K_n$. For $i > j$, $k_{ij} = 0$. For $i \geq j \geq 0$,

$$\sum_{s=1}^{n} r_{ik}b_{kj} = \sum_{s=j}^{j+2} r_{ik}b_{kj} = \sum_{s=1}^{3} r_{ik}b_{k1} = H_{i-1}(x, p, q) - H_{i-2}(x, p, q)(p+q) + H_{i-3}(x, p, q)pq = k_{ij}$$

which implies desired result.

References

[1] Burban, I.M., Klimyk, A.U., *P,Q-differentiation, P,Q-integration, and P,Q-hypergeometric functions related to quantum groups*, Integral Transforms and Special Functions, 2, 15-36, 1994.

[2] Chaichian, M., Demichev, A., Introduction to Quantum Groups, World Scientific, Singapore, 1996.

[3] Chari, V., Pressley, A., A Guide to Quantum Groups, Cambridge Univ. Press, Cambridge, 1994.

[4] Chakrabarti, R., Jagannathan, R.A., *(p, q)-oscillator realization of two-parameter quantum algebras,* Journal of Physics A: Mathematical and General, 24, L711, 1991.

[5] Jannussis, A., Brodimas, G., Mignani, L., *Quantum groups and Lie-admissible time evolution*, Journal of Physics A: Mathematical and General, 24(14), L775, 1991.

[6] Arik, M., Demircan, E., Turgut, E., Ekinci, L., Mungan, M., *Fibonacci oscillators*, Zeitschrift für Physik C Particles and Fields, 55(1), 89-95, 1992.

[7] Katriel, J., Kibler, M., *Normal ordering for deformed boson operators and operator-valued deformed Stirling numbers*, Journal of Physics A: Mathematical and General, 25(9), 2683, 1992.

[8] Jagannathan, R., Srinivasa Rao, K., *Two-parameter quantum algebras, twin-basic numbers, and associated generalized hypergeometric series*, arXiv:math/0602613, 2006.

[9] Smirnov, Y.F., Wehrhahn, R.F., *The Clebsch-Gordan coefficients for the two-parameter quantum algebra $SU_{p,q}(2)$ in the Lowdin-Shapiro approach*, Journal of Physics A: Mathematical and General, 25, 5563, 1992.

[10] Şahin, A. *On the Q analogue of Fibonacci and Lucas matrices and Fibonacci polynomials*, Utilitas Mathematica, 100, 2016.

[11] Cigler, J., *q-Fibonacci polynomials*, Fibonacci Quarterly, 41, 31-40, 2003.

[12] Cigler, J., *Einige q-Analoga der Lucas- und Fibonacci-Polynome*, Sitzungsberichte Abt.II.*, 211, 3-20, 2002.

[13] Cigler, J., *A new class of q-Fibonacci polynomials*, The Electronic Journal of Combinatorics, 10, R19, 2003.

[14] Rogers, L. J., *On a three-fold symmetry in the elements of Heine's series*, Proceedings of the London Mathematical Society, 24, 171–179, 1893.

[15] Rogers, L. J., *On the expansion of some infinite products*, Proceedings of the London Mathematical Society*, 24, 337–352, 1893.

[16] Szegő, G., *Ein Beitrag zur Theorie der Thetafunktionen*, S. B. Preuss. Akad. Wiss. Phys.- Math. Kl, 242–252, 1926.

[17] Andrews, G., The Theory of Partitions, Encyclopedia of Mathematics and Its Applications, Addison-Wesley, Reading, Mass.-London-Amsterdam, 1976.

[18] Jagannathan, R., Sridhar, R., *(p, q)-Rogers-Szegő Polynomial and the (p, q)-Oscillator*, arXiv:1005.4309v1[math.QA], 2010.

[19] Lee, G.Y., Kim, J.S., *The linear algebra of the k-Fibonacci matrix,* Linear Algebra and Its Applications, 373, 75-87, 2003.

[20] Kılıç, E., Taşcı, D., *The linear algebra of the Pell matrix*, Boletin de la Sociedad Matematica Mexicana, 2(11), 163-174, 2005.

[21] Lee, G.Y., Kim, J.S., Lee, S.G., *Factorizations and eigenvalues of Fibonacci and symmetric Fibonacci matrices*, Fibonacci Quarterly, 40(3), 203-211, 2002.

[22] Fonseca, C.M.da.,Petronilho, J., *Explicit inverses of some tridiagonal matrices*, Linear Algebra and Its Applications, 325,7–21, 2001.

[23] Şahin, A., Ramirez, J.L., *Determinantal and permanental representations of convolved Lucas polynomials*, Applied Mathematics and Computation, 281, 314-322, 2016.

[24] Şahin, A. *On the generalized Perrin and Cordonnier matrices*, Communications Faculty of Sciences University of Ankara Series A1 Mathematics and Statistics, 66(1), 242-253, 2017.

[25] Fonseca, C.M. da., *Unifying some Pell and Fibonacci identities*, Applied Mathematics and Computation, 236, 41-42, 2014.

[26] Kaygısız, K., Şahin, *A., Determinant and permanent of Hessenberg matrix and generalized Lucas polynomials*, Bulletin of the Iranian Mathematical Society.*, 39(6), 1065-1078, 2013.

[27] Anđelić, M., Du, Z., C.M. da Fonseca, Kılıç, E., *A matrix approach to some second-order difference equations with sign-alternating coefficients*, Journal of Difference Equations and Applications, 26:2, 149-162, 2020.

[28] Cahill, N.D., D'Errico, J.R., Narayan, D.A., Narayan, J.Y., *Fibonacci determinants*, College Mathematics Journal, 33, 221-225, 2002.

[29] Gibson, P.M., *An identity between permanents and determinants*, The American Mathematical Monthly, 76, 270-271, 1969.

Some Remarks on Riemannian Submersions Admitting An Almost Yamabe Soliton

Şemsi EKEN MERİÇ[1,*]

[1]*Mersin University, Faculty of Science and Arts, Department of Mathematics, Mersin, TURKEY*
semsieken@hotmail.com, ORCID: 0000-0003-2783-1149

Abstract

In this paper, we study the Riemannian submersions $\pi : M \to B$ whose total manifolds admit an almost Yamabe soliton. Here, we give some necessary conditions for which any fiber of π or B are almost Yamabe soliton or Yamabe soliton. Also, we calculate the scalar curvatures of any fiber and B and using them, we present the relations between the scalar curvatures of them and obtain some characterizations of such a soliton (that is, shrinking, steady or expanding).

Keywords: Riemannian manifold; Riemannian submersion; Almost Yamabe soliton.

Hemen Hemen Yamabe Soliton Kabul Eden Riemann Submersiyonlar Üzerine Bazı Notlar

Öz

Bu çalışmada total uzayı hemen hemen Yamabe soliton olan Riemann submersiyonlar ele alındı. Burada π'nin herhangi bir lifinin veya B manifoldunun birer Yamabe soliton veya hemen hemen Yamabe soliton olması için bazı gerekli koşullar verildi. Ayrıca liflerin ve B manifoldunun skalar eğrilikleri hesaplandı ve bunlar arasındaki ilişkiler ortaya koyularak söz konusu solitonun bazı karakterizasyonları (yani daralan, durgun veya genişleyen) elde edildi.

Anahtar Kelimeler: Riemann manifold; Riemann submersiyon; Hemen hemen Yamabe soliton.

1. Introduction

The concept of Yamabe flow was defined by Hamilton to solve the Yamabe problem in [1]. Yamabe solitons are self-similar solutions for Yamabe flows and they seem to be as singularity models. More clearly, the Yamabe soliton comes from the blow-up procedure along the Yamabe flow, so such solitons have been studied intensively (see [2-8]).

A generalization of Yamabe solitons was given in [2] as follows:

A Riemannian manifold M is said to be an almost Yamabe soliton, if there exists a vector field v on M which satisfies

$$\frac{1}{2}L_v g = (\tau - \mu)g, \tag{1}$$

where τ is the scalar curvature of M, μ is a smooth function, v is a soliton field for (M, g) and L is the Lie-derivative. An almost Yamabe soliton is denoted by (M, g, v, μ). Also, we say that an almost Yamabe soliton is steady, expanding or shrinking, if $\mu = 0$, $\mu < 0$ or $\mu > 0$.

From the above definition given by Eqn. (1), if μ is a constant, the almost Yamabe soliton is said to be the Yamabe soliton. It is obvious that Einstein manifolds are almost Yamabe solitons.

On the other hand, submersions are very interesting topic not only in differential geometry but also physics and mechanics, especially Riemannian submersions which are defined between Riemannian manifolds. Because, Riemannian submersions have many applications there. (for details, we refer to [9]).

Riemannian submersions were firstly studied by A. Gray [10] and B. O'Neill [11], independently. They presented some fundamental properties and formulas for Riemannian submersions and recently, such a theory has been intensively studied (we refer to [12-15]).

Considering above notions of almost Yamabe soliton and Riemannian submersion, the present paper contains some notes for Riemannian submersion in Section 2. The next section is about a Riemannian submersion π between Riemannian manifolds whose total space admits an almost Yamabe soliton. According to the soliton field (that is, such a field is vertical or horizontal), we obtain some characterizations for which any fiber of π or the target manifold is

a Yamabe soliton or an almost Yamabe soliton. Here, we calculate the extrinsic vertical and horizontal scalar curvatures and using them, we present the relationships between the scalar curvatures of any fiber or the target manifold and the characterization of almost Yamabe soliton (that is such a soliton is shrinking, expanding or steady).

2. Preliminaries

We recall here some basic notions from [9], as follows:

A differentiable map $\pi : (M,g) \rightarrow (B,g')$ is said to be a Riemannian submersion from Riemannian manifold M onto the Riemannian manifold B if it satisfies

(i) the derivative map π_* is onto,

(ii) $g_p(U,V) = g'_{\pi(p)}(\pi_{*p}U, \pi_{*p}V)$,

for any $U,V \in \Gamma(TM)$ and $p \in M$. Note that, for any $x \in B$, if $m-n=r$, $\pi^{-1}(x)$ of dimension r which is also a submanifold of M.

For any $p \in M$, we denote $\mathcal{V}_p = \ker \pi_{*p}$ such that it corresponds to the foliation of M determined by the fibers of Riemannian submersion π, since each $\mathcal{V}_p$ coincides with the tangent space of $\pi^{-1}(x)$ at p, $\pi(p) = x$. Hence, $\mathcal{V}_p$ is said to be the vertical space.

Denoting the complementary of the vertical distribution $\mathcal{V}$ by $\mathcal{H}$, we have

$$T_pM = \mathcal{V}_p \oplus \mathcal{H}_p.$$

Here $\mathcal{H}_p$ is said to be a horizontal space, for $p \in M$.

Some properties on a Riemannian submersion are given with the following:

Let π be a Riemannian submersion from M to B. Denoting the Levi-Civita connections by ∇ and ∇' of M and B, respectively. Then, for X, Z are basic vector fields π-related to $X',Z' \in \Gamma(TB)$ (i.e. $\pi_*(X) = X'$, $\pi_*(Z) = Z'$), the followings are hold:

(1) $g(X,Z) = g'(X',Z') \circ \pi$,

(2) $h[X,Z]$ is π-related to $[X',Z']$,

(3) $h(\nabla_X Z)$ is π-related to $\nabla'_{X'} Z'$,

(4) $[X,V]$ is the vertical, for any vertical vector field V.

Note that, two tensor fields $\mathcal{A}$ and $\mathcal{T}$ is determined by Riemannian submersion π on M. Also, these tensor fields are given by

$$\mathcal{A}(E,F) = \mathcal{A}_E F = v\nabla_{hE} hF + h\nabla_{hE} vF ,$$

$$\mathcal{T}(E,F) = \mathcal{T}_E F = h\nabla_{vE} vF + v\nabla_{vE} hF ,$$

for the vector fields E, F are tangent to M. Here the horizontal projection and vertical projection are respectively denoted by h and v and ∇ is the Levi-Civita connection of the total space.

We remark that the tensor field $\mathcal{T}$ vanishes on M if and only if any fiber is totally geodesic. Similarly, the tensor field $\mathcal{A}$ vanishes on M if and only if $\mathcal{H}$ is integrable.

Using O'Neill tensors $\mathcal{A}$ and $\mathcal{T}$, the followings are hold:

$$\nabla_U W = \mathcal{T}_U W + \hat{\nabla}_U W , \tag{2}$$

$$\nabla_U X = h(\nabla_U X) + \mathcal{T}_U X , \tag{3}$$

$$\nabla_X U = \mathcal{A}_X U + v(\nabla_X U) , \tag{4}$$

$$\nabla_X Y = \mathcal{A}_X Y + h(\nabla_X Y), \tag{5}$$

where $\hat{\nabla}_U W = \nabla_U W$, X, Y are tangent to $\mathcal{H}$ and U, W are tangent to $\mathcal{V}$. Indeed, such tensor fields satisfy

$$g(\mathcal{A}_E F, G) = -g(\mathcal{A}_E G, F), \tag{6}$$

$$g(\mathcal{T}_E F, G) = -g(\mathcal{T}_E G, F), \tag{7}$$

for any E, F, G are tangent to M.

Furthermore, the O'Neill tensors $\mathcal{T}$ and $\mathcal{A}$ satisfy

$$\sum_{j=1}^{r} g(\mathcal{T}_U U_j, \mathcal{T}_V U_j) = \sum_{i=1}^{n} g(\mathcal{T}_U X_i, \mathcal{T}_V X_i), \tag{8}$$

$$\sum_{j=1}^{r} g(\mathcal{A}_X U_j, \mathcal{A}_Y U_j) = \sum_{i=1}^{n} g(\mathcal{A}_X X_i, \mathcal{A}_Y X_i), \tag{9}$$

$$\sum_{j=1}^{r} g(\mathcal{A}_X U_j, \mathcal{T}_U U_j) = \sum_{i=1}^{n} g(\mathcal{A}_X X_i, \mathcal{T}_U X_i), \tag{10}$$

where $\{U_j\}_{1 \le j \le r}$ and $\{X_i\}_{1 \le i \le n}$ are orthonormal frames of vertical distribution $\mathcal{V}$ and horizontal distribution $\mathcal{H}$, respectively for any $X, Y \in \mathcal{H}$ and $U, V \in \mathcal{V}$.

Denote the Riemannian curvature tensors of B, M and any fiber respectively by R', R and $\hat{R}$. Then, we get

$$R(U,V,F,W) = \hat{R}(U,V,F,W) + g(\mathcal{T}_V F, \mathcal{T}_U W) - g(\mathcal{T}_U F, \mathcal{T}_V W),$$

$$R(X,Y,G,Z) = R'(X',Y',G',Z') \circ \pi - g(\mathcal{A}_Y G, \mathcal{A}_X Z) \\ + 2g(\mathcal{A}_X Y, \mathcal{A}_G Z) + g(\mathcal{A}_X G, \mathcal{A}_Y Z),$$

for any horizontal vectors X, Y, G, Z and vertical vectors U, V, F, W.

Moreover, denoting the mean curvature vector of any fiber by H which is given as

$$N = rH, \tag{11}$$

such that

$$N = \sum_{j=1}^{r} \mathcal{T}_{V_j} V_j, \tag{12}$$

where $\{V_1, V_2, ..., V_r\}$ is an orthonormal frame of $\mathcal{V}$. Also, remark that

$$\mathcal{T}_U V = g(U,V)H \tag{13}$$

is satisfied for U, V are tangent to $\mathcal{V}$ if and only if any fiber is totally umbilical submanifold. Indeed, the vector field N is zero on M if and only if any fiber is minimal.

Using Eqn. (12), one has

$$g(\nabla_E N, Z) = \sum_{j=1}^{r} g((\nabla_E \mathcal{T})(U_j, U_j), Z),$$

where any horizontal vector field Z and any vector field E.

Denoting the horizontal divergence of the horizontal vector field Z by $\breve{\delta}(Z)$ which holds

$$\breve{\delta}(Z) = \sum_{k=1}^{n} g(\nabla_{X_k} Z, X_k). \tag{14}$$

Here $\{X_1, X_2, ..., X_n\}$ is an orthonormal frame of $\mathcal{H}$. Therefore, from Eqn. (14), one has

$$\breve{\delta}(N) = \sum_{k=1}^{n} \sum_{j=1}^{r} g((\nabla_{X_k} \mathcal{T})(U_j, U_j), X_k).$$

(See [16], pp. 243).

The Ricci tensor on the total space of π is given as

$$Ric(U,W) = \hat{Ric}(U,W) - \sum_{k=1}^{n} g((\nabla_{X_k} \mathcal{T})(U,W), X_k) + g(N, \mathcal{T}_U W)$$
$$- \sum_{k=1}^{n} g(\mathcal{A}_{X_k} U, \mathcal{A}_{X_k} W) \tag{15}$$

$$Ric(X,Y) = Ric'(X',Y') \circ \pi + 2\sum_{k=1}^{n} g(\mathcal{A}_X X_k, \mathcal{A}_Y X_k)$$
$$+ \sum_{k=1}^{n} g(\mathcal{T}_{U_j} X, \mathcal{T}_{U_j} Y), \tag{16}$$

$$Ric(U,X) = -g(\nabla_U N, X) - \sum_{k=1}^{n} \{ g((\nabla_{X_k} \mathcal{A})(X_k, X), U)$$
$$+ 2g(\mathcal{A}_{X_k} X, \mathcal{T}_U X_k) \} + \sum_{j=1}^{r} g((\nabla_{U_j} \mathcal{T})(U_j, U), X) \tag{17}$$

where $\hat{Ric}$ and Ric' denote the Ricci tensors of fiber and B respectively. Here $\{U_j\}$ and $\{X_k\}$ are the orthonormal bases of the vertical and horizontal distributions respectively, for any $X, Y \in \mathcal{H}$ and $U, W \in \mathcal{V}$.

Taking into account the equalities Eqn. (15)-Eqn. (16), the extrinsic vertical scalar curvature $\tau|_{\mathcal{V}}$ and the extrinsic horizontal scalar curvature $\tau|_{\mathcal{H}}$ are given by

$$\tau|_{\mathcal{V}} = \sum_{j=1}^{r} Ric(U_j, U_j) = \sum_{j=1}^{r} \{\hat{Ric}(U_j, U_j) + g(N, \mathcal{T}_{U_j} U_j) \\ - \sum_{i=1}^{n} g((\nabla_{X_i} \mathcal{T})(U_j, U_j), X_i) - g(\mathcal{A}_{X_i} U_j, \mathcal{A}_{X_i} U_j)\} \tag{18}$$

$$\tau|_{\mathcal{H}} = \sum_{i=1}^{n} Ric(X_i, X_i) = \sum_{i=1}^{n} \{(Ric'(X_i', X_i') \circ \pi) - g(\nabla_{X_i} N, X_i) \\ + 2\sum_{k=1}^{n} g(\mathcal{A}_{X_i} X_k, \mathcal{A}_{X_i} X_k) + \sum_{j=1}^{r} g(\mathcal{T}_{U_j} X_i, \mathcal{T}_{U_j} X_i)\}. \tag{19}$$

Above equalities Eqn. (18)-Eqn. (19) imply

$$\tau|_{\mathcal{V}} = \hat{\tau} + \|N\|^2 - \|\mathcal{A}\|^2 - \breve{\delta}(N), \tag{20}$$

$$\tau|_{\mathcal{H}} = (\tau' \circ \pi) - \breve{\delta}(N) + 2\|\mathcal{A}\|^2 + \|\mathcal{T}\|^2, \tag{21}$$

where $\hat{\tau}$ and τ' are the scalar curvatures of any fiber of π and B respectively, such that $\|\mathcal{A}\|^2 = \sum_{i,j} g(\mathcal{A}_{X_i} U_j, \mathcal{A}_{X_i} U_j)$ and $\|\mathcal{T}\|^2 = \sum_{i,j} g(\mathcal{T}_{U_j} X_i, \mathcal{T}_{U_j} X_i)$.

Finally using Eqn. (20)-Eqn. (21), the scalar curvature τ on the base manifold M is given by

$$\tau = \hat{\tau} + (\tau' \circ \pi) + \|N\|^2 + \|\mathcal{T}\|^2 + \|\mathcal{A}\|^2 - 2\breve{\delta}(N).$$

3. Riemannian Submersions Admitting an Almost Yamabe Soliton

In the present part, we investigate the Riemannian submersion $\pi : M \to B$ between Riemannian manifolds whose total space M admits an almost Yamabe soliton. Here, we give some characterizations about any fibrer or B is an almost Yamabe soliton or a Yamabe soliton.

We recall the following lemma from [14]:

Lemma 1. Let π be a Riemannian submersion from M onto B. The horizontal distribution $\mathcal{H}$ is parallel with respect to ∇ on M if and only if the O'Neill tensors $\mathcal{A}$ and $\mathcal{T}$ vanish, identically.

Teorem 2. Let π be a Riemannian submersion admitting an almost Yamabe soliton (M, g, ν, μ) such that ν is vertical. Then, any fiber of π is an almost Yamabe soliton.

Proof. Because M is an almost Yamabe soliton, from Eqn. (1) we have

$$\frac{1}{2}\left\{g(\nabla_V \nu, U) + g(\nabla_U \nu, V)\right\} = (\tau - \mu)g(V, U), \tag{22}$$

for any $U, V \in \mathcal{V}$. Using Eqn. (2), one has

$$\frac{1}{2}\left\{g(\hat{\nabla}_V \nu, U) + g(\hat{\nabla}_U \nu, V)\right\} = (\tau|_V - \mu)g(V, U), \tag{23}$$

where $\hat{\nabla}$ is the Levi-Civita connection on any fiber of π. Putting the extrinsic vertical scalar curvature $\tau|_V$ of Eqn. (20) in Eqn. (23), it gives

$$\frac{1}{2}\left\{g(\hat{\nabla}_V \nu, U) + g(\hat{\nabla}_U \nu, V)\right\} = \left(\hat{\tau} + \|N\|^2 - \|\mathcal{A}\|^2 - \breve{\delta}(N) - \mu\right)g(V, U). \tag{24}$$

If we denote $\sigma = -\|N\|^2 + \|\mathcal{A}\|^2 + \breve{\delta}(N) + \mu$, then the equality Eqn. (24) follows

$$\frac{1}{2}(L_\nu g)(U, V) = (\hat{\tau} - \sigma)\hat{g}(U, V),$$

which means such a fiber of π is an almost Yamabe soliton.

Using Lemma 1, as particular case of Theorem 2, one has:

Remark 3. Let π be a Riemannian submersion admitting a Yamabe soliton (M, g, ν, μ) such that ν is vertical. Then, any fiber becomes a Yamabe soliton.

Teorem 4. Let π be a Riemannian submersion admitting an almost Yamabe soliton (M, g, ν, μ) such that ν is vertical. Then, the extrinsic horizontal scalar curvature $\tau|_{\mathcal{H}}$ satisfies

$$\tau|_{\mathcal{H}} - \mu = 0. \tag{25}$$

Proof. Because the total space M is an almost Yamabe soliton, from Eqn. (1) we get

$$\frac{1}{2}\{g(\nabla_X v, Z) + g(\nabla_Z v, X)\} = (\tau - \mu)g(X, Z), \tag{26}$$

for any the horizontal vectors X, Z. Considering Eqn. (4) in Eqn. (26), we have

$$\frac{1}{2}\{g(\mathcal{A}_X v, Z) + g(\mathcal{A}_Z v, X)\} = (\tau|_{\mathcal{H}} - \mu)g(X, Z). \tag{27}$$

Also, considering the properties of the tensor field $\mathcal{A}$ in the equality Eqn. (6), the left hand side of Eqn. (27) vanishes identically. For any $X, Z \in \mathcal{H}$, we have

$$(\tau|_{\mathcal{H}} - \mu)g(X, Z) = 0,$$

which gives Eqn. (25).

As a consequence of Theorem 4, we conclude the following:

Corollary 5. Let π be a Riemannian submersion admitting an almost Yamabe soliton (M, g, v, μ) be such that v is vertical. If $\mathcal{H}$ is parallel, the followings are hold:

(i) (M, g, v, μ) is shrinking if and only if the manifold B has positive scalar curvature.

(ii) (M, g, v, μ) is expanding if and only if the manifold B has negative scalar curvature.

(iii) (M, g, v, μ) is steady if and only if the manifold B has zero scalar curvature.

In this section, from now on, we suppose that the potential field of the almost Yamabe soliton is horizontal. Then, we have some theorems as follows:

Theorem 6. Let π be a Riemannian submersion admitting an almost Yamabe soliton (M, g, ξ, μ) such that ξ is horizontal. Then, the Riemannian manifold B is an almost Yamabe soliton.

Proof. Since (M, g) is an almost Yamabe soliton, from Eqn. (1), then we get

$$\frac{1}{2}\{g(\nabla_X \xi, Z) + g(\nabla_Z \xi, X)\} = (\tau - \mu)g(X, Z),$$

for any the horizontal vectors X, Z. Using Eqn. (5), one has

$$\frac{1}{2}\left\{g(h(\nabla_X\xi),Z)+g(h(\nabla_Z\xi),X)\right\}=(\tau|_{\mathcal{H}}-\mu)g(X,Z). \tag{28}$$

Putting Eqn. (21) in Eqn. (28), it follows

$$\frac{1}{2}\left\{g(h(\nabla_X\xi),Z)+g(h(\nabla_Z\xi),X)\right\}=\left\{(\tau'\circ\pi)+\|T\|^2+2\|\mathcal{A}\|^2\right.$$
$$\left.-\breve{\delta}(N)-\mu\right\}g(X,Z). \tag{29}$$

If we denote $\gamma=-\|T\|^2-2\|\mathcal{A}\|^2+\breve{\delta}(N)+\mu$, then Eqn. (29) is equivalent to

$$\frac{1}{2}\left\{g(h(\nabla_X\xi),Z)+g(h(\nabla_Z\xi),X)\right\}=\left\{(\tau'\circ\pi)-\gamma\right\}g(X,Z).$$

Here we note that $h(\nabla_X\xi)$ and $h(\nabla_Z\xi)$ are π-related to $\nabla'_{X'}\xi'$ and $\nabla'_{Z'}\xi'$, respectively. It follows

$$\frac{1}{2}\left\{g'(\nabla'_{X'}\xi',Z')+g'(\nabla'_{Z'}\xi',X')\right\}=(\tau'-\gamma)g'(X',Z'), \tag{30}$$

for any the vector fields X',Z' are tangent to B. Then, Eqn. (30) gives

$$\frac{1}{2}L_{\xi'}g'=(\tau'-\gamma)g', \tag{31}$$

which means the Riemannian manifold B is an almost Yamabe soliton with potential vector field ξ', such that $\pi_*(\xi)=\xi'$.

Considering Lemma 1, in particular case we have the following:

Remark 7. Let π be a Riemannian submersion admitting an almost Yamabe soliton (M,g,ξ,μ) such that ξ is horizontal. If $\mathcal{H}$ is parallel, then B becomes a Yamabe soliton.

Teorem 8. Let π be a Riemannian submersion with totally umbilical fibres admitting an almost Yamabe soliton (M,g,ξ,μ) such that ξ is horizontal. Then, the extrinsic vertical scalar curvature $\tau|_{\mathcal{V}}$ on $\mathcal{V}$ satisfies

$$\tau|_{\mathcal{V}}=\mu+g(H,\xi). \tag{32}$$

Here H is the mean curvature vector field of fiber.

Proof. Since the total space M of π is an almost Yamabe soliton, then from Eqn. (1), one has

$$\frac{1}{2}\{g(\nabla_U\xi,W)+g(\nabla_W\xi,U)\}=(\tau-\mu)g(U,W),$$

for any $U,W \in \mathcal{V}$. By using Eqn. (3), the last equation gives

$$\frac{1}{2}\{g(\mathcal{T}_U\xi,W)+g(\mathcal{T}_W\xi,U)\}=(\tau-\mu)g(U,W). \tag{33}$$

Also, using Eqn. (7) in the left hand side of Eqn. (33), it follows

$$g(\mathcal{T}_U W,\xi)=(\tau|_\mathcal{V}-\mu)g(U,W). \tag{34}$$

Finally, since π has totally umbilical fibres, using Eqn. (13) we have

$$g(H,\xi)=\tau|_\mathcal{V}-\mu, \tag{35}$$

which gives Eqn. (32).

Considering Theorem 8, we have the followings immediately:

Remark 9. Let π be a Riemannian submersion with minimal fibers admitting an almost Yamabe soliton (M,g,ξ,μ) such that ξ is horizontal. Then, the extrinsic vertical scalar curvature $\tau|_\mathcal{V}$ satisfies

$$\tau|_\mathcal{V}=\mu.$$

Using Remark 9, we infer the following:

Corollary 10. Let π be a Riemannian submersion with minimal fibres admittting an almost Yamabe soliton (M,g,ξ,μ) such that ξ is horizontal. If $\mathcal{H}$ is parallel, then we have the following:

(i) (M,g,ξ,μ) is shrinking if and only if any fiber has positive scalar curvature.

(ii) (M,g,ξ,μ) is expanding if and only if any fiber has negative scalar curvature.

(iii) (M, g, ξ, μ) is steady if and only if any fiber has zero scalar curvature.

Acknowledgement

References

[1] Hamilton, R., *"The Ricci flow on surfaces", in Mathematics and General Relativity*, Contemporary Mathematics, (71), 237-361, 1988.

[2] Barbosa, E., Ribeiro, E., *On conformal solutions of the Yamabe flow*, Archiv der Mathematik, (101), 79-89, 2013.

[3] Cao, H.D., Sun, X., Zhang, Y., *On the structure of gradient Yamabe solitons*, Mathematical Research Letters, (19), 767-774, 2012.

[4] Chen, B.-Y., Deshmukh, S., *Yamabe and quasi-Yamabe solitons on Euclidean submanifolds*, Mediterranean Journal of Mathematics, (15), 194, 2018.

[5] Deshmukh, S., Chen, B.-Y., *A Note on Yamabe solitons*, Balkan Journal of Geometry and Its Applications, 23(1), 37-43, 2018.

[6] Ma, L., Miquel, V., *Remarks on scalar curvature of Yamabe solitons,* Annals of Global Analysis and Geometry, 42, 195-205, 2012.

[7] Neto, B.L., *A note on (anti-)self dual quasi Yamabe gradient solitons,* Results in Mathematics, 71, 527-533, 2017.

[8] Seko, T., Matea, S., *Classification of almost Yamabe solitons in Euclidean spaces*, Journal of Geometry and Physics, 136, 97-103, 2019.

[9] Falcitelli, M., Ianus, S., Pastore, A.M., *Riemannian submersions and related topics,* World Scientific Publishing Co. Pte. Ltd. 2004.

[10] Gray, A., *Pseudo-Riemannian almost product manifolds and submersion*, Journal of Mathematics and Mechanics, (16), 715–737, 1967.

[11] O'Neill, B., *The fundamental equations of a Riemannian submersions*, Michigan Mathematical Journal, 13, 459-469, 1966.

[12] Akyol, M.A., Gündüzalp, Y., *Hemi-slant submersions from almost product Riemannian manifolds*, Gulf Journal of Mathematics, 4(3), 15-27, 2016.

[13] Akyol, M.A., Gündüzalp, Y., *Semi-invariant semi-Riemannian submersions*, Communications Faculty of Sciences University of Ankara Series A1-Mathematics and Statistics, 67(1), 80-92, 2018.

[14] Eken Meriç, Ş., Kılıç, E., *Riemannian submersions whose total manifolds admitting a Ricci soliton*, International Journal of Geometric Methods in Modern Physics, 16(12), 1950196 (12 pages), 2019.

[15] Özdemir, F., Sayar, C., Taştan, H.M., *Semi-invariant submersions whose total manifolds are locally product Riemannian*, Quaestiones Mathematicae, 40(7), 909-926, 2017.

[16] Besse, A.L., *Einstein manifolds*, Springer-Verlag, Berlin, Heildelberg, New York, 1987.

Synthesis and Optical, Thermal, Structural Investigation of Zinc-Borate Glasses Containing V$_2$O$_5$

Gökhan KILIÇ[1],*

[1]*Eskisehir Osmangazi University, Faculty of Science and Letters, Department of Physics, TR-26040 Eskisehir, Turkey*
gkilic@ogu.edu.tr, ORCID: 0000-0002-6762-6898

Abstract

Vanadium pentaoxide (V$_2$O$_5$) doped zinc borate (ZnB) oxide glasses that could be used in fiber optic cable cores in optoelectronics, in laser crystals in solar energy systems have been synthesized successfully. Structural characters of synthesized glasses were determined with differential scanning calorimeter (DSC) and Fourier-Transform infrared spectroscopy (FTIR). Glass transition (T_g), crystallization (T_c) and melting temperatures (T_m), and thermal stabilities (ΔT) of the glasses were determined and also their association with the change in V$_2$O$_5$ was explained. Structural units of boron and zinc that form the structure were determined according to FTIR data. As a result, it was determined that boron formed the glass matrix with BO$_3$, BO$_4$ and boroxol ring structural units; on the other hand, zinc contributed to the glass matrix with tetrahedral ZnO$_4$ and octahedral ZnO$_6$ structural units, and vanadium usually had modifier role in the structure with its VO$_4$ and VO$_5$ structural units. V$_2$O$_5$'s presence in the structure with increasing amount changes thermal, structural and physical properties. Among the properties that significantly change, the most important one is optical properties. Indirect optical band gaps, Urbach energies, refractive index values of these synthesized samples were determined, and quite clear shifts towards red region were observed in the transmittance and absorption spectra. Optical band gap decreased to 1.24 eV from 2.55 eV with increasing amount of V$_2$O$_5$; on the other hand,

Urbach energy was determined to increase to 0.630 eV from 0.246 eV. Densities, molar volumes of these synthesized glasses were also examined and commented on.

Keywords: ZnO; B₂O₃; V₂O₅; Zinc-Borate glass; FTIR.

V₂O₅ İçeren Çinko-Borat Camların Sentezi ve Optik, Termal, Yapısal İncelenmeleri

Öz

Optoelektronikte fiber optik kablo korlarında, laser kristallerinde ve güneş enerji sistemlerinde kullanılabilecek vanadium pentaoksit (V₂O₅) katkılı çinko borat (ZnB) oksit camlar başarıyla sentezlenmiştir. Sentezlenen camlara ait yapısal karakterler diferansiyel taramalı kalorimetre (DSC) ve Fourier dönüşümlü kızılötesi spektroskopisi (FTIR) ile belirlenmiştir. Camsı geçiş (*T_g*), kristallenme (*T_c*), erime sıcaklıkları (*T_m*) ve termal kararlılıklar (Δ*T*) belirlenerek V₂O₅ değişimiyle ilgisi açıklanmıştır. FTIR verilerine göre yapıyı oluşturan bor ve çinkonun yapısal birimleri belirlenmiştir. Borun cam matrisini BO₃, BO₄ ve boroksol halka yapısal birimleriyle oluşturduğu, çinkonun ise cam matrisine tetrahedral ZnO₄ ve oktahedral ZnO₆ yapısal birimleri ile katkıda bulunduğu, vanadyumun yapıda çoğunlukla VO₄ ve VO₅ yapısal birimleriyle yer alarak düzenleyici görev üstlendiği belirlenmiştir. V₂O₅ katkısının artması yapının termal, yapısal ve fiziksel özelliklerini değiştirmektedir. Belirgin biçimde değiştirdiği özelliklerin başında optik özellikler gelmektedir. Sentezlenen numunelere ait indirekt optik bant aralığı, Urbach enerjisi, kırılma indisi değerleri belirlenmiş, geçirgenlik ve absorpsiyon spektrumlarında kırmızı dalgaboyuna kaymalar net bir şekilde gözlenmiştir. Optik bant aralığı V₂O₅ artışıyla 2.55 eV dan 1.24 eV'a azalmış, buna karşılık Urbach enerjisi 0.246 eV'dan 0.630 eV'a arttığı belirlenmiştir. Ayrıca, sentezlenen numunelere ait yoğunluk, molar hacim incelenmiş ve yorumlanmıştır.

Anahtar Kelimeler: ZnO; B₂O₃; V₂O₅; Çinko-Borat cam; FTIR.

1. Introduction

Glass, an amorphous material, has an important place in respect to technology and science. Besides silicon dioxide (SiO₂), phosphorus pentoxide (P₂O₅), boron oxide (B₂O₃), and vanadium pentoxide (V₂O₅) are being used in the synthesis of glasses the most. Among these, B₂O₃ is known to be the best glass former [1, 2]. Borate glasses in which B₂O₃ establishes the glass network are very important optical materials due to their low melting points, high transmittance properties and high thermal stabilities [3]. They are frequently being used in the making of dielectric materials and used as isolation materials. Though they are being used as dielectric materials, the inclusion

of transition metal ions in the borate glass network leads to the achievement of semiconductor character or these glasses. Transition metals are nowadays being extensively used in glass science due to their presence in two or more valance states that alters the structural and optical characters [4-10].

It is possible to find examination studies performed on binary zinc-borate structures among transition metal doped borate glasses and also ternary structures and structures having more components in the literature [11-22]. Except for glass systems, it is possible to find zinc-borate ceramic structures, as well [23].

Zinc-borate glasses are being used in plasma screens and panels for high quality and performance [24, 25]. Zinc-borate glasses are promising materials for a large field including television panels and computer monitors. They are preferred due to having high voltage resistance in providing rapid surge in dielectric layers and being highly transparent. Since zinc borate glasses that do not contain lead possess all the aforementioned qualities, they are shown to be appropriate materials for applications that are in question [26].

Studies on vanadium due to their interesting optical, electrical and magnetic properties have significantly increased recently. Though studies on transition metal doped glasses can be found in the literature frequently [27-37], there are still components, compositions and properties that have not yet been studied. Glasses containing vanadium, which is a transition metal, show semiconducting properties since they contain V^{4+}, V^{5+} valance states [38-45]. Vanadium doped glasses are known to be n-type semiconductors for low V^{4+}/V^{5+} ratio [46]. Glasses with vanadium content have a wide range of use from the production of solid-state devices to memory and optical switching, devices like electrical threshold, and in the formation of fiber optics [47, 48]. Therefore, they are materials with potential for most electronic and optoelectronic applications [49]. In the literature, some characteristics of glasses having different compositions as a result of combining zinc-borate glass systems with V_2O_5 have been elaborated [50, 51].

In this study, ZnO-B_2O_3-V_2O_5 glasses doped with V_2O_5 and containing high ratio of ZnO, so they can find a use in optoelectronics were synthesized successfully. Compared borate glasses that are sensitive to humidity, these synthesized glasses are resistant to air, water; therefore, they are considered to be important since boron is able to find use in respect to technological applications. Structural and thermal properties of these synthesized glasses were examined in a detailed way and discussed. Characterization of this structure considered to become a potential material that could be used in fiber cable cores in optoelectronics, in laser settings and, also in solar energy systems was revealed.

2. Materials and Methods

2.1. Sample preparation

ZnO-B_2O_3 glass samples containing V_2O_5 were synthesized from chemicals having 99.5% purity (Alfa Aesar) according to $(100-x)(0.6ZnO-0.4B_2O_3).(x)(V_2O_5)$ $(x = 1, 2, 3, 4)$ composition. The method that was used in the synthesis of the glasses was melt-quenching method. Chemicals were weighed on an analytical scale having accuracy of 0.00001g, and then weighed chemicals were mechanically mixed for approximately 10 min and made uniform.

Prepared powder mixture was left in a porcelain crucible for 60 minutes in a Nabertherm LHT 02/17 LB brand high temperature furnace that was previously heated to 1100 °C for reaction to take place. At the end of the process, molten glass samples were shaped cylindrically in a steel mold and annealed for 60 minutes at 400 °C.

Figure 1: Synthesized ZnO-B_2O_3-V_2O_5 glass samples

Glass samples synthesized by this way (Fig. 1) were sliced with a Metkon brand Micracut 152 model cutting device with diamond disc for optical measurements having a diameter of 2.5 cm and a thickness of 2 mm; both surfaces of the cut samples were polished with a Metkon brand Forcipol 102 model polishing device. Some of the samples were grounded with a Retsch RM200 brand grinder to study their thermal and structural properties.

2.2. Characterization

Densities of glasses were determined with the principle of Archimedes. Samples were first weighed in the air with a KERN brand ABT 100-5m model analytical scale having an accuracy of 0.00001g, and then weighed again in immersion fluid. Ultra-pure water was selected as

immersion fluid. By using the measurements taken in the air and in the immersion fluid, densities of the samples were calculated with the below equation [52]:

$$D = \frac{W_a}{W_a - W_l} \cdot \rho_o \tag{1}$$

In this equation, W_a is the weight of the sample in the air, W_l is the weight of the sample in the fluid and ρ_o is the density of immersion fluid ($\rho_o = 0.998272$ g.cm^{-3}) at 20 °C. Molar volumes (V_m) of glass samples were calculated with the following equation:

$$V_m = \frac{\sum x_i M_i}{D} \tag{2}$$

Here, x_i is the mole ratio of the $i.^{th}$ component, M_i is the molecular weight.

Transmittance and absorption spectra of the glasses were determined with Analytik Jena SPECORD 210 UV-Vis Spectrophotometer with steps of 1 nm. In addition, in order to determine the uniformity of the sample, transmittance spectra were determined with scanning attachment of the device by using 1.5 cm piece of the surface. Absorption spectra were used to calculate optical band gaps and Urbach energies of the synthesized samples.

Refractive index due to optical band gap was calculated with the following empirical relation [53]:

$$\frac{(n^2 - 1)}{(n^2 + 2)} = 1 - \sqrt{\frac{E_0}{20}} \tag{3}$$

n, is the refractive index of the samples, E_0 is optical band gap.

In order to determine the structural properties, powdered forms of the samples were used and their FTIR spectra were obtained. FTIR analyses were performed at room temperature within the wavenumber range of 400-1400 cm^{-1} by using diamond ATR with a resolution of 4 cm^{-1}. Origin 2018 program was used to determine hidden bands in the spectrum.

Netzsch STA 449F3 simultaneous thermogravimetric analyze device was used in the determination of thermal properties. DSC measurements were made with approximately 50 mg of powdered sample between the range of room temperature and 1000 °C with increments of 1 °C. Glass transition, crystallization and melting temperatures were calculated from the obtained

graphs with ONSET method (Fig. 3). In addition, thermal stabilities (ΔT) belonging to glasses were calculated with the following equation:

$$\Delta T = T_c - T_g \tag{4}$$

Here T_c is the first crystallization temperature, T_g is glass transition temperature.

3. Results and Discussion

3.1. Density and molar volume

Sample densities and molar volume values calculated with the help of Eqn. (1) are given in Table 1. In addition, sample codes and ratio of components within the glass can also be seen. As you can see in Fig. 2, density values of the samples decreased regularly from 3.392 g.cm^{-3} to 3.329 g.cm^{-3} with increasing amount of V_2O_5. On the other hand, molar volume values increased from 22.910 cm^3.mol^{-1} to 24.289 cm^3.mol^{-1} almost linearly. V_2O_5's being a more complex molecule led to volume increase, in addition, since masses of shifting vanadium and zinc were close to each other, it resulted in decrease in the molar volume. Similar impact can also be found in the literature [54].
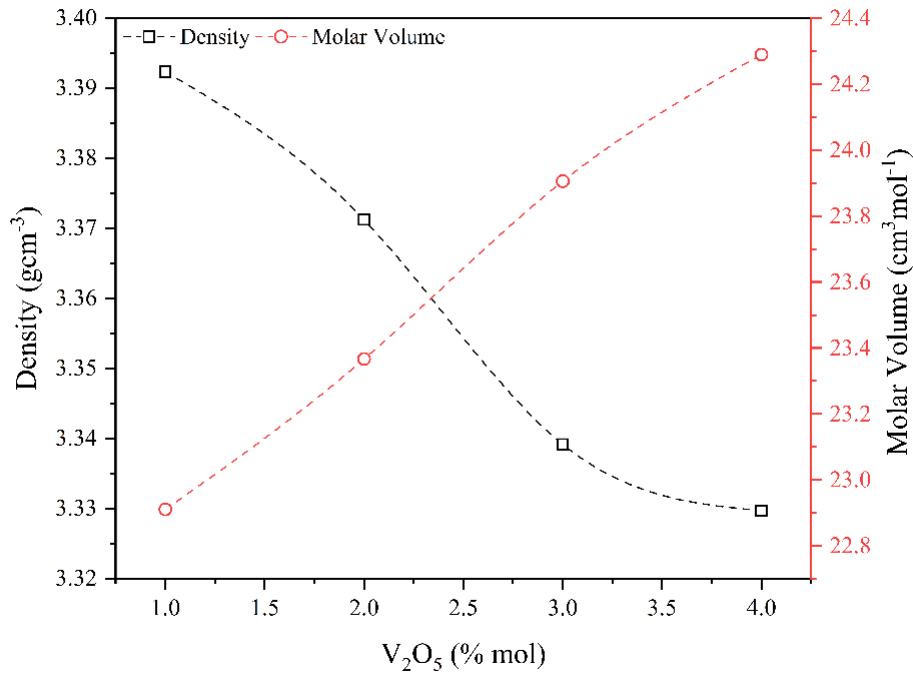
Figure 2: Change in density and molar volume values according to V_2O_5 concentration

Table 1: Sample codes, % compositions and calculated density and molar volume values of synthesized samples

Sample Code	ZnO mol %	B_2O_3 mol %	V_2O_5 mol %	Density g.cm^{-3} (±0.001)	Molar volume cm^3.mol^{-1} (±0.005)
ZBV1	59.40	39.60	1.00	3.392	22.910
ZBV2	58.80	39.20	2.00	3.371	23.366
ZBV3	58.20	38.80	3.00	3.339	23.906
ZBV4	57.60	38.40	4.00	3.329	24.289

3.2. Thermal properties

DSC thermograms belonging to synthesized ZBV glass samples are given in Fig. 3, and their glass transition temperatures, crystallization and melting temperatures are given in Table 2. As it can be seen in DSC thermograms, curves belonging to 4 samples are almost identical in respect to their shapes. 3 ambiguous exothermic peaks in the shape of shoulders are followed by 1 endothermic peak. Glass transition temperatures can be seen within the range of 530-550 °C and glass transition temperature has decreased with increasing amount of V_2O_5. First crystallization temperature was around 740 °C; the range of 818-833 °C was the region of second crystallization temperature. When we have reviewed the literature, we can see that various crystalline phases are mentioned between glassy transition temperature and melting temperature in similar systems [55]. These are $Zn_3B_2O_6$ crystalline phase around 680 °C and $Zn_3V_2O_8$ crystalline phase around 700 °C. In Nb_2O_5 doped zinc-borate glasses, $ZnNb_2O_6$ crystalline phase containing Nb is found around 740 °C.
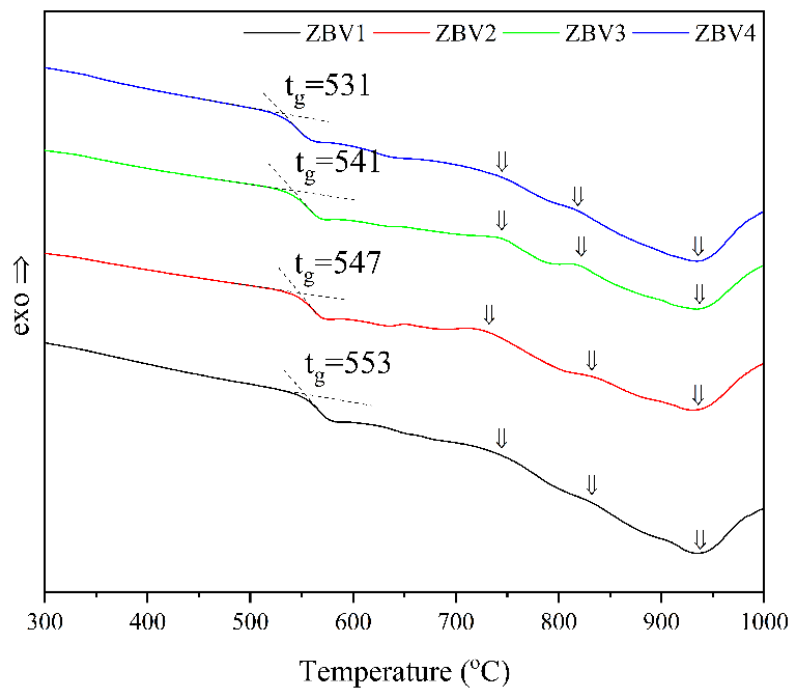
Figure 3: DSC thermograms belonging to samples

In the light of all these data, we estimate that the peak that we have observed in the proximity of 740 °C belong to $Zn_3V_2O_8$ and ZnV_2O_6 crystalline phases in the glasses that we have synthesized. The second crystallization temperature decreased with increasing amount of V_2O_5. Melting temperatures belonging to were almost the same and around 935 °C. Decrease in glass transition temperatures and crystallization temperatures remaining almost the same with increasing amount of V_2O_5 naturally resulted in increase in the thermal stability (ΔT). Glassy transition temperatures are reported to increase in tellurium and silicon-based glasses with the addition of Nb_2O_5, V_2O_5 in increasing amounts. Decrease in glass transition temperatures of the samples in this study with increasing concentration of V_2O_5 can be explained with bond enthalpy. While B-O bond enthalpy was 809 kJmol^{-1}, V-O bond enthalpy was lower (637 kJmol^{-1}). Substituting O-B-O bonds with weaker O-V-O connections lowers activation energy for structural reorganizations. Accordingly, glass transition temperature decreases with increasing V_2O_5.

Table 2: Glass transition, crystallization, melting temperatures and thermal stabilities of synthesized ZBV glasses

Sample Code	T_g (ºC)(± 1)	T_{c1} (ºC)(± 1)	T_{c2} (ºC)(± 1)	T_m (ºC)(± 1)	ΔT (ºC)(± 1.2)
ZBV1	553	743	833	935	190
ZBV2	547	730	831	933	183
ZBV3	541	743	820	935	202
ZBV4	531	743	818	935	212

3.3. Structural examination

FTIR spectra are given all together in Fig. 4. In addition, basic structural units of boron and vanadium and their corresponding localizations in our synthesized glasses are also given within this figure. In Fig. 5, deconvolutions of FTIR spectra belonging to samples are given. FTIR spectra were examined in three basic regions.

The first region is the 400-800 cm^{-1} region. In this region, vibrations belonging to various connections can be seen. The second region is between 800-1200 cm^{-1} and mostly vibrations belonging to BO_4 structural units of boron are observed in this region. The third region is the region around 1200-1500 cm^{-1} and mostly various vibrations corresponding to BO_3 structural unit of boron can be seen in these regions. Except for boron that forms the glass network, vibrations corresponding to various states of zinc and vanadium found in the glass can also be observed within these regions (Table 3).
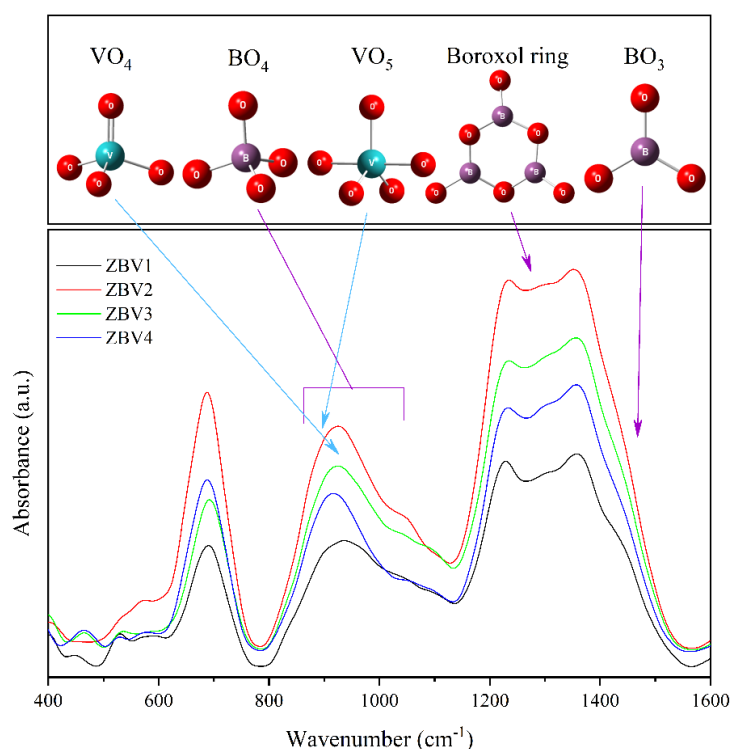
Figure 4: 400-1600 cm^{-1} region FTIR spectra and localizations of structural units belonging to ZBV samples

One or more intensive peaks can be seen in all regions. Bands found between 449-464 cm^{-1} within the first regions are known to belong to the vibrations in the ZnO$_4$ unit. Apart from this, O-V angular vibration is reported to correspond to 526-534 cm^{-1}, Zn-O stretching vibration correspond to 575-595 cm^{-1}, and B-O-B connection vibration correspond to the bands within 676-730 cm^{-1}. The most intense peak in this region belongs to the band around 680 cm^{-1} and shows the abundance of B-O-B connections within the structure.

Bands belonging to B-O stretching vibrations belonging to BO$_4$ unit in the second region are found within the ranges of 873-886 cm^{-1}, 930-939 cm^{-1}, 1042-1055 cm^{-1}. It is also known in V$_2$O$_5$ containing structures that the presence of bands belonging to the vibrations of VO$_5$ and VO$_4$ structural units are also found within the regions of 873-886 cm^{-1} and 930-939 cm^{-1} where B-O stretching vibrations have been encountered. Intensity of bands belonging to B-O vibration is known to decrease with increasing concentration of V$_2$O$_5$ in penta- and diborate groups within the range of 1103-1114 cm^{-1}; however, the intensity of the band belonging to B-O vibration in meta- and orthoborate groups increases within the range of 1222-1231 cm^{-1} found in the third region.
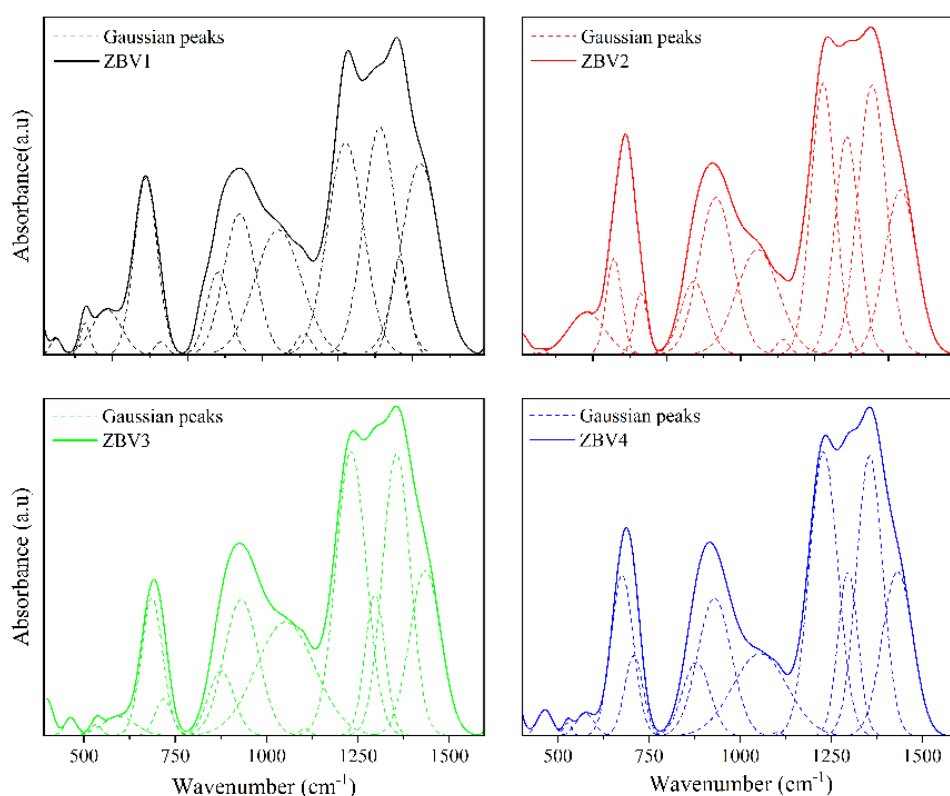
Figure 5: Deconvolution of FTIR spectra belonging to ZBV samples. Straight lines show the FTIR spectra belonging to samples and dashed lines show the Gaussian bands obtained from deconvolution

Table 3: Bands belonging to ZBV samples and corresponding vibrations

ZBV1	ZBV2	ZBV3	ZBV4	Vibrations	References
(cm^{-1})	(cm^{-1})	(cm^{-1})	(cm^{-1})		
449	458	464	464	Zn-O vibration in ZnO_4 structure	[56]
527	-	534	526	O-V angular deformation vibration	[57]
584	582	595	575	Zn-O stretching vibration	[58]
688	693	686	676	B-O-B connection vibration	[59]
729	730	718	708	B-O-B connection vibration	[60]
882	873	876	880	➢ B-O stretching vib. in BO_4 unit ➢ Stretching vib. of VO_5	[59]
939	933	931	930	➢ B-O stretching vibration in BO_4 unit ➢ Stretching vib. of VO_2 in VO_4 unit	[59]
1042	1046	1052	1055	Vibration belonging to tetrahedral BO_4 unit	[61]
1110	1114	1104	1103	B-O vibration in penta- and di- borate groups	[59]
1222	1223	1231	1229	B-O vibration in meta- and ortho- borate groups	[59]
1313	1287	1297	1296	B-O vibration in boroxol ring	[58]
1365	1355	1356	1356	➢ B-O-B connection vibration ➢ Zn-O-B connection vibration	[10] [59]
1421	1433	1435	1432	NBO B-O- stretching vibration in BO_3 unit	[62]

In the third region, it was observed that bands belonging to boroxol ring and BO_3 structure of boron was prominently found; nevertheless, bands belonging to B-O-B and Zn-O-B vibrations

were also present. Bands within the range of 1287-1365 cm^{-1} belong to B-O in the boroxol ring, bands in the 1421-1435 cm^{-1} regions belong to B-O- vibrations found in the BO$_3$ unit having non-bridging oxygen (NBO). Although the band around 1355 cm^{-1} is known to belong to B-O-B connection vibration, it was reported in some studies that it corresponded to Zn-B-O connection vibration in similar structures.

3.4. Optical properties

Transmittance spectra obtained with scanning 1.5 cm piece of the surface belonging to the synthesized glassed are given in Fig. 6 and transmittance and absorption spectra obtained from a single point of the samples are given in Fig. 7. Transmittance spectra obtained from surface scanning spectrophotometer were obtained from 16 different regions with intervals of 1 mm each. When compared with the transmittance curves found in these spectra, which were used to determine the uniformity of the samples, transmittance was seen to be similar in spectrum of every sample. This proves that a significant aggregation or bubble was not present and the samples had uniform distribution.
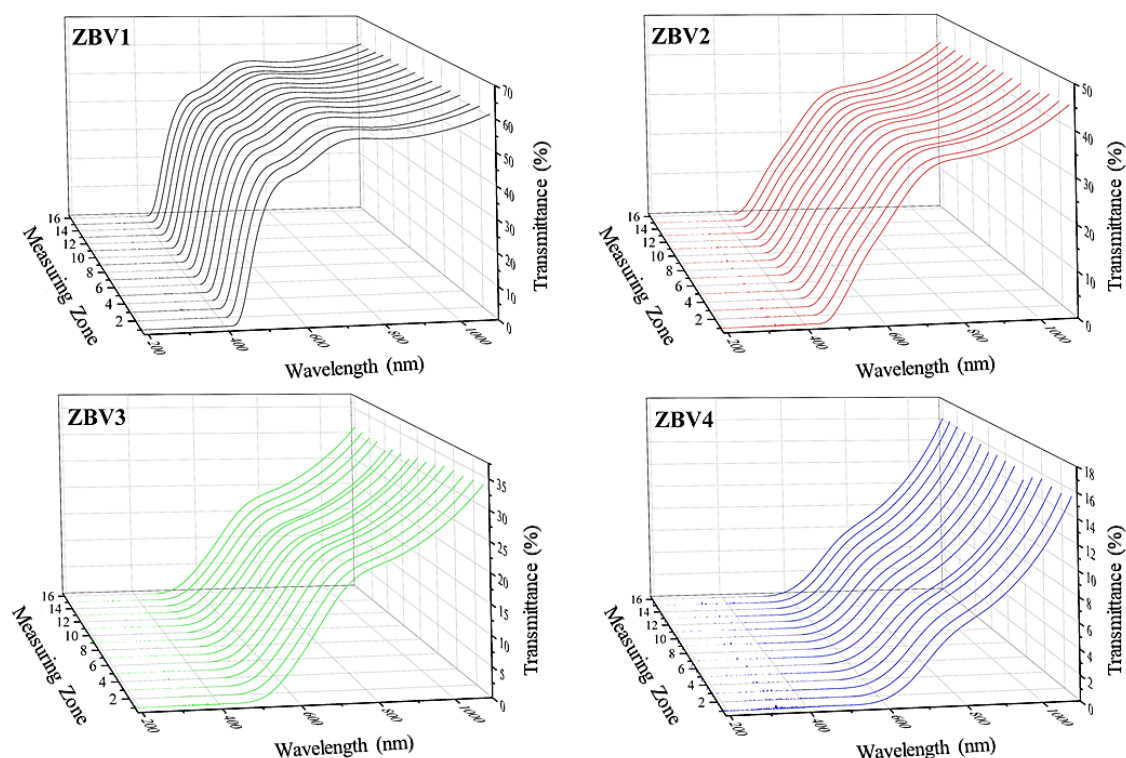
Figure 6: Transmittance spectra obtained by scanning approximately 1.5 cm regions of the samples

In Fig. 7, in which data obtained from a single point were evaluated collectively, absorption edges of spectra belonging to transmittance and absorption were observed to shift towards red (long wavelength) with increasing concentration of V$_2$O$_5$. Spectra shifted towards long

wavelength for approximately for 25 nm each. Transmittance value decreased significantly. Switching oxygen bond in the glass network and change in the number of non-bridging oxygen (NBO) in the network also changes absorption properties [54]. Shifting of the absorption edge towards long wavelength with increasing amount of V_2O_5 and also decrease in optical band gaps might be explained with this change.
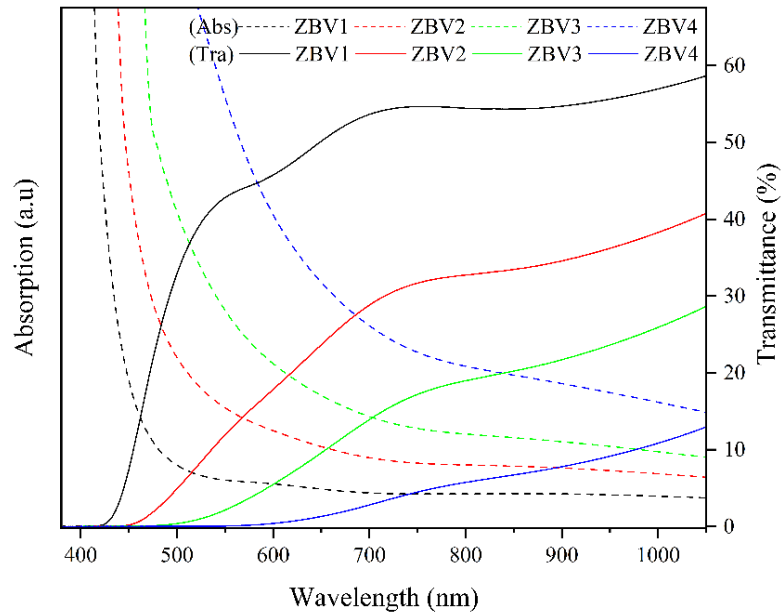
Figure 7: Absorption-transmittance spectra of ZBV samples against wavelength

Optical band gaps of synthesized glass samples were calculated by using absorption spectrum for indirect transitions. Absorption coefficient is given according to Lambert – Beer – Bouguer Law [63].

$$\alpha = 0.202 \left(\frac{A}{d} \right) \tag{5}$$

Here, A is the absorbance, d is the thickness of the sample. Photon energies belonging to wavelengths corresponding to linear part of the absorption spectrum were calculated with the help of the following equation [63]:

$$E = h\upsilon \tag{6}$$

Moreover, $(\alpha h\upsilon)^{1/2} \sim h\upsilon$ graphics were plotted for indirect transitions for each sample. In these equations, α is the absorption coefficient, h is the Planck constant, υ is photon frequency and in addition, $h\upsilon$ is the photon energy.

From the value of this line passing through the linear part of this plotted Tauc curve (Fig. 8) corresponding to $(\alpha h\upsilon)^{1/2} = 0$ optical band gap belonging to the sample is found. Optical band gaps of V_2O_5 doped glasses varied between 2.55 eV and 1.24 eV. Increase in V_2O_5 regularly reduced the optical band gap.
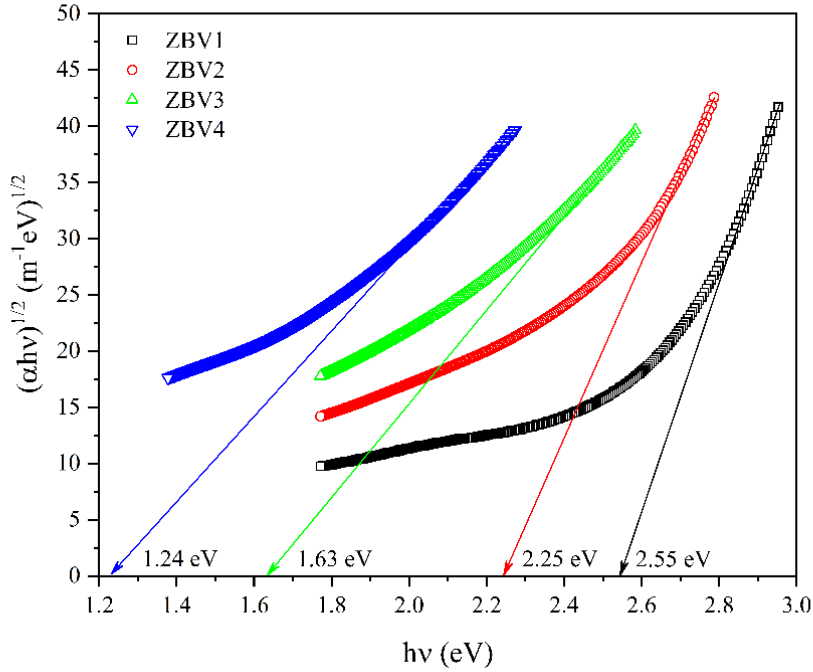
Figure 8: Tauc Plots belonging to ZBV samples

With the curve of the absorption edge in the semi-logarithmic plot (Fig. 9),

$$\Delta E = \left[\frac{d(ln\alpha)}{d(h\upsilon)}\right]^{-1} \tag{7}$$

Urbach Energies were calculated [63]. Fitting values of lines plotted from the straight part of the absorption edge were $R^2 > 0.99$. Here, *ΔE* is named as Urbach energy, *α* is absorption coefficient and *hυ* as photon energy.

A stable increase was observed in Urbach energies due to increase in V_2O_5 concentration. Urbach energy was calculated between the range of 0.246 eV and 0.630 eV. Urbach energy belonging to non-doped, pure 60% ZnO-40% B_2O_3 glass was calculated within the range of 0.17 eV [54]. This result is in line with the values that have been obtained in this study. Low Urbach energy value shows us that the structure of the synthesize glass structure is uniform and stable. Increase in V_2O_5 concentration in the glass network shows that the structure has become irregular and unstable [64].

Table 4: Optical band gap, Urbach energies and refractive indices of synthesized ZBV glasses

Sample Code	Optical band gap (eV)	Urbach energies (eV)	Refractive index
ZBV1	2.55	0.246	2.530
ZBV2	2.25	0.346	2.635
ZBV3	1.63	0.630	2.917
ZBV4	1.24	0.630	3.170

Refractive index is an important data for materials that are considered to be used in optoelectronics. Refractive indices were determined with the help of Eqn. (3) using optical band gaps data within the region corresponding to the absorption edge. Refractive indices of the samples were calculated within the range of 2.530-3.170. As it can be seen in Table 4, refractive index increased in direct proportion to increase in V_2O_5.
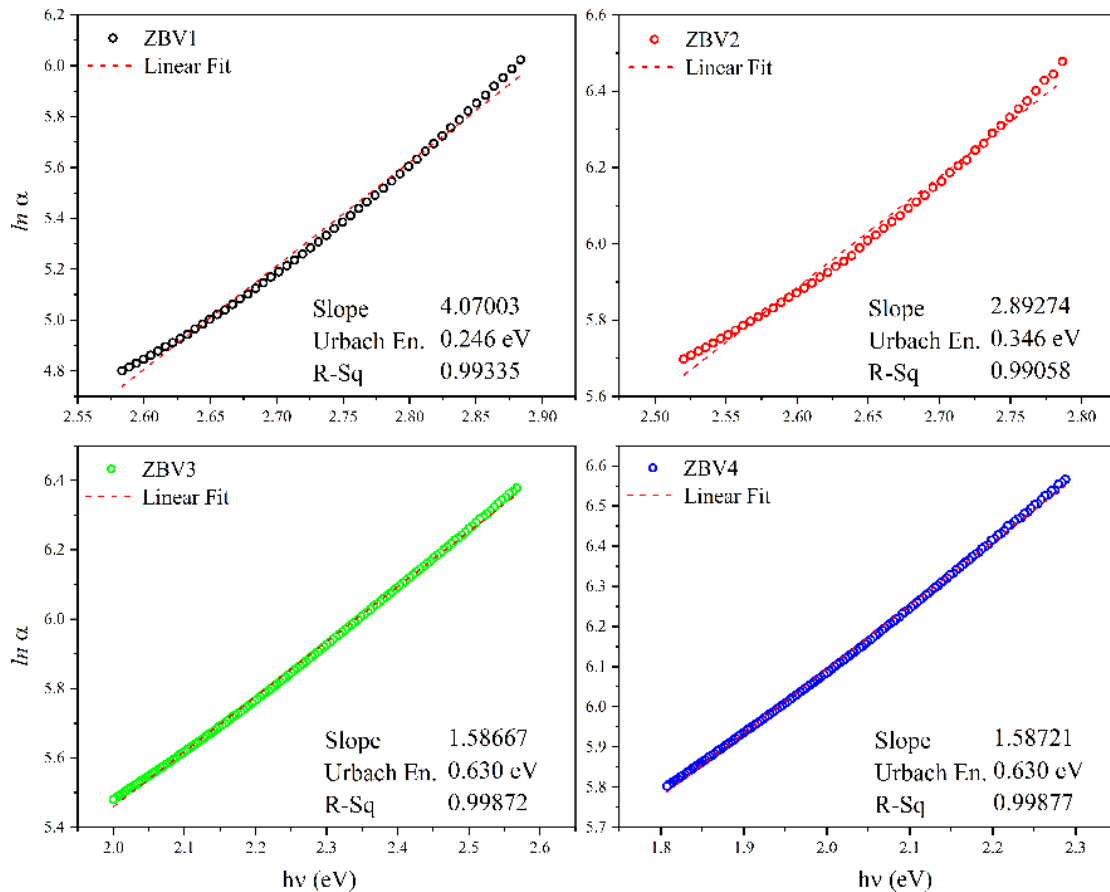
Figure 9: Urbach Energies, slopes, and R^2 fitting values of ZBV samples

4. Conclusions

Ternary zinc borate oxide glass samples doped with different ratios of V_2O_5 were synthesized successfully. Physical, structural, thermal, and optical characterization of these

synthesized samples were performed. Structural units were determined with FTIR. B_2O_3 was found to be present in the glass network in the structure of the boroxol ring, planar BO_3, tetrahedral BO_4. ZnO, acting as the organizer with its low concentration in the structures in which it is found, was determined to be present in the samples of this study in tetrahedral ZnO_4 and octahedral ZnO_6 structural units; and it was concluded that it might be present in the glass network as a glass former. Vanadium is present in the glass network with VO_4 and VO_5 structural unit. Increase in VO_5 shifted the absorption edge significantly towards the red region and correspondingly decrease optical band gap to 1.24 eV from 2.55 eV and as expected, led to increase in Urbach energy. Increase in Urbach energy proves that V_2O_5 renders the structure nonuniform and unstable. As a result of thermal characterization, V_2O_5 increase was found to decrease glass transition temperature to 531 °C from 553 °C. While density decreased with increasing amount of V_2O_5, molar volume values demonstrated increase, as well. Similar to molar volume, refractive index also increased. High refractive indices increasing to 3.170 from 2.530 showed that synthesized glasses are potential materials that could be used in optical system requiring high refractive index. These glasses, considered to find application in many fields of optoelectronics also have the property of being novel materials for solar energy systems due to their semiconducting properties.

References

[1] Kılıç, G., *Değişik bileşimli camların hazırlanması, fiziksel ve optik özelliklerinin incelenmesi*. PhD Thesis, Eskişehir Osmangazi University, Eskişehir, Turkey, 2006.

[2] Rao, R.B., Veeraiah, N., *Study on some physical properties of Li_2O-MO-B_2O_3: V_2O_5 glasses*, Physica B: Condensed Matter, 348, 256-271, 2004.

[3] El-Batal, H.A.R., Ezz-El-Din, F.M., *Interaction of γ-rays with Some Alkali Alkaline Earth Borate Glasses Containing Chromium*, Journal of the American Ceramic Society, 76, 523, 1993.

[4] Abdel-Baki, M., El-Diasty, F., *Role of oxygen on the optical properties of borate glass doped with ZnO*, Journal of Solid State Chemistry, 184, 2762-2769, 2011.

[5] El-Falaky, G.E., Gaafar, M.S., Abd El-Aal, N.S., *Ultrasonic relaxation in Zinc-Borate glasses*, Current Applied Physics, 12, 589-596, 2012.

[6] Sumalatha, B., Omkaram, I., Rao, T.R., Raju, Ch. L., *Alkaline earth zinc borate glasses doped with Cu^{2+} ions studied by EPR, optical and IR techniques*, Journal of Non-Crystalline Solids, 357, 3143-3152, 2011.

[7] Kumar, R.R., Bhatnagar, A.K., Rao, J.L., *EPR of vanadyl ions in alkali lead borate glasses*, Materials Letters, 57, 178-182, 2002.

[8] Rada, M., Rada, S., Pascuta, P., Culea, E., *Structural properties of molybdenum-lead-borate glasses*, Spectrochimica Acta A, 77, 832-837, 2010.

[9] Rao, T.R., Reddy, Ch.V., Krishna, Ch.R., Thampy, U.S.U., Raju, R.R., Rao, S., Ravikumar, R.V.S.S.N., *Correlation between physical and structural properties of Co^{2+} doped mixed alkali zinc borate glasses*, Journal of Non-Crystalline Solids, 357, 3373-3380, 2011.

[10] Singh, G.P., Kaur, S., Kaur, P., Kumar, S., Singh, D.P., *Structural and optical properties of WO_3-ZnO-PbO-B_2O_3 glasses*, Physica B: Condensed Matter, 406, 1890-1893, 2011.

[11] He, F., Wang, J., Deng, D., *Effect of Bi_2O_3 on structure and wetting studies of Bi_2O_3-ZnO-B_2O_3 glasses*, Journal of Alloys and Compounds, 509, 6332-6336, 2011.

[12] Lian, Z., Wang, J., Lv, Y., Wang, S., *The reduction of Eu^{3+} to Eu^{2+} in air and luminescence properties of Eu^{2+} activated ZnO-B_2O_3-P_2O_5 glasses*, Journal of Alloys and Compounds, 430, 257-261, 2007.

[13] Saritha, D., Markandeya, Y., Salagram, M., Vithal, M., *Effect of Bi_2O_3 on physical, optical and structural studies of ZnO-Bi_2O_3-B_2O_3 glasses*, Journal of Non-Crystalline Solids, 354, 5573-5579, 2008.

[14] Li, S., Chen, P., Li, Y., *Structural and physical properties in the system ZnO-B_2O_3-P_2O_5-R_nO_m*, Physica B: Condensed Matter, 405, 4845-4850, 2010.

[15] Aleksandrov, L., Komatsu, Iordanova, R., Dimitriev, Y., *Structure study of MoO_3-ZnO-B_2O_3 glasses by Raman spectroscopy and formation of $ZnMoO_4$ nanocrystals*, Optical Materials, 33, 839-845, 2011.

[16] Lakshminarayana, G., Buddhudu, S., *Spectral analysis of Sm^{3+} and Dy^{3+}: B_2O_3-ZnO-PbO glasses*, Physica B: Condensed Matter, 373, 100-106, 2006.

[17] Singh, H., Singh, K., Gerward, L., Singh, K., *ZnO-PbO-B_2O_3 glasses as gamma-ray shielding materials*, Nuclear Instruments and Methods in Physics Research B, 207, 257-262, 2003.

[18] Thulasiramudu, A., Buddhudu, S., *Optical characterization of Sm^{3+} and Dy^{3+}: ZnO-PbO-B_2O_3 glasses*, Spectrochimica Acta A, 67, 802-807, 2007.

[19] Mosner, P., Vosejpkova, K., Koudelka, L., Montagne, L., Revel, B., *Structure and properties of ZnO-B_2O_3-P_2O_5-TeO_2 glasses*, Materials Chemistry and Physics, 124, 732-737, 2010.

[20] Wu, J., Xie, C., Hu, J., Zeng, D., Wang, A., *Microstructure and electrical characteristics of ZnO-B_2O_3-PbO-V_2O_5-MnO_2 ceramics prepared from ZnO nanopowders*, Journal of the European Ceramic Society, 24, 3635-3641, 2004.

[21] Bale, S., Rahman. S., *Electrical conductivity studies of Bi_2O_3-Li_2O-ZnO-B_2O_3 glasses*, Materials Research Bulletin, 47, 1153-1157, 2012.

[22] Ji, L.N., Li, J.B., Liang, J.K., Sun, B.J., Liu, Y.H., *Phase relations and flux research for ZnO crystal growth in the ZnO-B_2O_3-P_2O_5 system*, Journal of Alloys and Compounds, 459, 481-486, 2008.

[23] Hu, Y., Wei, D., Fu, Q., Zhao, J., Zhou, D., *Preparation and microwave dielectric properties of $3ZnO·B_2O_3$ ceramics with low sintering temperature*, Journal of the European Ceramic Society, 32, 521-524, 2012.

[24] Raju, G.N., Reddy, M.S., Sudhakar, K.S.V., *Spectroscopic properties of copper ions in ZnO-ZnF_2-B_2O_3 glasses*, Optical Materials, 29, 1467-1474, 2007.

[25] Kim, D.N., Lee, J.Y., Huh, J.S., *Thermal and electrical properties of BaO-B_2O_3-ZnO glasses*, Journal of Non-Crystalline Solids, 306, 70-75, 2002.

[26] Masuda, H., Kimura, R., Sakamoto, N., *Properties and Structure of Glasses in the System BaO-B_2O_3-ZnO*, Journal of the Japan Institute of Metals, 63, 284, 1999.

[27] Kundu, V., Dhiman, R.L., Goyal, D.R., Maan, A.S., *Physical and electrical properties of semiconducting Fe₂O₃-V₂O₅-B₂O₃ glasses*, Journal of Optoelectronics and Advanced Materials, 2(7), 428-432, 2008.

[28] Saritha, D., Markandeya, Y., Salagram, M., Vithal, M., *Effect of Bi₂O₃ on physical, optical and structural studies of ZnO-Bi₂O₃-B₂O₃ glasses*, Journal of Non-Crystalline Solids, 354, 5573-5579, 2008.

[29] Toderaş, M., Filip, S., Ardelean, I., *Structural study of the Fe₂O₃-B₂O₃-BaO glass system by FTIR spectroscopy*, Journal of Optoelectronics and Advanced Materials, 3(8), 1121-1123, 2006.

[30] Schwarz, J., Ticha, H., *Some optical properties of BaO-PbO-B₂O₃ glasses,* Journal of Optoelectronics and Advanced Materials, 5(1), 69-74, 2003.

[31] Nagaraja, N., Sankarappa, T., Kumar, M.P., *Electrical conductivity studies in single and mixed alkali doped cobalt–borate glasses*, Journal of Non-Crystalline Solids, 354, 1503-1508, 2008.

[32] Chaudhry, M.A., Altaf, M., *Optical absorption studies of sodium cadmium phosphate glasses*, Materials Letters, 34, 213-216, 1998.

[33] Al-Hajry, A., Al-Shahran, A., El-Desoky, M.M., *Structural and other physical properties of barium vanadate glasses*, Materials Chemistry and Physics, 95, 300-306, 2006.

[34] Sharma, B.I., Robi, P.S., Srinivasan, A., *Microhardness of ternary vanadium pentoxide glasses*, Materials Letters, 57, 3504-3507, 2003.

[35] Ghosh, A., Bhattacharya, S., Ghosh, A., *Optical and other structural properties of some zinc vanadate semiconducting glasses*, Journal of Alloys and Compounds, 490, 480-483, 2010.

[36] Tawaki, D.M., Adlan, M.J.B., Abdullah, M.J., *DC electrical conductivity of semiconducting cobalt–phosphate glasses*, Journal of Non-Crystalline Solids, 357, 2152-2155, 2011.

[37] Mandal, S., Ghosh, A., *Electrical properties of lead vanadate glasses*, Physical Review B: Condensed Matter and Materials Physics, 49, 3131, 1994.

[38] Rao, R.B., Veeraiah, N., *Study on some physical properties of Li₂O-MO-B₂O₃: V₂O₅ glasses*, Physica B: Condensed Matter, 348, 256-271, 2004.

[39] Mott, N.F., *Conduction in glasses containing transition metal ions*, Journal of Non-Crystalline Solids, 1, 1-17, 1968.

[40] Austin, G., Mott, N.F., *Polarons in crystalline and non-crystalline materials*, Advances in Physics, 18, 41-102, 1969.

[41] Sen, S., Ghosh, A., *Structure and other physical properties of magnesium vanadate glasses*, Journal of Non-Crystalline Solids, 258, 29-33, 1999.

[42] Moustafa, Y.M., El-Damrawi, G., Meikhail, M.S., *Effect of Vanadium oxide on the structure and properties of lithium borate glasses*, Mans Science Bulletin C, 20, 71, 1993.

[43] El-Damrawi, G., Moustafa, Y.M., Meikhail, M.S., *Phase separation and NMR studies on sodium boro-silicate glasses containing V₂O₅*, Mans Science Bulletin C, 20, 83, 1993.

[44] Singh, K., Ratnam, J.S., *Electrical conductivity of the Li₂O-B₂O₃ system with V₂O₅*, Solid State Ionics, 31, 221-226, 1988.

[45] Mekki, A., Khattak, G.D., Holland, D., Chinkhota, M., Wenger, L.E., *Structure and magnetic properties of vanadium–sodium silicate glasses*, Journal of Non-Crystalline Solids, 318, 193-201, 2003.

[46] Ebendorff-Heidepriem, H., Riziotis, C., Taylor, E.R., *Novel photosensitive glasses*, Glass Science and Technology, 75, 54, 2002.

[47] Ghosh, A., *Transport properties of vanadium germanate glassy semiconductors*, Physical Review B: Condensed Matter and Materials Physics, 42, 5665, 1990.

[48] Sudarsan, V., Kulshreshtha, S.K., *Study of structural aspects of V_2O_5–P_2O_5–B_2O_3 glasses*, Journal of Non-Crystalline Solids, 258, 20-28, 1999.

[49] Ezz-Eldin, F.M., *Radiation effects on some physical and thermal properties of V_2O_5–P_2O_5 glasses,* Nuclear Instruments and Methods in Physics Research B, 159, 166-175, 1999.

[50] Sindhu, S., Sanghi, S., Agarwal, A., Kishore, N., Seth, V.P., *Effect of V_2O_5 on structure and electrical properties of zinc borate glasses*, Journal of Alloys and Compounds, 428, 206-213, 2007.

[51] Li, H., Lin, H., Chen, W., Luo, L., *IR and Raman investigation on the structure of (100-x)[0.33B_2O_3–0.67ZnO]–xV_2O_5 glasses*, Journal of Non-Crystalline Solids, 352, 3069-3073, 2006.

[52] Elkhoshkhany, N., El-Mallawany, R., Syala, E., *Mechanical and thermal properties of TeO_2–Bi_2O_3–V_2O_5–Na_2O–TiO_2 glass system*, Ceramics International, 42(16), 19218–19224, 2016.

[53] Dimitrov, V., Sakka, S., *Linear and nonlinear optical properties of simple oxides. II*, Journal of Applied Physics, 79, 1741-1745, 1996.

[54] Altaf, M., Chaudhry, M.A., Zahid, M., *Study of optical band gap of zinc-borate glasses*, Journal of Research (Science), 14(2), 253-259, 2003.

[55] Kaur, A., Khanna, A., Sathe, V.G., Gonzalez, F., Ortiz, B., *Optical, thermal, and structural properties of Nb_2O_5-TeO_2 and WO_3-TeO_2 glasses*, Phase Transitions, 86(6), 598-619, 2013.

[56] Mohamed, N.B., Yahya, A.K., Deni, M.S.M., Mohamed, S.N., Halimah, M.K., Sidek, H.A.A., *Effects of concurrent TeO_2 reduction and ZnO addition on elastic and structural properties of (90−x)TeO_2–10Nb_2O_5–(x)ZnO glass*, Journal of Non-Crystalline Solids, 356, 1626–1630, 2010.

[57] Laila, S., Supardan, S.N., Yahya, A.K., *Effect of ZnO addition and concurrent reduction of V_2O_5 on network formation and elastic properties of lead vanadate (55−x)V_2O_5–45PbO–(x)ZnO glass system,* Journal of Non-Crystalline Solids, 367, 14–22, 2013.

[58] Pascuta, P., Vladescu, A., Borodi, G., Culea, E., Tetean, R., *Structural and magnetic properties of zinc ferrite incorporated in amorphous matrix*, Ceramics International, 37, 3343–3349, 2011.

[59] Arora, S., Kundu, V., Goyal, D.R., Maan, A.S., *Effect of stepwise replacement of LiF by ZnO on structural and optical properties of LiF. B_2O_3 glasses*, Turkish Journal of Physics, 37, 229–236, 2013.

[60] Agarwal, A., Sheoran, A., Sanghi, S., Bhatnagar, V., Gupta, S.K., Arora, M., *Structural investigation and electron paramagnetic resonance of vanadyl doped alkali niobium borate glasses*, Spectrochimica Acta A, 75, 964–969, 2010.

[61] Jiao, Q., Yu, X., Xu, X., Zhou, D., Qiu, J., *Relationship between Eu³⁺ reduction and glass polymeric structure in Al₂O₃-modified borate glasses under air atmosphere*, Journal of Solid State Chemistry, 202, 65–69, 2013.

[62] Razali, W.A.W., Azman, K., Hashim, S., Alajerami, Y.S.M., Syamsyir, S.A., Mardhiah, A., Ridzwan, M.H.J., *Physical, Structural, and Luminescence Studies of Nd³⁺ Doped MgO–ZnO Borate Glass*, Optics and Spectroscopy, 115, 701–707, 2013.

[63] Kilic, G., Issever, U.G., Ilik, E., *Characterization of Er³⁺ doped ZnTeTa semiconducting oxide glass*, Journal of Materials Science: Materials in Electronics, 30(9), 8920-8930, 2019.

[64] Issever, U.G., Kilic, G., Peker, M., Ünaldi, T., Aybek, A.S., *Effect of low ratio V⁵⁺ doping on structural and optical properties of borotellurite semiconducting oxide glasses*, Journal of Materials Science: Materials in Electronics, 30 (16), 15156-15167, 2019.

Investigation on Optical Properties of Atmospheric Pressure Plasma Jets of N₂ Gas

Erkan İLİK[1,*], Çağrı DURMUŞ[2], Tamer AKAN[3]

[1]Eskisehir Osmangazi University, Faculty of Science and Letters, Department of Physics, TR-26040, Eskisehir, Turkey
eilik@ogu.edu.tr, ORCID: 0000-0003-2986-0015
[2]Eskisehir Osmangazi University, Graduate School of Sciences, TR-26040, Eskisehir, Turkey
501320191006@ogrenci.ogu.edu.tr, ORCID: 0000-0003-0174-0580
[3]Eskisehir Osmangazi University, Faculty of Science and Letters, Department of Physics, TR-26040, Eskisehir, Turkey
akan@ogu.edu.tr, ORCID: 0000-0003-0907-2724

Abstract

In this study, firstly, N₂ atmospheric pressure plasma jet (APPJ) system was presented. Nitrogen gas discharges are produced as jet using an AC power supply which can be adjusted between 6-18 kV and the frequency value of 13-20 kHz at atmospheric pressure. The change of length of produced atmospheric pressure nitrogen plasma jet, according to gas flow rate has been investigated and the produced jet length was approximately 2 cm for 5 L/min when the applied voltage was 18 kV and the frequency was 15 kHz. Nitrogen plasma jet produced at atmospheric pressure was examined with optical emission spectroscopy (OES) and the correlation between gas flow rate and emission spectra were investigated. Furthermore, electron temperature and electron density of atmospheric pressure nitrogen gas plasma jet were estimated under different flow rates of N₂ gas.

Keywords: Nitrogen; Atmospheric pressure plasma; N₂ APPJ; Electron temperature; Electron density.

N₂ Gazı Atmosferik Basınç Plazma Jetlerinin Optik Özeliklerinin İncelenmesi

Öz

Bu çalışmada öncelikle atmosferik basınçta plazma jet (APPJ) üretimine olanak sağlayan sistem tanıtılmıştır. Azot gazı deşarjları atmosferik basınçta 6-18 kV ve 13-20 kHz ayarlı AC güç kaynağı ile jet olarak üretilmiştir. Üretilen atmosferik basınç azot plazma jetin gaz akış hızına göre uzunluğunun değişimi incelenmiş olup, üretilen jet uzunluğu 5 L/dk gaz akış hızı, 18 kV voltaj ve 15 kHz frekans değerinde yaklaşık olarak 2 cm'dir. Atmosferik basınçta üretilen azot plazma jet, optik emisyon spektroskopisi (OES) ile incelenmiş ve gaz akış hızı ile emisyon spektrumlarındaki değişimler belirlenmiştir. Bununla birlikte, atmosferik basınç azot gazı plazma jetin elektron sıcaklığı ve elektron yoğunluğu azot gazının farklı gaz akış hızları için hesaplanmıştır.

Anahtar Kelimeler: Azot; Atmosferik basınç plazma; N₂ APPJ; Elektron sıcaklığı; Elektron yoğunluğu.

1. Introduction

Many studies have been carried out so far with gas discharge plasmas known as cold plasmas. Cold plasmas have many advantages such as the effects of low temperature, low electric field, and the chemical interactions of the active radicals have various applications. Cold plasmas are widely used in many applications such as sterilization, surface applications such as coating, activation, cleaning, polymerization, oxidation, nitriding, and medical treatments [1-4]. Instead of noble gases such as argon (Ar), helium (He), etc., nitrogen (N_2) gas has also used in these applications [5, 6]. Nitrogen gas plasmas have a vital importance because of the content of radical (reactive) and metastable particles. Molecular nitrogen does not react easily under normal conditions and is ineffective. However, the excited or dissociated N_2 species, especially atomic nitrogen (N) in the mixed gases containing N_2 or N_2^+ caused many reactions to be used in important applications. Different excited states of species such as N_2, N_2^+ and N are also formed in nitrogen plasmas and form important reactions [7]. The first excited state of nitrogen, the metastable triplet $N_2(A^3\sum_u^+)$, has a threshold energy of 6.2 eV and a lifetime of about 2 seconds. From this point of view, it is an important energy carrier, so it plays an effective role in N_2 plasma by making important mechanisms such as ionization, decomposition, plasma chemistry and gas heating [8]. Although $N_2(A)$ plays an important role in the basic processes controlling nitrogen discharge, it is known that the main energy storage is not by electronic metastable. It has been observed in previous studies that the $N_2(X^1\sum_g^+)$ state of the control mechanism is at vibration levels [9]. However, N atoms formed by the decomposition of nitrogen molecules used in metallic

nitriding are easily produced in nitrogen plasma. Observation of $N_2^+(B^2\textstyle\sum_u^+ \rightarrow X^2\textstyle\sum_g^+)$ transitions also indicates that N_2^+ is abundant [10]. Characteristic emissions and numerical calculations of species such as N_2, N_2^+, N^+, and N in low- and atmospheric pressure of nitrogen luminescent (glow) discharges have been examined [11, 12]. N_2 and N_2^+ species in nitrogen plasma play vital role in synthesis of new functional and mechanical materials as they have strong chemical activity. Production of anti-microbial low density polyethylene films and hydrophilic polymer structures [13], processing of hydroxyl cellulose films [14], GaN nanostructures containing nano-wire and nano-particles[15], nitrogen oxide processing [16], production of high activity plasma welding for the storage of silicon nitride films [17], modification of amorphous SiO_2 nanoparticles [18], single crystal production [19], modification of stainless steel surfaces (ion implantation) [20], treatment of indium tin oxide (ITO) films [21], graphene and graphite structures [22], surface modification of polyacrylonitrile copolymer structures [23], diamond building carbon (DLC) production [24], annealing Ta_2O_5 films [25] are examples of applications of material processing of cold plasma produced with low pressure nitrogen gas/gas mixtures.

According to the literature, there are a lot of applications by using N_2 APPJs, but the basic characteristics of the produced plasma are not examined in detail. In order to do that, a jet system which produces nitrogen gas plasmas at atmospheric pressure is designed and produced. Firstly, the behavior of nitrogen gas plasma in atmosphere medium according to different gas flow rate was investigated. Then, optical emission spectra (OES) of nitrogen plasmas (N_2 APPJs) were taken depending on gas flow rate. The possible atomic and molecular transitions in nitrogen plasma were obtained from the OES data in accordance with the literature. Finally, electron temperature (T_e) and electron density (n_e), which are one of the main parameters of nitrogen gas plasma, were calculated by Boltzmann two-line method. It is considered that this study would be a basis for determining the appropriate gas flow rate for N_2 plasmas in further experimental studies.

2. Materials and Methods

Designed system to produce N_2 APPJs and the scheme of N_2 APPJ system were given in Fig. 1 and Fig. 2, respectively. The atmospheric pressure plasma system used here is known as plasma jet.
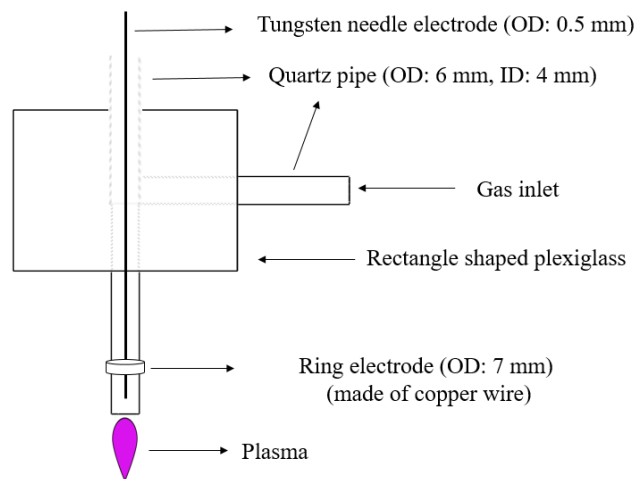
Figure 1: A schematic of N_2 atmospheric pressure plasma jet device
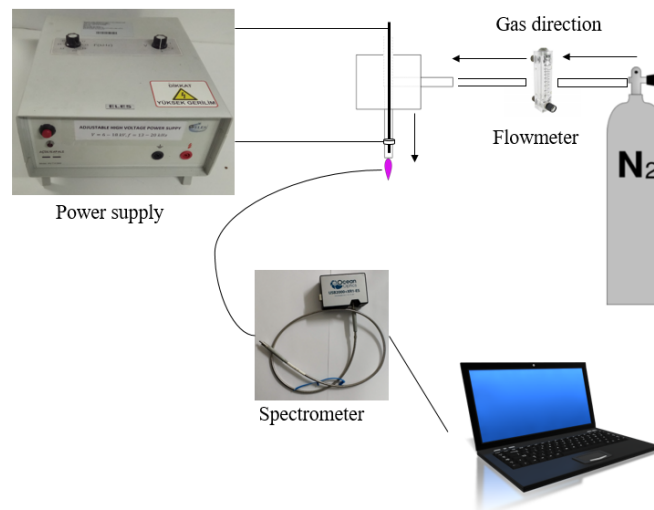

Figure 2: Close up view of APPJ system

The whole system was installed in a fume hood to protect against the stifling effects of nitrogen gas. In order to generate APPJ, three identical quartz glass pipes (OD: 6 mm, ID: 4 mm) were used. First pipe which was used as gas inlet was fixed on rectangle shaped plexiglass (50x25x37 mm). Other pipe which was fixed on the plexiglass was used to hold tungsten electrode. The tungsten electrode was extended approximately 3 mm to the nozzle of the pipe attached to gas outlet. The tungsten wire has 0.5 mm thickness. The distance of the ring electrode to the nozzle of the pipe was determined as a result of making a series of attempts. A ring electrode which was made of copper was connected to the end of the glass pipe. Then, a gas flowmeter (LZT M-6 flowmeter, 2-10 L/min) was connected to control gas flow rate to gas inlet of the system. Gas outlet of the pipe was mounted with pneumatic hose (OD: 10 mm, ID: 6 mm).

Nitrogen gas cylinder (Habas 99.999% purity) and its regulator were used to supply gas to the APPJ system. The connection between this gas cylinder and the fume hood is provided by a 6.5 mm diameter pneumatic hose. The alternating current (AC) power supply (ELES HV-711GK4), which can be adjusted between 6-18 kV and the frequency value of 13-20 kHz, was used for generating N_2 APPJ.

A spectrometer (Ocean Optics USB2000+), fiber optic cable and computer program (OceanView software) were used in order to examine the spectroscopic properties of N_2 APPJ as can be seen in Fig. 1. 10 mm wide slit (300 grooves/mm grating, the spectral resolution = 0.1 nm) were used to measure spectra in the sensitive range from 200-1100 nm. In order to avoid fluctuation of intensity, integration time of OES was fixed at 1 s through the experiment, and optical emission spectrometer was recalibrated priorly each measurement.

3. Results

In order to generate N_2 APPJ, the high voltage input was connected to the tungsten needle electrode. A ring electrode which was made of copper was connected to the end of the glass pipe. Then, N_2 gas was flowed through the glass pipe in the middle of the plexiglass. Gas sent from the nitrogen gas cylinder was read out from gas flowmeter, simultaneously. After all, when the AC voltage was applied between the electrodes, the nitrogen discharge was generated between the electrodes. When the flow rate of nitrogen gas was set at a certain value, the nitrogen gas discharge between the electrodes emerges as a N_2 APPJ. At different gas flow rates, generated N_2 APPJ was shown in Fig. 3.
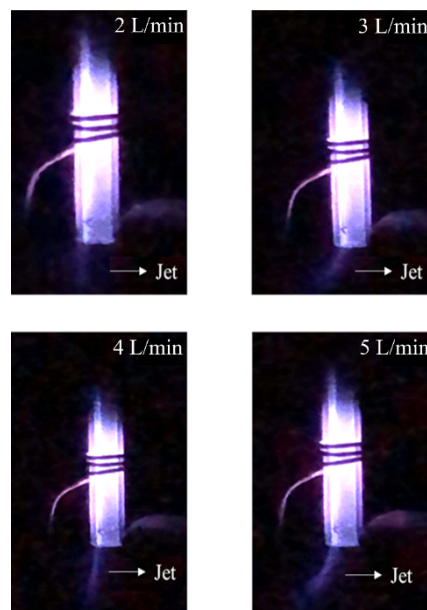
Figure 3: Atmospheric pressure nitrogen gas plasma jet photographs for different N_2 flow rates

We have achieved the longest jet length (about 2 cm) at 18 kV-15 kHz in N_2 APPJs that we produced in a similar diameter before. When we reduce the voltage to less than 18 kV, there is a decreasing in the intensity of the jet, thus its length. On the other hand, if we increase the frequency above 15 kHz, it turned to more intense plasma but similarly jet length decreased. Moreover, when the frequency value was adjusted below 15 kHz, the jet becomes unstable and discontinuous form. The distance between the ring electrode and the nozzle was set at 3 cm. Proper adjustment of this distance prior to the experiment affects the structure of the plasma formed in the atmosphere. It was seen that when the distance between the electrodes decreased, the plasma transformed into an arc form with a high intensity, in other respects when it increased, plasma formed only between the electrodes and could not reach the atmosphere.

The change of plasma jet length that can be released into the atmosphere according to the gas flow rate was also shown in the Fig. 4.
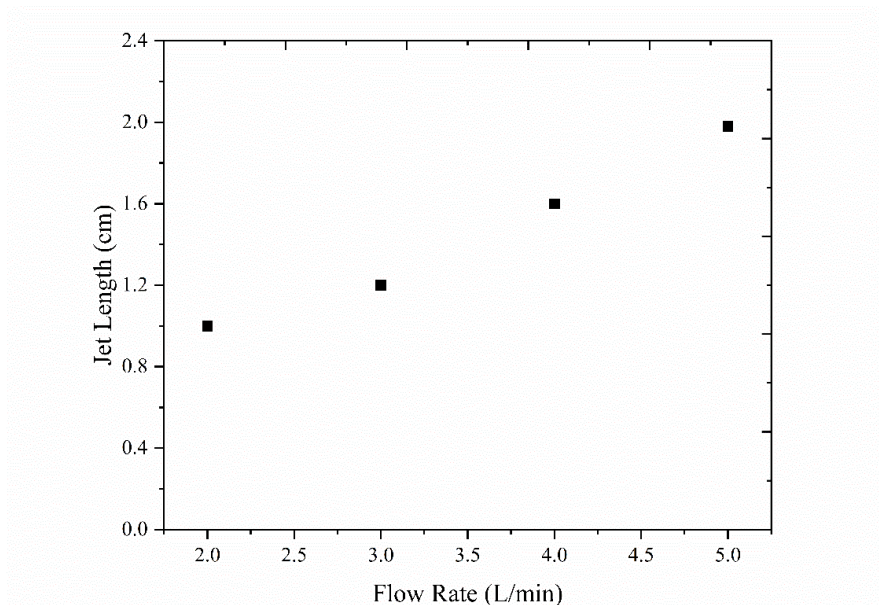
Figure 4: The change of plasma jet length according to the gas flow rate

As shown in Fig. 3 and Fig. 4, the length of APPJ was proportional to gas flow rate. This situation was related with high pressure formed inside the glass pipe. It was observed that high pressure nitrogen gas mixed with the atmosphere medium had been seen to ionize more easily. Spectra taken from the same distance of the N_2 APPJs were shown in Fig. 5.
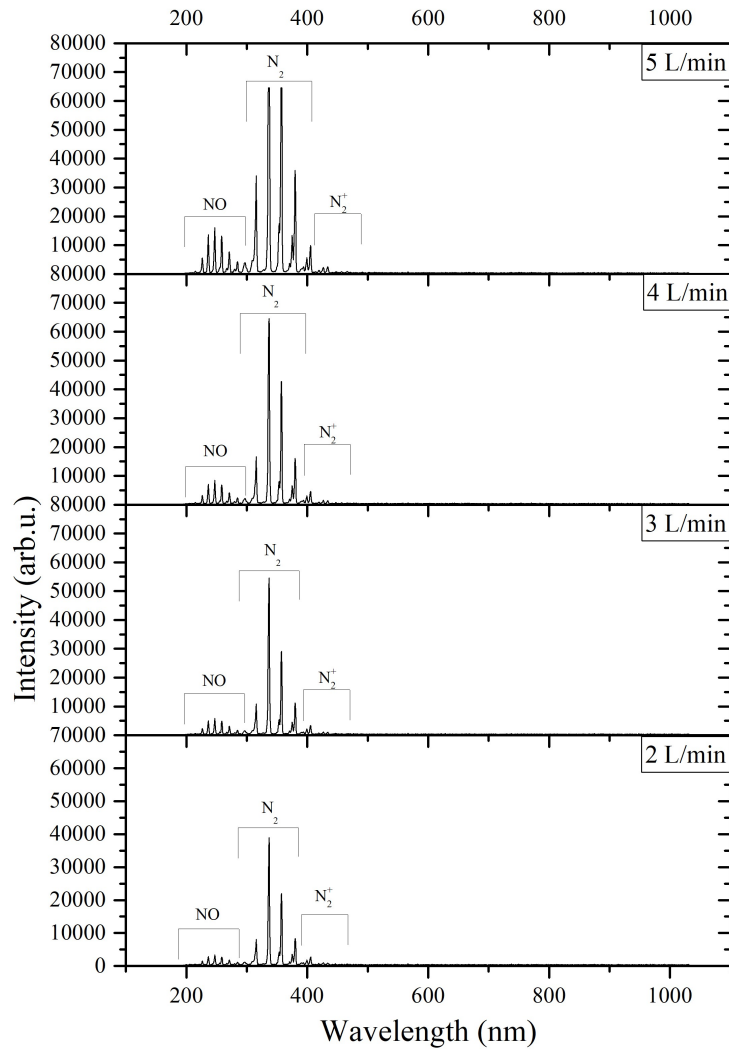
Figure 5: The optical emission spectra of N_2 APPJ at different gas flow rates

In the optical emission spectra taken for different nitrogen gas flow rates, various atom/atoms, molecules and radical particles were found in the N_2 APPJs [26]. Here, it was observed that the NO radical concentration was proportional to gas flow rate. Stated in other words, the NO radical concentration increases as gas flow rate increases. OH radicals (at 308 nm) were dominated by the NO radicals. Therefore, the wavelength corresponding to the OH radicals in the optical emission spectra was not marked and was only given in Table 1. The intensity of N atoms (747 - 870 nm) was determined to be quite low compared to other species such as N_2, N_2^+, etc. On the other hand, N_2 and N_2^+ peaks were observed to increase continuously up to 5 L/min (Fig. 6). As a result of ionization of nitrogen gas, this is an expected result and it is clearly seen from the Fig. 6 that ionization increases with increasing gas flow rate.
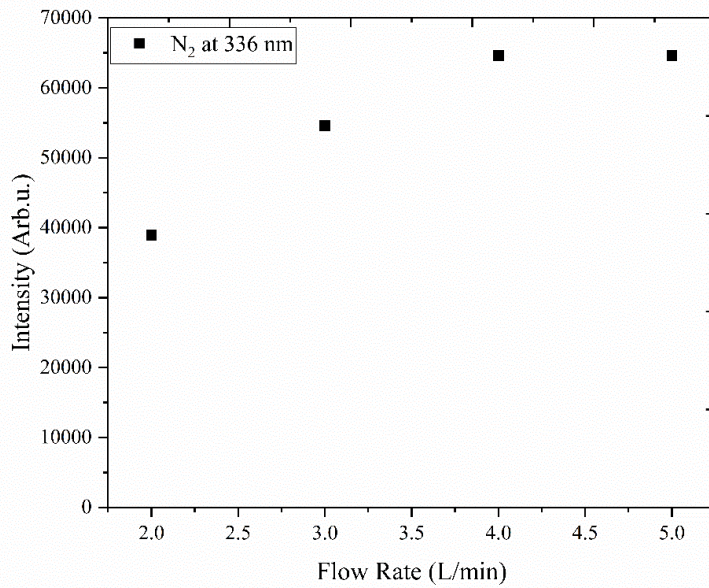
Figure 6: Change of N_2 emissions depending on gas flow rate

Furthermore, OES device used during the measurement reached the upper count limit at a flow rate of 5 L/min. When working in atmosphere medium, wavelengths of H, N and O are expected to be seen in the spectra. However, since the OH and NO radicals were formed by the interaction of H, N, and O atoms, these atoms were not directly observed in the spectra. OH and NO intensities were supposed to be suppressed by N_2. Observed transitions in N_2 APPJs were given in Table 1.

Table 1: Observed atomic and molecular transitions in N_2 APPJ [26]

Plasma Component	Wavelength (nm)	Transition	Excitation Energy (eV)
NO	204.70	$A^2\Sigma^+$, (v=2) – X, (v=0)	~5.46
	214.80	$A^2\Sigma^+$, (v=1) – X, (v=0)	~5.46
	226.20	$A^2\Sigma^+$, (v=0) – X, (v=0)	~5.46
NO	236.30	$A^2\Sigma^+$, (v=0) – X, (v=1)	~5.46
	247.10	$A^2\Sigma^+$, (v=0,) – X, (v=2)	~5.46
	258.70	$A^2\Sigma^+$, (v=0) – X, (v=3)	~5.46
	271.30	$A^2\Sigma^+$, (v=0) – X, (v=4)	~5.46
OH	308.00	$A^2\Sigma^+$ (v=0), – $X^2\Pi$, (v=0)	9,10
	315.90	$C^3\Pi_u$, (v=1) – $B^3\Pi_g$, (v=0)	11.30
	337.10	$C^3\Pi_u$, (v=0) – $B^3\Pi_g$, (v=0)	11.00
	353.60	$C^3\Pi_u$, (v=1) – $B^3\Pi_g$, (v=2)	11.30
	357.70	$C^3\Pi_u$, (v=0) – $B^3\Pi_g$, (v=1)	11.00
N2	370.90	$C^3\Pi_u$, (v=2) – $B^3\Pi_g$, (v=4)	11.50
	375.40	$C^3\Pi_u$, (v=1) – $B^3\Pi g$, (v=3)	11.30
	380.40	$C^3\Pi_u$, (v=0) – $B^3\Pi g$, (v=2)	11.00
	399.70	$C^3\Pi_u$, (v=1) – $B^3\Pi g$, (v=4)	11.30
	405.80	$C^3\Pi_u$, (v=0) – $B^3\Pi g$, (v=3)	11.00
	434.30	$C^3\Pi_u$, (v=0) – $B^3\Pi g$, (v=4)	11.00
	391.40	$B^2\Sigma_u^+$, (v=0) – $X^2\Sigma_g^+$, (v=0)	18.70
N2+	427.80	$B^2\Sigma_u^+$, (v=0) – $X^2\Sigma_g^+$, (v=1)	18.70
	470.90	$B^2\Sigma_u^+$, (v=0) – $X^2\Sigma_g^+$, (v=2)	18.70
N	746.80	$3s\ ^4P – 3p\ ^4S^0$	11.90
	870.30	$3s\ ^4P – 3p\ ^4D^0$	11.80

In the non-LTE plasmas, the electron temperature (T_e) can be calculated using Boltzmann approximation [27].

$$T_e = \frac{E_2 - E_1}{k} \left[\ln \left(\frac{A_2 g_2 I_1 \lambda_1}{A_1 g_1 I_2 \lambda_2} \right) \right]^{-1} \tag{1}$$
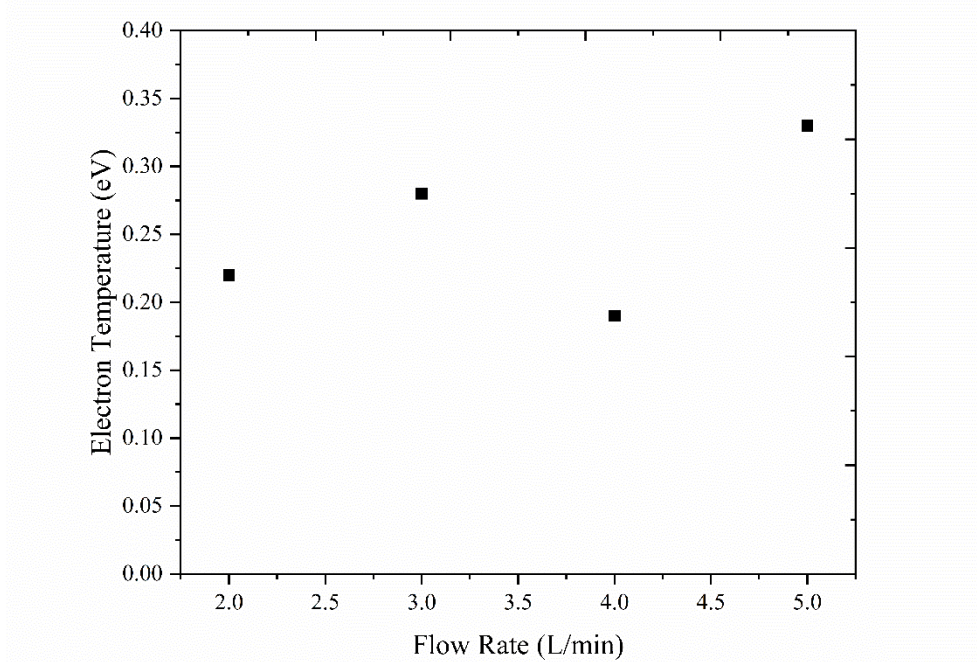
Here, sub index 1 and 2 correspond to two different electronic states of N_2. E_1 and E_2 represent the energy levels. λ_1 and λ_2 are wavelengths of emitted photons; I_1 and I_2 are measured relative intensities. g_1 and g_2 represent the statistical weights of these levels. A_1 and A_2 represent the transition probabilities. Furthermore, the electron density can be estimated as follows [28]:

$$n_e \cong 10^{18} T Z^{7/2} \left(\frac{1}{n_a} \right)^2 \left(\frac{2}{n_b} \right)^5 \ cm^{-3} \tag{2}$$

In Eqn. (2), n_b and n_a are the level of excited state and ground state, respectively. T is the electron temperature. Electron temperature of N_2 APPJ was estimated with using N atoms (at 747 nm and 870 nm) and the values of T_e varied from 0.19 eV to 0.31 eV for different gas flow rates as can be seen in Fig. 7. The electron densities for different gas flow rates were also calculated as can be seen in Fig. 8. The measurement results obtained in the experiment for this calculation are given in Table 2.

Table 2: Data used in electron temperature calculation

Flow Rate	Wavelength (nm)	Intensity (Arb.u.)	$A_1.g_1$ (s^{-1})	$A_2.g_2$ (s^{-1})	E_1 (eV)	E_2 (eV)
2 L/min	746	379	7.84×10^7	-	11.9	-
	870	362	-	4.32×10^7	-	11.75
3 L/min	746	377	7.84×10^7	-	11.9	-
	870	300	-	4.32×10^7	-	11.75
4 L/min	746	376	7.84×10^7	-	11.9	-
	870	393	-	4.32×10^7	-	11.75
5 L/min	746	434	7.84×10^7	-	11.9	-
	870	332	-	4.32×10^7	-	11.75

Figure 7: Electron temperature changing according to gas flow rate
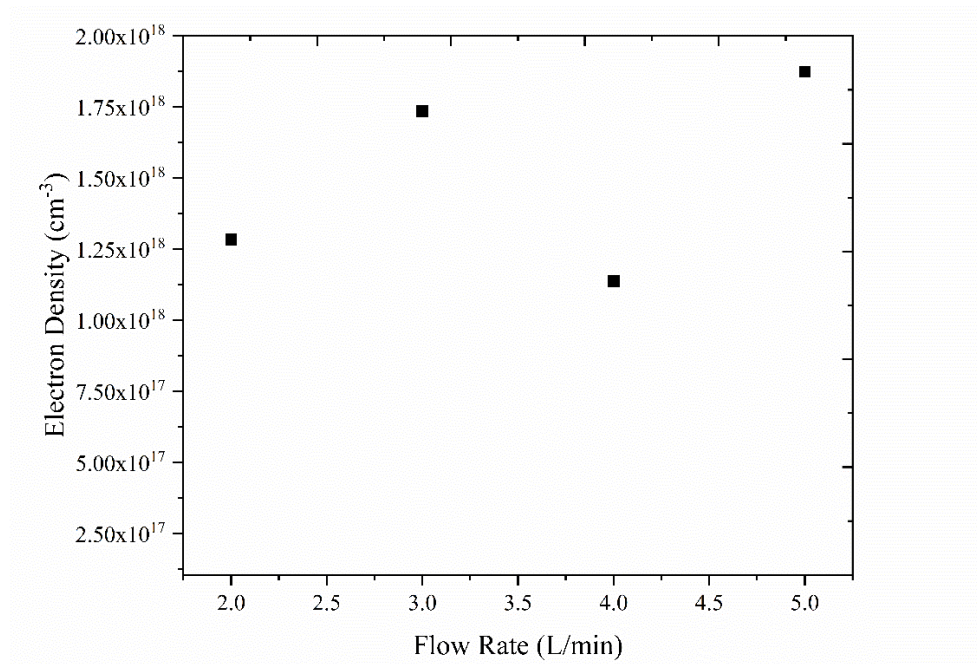
Figure 8: Electron density according to gas flow rate

As N_2 gas flow rate increased, there was no linear change in electron temperature. It is assumed that this result is due to the production of N_2 APPJ in the fume hood. At high gas flow rates, the jet draws towards the top of the furnace and leans towards the nearest electrode. Here, the outgoing plasma jet may tend to make a new ionization line. Since this ionization line can generate new types of reactions, it is thought that such variations are occurred in temperature

calculations. Similar to the change of electron temperature, as N_2 gas flow rate increased, there was no linear change in electron temperature. The electron densities obtained from the N_2 APPJ were between 1.14×10^{18} cm^{-3} and 1.87×10^{18} cm^{-3} values. It is thought that the reason for the decrease of electron density at high gas flow rates (especially at 4 L/min) is due to the ionization of gas atoms by free electrons. Similar results were obtained as the experiments were repeated. Calculated T_e and n_e values in accordance with the literature [27].

4. Conclusions

In this study, atmospheric pressure nitrogen gas plasmas (N_2 APPJs) were produced as a jet. The experiments were carried out in fume hood in order to protect from the effects of harmful gases which may occur in N_2 APPJs produced in atmospheric medium. The production of nitrogen gas plasma jet is quite difficult in comparison to noble gases. However, we have successfully produced plasma jet longer than 2 cm by using the alternating current power supply. The length of the jet was closely related to gas flow rate. It was determined that the jet length increased in proportion to the increase in gas flow rate. At high gas flow rates, APPJ bended towards the nearest electrode. The longest jet was observed at a gas flow rate of 4-5 L/min. However, therefore bending has also occurred at these flow rates. As the connection part of the ring electrode to the power supply in the system was close to the nozzle, it has been observed that the ionization line was directed towards this electrode as the length of the jet increases. The distance of the ring electrode to the end of the pipe was determined by trial and error. Plasma arc formation was observed if the ring electrode was close to the nozzle of the tube, and jet formation was not observed if the ring electrode was away from the nozzle of the tube. After that, the optical emission spectra were taken from 0.5 cm distance of the N_2 APPJ system. In the obtained spectra, as gas flow rate increased, N_2, N_2^+, and NO peaks increased proportionally. In addition, the OH peaks increased depending on gas flow rate, but these peaks were dominated by NO. Therefore, the wavelength corresponding to the OH radicals in the optical emission spectra was not marked and was only given in Table 1. Furthermore, electron temperature and electron density were calculated according to gas flow rate by using spectral line intensities of N atoms. Although the nitrogen gas flow rate increased, there was a relatively small increase in electron temperature, but a linear increase was not achieved. At the same time, the outgoing jet was trying to make a new ionization line. This is thought to increase the electron temperature and hence the electron density. Detailed studies on the electrical properties of N_2 plasma jet applications, in particular voltage and frequency changes, are planned for the future.

Acknowledgement

References

[1] Bogaerts, A., Neyts, E., Gijbels, R., Van der Mullen, J., *Gas discharge plasmas and their applications*, Spectrochimica Acta Part B: Atomic Spectroscopy, 57(4), 609-658, 2002.

[2] Petitpas, G., Rollier, J.-D., Darmon, A., Gonzalez-Aguilar, J., Metkemeijer, R., Fulcheri, L., *A comparative study of non-thermal plasma assisted reforming technologies*, International Journal of Hydrogen Energy, 32(14), 2848-2867, 2007.

[3] Tendero, C., Tixier, C., Tristant, P., Desmaison, J., Leprince, P., *Atmospheric pressure plasmas: a review*, Spectrochimica Acta Part B: Atomic Spectroscopy, 61(1), 2-30, 2006.

[4] Treumann, R.A., Kłos, Z., Parrot, M., *Physics of electric discharges in atmospheric gases: an informal introduction*, Planetary Atmospheric Electricity, Springer New York, 133-148, 2008

[5] Ahmed, K., Allam, T., El-sayed, H., Soliman, H., Ward, S., Saied, E., *Design, construction and characterization of ac atmospheric pressure air non-thermal plasma jet*, Journal of Fusion Energy, 33(6), 627-633, 2014.

[6] Allam, T., Ward, S., El-Sayed, H., Saied, E., Soliman, H., Ahmed, K., *Electrical parameters investigation and zero flow rate effect of nitrogen atmospheric nonthermal plasma jet*, Energy and Power Engineering, 6(12), 437, 2014.

[7] Ricard, A., Oh, S.G., Jang, J., Kim, Y.K., *Quantitative evaluation of the densities of active species of N_2 in the afterglow of Ar-embedded N_2 RF plasma*, Current Applied Physics, 15(11), 1453-1462, 2015.

[8] Ricard, A., Oh, S.-g., Guerra, V., *Line-ratio determination of atomic oxygen and $N_2(A_3\Sigma_u^+)$ metastable absolute densities in an RF nitrogen late afterglow*, Plasma Sources Science Technology, 22(3), 2013.

[9] Guerra, V., Sa, P., Loureiro, J., *Role played by the $N_2(A_3\Sigma_u^+)$ metastable in stationary N_2 and N_2-O_2 discharges*, Journal of Physics D: Applied Physics, 34(12), 1745, 2001.

[10] Loureiro, J., Sá, P., Guerra, V., *Role of long-lived $N_2(X^1\Sigma_g^+, v)$ molecules and $N2(A_3\Sigma_u^+)$ and $N_2(a'^1\Sigma_u^-)$ states in the light emissions of an N_2 afterglow*, Journal of Physics D: Applied Physics, 34(12), 1769, 2001.

[11] Hrycak, B., Jasiński, M., Mizeraczyk, J., *Spectroscopic characterization of nitrogen plasma generated by waveguide-supplied coaxial-line-based nozzleless microwave source*, IOP Publishing, 406(1), 012037, 2012.

[12] Rankovic, D., Kuzmanovic, M., Pavlovic, M.S., Stoiljkovic, M., Savovic, J., *Properties of argon–nitrogen atmospheric pressure DC arc plasma*, Plasma Chemistry and Plasma Processing, 35(6), 1071-1095, 2015.

[13] Karam, L., Casetta, M., Chihib, N.E., Bentiss, F., Maschke, U., Jama, C., *Optimization of cold nitrogen plasma surface modification process for setting up antimicrobial low density polyethylene films*, Journal of the Taiwan Institute of Chemical Engineers, 64, 299-305, 2016.

[14] Mahmoud, K., *Optical properties of hydroxyethyl cellulose film treated with nitrogen plasma*, Spectrochimica Acta Part A: Molecular and Biomolecular Spectroscopy, 157, 153-157, 2016.

[15] Gholampour, M., Abdollah-Zadeh, A., Shekari, L., Poursalehi, R., *From nanoparticles to nanowires of GaN with different hydrogen gas flow rates by PDC-PECVD*, Procedia Materials Science, 11, 304-308, 2015.

[16] Choi, J.S., Park, J.G., *Interface characterization of nitrogen plasma-treated gate oxide film formed by RTP technology*, Surface and Interface Analysis, 46(S1), 303-306, 2014.

[17] Shi, D., Xu, W., Miao, C., Ma, C., Ren, C., Lu, W., Zhang, Q., *A high-activity nitrogen plasma flow source for deposition of silicon nitride films*, Surface and Coatings Technology, 294, 194-200, 2016.

[18] Pan, G.-T., Chong, S., Yang, T.C.-K., Yang, Y.-L., Arjun, N., *Surface modification of amorphous SiO₂ nanoparticles by oxygen-plasma and nitrogen-plasma treatments*, Chemical Engineering Communications, 203(12), 1666-1670, 2016.

[19] Wang, J.C., Ye, Y.R., Lin, Y.H., *Light-addressable potentiometric sensor with nitrogen-incorporated ceramic Sm₂O₃ membrane for chloride ions detection*, Journal of the American Ceramic Society, 98(2), 443-447, 2015.

[20] Castro-Colin, M., Durrer, W., López, J.A., Ramirez-Homs, E., *Surface modification by nitrogen plasma immersion ion implantation on austenitic AISI 304 stainless steel*, Journal of Iron and Steel Research International, 23(4), 380-384, 2016.

[21] Praveen, T., Shiju, K., Predeep, P., *Influence of plasma treatment on Indium Tin Oxide electrodes*, Microelectronic Engineering, 131, 8-12, 2015.

[22] Bertóti, I., Mohai, M., László, K., *Surface modification of graphene and graphite by nitrogen plasma: Determination of chemical state alterations and assignments by quantitative X-ray photoelectron spectroscopy*, Carbon, 84, 185-196, 2015.

[23] Pal, D., Neogi, S., De, S., *Surface modification of polyacrylonitrile co-polymer membranes using pulsed direct current nitrogen plasma*, Thin Solid Films, 597, 171-182, 2015.

[24] Khatir, S., Hirose, A., Xiao, C., *Characterization of physical and biomedical properties of nitrogenated diamond-like carbon films coated on polytetrafluoroethylene substrates*, Diamond and Related Materials, 58, 205-213, 2015.

[25] Alers, G., Fleming, R., Wong, Y., Dennis, B., Pinczuk, A., Redinbo, G., Urdahl, R., Ong, E., Hasan, Z., *Nitrogen plasma annealing for low temperature Ta₂O₅ films*, Applied physics letters, 72(11), 1308-1310, 1998.

[26] https://www.nist.gov/pml/atomic-spectra-database, 06.03.2020.

[27] Shah, M., Ahmad, R., Iikhlaq, U., Saleem, S., *Characterization of pulsed DC nitrogen plasma using optical emission spectroscopy and Langmuir probe*, Journal of Natural Sciences and Mathematics, 53, 1-12, 2013.

[28] Marr, G.V., *Plasma spectroscopy*, Elsevier Publishing Company, 5, 1968.

Analyzing of Quantum Entanglement with Concurrence in the Deep Lamb-Dicke Regime

Rasim DERMEZ[1,2,*]

[1]*University of Afyon Kocatepe, Arts and Science Faculty, Department of Physics, 03200, Afyonkarahisar, Turkey*
[2]*University of Afyon Kocatepe, Afyon Vocational School, 03200, Afyonkarahisar, Turkey, dermez@aku.edu.tr, ORCID: 0000-0003-0038-801X*

Abstract

The entangled states of three-level of trapped ion and two phonons (into coherent state) in Λ configuration forming a Hilbert space of 12-dimensional (D) are analyzed. The concurrence is considered "such as a quantum measure" in trapped ion-coherent state system. Four values of Lamb-Dicke parameter (LDP), $\eta = 0.005, 0.07, 0.08$ and 0.09 are investigated by the worths of concurrence. We demonstrate that as η is increased, sudden birth of entangled states in the system is increased. Thus, establishing of entangled states can be tuned by LDP.

Keywords: Trapped ion-coherent system; Interaction Hamiltonians; Probability amplitudes; Frequency of harmonic trap.

Derin Lamb-Dicke Rejiminde Eş Zamanlılık ile Kuantum Dolanıklığın Analiz Edilmesi

Öz

12-boyutlu Hilbert uzayında **Λ** konfigürasyonunda iki fonon (kohorent durum içinde) ve üç-düzeyli tuzaklanmış iyon sisteminde dolanık durumlar analiz edildi. Eş zamanlılık;

tuzaklanmış iyon-koherent durum sisteminde "bir kuantum ölçümü olarak" düşünüldü. LDP'nin η = 0.005, 0.07, 0.08 ve 0.09 ile verilen dört değeri için dolanıklığın değerleri araştırıldı. LDP (η) arttıkça, sistemdeki dolanık durumların ani doğumunun arttığı gösterildi. Böylece dolanık durumların oluşturulması LDP ile ayarlanabilir.

Anahtar Kelimeler: Tuzaklanmış iyon-koherent sistemi; Etkileşim Hamiltonyenleri; Olasılık genlikleri; Harmonik tuzak frekansı.

1. Introduction

Entangled state is one of the central themes making characteristic between classical and quantum mechanics. Entanglement is an attractive physical phenomenon in which the overlap of two separable states is entangled state with any photon. Thus, entanglement shows a feature of non-local of quantum mechanics [1]. So far, most of the articles have been investigated on information theory, in fact, Einstein, Podolsky and Rosen (EPR) published that famous article to criticize quantum mechanics [2]. In the 1935, Niels Bohr published an article [3] with the same name as the EPR article. This famous paper introduced the entanglement with conversations on quantum theory. J. Bell conceived the quantum theory forecasts are in conflict with the local realistic theory [1]. In the 1935, Erwin Schrödinger acquired the EPR reasoning twice, first in his paper in Naturwissenschaften introducing "Verschrankung", where he advises the Schrödinger cat state, and secondly in a paper for the Cambridge Philosophical Society introducing entanglement [4]. Trapped ions systems are important for the entangled states works [5-8], concurrence C [9], negativity N [10, 11].

Pure qudit states and quantum correlation of one trapped ion system with respect to C and N are discussed by R. Dermez et al. [11]. In the internal states, very small optical wavelength of coupling of vibrational phonons have been achieved. This is named the deep Lamb-Dicke regime (LDR) described by LDP of small, $\eta << 1$, such as this study. LD limit is not necessarily appointed in typical experiments [12]. Such experiments act in named as beyond LDR where $\eta <$ 1 , for examples $\eta \approx 0.2$ [13] and $\eta \approx 0.25$ [14].

Product base and entangled base are shown generalization of Schmidt coefficients [15]. Entanglement of pure qudit states [16] and of mixed qudit states [17] are demonstrated by a quantum system with single-step dynamics under the Λ configuration. The calculations and graphs in these three articles differ from the traditional theoretical approach. Quantum entropy is offered for pure qudit states [18]. All entanglement measurements are known to test whether any given state is separable and entangled. Therefore, C and N are applied for pure states [19]. To

perform quantum computations in trapped ion it is advocated to use deeply phonon nonclassical states. For Fock states, squeezed [20], coherent states of odd-even [21], and their superpositions [22] were suggested.

In current quantum information theory, C is one of quantum entanglement measures. C is a useful measurement in quantum optics, especially in trapped ion. We report analytical results of the quantum entanglement for system via C for the deep LD regime and the Hilbert space of 12-D. We focus on the quantum dynamics in concurrence [11, 16] with respect to the total and the reduced density matrix. With help of Ref. [16] we have plotted the evolutions of C in the Figs. 2-6 for trapped ion-coherent system.

The rest of the paper is organized as follows. Section 2 discusses the growth of two unentangled qubits and analytical solutions in the trapped ion system. Section 3 describes how to obtain highly concurrence of system by the deep LD regime. The results and comments are given in Section 4.

2. Model and Solution of Trapped Ion-Coherent System

We study a trapped ion in a harmonic potential and two coherent states. Theoretical physical system is emerged via previous investigation [23, 24]. The Hamiltonian of system is $H_{total} = H_{ion} + H_1 + H_2$ and H_{ion} of trapped ion:

$$H_{ion} = \omega_g |g\rangle\langle g| + \omega_r |r\rangle\langle r| + 0|e\rangle\langle e| + \frac{p_x^2}{2m} + \frac{1}{2}m\nu^2 x_{ion}^2. \tag{1}$$

Here H_1 and H_2 are Hamiltonians of these interactions for excited-ground and excited-raman:

$$H_{e-g} = H_1 = \frac{\Omega}{2}e^{i(k_1 x_{ion} - \omega t)}|e\rangle\langle g| + hermitian\ c. \tag{2}$$

$$H_{e-r} = H_2 = \frac{\Omega}{2}e^{i(-k_2 x_{ion} - \omega t)}|e\rangle\langle r| + hermitian\ c., \tag{3}$$

where $\hbar = 1$, p_x and x_{ion} are momentum and the x-component of position of ion center of mass movement. The movement of the ion in the system is along the x-axis (one-D). Atomic levels of ion are given: $|e\rangle \rightarrow$ trapped ion excited level, $|r\rangle \rightarrow$ raman level energy, and $|g\rangle \rightarrow$ ground level in Fig. 1. The excited level energy is $\omega_e = 0$, raman level is ω_r, and ground level is ω_g in Eqn. (1). The mass center of trapped ion has been performed by the standard harmonic-oscillator of

H_{ion} in $p_x = i\sqrt{\dfrac{1}{2}mv}\left(a^+ - a\right)$ and $x_{ion} = \sqrt{\dfrac{1}{2}mv}\left(a + a^+\right)$. Here, a is annihilation operator and a^+ creation operator of the vibrational phonons. Two laser frequencies are ω_1 and ω_2, and Rabi frequency is Ω in Fig. 1. Ion-phonon total Hamiltonian is written as:

$$H = \left(\frac{\Omega}{2}e^{i\eta(a^+ + a)}|e\rangle\langle g| + v\,a^+ a - \delta|e\rangle\langle e| + \frac{\Omega}{2}e^{-i\eta(a + a^+)}|e\rangle\langle r|\right) + h.c., \tag{4}$$

here LPD is $\eta = k/2mv$, v is harmonic trap frequency, and $\delta = v\eta^2$. We have taken the base vectors as follow:

$$|e\rangle = \begin{pmatrix} 1 \\ 0 \\ 0 \end{pmatrix},\ |r\rangle = \begin{pmatrix} 0 \\ 1 \\ 0 \end{pmatrix},\ |g\rangle = \begin{pmatrix} 0 \\ 0 \\ 1 \end{pmatrix}. \tag{5}$$

$\widetilde{H} = U^+ H U$ is transformed Hamiltonian. The Hamiltonian in Eqn. (4) is found as follows after the transmission process. The optical Λ configuration can be equal to a cascade Ξ scheme for two coherent states. Trapped ion-coherent state is covered by unitary transformation. Matrix of transformation, namely U is written as [23],

$$U = \frac{1}{2}\begin{pmatrix} 0 & \sqrt{2} & \sqrt{2} \\ -\sqrt{2}B[\eta] & B[\eta] & -B[\eta] \\ \sqrt{2}B[-\eta] & B[-\eta] & -B[-\eta] \end{pmatrix}. \tag{6}$$
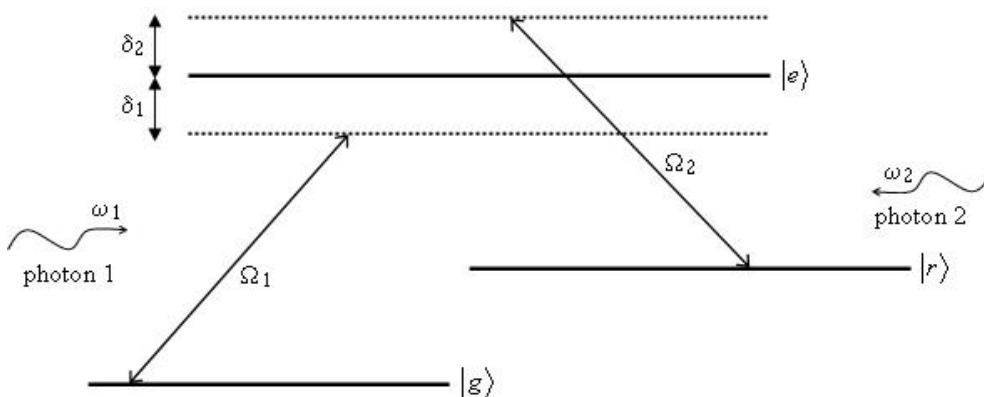
Figure 1: Figure of three internal electronic levels of trapped ion-coherent system. Time is given by dimensionless for ion-coherent system, the other coupling parameters are allowed to be $\Omega = \Omega_1 = \Omega_2$, $\omega = \omega_1 = \omega_2$, and $\delta = \delta_1 = \delta_2$

Here displacement operators of Glauber, $B(\eta) = e^{(i\eta(a+a^+))}$, $B(-\eta) = e^{(-i\eta(a+a^+))}$ are achieved. $\widetilde{H}$ is written as $\widetilde{H} = \widetilde{H}_0 + \widetilde{V}$, here

$$\widetilde{H}_0 = v(|r\rangle\langle r| - |g\rangle\langle g|) + \upsilon\eta^2 + \upsilon a^+ a, \tag{7}$$

$$\widetilde{V} = -i\frac{\sqrt{2}v\eta}{2}(a^+|e\rangle\langle r| - a^+|e\rangle\langle g| + hermitian\ c.) \tag{8}$$

The deep LD regime is allowed between the 0.005 and 0.9. Under the unitary transformation method [23], an early state $|\psi(0)\rangle$ is given by

$$|\psi(t)\rangle = U_0^+ U e^{-it\widetilde{H}_0} K(t) U^+ |\psi(0)\rangle, \tag{9}$$

where $K(t)$ is a propagator vector; $e^{(-it\widetilde{H}_0)}$ is the transformation of Shrödinger picture, and $U_0 = \exp(-i\omega t|e\rangle\langle e|)$ is the transformation matrix [23]. Trapped ion-coherent state system evolves in the Λ scheme. The propagator is written as:

$$K(t) = \frac{1}{2}\begin{pmatrix} Cos(\Lambda t) & -\varepsilon Sa^+ & -\varepsilon Sa \\ \varepsilon aS & 1+\varepsilon^2 aGa^+ & \varepsilon^2 aGa \\ \varepsilon a^+ S & \varepsilon^2 a^+ Ga^+ & 1+\varepsilon^2 a^+ Ga \end{pmatrix}, \tag{10}$$

here $\varepsilon = v\eta/\sqrt{2}$, $\Lambda = \varepsilon\sqrt{2a^+a+1}$, $G = \frac{Cos(\Lambda t)-1}{\Lambda^2}$ and $S = \frac{Sin(\Lambda t)}{\Lambda}$. We consider the parameters for trapped ion-coherent state with an application. We take $v = 10^7$ Hz and $\omega_{eg} = 5\times10^{15}$ Hz With first order terms of our system, we have taken $a = 1$ and $b = 0.005$ for two coherent states. Trapped ion normalization condition is exactly $\left[\frac{1}{\sqrt{2}}\right]^2 + \left[-\frac{1}{\sqrt{2}}\right]^2 = 1$, and two phonons normalization condition is approximately $\|a\|^2 + \|b\|^2 = |1|^2 + |0.005|^5 \cong 1$. So, the earliest of ion-coherent state system is given as:

$$|\psi(0)\rangle = \frac{1}{\sqrt{2}}[|g\rangle - |r\rangle] \otimes (a|0\rangle + b|1\rangle), \tag{11}$$

here the phonon levels are $\langle 0| = (1,0)$, and $\langle 1| = (0,1)$. The new formula of system is given as

$$|\psi(0)\rangle = \frac{1}{\sqrt{2}} \big[|g\rangle - |r\rangle\big] \otimes \left(\sum_{n=0}^{\infty} F_n(b)|n\rangle \right). \tag{12}$$

We have used the coherent state by means of the zero-order and first-order terms of LDP such as η^0, η^1. This system is transformed to an early separable state,

$$|\psi K(t)\rangle = |\widetilde{\psi}(0)\rangle = U^+|\psi(0)\rangle = \sum_{\sigma,m} N_{\sigma,m}(t)|\sigma,m\rangle. \tag{13}$$

In Eqn. (11), our system is produced in respect of $\sum\limits_{\sigma,m} N_{\sigma,m}(t)|\sigma,m\rangle$. The twelve of system's probability amplitudes are written as:

$$N_{e0}(t) = \left[\cos\left(\sqrt{\frac{1}{2}}t\right) + \frac{\eta i}{\sqrt{2}} \sin\left(\sqrt{\frac{1}{2}}t\right) \right] \exp[-ti/\eta] \tag{14}$$

$$N_{e1}(t) = b \cos\left(\sqrt{\frac{3}{2}}t\right) \exp[-ti/\eta] \tag{15}$$

$$N_{e2}(t) = -\frac{\eta i}{\sqrt{5}} \sin\left(\sqrt{\frac{5}{2}}t\right) \exp[-2ti/\eta] \tag{16}$$

$$N_{r0}(t) = \frac{b}{\sqrt{3}} \sin\left(\sqrt{\frac{3}{2}}t\right) \exp[-ti/\eta] \tag{17}$$

$$N_{r1}(t) = \frac{\eta i}{\sqrt{2}} \left[\frac{3}{2} + \frac{2}{5} \cos\left(\sqrt{\frac{5}{2}}t\right) \right] \exp[-2ti/\eta] \tag{18}$$

$$N_{g1}(t) = \left[\sin\left(\sqrt{\frac{1}{2}}t\right) - \frac{\eta i}{\sqrt{2}} \cos\left(\sqrt{\frac{1}{2}}t\right) \right] \exp[-ti/\eta] \tag{19}$$

$$N_{g2}(t) = b\sqrt{\frac{2}{3}} \sin\left(\sqrt{\frac{3}{2}}t\right) \exp[-ti/\eta] \tag{20}$$

$$N_{g3}(t) = -\frac{\sqrt{3}}{5} \eta i \left[1 - \cos\left(\sqrt{\frac{5}{2}}t\right) \right] \exp[-2ti/\eta] \tag{21}$$

and four amplitudes are zero: $N_{e3}(t) = N_{r2}(t) = N_{r3}(t) = N_{g0}(t) = 0$. In Eqns. (14) to (21), the first index σ is the states of atomic (g, r, e), second index m is the vibrational quantum numbers (0, 1, 2, 3). The vibrational coherent state is indicated by a four-dimensional (four-D) Hilbert space $\mathbf{H}_p$ and subsystem of trapped ion is shown by a three-D Hilbert space $\mathbf{H}_i$. Therefore, the trapped ion-coherent states are C^{12} D of Hilbert space. In the equations, t is dimensionless time scaled by $\nu\eta$ (harmonic trap frequency-LDP). For the analytical expressions in Eqn. (22), we have ignored the second-order, third-order and forth-order terms. For trapped ion-two coherent state, the final state vector is given as:

$$\left|\psi_{final}(t)\right\rangle = \sum_{m=0}^{3}\left(A_m(t)|e,m\rangle + B_m(t)|r,m\rangle + C_m(t)|g,m\rangle\right). \tag{22}$$

These coefficients of the final vector are

$$A_m(t) = \frac{1}{\sqrt{2}} e^{-i\omega t/\nu\eta}\left[N_{rm}(t) + N_{gm}(t)\right], \ (m = 0,1,2,3), \tag{23}$$

$$B_0(t) = -\frac{1}{\sqrt{2}} N_{e0}(t) + \frac{1}{2} N_{r0}(t) - \frac{i\eta}{2} N_{g1}(t) \tag{24}$$

$$B_1(t) = -\frac{i\eta}{\sqrt{2}} N_{e0}(t) - \frac{1}{2} N_{r1}(t) + \frac{1}{2} N_{r1}(t) - \frac{1}{2} N_{g1}(t) \tag{25}$$

$$B_2(t) = -\frac{1}{\sqrt{2}} N_{e2}(t) - \frac{i\eta}{\sqrt{2}} N_{g1}(t) - \frac{1}{2} N_{g2}(t) \tag{26}$$

$$B_3(t) = -\frac{1}{2} N_{g3}(t) \tag{27}$$

$$C_0(t) = \frac{1}{\sqrt{2}} N_{e0}(t) + \frac{1}{2} N_{r0}(t) - \frac{i\eta}{2} N_{g1}(t) \tag{28}$$

$$C_1(t) = -\frac{i\eta}{\sqrt{2}} N_{e0}(t) + \frac{1}{2} N_{r1}(t) + \frac{1}{2} N_{r1}(t) - \frac{1}{2} N_{g1}(t) \tag{29}$$

$$C_2(t) = \frac{1}{\sqrt{2}} N_{e2}(t) + \frac{i\eta}{\sqrt{2}} N_{g1}(t) - \frac{1}{2} N_{g2}(t) \tag{30}$$

$$C_3(t) = -\frac{1}{2} N_{g3}(t) \tag{31}$$

here ω_{eg} is the frequency of resonance of excited-ground level, $\omega = \omega_{eg} - \eta^2 \nu$, i is ion index, and i is a complex number. We have illustrated the C of pure qudit states as $l \otimes l'(l \leq l')$ in Figs. 2-6. We found that the final state vector $|\psi_{final}(t)\rangle$ is superposition of twelve function in Eqn. (23-31).

In our model, these dimensions (D) of Hilbert space are $l = 4$ for the two-phonons and $l' = 3$ for the trapped ion subsystem. We have used a reduced density operator $\rho_{ion} = Tr_{phonon}(\rho_{ion-p})$ by the help of Eqn. (32). A measurement for pure qudit states can be optimized by a generalized C [6, 18, 19]. The total density operator ρ_{ion-p} is shown by a 12×12 D matrix in the base of $|i, p\rangle$. Taking trace over the phonon system, 3×3 reduced density operator, ρ_{ion} is given as,

$$\rho_{ion} = Tr_{phonon}(\rho_{ion-phonon}) = \begin{pmatrix} Tr|e\rangle\langle e| & Tr|e\rangle\langle r| & Tr|e\rangle\langle g| \\ Tr|r\rangle\langle e| & Tr|r\rangle\langle r| & Tr|r\rangle\langle g| \\ Tr|g\rangle\langle e| & Tr|g\rangle\langle r| & Tr|g\rangle\langle g| \end{pmatrix} \tag{32}$$

where diagonal terms, $|e\rangle\langle e|$, $|r\rangle\langle r|$ and $|g\rangle\langle g|$ are a 4×4 square matrix. With respect to Eqn. (32), fully density operator of the system is written as:

$$\rho_{ion-phonon} = (|Z\rangle\langle Z|) \tag{33}$$

where $|Z\rangle\langle Z|$ is a 12×12 D square matrix in the 12-D Hilbert space. With Eqn. (33), the analytic solution of the total density operator is

$$\rho_{ion-phonon} = U^+(t)[\rho^i(0) \otimes \rho^p(0)]U(t). \tag{34}$$

3. The Measure of Concurrence, Deep LD Regime and Discussion

Concurrence is important in quantum entanglement measures. We investigate the entanglement by the concurrence for deep LD regime in the system and explain it. The coherent state is shown by a four D H_p of a quadrit. So, the early state in Section 2 derives in the Hilbert

space $H = H_i \otimes H_p$ D. In a pure qudit state $|\psi(t)\rangle$ the density matrix of the system is shown by $\rho_{ion-phonon} = |\psi(t)\rangle\langle\psi(t)| = |Z\rangle\langle Z|$ in Eqns. (32) and (33). Concurrence is first reported in the literature as a quantum entanglement measurement in Ref [25] for two qubits. For any arbitrary bipartite pure state is written [25]

$$Concurrence = \sqrt{2(Tr(\rho_{ion-phonon}) - Tr(\rho_{ion}^2))}. \tag{35}$$

where $\rho_{ion} = Tr_{phonon}(\rho_{ion-p})$ is the reduced density matrix in Eqn. (32). So that, in Figs. 2-5 time evolution of C have been plotted by $\eta = 0.005, 0.07, 0.08,$ and 0.09. We have obtained high amount of entanglement for four values of LDP. This is called "deep LD regime" is qualified by $\eta = 0.005$, the other way, it is known that "beyond LD regime" is $\eta = 0.5$.
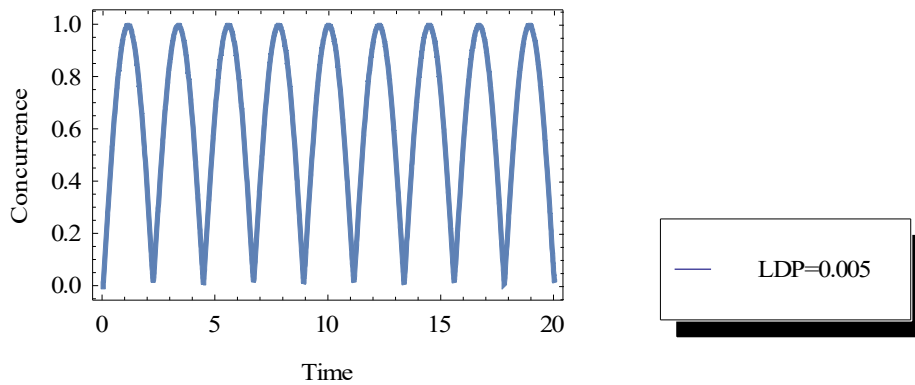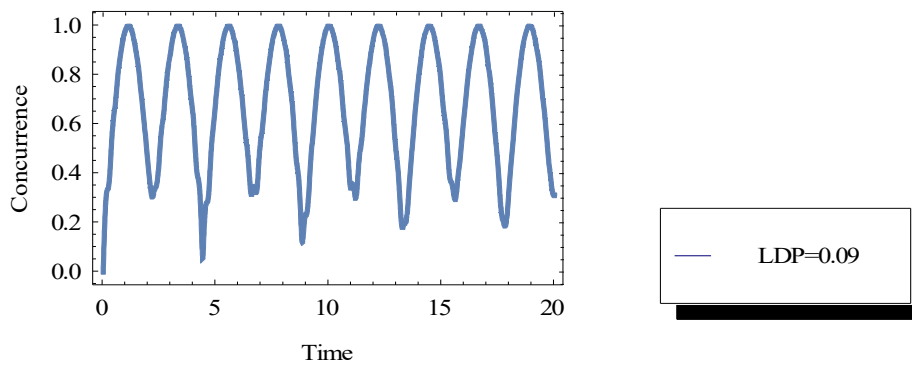

Figure 2: The time change of C is given by $\eta = 0.005$, first value of deep LD regime. The earliest state of trapped ion-coherent state system is $|\psi(0)\rangle = \frac{1}{\sqrt{2}}[|g\rangle - |r\rangle] \otimes (a|0\rangle + b|1\rangle)$, with $a = 1$, $b = 0.005$. Assumption parameters are given for $\nu = 1 \times 10^7$ Hertz and $\omega_{eg} = 5 \times 10^{15}$ Hertz
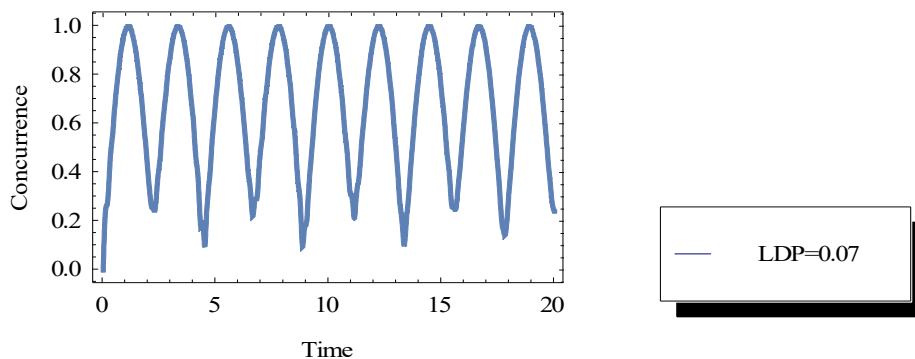
Figure 3: The time change of C is given by $\eta = 0.07$ second value of deep LD regime. Other assumptions parameters are the same as Fig. 2 in the system
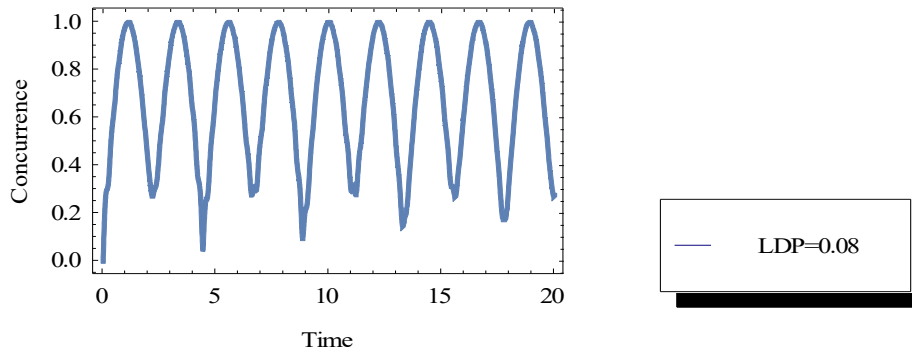
Figure 4: The time change of C is given by $\eta = 0.08$, third value of deep LD regime. Other assumption parameters are the same as Fig. 2 in the system


Figure 5: The time change of C is given by $\eta = 0.09$, fourth value of deep LD regime. Other assumption parameters are the same as Fig. 2 in the system

Table 1: The eight values of concurrence for two optimum time, $t = 4.2$ and $t = 3.50$ via Figs. 2-5

	Fig. 2, b=0.005, $\eta = 0.005$	Fig. 3, b=0.005, $\eta = 0.07$	Fig. 4, b=0.005, $\eta = 0.08$	Fig. 5, b=0.005, $\eta = 0.09$
Concurrence, t=4.2	0.336	0.381	0.349	0.383
Concurrence, t=3.50	0.999	0.971	0.971	0.969

In this paper, we measured quantum entanglement with concurrence in the deep LD regime distinctively from the other paper [16]. The values of concurrence for two optimum time are given in Table 1. We have taken the harmonic trap frequency as 10^7 Hz in Figs. 2-6. The maximum value of concurrence is interestingly recorded $C = 0.999$ for $\eta = 0.005$ in Table 1. The four different values of η are determined and taken into consideration in this study. When we checked the literature we didn't see that it has been worked with 0.005 value. We report the quantum dynamics of C as a function of LDP in Fig. 6 with two graphics for two optimum time. Our previous analytical results [16, 26, 27] are in similar with Figs. 2-6. Negativity and quantum

entropy, which are the other elaborated measurements from the measurement family defining the entanglement concept, have also been studied in the literature [6, 8, 11, 18, 26, 27, 29].
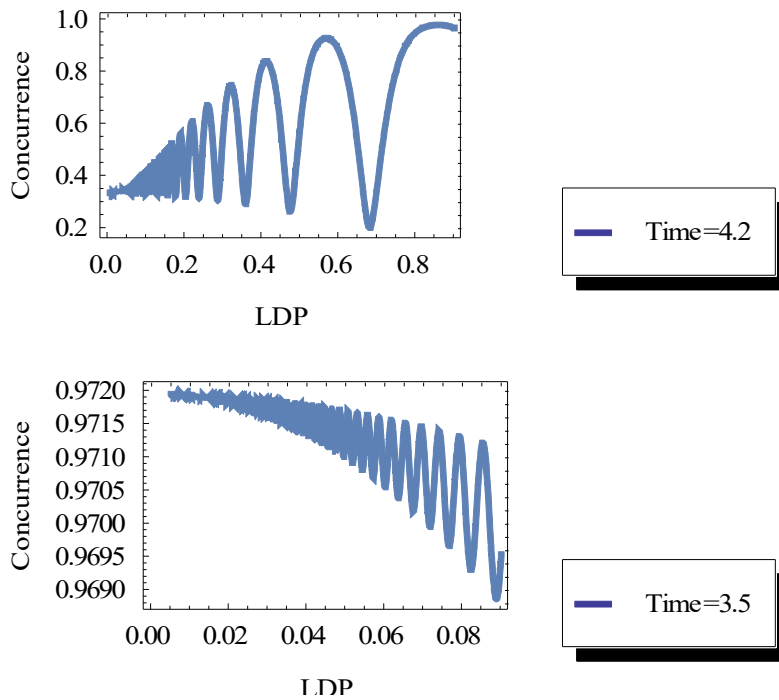
Figure 6: The η evolution of C is given for $t = 4.2$ and $t = 3.5$ (from $\eta = 0.005$ to $\eta = 0.09$). The other coupling parameters are the same as Fig. 2 in the system

We propose the quantum dynamics with concurrence for coupling parameters. We have detected different dynamical features in C in reaction to increasing η. In Fig. 3, C oscillates between minimum value $C = 0$ and the highest value $C = 0.999$ at $t = 3.50$ for $\eta = 0.005$. This time is maximally entangled state at the optimum time in Table 1. By this method, we have observed that the maximally entangled states do not collapse in system. The presence of robust entanglement in trapped ion-coherent state the system has been recognized by Fig. 6.

If parameters of the system are $\eta = 0.09$ and at $t = 3.50$, a concurrence measurement becomes 0.969 in Table 1. We explore with C that the measurement degrees have a sudden birth of entangled state in parallel with raising η, and this is in comparison to the previous observations [6, 26-30]. In Fig. 1, two internal electronic levels of trapped ion can be built by a qubit, such as three internal levels can play a role of a qutrit in the quantum Rabi model. They suggested the quantum simulations of the Rabi model in single trapped ion with deep $\eta = 0.06$ [31], similar to our suggestion in this study for LDP. These articles similar to our model [32, 33] have been proposed a design for creating odd and even coherent states of trapped ion with respect to laser excitation of two vibration modes.

4. Conclusions

In summary, we have presented quantum entanglement of trapped ion-coherent system in the Λ scheme by the unitary transformation. Quantum mechanical expressions such as: the final state, density operator and reduced density operator have been normalized in analytical high-level calculations. We concentrate the concurrence through the definition of variance deep LD regime. These plots are obtained by concurrence which is consistent with quantum corrections. Quantum entanglement is discussed by an elaborated measure which is *C*. The quantum dynamics of interactions between trapped ion and coherent state determine the extent of coupling parameters such as Rabi and harmonic trap frequencies. Entangled states of the trapped ion-coherent system can be called pure qudit states. Because, strong quantum correlations can arise between higher dimensional such as qubits or qutrits.

These pure qudit states are calculated and analyzed by η. When concurrence is given sudden birth, quantum entanglement among trapped ion qutrit-phonon quadrit states is generalized. The results are summarized as follows: (1) quantum entanglement is seen to have the capacity in our system and the amount of concurrence is $C = 0.999$; (2) C depends on four deep different LDPs; (3) This extracts that such entanglement is connected with η.

We achieved the long-lived entanglement in the deep LD regime. Maximally entangled states as demonstrated through our system can be important for researchers with trapped ions. The extending of life time can be succeeded with Rabi frequences and η. These new approaches and results can provide useful data for identification of the life time of entanglement in future theoretical studies.

Acknowledgments

References

[1] Bell, J., *Speakable and Unspeakable in Quantum Mechanics*, Cambridge University Press, 1987.

[2] Einstein, A., Podolsky, B., Rosen, N., *Can quantum-mechanical description of physical reality be considered complete?,* Physical Review, 47, 777-780, 1935.

[3] Bohr, N., *Can quantum-mechanical description of physical reality be considered complete?*, Physical Review, 48, 696-702, 1935.

[4] Schrödinger, E., *Die gegenwrtige situation in der quantenmechanik*, Naturwissenschaften, 23, 844-849, 1935.

[5] Cirac, J.I., Zoller, P., *Quantum computations with cold trapped ions,* Physical Review Letters, 74, 4091, 1995.

[6] Landsman, K.A., Wu, Y., Leung, P.H., Zhu, D., Linke, N.M., Brown, K.R., Duan, L.M., Monroe, C., *Two-qubit entangling gates within arbitrarily long chains of trapped ions*, Physical Review A, 100, 022332, 2019.

[7] Abdel-Aty, M., *Qualitative aspects of the entanglement in the three-level model with photonic crystals*, Applied Physics B, 81, 193-203, 2005.

[8] Wong-Campos, J.D., Moses, S.A., Johnson, K.G., Monroe, C., *Demonstration of two-atom entanglement with ultrafast optical pulses*, Physical Review Letters, 119, 230501, 2017.

[9] Wootters, W.K, *Entanglement of formation of an arbitrary state of two qubits*, Physical Review Letters, 80, 2245, 1998.

[10] Vidal, G., Werner, R.F., *Computable measure of entanglement*, Physical Review A. 65, 032314, 2002.

[11] Dermez, R., Khalek, S.A., Kara, K. Deveci, B., Gunaydin, G.N., *Full-trapped three-level ion in the Lamb-Dicke limit: Analyzing and comparing quantum entanglement measures of two qudits*, Journal of Russian Laser Research, 33, 42-51, 2012.

[12] James, D.F.V., *Quantum computation and quantum information theory*, Applied Physics B, 66, 181-190, 1998.

[13] Monreo, C.D., Meekhof, M., King, B.E., Wineland, D.J., *A Schrödinger cat superposition state of an atom*, Science, 272, 1131-1136, 1996.

[14] Wei, L.F., Liu, Y., Nori, F., *Engineering quantum pure states of a trapped cold ion beyond the Lamb-Dicke limit*, Physical Review A, 70, 063801, 2004.

[15] Guo, Y., Du, S., Li, X., Wu, S., *Entangled bases with fixed Schmidt number*, Journal of Physics A: Mathematical and Theoretical, 48(24), 245301, 2015.

[16] Dermez, R., Müstecaplıoğlu, Ö.E., *Long-lived entangled qudits in a trapped three-level ion beyond the Lamb–Dicke limit*, Physica Scripta, 71, 015304, 2009.

[17] Nieuwenburg, E., Zilberberg, O., *Entanglement spectrum of mixed states*, Physical Review A, 98, 012327, 2018.

[18] Neumann, J.V., *Mathematical foundations of quantum mechanics*, Princeton University Press, N.J., 1995.

[19] Dermez, R., *Concurrence and negativity as a family of two measures elaborated for pure qudit states*, Journal of Russian Laser Research, 38, 408-415, 2017.

[20] Zheng, S.B., Kuang, L.M., Gao, K.L., *Two-mode squeezed states and their superposition in the motion of two trapped ions*, Physical Letters A, 300, 427-431, 2002.

[21] Zheng, S.B., *Preparation of motional macroscopic quantum-interference states of a trapped ion*, Physical Review A, 58, 761, 1998.

[22] Zheng, S.B., *Control of motional states of a trapped ion*, Physical Letters A, 248, 25-28, 1998.

[23] Müstecaplıoğlu, Ö.E., *Motional macroscopic quantum superposition states of a trapped three-level ion*, Physical Review A, 68, 023811, 2003.

[24] Sakurai, J.J., *Modern Quantum Mechanics*, Addison-Wesley Publishing Company, 489p., 1994.

[25] Hill, S., Wooters, W.K., *Entanglement of formation of an arbitrary state of two qubits*, Physical Review Letters, 80, 2245, 1998.

[26] Dermez, R., *Generalized concurrence and negativity in time-dependent $C^3 \otimes C^5 = C^{15}$ dimensional ionic–phononic systems*, Journal of Russian Laser Research, 37, 572-580, 2016.

[27] Dermez, R*., Comparing concurrence and negativity in time-dependent ionic-phononic system with fifteen dimensional density matrix*, IOP Publishing Journal of Physics: Conference Series, 766, 012012, 2016.

[28] Anvar, S.J., Ramzan, M., Khan, M.K., *Dynamics of entanglement and quantum Fisher information for N-level atomic system under intrinsic decoherence*, Quantum Information Process, 16, 142, 2017.

[29] Liao, Q.H., Wu, J.F., Wang, P., *Properties of entanglement between the two trapped ions*, Indian Journal of Physics, 91(12) 1615, 2017.

[30] Zhang, C.L., Liu, W.W., *Generation of W state by combining adiabatic passage and quantum Zeno techniques*, Indian Journal of Physics, 93, 67-73, 2019.

[31] Pedemales, L.S., Lizuain, I., Felicetti, S., Romero, G., Lamata L., Solano, E., *Quantum Rabi model with trapped ions*, Scientific Reports, 5, 15472, 2015.

[32] Filho, R.L.M., Vogel, W., *Even and odd coherent states of the motion of trapped ion*, Physical Review Letters, 76, 608, 1996.

[33] Khalek, S.A., *Quantum Fisher information flow and entanglement in pair coherent states*, Optical and Quantum Electronics, 46, 1055-1064, 2014.

Comparing Different Approaches to Form Cobalt Oxide Layer on CoPt

Nanoparticles

Dogan KAYA[1,*], Idris ADANUR[2], Mustafa AKYOL[3], Faruk KARADAG[2], Ahmet EKICIBIL[2]

[1]Cukurova University, Vocational School of Adana, Department of Electronics and Automation, Adana, Turkey
dogankaya@cu.edu.tr, ORCID: 0000-0002-6313-7501
[2]Cukurova University, Faculty of Art and Sciences, Department of Physics, Adana, Turkey
adanuridris@gmail.com, ORCID: 0000-0002-0160-5074
[3]Adana Alparslan Turkes Science and Technology University, Faculty of Engineering, Materials Engineering Department, Adana, Turkey
makyol@atu.edu.tr, ORCID: 0000-0001-8584-0620
[2]Cukurova University, Faculty of Art and Sciences, Department of Physics, Adana, Turkey
fkaradag@cu.edu.tr, ORCID: 0000-0001-7862-9085
[2]Cukurova University, Faculty of Art and Sciences, Department of Physics, Adana, Turkey
ahmetcan@cu.edu.tr, ORCID: 0000-0003-3071-0444

Abstract

We have studied the effect of preparation methods, under argon gas and in the air environment, on the cobalt oxide formation of CoPt nanoparticles by the polyol process. The formation of cobalt oxide for both samples was investigated by the x-ray diffraction (XRD) method and cobalt oxide peaks are observed in the air prepared sample. Rietveld refinement analyses revealed that all samples exhibit a chemically distorted cubic crystal structure. The average particle size was determined <8 nm by scanning electron microscopy (SEM) and energy-dispersive x-ray spectroscopy (EDS) was revealed the chemical compositions with possible oxygen formation in the structure. The blocking temperature is reduced to 28 K in the air prepared sample due to cobalt oxide formation. The hysteresis gap disappeared above the blocking temperature and no saturation is observed up to ±5 T external field due to the system switching

from ferromagnetic state to paramagnetic state. Similarly, the coercive field was decreased from 1021 Oe to zero with increasing the temperature from 5 K to 300 K. The formations of the cobalt oxide layer did not interact with CoPt nanoparticles, therefore, the maximum exchange bias was observed about 93 Oe at 5 K.

Keywords: CoPt NPs; Cobalt oxide formation; Polyol; XRD; SEM; PPMS.

CoPt Nanoparçacıkların Üzerine Kobalt Oksit Tabakası Oluşturmada Farklı Yaklaşımların Karşılaştırılması

Öz

Polyol yöntemi ile hazırlanan CoPt nanoparçacıklarının üzerine oluşturulan kobalt oksit oluşumunun argon gazı ve hava ortamında etkilerini çalıştık. Her iki numune için kobalt oksit oluşumu, x-ışını kırınımı (XRD) yöntemi ile araştırıldı ve hava ile hazırlanan numunede kobalt oksit oluşumu gözlendi. Rietveld düzeltme analizleri, tüm numunelerin kimyasal olarak düzenli olmayan bir kübik kristal yapı sergilediğini ortaya çıkarmıştır. Ortalama parçacık boyutu, taramalı elektron mikroskopisi (SEM) ile <8 nm olarak belirlendi ve x-ışını enerji dağılımlı spektrometre (EDS) yapıda olası oksijen oluşumuna sahip kimyasal bileşimleri ortaya çıkardı. Hava ortamında hazırlanan numune ile kobalt oksit oluşumu nedeniyle bloke etme sıcaklığı 28 K sıcaklığa düşürülmüştür. Histeresis açıklığı engelleme sıcaklığının üzerinde kayboldu ve sistemin ferromanyetik durumdan paramanyetik duruma geçmesi nedeniyle ±5 T dış alanda doygunluk manyetizasyonu gözlenmedi. Benzer şekilde, sıcaklığı 5 K'den 300 K'ne yükselterek zorlayıcı alan 1021 Oe'den sıfıra düşürüldü. Kobalt oksit tabakası oluşumları CoPt nanoparçacıkları ile etkileşime girmedi, bu nedenle maksimum değişim eğilimi 5 K'de yaklaşık olarak 93 Oe gözlemlendi.

Anahtar Kelimeler: CoPt nanoparçacıklar; Kobalt oksit oluşumu; Polyol; XRD; SEM; PPMS.

1. Introduction

Magnetic nanoparticles (NPs) with size below 10 nm have attracted enormous interest for future device applications, such as, high density magnetic hard disk devices, permanent magnets, medical applications, etc. [1-3]. Although the small size leads to enhance physical and magnetic properties, superparamagnetic behaviour is an undesirable situation for recording media applications due to the thermal fluctuation and instability [4]. To govern the magnetism in ferromagnetic materials, such as Fe, Co, and Ni, usually doping paramagnetic or diamagnetic metal atoms, Pt, Pd, Mn, Au, Ag, etc. are a preferred idea to reduce the size and desired level of

magnetism in the sample [5]. Since Fe, Co, FePt, FePd, or CoPt nanoparticles are widely used for applications due to their chemical stability [6-10]. Controlling size, shape, and magnetism of these NPs need to focus further progresses.

Cobalt nanoparticles are widely preferred in technological applications due to its strong natural ferromagnetic order and chemical stability [11]. Particularly, chemically prepared CoPt NPs exhibits excellent magnetic properties and catalytic activities [12, 13] when the size reduced below 10 nm. The formation of cobalt oxide (CoO, Co_2O_3, or Co_3O_4) on CoPt nanoparticles provides a chemical and thermal stability of magnetic application as well as in Li-ion batteries, optical devices, catalysts, gas and humidity sensors properties [14-16]. There are several methods which result in high-quality cobalt oxide formation on clusters by polyol process, solgel method, thermal composition, etc. [17-19] techniques are widely used for the synthesis of these NPs to enhance and control the magnetic properties of the NPs. Among them, polyol process provides more control on particle nucleation, growth, and agglomeration of metal NPs so that the particle size can be easily reduced below 10 nm and forming a shell on core structure is possible with two steps polyol process. When the antiferromagnetic nature of cobalt oxide interacts with ferromagnetic CoPt layer, exchange bias can emerge regarding with a small particle size of CoPt.

In this paper, we aimed to investigate the morphologic and magnetic properties of the two-step synthesis of cobalt oxide on CoPt nanoparticles under Ar gas and in the air environment by polyol process. After determined oxide formation in the samples with XRD spectrometry, Rietveld refinement provided the structural information in the samples. We have investigated magnetic properties as a function of temperature at zero-field cooled (ZFC) and field cooled (FC), besides as a function of applied external field up to ±5 T at 5 K, 60 K, and 300 K. We showed that the magnetic properties below the blocking temperature are fairly large despite a striking change of magnetism at higher temperatures.

2. Materials and Methods

We conducted two-step processes to syntheses of cobalt oxide on CoPt NPs using polyol method. The first phase is preparing CoPt particles which is mixture of 0.2026 g $Co(acac)_2$ (Sigma-Aldrich ≥99.0%), 0.3097 g $Pt(acac)_2$ (Sigma-Aldrich ≥97.0%), and 6.4909 g 1,2-hexadecanediol (Sigma-Aldrich ≥90%) with 60 ml diethyl ether solution in a three-necked round-bottom flask fitted with a condenser at room temperature. We stirred for long enough under Ar gas flow to obtain a homogeneous mixture before adding 4.7824 mL oleic acid, and 4.9578 mL oleylamine surfactants. The mixture was heated to 200 °C and waited for 20 min with continuous string. Following, the mixture was cooled to RT and hexane and ethanol washing centrifugation

cycles were performed with 9000 rpm for 10 min. The second phase is forming a cobalt oxide layer on pre-prepared CoPt NPs using the same procedure. We conducted two different methods: (a) under Ar gas (CP-Ar) and (b) under air (CP-Air). Once, the dust CoPt sample is dried, 0.1025 g CoPt and 0.2026 g Co(acac)$_2$ were mixed with 3.0228 g 1,2-hexadecanediol in 40 ml diethyl ether. Then the mixture temperature was again elevated to 200 °C and waited for 20 min.

X-ray powder diffraction (XRD) data were acquired at room temperature on a PANaylitical diffractometer with Cu-Kα radiation (λ=1.54 Å) for the structural characterization of as-prepared NPs. FEI scanning electron microscopy (SEM) images are collected at 20 kV to obtain the average particle size and the ratio of the NPs compositions were calculated from energy dispersive X-ray spectroscopy (EDS) data. To explore the effect of cobalt oxide formation on the magnetic properties of CoPt NPs a variable temperature 9 T Quantum Design physical property measurement system (PPMS) with a vibrating sample magnetometer (VSM) system was used for *M-T* (at zero field cooled, ZFC, and field cooled, FC) and *M-H* field measurements at 5 K, 60 K and 300 K under ±5 T field.

3. Results

Figure 1 shows x-ray diffraction (XRD) data (black circle) and Rietveld refinements (solid red line) for as-prepared CP-Ar and CP-Air NPs. The peaks at 2θ = 40.4°, 47.1°, 68.7°, 82.8° and 87.4° for both samples correspond to the (111), (200), (220), (311) and (222) lattice planes of cubic phase [20], respectively. As seen in Figure 1, both samples are produced with high purity by polyol method. However, Figure 1(b) reveals additional peaks due to cobalt oxide formation in the CP-Air sample structure. The peak at 2θ=31° belongs to Co$_2$O$_3$ formation [21, 22] and the peaks at 2θ = 43.9°, and 50.9° correspond to cobalt oxide formation on the CoPt structure [23]. This reveals that the oxide formation is only possible under air condition. To explore lattice constant (*a*), lattice angle (*α*), unit cell volume (*V*), and Bragg positions of the samples (see Figure 1), we were carried out Rietveld refinements of XRD data using Full Prof software. We investigated the crystalline symmetry as the $Fm\overline{3}m$ (JCPDS: 15-0806) space groups of fcc-Co cubic phases for both samples from the simulation [24]. The lattice constants were found to be 3.86 Å and 3.88 Å for the samples prepared under Ar pressure and air, respectively [25]. The $d_{(111)}$ spacing is calculated via Rietveld refinement and found to be 2.23 Å and 2.24 Å for CP-Ar and CP-Air NPs, respectively. These slight shifts of the lattice constant and the spacing might be due to the oxygen formation in the CP-Air sample structure. Scherrer's equation is used to calculate the average size of the single crystalline domain, D_p (nm) for both samples which are presented in Figure 1. The crystalize sizes are calculated as 3.80 nm and 5.05 nm for CP-Ar and CP-Air NPs, respectively. This increase is due to cobalt-oxide formation in the structure.
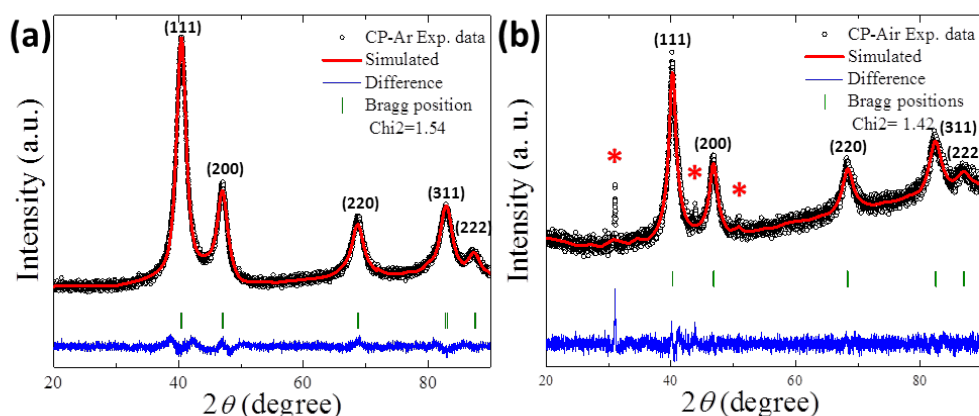
Figure 1: (a-b) XRD patterns (black circle) of cobalt oxide on CoPt NPs under Ar gas and Air, respectively, after Rietveld refinement which provide simulated data (solid red line), differences (solid blue line), and Bragg positions (green bar) with low Chi2. (*) show cobalt-oxide formations

Table 1: Agreement factor (χ), lattice constant (a), lattice angle (α), and unit cell volume (V) of cobalt oxide on CoPt NPs are obtained after Rietveld refinement. XRD peak widths are used to calculate the crystallite size (D_p) by the Scherrer formula. Several SEM images are investigated for the average particle size

Sample	χ^2	$a=b=c$ (Å)	V (Å^3)	Crystallite size D_p (nm)	Average particle Size (nm)
CoPt$_{1.12}$O$_{1.93}$ Under Ar	1.54	3.8627	57.63	3.80±0.43	7.92±0.052
CoPt$_{1.24}$O$_{3.4}$ Under Air	1.42	3.8812	58.46	5.05±0.41	5.99±0.039

Air-stable nanoparticle imaging has been performed with SEM technique which revealed monodisperse particle distribution for the samples. Figure 2(a-b) show CP-Ar and CP-Air samples formation with a 400000x and 500000x magnifications, respectively. We observed NPs distributed on the surface without adhesion due to the successful process the covering NPs with oleic acid and oleylamine surfactants. Some areas in Figure 2(b) without nanoparticles correspond to possible cobalt oxide formation which results in the disappearance of the NPs in the area. Figure 2(c-d) show the number of particles vs. particle size histogram that were fitted with the log-normal distribution (solid blue line). By fitting, the average particle sizes found to be 7.92 nm and 5.99 nm with narrow size distribution for CP-Ar and CP-Air samples (see Figure 2), respectively. We were calculated the compound stoichiometry via averaged weight and atomic percentages EDS data from five different areas which were averaged as C:55.67, O:21.13, Co:10.93 and Pt:12.28 for CP-Ar and C:50.90, O:29.63, Co:8.69 and Pt:10.78 for CP-Air samples. In the first phase, we obtained CoPt$_{2.3}$ NPs. Adding only Co under Ar gas and air conditions resulted in CoPt$_{1.12}$O$_{1.93}$ and CoPt$_{1.24}$O$_{3.4}$ compounds, respectively. The EDS stoichiometric calculation is also showed that producing in the air led to more cobalt oxide formation in the sample.
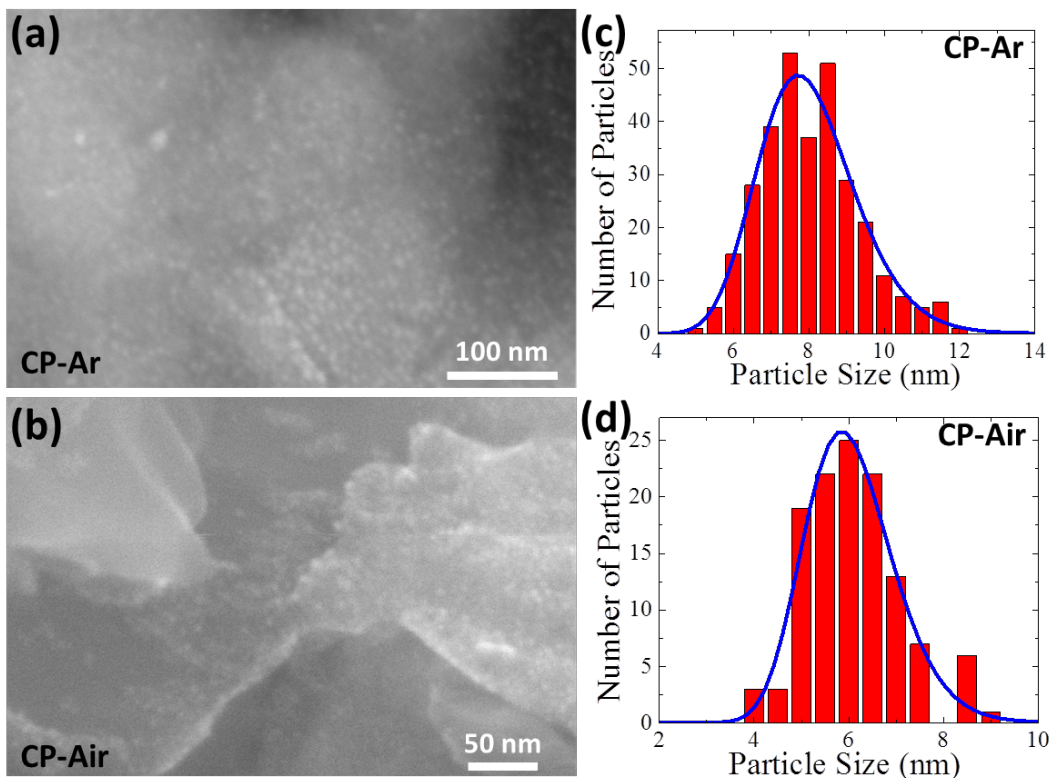
Figure 2: (a-b) SEM images of CP-Ar and CP-Air NPs. (c-d) The average particle size (red bar) distributions fitted by a log-normal distribution (solid blue line) inset plot for both samples

To investigate the effect of the oxidation process on the magnetic properties, we first measured zero-field cooled (ZFC) and field-cooled (FC) cycles for CP-Ar (black) and CP-Air (red) nanoparticles between 5 K and 300 K with applying 500 Oe external field. We observed typical ferromagnetic signal at low temperature for both samples (see Figure 3(a)). Well defined maximum of ZFC curve exhibits a superparamagnetic blocking temperature, T_B, for CP-Ar and CP-Air samples which are about 60 K and 28 K, respectively. These sharp decreases are usually observed when the particles exhibit uniform distribution [26]. Besides, increasing particle size results in an increase in T_B due to increased anisotropy in the structure. We observed from XRD and *M-T* data that there is no cobalt-oxide formation in CP-Ar sample which has a similar behaviour temperature-dependent magnetization curve and T_B with earlier findings [26, 27]. Once, the cobalt oxide layer is formed on CoPt particles, the ferromagnetic signal in the CP-Air sample is reduced due to CoO antiferromagnetic contribution.
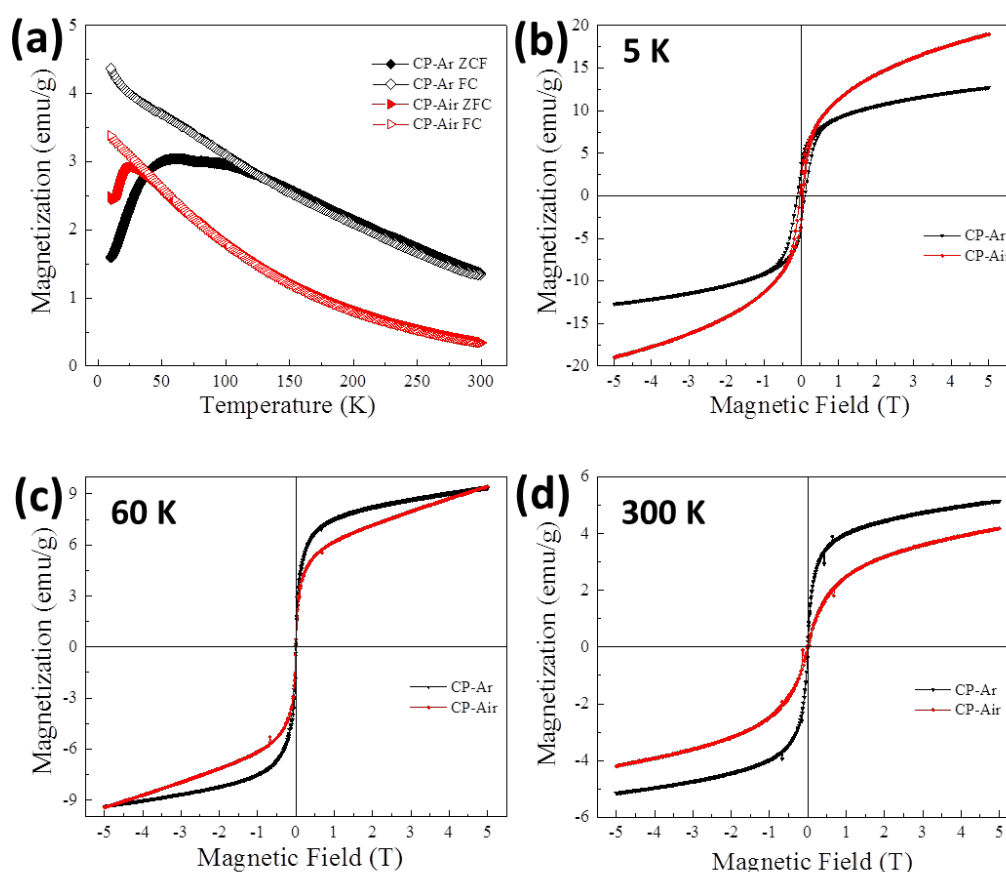
The hysteresis loops of CP-Ar (black) and CP-Air (red) samples are shown in Figure 3(b-d) at 5 K, 60 K and 300 K by applying a ±5 T magnetic field. While a strong ferromagnetic signal is observed for CP-Ar (black) particle at 5 K, the superparamagnetic signal became dominant with losing the hysteresis at 60 K and 300 K which are above T_B for both samples. The hysteresis loops could not be saturated at any temperature up to ±5 T applied field. We summarized the calculated

values of blocking temperature (T_B), coercive field (H_c), exchange bias (H_{EB}), and remanent magnetization (M_R) at 5 K for CP-Ar and CP-Air NPs in Figure 3. CP-Ar and CP-Air exhibit relatively large H_c about 1021 Oe and 421 Oe at 5 K, respectively. Above T_B, H_c has vanished due to a shift from ferromagnetic state to superparamagnetic state. Similar values are calculated for samples that exhibit relatively low 93 Oe and 8 Oe of H_{EB}, at 5 K and there is no H_{EB} at 60 K and 300 K. This is probably because ferromagnetic-paramagnetic CoPt does not interact with antiferromagnetic CoO layer.

Table 2: Blocking temperature (T_B), coercive field (H_c), exchange bias (H_{EB}), and remanent magnetization (M_R) for CP-Ar and CP-Air NPs measured at 5 K

Sample	T_B (K)	H_c (Oe)	H_{EB} (Oe)	M_R (emu/g)
CoPt$_{1.12}$O$_{1.93}$ Under Ar	60	1021 ± 10.2	93 ± 0.9	3.47
CoPt$_{1.24}$O$_{3.40}$ Under Air	28	421 ± 4.2	8 ± 0.1	2.4

We calculate the uniaxial anisotropy constant, K_u, as a function of particle volume, V, by: $T_B = K_u V / 25 k_B$ where k_B is the Boltzmann constant (1.38×10^{-16} erg/K) [27, 28]. The maximum moment value is found as 8.02×10^5 erg/cm^3 and 8.54×10^5 erg/cm^3 for CP-Ar and CP-Air NPs, respectively. These are similar to earlier report of CoPt NPs as 1.0×10^6 erg/cm^3 for the blocking temperature of 60 K [29]. An effective magnetic moment, μ_{eff} is a value of the magnitude of the paramagnetism in the CoPt due to Pt. We can calculate moment by $\mu_{eff} = (M M_S)/(N_A \beta)$. Here, M is the molecular weight of samples, M_S is saturation magnetization of sample, N_A is the Avogadro's number and β is the conversion factor that is 9.27×10^{-21} erg/Oe. The samples did not exhibit full saturation however we were taken into account the maximum magnetization for CP-Ar and CP-Air NPs with ± 5 T external field at 5 K and we calculated μ_{eff} $0.70 \mu_B$ and $1.21 \mu_B$, respectively. So, the paramagnetic effect is in CP-Air NPs increased with the increased ratio of Pt in the compound.

Figure 3: (a) Zero-field cooled (ZFC) and field-cooled (FC) cycles for CP-Ar (black) and CP-Air (red) nanoparticles between 5 K and 300 K. (b-d) Magnetic hysteresis loops of CP-Ar (black) and CP-Air (red) NPs measured at 5 K, 60 K and 300 K, respectively

The magnetization of samples increased from 5 emu/g at 300 K to 19 emu/g at 5 K with an applied field of ±5 T. However, the 5 T field remain incapable to saturate both samples due to the large particle size in the samples. The remanent magnetizations, M_R, of samples are found to be 3.47 emu/g and 2.4 emu/g for CP-Ar and CP-Air samples, respectively. We observed zero M_R at 60 K and 300 K due to the paramagnetic signal overcomes the ferromagnetic signal of CoPt NPs above T_B. Although oxidation process highly effective method to produce chemically and thermally stable the NPs, the effect of oxidation results in reduce in magnetic properties such as T_B, H_c, H_{EB}, and the effective magnetic moment. The ferromagnetic origin at room temperature is due to uncompensated surface spins with uncompensated spins. These spins strongly coupled to the CoO antiferromagnetic layer which is usually observed small NPs less than 10 nm [30]. Below the blocking temperature the magnetization of CP-Air sample increase as expected.

4. Conclusions

In summary, we have prepared the addition of Co on CoPt nanoparticles under argon gas and in the air environment. XRD results showed that there are three additional peaks of oxide

formation in the CP-Air sample. The SEM images revealed that the average particle sizes are less than 8 nm which is important for practical applications. Besides reasonable high coercive field, exchange bias, and remanent magnetization were obtained at 5 K, above blocking temperature all these vanishes due to dominant paramagnetic signal in the sample structure. We can also conclude that the cobalt oxide formation does not interact with CoPt samples. Although the samples exhibit an increase in saturation magnetization with decreasing temperature, in order to reach total saturation more than ±5 T external field is required. The effect of the CoO thickness on the CoPt core remains a major problem for nanoparticles and require further study with high-resolution imaging techniques.

Acknowledgement

References

[1] Ethirajan, A., Wiedwald, U., Boyen, H.-G., Kern, B., Han, L., Klimmer, A., Weigl, F., Kästle, G., Ziemann, P., Fauth, K., Cai, J., Behm, R.J., Romanyuk, A., Oelhafen, P., Walther, P., Biskupek, J. and Kaiser, U., *A Micellar Approach to Magnetic Ultrahigh-Density Data-Storage Media: Extending the Limits of Current Colloidal Methods*, Advanced Materials (Weinheim, Germany), 19(3), 406-410, 2007.

[2] Plumer, M.L., Van Ek, J. and Weller, D., *The physics of ultra-high-density magnetic recording*, Springer Science & Business Media, 2012.

[3] Weller, D., Moser, A., Folks, L., Best, M.E., Wen, L., Toney, M.F., Schwickert, M., Thiele, J. and Doerner, M.F., *High Ku materials approach to 100 Gbits/in2*, IEEE Transactions on Magnetics, 36(1), 10-15, 2000.

[4] Himpsel, F., Ortega, J., Mankey, G. and Willis, R., *Magnetic nanostructures*, Advances in physics, 47(4), 511-597, 1998.

[5] Jiles, D., *Introduction to magnetism and magnetic materials*, CRC press, 2015.

[6] Alloyeau, D., Ricolleau, C., Mottet, C., Oikawa, T., Langlois, C., Le Bouar, Y., Braidy, N. and Loiseau, A., *Size and shape effects on the order–disorder phase transition in CoPt nanoparticles*, Nature Materials, 8, 940, 2009.

[7] Barmak, K., Kim, J., Lewis, L.H., Coffey, K.R., Toney, M.F., Kellock, A.J. and Thiele, J.-U., *On the relationship of magnetocrystalline anisotropy and stoichiometry in epitaxial $L1_0$ CoPt (001) and FePt (001) thin films*, Journal of Applied Physics, 98(3), 033904, 2005.

[8] Chen, Q., Qin, Z., Gan, Q., Xinqi, C., Hai, W., Daming, S., Bixiao, W., Lifeng, X. and Yiwen, T., *Designing 3D interconnected continuous nanoporous Co/CoO core–shell nanostructure electrodes for a high-performance pseudocapacitor*, Nanotechnology, 28(8), 085401, 2017.

[9] Lin, J., Zhou, W., Kumbhar, A., Wiemann, J., Fang, J., Carpenter, E.E. and O'Connor, C.J., *Gold-coated Iron (Fe@Au) nanoparticles: Synthesis, characterization, and magnetic field-induced self-assembly*, Journal of Solid State Chemistry, 159(1), 26-31, 2001.

[10] Mori, K., Kondo, Y. and Yamashita, H., *Synthesis and characterization of FePd magnetic nanoparticles modified with chiral BINAP ligand as a recoverable catalyst vehicle for the asymmetric coupling reaction*, Physical Chemistry Chemical Physics, 11(39), 8949-8954, 2009.

[11] Wu, N., Fu, L., Su, M., Aslam, M., Wong, K.C. and Dravid, V.P., *Interaction of fatty acid monolayers with Cobalt nanoparticles*, Nano Letters, 4(2), 383-386, 2004.

[12] Chen, M. and Nikles, D.E., *Synthesis of spherical FePd and CoPt nanoparticles*, Journal of Applied Physics, 91(10), 8477-8479, 2002.

[13] Sobal, N.S., Ebels, U., Möhwald, H. and Giersig, M., *Synthesis of Core−Shell PtCo Nanocrystals*, Journal of Physical Chemistry B, 107(30), 7351-7354, 2003.

[14] Gopinath, S., Sivakumar, K., Karthikeyen, B., Ragupathi, C. and Sundaram, R., *Structural, morphological, optical and magnetic properties of Co_3O_4 nanoparticles prepared by conventional method*, Physica E: Low-dimensional Systems and Nanostructures, 81, 66-70, 2016.

[15] Liang, Y., Li, Y., Wang, H., Zhou, J., Wang, J., Regier, T. and Dai, H., *Co_3O_4 nanocrystals on graphene as a synergistic catalyst for oxygen reduction reaction*, Nature Materials, 10(10), 780-786, 2011.

[16] Shatrova, N., Yudin, A., Levina, V., Dzidziguri, E., Kuznetsov, D., Perov, N. and Issi, J.-P., *Elaboration, characterization and magnetic properties of cobalt nanoparticles synthesized by ultrasonic spray pyrolysis followed by hydrogen reduction*, Materials Research Bulletin, 86, 80-87, 2017.

[17] Izu, N., Matsubara, I., Uchida, T., Itoh, T. and Shin, W., *Synthesis of spherical cobalt oxide nanoparticles by a polyol method*, Journal of the Ceramic Society of Japan, 125(9), 701-704, 2017.

[18] Salavati-Niasari, M., Khansari, A. and Davar, F., *Synthesis and characterization of cobalt oxide nanoparticles by thermal treatment process*, Inorganica Chimica Acta, 362(14), 4937-4942, 2009.

[19] Sinkó, K., Szabó, G. and Zrínyi, M., *Liquid-phase synthesis of cobalt oxide nanoparticles*, Journal of Nanoscience and Nanotechnology, 11(5), 4127-4135, 2011.

[20] Sun, X., Jia, Z., Huang, Y., Harrell, J., Nikles, D., Sun, K. and Wang, L., *Synthesis and magnetic properties of CoPt nanoparticles*, Journal of Applied Physics, 95(11), 6747-6749, 2004.

[21] Aksoy Akgul, F., Akgul, G. and Kurban, M., *Microstructural properties and local atomic structures of cobalt oxide nanoparticles synthesised by mechanical ball-milling process*, Philosophical Magazine, 96(30), 3211-3226, 2016.

[22] Wang, X., Ge, H., Ye, Q., Si, P. and Chen, H., *Weak Ferromagnetism and Exchange Bias in Antiferromagnetic Cobalt Oxide Nanoparticles*, Journal of Magnetics, 23(4), 487-490, 2018.

[23] Qiu, B., Guo, W., Liang, Z., Xia, W., Gao, S., Wang, Q., Yu, X., Zhao, R. and Zou, R., *Fabrication of Co_3O_4 nanoparticles in thin porous carbon shells from metal–organic frameworks for enhanced electrochemical performance*, RSC advances, 7(22), 13340-13346, 2017.

[24] Liu, Y., Yang, Y., Zhang, Y., Wang, Y., Zhang, X., Jiang, Y., Wei, M., Liu, Y., Liu, X. and Yang, J., *A facile route to synthesis of CoPt magnetic nanoparticles*, Materials Research Bulletin, 48(2), 721-724, 2013.

[25] Trung, T.T., Nhung, D.T., Nam, N.H. and Luong, N.H., *Synthesis and Magnetic Properties of CoPt Nanoparticles*, Journal of Electronic Materials, 45(7), 3621-3623, 2016.

[26] San, B.H., Lee, S., Moh, S.H., Park, J.-G., Lee, J.H., Hwang, H.-Y. and Kim, K.K., *Size-controlled synthesis and characterization of CoPt nanoparticles using protein shells*, Journal of Materials Chemistry B, 1(10), 1453-1460, 2013.

[27] Tournus, F., Tamion, A., Blanc, N., Hannour, A., Bardotti, L., Prével, B., Ohresser, P., Bonet, E., Epicier, T. and Dupuis, V., *Evidence of L1$_0$ chemical order in CoPt nanoclusters: Direct observation and magnetic signature*, Physical Review B, 77(14), 144411, 2008.

[28] Frommen, C., Malik, S., Würfel, J.U., Rösner, H. and Didschies, C., *Synthesis and magnetic properties of CoPt$_3$ nanoparticle assemblies containing copper*, Materials Letters, 58(6), 953-958, 2004.

[29] Rooney, P.W., Shapiro, A.L., Tran, M.Q. and Hellman, F., *Evidence of a Surface-Mediated Magnetically Induced Miscibility Gap in Co-Pt Alloy Thin Films*, Physical Review Letters, 75(9), 1843-1846, 1995.

[30] Dai, Q. and Tang, J., *The optical and magnetic properties of CoO and Co nanocrystals prepared by a facile technique*, Nanoscale, 5(16), 7512-7519, 2013.

Numerical Investigation and Water Tunnel Experiment for F35 Fighter Jet

Haci SOGUKPINAR[1,*], Serkan CAG[2], Bulent YANIKTEPE[3]

[1]*University of Adiyaman, Vocational School, Department of Electric and Energy, Adiyaman, Turkey*
hsogukpinar@adiyaman.edu.tr, ORCID: 0000-0002-9467-2005

[2]*University Adiyaman, Vocational School, Department of Machinery and Metal Technology, Adiyaman, Turkey*
scag@adiyaman.edu.tr, ORCID: 0000-0003-1088-448X

[3]*Korkut Ata University, Faculty of Engineering, Department of Energy Systems Engineering, Osmaniye, Turkey*
byaniktepe@osmaniye.edu.tr, ORCID: 0000-0001-8958-4687

Abstract

In this paper, a low-speed aerodynamic flow structure of the original F35 aircraft model was investigated in a closed-circuit water tunnel experiment, and the investigation was also conducted numerically by using a computational fluid dynamic (CFD) approach. Both studies were performed for the model with a chord length of c =168 mm and wing sweepback angle of Λ = 21.59°, thickness 5 mm and beveled leading edges with an angle of 45°, and for the Reynolds numbers 10.000 at the angle of attack from 5° to 25° with the airflow speed of 0.6 cm/s. For the experimental part, dye visualization and Particle Image Velocimetry (PIV) experiments were performed, and for the numerical part, SST turbulence model was used to solve the flow field around model aircraft and obtained data were compared with experiment. Detail about the flow field including, the development of leading-edge vortex and formation of vortex breakdown and interactions were discussed and presented. Leading-edge vortices were partially developed at the angle of 5°, vortex breakdown pronounced at the angle of 10°, as the increasing angle of attack, location of vortex breakdown moved further up to the front side. At 25°, there was no complete stall condition, and the location of the vortex breakdown stayed on the wing surface.

F35 Savaş Uçağının Deneysel ve Nümerik Yöntemlerle İncelenmesi

Öz

Bu makalede, orijinal F35 uçak modelinin düşük hızda aerodinamik akış yapısı kapalı devre su tüneli deneyinde araştırılmış ve ayrıca hesaplamalı akışkanlar dinamiği (CFD) yaklaşımı kullanılarak sayısal olarak incelenmiştir. Her iki çalışma için, kiriş uzunluğu c = 168 mm, kanat geri süpürme açısı Λ = 21.59°, pah açısı 45°, et kalınlığı 5 mm, Reynolds sayısı 10.000 ve akış hızı 0,6 cm/s olan parametreler kullanılarak 5°-25° aralığındaki hücum açıları için araştırma yapılmıştır. Deneysel kısım için boya görselleştirme deneyi ve parçacık görüntü hız ölçümü (PIV) deneyleri yapılmış, nümerik yöntem olarak SST türbülans modeli kullanılmıştır, elde edilen veriler deneysel ve nümerik sonuçlarla kıyaslanmıştır. Ön kenar girdabının oluşması ve girdap dağılması/çökmesi ve akış alanı ile ilgili etkileşimler araştırılmış ve elde edilen veriler tartışılmıştır. Ön kenar girdap oluşumu 5°'de kısmen başlamış, 10°'de girdap kırılması belirginleşmiş ve hücum açısının artmasına bağlı olarak girdap çökme noktası ön tarafa doğru ilerlemiştir. 25°'lik hücum açısına gelindiğinde girdap çökme/dağılma noktası tepe noktasına kadar ilerlememiş, kanat üzerinde kalmış, uçağın bütünüyle stol'a girme durumu gözlemlenmemiştir.

***Anahtar Kelimeler:*** F35 savaş uçağı; LEV; Girdap çökmesi; Girdap; PIV; Boya görüntüleme.

1. Introduction

The efficiency of aircraft is the main subject of scientific research in parallel with the rapid development of the aviation sector. Great attention is given to increase aerodynamic efficiency to travel long distances without refueling and reducing operating costs, besides, to increase payload and decrease fuel consumption. Although accurate prediction of the maximum lift coefficient and lift to drag ratio are the main issue but prediction of low-speed flow field behavior of aircraft poses considerable challenges from the aerodynamics point of view [1]. Reynold's number dependency of flow and reliability of many other factors is the most challenging task. Because most of the experiments were performed with limited sub-scale models [2]. On the other hand, in the last 4 decades, CFD has evolved with increasing quality of the powerful computer, and the application of CFD has accelerated the process of aerodynamic design and joined the wind tunnel and flight test as a critical tool of the trade [3]. Reynolds Averaged Navier-Stokes (RANS) equations with varied turbulence models have been widely used for laminar or turbulent flow

simulations [4] and consistent prediction is possible with experimental observations. Particle image velocimetry (PIV) and dye visualization experiment are other methods to investigate low-speed flow field behavior over or behind blunt objects. In this method, fluid is seeded with small tracer particles or dye, and the motion of these particles is traced in the water channel then the flow regime of fluid is revealed with the help of optical devices. These two methods have been mainly used to investigate unmanned combat air vehicle (UCAV) with non-slender delta wing configuration [5, 6]. The development of leading-edge vortex (LEV) and vortex breakdown are two important phenomena and have a strong influence on wing aerodynamics. A well-documented example of LEV is generated by aircraft with highly swept delta-shaped wings [7] and under correct conditions, LEV can augment lift generation for the air vehicle [8]. Flow structures at the trailing-edge side of diamond and lambda wings were investigated in a water channel experiment and variation of flow field regime, development of LEV, and vortex breakdown concerning the angle of attack were reported [9]. Boundary layer separation induces these vortex phenomena and happens by rolling up of viscous flow sheet [10] and the separation happens due to a sharp leading edge and angle of attack [11]. Unsteady wake flow of NASA Common Research Model under low-speed stall conditions was investigated by using PIV and Detached Eddy Simulation (DES) method and obtained data were compared with other methods [1]. In other PIV experiments, the results indicate that the stereo PIV is suitable and effective to investigate practical, complex velocity fields, at least qualitatively, in the large-scale low-speed wind tunnels [12]. On the other hand, the majority of PIV application stays in low-speed application but speed ranges are increasing gradually to high-speed applications such as transonic, supersonic [13], and hypersonic speeds [14]. The F35 is a new and best-in-class fighter jet. F-35 Lightning II is a true 5th Generation trivariate, multiservice air system. It provides outstanding fighter class aerodynamic performance, supersonic speed, all-aspect stealth with weapons, and highly integrated and networked avionics [15]. This aircraft is a joint production project of different countries and is now in the production process. Field tests continue with deliveries and there are sometimes positive and sometimes negative news about the plane in the media almost every day. As this plane is still new, scientists have just begun researching. For instance, PIV and Dye visualization experiments are more common for delta wind in the literature. However, there are no extensive researches related low-speed aerodynamic properties of this aircraft. Therefore, in this study, low-speed aerodynamic characteristics of an F35 fighter jet model were investigated by using dye visualization, Particle Image Velocimetry (stereo-PIV), and SST turbulence method. This paper also wants to compare numerical and experimental investigations to understand complex flow physics and to validate the simulation accuracy of the Computational Fluid Dynamics (CFD) approach.

2. Experimental Approach

The F35 aircraft configuration is given in Fig. 1. The full-scale configuration has a thickness of 5 mm, mean aerodynamic chord length of 168 mm, bevel angle of 45°, and wing sweepback angle of the main wing is $\Lambda = 20.96°$ and lower surface area of 137 cm^2. The full-scale model was tested in a closed-circuit water channel experiment at the Department of Mechanical Engineering at Osmaniye Korkut Ata University. The closed-loop, open water channel experiment setup is given in Fig. 2. The experimental system consists of a water channel with dimensions of 750×1000×8000 mm (height × width × length) between two water tanks.
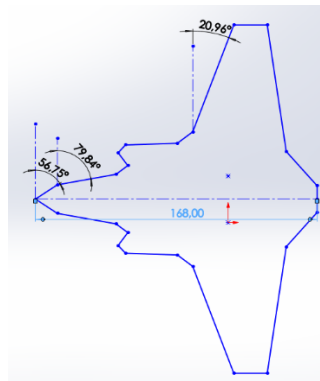
Figure 1: F35 aircraft configuration

Total water depth is 52 cm in the channel, water level under the wing is 20 cm and over the wing is 16 cm. The wall of the channel made from 15 mm thick transparent Plexiglas. The test was performed at a free stream velocity of 0.6 cm/s which corresponds to chord-based Reynolds number of 10.000. To provide uniform flow, there is a current regulator before the contraction section. Before the test section, water was directed into a settling chamber and passed through a honeycomb section where there is a channel contraction with the ratio 2:1. These two arrangements were used to preserve the turbulence intensity below 0.1%. Rhodamine 6G was used in the dye experiment, which shines under 532 nm laser light and was recorded using a SONY HD-SR1camera. The dye was injected at the apex from a certain height with a plastic pipe. There is a needle at the end of this pipe, which is placed in a channel along the central axis in the model aircraft. In the present dye experiment, the plan and side view flow pattern of the model was captured and presented at the angle of attack from 5° to 25°.

Figure 2: The closed-loop, open water channel experiment setup

Stereoscopic Particle Image Velocimetry (stereo-PIV) technique provides information about the instantaneous or time average values of flow structure by measuring the velocities of small metal-coated solid particles at the micron size, which is moving at the same speed as the fluid in the flow. In this experiment, 10-micrometer silver-coated plastic particles were added into water. Although the densities of the particles (1100 kg/m³) are relatively higher than the density of the water, they move almost at the same speed as the water due to their micron size. A double pulsed 120 mJ power unit was used to produce a laser beam and converted into 1 to 2 mm thickness laser beam using an optical instrument. The time interval between consecutive pulses was set to 1.5 ms for all measurements. The pulsed laser unit can send up to 15 laser beam pairs per second. The consecutive motion of particles was recorded with a CCD camera with a resolution of 1600×1186 pixels. The camera-equipped lens with 60 mm focal length and 900 consecutive images were taken for each continuous run with an acquisition frequency of 15 Hz. Detail information about parameters, experimental, and PIV systems are available at the Ref. [16-20].

3. Numerical Approach

The flow field over the X45 wing was simulated by using commercial software COMSOL. Reynolds-Averaged Navier-Stokes (RANS) equation was applied for the conservation of momentum and the continuity. Turbulence effects were modeled by using the Menter Shear-Stress transport (SST) model with realizability constraints. The SST model is also called the low-Reynolds number model and this model resolves the flow field all the way down to the wall. SST model is expressed in terms of k and ω with Eqn. (1) and Eqn. (2) [21-23].

$$\rho \frac{\partial k}{\partial t} + \rho u. \nabla k = P - \rho \beta_0^* k\omega + \nabla.((\mu + \sigma_k \mu_T)\nabla_k) \tag{1}$$

$$\rho \frac{\partial \omega}{\partial t} + \rho u. \nabla \omega = \frac{\rho \gamma}{\mu_T} P - \rho \beta \omega^2 + \nabla.\left((\mu + \sigma_\omega \mu_T)\nabla_\omega\right) + 2(1 - f_{v1})\frac{\rho \sigma_{\omega 2}}{\omega}\nabla \omega. \nabla k \tag{2}$$

where, P is the static pressure and can be represented with the Eqn. (3).

$$P = \min\left(P_k, 10\rho\beta_0^* k\omega\right) \tag{3}$$

Here, P_k production term and it is expressed with Eqn. (4).

$$P_k = \mu_T\left(\nabla u : (\nabla u + (\Delta u)^T) - \frac{2}{3}(\nabla . u)^2\right) - \frac{2}{3}\rho k \nabla . u \tag{4}$$

Turbulence viscosity is expressed with Eqn. (5),

$$\mu_T = \frac{\rho a_1 k}{\max\left(a_1\omega, S f_{v2}\right)} \tag{5}$$

where, S is the characteristic magnitude of the mean velocity gradients and is expressed with the help of Eqn. (6).

$$S = \sqrt{2 S_{ij} S_{ij}} \tag{6}$$

The interpolation functions f_{v1} and f_{v2} are represented with the Eqn. (7) and Eqn. (8).

$$f_{v1} = \tanh\left(\min\left[\max\left(\frac{\sqrt{k}}{\beta_0^* \omega l_\omega}, \frac{500\mu}{\rho\omega l_\omega^2}\right), \frac{4\rho\sigma_{\omega 2} k}{\max\left(\frac{2\rho\sigma_{\omega 2}}{\omega}\nabla\omega.\nabla k, 10^{-10}\right) l_\omega^2}\right]^4\right) \tag{7}$$

$$f_{v2} = \tanh\left(\max\left(\frac{\sqrt{k}}{\beta_0^* \omega l_\omega}, \frac{500\mu}{\rho\omega l_\omega^2}\right)^2\right) \tag{8}$$

where, l_ω is the distance to the closest wall. For SST, default model constants are given by,

$$\beta_1 = 0.075, \gamma_1 = \frac{5}{9}, \sigma_{k1} = 0.85, \sigma_{\omega 1} = 0.5, \beta_2 = 0.0828, \gamma_2 = 0.44, \sigma_{k2} = 1.0,$$

$$\sigma_{w2} = 0.856, \beta_0^* = 0.09, \sigma_1 = 0.31$$

For this calculation flow type was set to incompressible and gravity effect provided in the *z*-direction. The delta wing had a chord length of $C = 168$ mm with a wing sweepback angle of $\Lambda = 21.59$. Wind speed was set to 0.058 m/s. Reynold's number was taken as 10,000 and flow over the boundary conditions of the wing was assumed to be turbulent. In a low Reynolds number model, the equations are integrated through the boundary layer to the wall, this allows a no-slip condition to be applied to the wing surface, therefore X45 wing was modeled as a solid wall with no-slip conditions and other boundaries was modeled as a free stream. The algebraic multigrid (AMG) solver with the generalized minimal residual (GMRES) method (a commercial version built-in COMSOL) was chosen because it is an iterative method for solving very large systems of

linear equations and provides robust solutions for large CFD simulations [24]. In the fluid flow problem, there are millions of equations or unknowns, proportional to the number of nodes in the finite element mesh therefore it is so expensive to solve with the direct solver. On the other hand, the iterative solver uses much less memory. Reynolds-Averaged Navier-Stokes (RANS) equation is solved in terms of averaged velocity and pressure fields in time. The turbulence effect is computed with two equations SST turbulence model. On the surface of the model aircraft, free triangular mesh type was applied and the minimum element size was limited as 0.0001 and maximum was set to 0.0005 then a total 177.766 triangular mesh element was generated. For the 3D computational domain, the tetrahedral mesh type was chosen and the minimum element size was limited to 0.0001 and maximum growth rate set to 1.25 and finally, 6 million tetrahedral mesh elements were generated. Low numbers of mesh lead to a calculation error, while too much mesh increases the calculation time considerably. If only the mesh number is in a certain range, the results are more agreement with the experimental data. For the numerical calculation in the literature, only criteria are generally compliant with the experiment. Therefore, the effect of the mesh number on the numerical results was carefully tested in preliminary calculations and the mesh configuration more agreement with the experiment was set. COMSOL has an integrated mesh generation and quality control module and mesh quality are generally checked in terms of skewness of the mesh element. In this study, mesh quality was checked and the average element quality was calculated 0.65, and minimum was 0.19. Mesh quality 1 is the best possible and it indicates an optimal element in the chosen quality measure and 0 is the worst. In general, elements with a quality below 0.1 are considered as poor quality for many applications [25]. Mesh distribution is given in Fig. 3. The simulation was carried out for the full model aircraft. To eliminate domain size effect on the calculation results, the computational domain size was extended at least over 10 times the chord length of the model. The upstream boundary was placed 20 mean aerodynamic chords in front of the apex, 20 mean aerodynamic chords behind the tail, and 10 mean aerodynamic chords above and below the pressure and suction side. This configuration is consistent with other numerical studies [26]. The inlet port was set to velocity inlet and outlet port was set to pressure outlet with zero atmospheric pressure and no-slip boundary condition was applied for the surface of the model. The computation was carried out with a server with 32 processors and 64 GB RAM. Detailed information about numerical method and equations are available at the Ref. [27, 28]
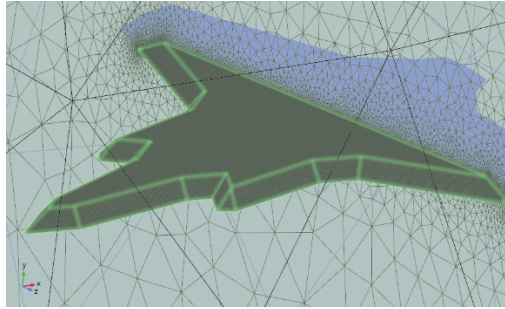
Figure 3: Mesh distribution around model aircraft

4. Results and Discussion

Dye visualization of the flow field structure of the model aircraft for the thickness of 5 mm in the plan view is presented in Fig. 4 at the angle of attack from 5° to 25°. At the lower angle of attack at $\alpha = 5°$, flow is almost conventional and moves very orderly until at the end of the trailing edge side of the wing. However, at $\alpha = 10°$ small scale leading-edge vortex (LEV) develops and rotation of flow is evident at the lower side of the front body. Turbulence intensity increases compare to the previous image and there is cross current on the wing surface with lateral mixing. When the angle of attack increased to $\alpha = 15°$, LEV and vortex breakdown are quite prominent on the main wing. By the time $\alpha = 20°$ is reached, flow is swirling from beginning to end and spiral vortex breakdown happens under the main wing surface. When the angle of attack increased to $\alpha = 25°$, the size of rotation and turbulence increases and the location of the vortex breakdown moves forward. Although LEV keeps up its flow regime on the front side, it became quite unstable, and ruptures in flow become more common.

Figure 4: Dye visualization of the plan view with the formation and development of LEV and vortex breakdown

Fig. 5 shows the lower surface computational flow field with the formation and development of LEV and vortex breakdown. At the lower angle of attack such as $\alpha = 5°$, streamline flowing under the surface of the model aircraft without lateral mixing and fluid flows in parallel layers until at the end of trailing edge side of wing or tail but behind the aircraft, small scale cross-currents or lateral mixing happens. When the increasing angle of attack up to $\alpha = 10°$, a part of the flow field keeps flow regime the same but small-scale vortex develops along the leading-edge side of the body. The size of rotation is small and the cycle frequency is low. By the time $\alpha = 15°$ is reached, LEV is quite prominent, cycle frequency decreases, the radius of core

371

increases and vortex breakdown is happening on the wing surface. At this angle, the LEV gets under the influence of a larger and stronger vortex, which is the precursor of the vortex breakdown. At $\alpha = 20°$, the vortex with a lower loop frequency appears to increase the effectiveness and disrupt normal LEV formation where circulating frequency decreases, size of LEV increases, and location of vortex breakdown moves to further up to the front side of the model. When the angle of attack increased to $\alpha = 25°$, irregularities in the flow structure and size of vorticity increases at the rear side of the model, and the location of the vortex breakdown moves a little bit further to the front side. When the experimental and theoretical results are compared, there is a good correlation between the experiment and the numerical approach at the angle of attack from 5° to 25°.
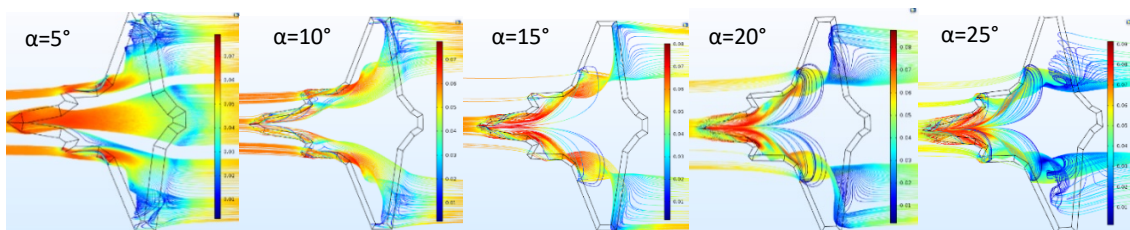
Figure 5: Computational visualization of the plan view with the streamline velocity field with the formation and development of LEV and vortex breakdown

Fig. 6 shows PIV time-averaged vorticity field at the angle of attack from 5° to 25°. In the vorticity image, solid dark lines represent clockwise rotation, while dotted lines express a counterclockwise loop. At $\alpha = 5°$, streamlines move in parallel layers and no disruption between the streamlines but vorticity image indicates two small scale formation of vortex area under the wing surface where one of them is on the body and the other is on the wing. The figures show the symmetric vortex area on both sides of the body and the wing surface. Both vorticity images represent LEV formation, but since the body does not consist of a single geometry like a simple delta wing, one represents LEV formation on the front while the other represents LEV formation on the wing. The same situation is seen also in Fig. 5 where fluids from different regions create both LEV separately and join at the back. As is seen in Fig. 6 ($\alpha = 5°$) LEV develops along from front to the back across the entire wing surface and there is no situation to imply vortex breakdown but by the time $\alpha = 10°$ is reached, it appears that LEV flow regime ends at the backside of the wing where an irregular vortex area is formed and this proves the location and formation of vortex breakdown on the wing. When the angle of attack increased to $\alpha = 15°$, LEV intensity decreases and the area it covers narrows, and LEV regime appears to be structurally impaired along the LEV axis. As the increasing angle of attack up to $\alpha = 20°$ flow regimes of the LEV shortens further and the point where the LEV ends is the beginning of the vortex breakdown. Finally, by the time $\alpha =$

25° is reached, LEV regime disrupts, location of the vortex breakdown moves forward and expands, and undesirable other vortex areas form in different places.
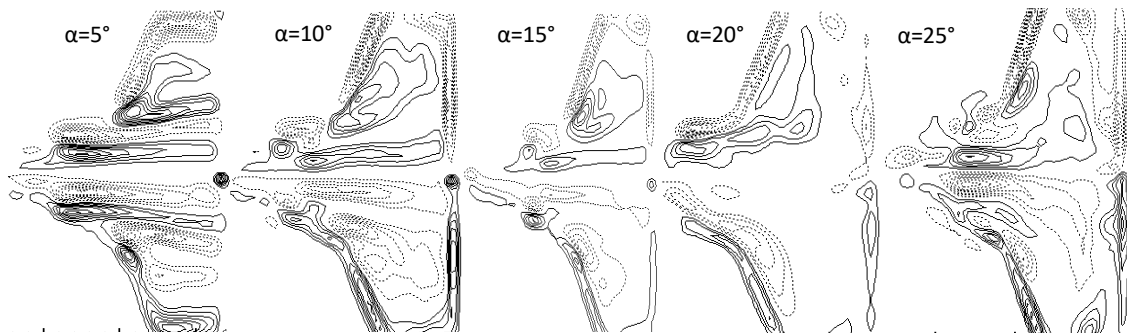

Figure 6: Patterns of the time-averaged vorticity, <ω> field of the model aircraft with the angle of attack

The plan view vorticity contour on the surface as a function of the angle of attack is given in Fig. 7. At $\alpha = 5°$, The LEV regime extends from front to toe appears symmetrically on both sides of the body. Two LEV regimes are seen also in other previous figures. The first one is on the front, thinner and shorter, while the other is longer and wider, it covers the majority of the body from front to back. The LEV at the front extends along the outer line, while the LEV at the rear extends along the starting line of the wing on the body. Besides, there is a weaker third LEV regime on the wing closer to the tip. It was also observed in PIV experiments where three LEV regimes were formed and are seen in Fig. 6 ($\alpha = 15°$). The main reason for the formation of different LEV flow regime is caused by the fact that the plane is not composed of a uniform geometry. By the time, $\alpha = 10°$ is reached, LEV regime in the front and on the body narrows, however third LEV, consist of two parts, in the middle outer part of the wing has expanded and strengthened. Apart from these three LEV flow regimes, it is seen that the fourth but irregular eddy currents begin to form on the backside of the wing. These irregular currents are the precursors of the vortex breakdown. When the angle of attack increased to $\alpha = 15°$, the LEV regime on the middle body almost disappears, and the vortex area on the wings bends towards the edge and the second part of the third vortex becomes stronger. Irregular flows at the backside become stronger and merge to form vortex breakdown, and now covers at the middle backside of the wing. As the increasing angle of attack up to $\alpha = 20°$, LEV transforms into a different vortex area on the wingtip, LEV regime retains its dominance in the front, and almost disappears in the middle part. The size of the vortex breakdown increases and location moves further up to the front side. Finally, by the time $\alpha = 25°$ is reached, LEV regime almost disperses, and the location of the vortex breakdown moves further but there is still LEV regime in the front side, and the size of the core increases close to wingtip.
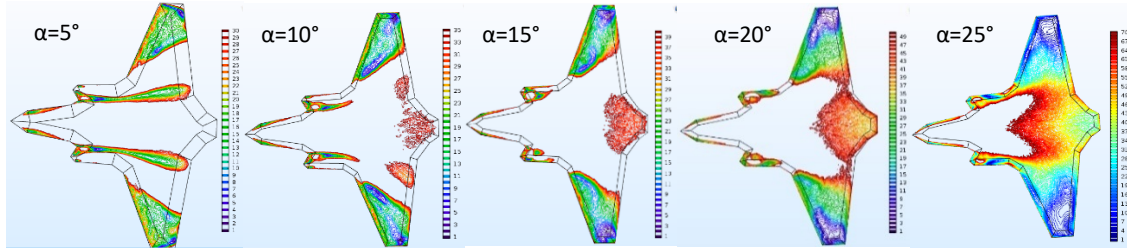
Figure 7: Comparison of pattern of vorticity contour on the surface as a function of angle of attack

PIV streamline data of the F35 aircraft model is given in Fig. 8. At the angle of attack 5°, the flow regime is quite linear, and there is almost no turbulence happens on the surface. When the angle of attack increased to 10°, streamlines converge along the outer front lines of the model and indicates the formation of LEV. As the angle of attack increases, the flow lines get closer and tighter and show a circular behavior along the outer line of the wing. By the time $\alpha = 20°$ is reached, the figure indicates a vortex area on the outer side of the wing, which was also reported in Fig. 6 ($\alpha = 20°$). Finally, by the time $\alpha = 25°$ is reached, the severity of the vorticity on the wing surface increases, and a circular core forms in the upper part.
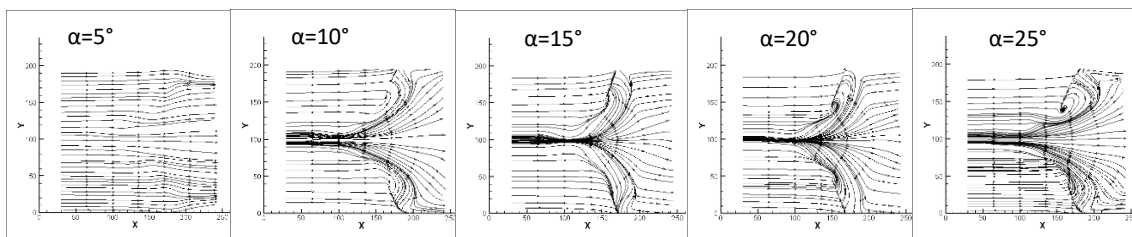
Figure 8: Comparison of near-surface patterns of streamline topology of PIV experiment

5. Conclusions

A computational and experimental study was conducted for the F35 fighter jet configuration. In the experiment dye visualization and particle image velocimetry (PIV) techniques were used and plan view velocity field and vorticity pattern were presented. For the numerical part, Reynolds Average Navier Stokes (RANS) theorem equations with SST turbulence model were solved for incompressible flow around the wing surface and, were compared with experimental data to validate simulation accuracy of computational fluid dynamic approaches. In the dye visualization experiment, LEV development started at $\alpha = 10°$ vortex breakdown pronounced at 15°. When the increasing angle of attack, the location of the vortex breakdown moved further to the front side with increasing size and severity but never reached the apex. In the numerical study, vortex breakdown was observed firstly at the angle of 15°. As the increasing angle of attack, the size of the core increased with decreasing frequency. At 25°, there was still LEV regime in the front even it was small and there was no complete stall. In PIV experiment,

LEV development started at $\alpha = 5°$, three different LEV regimes were observed on the model. With the increasing angle of attack to 10°, a vortex area, transverse to the back of the plane was observed, which indicated the formation of a vortex breakdown. As the increasing angle of attack, LEV distance shortened and dispersed structurally, location of vortex breakdown moved to the front side but there was no complete stall condition observed. In the pattern of vorticity contour of numerical data, LEV pattern developed at the angle of attack at 5°, vortex breakdown showed signs of formation at 10° and became evident at 15° on the backside. With the increasing angle of attack, the area of irregular vortex formation (vortex breakdown) expanded and moved forward. In PIV experiment, streamline topology of the model was plotted and a steady flow was observed at 5°. As the increasing angle of attack, flow lines were gathered along the contours of the model and showed LEV formation. At 25°, the rotation core appeared to occur near the tip of the wings.

When the numerical results are compared with the experimental observations, there is a good agreement between them. The installation and operating costs of the experimental systems are quite high therefore, in the modern design process, the computational fluid dynamics method becomes an important analysis method together with the experiment. Experimental systems have the advantage of dealing with "real" fluid and can produce a much wider range of global data than CFD, but the experiment does not produce data in a wide range of Reynolds numbers. For example, it is subject to an important wall and boundary system fixes and is not very suitable for providing flow details. In modern aircraft design, it is necessary to focus on CFD with experimental systems.

Nomenclature

c_P	Pressure coefficient
c_L	Lift coefficient
f_{w1}	Damping fuction
P	Static pressure
P_∞	Free stream pressure
U_r	Relative velocity
U_∞	Free stream velocity (wind velocity)
v	Kinematic viscosity
c	Airfoil chord
t	Percentage of the maximum thickness
k	Turbulence kinetic energy
κ	Von Kármán constant,
l_{ref}	Reference length scale
L	Length scale of flow
ε	Turbulence dissipation rate
ω	Specific dissipation rate
ω_t	wall vorticity at the trip
ρ	Density

ρ_∞	Freestream density
μ	Dynamic viscosity
S	magnitude of the vorticity,
$\tilde{S}$	Modified vorticity
S_{ij}	Mean strain rate
Ω_{ij}	Mean rotation rate
μ_{eff}	Effective dynamic viscosity
α	Angle of attack
$\emptyset$	Scalar quantity of the flow
CFD	Computational Fluid Dynamics
NACA	National Advisory Committee for Aeronautics
NASA	National Aeronautics and Space Administration

Acknowledgement

References

[1] Waldmann, A., *Unsteady wake flow analysis of an aircraft under low-speed stall conditions using DES and PIV*, In 53rd AIAA Aerospace Sciences Meeting, 1096, 2015.

[2] Yokokawa, Y., Murayama, M., Ito, T., Yamamoto, K., *Experiment and CFD of a high-lift configuration civil transport aircraft model*, In 25th AIAA aerodynamic measurement technology and ground testing conference, 3452, 2006.

[3] Johnson, F.T., Tinoco, E.N., Yu, N.J., *Thirty years of development and application of CFD at Boeing Commercial Airplanes, Seattle*, Computers & Fluids, 34(10), 1115-1151, 2005.

[4] Sogukpinar, H., *Numerical investigation of influence of diverse winglet configuration on induced drag*, Iranian Journal of Science and Technology, Transactions of Mechanical Engineering, 44, 1-13, 2019.

[5] Gursul, I., Gordnier, R., Visbal, M., *Unsteady aerodynamics of nonslender delta wings*, Progress in Aerospace Sciences, 41(7), 515-557, 2005.

[6] Canpolat, C., Yayla, S., Sahin, B., Akilli, H., *Dye visualization of the flow structure over a yawed nonslender delta wing*, Journal of Aircraft, 46(5), 1818-1822, 2009.

[7] Muir, R.E., Arredondo-Galeana, A., Viola, I.M., *The leading-edge vortex of swift wing-shaped delta wings*, Royal Society Open Science, 4(8), 170077, 2017.

[8] Jardin, T., David, L., *Spanwise gradients in flow speed help stabilize leading-edge vortices on revolving wings*, Physical Review E, 90(1), 013011, 2014.

[9] Yaniktepe, B., Rockwell, D., *Flow structure on diamond and lambda planforms: Trailing-edge region*, AIAA journal, 43(7), 1490-1500, 2005.

[10] Yaniktepe, B., Ozalp, C., Canpolat, C., *Aerodynamics and flow characteristics of X-45 delta wing planform*, Kahramanmaras Sutcu Imam University Journal of Engineering Sciences, 19(1), 1-10, 2016.

[11] Canpolat, C., Yayla S., Sahin, B., Akilli, H., *Observation of the Vortical Flow over a Yawed Delta Wing*, Journal of Aerospace Engineering, 25, 613-626, 2012.

[12] Watanabe, S., Kato, H., *Stereo PIV applications to large-scale low-speed wind tunnels*, In 41st Aerospace Sciences Meeting and Exhibit, 919, 2003.

[13] Watanabe, S., Mungal, M.G., *Velocity field measurements of mixing-enhanced compressible shear layer*s, AIAA, 99-0088, 1999.

[14] Humphreys, W.M., *A survey of particle image velocimetry applications in Langley Aerospace Facilities*, AIAA Paper, 93-0411, 1993.

[15] Wiegand, C., *F-35 Air vehicle technology overview*, 2018 Aviation Technology, Integration, and Operations Conference, 1-28, 2018.

[16] Raffel, M., Willert, C.E., Wereley, S.T., Kompenhans, J., *Particle image velocimetry: A practical guide*, 2nd ed., Springer, 2007.

[17] Arroyo, M.P., Greated, C.A., *Stereoscopic particle image velocimetry*, Measurement Science & Technology, 2(12), 1181-1186, 1991.

[18] Westerweel, J., *Digital particle image velocimetry, Theory and Application*, Delft University Press, 1993.

[19] Adrian, R.J., *Twenty years of particle image velocimetry*, Experimental Fluids, 39, 159–169, 2005.

[20] Raffel, M., Willert, C.E., Wereley, S.T., Kompenhans, J., *Particle image velocimetry: A practical guide, 2nd ed.*, Springer, 2007.

[21] Menter, F.R., *Two-equation Eddy-viscosity turbulence models for engineering applications*, AIAA Journal, 32(8), 1598-1605, 1994.

[22] Menter, F.R., Kuntz, M., Langtry, R., *Ten years of ındustrial experience with the SST turbulence model*, Turbulence Heat and Mass Transfer, 4, 625-632, 2003.

[23] COMSOL CFD Module user guide, http://www.comsol.com (Accessed on April 8, 2019).

[24] Fontes, E., *Using the algebraic multigrid (AMG) method for large CFD simulations*, https://www.comsol.com (Accessed on April 8, 2019).

[25] Sogukpinar, H., *Effect of hairy surface on heat production and thermal insulation on the building*, Environmental Progress & Sustainable Energy, e13435, 1-8, 2020.

[26] Cummings, R.M., Scott, A.M., and Stefan, G.S., *Numerical prediction and wind tunnel experiment for a pitching unmanned combat air vehicle*, Aerospace Science and Technology, 12(5), 355-364, 2008.

[27] Sogukpinar, H., *Low speed numerical aerodynamic analysis of new designed 3D transport aircraft*, International Journal of Engineering Technologies, 4(4), 153-160, 2019.

[28] Sogukpinar, H., *Numerical calculation of wind tip vortex formation for different wingtip devices*, INCAS Bulletin, 10(3), 167-176, 2018.

The Effect of Morphology of Photoanode on Photovoltaic Properties of ZnO-DSSC

Halil EŞGİN[1],*, Yasemin ÇAĞLAR[2]

[1]*Cukurova University, Central Research Laboratory, Adana, Turkey*
esginhalil@gmail.com, ORCID: 0000-0001-6659-5519
[2]*Eskisehir Technical University, Faculty of Science, Department of Physics, Yunusemre Campus,*
Eskisehir, Turkey
yasemincaglar@eskisehir.edu.tr, ORCID: 0000-0001-8462-0925

Abstract

In this work, ZnO nanopowders with different morphology such as nanoleafy and nanosphere were synthesized by hydrothermal method. The X-ray Diffraction (XRD) spectra have showed that ZnO nanopowders synthesized in different morphologies have a highly crystallized hexagonal structure. Scanning Electron Microscopy (SEM) was used to examine the morphology of nanopowders and revealed that they were formed in the nanoleafy and nanosphere structure. Dye-Sensitized Solar Cell (DSSC) fabrication was performed by using ZnO nanopowders as a photoelectrode. The Dye-Sensitized Solar Cells (DSSCs) were immersed in N719 dye at 4h and the performance of the cells (conversion efficiency, open circuit voltage, fill factor and short circuit current) of ZnO-DSSCs were obtained. It has been observed the highest efficiency value of 1.59% for nanosphere ZnO:DSSC.

Keywords: ZnO nanopowders; Hydrothermal method; DSSC.

ZnO-DSSC'lerin Fotovoltaik Özelliklerine Fotoanodun Morfolojisinin Etkisi

Öz

Bu çalışmada, nano küre ve yaprak benzeri gibi farklı morfolojiye sahip ZnO nanotozları hidrotermal yöntemle sentezlenmiştir. Farklı morfolojilerde sentezlenen ZnO nanotozlarının, hegzagonal yapıda kristallendikleri XRD spektrumlarından belirlenmiştir. Nanotozların morfolojisini incelemek için Taramalı Elektron Mikroskobu (SEM) kullanılmış ve yapılarda nano boyutta yaprağımsı ve küresel fomlar gözlenmiştir. DSSC fabrikasyonu, farklı morfolojilerde ZnO tozları kullanılarak yapılmıştır. DSSC'ler 4 saat N719 boyasına daldırılmış ve ZnO-DSSC'lerin hücrelerinin pil performansları (kısa devre akımı, açık devre voltajı, verimi ve dolum faktörü) belirlenmiştir. En yüksek verim değeri, küre benzeri nano yapıya sahip ZnO: DSSC için %1.59 olarak bulunmuştur.

Anahtar Kelimeler: ZnO nanotozları; Hidrotermal metot; DSSC.

1. Introduction

Until now, due to the increasing energy demand and fossil fuel consumption, finding approaches to convert light from solar to electrical energy has become the focus of the world energy field. The most common and reliable energy source is the light from the sun. However, the cost and efficiency of solar power generation are one of the biggest barriers to transition to environmentally friendly and sustainable technology. DSSCs, which are the third-generation photovoltaic devices, has attracted great attention in the last two decades due to its good aspects such as low production cost, simple production process and higher energy conversion efficiency. DSSCs have many advantages compared to other photovoltaic devices due to their superior performance even under low intensity light, low reflection angle and high temperature conditions.

Various factors play important roles in the selection of semiconductors in DSSCs. First of all, the selected semiconductor should facilitate charge separation, effective electronic coupling and minimize recombination. Hence, the semiconductor must have band energy and density of state compatible with the energy levels of the dye. Secondly, the semiconductor morphology should offer a high surface area to provide high light absorption through the dye layer, while at the same time it should provide good electrical conduction to the substrate [1].

In DSSCs, charge separation takes place by electron transfer from the dye excited under light to the conduction band of the photoanode. Generally, titanium oxide (TiO_2) has been used as a photoanode in DSSCs. But zinc oxide (ZnO), which has better electrical properties than TiO_2, is considered to be the best alternative to be used in DSSCs [2].

The circuit elements to be prepared with nanostructured semiconducting materials may exhibit a different characteristic from the electronic circuit elements prepared with typical

semiconductors, resulting in the change of the electronic circuit performances of these materials. In order to increase the efficiency of DSSCs, some studies have been performed for the preparation of ZnO films, which are promising as photo-anodes in different morphologies [1-3]. In the literature, the techniques such as hydrothermal [4], thermal decomposition [5], microwave assisted hydrothermal [6], sol-gel method [7] are used to obtain ZnO nanopowder. The hydrothermal method is a method based on high-pressure crystallization from high temperature aqueous solutions. Due to the advantages such as low cost, low temperature, potential controllability in terms of shape and size, the unexpected hydrothermal method allows the formation of nano-morphologies that cannot be obtained by conventional reactions and their associated traditional methods [8].

Nanostructured ZnO can be produced in different morphologies such as sphere, nanowire, nanosheets, and nanoflower with this method. Morphology has a significant effect on DSSC efficiency. In recent years, ZnO nanostructure has been produced in different morphologies by hydrothermal method and DSSCs have been created using these powders. Zhu et al. [9] produced ZnO crystals with different morphologies, such as micro rods, hierarchical microspheres and hollow microspheres by hydrothermal method. They found the efficiency (1.42%) of DSSC made with ZnO in hierarchical microspheres structure higher than that of DSSC in other morphology. They attributed the reason for this high efficiency to better hierarchical microspheres to absorb higher dye molecules and better light scattering. Wang and his colleagues [10] synthesized nanorod and nanoflower like ZnO nanocrystals by hydrothermal method using hexadecyl trimethyl ammonium bromide (CTAB). They observed that the efficiency (1.37%) of DSSC produced with nanoflower ZnO was higher than that of DSSC using nanorod. The authors said that the capacity of the flower structure to absorb the dye increases efficiency because it is more than the rod structure. Three-dimensional (3D) ZnO hierarchical microspheres consisting of nanorods were synthesized by Li et al. [11] by hydrothermal method without any surfactant. The authors changed the morphology of ZnO powders by changing reaction conditions such as reaction temperature and reaction time. They found the efficiency of the DSSC produced with the nanosheet ZnO to be 3.75%. They emphasized that nanorod ZnO hierarchical structures show excellent photoelectric properties due to the high surface area and relatively fast electronic transmission path.

One of the parameters played an important role on the electrical performance of DSSCs is the structural morphology of the photoanode. Therefore, in this study, ZnO nanostructures were obtained at two different morphologies by hydrothermal synthesis method and the effects of these structures on the cell parameters have been investigated in detail.

2. Experimental Details

2.1. Deposition of ZnO nanopowders

The ZnO nanopowders were synthesized by the hydrothermal method. Zinc nitrate hexahydrate ($Zn(NO_3)_2.6H_2O$, Sigma-Aldrich) and sodium hydroxide (NaOH, Sigma-Aldrich) were used as initial materials for the ZnO nanopowders. Sodium dodecyl sulfate ($NaC_{12}H_{25}SO_4$, Sigma-Aldrich, SDS) and N-(1-Naphthyl) ethylenediamine dihydrochloride, (Sigma Aldrich, NND) were used as surfactant. SDS was used in the sample named as ZnO-1 and NND was used in the sample named as ZnO-2. To obtain a starting solution, $Zn(NO_3)_2.6H_2O$ and surfactant were dissolved in water by mixing the appropriate stoichiometric ratios of initial materials in 10 minutes and stirred for 30 minutes. After adding NaOH to starting solution by dropwise, the resulting solution was placed to 100 mL capacity of Teflon coated stainless steel autoclave. The teflon-lined stainless-steel autoclave was heated at 140 °C for 12 h. Subsequently, the autoclave was then left to cool at room temperature. The final white precipitates were collected by centrifugation and washed with deionized water and ethanol respectively. The ZnO powder were dried in an oven at 60 °C.

2.2. DSSC fabrication

Firstly, Fluorine-doped tin oxide (FTO) substrates were cleaned for 15 minutes in an ultrasonic bath and were dried in nitrogen ambient. The paste of ZnO-1 and ZnO-2 nanopowders were made using ethanol, Triton-X 100 and acetyl acetone. The obtained pastes were spread onto the FTO glass using the doctor blade method. In this method, plastic tapes were used to squeeze the paste onto the FTO substrate. The ZnO-1 and ZnO-2 films were annealed for 4 h at 450 °C in air and then cooled. And then, the ZnO films were immersed into a 0.5 mM N719 for 4 hours. Finally, the dye loaded films were combined with Pt counter electrodes to give shape to DSSCs, such as sandwich-type, using a sealing tape. The cell active area is 0.36 cm^2. The schematic structure and arrangement of each component of the obtained DSSC is shown in Fig. 1.
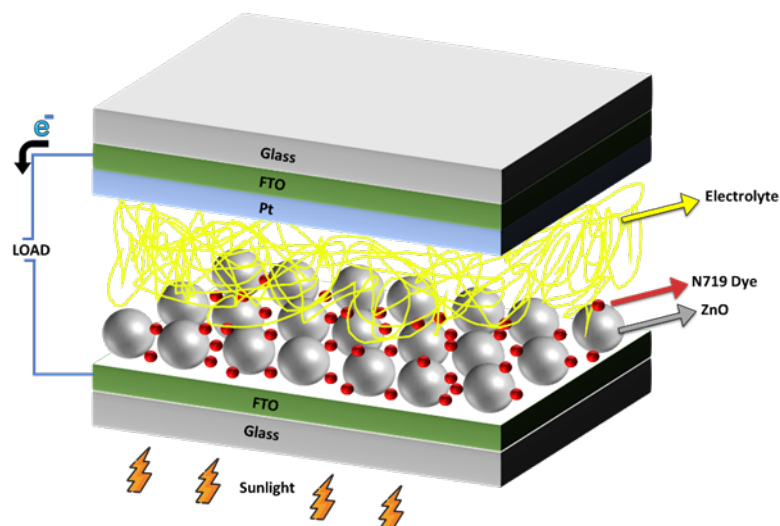
Figure 1: The components of a DSSC

The structure consists of conductive glass substrates (FTO), a dye-sensitive metal oxide semiconductor electrode (ZnO), a dye material (N719), a catalyst counter electrode (Pt) and an electrolyte solution (Iodolyte) placed between the two electrodes.

2.3. Characterization of ZnO and DSSCs

X-ray diffraction (XRD, Rigaku SMARTLAB) was used to analyse the phase of ZnO nanopowders. The morphology of ZnO nanopowders have been performed with TESCAN MAIA3 Scanning Electron Microscopy (SEM). The reflectance and absorbance measurements were performed with SHIMADZU UV-2450 spectrophotometer. The photovoltaic measurements of the DSSCs were recorded employing a solar cell measurement system (FYTRONIX OPTOSENSE).

3. Results and Discussion

Fig. 2 shows the XRD pattern of produced ZnO-1 and ZnO-2. All of the diffraction peaks are in good agreement with hexagonal structure and in polycrystalline form (ICCD card no 01-079-02006). No other characteristic peaks of the surfactant, reactant or $Zn(OH)_2$ are found. It has been found that the production method is suitable to obtain fairly pure products. The intensities of the diffraction peaks of ZnO-1 appear to be higher compared to ZnO-2 obtained using NND. This can be explained by the higher crystallinity and particle size of the ZnO-1 nanopowder, taking into account the structural parameters shown in the Table 1.
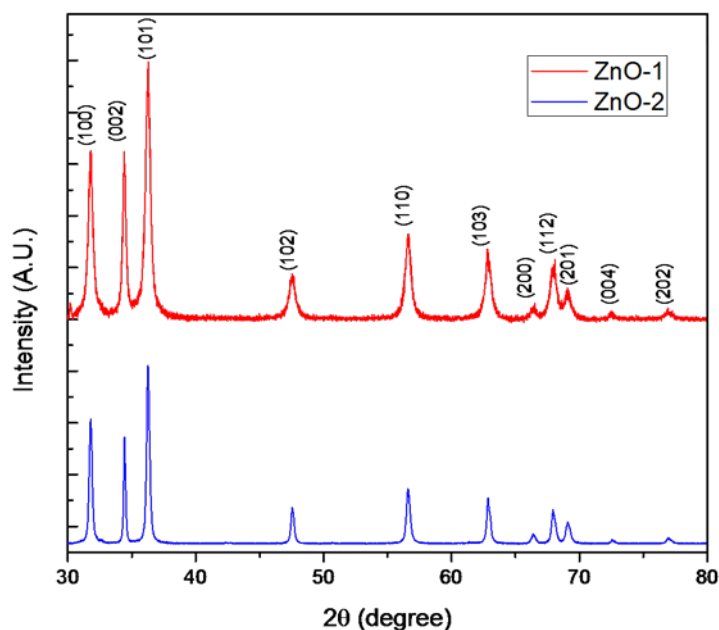
Figure 2: The X-ray diffraction pattern of the ZnO-1 and ZnO-2 nanopowders

Using different surfactants in the starting solution led to a change in crystallinity and particle size. According to the Debye-Scherrer formula, the average crystallite sizes of ZnO-1 and ZnO-2 are calculated through the (101) planes as 65.48 nm, 38.60 nm respectively.

Table 1: Structural parameters of the ZnO nanopowders

|	(hkl)	2θ (degree)	d (Å)	D (nm)		(hkl)	2θ (degree)	d (Å)	D (nm)
	(100)	31.756	2.8155			(100)	31.743	2.8167	
	(002)	34.428	2.60286			(002)	34.404	2.6046	
	(101)	36.231	2.47738	65.48		(101)	36.240	2.4768	38.60
	(102)	47.529	1.91151			(102)	47.536	1.9112	
	(110)	56.582	1.62527			(110)	56.608	1.6246	
ZnO-1	(103)	62.846	1.47750		**ZnO-2**	(103)	62.736	1.4798	
	(200)	66.386	1.4070			(200)	66.27	1.4092	
	(112)	67.931	1.37874			(112)	67.952	1.3784	
	(201)	69.059	1.35895			(201)	69.05	1.3590	
	(004)	72.551	1.30191			(004)	72.46	1.3033	
	(202)	76.908	1.23864			(202)	76.92	1.2385	

The effect of using different surfactants on morphology of ZnO nanopowders was determined by examining SEM images. The SEM images of the ZnO nanopowders are given in Fig. 3.
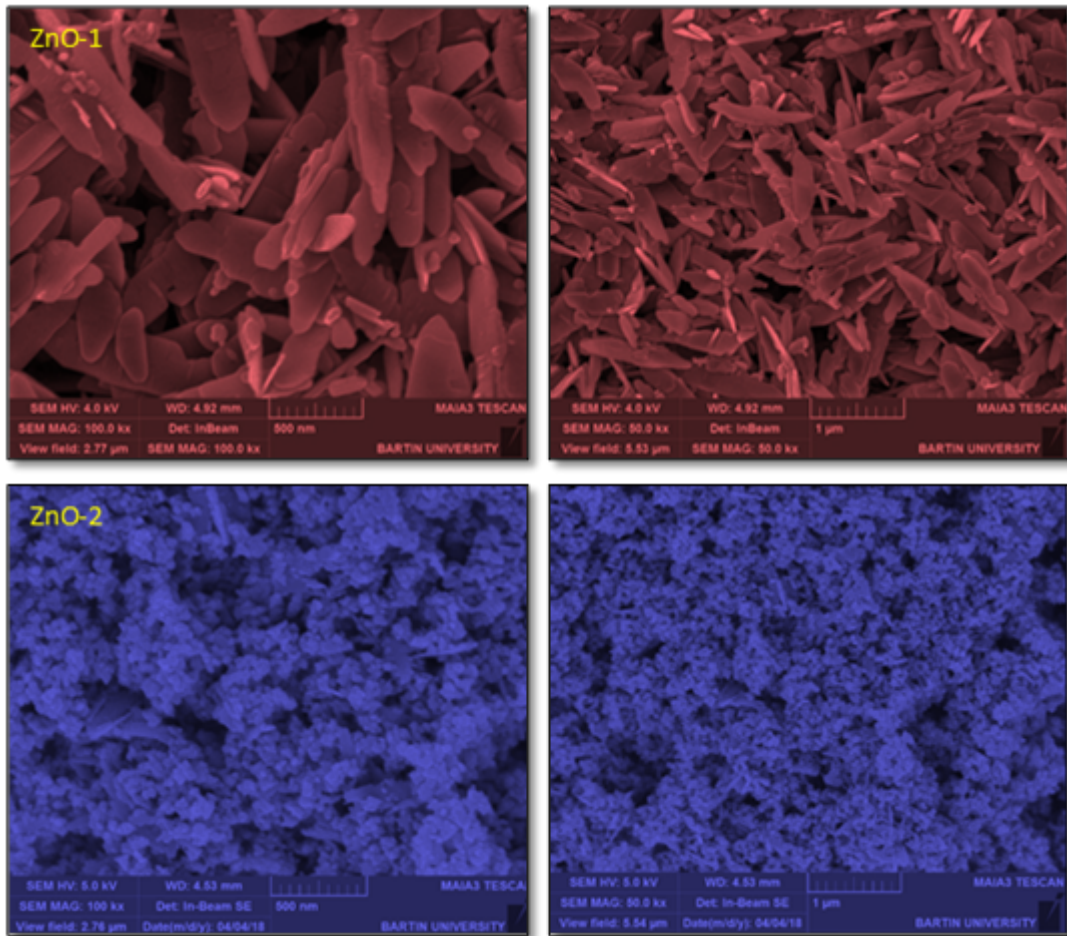
Figure 3: SEM images of the ZnO-1 and ZnO-2 nanopowders (left side ×100k, right side ×50k)

As seen from these images, ZnO-1 nanopowder prepared with SDS surfactant in starting solution has a sheet-like shape (nanoleafy) structure. ZnO-2 nanopowder is composed of nanospheres. The structure of ZnO-1 nanopowder consists of approximately 500×200×30 nm nanoleafy ZnO nanostructures, while ZnO-2 nanopowder consists of approximately 40 nm nanospheres. Both samples were found to have a homogeneous distribution.

The energy band diagram of DSSC, which shows the HOMO / LUMO levels of the N719 dye, the working function of the FTO, the reduction potential of the electrolyte and the conduction band (CB) and valance band (VB) band levels of ZnO, is schematically shown in Fig. 4. Accordingly, ZnO's CB and VB energy levels are lower than the N719 paint's LUMO and HOMO energy levels. Therefore, the photogenerated electrons in the dye can be collected from ZnO and quickly transferred to the FTO.
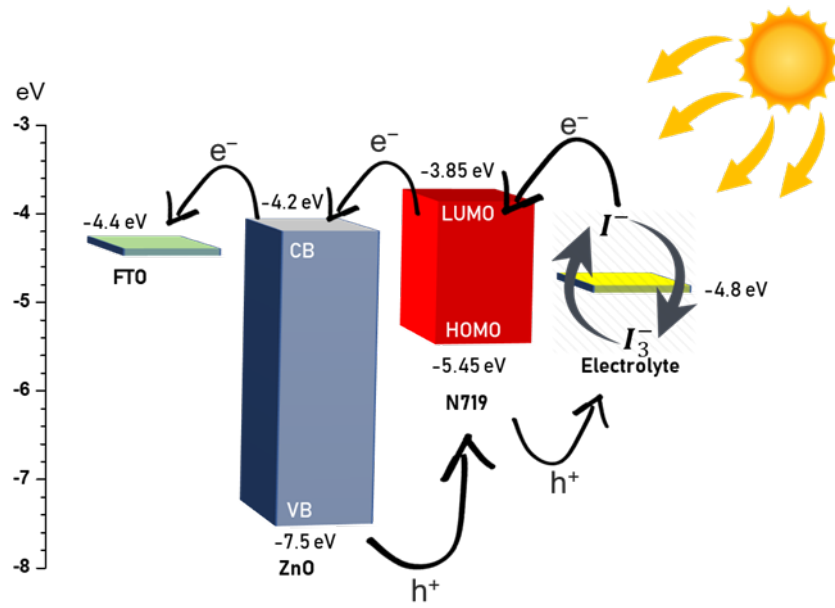
Figure 4: Schematic energy band diagram for FTO, ZnO and N719 dye

The energy conversion efficiency (*n%*) of the DSSCs varies depending on the short circuit photo current density (J_{sc}), open circuit photovoltage (V_{oc}), the filling factor of the cell (*FF*) and the intensity of the incident light (P_{in}) [12]. Based on the solar cell parameters of DSSCs, cell efficiency (*η*) and fill factor (*FF*) can be defined as follows:

$$\eta(\%) = \frac{FF x V_{oc} x I_{sc}}{P_{in}} x100 \tag{1}$$

$$FF(\%) = \frac{V_{max} x I_{max}}{V_{oc} x I_{sc}} x100 \tag{2}$$

where V_{max} and I_{max} are the voltage and current at maximum power output, respectively [13]. The interaction of photo anodes, dye molecules, FTO substrates, counter electrodes and electrolytes with each other is highly effective on the solar cell parameters mentioned above. The basis of the operation of the DSSCs is that the dye molecules attached to the photo anode absorbs the photons from sunlight and turn themselves into the excited state. The electric field caused by the difference between the energy levels of photo anode and dye molecules drags the excited electrons into the conduction band of the ZnO photoanode. Then the electron moves to the counter electrode (CE) to complete the circuit [14].
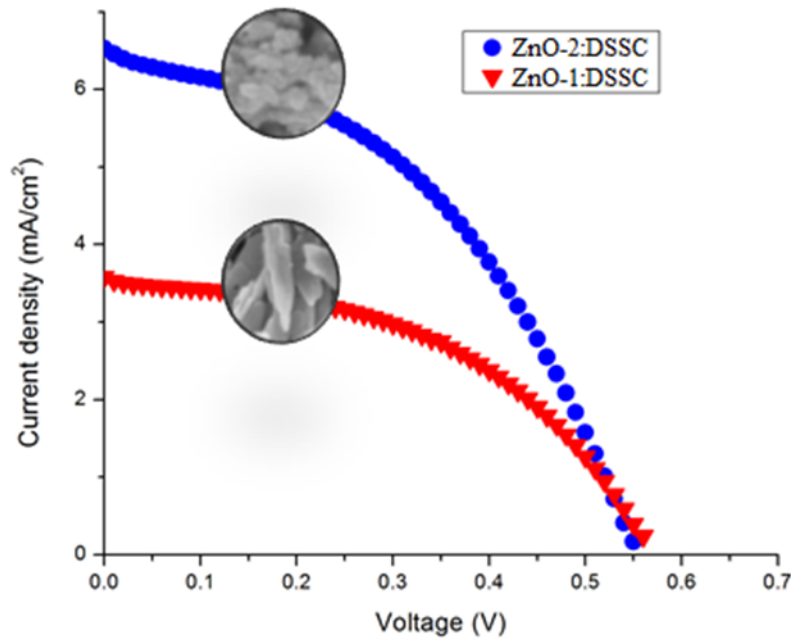
Figure 5: *J-V* graph of ZnO-DSSCs

Table 2: The photovoltaic parameters of ZnO-DSSCs

| DSSC	J_{sc} (mA/cm^2)	V_{oc} (V)	n (%)	FF (%)
ZnO-1:DSSC	3.58	0.56	1.02	51
ZnO-2:DSSC	6.53	0.55	1.59	44

The current density vs voltage graph of the DSSCs is given in Fig. 5 and corresponding parameters such as J_{sc}, V_{oc}, FF and n% values are summarized in Table 2. The V_{oc} values of both DSSCs are around 0.55 V. Because the difference between the potential of the redox couple in the electrolyte and the quasi Fermi level energies of ZnO, this value did not change [9]. However, the DSSC parameters made with nanosphere ZnO are higher than the parameters of the cell made with nanosheet ZnO. As known, the greater the amount of dye loading in a DSSC, the greater the photo-current density. At the same time, a greater amount of dye loading ensures that the incident lights are completely absorbed, resulting in a greater short circuit current density. To determine this, the absorbance wavelength measurements of the films immersed for 4 hours in N719 dye were taken and given in Fig. 6. As seen from this figure, the ZnO-2 film has a higher absorbance value than the other film in the visible region. Also, the observed peak at about 385 nm belongs to absorption edge of ZnO.
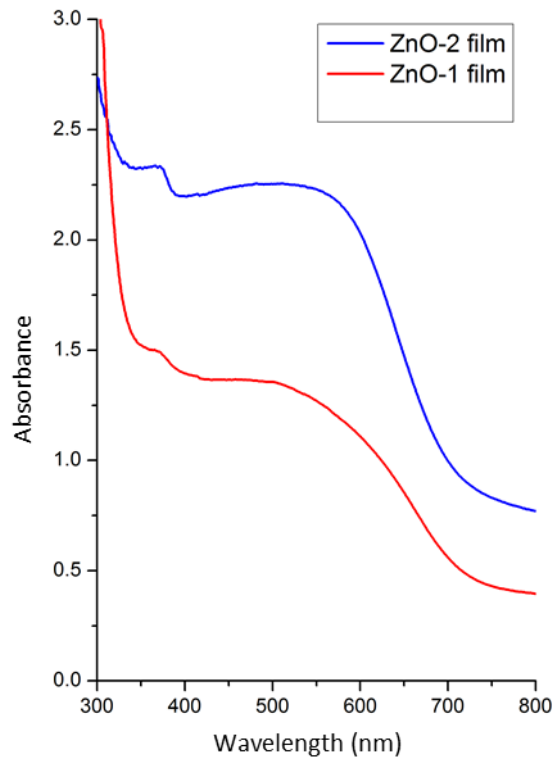
Figure 6: Absorbance graphs of ZnO-1 film and ZnO-2 film

Consequently, the more dye loading is done, the more photogenic electrons and higher photo current. Also, considering that the ZnO-2 film is in nanosphere morphology, its surface area is higher than that of the nanoleafy film. This increase in surface area increased dye loading and consequently increased cell efficiency to 1.59%.

Another way to improve photocurrent is to create higher scattering ability of the photoanode. To investigate the light scattering properties of ZnO films, reflectance spectra were also measured and shown in Fig. 7. The R% value of nanosheet film (ZnO-2 film) was 76% at 400-800 nm, which was higher than the other film. The high reflectance value increased the photocurrent value of ZnO-2:DSSC compared to other DSSC. Therefore, the fact that nanosphere structured ZnO films have higher dye loading and light scattering ability compared to nanoleafy films contributed to high efficiency, resulting in increased photocurrent density and overall power conversion efficiency.
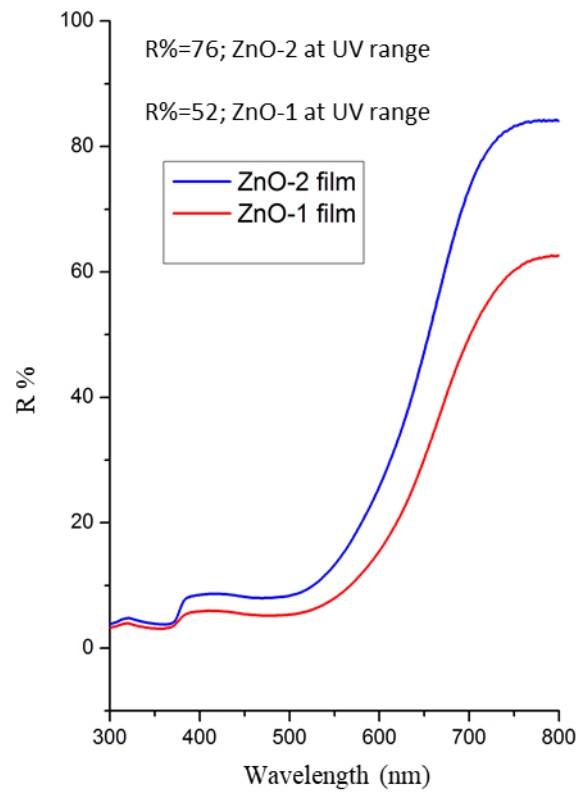
Figure 7: Reflectance graphs of ZnO-1 film and ZnO-2 film

4. Conclusion

In the study, the effect of ZnO photoanodes morphologies on solar cell parameters was investigated. For this purpose, ZnO nanospheres and nanoleafy powders with different morphologies were synthesized by hydrothermal synthesis method and used as photoanode in DSSCs. It has been determined that the synthesized nanopowders have high homogeneity and good crystallinity by structural and morphological analysis. It has been seen from the absorbance curves that ZnO-2 film has higher dye absorption capacity. Thus, ZnO-2 nanospheres absorbed more dye and showed higher device performance with much smaller grain size. In addition, ZnO-2 film with higher reflectance values, more light scattering, contributed positively to the efficiency. DSSC photoelectrodes were successfully fabricated using N719 dye sensitized ZnO nanopowders. DSSC fabricated with prepared ZnO nanosphere attains a reasonable overall conversion efficiency of 1.59%, with good J_{SC} of 6.53 mA/cm^2, V_{OC} of 0.55 V and FF of 0.44 under sunlight intensity of 100 mW/cm^2.

Acknowledgement

References

[1] Baxter, J.B., Aydil, E.S., *Dye-sensitized solar cells based on semiconductor morphologies with ZnO nanowires,* Solar Energy Materials and Solar Cells, 90(5), 607–622, 2006.

[2] Chandiran, A.K., Abdi-Jalebi, M., Nazeeruddin, M.K., Grätzel, M., *Analysis of Electron Transfer Properties of ZnO and TiO₂ Photoanodes for Dye-Sensitized Solar Cells*, ACS Nano, 8(3), 2261–2268, 2014.

[3] Xu, F., Sun, L., *Solution-derived ZnO nanostructures for photoanodes of dye-sensitized solar cells*, Energy & Environmental Science, 4(3), 818–841, 2011.

[4] Qiu, Y., Chen, W., Yang, S., *Facile hydrothermal preparation of hierarchically assembled, porous single-crystalline ZnO nanoplates and their application in dye-sensitized solar cells*, Journal of Materials Chemistry, 20(5), 1001–1006, 2010.

[5] Alp, E., Araz, E.C., Buluç, A.F., Güner, Y., Değer, Y., Eşgin, H., Dermenci, K.B., Kazmanlı, M.K., Turan, S., Genç, A., *Mesoporous nanocrystalline ZnO microspheres by ethylene glycol mediated thermal decomposition*, Advanced Powder Technology, 29(12), 2018.

[6] Krishnapriya, R., Praneetha, S., Murugan, A.V., *Investigation of the effect of reaction parameters on the microwave-assisted hydrothermal synthesis of hierarchical jasmine-flower-like ZnO nanostructures for dye-sensitized solar cells*, New Journal of Chemistry, 40(6), 5080–5089, 2016.

[7] Rani, S., Suri, P., Shishodia, P.K., Mehra, R.M., *Synthesis of nanocrystalline ZnO powder via sol–gel route for dye-sensitized solar cells*, Solar Energy Materials and Solar Cells, 92(12), 1639–1645, 2008.

[8] Xu, H., Wang, H., Zhang, Y., He, W., Zhu, M., Wang, B., Yan, H., *Hydrothermal synthesis of zinc oxide powders with controllable morphology*, Ceramics International, 30(1), 93–97, 2004.

[9] Zhu, S., Tian, X., Chen, J., Shan, L., Xu, X., Zhou, Z., *A Facile Approach to Construct Multiple Structured ZnO Crystals by Trisodium Citrate-Assisted Hydrothermal Growth Toward Performance Enhancement of Dye-Sensitized Solar Cells*, Journal of Physical Chemistry C, 118(30), 16401–16407, 2013.

[10] Wang, C., Zhang, X., Wang, D., Yang, Z., Ji, W., Zhang, C., Zhao, Y., *Synthesis of nanostructural ZnO using hydrothermal method for dye-sensitized solar cells*, Science China Technological Sciences, 53(4), 1146–1149, 2010.

[11] Li, D., Li, Y., Zhang, Y., Chang, F., *Facile synthesis of three-dimensional ZnO hierarchical microspheres composed of well-ordered nanorods by hydrothermal method*, Results in Physics, 12, 953–958, 2019.

[12] Hongsith, K., Hongsith, N., Wongratanaphisan, D., Gardchareon, A., Phadungdhitidhada, S., Singjai, P., Choopun, S., *Sparking deposited ZnO nanoparticles as double-layered photoelectrode in ZnO dye-sensitized solar cell*, Thin Solid Films, 539, 260–266, 2013.

[13] Khan, M.Z.H., Al-Mamun, M.R., Halder, P.K., Aziz, M.A., *Performance improvement of modified dye-sensitized solar cells*, Renewable and Sustainable Energy Reviews, 71, 602–617, 2017.

[14] Rathnasamy, R., Thangasamy, P., Thangamuthu, R., Sampath, S., Alagan, V., *Green synthesis of ZnO nanoparticles using Carica papaya leaf extracts for photocatalytic and*

photovoltaic applications, Journal of Materials Science: Materials in Electronics, 28(14), 10374–10381, 2017.

Investigation of Structural Properties and Martensitic Phase Transformations in Heat-treated Ni-25.5 at. %Ta High Temperature Shape Memory Alloys

Koksal YILDIZ[1],*

[1]*Firat University, Faculty of Science, Department of Physics, Elazig, TURKEY*
kyildiz@firat.edu.tr, ORCID: 0000-0002-3484-4653

Abstract

The effect of heat treatment performed at 800 °C, 900 °C and 1000 °C for 1 hour on structural and martensitic transformation properties of Ni-25.5 at.%Ta high temperature shape memory alloy has been examined. Morphological observations by SEM-EDS showed that the heat treatment affected directly microstructural properties of the alloy. Microstructure of the heat treated samples is composed of intermetallic Ni-rich Ni_8Ta and Ta-rich $NiTa_2$ compound in the Ni_3Ta matrix. In addition to these phases, orthorhombic Ni_3Ta phase was only observed in the sample heat-treated at 1000 °C. Structural investigations of alloy the samples by XRD indicated that the martensitic crystal orientation of the samples changed with heat treatments. DSC measurements revealed that all the samples displayed high temperature shape memory behavior with martensitic transformation temperatures of above 200 °C. Vicker's microhardness measurements showed that the microhardness of the alloy influenced dramatically by applying heat treatments, especially at 800 and 900 °C.

Keywords: Ni_3Ta; Martensite; Heat treatment.

Isıl İşlem Uygulanmış Ni-25,5 at. %Ta Yüksek Sıcaklık Şekil Hatırlamalı Alaşımlarındaki Yapısal Özelliklerin ve Martensitik Faz Dönüşümlerinin İncelenmesi

Öz

1 saat boyunca 800 °C, 900 °C ve 1000 °C'de gerçekleştirilen ısıl işlemin, Ni-25,5 at.% Ta yüksek sıcaklık şekil hatırlamalı alaşımının yapısal ve martensitik dönüşüm özellikleri üzerindeki etkisi incelenmiştir. SEM-EDS analizleri ile gerçekleştirilen morfolojik gözlemler, ısıl işlemin alaşımın mikroyapısal özelliklerini doğrudan etkilediğini gösterdi. Isıl işlem uygulanmış numunelerin mikroyapısı, Ni_3Ta anafazı içerisinde dağılmış olan Ni oranınca zengin Ni_8Ta ve Ta oranınca zengin $NiTa_2$ intermetalik bileşiklerinden oluşur. Bu ikincil fazlara ek olarak, ortorombik Ni_3Ta fazı sadece 1000 °C'de ısıl işleme tabi tutulmuş numunede gözlenmiştir. XRD analizleri ile gerçekleştirilen yapısal analizler, numunelerin martensitik kristal yönelimlerinin ısıl işlemlerle değiştiğini göstermiştir. DSC ölçümleri, tüm numunelerin 200 °C'nin üzerindeki martensitik dönüşüm sıcaklıkları ile yüksek sıcaklık şekil hatırlama davranışı gösterdiğini ortaya koymuştur. Vickers mikro sertlik ölçümleri, alaşımın mikro sertliğinin özellikle 800 ve 900 °C'de uygulanan ısıl işlemlerden dramatik bir şekilde etkilendiğini gösterdi.

Anahtar Kelimeler: Ni_3Ta; Martensite; Isıl işlem.

1. Introduction

Shape memory alloys (SMAs) belong to a specific class of smart materials that can remember or retain their previous shape when exposed to thermomechanical or magnetic stimuli. Due to their unique and superior properties, these alloys have become very popular and attracted great interest in many commercial applications in recent years [1, 2]. Binary Ni-Ti alloy is already the most well-known and widely used SMA group and its martensitic transformation temperature is generally below 100 °C. However, at the present time, there is a need for SMAs with higher martensitic transformation temperatures of above 100 °C for high temperature applications, and there are many industrial application areas, at which high temperature SMAs are popular, e.g. sensors and actuators in automotive industry, rocket technologies, nuclear reactor systems and safety devices [3, 4]. Additionally, high-temperature SMAs should have reason for recoverable strain levels, long-term stability, plastic deformation, and adequate environmental resistance [5].

In recent years, binary Ni-Ta alloys, which have high melting temperature and exhibit excellent features in harsh environmental conditions, have attracted attention as a remarkable candidate material, especially for high temperature applications [6]. In 2008, Firstov *et al.* [7] discovered that the intermetallic Ni_3Ta compound also exhibited shape memory behavior with a

martensitic transformation temperature of above 300 °C. Thus, a new candidate material has been joined in SMA family. The martensitic transformation in intermetallic Ni_3Ta compound occurs resulting in transformation of tetragonal austenite phase to monoclinic martensite phase [8]. The possible phases in the phase diagram of binary Ni-Ta system are liquid solution, Ni-rich fcc-A1, and Ta-rich bcc-A2 solid solutions and intermetallic Ni_8Ta, Ni_3Ta, Ni_2Ta, NiTa and $NiTa_2$ compounds [9, 10]. However, there have been some uncertainties about crystal structures and properties of intermetallic phases in the Ni-Ta system. For example; intermetallic Ni_3Ta is polymorphic with three different crystal structures (orthorhombic Pmmn-Ni_3Ta, tetragonal $I4$/mmm-Ni_3Ta and monoclinic $P2_1$/m-Ni_3Ta) and which polymorphic phase is stable is still controversial. In addition, the mechanism of the shape memory effect exhibited by the intermetallic Ni_3Ta phase is also unclear [6]. Eventually, it is very important to understand the functional behaviors, such as shape memory effect, and characteristics of intermetallic phases in the binary Ni-Ta system.

The main purpose of this work was to examine the effect of heat treatment performed at 800 °C, 900 °C and 1000 °C for 1 hour on martensitic transformation behavior, morphological and structural properties of high temperature Ni-25.5 at.% Ta SMA were systematically examined by means of DSC, XRD, SEM-EDS and Vicker's microhardness measurements. The effects of heat treatments performed at high temperatures on some physical properties of the non-stoichiometric Ni-Ta SMA, which exhibits shape memory behavior, are studied for the first time.

2. Materials and Methods

The Ni-25.5Ta (at.%) alloy was produced by using high purity nickel (Ni) and tantalum (Ta) powders in an arc-melting furnace under vacuum. The ingot was homogenized at 1400 °C for 4 hours in a furnace. After the homogenization process, the ingot was cut to different sizes for heat treatments to be performed at different temperatures. The samples were heat treated at 800 °C, 900 °C, and 1000 °C for 1 hour. Sample groups without heat treatment and subjected to heat treatment at 800 °C, 900 °C, and 1000 °C temperatures were labeled as NiTa-0, NiTa-800, NiTa-900 and NiTa-1000, respectively.

Transformation properties of the samples were examined by differential scanning calorimeter (SII NanoTechnology EXSTAR DSC 7000) measurements taken in a nitrogen gas atmosphere at a heating/cooling rate of 10 °C/min. Structural analysis of the samples were realized by taking X-ray diffractometer (Bruker Discover D8 XRD) patterns using Cu K_α radiation at room temperature. Morphological properties and chemical analysis of the samples were studied by carrying out scanning electron microscope (SEM, LEO EVO 40) images equipped with an

energy-dispersive X-ray spectrometer (EDS). The Vicker's microhardness measurements of the samples were performed by using Emco Test DuraScan at a load of 300 g and repeated for five times for each sample.

3. Results and discussion

Fig. 1 displays SEM images of NiTa-0, NiTa-800, NiTa-900 and NiTa-1000 samples. In Fig. 1-a, small-sized gray structures in the matrix of the NiTa-0 sample are clearly visible. From the EDS spectra, it was concluded that the chemical compositions of the matrix and grey structures were composed of 73.69 at.% Ni + 26.31 at.% Ta and 16.97 at.% Ni + 83.03 at.%Ta elements, respectively. According to EDS analyses, it is concluded that this area contains intermetallic Ta-rich $NiTa_2$, which has 1-3 μm in size, sparsely dispersed in the Ni_3Ta matrix. However, Ta content of grey structures in NiTa-0 sample is much higher than that in stoichiometric $NiTa_2$ compound and it is well-known that $NiTa_2$ is only phase with high Ta content in the binary Ni-Ta system. On account of this, it is thought that high Ta content of grey structures in the NiTa-0 sample may be a result of homogenization process. From this, it has been seen that the homogenization condition was not enough to form single phase supersaturated structure. In addition to small-sized Ta-rich $NiTa_2$ precipitate phase in the Ni_3Ta matrix (Fig. 1-a), Ni-rich Ni_8Ta precipitate phases were also observed, containing 83.94 at.% Ni + 16.06 at.% Ta, at different regions of the NiTa-0 sample. Biffi *et al.* [11] detected intermetallic Ni_8Ta and Ni_2Ta precipitates in microstructure of $Ni_{75}Ta_{24}B_1$ alloy homogenized at 1400 °C for 4 h. On the other hand, Firstov *et al.* [7] reported that the Ni_8Ta and Ni_2Ta precipitate phases located in the grain boundaries of the Ni_3Ta matrix were disappeared after the same homogenization condition as in Ref. [11]. They did not observe intermetallic $NiTa_2$ compounds in their alloy samples. Eventually, optimal homogenization condition for Ni-Ta alloys are needed to obtain single Ni_3Ta phase structure.
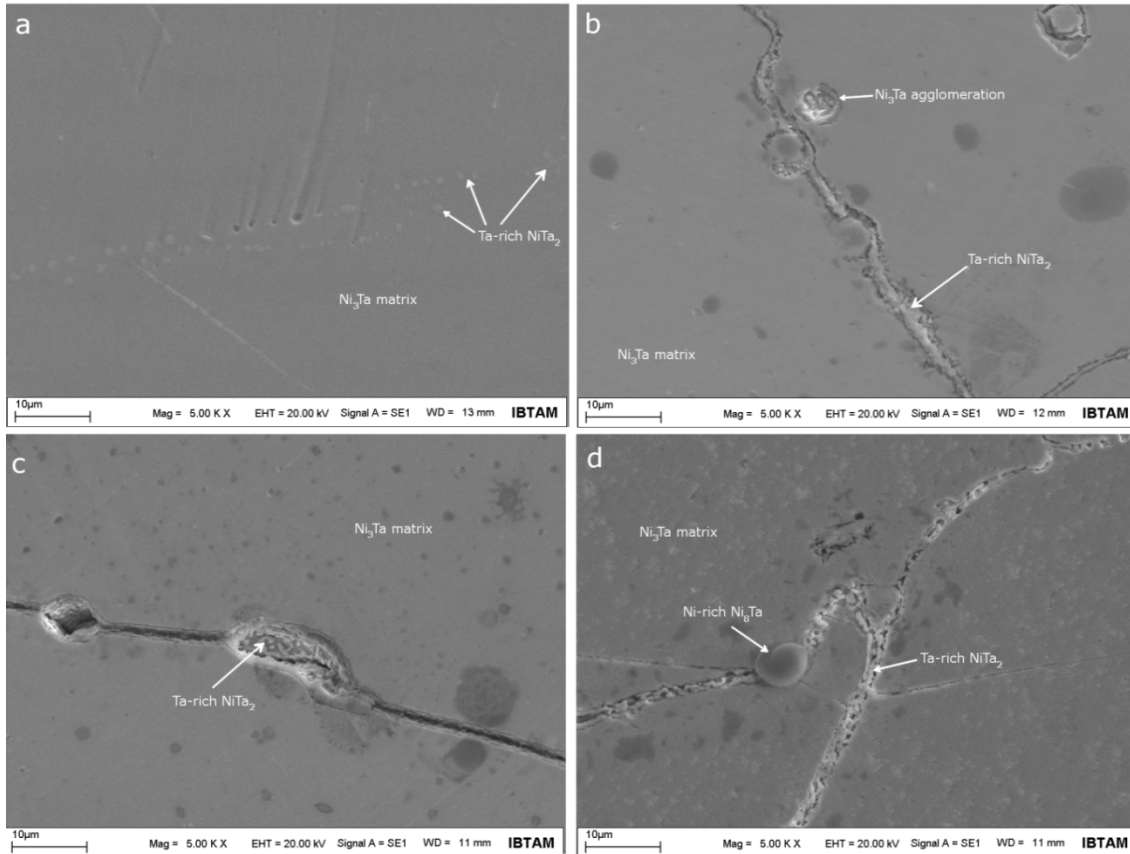
Figure 1: SEM images of (a) NiTa-0, (b) NiTa-800, (c) NiTa-900 and (d) NiTa-1000 alloy samples

The surface morphology of NiTa-800 sample is presented in Fig. 1-b. The heat treatment at 800 °C led to change in the microstructure of the alloy. The microstructure of NiTa-800 sample contains a large of cracks. Firstov *et al.* [7] reported that intergranular cracks were formed on the surface of Ni_3Ta alloy after homogenization process. However, it could be clearly seen that some secondary phase precipitates in the NiTa-800 sample located in the crack. In order to determine chemical composition of this secondary phase in the crack, point EDS analysis was made. According to EDS analysis, its chemical composition is 30.56 at.% Ni + 69.44 at.% Ta and it is concluded that this phase located in the crack is the Ta-rich $NiTa_2$ phase. From here, it was understood that the Ta-rich $NiTa_2$ phase nucleated and grown in the cracks. Also, in Fig. 1-b, structural agglomerates are observed in some areas of the matrix. According to EDS analysis taken, it was determined that this agglomerate structure in Fig. 1-b chemically included 72.65 at.% Ni + 27.35 at.% Ta elements and this is close to matrix composition. As a result, these agglomerates are not any secondary phases.

SEM image of the NiTa-900 sample is shown in Fig. 1-c. It is obvious that microstructural characteristics of the NiTa-900 sample are similar to that of the NiTa-800. EDS results revealed that the chemical composition of the gray structures in the crack was 20.13 at.% Ni + 79.87 at.%

Ta and these gray structures are the Ta-rich $NiTa_2$ phase as well as observed in NiTa-800 sample. In contrast, the agglomerates observed in NiTa-800 sample disappeared in NiTa-900 sample. In addition, intermetallic Ni_8Ta phase was also detected in some regions of NiTa-900 sample.

Fig. 1-d displays SEM image of the NiTa-1000 sample. Its microstructure contains many cracks and Ta-rich $NiTa_2$ phase (23.76 at.% Ni + 76.24 at.% Ta) located in these cracks. The chemical composition of NiTa-1000 matrix is 74.25 at.% Ni + 25.75 at.% Ta. In addition to these observations, a big-sized structure located on the crack is also visible in Fig. 1-d. Its chemical composition was analyzed by taking EDS spectrum and it is identified as Ni_8Ta phase with 86.68 at.% Ni + 13.32 at%Ta composition. Apart from similar morphological features of NiTa-1000 sample compared to NiTa-800 and NiTa-900 samples, a phase region exhibiting quite different morphological features were also observed in the NiTa-1000 sample. Fig. 2 shows the SEM image of this region. Chemical composition of these structures in Fig. 2 was determined by taking EDS spectra. According to EDS spectra, thin white structures contained 77.2 at.% Ni + 22.8 at.% Ta. From the results of EDS spectra, it is thought that thin white structures are orthorhombic Ni_3Ta phase. Aballe *et al.* [12] showed that prolonged aging process at 800 °C or above could be caused formation of the stable orthorhombic Ni_3Ta phase in Ni-25wt.% Ta-10wt.% Cr alloy by replacing the b.c.t. Ni_3Ta. Likewise, Kosorukova *et al.* [13] reported that as aging temperature increased the stable orthorhombic Ni_3Ta phase was formed in the Ni_3Ta alloy, as a result of diffusional phase transformation mechanism. Consequently, the results indicated that heat treatment performed at 1000 °C led to starts diffusional phase transformation in the Ni-25.5Ta (at.%) alloy.

The crack formation in the microstructure of the binary Ni-Ta shape memory alloy is an important issue after homogenization process. It is thought that cracks in the Ni-Ta SMA have a negative effect on its physical properties. Although there are some suggestions to hinder crack formation in the Ni-Ta SMAs [7], Yildiz [14] reported that it might be prevented from the crack formation by changing homogenization condition of Ni-Ta SMA.
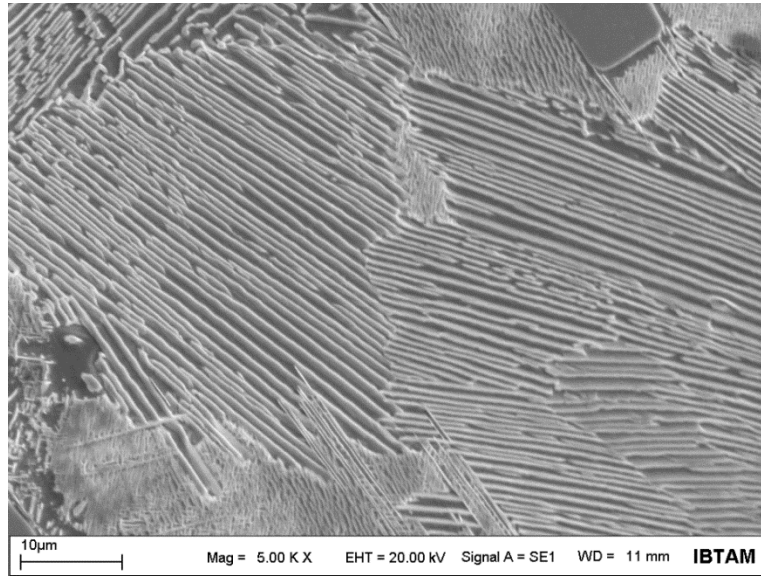
Figure 2: A SEM image showing the stable orthorhombic Ni₃Ta phase in NiTa-1000 sample
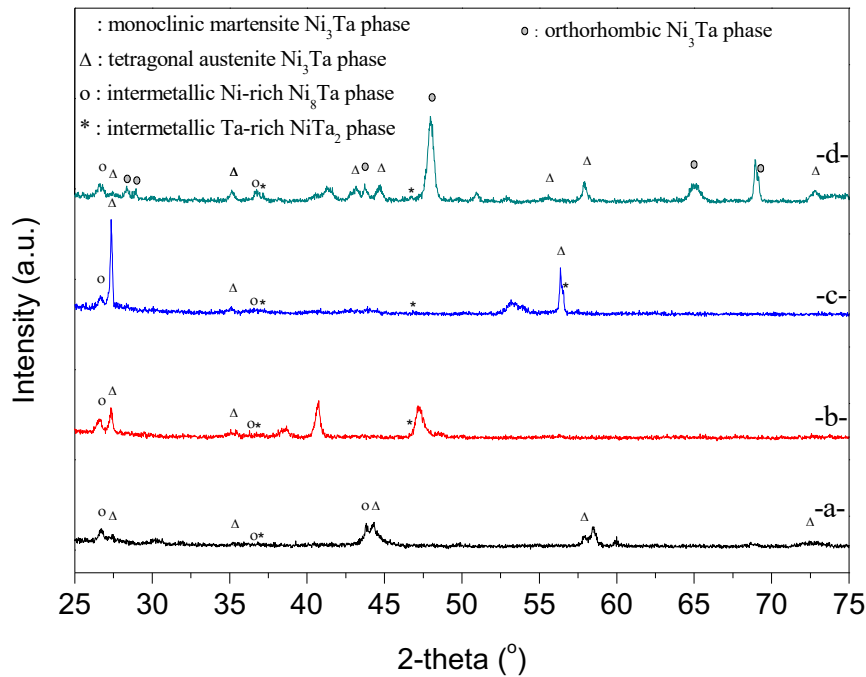

Figure 3: XRD patterns of (a) NiTa-0, (b) NiTa-800, (c) NiTa-900 and (d) NiTa-1000 samples

XRD patterns of NiTa-0, NiTa-800, NiTa-900 and NiTa-1000 samples are illustrated in Fig. 3. The XRD results are in good harmony with the SEM-EDS analysis of the samples. Fig. 3 demonstrates that NiTa-0, NiTa-800 and NiTa-900 samples contain structurally four different phase components: monoclinic martensite Ni_3Ta phase (PDF: 01-073-7070), tetragonal austenite Ni_3Ta phase (PDF: 00-018-0893), and intermetallic Ni_8Ta (PDF: 00-023-0438) and $NiTa_2$ (PDF: 01-072-2592) compounds. However, XRD pattern of NiTa-1000 sample also includes

orthorhombic Ni_3Ta phase (PDF:03-065-2588) in addition to mentioned phases above. The 2θ peak positions of the all phases are also in accordance with the literature [7, 8, 15, 16] and the corresponding phases are marked on patterns. Also, as expected, all samples contained austenite phase at room temperature [11, 13, 17]. The XRD pattern of NiTa-0 sample display in Fig. 3-a. Compared to the XRD patterns in Figs. 3-b and c, it is clear that the heat treatments performed at 800 °C and 900 °C resulted in significant changes on the crystallographic properties of the alloy. The main martensite phase peak located at $2\theta \approx 43.8^{\circ}$ in the XRD pattern of NiTa-0 sample was completely disappeared. However, the peak intensity at $2\theta \approx 27.4^{\circ}$, which is quite weak in the XRD pattern of the NiTa-0 sample, increases in the XRD pattern of NiTa-800 sample. As can be seen from the XRD pattern in Fig. 3-c, intensity of this peak is maximum for NiTa-900 sample. These results indicated that the heat treatments at 800 °C and 900 °C directly affected the martensite phase orientation of alloy. Both number and intensities of the $NiTa_2$ peaks in Fig. 3-c were also increased. This is in good agreement with the SEM observations in Figs. 1-b and c. Finally, from the XRD pattern of NiTa-1000 sample, as shown in Fig. 3-d, it can be clearly seen that the number of related phase peaks increased considerably. The maximum intensity peak in Fig. 3-d is the reflection at $2\theta \approx 47.9^{\circ}$ and the diffraction peaks for martensite and orthorhombic phases overlapped. This peak does not exist in the XRD pattern of NiTa-900 sample. The intensity of peak at $2\theta \approx 27.4^{\circ}$ in Fig. 3-d is lower than that in the XRD pattern of NiTa-900 sample. Consequently, according to the XRD patterns of all samples in Fig. 3, it is revealed that the crystallographic orientation of martensite phase in the Ni-25.5Ta (at.%) alloy is very sensitive to heat treatments applied at 800 °C, 900 °C, and 1000 °C.

Reverse (martensite to austenite) and forward (austenite to martensite) transformation temperatures of the samples were determined by carrying out DSC scans during heating and cooling curves, as shown in Fig. 4. Austenite start (A_s), austenite finish (A_f), martensite start (M_s) and martensite finish (M_f) temperatures, transformation hysteresis (A_f-M_f) values are tabulated in Table 1. The DSC results in Table 1 indicate that all the samples exhibit high temperature shape memory behavior. It can be also seen that the transformation characteristics of all the samples are well consistent with works in literature [7, 11]. The reverse and forward transformation temperatures were not affected strongly by heat treatment, whereas reverse and forward transformation peak intensities were influenced. The transformation peaks of NiTa-800, NiTa-900 and NiTa-1000 samples are stronger than those of NiTa-0 sample. It is well-known that the heat exchanged during martensitic transformation is related to the amount of martensite phase in the sample [11]. Therefore, it has been concluded that, as a result of heat treatment, the amount of martensite phase in NiTa-800, NiTa-900 and NiTa-1000 samples increased, compared to NiTa-0 sample. This is in a good accordance with the XRD patterns.
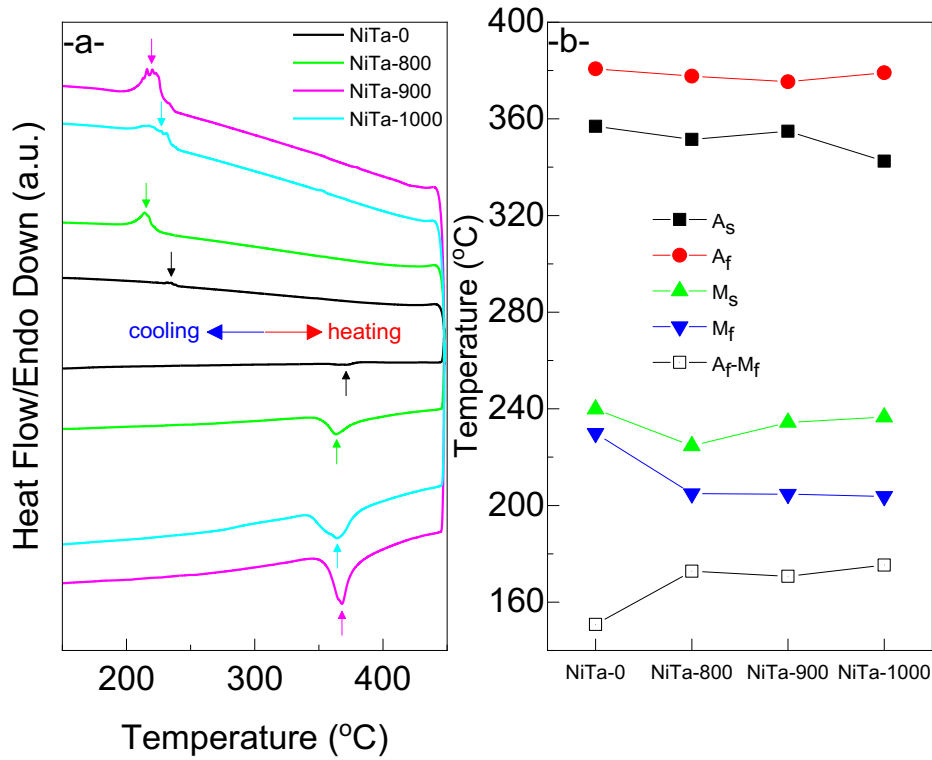
Figure 4: (a) DSC scans of the alloy samples on heating and cooling. (b) Variations of transformation temperatures and hysteresis values of the samples

Table 1: Transformation temperatures and hysteresis values of NiTa-0, NiTa-800, NiTa-900 and NiTa-1000 samples

	A_s(°C)	A_f(°C)	M_s(°C)	M_f(°C)	A_f-M_f(°C)
NiTa-0	356.9	380.7	239.9	229.9	150.8
NiTa-800	351.5	377.7	224.7	204.9	172.8
NiTa-900	354.9	375.4	234.4	204.7	170.7
NiTa-1000	342.5	379.1	236.6	203.8	175.3

Fig. 5 presents variations of the average Vicker's microhardness values of NiTa-0, NiTa-800, NiTa-900 and NiTa-1000 alloy samples. The calculated average Vicker's microhardness values of NiTa-0, NiTa-800, NiTa-900 and NiTa-1000 samples are 460±12, 413.4±7.68, 494.2±13.36 and 460.2±12.96 Hv$_{0.3}$, respectively. The results indicated that heat treatments, especially at 800 and 900 °C, caused a significant change in the microhardness of the alloy.

Another remarkable result is that the average microhardness of NiTa-0 and NiTa-1000 samples are almost the same. Therefore, it has been concluded that the cracks in the microstructure of the alloy samples did not cause significant changes in mechanical behaviors of the samples. However, it is believed that differences in the average microhardness values of NiTa-800 and NiTa-900 samples are closely related to the structural properties of these samples. El Bougory [18] reported that microhardnesses of $Ni_{51}Ti_{49}$ and $Ni_{47}Ti_{49}Co_4$ shape memory alloys altered by the effect of thermal aging and these changes were attributed to change occurring in volume fraction and size of hard precipitates in the microstructures of alloys and also the morphology of martensite plates. Aballe *et al.* [12] noted that heat treatments applied to Ni-Ta-Cr alloys affected the microstructural properties of alloys, resulting in changes in the hardness of alloys. Kojima *et al.* [19] reported that the microhardness of Ni_3Ta compounds subjected to high-energy ion irradiation changed due to changes in lattice structure of the compound.
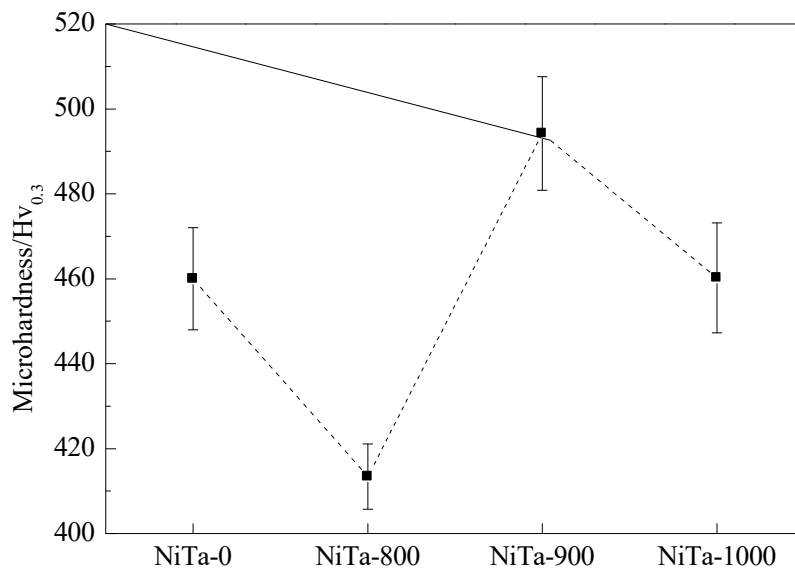
Figure 5: Variation of the average microhardness values of NiTa-0, NiTa-800, NiTa-900 and NiTa-1000 samples

4. Conclusions

Morphological investigations showed that the microstructure of Ni-25.5Ta (at.%) high temperature SMAs changed with applying heat treatment at 800 °C, 900 °C, and 1000 °C. The microstructure of NiTa-0 sample includes intermetallic Ni_8Ta and Ta-rich $NiTa_2$ compounds distributed in Ni_3Ta matrix, whereas the microstructures of NiTa-800, NiTa-900 and NiTa-1000 samples are consisting of Ni_8Ta and Ta-rich $NiTa_2$ compounds and many cracks in Ni_3Ta matrix.

SEM-EDS observations also revealed that the NiTa-1000 sample has the stable orthorhombic Ni_3Ta phase, which is a result of heat treatment at 1000 ºC. It was observed that volume frictions of intermetallic Ni_8Ta and Ta-rich $NiTa_2$ phases are higher than those of the NiTa-800, NiTa-900 and NiTa-1000 samples. Thermal measurements revealed that all the samples exhibited high temperature shape memory alloy behavior and the heat treatment processes did not affect that. Structural analysis indicated that XRD patterns of all samples were in good consistent with their SEM-EDS observations. The XRD results also demonstrated that the martensitic phase orientation of Ni-25.5Ta (at.%) high temperature SMA was very sensitive to heat treatment. It was deduced that Vicker's microhardness values of the samples changed by applying heat treatment, especially at 800 ºC and 900 ºC. This was attributed to change in martensitic phase orientation.

Acknowledgement

References

[1] Jani, J.M., Leary, M., Subic, A., Gibson, M.A., *A review of shape memory alloy research, applications and opportunities*, Materials and Design, 56, 1078-1113, 2014.

[2] Taşkan, E., Bulak, S., Taşkan, B., Şaşmaz, M., El Abed, S., El Abed, A., *Nitinol as a suitable anode material for electricity generation in microbial fuel cells*, Bioelectrochemistry, 128, 118-125, 2019.

[3] Rudajevová, A., Pospíšil, J., *Shape memory behavior of a Ni_3Ta alloy pre-deformed in compression*, Materials Science and Engineering A, 527, 2900-2905, 2010.

[4] Wu, K., Ma, J.L., *A review of high-temperature shape memory alloys*, Proceedings of the SMST, p.153, 2000.

[5] Ma, J., Karaman, I., Noebe, R.D., *High temperature shape memory alloys*, International Materials Reviews, 55, 257-315, 2010.

[6] Zhou, Y., Wen, B., Ma, Y., Melnik, R., Liu, X., *First-principles studies of Ni-Ta intermetallic compounds*, Journal of Solid State Chemistry, 187, 211-218, 2012.

[7] Firstov, G.S., Koval, Y.N., Van Humbeeck, J., Ochin, P., *Martensitic transformation and shape memory effect in Ni_3Ta: A novel high-temperature shape memory alloy*, Materials Science and Engineering A, 481-482, 590-593, 2008.

[8] Koval, Y.N., Firstov, G.S., *Nickel-tantalum-New object for investigation of martensitic transformations*, Metallofizika i Noveishie Tekhnologii, 29(6), 815-821, 2007.

[9] Ansara, I., Selleby, M., *Thermodynamic analysis of the Ni-Ta system*, Calphad, 18, 99-107, 1994.

[10] Nash, A., Nash, P., *The Ni-Ta (Nickel-Tantalum) system*, Bulletin of Alloy Phase Diagrams, 5, 259-265, 1984.

[11] Biffi, C.A., Agresti, F., Casati, R., Tuissi, A., *Ni₃Ta high temperature shape memory alloys: effect of B addition on the martensitic transformation and microstructure*, Materials Today: Proceedings, 2S, 813-816, 2015.

[12] Aballe, M., Ramaswamy, V., West, D.R.F., *Intermetallic compound precipitation from solid solution in some Ni-Ta and Ni-Ta-Cr alloys*, Journal of the Less-Common Metals, 39, 287-292, 1975.

[13] Kosorukova, T., Firstov, G., Noël, H., Ivanchenko, V., *Crystal structure changes in the Ni₃Ta intermetallic compound*, Chemistry of Metals and Alloys, 6, 196-199, 2013.

[14] Yildiz, K., *Thermally induced martensitic transformation and structural properties in Ni-Ta high-temperature shape memory alloys*, The European Physical Journal Plus, 134, 11, 2019.

[15] Larson, J.M., Taggart, R., Polonis, D.H., *Ni₈Ta in nickel-rich Ni-Ta alloys*, Metallurgical and Materials Transactions B, 1, 485-489, 1970.

[16] Kripyakevich, P.I., Pylaeva, E.N., *Crystal structure of the compound Ta₂Ni*, Journal of Structural Chemistry, 3, 30-32, 1962.

[17] Kosorukova, T.A., Firstov, G.S., Koval, Y.N. Van Humbeeck, J., Zhuravlev, B., *Phase transformations and shape memory behavior in Ni₃Ta-based intermetallics*, Materials Today: Proceedings 2S, 793-796, 2015.

[18] El-Bagoury, N., *Comparative study on microstructure and martensitic transformation of aged Ni-rich NiTi and NiTiCo shape memory alloys*, Metals and Materials International, 22, 468-473, 2016.

[19] Kojima, H., Yoshizaki, H., Kaneno, Y., Semboshi, S., Hori, F., Saitoh, Y., Okamoto, Y., Iwase, A., *Lattice structure transformation and change in surface hardness of Ni₃Nb and Ni₃Ta intermetallic compounds induced by energetic ion beam irradiation*, Nuclear Instruments and Methods in Physics Research Section B, 372, 72-77, 2016.